DESIGN OF A MULTISPECTRUM CANDU REACTOR FOR BURNING ACTINIDES

An Approach of Non-Proliferation and Nuclear Fuel Recycling

DESIGN D'UN RÉACTEUR CANDU À MULTISPECTRE POUR BRÛLER LES ACTINIDES

Une Approche vers la Non-Prolifération et pour le Recyclage du Combustible Nucléaire

A Thesis Submitted to the Division of Graduate Studies of the

Royal Military College of Canada

By

MOHAMED SALAH M. HUSSEIN

M.A.Sc, M.Sc., PGDip. IT, PGDip. Rad., B.Sc.Physics

In Partial Fulfillment of the Requirements for the Degree of

Doctor of Philosophy

May 2017

Abstract

With the end of the Cold War between the United States and the former USSR (currently Russia), a series of disarmament treaties were implemented, where a large number of nuclear warheads were dismantled thereby providing a large quantity of highly-enriched fissile materials. An approach has been developed to burn these materials in a novel Multispectrum CANDU Reactor (MSCR) based on CANDU 6 design, consisting of a separated thermal and fast neutron-spectral core.

Reactor coupling theory for a combined thermal/fast core was examined with a comparison of an analytical model to numerical computations with the MCNP6 and Serpent reactor physics codes, considering the simulation of a Deuterium Critical Assembly. A further benchmark was carried out to assess the validity of the tools using the Serpent and MCNP6 codes for burnup calculations with natural uranium fuel for the CANDU 6 Gentilly-2 reactor and burnup calculations made with the WIMS-AECL 3.1.2.1 code. Finally, with this validation of the tools, the Serpent code was then applied to the design of the MSCR.

Six models of the reactor were designed in a pressure-tube configuration using the Serpent reactor physics code by examining various sizes for the core radius, lattice pitch, type of fuel and number of fuel channels used in the fast core (i.e., 19.9% of enriched uranium or 13.9% of enriched plutonium). A helium coolant is used for the fast core. The outer/thermal core is fuelled with natural uranium with heavy water as both moderator and coolant. Both cores employ a 37-element fuel bundle design as currently used in CANDU reactors, with Zircaloy-4 sheathing for the thermal core and Stainless Steel 316L(N)SS for the fast one. The core size and enrichment level were optimized according to criticality requirements with an appropriate safety margin for the complete reactor.

This analysis examined several metrics for the six-reactor designs to ensure safety and non-breeding conditions. The current analysis investigated the excess reactivity, regeneration factor, radial and axial flux distributions, reactor power density and generated power for each core, form factor, core burnup, actinide concentration, and consumption rate of fissile isotopes.

The amount of destruction of diluted weapons-grade material in the MSCR depends on the size of the fast core, the number of fuel channels and the lattice pitch. For the two uranium-fuelled models, Model (II) had the highest percentage (10.7%) of destruction of fissile isotopes for 1000 days of operation without refuelling while, for the plutonium-fuelled models, Model (IV) had the highest percentage of fissile destruction at 15.3% operating for 2600 days. Model (VI) provides the highest consumption rate for 420 days before subcriticality is reached. However, Models (II, IV, V and VI) have a high form factor above that required for an appropriate safety margin. This work has demonstrated that the destruction of fissile isotopes from dismantled nuclear weapons can be successfully achieved in an MSCR based on a reactor physics study.

Résumé

Avec la fin de la Guerre froide entre les États-Unis et l'ancienne URSS (maintenant la Russie), on a appliqué une série de traités de désarmement qui prévoient qu'un grand nombre d'ogives nucléaires allaient être démantelées, ce qui produirait de grandes quantités de matières fissiles hautement enrichies. Une technique a été développée pour brûler ces matières dans un nouveau concept de réacteur nucléaire appelé Réacteur CANDU Multispectre (RCMS) basé sur le design du réacteur présent CANDU 6 et consistant en un cœur en deux zones, une à prédominance de neutrons thermiques et l'autre dans laquelle les neutrons rapides sont majoritaires.

On a examiné la théorie du couplage de réacteur pour un cœur combiné thermique/rapide et les résultats ont été comparés avec des résultats correspondants produits par les codes numériques de physique du réacteur MCNP6 et Serpent pour la simulation de l'Assemblage critique au deutérium. Les deux codes ci-dessus (MCNP6 et Serpent) ont été aussi vérifiés via la simulation du réacteur CANDU6 Gentilly-2 alimenté avec de l'uranium naturel, y compris les calculs de la combustion, ceux-ci étant comparés aux calculs effectués par le code WIMS-AECL. Une fois les outils validés, ceux-ci ont été appliqués au design du RCMS.

Six modèles du réacteur ont été conçus selon une configuration basée sur des tubes de force à l'aide du code de physique du réacteur Serpent et on a examiné plusieurs grandeurs pour le rayon du cœur, le pas de réseau, et la composition du combustible utilisé pour le cœur rapide (i.e., un enrichissement de 19.9% pour l'uranium enrichi ou une teneur de 13.9% pour le combustible riche en plutonium). Pour le cœur rapide, on a prévu un caloporteur fait d'hélium. Le cœur externe est le cœur thermique alimenté à l'uranium naturel et utilisant de l'eau lourde tant comme caloporteur que modérateur. Les deux cœurs utilisent des grappes de combustible à 37 crayons tout comme les grappes utilisées présentement dans les réacteurs CANDU. Les grappes destinées au cœur thermique ont des gaines en Zircaloy-4 tandis que celles pour le cœur rapide ont des gaines en acier inoxydable SS316L(N). La taille du cœur et les niveaux d'enrichissement ont été optimisés en tenant compte des exigences en matière de criticité tout en maintenant une marge de sûreté appropriée pour tout le réacteur.

Cette analyse a examiné plusieurs métriques pour les six designs du réacteur afin d'assurer la sûreté et des conditions ne menant pas à la surrégénération. Ce présent travail a aussi étudié la réactivité excédentaire, le facteur de régénération, les distributions radiales et axiales des flux neutroniques, la densité de puissance du réacteur, la puissance produite par chacun des cœurs, le facteur de forme, le « burn-up », les concentrations des actinides, et les taux de consommation des isotopes fissiles.

Les quantités de matériaux détruits provenant des matières des ogives nucléaires dans le RCMS dépendent de la taille du cœur, le nombre de canaux de combustible et le pas de réseau. Pour les modèles utilisant deux enrichissements d'uranium, le Modèle (II) avait le pourcentage le plus élevé (10.7%) de destruction d'isotopes fissiles pour 1000 jours d'exploitation sans recharge. Cependant, pour les modèles basés sur le plutonium, le Modèle (IV) avait le plus haut pourcentage de destruction de matières fissiles avec 15.3% , après 2700 jours d'exploitation. Le Modèle (VI) fournissait le taux de combustion le plus élevé jusqu'à ce qu'il devienne sous-critique après 420 jours. De leur côté, les Modèles II, IV, V at VI avaient un facteur de forme plus élevé que la valeur procurant une marge de sûreté acceptable. Le présent travail a démontré que la destruction des isotopes fissiles provenant des ogives nucléaires démantelées peut être effectivement réalisée dans un RCMS sur la base d'une étude en physique du réacteur.

Acknowledgements

I would like to express my sincerest gratitude to my advisors Prof. Dr. Brent Lewis and Prof. Dr. Hugues Bonin for their continuous support during my Ph.D. study and related research and for their patience, motivation, and immense knowledge. Their guidance helped me throughout my research as well as the writing and reviewing of this thesis. I could not have imagined having better advisors and mentors for my Ph.D. study. I owe my deepest sense gratitude to Prof. Dr. Paul Chan for his encouragement and his valuable advice. I would like to express my thanks to Dr. Hartmut Schmider the scientific computing specialist of HPCVL at Queen's University for his help in sitting up the software.

It is my radiant sentiment to place on record my best regards to Mrs. Kim Sampson, Mr. Brent Ball, and Mr. Bob Whitehead for their valuable technical helps. I would like to express my deepest gratitude and special thanks to the administration of Department of Chemistry and Chemical Engineering and the Registration’s officers at RMCC for their exceptional and appreciated help.

I am grateful for having a chance to meet so many wonderful colleagues and professionals who helped me during my Ph.D. track at RMCC. I also offer my regards and blessings to all of those who supported me in any respect during the completion of the project.

I would like to also express my appreciation to NSERC and UNENE for their supporting to this project.

I would also like to send my love and deepest thanks to my mother, my father, my wife (Ghada Ismail), my siblings (Ahmed, Mahmoud, Islam, Manal and Ashgan) and my children (Marwa, Yara, Khaled, Nour and Rabaa) for standing by me and supporting me throughout this remarkable journey.

Statement of Originality

I hereby certify that all of the work described within this thesis is the original work of the author. Any published (or unpublished) ideas and/or techniques from the work of others are fully acknowledged in accordance with the standard referencing practices.

Mohamed S. Hussein

(May, 2017)

Table of Contents

List of Figures

List of Tables

Abbreviations

MSCR	Multispectrum CANDU-based reactor
DCA	Deuterium Critical Assembly
MOX	Mixed Oxide Fuels (Pu and U)
MCNP	Monte Carlo N-Particle Transport Code is a software package for simulating nuclear processes. It is developed by Los Alamos National Laboratory since at least 1957 with several further major improvements .
Serpent	Serpent is a multi-purpose three-dimensional continuous-energy Monte Carlo particle transport code, developed at VTT Technical Research Centre of Finland, Ltd.
WIMS-AECL	WIMS·AECL is a deterministic code general-purpose lattice cell code, validated and applied over a wide range of lattices of which CANDU lattices
LW	Light water
HW	Heavy Water
TLE	Track Length Estimator flux (cm^{-2}) normalized flux calculated by MCNP flux tally per equal the sum of track lengths divided by volume of the cell and number of histories.
NU	Natural Uranium (uranium with ~0.71 wt.% U-235 in U-235+U-238)
TRU	Transuranic nuclides (see TRUMOX).
Radiotoxicity	A measure of harm to humans focusing on the cancer causing potential due to the decay of an ingested, inhaled or injected radionuclide inside the body.
TRUMOX	MOX mixed with transuranic nuclides (Np, Pu, Am)

Nomenclatures

k_{11}	Average number of next generation fission neutrons in the inner fast region resulting from a single fission neutron being born in the inner fast region
k_{22}	Average number of next generation fission neutrons in the outer thermal region resulting from a single fission neutron born in the outer thermal region
k_{21}	Average number of next generation fission neutrons in the thermal region (subscript 2) resulting from a single fission neutron born in the inner fast region (subscript 1) and diffused to the thermal region
k_{12}	Average number of next generation fission neutrons in the inner fast region (subscript 1) resulting from a single fission neutron born in the thermal region (subscript 2)
k_{∞}	Infinite multiplication factor
k_{eff}	Effective multiplication factor
ρ	System reactivity, i.e. the quantitative measure of departure from criticality for the reactor
Lp	Size of the lattice pitch in the fast or thermal core (cm)
En	Concentration of fissile actinides (%)
Fc	Number of fuel channels
$R_{a,fast\ core}$	Uranium-238 absorption rate in the inner fast core (atoms $cm^{-3}\ s^{-1}$)
$R_{a,thermal\ region}$	Uranium-238 absorption rate in the thermal region (atoms $cm^{-3}\ s^{-1}$)
$R_{a,total}$	Total uranium-238 absorption rate, multispectrum reactor (atoms $cm^{-3}\ s^{-1}$)
R_f	Total fission rate (fission $cm^{-3}\ s^{-1}$)
$R_{f,1}$	Total fission rate in the inner fast region (fission $cm^{-3}\ s^{-1}$)
$R_{f,2}$	Total fission rate in the thermal region (fission $cm^{-3}\ s^{-1}$)
$R_{f,1\leftarrow 2}$	Fission rate in the inner region triggered by neutrons born in the outer region (fission $cm^{-3}\ s^{-1}$)
$R_{f,2\leftarrow 1}$	Fission rate in the inner region triggered by neutrons born in the outer region (fission $cm^{-3}\ s^{-1}$)
$N_D(U_{235})$	Number density of uranium isotope (U-235)
$R_{np,th}$	Thermal Neutron Production Rate (n s^{-1})
$N_D(U_{238})$	Number density of uranium isotope (U-238)
φ	Average total neutron flux (n $cm^{-3}\ s^{-1}$)
$\varphi_{1\leftarrow 2}(E_i)$	Neutron flux of energy group E_i that diffused from the thermal region (2) to
$\varphi_{2\leftarrow 1}(E_i)$:	Neutron flux of energy group E_i that diffused from to the fast region (1) the thermal region
ϕ	Angular neutron flux

Φ	Track Length Estimator flux (cm^{-2}) normalized flux calculated by MCNP flux tally it is equal to the sum of track lengths divided by volume of the cell and number of histories
$\varphi(E)$	Neutron flux at the energy (E) (n cm^{-2} s^{-1})
$\sigma_f(E_i)$	Average microscopic fission cross section at energy bin E_i (cm^2)
$\sigma_{f,th}$	Average microscope fission cross section for the thermal group (cm^2)
σ_c	Microscopic capture cross section (cm^2)
ν	Average number of neutrons liberated per fission
α	Capture-to-fission ratio
σ_a	Microscopic absorption cross section (cm^2)
$\sigma_{a,th}$	Average microscopic absorption cross for the thermal group (cm^2)
$\sigma_{a,f}$	Average microscopic absorption cross for the fast group (cm^2)
σ_s	Microscopic elastic scattering cross section (cm^2)
$\sigma_{s,th}$	Microscopic elastic scattering cross section at 0.0253 eV (cm^2)
$\sigma_{s,f}$	Microscopic elastic scattering cross section at 14 MeV (cm^2)
Σ_a	Macroscopic absorption cross section (cm^{-1})
Σ_s	Macroscopic elastic scattering cross section (cm^{-1})
$\Sigma_{s,m}$	Macroscopic elastic scattering cross section for the moderator (cm^{-1})
N^i	Atom density of nuclide (atoms cm^3
N_f	Atom density of the fuel (atoms cm^3)
n	neutron
P	Reactor thermal power (W)
V_f	Volume of the fuel (cm^3)
V_m	Volume of the moderator (cm^3)
$CR(\vec{r},t)$	Conversion ratio
FP	Fission material produced
FD	Fission material destructed
$RR^{FP}_{c(n,\gamma)}(\vec{r},t)$	Rate of production of fissile material
$RR^{FD}_{a}(\vec{r},t)$	Rate of destruction of fissile material
η	Regeneration factor
R_1	Radius of the fast core of multispectrum Candu reactor Models (III) and (IV)
R_2	Radius of the fast core of multispectrum Candu reactor Models (I), (II) and (V)
R_3	Radius of the fast core of multispectrum Candu reactor Model (VI)
ρ_T	Density of material at certain temperature
$\rho_{(fuel\ in\ the fast\ core)}$	Density of MOX fuel in the fast core

Chapter 1.

Introduction

1.1. Synopsis

With the end of the cold war between the United States and the former USSR, both countries implemented the "Strategic Arms Limitation Talks," SALT I and SALT II, followed by "Strategic Arms Reductions Talks," START I, START II treaties. This led to the "Strategic Offensive Reductions Treaty," SORT 2002 and NEW START, by 2010. Figure (1-1) shows the consequence of the large number of nuclear warheads that have been dismantled according to these treaties up to July 2017.

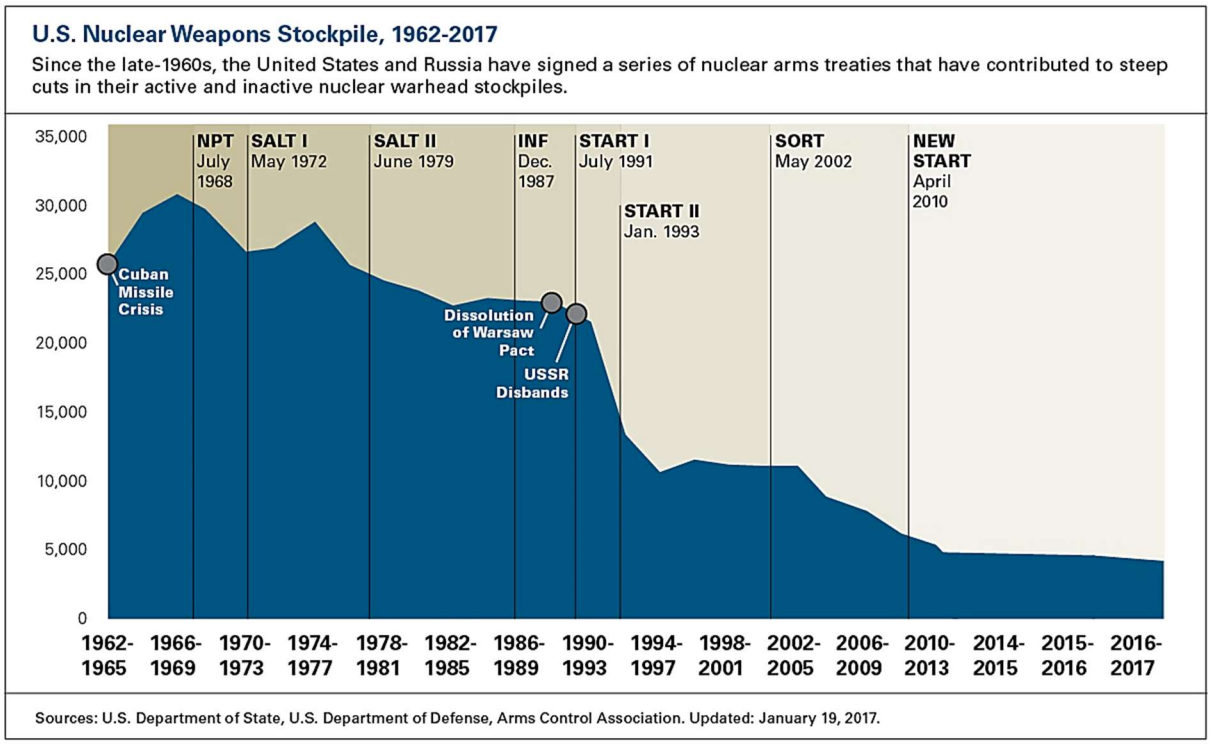

Figure (1-1): U.S. Nuclear Weapon Stockpile 1962-2016[1]

The material from dismantled nuclear warheads could provide many years of electricity production for peaceful uses. However, it cannot be used to fuel existing nuclear reactors because

of its high fissile concentration, which causes high reactivity and power peaking within the present reactor core.

In general, actinides are defined as the heavy elements series that contains elements with atomic numbers 89 to 103 and is the third group in the periodic table. e.g. of these elements start from Ac-89, Th-90, Pa-91, U-92, Np-93, Pu-94, Am-95, Cm-96, Bk-97 up to Lr-103. The most probable actinides isotopes that may found as a fuel or as a result of neutron capture interactions in the nuclear reactors are from Th-90 up to Cm-96. The fissile actinides isotopes are (U-233, U-235, and Pu-239 and Pu-241). The fissile actinides are high enrichment uranium (U-235 ~90%) and high enrichment plutonium (Pu-239 ~93%). Some interactions in the uranium and thorium fuel cycles will be presented in section 2.1.

At best, in order to reuse this material in the current nuclear power plants (NPPs), it could be burned with natural uranium dioxide fuel or blended with uranium dioxide from spent fuel burned in CANDU®[1] reactors. Alternatively, it could be mixed with depleted uranium, which is produced as a tail of the enrichment fuel process for Light Water Reactors (LWR) reactors. However, these approaches would need a very long time to dispose of the large quantity of nuclear-warhead material.

On the other hand, the reprocessing of spent fuel, such as the extraction of fissile actinide materials for use in mixed oxide fuels, is an important way to reduce the end waste from nuclear power plants. Using reprocessed spent fuel in current reactors is becoming a popular option to help close the fuel cycle as an economical option.

The destruction or burning of actinides from dismantled nuclear weapons or recycled spent fuels, to convert them from long-lived actinides isotopes to short-lived fission products isotopes,

---

[1] The CANDU® (short for CANada Deuterium Uranium) reactor is a Canadian invention. CANDU® is registered trade mark by Atomic Energy of Canada Limited (AECL). In the rest of this thesis, the registered trade mark (®) will not be repeated when the acronym "CANDU" is written.

requires the utilization of fast reactor technology to provide the necessary high-energy neutron (fast) flux to transmute the actinides. In other words, the fuel cycle would be closed with fast reactors used to burn the long-lived actinides from dismantled nuclear warheads or recovered from spent fuel. However, while many countries continue to pursue fast reactors, these development reactor types are high cost ventures with a reliability risk that still require significant development. Therefore, the burning of actinide mixed oxides in a nuclear reactor requires an appropriate reactor design. Such a design would have the features of a thermal neutron CANDU reactor, along with a fast reactor, all in one system. This coupled system leads to a multispectrum CANDU-based reactor (MSCR) that can be used for the burning of fissile actinides (highly enriched ^{239}Pu or ^{235}U) from dismantled nuclear warheads or as recovered from spent fuel. The suggested system in this dissertation will have not only a strong political and non-proliferation feasibility, but also provide environmental and economic advantages.

1.2. Economic, Environmental and Political Challenges of Burning Actinides

As the energy demand increases globally, in light of environmental concerns of fossil fuels and the limited power density from other energy sources, the interest in fission nuclear power is increasing. Nuclear fission energy stands today as a relatively well-developed option to produce electric power with a high-energy density. Nuclear energy involves a technology that depends strongly on materials performance. It represents the best known peaceful use of the atom. However, there are many domestic and international challenges that limit the growth of nuclear power. The proposed design for a multispectrum CANDU reactor is based on the exceptional features of the CANDU reactor. Such a design could overcome some of the economic, environmental and political challenges that face traditional nuclear reactors. The next subsections will introduce the challenges briefly and how the multispectrum reactor design can meet these difficulties.

The economic challenges of nuclear power have been a key barrier to the construction of new reactors around the world. The lack of competitiveness with other energy sources arises mainly from its capital intensity. The ongoing electricity sector requires a greater emphasis on economic competition. The cost of generating electricity consists of three main components: (i) the capital cost of constructing the generating facility, (ii) the annual fuelling, operations and maintenance

costs, and (iii) the waste management expenses. An additional component in the case of nuclear power is that of decommissioning [2]. Both decommissioning and dealing with radioactive wastes are expensive processes. The cost of managing long-lived radioactive waste could be decreased with the reuse of highly-enriched actinides. The weights of these components are different from one country to another according to their nuclear policy, e.g. whether fuel recycling is an important consideration. The economic feasibility is different for each country according to the availability of other energy resources in the country and its developing plans. The introduction of the multispectrum CANDU reactor could provide economic feasibility because it deals with the fissile actinides in the nuclear waste and the high enrichment actinides (^{239}Pu and ^{235}U) obtained from dismantled nuclear warheads that contain a large amount of energy yet to be extracted. In addition, the long fuel cycle of some designs of MSCR may have a further economic impact.

The potential impact of nuclear accidents has also been a topic of significant debate practically since the first reactors were constructed. Public concerns about nuclear power require that safety issues be addressed, particularly in light of past accidents at Three Mile Island, Chernobyl and later at Fukushima. Such interests, therefore, focus not only on the reliability and safety of the reactor design but also on the ability to meet the challenges of dealing with the nuclear waste (spent fuel management).

From engineering and reliability viewpoints, there are essentially two routes toward providing a safe reactor system:

a) ***The first route*** is the reactor design in which, if an accident occurs, the reactor could recover, and the damage does not spread, even if no protective, automatic or deliberate action, is taken.

b) ***The second route*** is to incorporate protective systems, preferably with redundancies, that mitigate the effects of an accident.

There are three levels of safety:

(i) The first level is in the design of the reactor and its components;

(ii) The second level refers to protection measures to halt or deal with component failures;

(iii) The third level includes mitigation measures to limit the consequences of accidents.

The first level is in accordance with route (a) of making the system safe as identified above, whereas the second and third levels fall under the area of route (b) [2].

The proposed multispectrum CANDU reactor design consists of an internal fast core used for burning high fissile concentration fuel and an external thermal core as described in Chapter 7. This reactor specifically introduces an additional level of safety. A more tolerant design is introduced in which each core (fast and thermal) are independently subcritical or at least one of them is subcritical. The diffusion of neutrons from one core to another drives the whole reactor to criticality. As such, an alteration in any one of the two cores is enough to shut down the whole reactor.

The political regulation of the peaceful use of nuclear energy was initiated by the "Atoms for Peace" landmark speech made by Dwight Eisenhower to the United Nations General Assembly on 8 December 1953 [3]. This milestone speech addressed the world's widespread fear and discontent from recently developed atomic technology and weapons. Eisenhower's proposal was sketchy, but it was enough to generate serious discussions that led, in 1957, to the creation of an international nuclear regulatory agency (i.e., the International Atomic Energy Agency). Eisenhower sought to transform nuclear technology into a peaceful and humanitarian pursuit by focusing on nuclear energy development. His promotion of nuclear energy led to its widespread use through the US and the world during the early decades of the cold war.

By 1960s, the *"Nuclear Non-proliferation Treaty (NPT)"* provided a means to curb and control the production and proliferation of nuclear weapons and nuclear weapons' material. While providing significant restrictions on nuclear weapons development, Article IV of the NPT establishes the access to nuclear technology for peaceful purposes as an "*inalienable right, the spread wide of peaceful use of nuclear technology is organized by the obligation of the states with the NPT Treaty and additional protocols"*.[4]. Therefore, finding a system, such as the multispectrum CANDU reactor, that can support non-proliferation and reduce stockpiles of dismantled nuclear weapons represents a challenge.

The goal could be summarized as:

1) Verification of a couple reactor theory using probabilistic (MCNP and Serpent) codes.
2) Validate Serpent code for burnup calculations.
3) Design the multispectrum CANDU reactor for burning actinides from dismantled nuclear weapons.
4) Calculate the reactor physics parameters in order to assess the MSCR Models.
5) Assess the safety breeding criteria of the MSCR-Models.
6) Investigate the technical feasibility of the MSCRs for reducing the world stockpile of weapons-grade high enrich uranium and plutonium as well as recycling used nuclear fuel.

1.3. New Reactor Design and Advanced Fuel Cycle Initiative (AFCI)

The current once-through nuclear fuel cycle uses less than one percent of the energy available in the natural uranium, so there is a need for a much more efficient use of uranium resources by breeding and fissioning plutonium. The advanced Fuel Cycle Initiative (AFCI) and the Generation IV Nuclear Fuel Cycle Initiative (GIF) identified the following goals to help the industry make informed decisions about the potential of advanced fuel cycle technologies [5]:

1. Reduce high-level waste volume.
2. Reduce radiotoxicity and long term heat generation of spent nuclear fuel.
3. Provide sustainable fuel source for nuclear technology.
4. Reduce long-term inventories of plutonium (non-proliferation initiative);
5. Enable recovery of the energy contained in the spent fuel; and
6. Support the future operation of Generation IV nuclear energy systems.

Accomplishing these steps requires the use of complex chemical and nuclear reaction processes that can be conducted in a manner that is safe, cost-effective, environmentally friendly, and proliferation-resistant. There are different scenarios to achieve these goals. One of these scenarios is the use of mixed oxide (MOX) fuels in traditional light and heavy water reactors. The

other scenarios introduce new nuclear reactor designs which meet the AFCI objectives such as Generation IV nuclear reactor designs.

The design of a multispectrum reactor introduces a modification of the traditional CANDU reactor design that particularly meets the goals of the AFCI. Accordingly, a new reactor design is needed to burn the high-enrichment fuels that contain actinides from dismantled nuclear weapons and from actinides in nuclear waste in order to utilize their stored energy. In particular, the multispectrum CANDU-based reactor works as an actinide burner as well as a power reactor. The current design of a multispectrum CANDU nuclear reactor can also meet environmental and political requirements vital from a new generation of reactor design applicable to the AFCI requirements.

1.4. Features of the CANDU Reactor for the Design Basis of an MSCR

The heavy water Canadian Deuterium Uranium (CANDU) reactor design offers significant benefits in the transmutation of actinides[6]. The CANDU reactor offers a wide flexibility due to its high neutron economy and the online fuelling with a simple, compact fuel bundle design. The online refuelling provides access to the CANDU core making it a unique base design applicable to a multispectrum reactor. The neutron economy is produced by a combination of heavy water coolant and separate heavy water moderator along with low-neutron-absorption materials in the core assembly. The fuel bundle design of 37 or 43 elements in a circular multi-ringed arrangement provides for flexible fuel content, including integrated poison and varied fuel enrichments. The online refuelling allows the bundle to shift through the same fuel channel or from one fuel channel to another. Online access to the core would help the uniformity of burnup along each region. It would also help stabilize the form factors and other safety factors in addition to extending the refuelling time [7].

1.5. Overview of the Multispectrum CANDU Based Reactor

The multispectrum CANDU based reactor consists of two cores. The internal core is a fast neutron core dedicated for burning actinides fuelled with MOX fuel with an enrichment in ^{235}U (up to 19.9%) or a high concentration of ^{239}Pu (up to 14.13% of fissile materials with 13.89% of ^{239}Pu). In the case of MOX fuel, ^{239}Pu from dismantled nuclear weapons is blended with depleted

uranium (0.25% of ^{235}U from the tail product of enrichment process). There is no moderator, and the coolant is a helium gas at a pressure of 6 MPa. This coolant has a small slowing down power or moderation in order to keep a fast-neutron economy in the fast core. In the fast core, the structure, pressure tubes and bundles are proposed to be made from stainless steel of type SS316.

The external core is the thermal core fuelled by natural uranium with heavy water coolant and moderator and principally generates most of the reactor power. Both cores, or at least one core, are independently subcritical, but the diffusion of the neutrons from one core to another can drive the whole reactor to criticality. The two cores are separated by two stainless steel partition walls. The volume between the two partition walls is filled by helium gas at 0.1 MPa to prevent heat dissipation from one core to another and to keep the temperature of the moderator in the thermal core at a reasonable temperature. The pressure tube and fuel bundle of the thermal core are proposed to be made from Zircaloy-2 like a conventional CANDU 6 reactor. Additional details of the multispectrum reactor are presented in Chapter 7.

The simulation of the multispectrum CANDU based reactor design is accomplished with two transport codes MCNP6 (Monti-Carlo N-Particles), and the Serpent code (three-dimensional continuous-energy Monte Carlo reactor physics burnup calculation code).

1.6. Preliminary MSCR Design Concept Using and Validating Mathematical Models.

In the current dissertation, the focus is on the burning of actinides from dismantled nuclear weapons (e.g., isotopes of U-235 and Pu-239) by providing a preliminary design concept of a multispectrum CANDU nuclear reactor that is based on the characteristics of the well-established CANDU 6 nuclear reactor. The aim of the multispectrum reactor (also called a coupled fast–thermal system) is to combine the advantages of a thermal reactor with those of a fast reactor into a single system. The system is used for burning actinides mainly in the fast core as well as producing electricity where the entire reactor power is normalized to the CANDU 6 power reactor (2180 MW_{th} or ~600 MW_e)

This design avoids breeding in the whole reactor which makes for efficient elimination or burning of the actinides. For the fresh fuel, the fissile isotopes considered are: U-235 and Pu-239, with fissile isotope ratio 19.9% and 13.89% respectively, which are specifically consumed in the

fast core region. These fissile fuels are blended with depleted uranium and used as the fuel in the fast core. This design specifically takes advantage of the fast spectrum to maximize the burning of the actinides. The reactor is designed to be easily controllable, highly safe, sustainable, and would significantly reduce the long-term radiotoxicity of spent nuclear fuel through recycling.

The dissertation is based on the use of reactor physics and coupled-reactor theory for the burning of actinides in the fast core. This investigation requires the verification and the validation of the codes used for the design. The thesis is organized as follows: Chapter 1 provides an introduction of the background history and the need for actinide burning as well as the goals of the thesis; Chapter 2 gives a literature review describing actinide transmutation, and sources of actinides from nuclear waste reprocessing and dismantled nuclear weapons (covering the Megawatt to Megaton program, use of MOX fuel and actinide burning in CANDUs, as well as the concept of fast-thermal power breeder reactors and coupled systems); Chapter 3 describes reactor physics theory including the development of the neutron transport equation and methods of solution, burnup analysis and coupled-reactor theory, and concepts for a fast and breeder reactor system; and Chapter 4 details the simulation methodology for the codes used to design the reactor and approximations taken. The results of the work are presented in Chapter 5 that presents a verification of the coupled-reactor theory for a Deuterium Critical Assembly (DCA) providing a validation of the Serpent code. Chapter 6 describes the simulation of a traditional CANDU 6 reactor as an additional code validation exercise. With this validation of the various tools, different designs of the multispectrum reactor are proposed and developed in Chapters 7 and 8 using the Serpent code as a means to effectively burn high-enrichment uranium and plutonium, respectively, while meeting safety considerations. Finally, Chapters 9 provides a conclusion of the work and Chapter 10 highlights recommendations for future work.

Chapter 2.

Background and Literature Review

The most probable isotopes that could be used as nuclear reactor fuels are derived from the elements of thorium, uranium, and plutonium. Also, due to successive neutron capture interactions in the nuclear reactor fuel, other higher actinides might be found. The concentrations of isotopes in the reactor core depend mainly on the type of the nuclear reactor, in other words, the main neutron flux distribution per energy bin plus the isotopic content of the fresh fuel elements.

2.1. Neutron Spectra and Actinide Transmutation

Fission neutrons are generated with an average energy of about 2 MeV, some neutrons reaching up to 14 MeV. They are scattered by heavy nuclei with the major energy loss occurring through interactions with light nuclei, where they lose a relative amount of energy $\Delta E/E \geq 1/A$, where A is the mass number of the scattering nucleus. Scattering does not directly result in a transmutation, i.e., a change of the charge number Z or the number of neutrons N of the original nucleus [Z,N], but it alters the energy distribution of neutrons (the neutron spectrum), in addition to changing the direction of the trajectory of the neutron. After a certain number of collisions, particularly with the light hydrogen isotopes in the moderator of light water reactors (or deuterium in heavy water reactors), neutrons are thermalized.

Most transmutations in fission reactors are initiated by neutron absorption. These reactions cause either fission, and hence generation of fission products, or neutron capture followed typically by γ-ray emission, leaving a nucleus of the same element but with one additional neutron: [Z, N] (n, γ) [Z, N+1]. Furthermore, there are transmutations by (n, 2n)-reactions, resulting in a nucleus of the same element but with one less neutron, [Z, N] (n, 2n) [Z, N-1]. Additional Z or N changing interactions are radioactive decays: β^-, β^+, and α-decays, leading to [Z+1, N], [Z-1, N], and [Z-2, N-2], respectively. Figure (2-1) (a and b) shows the most probable interactions for creating actinides in the nuclear reactor along with the nuclear transformation or radioactive decay schemes. Thorium-based fuels are not considered in the current work. Therefore, only interactions and transmutations shown in Figure (2-1-a) will be treated in the current dissertation. These

interactions represent the most probable transmutations in a thermal reactor and the interactions in the dashed lines represent the major transmutations in a fast core.

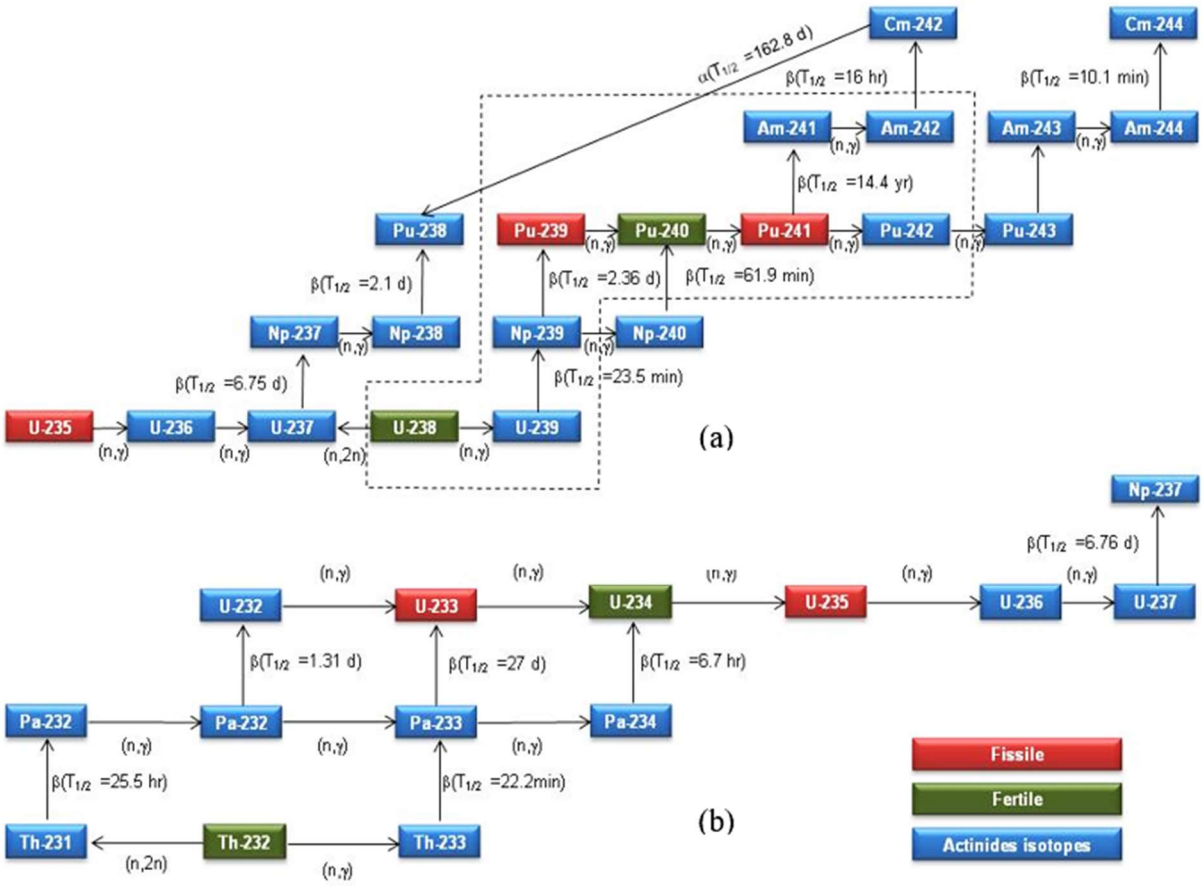

Figure (2-1) (a, b): The Most Probable Nuclear Interactions of Actinides inside the Nuclear Reactors (a) for Uranium Cycle and (b) for Thorium Cycle.

a) Actinides from Recycling Nuclear Waste

Actinides represent a substantial part of the nuclear waste. Figure (2-2) [8] shows the average lifetime for decay heat in the disposed waste. The average lifetime for decay heat from the high-level radioactive actinides produced as part of nuclear waste in the reactor is approximately a hundred thousand years compared with just a few hundred years for that from the fission products.

Since the chemical processes involved in extracting actinides are well known, efficient, safe and economically feasible, the option of chemical extraction of these highly radioactive actinides from the nuclear waste and burning them neutronically in a nuclear reactor is very promising. The advantages of this option are the destruction of plutonium to eliminate proliferation concerns, the production of additional energy from the plutonium and the actinides, and the burning of the minor actinides. Consequently, actinide burning is a very effective process at reducing the disposal heat load and long-term radiation hazard that are important considerations in future reactor designs[8].

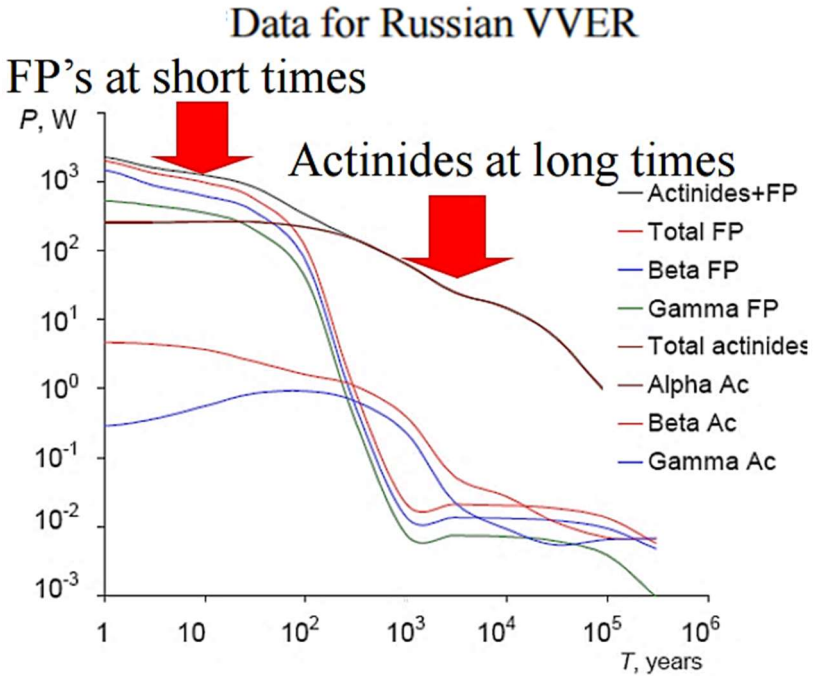

Figure (2-2): Spent Fuel Heat Load Contribution [8]

(Data for Russian VVER)

The destruction of transuranic elements (Pu, Np, Am and Cm) can be achieved mostly through fission, resulting in fewer minor actinides requiring long-term waste disposal. The plutonium-based mixed oxide fuel is the main fuel type produced from the recycle of actinides from spent nuclear fuel. In the case of extraction, the plutonium is fed into the MOX feedstock and the other minor actinides (Np, Am and Cm) are collected and either stored or fabricated into direct irradiation targets. However, the use of grouped extraction methods to produce MOX is also being developed due to their increased simplicity and proliferation resistance.[9]. The bulk of the actinide material is plutonium (~84.5 wt% of the extracted bulk) providing the necessary fissile content,

but the minor actinides and the larger Pu-240 content increase the neutron capture and thus affect the loading necessary for a fuel with suitable burnup [10].

Figure (2-3) and Figure (2-4) present the capture and fission neutron cross sections of some fissionable and fissile actinides. It is obvious that the fission cross sections for the fast neutrons are significantly higher than the capture cross sections in the same energy range.

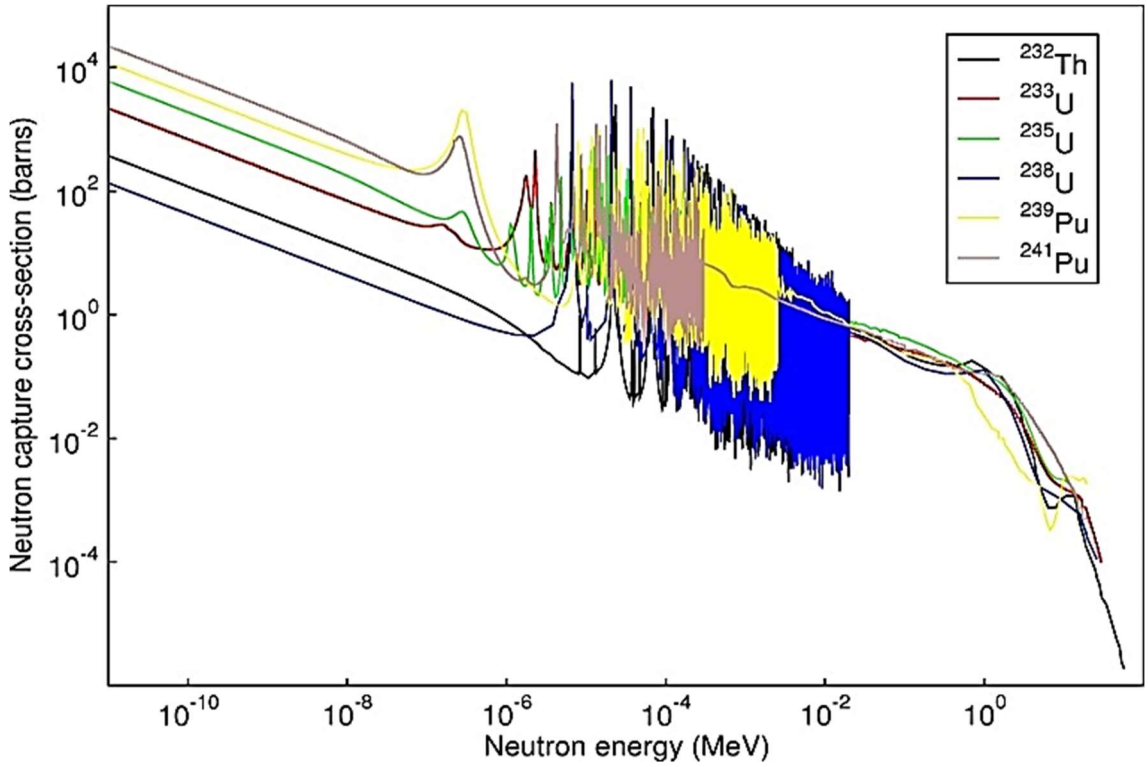

Figure (2-3): Neutron Radiative Capture Interaction Cross Sections for some Fissionable and Fissile Actinides Isotopes.(Nuclear Data Center at KAERI)[11].

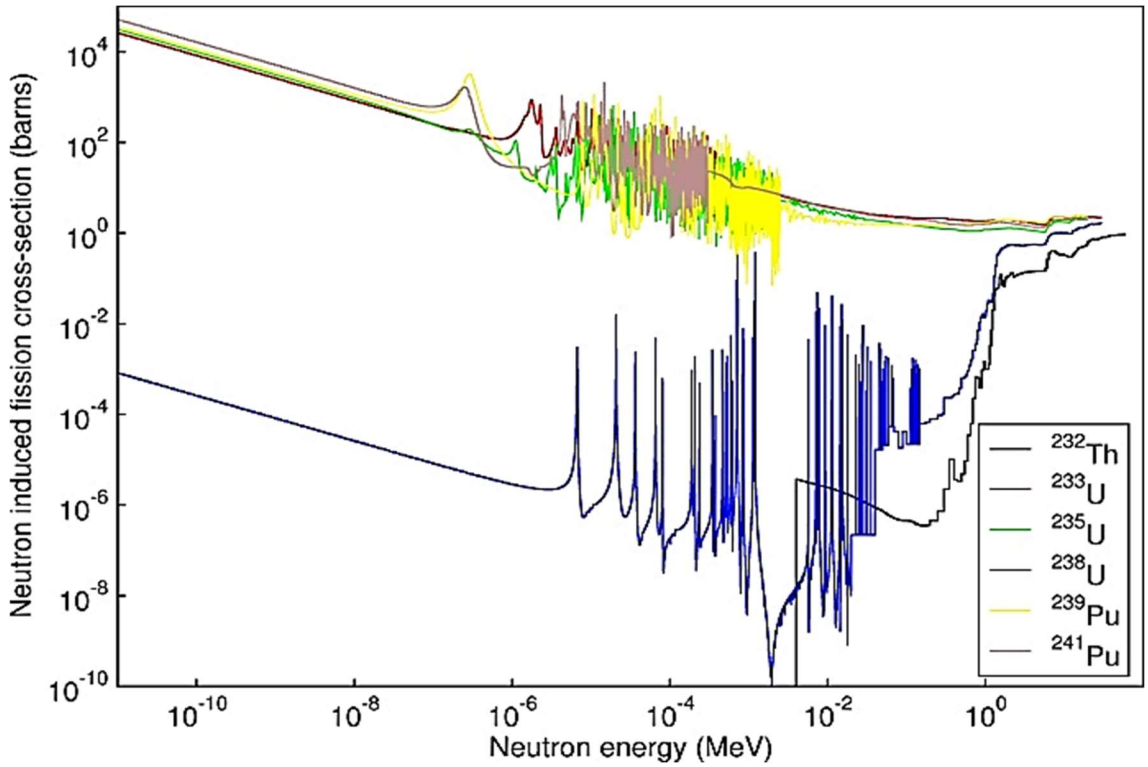

Figure (2-4): Neutron Fission Interaction Cross Sections for Fissionable and Fissile Actinides Isotopes.(Nuclear Data Center at KAERI)[11].

Figure (2-5) and Figure (2-6) present the percentage of plutonium, curium and transuranic isotopes that can be destroyed in a thermal and fast reactor, respectively. This diagram shows the advantages of the fast neutron flux or fast reactor over the thermal. Therefore, the fast reactor could be an important approach for burning actinides. Consequently, this approach has a tremendously positive effect on the average lifetime of spent nuclear fuel, Figure (2-5) and Figure (2-6) demonstrate the possibility of actinide burning in the fast neutron flux. These figures represent one of the strong motivations for the current work.

The objective of minor actinide (Np, Am and Cm) burning for implementation on a commercial scale in current and new build thermal reactors is that it can be done in a much shorter timescale and therefore represents an important end-point in its own right. These reactors are already in operation or being built and large-scale minor actinide burning sufficient to stabilize the minor actinide inventory could be achieved possibly within 20 to 30 years, much sooner than what could be reasonably expected for the development of fast reactors. The capacity to demonstrate

the stabilization of long-lived radionuclides would be helpful in justifying a new nuclear build, especially if many countries were to adopt an aggressive new-build construction program. [12].

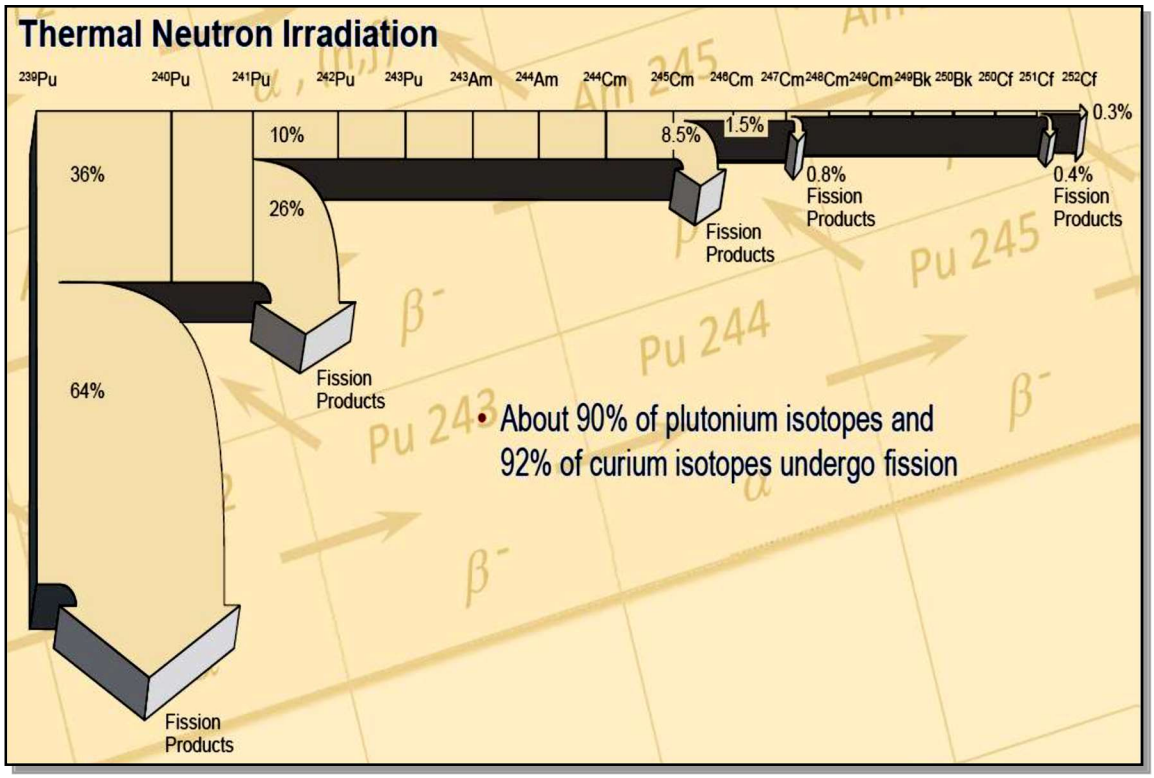

Figure (2-5): Percentage of Plutonium, Curium and Transuranic Isotopes that Can be Destroyed in Thermal Reactor [8]

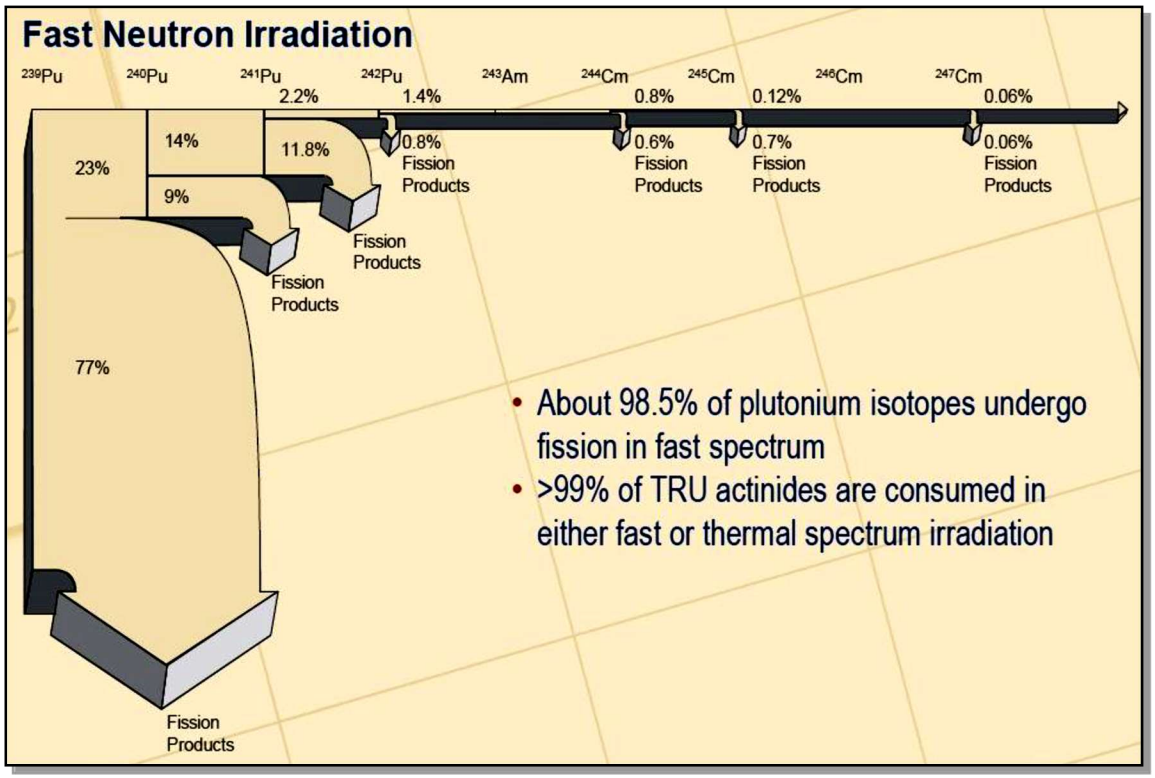

Figure (2-6): Percentage of Plutonium, Curium and Transuranic Isotopes that Can be Destroyed in Fast Reactor [8].

2.2. Actinides from Dismantled Nuclear Warheads

For more than three decades, concern has centered on the possibility that uranium intended for commercial nuclear power might be diverted for use in weapons. As mentioned, the United States and countries of the former USSR have signed a series of disarmament treaties [13] to reduce the stored amount of weapons-grade nuclear material by about 80%. Figure (2-7) shows the estimated nuclear warhead inventories of the United States and Russia 1977-2018. As shown in Figure (1-1), by 2018, the nuclear warhead inventory of the United States will decrease to less than one-fifth of its stockpile value in 1977. Similarly, the Russian nuclear warhead inventory would be reduced by one-eighth of the value at peak value in 1987. The consequence of these disarmaments is producing a large amount of high-concentration fissile nuclear material, mainly Pu-239 and U-235. Accordingly, the attention is focused on the role of military uranium and plutonium as a major source of fuel for commercial nuclear power.

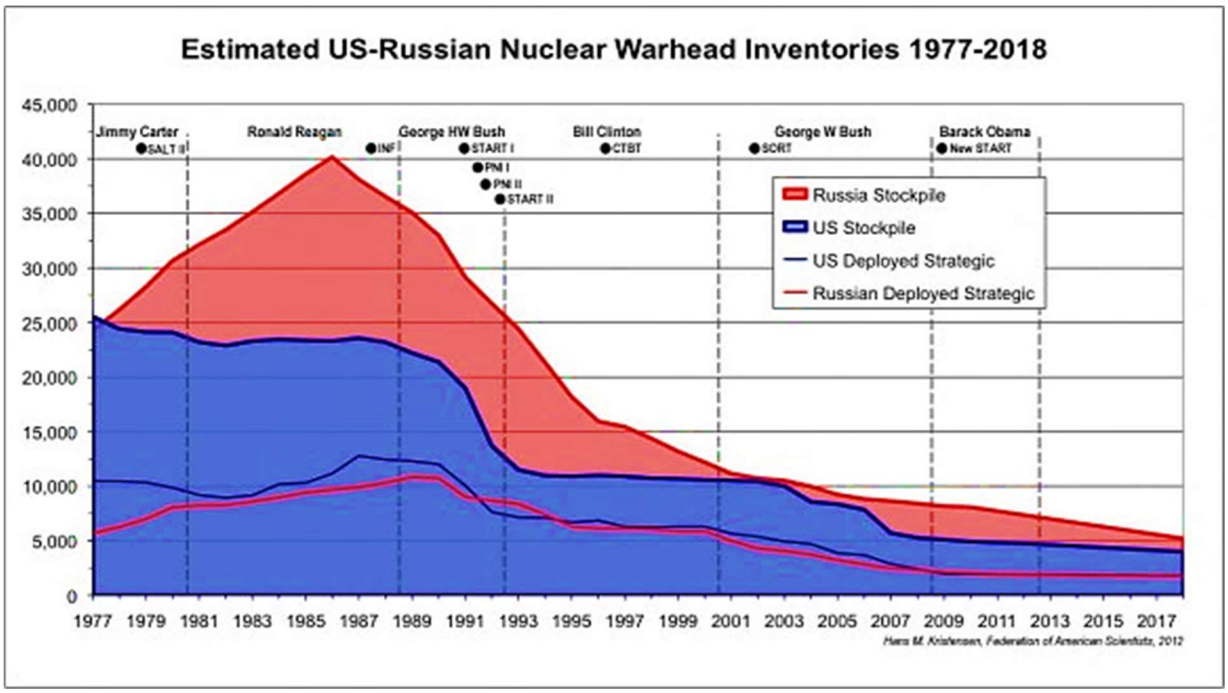

Figure (2-7): Estimated of Nuclear Warhead Inventories of the United States and Russia 1977-2018 [14]

Weapons-grade highly enriched uranium (HEU) (~90% U-235) is evaluated at about 2000 tons. This HEU can be blended down with uranium containing very low levels of U-235 from depleted uranium produced as a tail from the enrichment process (~0.2% to ~0.25% of U-235) or from fuel recycling of nuclear waste (less than ~0.2% from PHWR or ~ <0.9% from PWR). As such, natural-equivalent uranium would be produced to be used in traditional commercial reactors. This redirection could displace more than 10,600 tons of U_3O_8 production from mines each year[14][15].

The world's stockpiles of weapon-grade of plutonium (which has over ~93% Pu-239) are reported to be some 260 tons[14].This military plutonium can be blended with depleted uranium oxide to form a mixed oxide fuel, which can be used safely in conventional reactors. MOX fuel and slightly enriched uranium (SEU) can also be used in a thorium-fuelled reactor, which represents a promising nuclear fuel for the future. After the low enriched uranium (LEU) or MOX fuel is burned in power reactors, the spent fuel is no longer suitable for use in weapons.

Plutonium from derived nuclear weapons materials is primarily Pu-239 (~92.7%), with some Pu-240 (~7.0%) and trace amounts of Pu-241 ($4.4E^{-4}$ %) in which Am-241 represents the

balance[16]. Pu-239 is fissile and Pu-240 is easily transmuted by neutron capture (n, ɣ) into Pu-241 which is also fissile. The plutonium in the weapon-grade material is usually in a metallic form, so it needs to be converted into plutonium oxides and then blended with natural or depleted uranium to produce MOX fuel with a suitable fissile concentration level. The level of the fissile concentration depends on the target reactor. The production of mixed oxide fuel for LWR reactors is quite mature and the fabrication technologies for such fuels are well developed and already employed on an industrial scale [17].

2.3. The Megatons to Megawatts™ Program

", *Megatons to Megawatts continue to be the most successful non-proliferation program in history as it provides a reliable source of fuel for nuclear power plants, while making the world safer*, said John K. Welch, the retired president and CEO of Centrus Energy Corp[15]. "*The Megatons to Megawatts Program made a substantial contribution both to the elimination of nuclear weapons material and to nuclear energy generation in the United States. Nearly every commercial nuclear reactor in the United States received nuclear fuel under the program,*", said US, former Energy Secretary Ernest Moniz[18].

The Megatons to Megawatts Program is a government-to-government agreement signed in February 1993 between the United States and Russia. This program, implemented through a non-proliferation agreement, is to convert HEU taken from dismantled Russian nuclear weapons into LEU fuel for LWR's of the USA. As of December 2013, Russia shipped the last cylinders of low enriched uranium from the Port of Baltimore to the USA's facility in Paducah, Ky. Since 1995, the United States Enrichment Corporation (USEC) has purchased more than 14,000 metric tons of low-enriched uranium that was down-blended from 500 metric tons of weapons-grade highly enriched uranium. This material has been extracted from the equivalent of 20,000 dismantled Russian nuclear warheads. This 20-year program supported approximately 20% of the electricity supply from nuclear power in the USA [15].

2.4. Burning Plutonium Mixed Oxide Fuels in CANDU Reactor

Plutonium burning using MOX has been fully used in both light and heavy water reactors. There has been extensive operational experience with partial core loading (10-30%) of plutonium MOX in many pressurized water and boiling water reactors[15] [19].

There has also been a significant interest in the use of CANDU reactors for plutonium disposal from nuclear weapons materials or spent LWR fuel by Ontario Hydro and Atomic Energy of Canada Limited (AECL) [20]. AECL has more than 30 years of experience in Pu-MOX fuel research and development [21]. Fuel fabrication and irradiation testing has been conducted on plutonium MOX CANDU fuels in the ZED-2 reactor and the National Research Universal (NRU) reactor [20],[22]. A detailed analysis of the possibility of using some of the Bruce CANDU reactor units as plutonium-burners was performed [23].

Morreale [6][19] investigated the feasibility of actinide transmutation using a new blended oxide fuel design in the proven CANDU reactor system. This capability to reuse once-through fuel material demonstrates the complementary nature of the CANDU system to synergistically interface with LWR designs. It demonstrates the benefits of increased energy generation from the fuel and reduced legacy impacts of the nuclear fuel cycle. The evaluation of the detailed neutronic behaviour of the actinide fuel and its implications on CANDU reactor operations did not reveal any major complications in the implementation of such an advanced fuel cycle. Also, Morreale demonstrated that the TRUMOX-30 CANDU-900 system can provide a significant reduction in the net inventory of actinides from waste reprocessing. With an initial actinide content of approximately 520 g per bundle, the actinide conversion for this design was approximately 34.76%. The longer burnup cycle of the TRUMOX-30 fuel reduces the daily fuel bundle requirements for fuelling of the core to 1/3 of that of a natural uranium (NU) CANDU.

Recently, Hyland [24] studied the heavy water reactor (HWR) as an intermediate burner of transuranic elements (plutonium, americium, curium, and neptunium) from LWR spent fuel, prior to further transmutation in a sodium cooled fast reactor. In this study, the simulation of the HWR was performed using the lattice cell code WIMS-AECL 3.1, and the sodium cooled fast reactor was modelled using the Monte Carlo code Serpent. The basic safety criteria were analyzed for

both the HWR and the fast reactor models. The VISION fuel cycle systems was used to model the dynamic simulations to determine the impact of transitioning to actinide burning fuel cycles.

Five fuel cycles were modeled in the Hyland study, in order to determine the impact of an intermediate burner HWR:

1: A reference case, once-through LWR;

2: LWRs, transitioning to fast reactors;

3: LWRs, transitioning to HWR intermediate actinide burners, then to fast reactors;

4: LWRs, transitioning to both HWR intermediate burners and LWR-derived fuel fast reactors; and

5: an LWR to HWR modified open fuel cycle (no fast reactors).

This work [24] concluded that:

- Fuel cycles that include a transition to fast reactors have the most favorable impact on sustainability metrics, such as uranium consumption. Relative to a reference once-through LWR case, a transition to fast reactors reduces consumption by 70%.
- Fuel cycles utilizing HWRs as intermediate burners of minor actinides give a smaller reduction in uranium requirements of 55-59%.
- The fuel cycles studied significantly reduced the amount of spent fuel requiring long term storage. 527 kt of spent fuel in the reference once-through LWR case is reduced by 76% to 126 kt in the LWR to HWR modified open fuel cycle, and by 98% to 10 kt for the fast reactor scenarios.
- The determination of the actinide burning abilities of the different fuel cycles is complicated by the concentration of minor actinides (i.e. Am and Cm) in the fast reactor fuel.
- If a sufficient number of fast reactors are built in relation to the supply of fuel from LWR or HWRs, the scenario runs out of minor actinides, and is forced to “borrow” these elements from an outside region. However, since these scenarios are forced to import

minor actinides, they do a sufficient job of dispositioning actinides that helps to offset the manufacturing costs of the fuel.

2.5. Coupled Fast-Thermal Power Breeder Reactor Concept

The theory of coupled reactors was pioneered by Avery [25]in the 1950's. As presented in Figure (2-8), the basic design concept of the coupled fast-thermal system consists of an inner fast core surrounded by a thermal region which includes an inner blanket and a moderator annulus.

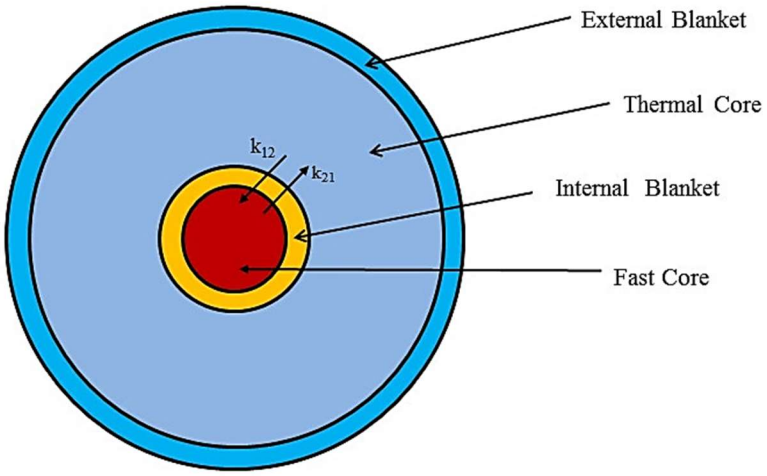

Figure (2-8): General Model of a Double Zone Reactor.
(The dimensions of each zone do not represent the real optimized size).

The internal core typically has a dominant fast neutron spectrum, while the external core has a dominant thermal neutron spectrum. Both regions would be independently subcritical on their own. The combination of the two regions is designed so that any neutron leakage between them can provide sufficient reactivity to drive the combined system to criticality. The thermal fissions arise from thermal neutrons that have slowed down in the moderator annulus and diffused back into the inner blanket. The fast and thermal cores are coupled together in the sense that, in each of the fuel assemblies, some of the neutrons causing fissions were born in the other region. Each of the regions is subcritical when uncoupled from the other, and, in particular, the overall system is not critical dependent on fast neutrons alone.

The coupled system introduced by Avery combines the high breeding ratio of fast reactors, although subcritical on fast neutrons, and the long neutron lifetime of thermal reactors. To bring the overall neutron lifetime of the coupled fast-thermal system into the thermal range, thermal fission must constitute an important fraction of the total fissions. Hence the volume of the thermal region must be larger than the volume of the fast core. Due to the diffusion of the thermal neutrons from the thermal core to the fast one, the thermal fissions are important towards driving and maintaining the chain reaction in the fast core. This contribution in the total reactor criticality is demonstrated by the criticality factor k_{21} in the diagram, which represents the substantial need for a coupling of the thermal region to the fast region. Unless enough reactivity is added to the fast system to bring it close to criticality on its own, the kinetics of the reactor will be representative of a thermal system. The subcriticality of the fast core thus serves as a safety margin against a prompt excursion in a fast system. While it is necessary to obtain sufficient coupling from the thermal region to the fast core, it is also important to introduce a barrier which sufficiently isolates the fast system from low-energy neutrons. In other words, the fissions of fissile fuel in the fast core should be generated mainly from fast neutrons in order to obtain a breeding ratio comparable of an all-fast reactor. The close proximity of the inner blanket to the fast core and the absence of a moderator in between them make this coupling requirement possible. The inner blanket thus serves as a reflector for the fast core as well as a breeding blanket for both the fast and thermal systems. The breeding effect compensates for the burning of U-235 in the inner blanket. The moderator is surrounded by an outer blanket, normally made of depleted uranium, which captures thermalized and unthermalized neutrons that have diffused outward, burning its U-235 content and promoting conversion from fertile to fissile fuel. These blankets are not applicable in the current multispectrum reactor because the target is to burn more actinides than breeding them.

Avery and his team conducted experiments on the ZPR-Ill assembly at the Argonne Fast Critical Facility. In this experiment, the fuel of the fast core was composed of 93% enriched U-235 and depleted uranium [26]. The experimental results were compared with those for an all-fast reactor. It was demonstrated that the coupled fast-thermal breeder can achieve the goal of a breeder reactor with a lower critical mass of fissile fuel and a breeding ratio only slightly less than an all-fast reactor. It was also concluded that the fast-thermal system had a significant (approximately 4%) margin of safety against an excursion as a fast system. As well, the radial maximum-to-

average power ratio or the so-called form factor in the fast core was significantly improved in the coupled fast-thermal system, going from 1.3 down to 1.1. This allowed for a more uniform radial flux distribution in the central fast core. Moreover, the coupled reactor has a neutron lifetime significantly longer than that for the all fast reactor, making the fast-thermal reactor system easier to control. It was found (as seen in Figure (2-8)) that the contribution from the thermal core to the fast core (i.e., the coupling coefficient k_{21}) is significantly larger than that of the criticality contribution from the fast to the thermal core (k_{12}). The verification of coupled reactor theory and its application in the Deuterium Critical Assembly will be presented in Chapter 5.

The criticality factors k_{eff}, k_{11} and k_{22} could be computed with MCNP along with the coupling coefficients k_{12} and k_{21} that can be calculated from Equations (2-1) and (2-2):

$$k_{12} = \frac{R_{f,1-2}}{(R_{f,1} + R_{f,2})} \times k_{eff} \tag{2-1}$$

$$k_{21} = \frac{R_{f,2-1}}{(R_{f,1} + R_{f,2})} \times k_{eff} \tag{2-2}$$

The coupling formula of k_{eff} is presented by Nishihara's work[27], given by Equation (2-3):

$$k_{eff} = \frac{1}{2}\left[k_{11} + k_{22} + \sqrt{(k_{11} - k_{22})^2 + 4k_{12} \cdot k_{22}}\right] \tag{2-3}$$

where

$R_{f,1}$: is the fission rate in the inner region (fission cm^{-3} s^{-1}),

$R_{f,2}$: is the fission rate in the outer region (fission cm^{-3} s^{-1}),

$R_{f,1-2}$: is the fission rate in the inner region caused by neutrons born in the outer region (fission cm^{-3} s^{-1}), and

$R_{f,2-1}$: is the fission rate in the outer core caused by neutrons born in the inner region (fission cm^{-3} s^{-1});

k_{11}: is the average number of next generation fission neutrons in the inner fast region resulting from a single fission neutron born in the inner fast region,

k_{22}: is the average number of next generation fission neutrons in the outer thermal region resulting from a single fission neutron born in the outer thermal region,

k_{21}: is the average number of next generation fission neutrons in the outer thermal region resulting from a single fission neutron born in the inner fast region, and

k_{12}: is the average number of next generation fission neutrons in the inner fast region resulting from a single fission neutron born in the outer thermal region.

2.6. HERBE and other Coupled Reactor Systems

The coupled fast-thermal core HERBE at the RB[2] zero power heavy water reactor in Vinča was designed for experimentation with fast neutron fields[28]. The requirements for minimum modifications in the RB construction, and application of available fuel, restricted the design flexibility of the coupled system. Thus, the RB core is optimized with a central fast core of natural uranium that is surrounded by a neutron filter zone (cadmium and natural uranium) and converter zone (enriched uranium fuel, without moderator). The coupling region is heavy water. The thermal core is formed of heavy water with an 80% enriched uranium lattice using a 12-cm pitch. The criticality of the system is obtained by adjusting the moderator level. The critical heavy water levels were measured for normal reactor operation and some simulated accidental conditions. The coupled fast thermal system HERBE, as shown in Figure (2-9), has an overall radius of 100 cm, an inner fast core of about 20 cm radius surrounded by a 30-cm thick thermal region and a D_2O outer reflector.

[2] RB is the reactor name in Vinča, Institute of Nuclear Sciences, Belgrade, Serbia and Montenegro Center for Nuclear Technologies and Research

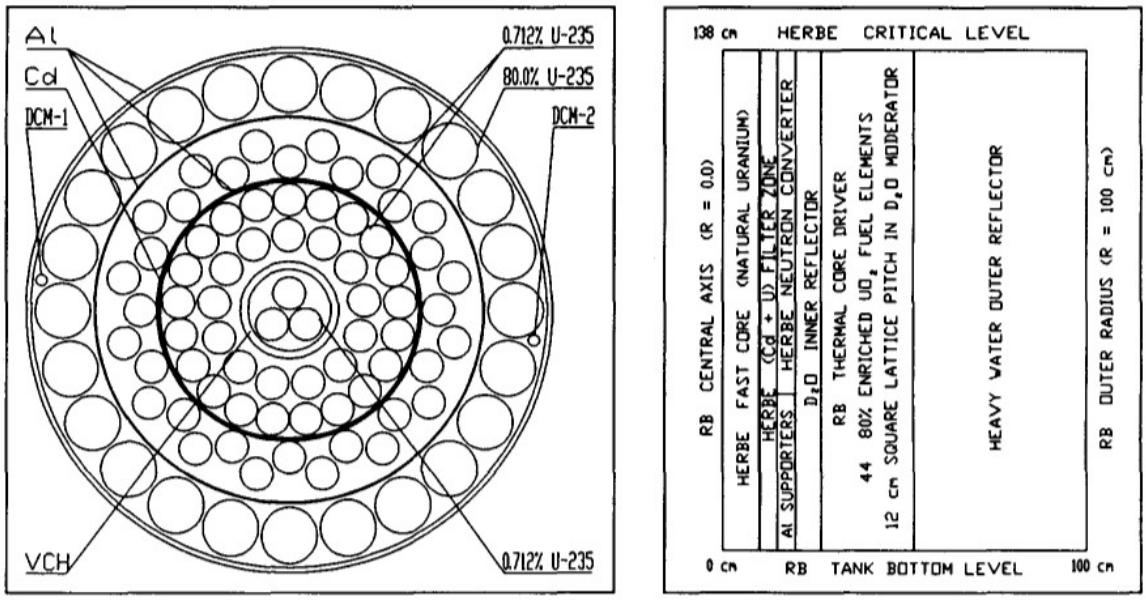

A) HERBE Fast Zone Horizontal Cross Section **B) Vertical Cross Section of the RB Reactor**

Figure (2-9): The Coupled Fast Thermal System HERBE[28]

The inner fast core basically contains natural uranium fuel elements surrounded by high neutron absorbing zones (cadmium layer). The outer core (thermal region) is moderated by heavy water and includes 44 fuel channels having a 12-cm square lattice pith. Each fuel channel includes 13 fuel segments composed of 80% enriched UO_2 fuel. One of the main objectives of the HERBE system was for validation of computer codes for calculation of reactor cells with large heterogeneous regions filled with air and high-absorption material.

The calculation of two-group radial neutron flux distributions was carried out with the computer code MCNP (version 4B2) and validated experimentally from measurements using gold foils. In this exercise, the criticality factors k_{11}, k_{22} and the criticality coefficients k_{12} and k_{21} were calculated and validated.

Avery [25] analysis has been the bases of many works and the governing equations have also been re-derived by Komata [29] and Kobayashi[30]. In particular, Kobayashi extended Avery's work where the nodal equations in each reactor [31] region could be rigorously derived from multigroup diffusion theory without the need for any approximations. An exact expression for the

coupling coefficients and the neutron lifetimes are presented in this treatment. An approach using a multigroup transport theory was also introduced by Kobayashi[31]. Nishihara[27] used an experimental Deuterium Critical Assembly (DCA) to verify the theory of coupled reactors employing the TWOTRAN[3] code. As part of the current thesis work, the DCA is also simulated in order to verify the coupled-reactor theory and to validate both the MCNP and the Serpent codes as detailed in Chapter 5. Allen's Master degree thesis [32] also used the Monte Carlo probabilistic computer code to simulate a CANDU as a Coupled Reactor.

As previously mentioned, Allen [32] was able to develop a mathematical model of a multispectrum CANDU reactor using the MCNP code for a Gentilly-2 CANDU 6 reactor design. This coupled reactor design consisted of two reactor regions with an internal fast core (which represents about one fourth of the whole reactor core volume) and an external thermal core. The inner fast core contributed only a small fraction of the total power of the reactor. The purpose of the fast core was to burn mainly actinides and breed new fissile materials, while the thermal core's contribution was for power generation. Allen optimized his model by maximizing the excess reactivity, lowering the form factor and maximizing the breeding ratio. The method of Gauss' Steepest Descent was used for this optimization procedure. A number of optimum reactor configurations were proposed for the multispectrum CANDU, which exhibited an excellent form factor of less than 1.3 as is required for safe reactor operation.

[3]TWOTRAN is designed to solve the multigroup discrete ordinates approximation to the two- dimensional Boltzmann equation for particle transport problems in x-y, r-z and r-theta geometries. [27].

Chapter 3.

Theory

3.1. Nuclear Reactor Calculations

The most fundamental evaluation quantities of the nuclear design calculation are the effective multiplication factor (k_{eff}) and the neutron flux distribution. Also, the excess reactivity, control rod worth, reactivity coefficient, power distribution, among others, are unquestionably inseparable from the nuclear design calculation. Some of these quantities can be derived by secondary calculations from the effective multiplication factor or neutron flux distribution. The theory and methodology to calculate the effective multiplication factor and the neutron flux distribution in calculational programs using different computer codes are discussed in the following sections. A full nuclear reactor design requires a significant amount of work including a reactor core calculation and nuclear plant analysis. The nuclear core calculation is performed to determine the nuclear, thermal, and composite properties of the system. A nuclear plant analysis is done to determine dynamic and control properties, start up and stability, and safety by modeling pipes and valves of the coolant system, coolant pump, control system, steam turbine and condenser etc. (as connected to the reactor partition wall and core)[33][34]. The current work specifically provides a preliminary design of the Multispectrum CANDU-based reactor (MSCR) for the burning of actinides. However, for this analysis, only a reactor core calculation is carried out to limit the scope of the study, which focusses on a reactor core analysis for the effective multiplication factor (k_{eff}), the regeneration factor (η), the neutron flux distribution, the excess reactivity, power distribution, relative power generated from each core, the form factors, and fuel burnup calculations. The transport of neutrons through materials in the reactor is determined by the Boltzmann transport equation as discussed below.

3.2. Neutron Multiplication Factor

From the time that a neutron chain reaction was first experimentally verified with the CP-1 critical pile in 1942 to the Gen IV reactor designs of today, the principal measure of the capability for a system to initiate and maintain a neutron chain reaction is the k-effective (k_{eff}) or eigenvalue factor. The metric for criticality can be looked at in several ways. The simplest definition of the k-

effective (k_{eff}) is the average number of fission events that result from the neutrons emitted from a single original fission event. If this number is one, then the rate of fission reactions will be maintained and constant over time. If greater than one, the reaction rate will increase with time (supercritical system) and if less than one, it will decrease with time (subcritical system):

$$k_{eff} = \frac{fission\ in\ generation\ N+1}{fission\ in\ generation\ N} = \frac{fission\ neutron\ production\ rate}{neutron\ leakage\ rate + neutron\ absorption\ rate} \tag{3-1}$$

For this equation, the important physical parameters are the neutron cross sections, which give the probabilities of various reactions occurring when neutrons interact with nuclei. The most important reaction types are fission, absorption (the sum of fission and non-fission capture), and scattering reactions. The particular forms and energy shapes of the cross sections have a strong effect on criticality [33] [35].

3.3. Neutron Transport Equation

There are several methods for determining the distribution of neutrons in lattice cells of the reactor, one of the most widely used being neutron transport theory. The basis of transport theory is to determine the neutron population in space in terms of position, energy, direction and time within a given volume. Primarily, this is a counting problem where an arbitrary volume, *V*, contains a number of neutrons, *n*, with a trajectory within an angle $\widehat{\Omega}$ and energy interval of *dE* about energy *E*. The change of neutron population in *V* is a result of the sum of the gain and loss terms.

The transport of neutrons through some material is governed by the neutral particle Boltzmann transport equation, one form of which is given by:

$$\nabla \cdot J(r,E) + \Sigma_t(\vec{r},E)\varphi(\vec{r},E) = \frac{\chi(\vec{r},E)}{k_{eff}} \int_0^\infty dE' \nu(E') \Sigma_f \varphi(\vec{r},E') + \int_0^\infty dE' \Sigma_s(\vec{r},E' \longrightarrow E)\varphi(\vec{r},E') \tag{3-2}$$

where, $\varphi(\vec{r},E)\ and\ J(r,E)$ are the neutron flux and the neutron current as a function of position and energy, and $\chi(\vec{r},E)$ is the distribution of fission neutrons at the position r and energy E. Equation (3-2)[36], gives the balance of the different reactions that can occur with neutrons at a

given point and energy, along with the eigenvalue, denoted by k_{eff}. Each of the terms in the equation denotes loss mechanisms for the neutrons (on the left-hand side of the equation) or gain mechanisms for neutrons (on the right-hand side):

$\nabla \cdot J(\vec{r}, E) =$ diffusion rate of loss.

$\Sigma_t(\vec{r}, E)\varphi(\vec{r}, E)$ = interaction rate of loss.

$\chi(\vec{r}\,, E) \int_0^\infty dE' \nu\,(E')\Sigma_f \varphi(\vec{r}, E')$ = fission neutron production rate.

$\int_0^\infty dE' \Sigma_s\,(\vec{r}, E' \longrightarrow E)\varphi(\vec{r}, E')$ = rate of neutrons emerging from scattering reactions.

This equation is solved for the flux and then integrated over all energies and over spatial regions of interest. It can be altered to solve for (k_{eff}) by picking the spatial integration region such that all of the fissionable material is included and such that escaping neutrons do not re-enter the spatial integration region and cause fission so that:

$$\langle \vec{\nabla} \cdot \vec{J} \rangle + \langle \Sigma_t, \varphi \rangle = \frac{1}{k_{eff}} \langle \upsilon \Sigma_f, \varphi \rangle + \langle \Sigma_s, \varphi \rangle \tag{3-3}$$

Here the shorthand integral vector notation means for any arbitrary vectors:

$$\langle \mathrm{a} \cdot b \rangle = \int_V dr' \int_0^\infty dE\; a(\vec{r}, E) b(\vec{r}, E) \tag{3-4}$$

This equation can be reorganized where:

$$\Sigma_t = \Sigma_a + \Sigma_s \tag{3-5}$$

$$k_{eff} = \frac{\langle \upsilon \Sigma_f, \varphi \rangle}{\langle \vec{\nabla} \cdot \vec{J} \rangle + \langle \Sigma_a, \varphi \rangle} \tag{3-6}$$

The angular time dependent transport equation can be written in the form

$$\frac{1}{v}\frac{\partial\phi(\vec{\mathrm{r}},\mathrm{E},\hat{\Omega},\mathrm{t})}{\partial\mathrm{t}} = \int_0^{\infty}\mathrm{dE}'\int_{4\pi}\Sigma_{\mathrm{s}}\left(\vec{\mathrm{r}},\mathrm{E}'\longrightarrow\mathrm{E},\hat{\Omega}'\longrightarrow\hat{\Omega},t\right)\phi(\vec{\mathrm{r}},\mathrm{E}',\hat{\Omega}',t)d\hat{\Omega}'$$
$$+\frac{\chi(\mathrm{E})}{4\pi}\int_0^{\infty}dE\int_{4\pi}\chi(\mathrm{E})\,\nu\,\Sigma_{\mathrm{f}}(\vec{\mathrm{r}},\mathrm{E}'\mathrm{t})\phi(\vec{\mathrm{r}},\mathrm{E}',\hat{\Omega}',t)d\hat{\Omega}'+S_{ex}(\vec{\mathrm{r}},\mathrm{E},\hat{\Omega},t) \qquad (3\text{-}7)$$
$$-\hat{\Omega}\cdot\nabla\phi(\vec{\mathrm{r}},\mathrm{E},\hat{\Omega},\mathrm{t})-\Sigma_{\mathrm{t}}(\vec{\mathrm{r}},\mathrm{E},\mathrm{t})\phi(\vec{\mathrm{r}},\mathrm{E},\hat{\Omega},\mathrm{t})$$

Here, S is the neutron source, Σ_t is the macroscopic total cross section, and ϕ is the angular neutron flux. This equation represents the balance between gain and loss in the unit volume. The neutrons are characterized by kinetic energy E (velocity v) and are traveling in a specific direction $\hat{\Omega}$ at a time t and a position $\vec{r}$; Σ_s and Σ_f are the macroscopic scattering and fission cross sections, respectively; and v is the average number of neutrons emitted per fission and the product $v\Sigma_f$ is treated as a neutron production[35][37].

The term $\frac{1}{v}\frac{\partial\phi}{\partial\mathrm{t}}$ is the time change of the neutrons given by the balanced relation involving the net gain of neutrons appearing from the neutron source S, and the net rate loss of neutrons due to nuclear collisions (absorption or scattering). It should be noted that the changes in angle and energy of neutrons are also included in the gain and loss terms.

- Neutrons are created at certain energies and in a given direction from three mechanisms: scattering, fission, and external neutron sources. The first term on the right-hand side (R.H.S.) of the equation defines the scattering source term

$$\int_0^{\infty}\mathrm{dE}'\int_{4\pi}\Sigma_{\mathrm{s}}\left(\vec{\mathrm{r}},\mathrm{E}'\longrightarrow\mathrm{E},\hat{\Omega}\longrightarrow\hat{\Omega}',t\right)\phi(\vec{\mathrm{r}},\mathrm{E}',\hat{\Omega}',t)d\hat{\Omega}'$$

  that represents the number of target neutrons scattering into E and $\hat{\Omega}$ from another energy E′and direction $\hat{\Omega}'$

- The second term on the R.H.S.

$$\frac{\chi(\mathrm{E})}{4\pi}\int_0^{\infty}dE\int_{4\pi}\chi(\mathrm{E})\,\nu\,\Sigma_{\mathrm{f}}(\vec{\mathrm{r}},\mathrm{E}'\mathrm{t})\phi(\vec{\mathrm{r}},\mathrm{E}',\hat{\Omega}',t)d\hat{\Omega}'$$

is the fission source and it indicates the neutrons production by fission over the whole range of energies which are distributed with an isotropic probability in direction (1/4π) and probability χ(E)

in energy (E). χ(E) is the fission spectrum and it is dependent on the nuclide undergoing fission and the energy of the incident neutrons.

- The third term on the R.H.S. $S_{ex}(\vec{r}, E, \hat{\Omega}, t)$, is an external source term usually used for the startup of the reactor such as with a neutron source such as $Am(\alpha, n)Be$; $Pu(\alpha, n)Be$ or ^{252}Cf .
- The fourth term on the R.H.S., $\hat{\Omega} \cdot \nabla\phi(\vec{r}, E, \hat{\Omega}, t)$, is a streaming term.
- The fifth term, $\Sigma_t(\vec{r}, E, t)\phi(\vec{r}, E, \hat{\Omega}, t)$, is the absorption term.

3.3.1. Approximations to the Transport Equation:

The transport equation (3-7) has ten independent variables: x, y, z, v_x, v_y, v_z, $\hat{\Omega}_x, \hat{\Omega}_y$, $\hat{\Omega}_z$ and t. If an angular approximation is applied for a one-dimensional solution, the streaming term $\hat{\Omega}_x \cdot \nabla\phi(\vec{x},)$, where $\hat{\Omega}_x = \overrightarrow{\cos\theta} = \mu$, the total number of variables collapses to seven.

Moreover, the dependence of the collision cross section Σ_s (r,$E' \rightarrow E$) on the particle energy (or velocity v) is extremely complicated because of the collision dynamics. The general form of the transport equation is an integro-differential equation making it difficult to solve by computer. Some methods of solution and approximations have to be considered[35]. Three ways are available to solve the transport problem:

1. Approximating the form of the equation itself e.g. diffusion theory;
2. Consideration of the problem for which the form of the transport equation can be simplified (see below); and
3. Using a probabilistic simulation techniques such as a Monte Carlo method.

The approximations to the geometry, energy dependence or angular dependence are normally introduced:

1- Geometrical approximations:

   b) Isotropic, homogeneous media.

   c) Infinite media or half-spaces

d) One dimensional plane, spherical, or cylindrical geometry.

e) Periodic lattice and symmetries.

2- Energy approximations:

a) One-speed approximation.

b) Multigroup energy descriptions.

c) Expansion of the energy dependence in polynomial.

d) Simple models of the collision kernels.

3- Angular dependence approximations:

- Isotropic sources.
- Isotropic scattering
- Expansion of collision kernels in Legendre Polynomials in angle.

A) Importance of Neutron Flux Distribution Knowledge

The determination of the multiplication factor (k_{eff}), (or the reactivity), represents an important part of reactor analysis. The flux profile (in space and energy) is also needed to obtain other engineering parameters for the design of the reactor. The most important use of the calculated flux is to determine the amount of energy that will be deposited in various spatial regions (usually in the fuel elements) of the reactor. This is found by integrating the flux over the deposition region utilizing an energy deposition factor for each of the different neutron reactions that can occur:

$$E_{deposited} = \sum_{i=1}^{I} N_i \sum_{x} \int_{0}^{\infty} \varepsilon_{ix}(E) \int_{V} \sigma_{ix}(\vec{r}, E)\phi(\vec{r}, E)d\vec{r}\, dE \qquad (3\text{-}8)$$

where, the $\varepsilon_{ix}(E)$ factor represents the energy deposition for reaction *x* in isotope *i* at energy *E*. The energy deposition is important for the thermal hydraulic design. Other uses of the neutron flux in the reactor analysis process are in:

(1) the determination of the fuel burnup or the variation of the nuclide densities that occur in an operating reactor due to different interactions of the neutrons flux with the different materials in the reactor, especially the fuel.

(2) the nuclide density of fissionable isotopes for the type of reactor for conversion or breeding purposes.

(3) the determination of the asymptotic concentrations of neutron-absorbing intermediate fission products whose presence have a strong effect on the (k_{eff}) and the neutron flux distributions.

(4) the analysis of the time-varying dependence of (k_{eff}) and the neutron flux distribution, which provides needed information for control of the reactor total power and the power density spatial distribution with time.

3.3.2. Methods of Solution of Transport Equation.

The control of the reactor neutron spectrum (i.e., energy dependence) has a strong effect on the reactor operating characteristics and provides for the thermal hydraulic design. In general, the following time dependences occur: (i) neutron flux variations, quickly-varying changes due to power and reactor control, and (ii) slower time-dependent changes due to material transformations and fuel burn up. Computer codes that are used to solve for the time-independent, steady-state neutron flux, fall into two categories:

(1) Deterministic: Discrete ordinates, integral transport, diffusion theory; and

(2) Probabilistic: Monte Carlo Method.

Each of these methods has advantages and disadvantages. Both types of approaches are used in this toolset because of the relative advantages and disadvantages of the two different approaches.

i. Deterministic Solutions

Deterministic methods involve the numerical subdivision of the independent variables of space, energy, and direction into computational subdivisions, with a subsequent reformulation of the continuous-variable Boltzmann equation into a set of discrete variable equations for each *phase cell* (i.e., the combination of a space, energy and direction subdivision). The flow of particles through space causes a linkage among the spatial subdivisions, and the scattering process causes a

linkage among the energy and directional subdivisions. Specialized deterministic computer codes solve these coupled linear algebraic equations, thereby providing the neutron flux in each phase cell. The desired flux integrals are approximated by summations over the appropriate cells for the engineering parameters (including (k_{eff})) of interest[37]. Because the basic formation of the deterministic solution requires this extensive subdivision, deterministic methods naturally provide the detailed information in space and energy that the reactor design process requires. In addition to this wide range of information, the deterministic methods also tend to be fast, accurate, and amenable to acceleration and convergence improvement methods from well-developed numerical analysis techniques. The three predominant types of deterministic methods are:

(1) The *discrete ordinates* method that subdivides all three independent dimensions—

space, energy, and direction.

(2) The *integral transport* method (also called the collision probability method) that subdivides only space and energy. Space is again divided into a grid, but the grid regions tend to be larger and less regular than for the discrete ordinates method. The energy variable is again handled using a multigroup method. The WIMS-AECL code uses the collision probability method to solve the transport equation for flux and the infinite multiplication factor and for burnup calculations.

(3) The *diffusion theory* method simplifies the directional dependence by assuming a nearly isotropic flux (i.e., an approximately equal number of neutrons traveling in all directions). The spatial treatment again utilizes a regular grid of spatial elements connected to their immediate neighbours and the energy treatment again employs a multigroup approach. This is the simplest and fastest of the deterministic methods, but the direction approximation is the most extreme, limiting its usefulness for calculations near sources or strong absorbers. The primary use of diffusion theory is for a full-reactor calculation in which the reactor assemblies have been homogenized, so that strong absorbers and fission/scattering sources have been mathematically spread out[38].

ii. Probabilistic Solutions

Probabilistic (Monte Carlo) methods solve for the neutron flux by simulating particle transport rather than by numerically solving the Boltzmann transport equation itself (although the simulation algorithm can be derived from the transport equation as well as from the physics).

The Monte Carlo particle simulation involves the use of an algorithm in which the interactions faced by a neutron in its lifetime are simulated in the computer code, in the order in which they arise. For each Monte Carlo decision, the outcome is determined from mathematical probability densities that nuclear physics experiments provided for the physical effect being simulated. For criticality problems, neutrons are born in "batches" or "generations" of particles (generally hundreds to thousands of particles for each one of hundreds to thousands of generations). The Monte Carlo Calculations Scoring or Tallying are shown in the Appendix (A). The interactions that are faced by each fission-produced neutron are:

(1) An initial position is chosen for the particle based on fission sites from the previous generation (or assumed for the first generation);

(2) An initial energy is chosen from the known probability distribution of fission neutrons from the appropriate fissionable nuclide (and possibly depending on the energy of the neutron inducing the fission).

(3) An initial direction is chosen from an isotropic distribution.

(4) The distance travelled to the next collision site is chosen. Actually, this is done in two steps: the number of mean free paths to the next collision is chosen and then this is translated into a distance based on the materials and geometry of the problem (this second step takes up the majority of the computer time needed by the Monte Carlo code). If this distance is greater than the distance to the edge of the volume being calculated, the particle is deemed to have escaped and its history is terminated.

(5) The type of collision is determined from the macroscopic cross sections of the material present at the collision site. If the reaction is a neutron absorption reaction, the particle history is

terminated; if the absorption reaction is fission, the location of the collision is stored as a potential starting point for the next generation of neutrons.

(6) If the collision is a scattering reaction, the new energy and direction are chosen from the scattering distributions for the material, and the simulation returns to step (4).

For each of the simulated particles, the code keeps track of information of interest: the average flux values in the regions of the problem, the energy deposition in the regions of the problems, and the number of new fission neutrons produced by the generation. This last one is of particular interest since the ratio of new fission neutrons to the number of neutron particle histories followed in the generation gives an estimate of (k_{eff}) for the generation in Equation (3-1). The statistical processing of these (k_{eff}) estimates provides the code its final estimate of (k_{eff}), with statistical uncertainty (estimated standard deviation). This simplified description has assumed that the exact physical probabilities are utilized to determine the outcome of every decision; when this is done, the resulting simulation is termed an *analog* simulation. More sophisticated statistical treatments are included in modern computer codes that utilize nonphysical distributions with corrections (in a defined particle *weight*) to keep the results of the simulation unbiased. These can be shown to improve the efficiency of the simulation. These methods are called "variance reduction" methods, although this is somewhat of a misnomer because many of these methods increase the efficiency by saving computer time, not by reducing variance. A key feature of Monte Carlo codes is that the accuracy of the results delivered by the method depend on the number of particle histories followed (N) by the ratio $1/N$. This fact severely limits the efficiency of Monte Carlo methods to deliver precise results, especially for region-dependent values of flux and energy deposition. The result is that Monte Carlo methods are generally much more efficient in calculating system-wide parameters such as (k_{eff}) than they are for calculating detailed spatial parameters such as energy deposition profiles.

For the current thesis work, probabilistic solutions with the Monte Carlo codes MCNP6 and Serpent Code 1.1.19 are used to design and simulate the Deuterium Critical Assembly and the multispectrum CANDU reactor. The deterministic code WIMS-AECL 3.1 is used to validate the Serpent code calculations as shown in Chapter 6.

3.4. Fast Reactor Physics

Fast reactors differ from thermal reactors in several aspects and require a special treatment. The parasitic capture cross sections in the fuel, coolant and structure decrease with increasing neutron energy faster than the fission cross section. Thus, the neutron economy is improved in the fast region of the neutron spectrum. This is achieved by avoiding the use of moderator materials as coolants. Since the fission cross section is less in a fast reactor than in a thermal reactor, a fast reactor will contain much more fissile fuel than a thermal reactor for the attainment of a critical mass as a fast reactor alone. In the current thesis, the fast core or the fast neutron region is subcritical because of the selection of the geometrical properties (core radius, lattice pitch and number of fuel channels), with the diffusion of neutrons between the fast (internal core) and thermal cores (external core) driving the whole reactor to criticality[39][38].

Fast reactor cores, having no moderator, are very compact in size. This leads to a higher power density necessitating the use of efficient coolants [40] such as liquid metals. Sodium, lead, and a sodium-potassium eutectic (that is liquid at room temperature), bismuth-lead eutectic or helium gas are investigated in the simulations of the design of the multispectrum CANDU-based reactor for this work.

In a traditional fast reactor, a small core implies a relatively large amount of neutron leakage from its surface. A reflector is avoided and replaced by a blanket to intercept the leaking neutrons into the breeding material[41]. The multiplication and energy production in the blanket must be accounted for from the perspective of power production. In the current work, there is no blanket but the fast core is in a central region of the multispectrum reactor and the diffused neutrons from the fast core are captured in the surrounding fuel channels of thermal core. The flux profile in the region between the two cores will be presented in Chapters 7 and 8.

3.4.1. Conversion Chains

The ultimate goal of traditional fast reactors is to breed fuel to enable nuclear reactors to power our planet for several millennia. For the fast breeder reactor, in order to achieve breeding, a fertile isotope (^{238}U, ^{240}Pu, ^{232}Th, ^{234}U) must be converted via neutron capture (n, γ) into a fissile isotope (^{239}Pu, ^{241}Pu, ^{233}U, ^{235}U) [7].The two important conversion chains are shown in Figure (2-4). Most

of the fertile and fissile isotopes appearing in Figure (2-6) are long-lived alpha emitters ($T_{1/2} \geq 10^4$ year) so that, with the exception of ^{241}Pu, they can be considered stable with regard to a mass balance. ^{241}Pu is also a beta emitter with a half-life short enough to require consideration in the fuel cycle calculation. Ignored in Figure (2-6) are fission reactions (*n*, *f)* by all isotopes, as well as neutron capture reactions by the short-lived beta emitters[39].

3.4.2. Conversion Ratio and Breeding Requirements

The degree of conversion that occurs in a reactor is denoted by the general term *conversion ratio,* CR, which is defined as

$$CR(\vec{r},t) = \frac{Fissile\ Material\ Produced}{Fissile\ Material\ Destroid} = \frac{FP}{FD} = \frac{RR^{FP}_{c(n,\gamma)}\ (\vec{r},t)}{RR^{FD}_{a}(\vec{r},t)} \tag{3-9}$$

Here, the fissile material produced is FP = $RR^{FP}_{c(n,\gamma)}\ (\vec{r},t)c$ and the fissile material destroyed is $RR^{FD}_{a}(\vec{r},t)$ during a fuel cycle, i.e., between periodic refuelling. The $RR^{FP}_{c(n,\gamma)}\ (\vec{r},t)$ and $RR^{FD}_{a}(\vec{r},t)$ terms are the capture and absorption reaction rates. The conversion rate $CR(\vec{r},t)$ is a property that depends on space and time, and depends mainly on the flux and fuel distribution inside the reactor[39] [42].

The average conversion ration can be calculated for the reactor

$$\overline{CR} = \frac{\int_0^{T_f} dt\ \int_{V_c} RR^{FP}_{c(n,\gamma)}\ (\vec{r},t)\ dV}{\int_0^{T_f} dt\ \int_{V_c} RR^{FD}_{a}\ (\vec{r},t)\ dV} \tag{3-10}$$

where, the integration is taken all over the entire reactor. $\overline{CR}$ is also averaged over the reactor core volume V_c. The reactor is said to be a breeder or a converter according to the value of $\overline{CR}$. A reactor is called a *breeder* if the conversion ratio is greater than unity. In this case, the conversion ratio is called a *breeding ratio,* BR; hence

$$Breeder: BR = CR > 1.0 \tag{3-11}$$

A reactor for which the conversion ratio is less than unity is called a *converter*,

$$Converter: CR = CR < 1.0 \quad (3\text{-}12)$$

In the current work, the breeding should be avoided because the goal of the multispectrum reactor design is to burn fissile actinides from dismantled nuclear weapons, so the multispectrum reactor must be designed to be a converter of fissile materials. Therefore, basic reactor physics is needed to check the conversion ratio, which depends on certain reactor physics parameters.

It is possible for a nuclear reactor to breed over a broad neutron energy spectrum, but adequate breeding ratios can be achieved for a given energy spectrum only by carefully selecting the appropriate fissile isotopes for that spectrum. Recall from the fission process that

ν_f = Number of neutrons per fission,

η = Number of neutrons produced per neutron absorbed, or regeneration factor, and

α = Capture-to-fission ratio $\frac{\sigma_c}{\sigma_f}$

If η is the average number of new neutrons for each neutron absorbed in the fuel averaged over the neutron flux spectrum, these parameters are related by:

$$\overline{\eta}(E) = \frac{\overline{\nu}_f(E)\ \overline{\sigma}_f(E)}{\overline{\sigma}_f(E)} = \frac{\overline{\nu}_f\ (E)\,\overline{\sigma}_f(E)}{1 + \frac{\overline{\sigma}_c(E)}{\overline{\sigma}_f(E)}} = \frac{\overline{\nu}_f(E)\,\overline{\sigma}_f(E)}{1 + \overline{\alpha}(E)} \quad (3\text{-}13)$$

The parameters $\overline{\nu}_f$ and $\overline{\alpha}$ are measured quantities, while $\overline{\eta}$ is a derived quantity. For each of the primary fissile isotopes, ν_f is constant for neutron energies up to about 1 MeV (~2.9 for ^{239}Pu and ~2.5 for ^{233}U and ^{235}U) and slowly rises at higher energies. On the other hand, α varies considerably with energy and between isotopes. For ^{239}Pu and ^{235}U, α rises sharply in the intermediate energy range between 1 eV and 10 keV and then drops again at higher energies; for ^{233}U, α never rises appreciably. This behaviour of ν and α leads to the variations of η with energy are shown in Figure (3-1).

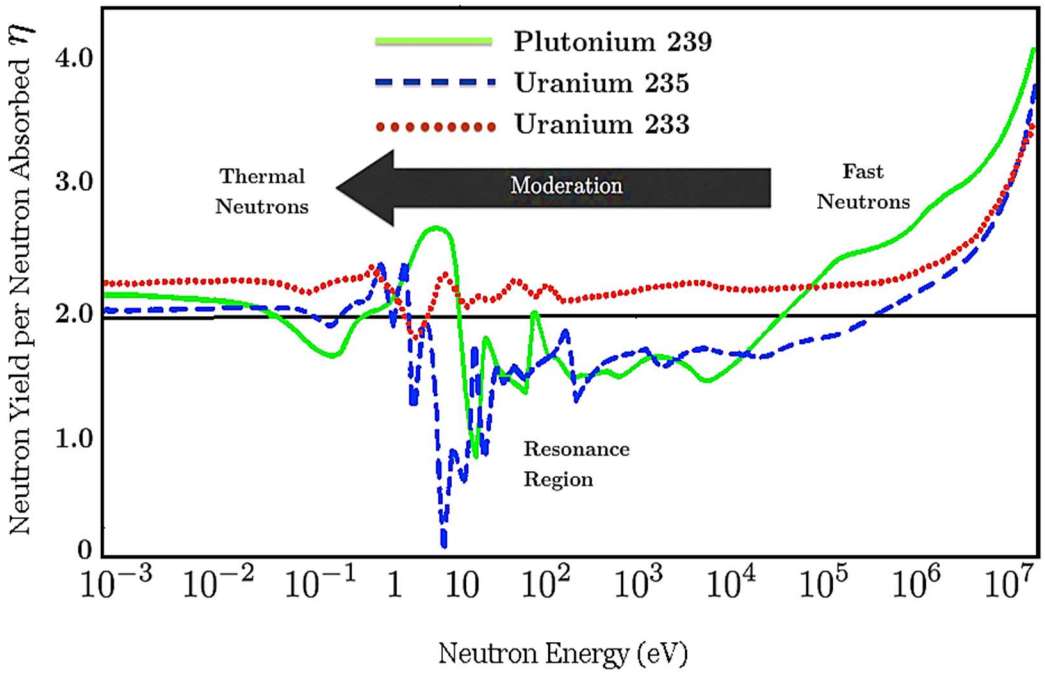

Figure (3-1): Neutrons Produced per Absorption vs. Energy for Fissile Isotopes [38]

In order to appreciate the significance of Figure (3-1), it is useful to establish the minimum criterion for breeding. Consider a simple neutron balance for which the basis is one neutron absorbed by a fissile nucleus (which is equivalent to the destruction of 1 fissile nucleus). In order to breed, the next generation of neutrons must, at a minimum, replace that 1 destroyed fissile nucleus. The number of neutrons produced by this absorbed neutron is η. Let us examine the fate of these η neutrons:

- One neutron must be absorbed in a fissile isotope to continue the chain reaction;
- L neutrons are lost unproductively, by parasitic absorption or by leakage from the reactor.

For the present purpose of this work, the neutron absorption by any material other than fissile or fertile materials is parasitic. Hence, from the neutron balance, $[\eta - (1 + L)]$ is the number of neutrons captured by the fertile material. Since this value represents the number of new fissile nuclei produced, and since the basis of the neutron balance is the destruction of one fissile nucleus, therefore, $[\eta - (1 + L)$ must be $\geq 1]$ to replace the one destroyed fissile nucleus, i.e., for the breeding to occur. This relation defines a minimum value for η for breeding. Rewriting this relation gives $[\eta \geq 2 + L]$. Since the loss term is always greater than zero,

$$\eta > 2 \tag{3-14}$$

Then the condition (3-14) becomes a further simplified minimum criterion for breeding. The quantity $[\eta - (1 + L)]$ is the ratio of fissile nuclei produced to fissile nuclei destroyed for this simplified model; hence, from Equations (3-9) and (3-10), it is equal to the breeding ratio,

$$BR = \eta - (1 + L) \tag{3-15}$$

Therefore, a high value of η results in a high breeding ratio. This expression for breeding ratio is useful as a conceptual guide.

Now, one can re-examine Figure (3-1), considering the criterion (3-14) that η must be greater than 2.0 to breed. In a thermal reactor, most of the fissile absorptions occur in the 0.01–1 eV range. In a fast spectrum reactor using mixed oxide (UO_2-PuO_2) fuel, about 90% of the fissile absorptions occur above 10 keV. An examination of Figure (3-1) reveals that ^{239}Pu is the best choice for breeding in a fast reactor, with ^{233}U a possibility and ^{235}U doubtful. The figure also shows that ^{233}U is the only realistic candidate for breeding in a thermal reactor [39].

These observations are reinforced by Table (3-1), which compares η for the three fissile isotopes averaged over typical LWR and fast spectrum reactor spectra. If the relative loss events characterized by *L* in Equations (3-15) can be made about the same for a fast spectrum reactor and a thermal breeder reactor, the results of Figure (3-1) and Table (3-1) show that larger breeding ratios can be achieved with fast reactors. Moreover, even higher breeding ratios can be obtained from fast reactors that use metal (U-Pu), carbide (UC-PuC), or nitride (UN-PuN) fuel, partly because the average neutron energy for these fuels is higher and these fuels have greater fissile and fertile material densities.

Table (3-1) : Value for Regeneration Factor (η) Averaged over Fast and Thermal Spectra [39]

η -averaging spectrum type	^{239}Pu	^{235}U	^{233}U
Average over thermal spectrum (0.025 eV) (This value is needed for CANDU)	2.04	2.06	2.26
Average over a typical oxide-fueled fast reactor spectrum	2.45	2.10	2.31

One may proceed to treat such a system using a subdivision into a fast group for neutrons of energy above 1.35 MeV, the fission threshold of ^{238}U, and a thermal group for energies below it. From Figure (2-6), the fast neutron flux represents the best medium for burning actinides. The philosophy of the current design simulation is to introduce a reactor design that can work as a power reactor, where the main nuclear power can be extracted from the thermal core, while the fast core is working as an actinides burner. Consequently, it is necessary to introduce a brief description about the fast reactor and applicable conditions to avoid breeding in the multispectrum reactor.

3.5. Burnup Analysis

One of the most important analysis that is needed for the current thesis is the burnup analysis of the reactor's fuel for a user-specified period of time to update the isotopic contents of the fuel. The fuel composition changes with time due to irradiation effects and radioactive decay. These effects must be taken into account in the design of the reactor. In fact, it may be the primary design consideration of the reactor itself. The isotopic mix changes for two reasons: (a) from irradiation effects (primarily due to fission and transmutation) and, (b) from radioactive decay. Figure (2-1) shows the transmutation decay and the most probable nuclear interactions of actinides inside the nuclear reactors for the uranium and thorium cycles[7].

In general, Equation (3-16) [35] shows the rate of change of isotopic concentrations in the reactor, with some combination of these terms involving decay and transmutation:

$$\frac{dN_j(t)}{dt} = \gamma_j \sum_g \Sigma_{fg}\phi_g + \sum_{i\neq j}\left(\lambda^{i\to j} + \sum_g \sigma_g^{i\to j}\phi_g\right)N_i - \sum_{i\neq j}\left(\lambda^i + \sum_g \sigma_{ag}^i\phi_g\right)N_i \quad (3\text{-}16)$$

γ_j = fraction of fission events resulting in isotope j,

$\lambda_{i\to j}$ = decay constant from isotope i to isotope j,

λ_j = total decay constant for isotope j,

$\sigma_{i\to j}$ = transmutation cross section from isotope i to isotope j,

$\sigma_{a\,j}$ = total loss cross section for isotope i.

A number of Ordinary Differential Equations based on Equation ((3-16) could be generated to calculate the concentrations of each isotope. The primary consequence of the burnup is a drop-in *k*-effective as the fuel depletes and the fission products accumulate. This drop is compensated by the build-up of new fissile isotopes (notably Pu-239 from U-238 neutron absorption in uranium-fueled reactors). In some models of the current multispectrum reactor, as will be seen in Chapters 7 and 8, some fissile fuel materials are bred in the fast core and some in the surrounding thermal fuel channels.

All the light water reactors, boiling and pressurized water reactors, are refuelled in batches when the reactor is shut down. The fresh fuel assemblies replace the most burned-out assemblies at scheduled shutdowns with the remaining assemblies often moved ("shuffled") to new positions to optimize the reactor operating characteristics. In the CANDU reactor, the on-line refuelling helps to shuffle the fuel bundle axially to maintain the flux distribution as flat as possible and consequently to produce a uniform distribution of fuel burnup. Presently, due to limitations of the refuelling machines, the partly spent fuel bundles are not shuffled in the radial direction (from one channel to another).

A second consequence of importance for thermal reactors is the building-in of the intermediate fission product chain isotopes with particular high absorption cross sections, notably Xe-135 and Sm-149. When the reactor is shutdown, Sm-149 (which is stable, but a daughter of radioactive Pm-149) rises to a new equilibrium, whereas Xe-135, being radioactive, decays[42]. When the reactor is restarted, the equilibrium for both isotopes re-establish. Because of the expected drop in *k*-effective, extra fuel is built into the reactor at the beginning of the core life, which in turn requires a more extensive control system to counteract this initial "extra" *k*-effective. This is referred to as "excess reactivity" with the "reactivity" generally defined as:

$$\rho = \frac{k_{eff} - 1}{k_{eff}} \tag{3-17}$$

Many core designs include built-in absorbers, referred to as "burnable poisons" that reduce the control problems that this excess reactivity introduces. These absorbers reduce the initial *k*-effective—allowing less absorbing control systems to be used but are generally designed to be burned up before the end of the cycle so as to not shorten significantly the core lifetime.

Chapter 4.

Methodology

The objective of this work is the preliminary design of a multispectrum CANDU based reactor for the burning of actinides from dismantled nuclear weapons. The fast core is used as an actinide burner, while the thermal core becomes a power generator. To achieve this goal, a verification of coupled-reactor theory is required using the stochastic codes, MCNP and Serpent. A validation of the Serpent code for calculation of the necessary physical parameters, including the power density distribution and the burnup, is needed. With validation, the Serpent code can be used for the design of the multispectrum reactor. Accordingly, the thesis consists of the following two parts:

- Part I:

This part includes two components: (i) verification of coupled-reactor theory considering a Deuterium Critical Assembly, DCA, using the Monte Carlo N-Particle Transport (MCNP) code and Serpent code. This verification is presented in Chapter 5. (ii)The second component of the work consists of the validation of the Serpent code for a burnup calculation with the simulation of a single core for a CANDU 6 reactor. This is accomplished by comparing reactor physics parameters such as the multiplication factor, total neutron flux, radial and axial flux distributions, radial and axial power distributions in certain fuel channel(s), and a burnup calculation using both MCNP6.1 and Serpent1.1.19 codes that can be further compared to the WIMS-AECL 3.1.2.1 code[43].

The significance of this part is to establish confidence in the reactor physics parameters calculated with the Serpent code for comparison to those calculated by MCNP6 and WIMS -AECL This validation is presented in Chapter 6. Once verified, the Serpent code may be used to design the multispectrum CANDU based reactor in Chapters 7 and 8.

- Part II:

In this second part, as detailed in Chapters 7 and 8, the design of the multispectrum CANDU based reactor is presented. This part specifically consists of a study of the effects of design parameters for the multispectrum CANDU based reactor such as the lattice pitch, fuel enrichment,

and the performance of the reactor in terms of the distributions of the neutron flux, multiplication factors, regeneration factors among others.

Different models of the multispectrum CANDU reactor were simulated for different decision variables and degrees of freedom:

1. Lattice pitch of the fast core;
2. Fissile concentration of the fresh fuel of the fast core (enrichment of uranium or plutonium);
3. Number of fuel channels in the fast core; and
4. Radius of the fast core (in which three radii were considered: R_1 =137.32 cm, R_2 =108.86 cm and R_3 =80.39 cm).

Table (4-1) depicts the multispectrum CANDU reactor models investigated in the thesis. For each model, the following parameters were calculated to assess the performance of the reactor design: the multiplication factor, flux distribution, regeneration factor, form factor, power density distribution, and the fuel burnup, discharge burnup, and the percentage of destructed fissile materials.

Table (4-1): Overview of the Specifications for Various Multispectrum Reactor Models Used in this Study

Chapter	Model	Radius of the fast core (cm)	Number of fuel channels in the thermal core	Number of fuel channels in the fast core	Lattice pitch of the fast core (cm)	Fuel type of the fast core and concentration of fissile materials (Enrichment)	Calculated parameters
7	I	R_2=108.86	320	32	28.575	^{235}U (19.9%)	Excess Reactivity Multiplication Factor Regeneration Factor, Flux Distribution, Power Distribution, Form Factor, Fuel Burnup, and Changes of Atomic Densities of Actinides
	II	R_2=108.86	320	148	14.575		
8	III	R_1=137.32	292	52	28.575	Fissile material concentration 14.13% (^{239}Pu 13.89%)	
	IV	R_1=137.32	292	240	14.287		
	V	R_2=108.86	320	144	14.287		
	VI	R_3=80.39	348	76	14.287		

For the reactor of radius R_2=108.86 cm, a model was built assuming only high enriched uranium in the fast core (Chapter 7). However, ^{239}Pu was also used for the fast core to investigate the performance of cores of various radii (i.e., R_1, R_2, and R_3) (Chapter 8).

4.1. Computational Tools used in the Thesis

1) The PC-HPZ820 with 16 core and 64 Giga Ram is used in the coding and testing mode
2) Serpent code is run on the Linux platform while MCNP5 and MCNP6 were run on the Windows and Linux platform.
3) The computations of MCNP and Serpent codes for deuterium critical assembly models, CANDU6 model, and the MSCR Models are run in the high-performance Virtual Lab (HPCVL).
4) The models need an intensive calculations capability so using High-performance parallel computing is essential with using shared MPI memory
5) The average burnup calculations for full core MSCR models is between 20 to 30 days per model.
6) MATLAB and Microsoft-Excel software are used for results analyses.

Chapter 5.

Design of the Deuterium Critical Assembly

Designing a multispectrum CANDU-based reactor as a possible actinide burner requires a verification of the theory of coupled reactors using neutron transport codes. The term 'coupled' means that, in each of the regions, some of the fission neutrons are born in the other region. The numerical verification of the coupled reactors theory is performed by modeling the Deuterium Critical Assembly (DCA) using the MCNP5 code. The multiplication factors and coupling coefficients for a two-region DCA are calculated then compared with calculations and experimental results, as performed by Nishihara [27] using the TWOTRAN code [44] and DCA experiment. As a part of the current work, the numerical validation or verification of the Serpent code [45] for a multi-point reactor are required. In the current chapter, the simulation of the Deuterium Critical Assembly (DCA) is performed using the Serpent code. The effective multiplication factor k_{eff}, the criticality factors (k_{11} and k_{22}) and the coupling coefficients ($k_{12}$and $k_{21,}$) is computed using the Serpent code and compared with the values computed with from MCNP code and with the calculation of coupled reactors theory.

5.1. The Coupled Reactor Theory

The theory of a coupled reactor was first pioneered by Avery [20][23]. The theory was modified and extended by Komata [29], and Kobayashi [31] and [27]. A brief mathematical formulation of the nodal equations of the coupled reactor system was derived by Kobayashi [31].

For the two-region reactor model such as the Deuterium Critical Assembly (DCA), one can obtain easily the multiplication factor k_{eff} from Equation (5-1) which is related to regional criticality factors k_{11} and $k_{22,}$ and the coupling coefficients k_{12} and k_{21}

$$k_{eff} = \frac{1}{2}\left[k_{11} + k_{22} + \sqrt{(k_{11} - k_{22})^2 + 4k_{12} \cdot k_{21}}\right] \qquad (5\text{-}1)$$

The coupling coefficients k_{21} and k_{12} could be calculated from Equation (5-2) and (5-3) respectively.[32] In Equations (5-2) and (5-3), the sum in the denominator represents the fission

rate in the inner region $R_{f,1}$ plus the fission rate in the outer region $R_{f,2}$. This is equal to the total fission rate as directly related to the effective multiplication factor k_{eff} of the whole system. The ratio of either $R_{f,1\leftarrow 2}$ and $R_{f,2\leftarrow 1}$ over the total fission rate represents the fraction of the k_{eff} value which corresponds to the contribution of one region to the other. The total reaction rates $R_{f,1}$ and $R_{f,2}$ in each core can be calculated through Equation (5-4) where $\varphi_1(E_i)$ and $\varphi_2(E_i)$ can be defined as follows: (A) The normalized flux $\varphi_1(E_i)$ is the flux in the fast core, which is due to the fissions in the fast core plus the contribution of the fast neutrons flux $\varphi_1(E_i)_{1\leftarrow 2}$ as diffused from the thermal core to the fast core for an energy E_i , and (B), the normalized thermal flux $\varphi_2(E_i)$ is the thermal neutron flux in the thermal core, which is due to the fissions and subsequent slowing down in the thermal core plus the contribution of the flux $\varphi_2(E_i)_{2\leftarrow 1}$ diffused from the fast core to the thermal core.

The average fission cross sections were calculated for each neutron energy group (thermal, epithermal and fast). In order to calculate the values of the coefficients k_{21} and k_{12}, the fluxes, $\varphi_1(E_i)$ and $\varphi_2(E_i)$ at each energy group were calculated using an F4 tally in MCNP (or the cell detectors in case of Serpent simulation (Section 5.4). Consequently, the fission rates $R_{f,1}$ and $R_{f,2}$, $R_{f,1\leftarrow 2}$ and $R_{f,2\leftarrow 1}$can be calculated using Equations (5-4) and (5-5):

$$k_{12} = \frac{R_{f,1\leftarrow 2}}{(R_{f,1} + R_{f,2})} \times k_{eff} \tag{5-2}$$

$$k_{21} = \frac{R_{f,2\leftarrow 1}}{(R_{f,1} + R_{f,2})} \times k_{eff} \tag{5-3}$$

$$R_{f,n_{(n=1\ or\ 2)}} = \left(N_D(U_{235}) \sum_i^3 \left[\sigma_f(E_i) \times \varphi_n(E_i)\right] \right) + \left(N_D(U_{238}) \sum_i^3 \left[\sigma_f(E_i) \times \varphi_n(E_i)\right] \right) \tag{5-4}$$

$$R_{\substack{f,1\leftarrow 2 \\ or\ 2\leftarrow 1}} = \left(N_D(U_{235}) \sum_{i}^{3} \left[\sigma_f(E_i) \times \varphi_{\substack{1\leftarrow 2 \\ or\ 2\leftarrow 1}}(E_i) \right] \right) + \left(N_D(U_{238}) \sum_{i}^{3} \left[\sigma_f(E_i) \times \varphi_{\substack{1\leftarrow 2 \\ or\ 2\leftarrow 1}}(E_i) \right] \right) \quad (5\text{-}5)$$

where

k_{11}: is the average number of next generation fission neutrons in the inner fast region resulting from a single fission neutron born in the inner fast region;

k_{22}: is the average number of next generation fission neutrons in the outer thermal region resulting from a single fission neutron born in the outer thermal region;

k_{21}: is the average number of next generation fission neutrons in the outer thermal region resulting from a single fission neutron born in the inner fast region;

k_{12}: is the average number of next generation fission neutrons in the inner fast region resulting from a single fission neutron born in the outer thermal region;

$R_{f,1}$: is the fission rate in the inner region or the fast region (fission cm^{-3} s^{-1});

$R_{f,2}$: is the fission rate in the outer region or the thermal region (fission cm^{-3} s^{-1});

$R_{f,1\leftarrow 2}$: is the fission rate in the inner region triggered by neutrons born in the outer region (fission cm^{-3} s^{-1});

$R_{f,2\leftarrow 1}$: is the fission rate in the outer core triggered by neutrons born in the inner region (fission cm^{-3} s^{-1});

$N_D(U_{235})$: is the number density of uranium isotope (U-235);

$N_D(U_{238})$: is the number density of uranium isotope (U-238);

$\sigma_f(E_i)$:is the fission cross section at energy group E_i;

$\varphi_{1\leftarrow 2}(E_i)$: is the neutron flux of energy group E_i that diffused from the thermal region (2) to the fast region (1), and

$\varphi_{2\leftarrow1}(E_i)$: is the neutron flux of energy group E_i that diffused from to the fast region (1) the thermal region (2).

The advantage of using the theory of coupled reactors consists in the consist of gain a better understanding in the criticality factor for each region rather just for the whole system, which helps in improving the physical understanding of the detailed characteristics of the multispectrum system as an actinide burner.

5.2. Deuterium Critical Assembly

The DCA has a cylindrical geometry with an outer radius of 150.25 cm. It consists of two reactor core regions. The inner region has a dominant fast neutron energy spectrum, while the outer region has a dominant thermal energy spectrum. The inner and outer regions are separated by an air gap of thickness 9.2 cm as shown in Figure (5-1) The inner region or fast neutron flux core is loaded with 2.7 wt% U-235/U enriched metallic uranium fuel rods in aluminum clad surrounded by light water coolant. The lattice pitch of the fast core has a small value (1.9 cm) to minimize as much as possible the moderation of the fast neutrons by light water. It consists of 140 fuel rods distributed within a square lattice with a lattice pitch (1.9 cm). The middle cell of the inner region consists of an air tube of inner radius 1.5 cm and an aluminum wall of thickness 0.2 cm. The inner core consists of an aluminum cylinder of inner radius 16.8 cm and outer radius 17.5 cm. The outer region or the thermal core is loaded with 1.2 wt% U-235/U enriched metallic uranium rods in aluminum clad of thickness 1.3 mm surrounded by heavy water. The thermal core lattice was optimized to 474 fuel clusters in a square lattice cells with a thermal lattice pitch of 9.66 cm. Each cluster has four fuel rods for total of 1896 fuel rods

In the outer thermal core, heavy water is used as moderator and coolant. The inner radius of the outer core is 33.851 cm and the outer radius is 133.875 cm. The outer core is surrounded by two heavy water reflectors. The outer reflector thickness is 16.375 cm and the inner reflector thickness is 4.351 cm. In both cores, the fuel rod diameter is 1.45 cm and its length is 200 cm. Both regions would be independently subcritical on their own when the levels of light water and heavy water are at the mid height (100cm) in both cores.

The combination of the two regions is designed in such a way that the neutron leakage between them can provide sufficient reactivity to drive the combined system to criticality. The details of the Deuterium Critical Assembly (DCA) are shown in Figure (5-1) [27].

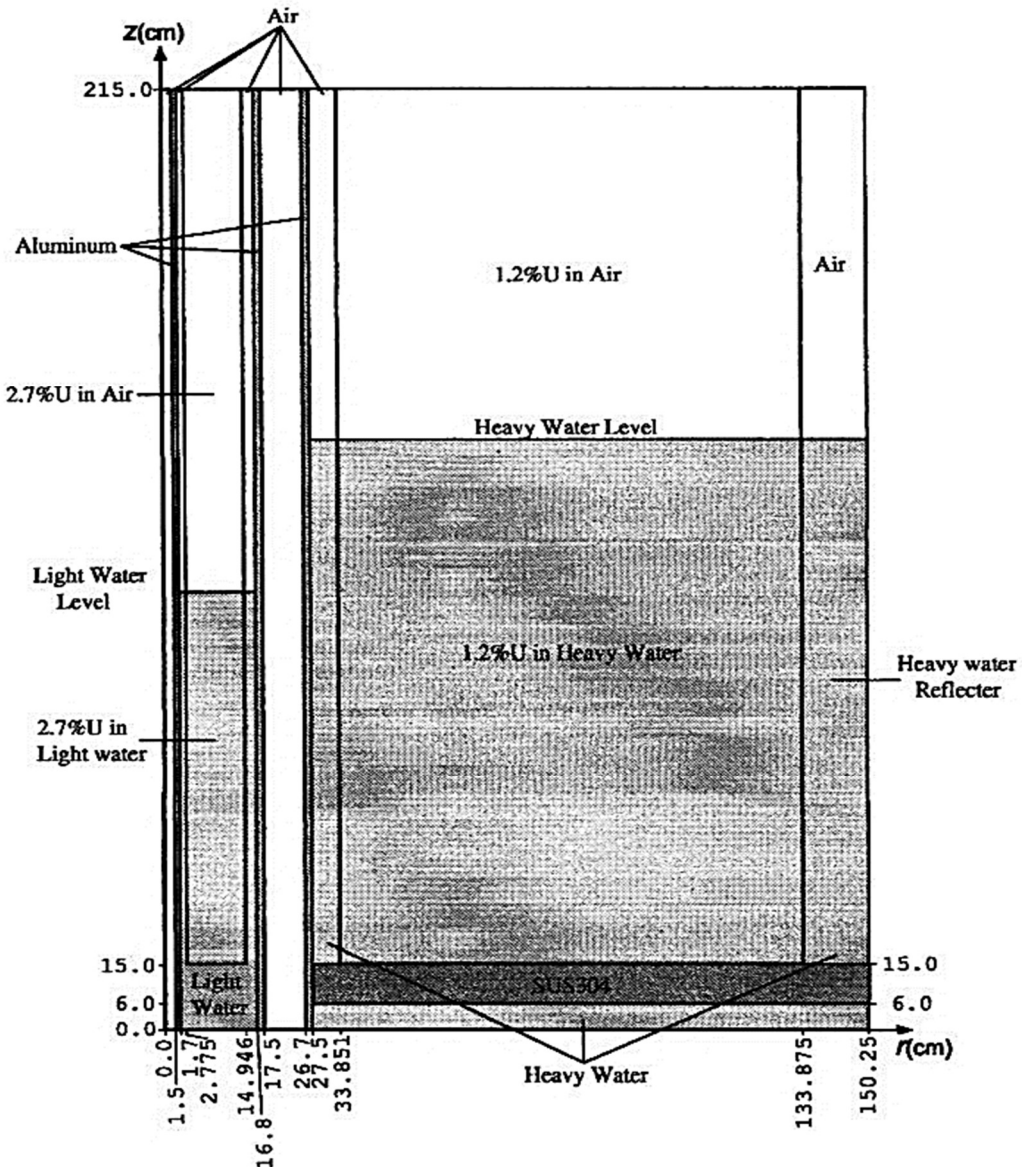

Figure (5-1): Diagram of the Deuterium Critical Assembly (DCA).

The Shape and Dimensions of the Fuel Clusters are Presented in Details in[27]**.**

There are some data that were not included in the Nishihara's [27] published work of the DCA model. These unknown data values are used as a degree of freedom for the DCA optimization. The missing data include: 1) the number of fuel pins in the thermal region, 2) the lattice pitch of the

thermal region and, 3) the thickness of the aluminum clad of the fuel in the whole DCA reactor. An MCNP5 model is created with the exact dimensions and structures using only these three degrees of freedom. The constraints in this simulation include: i) the two regions should be subcritical on their own, and ii) the values of the criticality factors as published by Nishihara [27] are when the light and heavy water (LW and HW) levels in the two regions are at a height of 100 cm. The lattice pitch and number of fuel pins per lattice in the thermal region were optimized.

The optimum values of the thermal lattice pitch are 9.66 cm and the number of fuel pins is 4 pins per lattice cell. The last degree of freedom (or the remaining unknown value) is the thickness of the aluminum cladding. The clad thickness was changed from 0.5 mm up to 1.5 mm. Then, the criticality factors k_{eff}, k_{11} and k_{22} were compared using the same values under the same conditions as the results of Nishihara [1] (as shown in Table (5-1)).

Table (5-1): Determination of the Optimum Value of the Aluminum Cladding Thickness

	Al-Clad thickness (cm)	k_{eff} at F100-T100	k_{22} at F100-T100	k_{11} at F100-T100
Reference data[27]	not included	1.020	0.988	0.810
Current calculations	0.1300	1.0234	0.9983	0.7424

The thermal core lattice was optimized to 474 fuel clusters in a square lattice cell. The thermal lattice pitch is 9.66 cm. Each cluster has four fuel rods for a total of 1896 fuel rods. The aluminum clad thickness of the fuel rod is optimized to 1.3 mm. This optimum value provides the closest value to the criticality factors produced by Nishihara [27] as shown in Table (5-1).

5.3. Numerical Verification of the Theory of Coupled Reactors for the Deuterium Critical Assembly (DCA) Using MCNP5

The probabilistic computer code MCNP5 (Monte Carlo N-Particle) [46] is used to simulate the DCA experiment [47]. The nuclear data library used with MCNP5 is ENDF/B-VI.5, which is the same library used with TWOTRAN[44] in Nishihara's work[27]. The materials' temperatures were set at a room temperature of 293.6 K. The criticality factors k_{eff}, k_{11} and k_{22} were computed with MCNP5 along with the coupling coefficients k_{12} and k_{21} from Equations (2-1) and ((2-2). The coupling between the two DCA regions is verified by comparing k_{eff} calculated by Equation ((2-3) with the value computed directly by MCNP5 and that computed by Nishihara [27] with the TWOTRAN code.

5.3.1. Methodology

The DCA model is designed using MCNP5 code[46][48], Figure (5-2) shows the vertical section and Figure (5-3) shows the horizontal cross section of the DCA, the lattice pitch of each core, and fast core cross section.

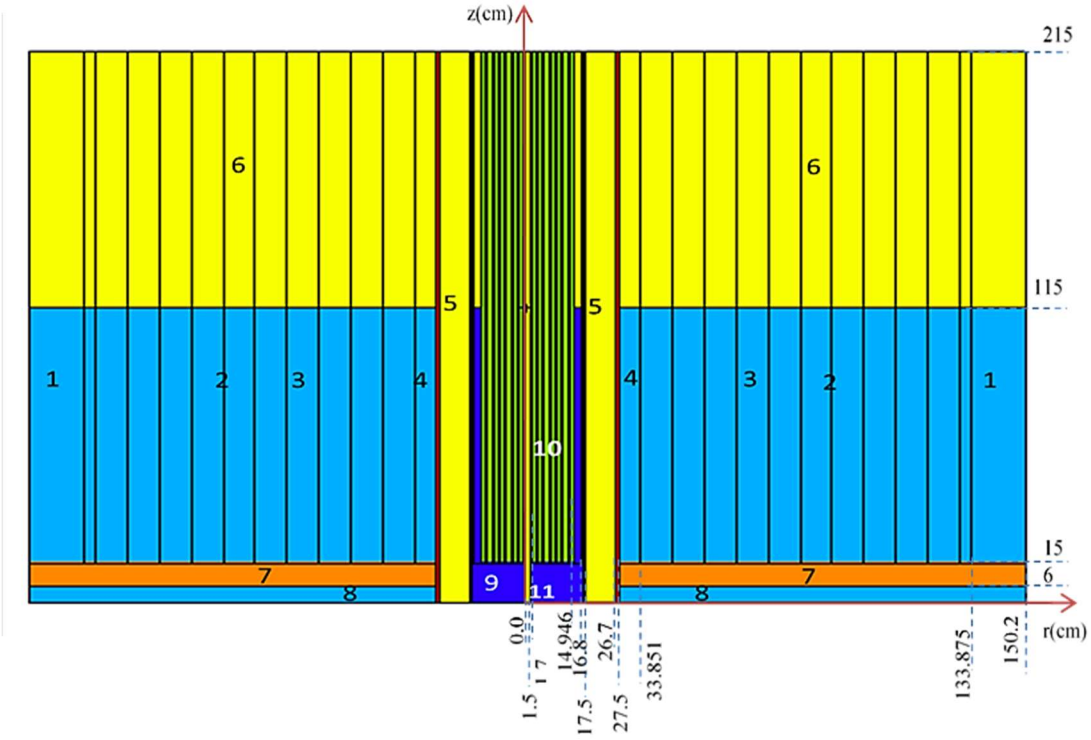

(1) Heavy water external reflector.
(2) Thermal core fuel lattice.
(3) Heavy water moderator.
(4) Internal heavy water reflector.
(5) Air gap
(6) Air upper the thermal core
(7) Steel (SUS340)
(8) Heavy water.
(9) Light water in the fast core
(10) Fast core fuel lattice.
(11) Aluminum tube in the middle of the fast core of wall thickness 0.2 mm. it contains air.

Figure (5-2): MCNP Model of the Deuterium Critical Assembly (Vertical Cross Section)

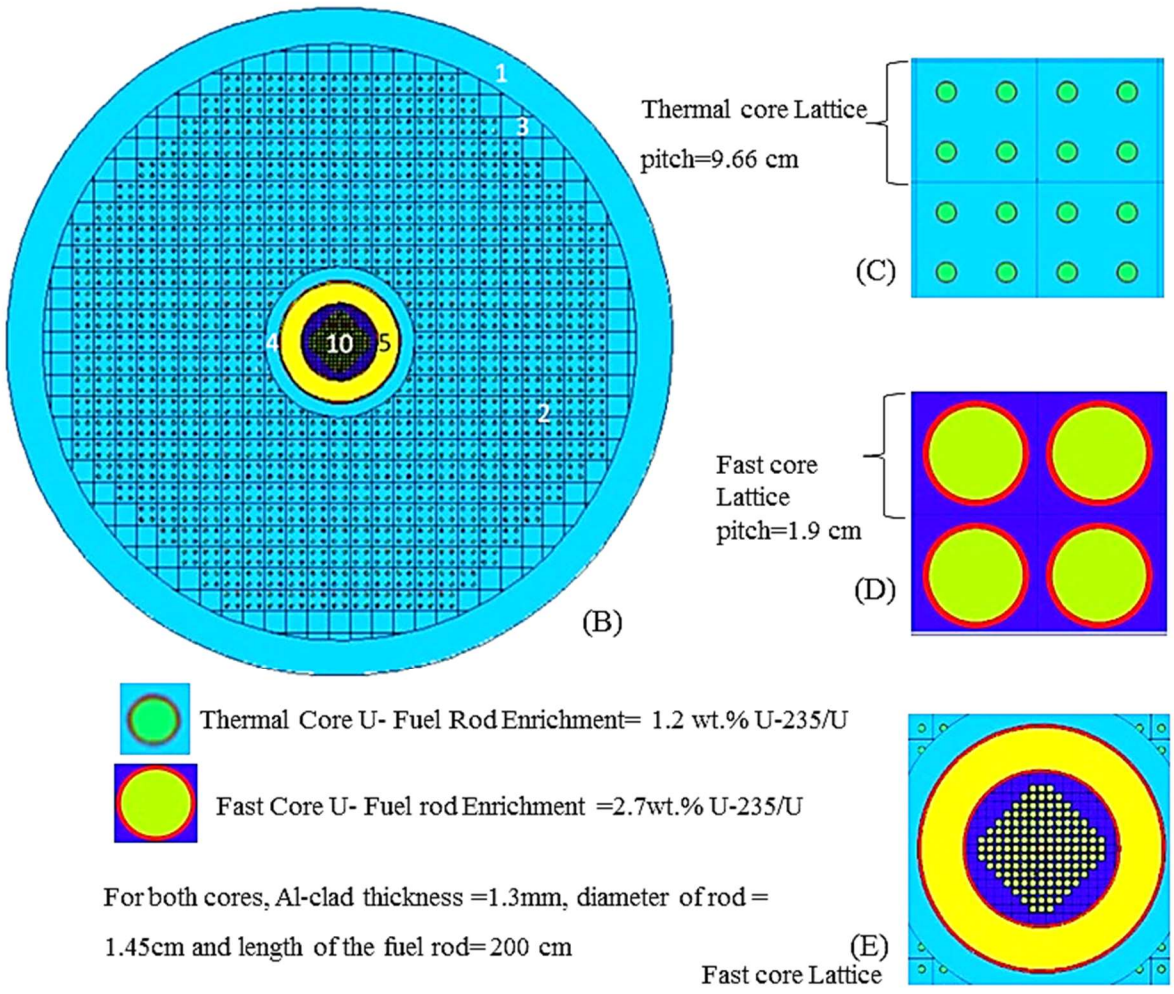

Figure (5-3): MCNP Model of the Deuterium Critical Assembly (Horizontal Cross Section)

The simulation steps can be summarized as follows:

1) To find the optimum value of the number of cycles and number of neutrons per cycle to be used in the criticality calculations, the DCA model designed by MCNP5 code were run at different number cycles with a different number of neutrons per cycle

2) These simulations are run for the cases of both light water and heavy water at 100 cm in the fast and thermal core. The best convergence of k_{eff} value was obtained for the number of neutrons and the number of cycles set at 10000 neutrons per cycle and 500 cycles respectively. These values represent the first converging value of k_{eff}. as shown in Figure (5-4)

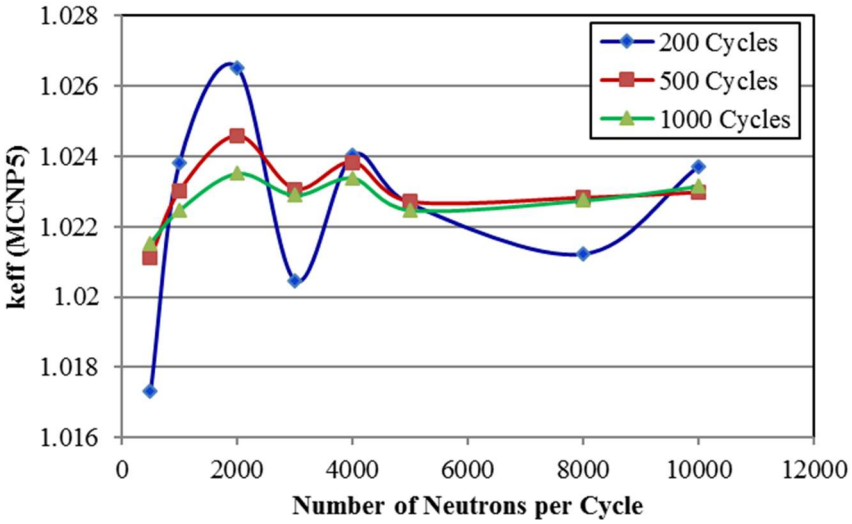

Figure (5-4): The Convergence Value of k_{eff} with the Number of Cycles and Number of Neutron Per Cycle Using MCNP5

3) As the DCA model was optimized, the coupling theory was verified by driving the system to criticality. Different values of criticality factors k_{eff}, k_{11} and k_{22} and corresponding values of coefficients k_{12} and k_{21} were calculated by changing the level of heavy water in the thermal region and setting the light water level at 100 cm in the fast region, and vice versa.

4) The criticality factor k_{11} was calculated by setting the importance of neutrons in the thermal part at a zero value and calculating the k_{eff} of the system, which represents only the criticality coefficient k_{11} of the fast region. Similarly, the criticality factor k_{22} was calculated by setting the importance of the neutrons in the fast region to a value of zero.

5) By using the flagged cell tally CF4 in the MCNP5 [47] code, the neutron fluxes ($\varphi_{1\leftarrow 2}$ *or* $\varphi_{2\leftarrow 1}$) for three energy groups that diffuse from the thermal region to the fast region and vice versa can be calculated. Here the flagged cell is the cell between the fast core and the thermal core that is used for the calculation of the average neutron flux as diffused from one region to another. In the current model, the air gap cell (cell 5) is used as a flagged cell to calculate the flag fluxes.

6) The fission rates $R_{f,1-2}$ and $R_{f,2-1}$ can be calculated, and then the coupling coefficients k_{12} and k_{21} can be found from Equations (5-4) and (5-5), respectively. Both k_{11} and k_{22} were calculated for various the levels of water in the fast and thermal regions, respectively.

7) The average cross sections were calculated for each neutron energy group (thermal, epithermal and fast) corresponding to energy ranges 10^{-11} eV to 0.625 eV, 0.625 eV to 0.1 MeV and 0.1 MeV to 14 MeV, respectively. The fission rates $R_{1\rightarrow 2}$ and $R_{2\leftarrow 1}$ were also calculated. Consequently, the coupling coefficients k_{21} and k_{12} can be calculated from Equations (5-2) and (5-3), respectively.

The multiplication factor k_{eff} calculated from the coupling Equation (5-1) were compared with the multiplication factors k_{eff} that were evaluated numerically with MCNP5 for the system for different levels of heavy and light water in the two regions.

5.3.2. Results and Discussion

The dependence of the multiplication factor k_{eff}, and criticality factors k_{11} and k_{22} and coupling coefficients k_{12} and k_{21} for different levels of heavy water in the thermal region, with the level of light water in the fast region set at 100 cm, is shown in Figure (5-5) and Figure (5-6). While the dependence of factors k_{eff} , k_{11} and k_{22} and coefficients k_{12} and k_{21} at different levels of light water in the fast region, with the level of heavy water in the thermal region set at 100 cm, are shown in Figure (5-7), Figure (5-9).and Figure (5-9)

1) In Figure (5-5) as the heavy water level is increased in the thermal region, the criticality factors of this region k_{22} increase gradually. Consequently, the criticality coefficient k_{12} increases as more neutrons diffuse from the thermal region to the fast one, resulting in more fission interactions. There is a small increase in the criticality coefficient k_{21} due to an increase in the fission rate in the fast core because there is a small number of neutrons diffusing from the fast to the thermal region. These values affect the total values of k_{eff} at each heavy water level. The value of k_{11} is not changed because it is calculated independently at a fixed level of light water in the thermal core.

2) Figure (5-6) represents the detailed behaviour of the change of the multiplication factors k_{eff} from the MCNP5 calculations, the coupling equation calculations and those calculated by

[27] using the TWOTRAN [44] code as the heavy water level increases from 0 to 200 cm. Very good agreement is seen between the k_{eff} value calculated directly by MCNP5 and that calculated from the coupling theory, with an overall percentage difference between these results being 1.6%. Therefore, the coupling theory is verified through the MCNP5 code[46] .

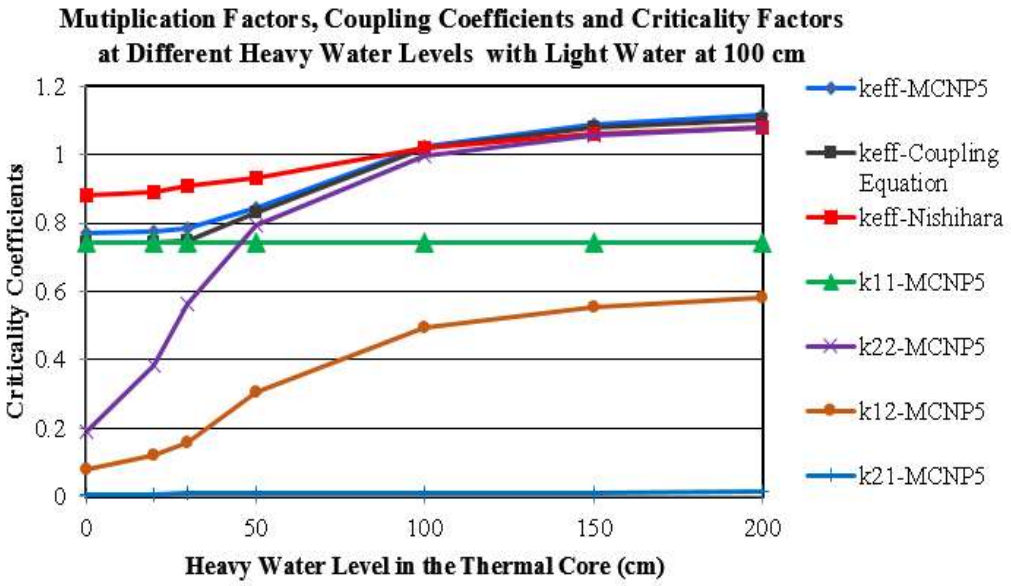

Figure (5-5): Criticality Factor and Coupling Coefficients at Different Heavy Water Levels in the Thermal Core with Light Water Level at 100 cm in the Fast Core.

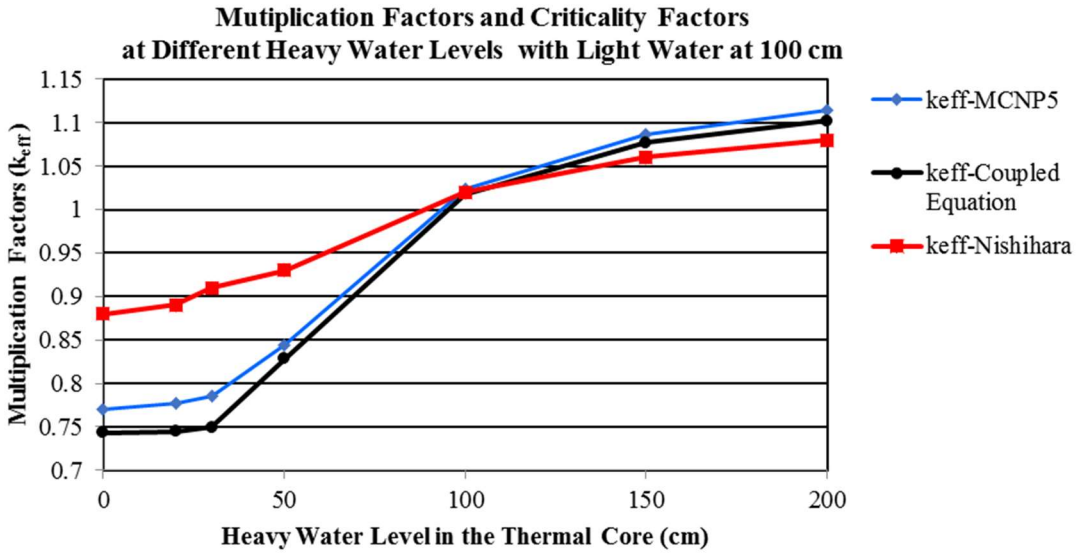

Figure (5-6): Criticality Factors at Different Heavy Water Levels in the Thermal Core with Light Water at 100 cm in the Fast Core.

3) From Figure (5-7) as the light water level is increased in the fast region, the criticality factor of this region, k_{11}, increases sharply until the light water level is around 25 cm. Then it increases gradually until the light water level reaches 100 cm. This result is due to light-water moderation in the fast core. But, as the level of light water increases, the rate of neutron absorption also increases thereby providing a flattening of the criticality factor k_{11} as the value of the fast core.

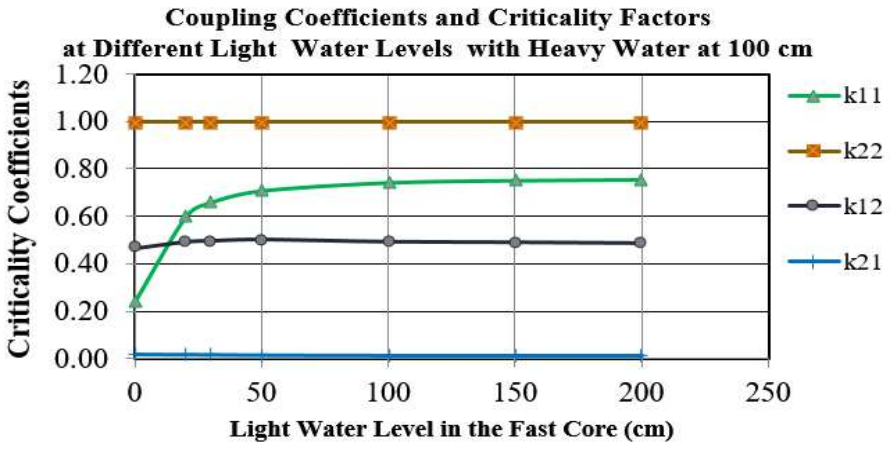

Figure (5-7): Criticality Factor and Coupling Coefficients at Different Light Water Levels in the Fast Core with Heavy Water at 100 cm in the Thermal Core.

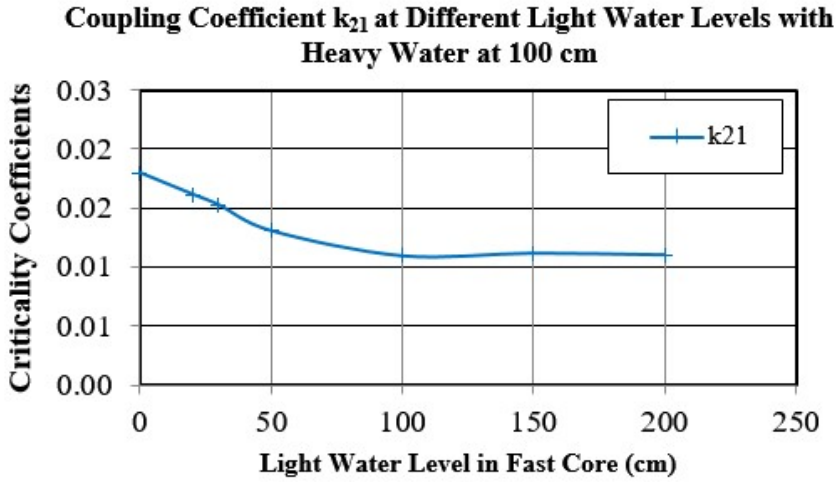

Figure (5-8): Variation of Coupling Coefficient k_{21} at Different Light Water Levels in the Fast Core with Heavy Water at 100 cm in the Thermal Core.

4) From Figure (5-8) the coupling coefficient k_{21} decreases slightly as the light water level increases in the fast region until the its level reaches to 100 cm. This slightly decrease in the diffusion of neutrons from the fast to thermal region is due to the absorption of the neutrons in the fast region by the light water in addition to slight moderation that increases the neutron absorption. The rate of this neutrons diffusion comes to constant value when the level of water become 100 cm in the fast region and above, because of the difference between the rate of absorption and rate of production of the neutrons from fast fission equal constant value. Consequently, the rate of diffusion of neutrons from the fast region to the thermal region or the reaction rate by these neutrons becomes constant value.

5) From Figure (5-6) and Figure (5-9), the contribution of the thermal region to the values of k_{eff} is more important than that of the fast one due to its larger volume and the amount of fuel in the thermal region in addition to the contribution of the heavy water moderation and reflectors in the thermal fission.

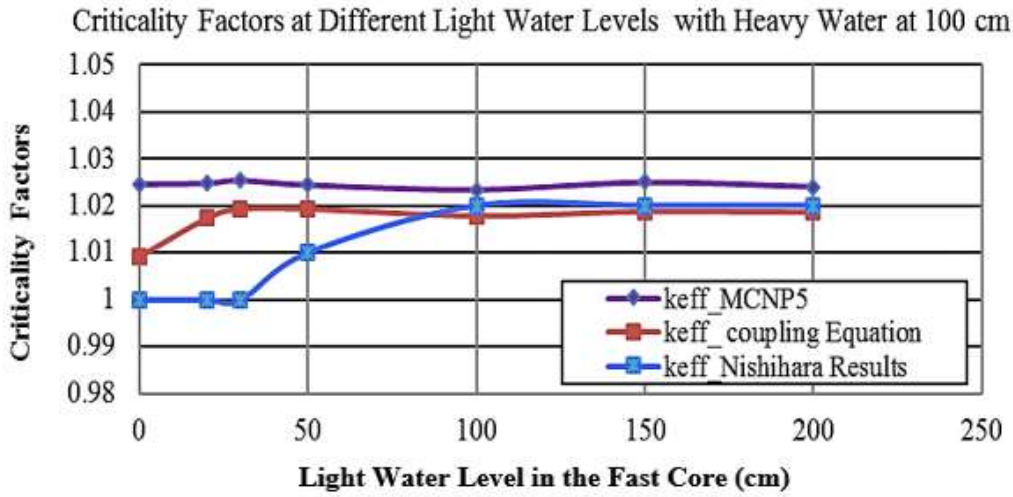

Figure (5-9): Variation of Multiplication Factor at Different Light Water Levels in the Fast Core with Heavy Water at 100 cm in the Thermal Core.

6) As shown in Figure (5-6), when the light water level is fixed at 100 cm in the fast region while the level of heavy water in the thermal region changes from zero to 100 cm, there is a reasonable agreement between the values of k_{eff} as calculated by MCNP5 and those calculated by [27] using the code [44] with a percentage difference of 8%. When the level of heavy water in the thermal region changes from 100 to 200, very good agreement is observed (with a percentage difference of 1.2%). For both cases, the average percentage difference is 4.6%.

7) As shown in Figure (5-9), when the level of heavy water is set at 100 cm in the thermal region, while changing the level of light water in the fast region shows excellent agreement within 2.7%, for k_{eff} as calculated by MCNP5 and that calculated by [27] with the code in Ref. [44]

8) The values of k_{eff} calculated by MCNP5 code are in excellent agreement with those calculated from the coupling Equation (5-2). The minor differences in the results may due to: (a) the use of a three energy group model in the present DCA work rather than a four energy groups as considered in the work of Nishihara [27], (b) the use of a different cross section library, and (c) the inaccuracy of the TWOTRAN code [44] at this energy range for fast reactor criticality calculations.

5.4. Validation of Serpent Codes Using the Application of the Theory of Coupled Reactors for the Deuterium Critical Assembly.

The DCA model was simulated and compared with the results from MCNP5 [46]. The nuclear data library used with both MCNP5 and Serpent is ENDF/B-VII. The multiplication factor k_{eff}, and criticality factors (k_{11} and k_{22}) were computed with both codes along with the coupling coefficients k_{12} and k_{21} from Equations (5.2) and (5.3). The coupling between the two DCA regions is validated by comparing k_{eff} as calculated by Equation (5.1) with that computed by MCNP5 and Serpent. The flux is also calculated in addition to the criticality coefficient and criticality factors.

The components (a), and (b) of the Figure (5-10) show the vertical and horizontal cross sections of the DCA model for a level of heavy water and light water in the thermal and fast regions set at 100 cm in the Serpent models. The components (c), (d) and (e) show close-up views of the lattice pitch of the thermal and fast cores model simulated using the Serpent code.

Due to the limitations of the Serpent code for temperatures less than 300 K, the temperature in the Serpent code is set at 300 K, while the temperature of the MCNP5 code is set to the closest value in the chosen library at 293.6 K. Some of the MCNP5 models were run at 300 K but there is no significant difference with this small temperature difference. To realize the DCA criticality condition, the aluminum clad thickness in the whole DCA was optimized to the value of 1.3 mm as presented in Table (5-1). The models were optimized to realize the DCA criticality condition. The fast core and thermal core should be subcritical independently when the levels of light water and heavy water are at 100 cm height. In both simulation models for the calculation of k_{11} and k_{22}, the air gap (cell 5 in Figure (5-10) is added to the thermal region only. The reason for the air gap in the thermal core is to consider the neutrons that may escape from the thermal core and back to it through the air gap.

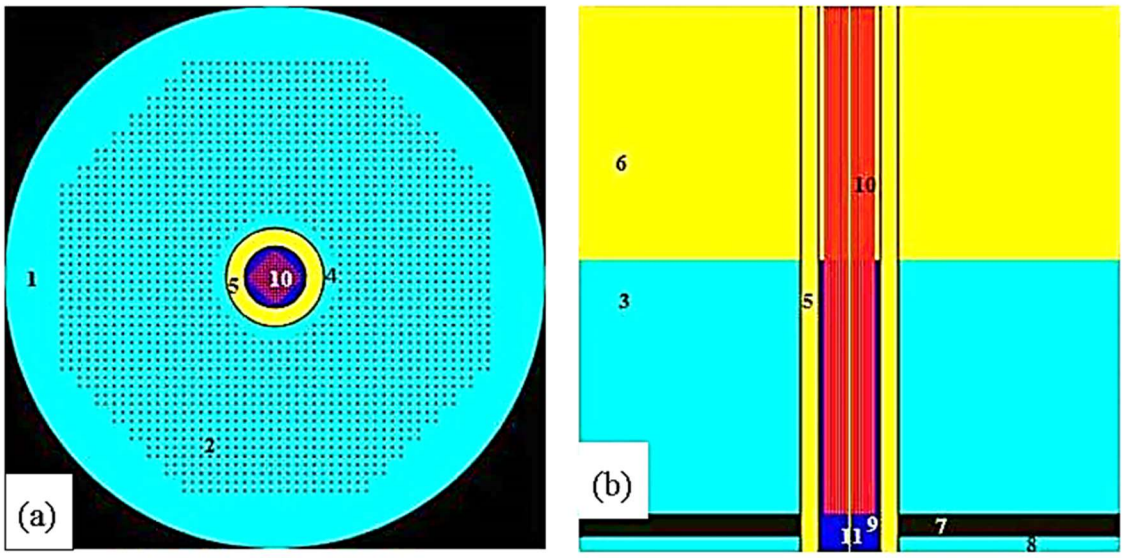

(1) Heavy water external reflector.
(2) Thermal core fuel lattice.
(3) Heavy water moderator and coolant
(4) Internal heavy water reflector.
(5) Air gap
(6) Air above the thermal core
(7) Steel (SUS340)
(8) Heavy water.
(9) Light water in the fast core (coolant)
(10) Fast core fuel lattice.
(11) Aluminum tube in the middle of the fast core of wall thickness 0.2 mm. It contains air.

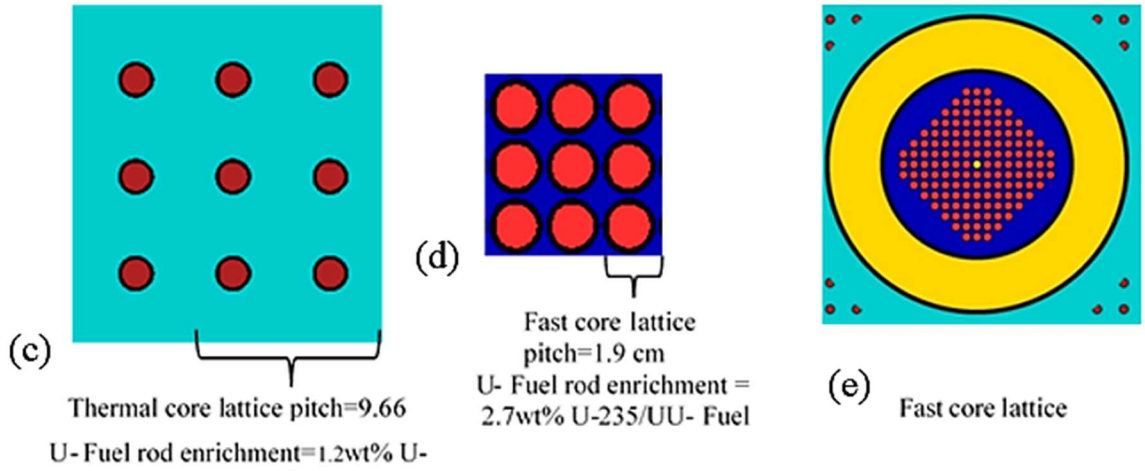

For both cores, Al-clad thickness =1.4 mm, diameter of rod = 1.45cm and length of the fuel rod= 200 cm

Figure (5-10): Serpent Model of the Deuterium Critical Assembly

5.4.1. Methodology

To find the optimum value of the number of cycles and number of neutrons per cycle to be used in the criticality calculations, the DCA model designed by Serpent code was run at a different number of cycles with a different number of neutrons per cycle as shown in Figure (5-11).

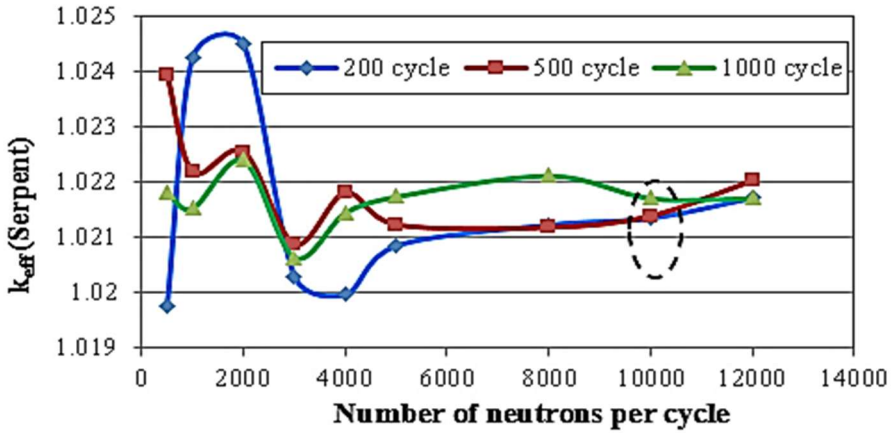

Figure (5-11): The Convergence Value of k_{eff} with the Number of Cycles and Number of Neutron per Cycle Using Serpent

These simulations are run for both cases of both light water and heavy water at 100 cm in the fast and thermal core. The best convergence of the k_{eff} value was obtained for the number of neutrons and the number of cycles set at 10,000 neutrons per cycle and 1,000 cycles respectively. These values represent the first converging value of k_{eff}.

As the DCA model was optimized and the coupling reactor theory was verified by driving the system to criticality. Different values of criticality factors k_{eff}, k_{11} and k_{22} and corresponding values of coupling coefficients k_{12} and k_{21} were calculated by changing the level of heavy water in the thermal region and setting the light water level at 100 cm in the fast region, and vice versa. The simulation and calculations steps are the same steps as shown in Section 5.3.1.

MCNP and Serpent calculate the track length estimator flux (TLE-flux), which is defined as the sum of total track lengths of the neutrons per number of track lengths per volume of the cell. The units of track length estimator flux are in n cm^{-2}. The relation between the track length estimator flux and actual flux in n cm^{-2} s^{-1} is shown in Appendix (A). In the current calculation of the fission rates, Equations (5-4) and (5-5) where used for the calculation of k_{12} and k_{21} in

Equations (5-2) and (5-3). Therefore, k_{12} and k_{21} are calculated from the neutron track length estimator flux using the F4 flux tally and the CF4 flagging tally given in MCNP5. The flagging flux of the thermal core is defined as the part of the flux contributed from the thermal core having passed to the fast core. The flagging cell used is the air gap cell is cell 5 in Figure (5-10).

There is a limitation of Serpent for the flagging of the cell flux detector. However, given the agreement between the TLE-flux values in the fast core $\Phi_1(\mathrm{E_i})$ and thermal core $\Phi_2(\mathrm{E_i})$ as calculated with MCNP5 and Serpent, the flag-weighted TLE-flux from MCNP5 can be used to calculate the flagged TLE-flux in Serpent. These fluxes are normalized to the number for the neutron history and volume. The flagged flux from the thermal core in the air gap of cell, $\Phi_n(E_i)_{1\leftarrow 2}(Serpent)$ can be calculated by multiplying the thermal TLE-flux $\Phi_2(\mathrm{E_i})$ from Serpent times the ratio between the flagging TLE-flux $\Phi_n(E_i)_{1\leftarrow 2}(MCNP)$ and the thermal TLE-flux of the core $\Phi_2(\mathrm{E_i})(MCNP)$. This ratio is called flag weighted flux shown in Equation (5-6). The same method is used to calculate the flagging flux from the fast core to the thermal one:

$$\varphi_n(E_i)_{\substack{1\leftarrow 2 \\ or\ 2\leftarrow 1}}(Serpent) = \frac{\Phi_n(E_i)_{\substack{1\leftarrow 2 \\ or\ 2\leftarrow 1}}(MCNP)}{\Phi_n(E_i)\ (MCNP)} \times \Phi_n(E_i)\ (Serpent) \qquad (5\text{-}6)$$

where, i=1,2 or 3 represents the bin of thermal, epithermal or fast energy, respectively and, n=1 for the fast core flux and n=2 for the thermal core flux.

5.5. Comparison between Results of MCNP5 and Serpent Codes

5.5.1. Comparison between Track Length Estimator Flux calculated by MCNP5 and Serpent Codes

Figure (5-12) to Figure (5-15) present the track length estimator fluxes are given by the tally F4 in MCNP5 and the cell flux detector in Serpent. These are the fluxes at each energy bin as normalized to the volume and number history. Excellent agreement is observed for the fluxes as calculated by MCNP5 and Serpent. Therefore, the following discussion applies to the flux results from both codes.

1) Figure (5-12) represents the flux distribution in the thermal core with an increasing level of light water in the fast core for the three energy groups. As the light water level increases,

the fast and epithermal fluxes decrease due to moderation in the light water. Consequently, the thermal fluxes increase gradually. Above 100 cm, the thermal fluxes and the epithermal fluxes are increase very slowly while the fast fluxes are almost constant.

2) A small increase in the thermal and epithermal fluxes are due to more moderation with an increased level of light water. Also as the light water increases, more moderation occurs for neutrons that have diffused from the thermal core thereby increasing the thermal flux in the fast core.

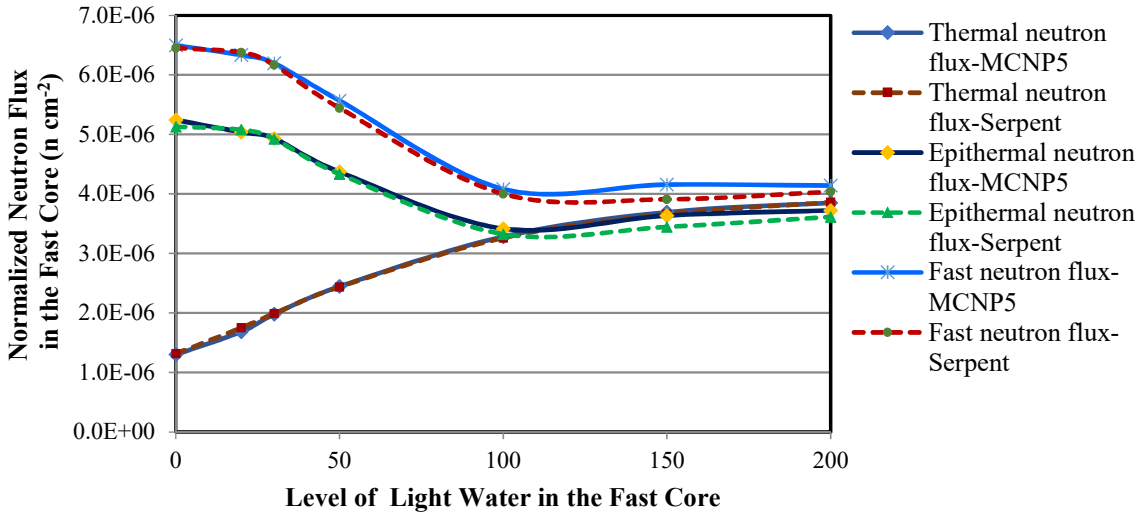

Figure (5-12): Variations of the Normalized Fluxes in the Fast Core for Different Levels of Light Water in the Fast Core, for a Heavy Water Level of 100 cm in the Thermal Core.

3) Figure (5-13) presents the effect due to changing the heavy water in the thermal core on the three group fluxes in the fast core. As the heavy water level increases, the fluxes for the three groups decrease. The fast and epithermal fluxes are decreasing strongly due to the strong effect of moderation in heavy water. Consequently, more absorption, fission and radioactive capture occur in the thermal core. Therefore, the thermal flux in the fast core also decreases. The neutron fluxes for all three groups reach a constant value when the level of heavy water exceeds 100 cm because the rate of fission is then almost equal to the rate of absorption and moderation.

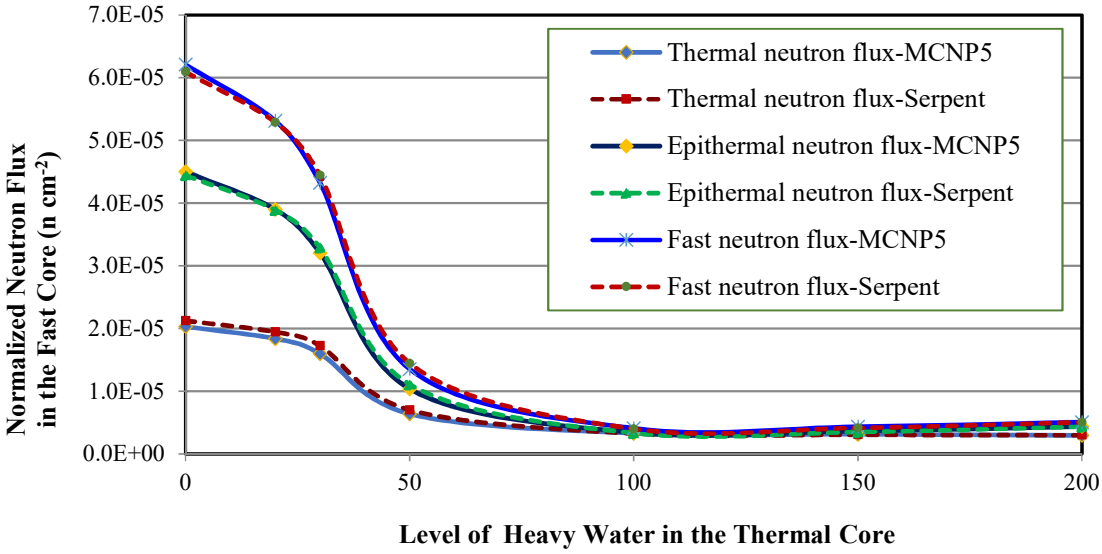

Figure (5-13) Variations of the Normalized Fluxes in the Fast Core for Different Levels of Heavy Water in the Thermal Core, and for a 100 cm Light Water Level in the Fast Core.

4) In Figure (5-14), as the light water level increases in the fast core, the only significant change in the thermal core occurs for the epithermal flux. This is due to the moderation effect of the light water on the fast neutrons generated in the fast core before it defused to the thermal one. The other group fluxes are not significantly changed with the large difference between the volumes and amount of fuel in the fast and thermal cores.

5) From Figure (5-15), as the heavy water level increases in the thermal core, the fast neutron flux level decreases due to moderation. The epithermal and thermal fluxes increase and come to constant values at a heavy water level of 150 cm when the rates of moderation from the fast-to-epithermal and from epithermal-to-thermal group regions are similar.

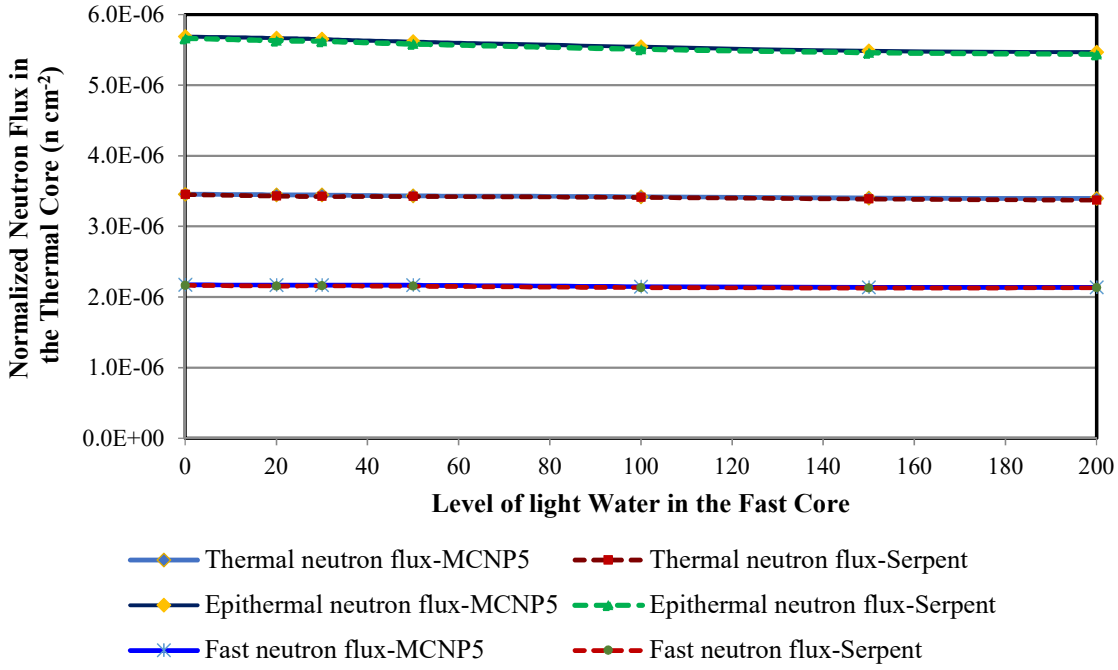

Figure (5-14): Variations of the Normalized Fluxes in the Thermal Core for Different Levels of Light Water in the Fast Core, and for a 100 cm Heavy Water Level in the Thermal Core

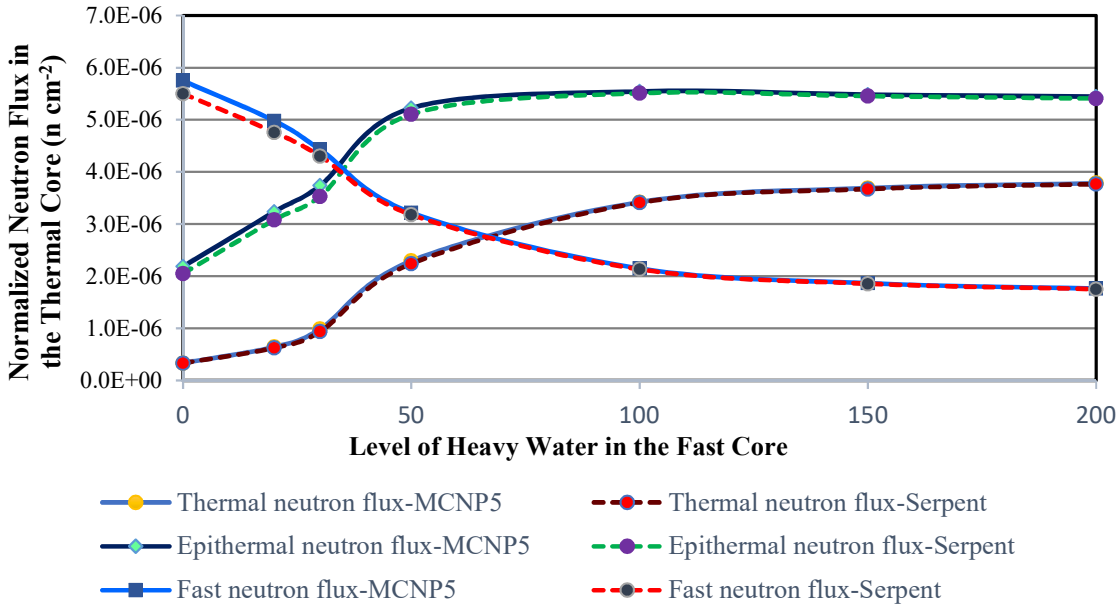

Figure (5-15): Variations of the Normalized Fluxes in the Thermal Core for Different Levels of Heavy Water in the Fast Core, and for a 100 cm Light Water Level in the Fast Core.

5.5.2. Comparison between Criticality Factors and Criticality Coefficients Calculated by the Codes MCNP5 and Serpent.

The multiplication factors k_{eff} from the coupling Equation (5-1), and based on the criticality factors k_{11}, k_{22}, and the coupling coefficients k_{12}, k_{21} from both MCNP5 and Serpent, can be compared with the multiplication factors k_{eff} calculated numerically and independently by both the MCNP5 and Serpent codes.

- ***At Fixed Level of the Heavy Water in the Thermal Core***

In this subsection, the heavy water in the thermal is fixed at 100 cm while the light water in the fast core is varied from 0 to 200 cm. From Figure (5-16), there is a consistency for the criticality factors k_{11}, k_{22} and coupling coefficients k_{12} and k_{21} as calculated with MCNP5 and Serpent. The multiplication factor k_{eff} calculated by both methods match.

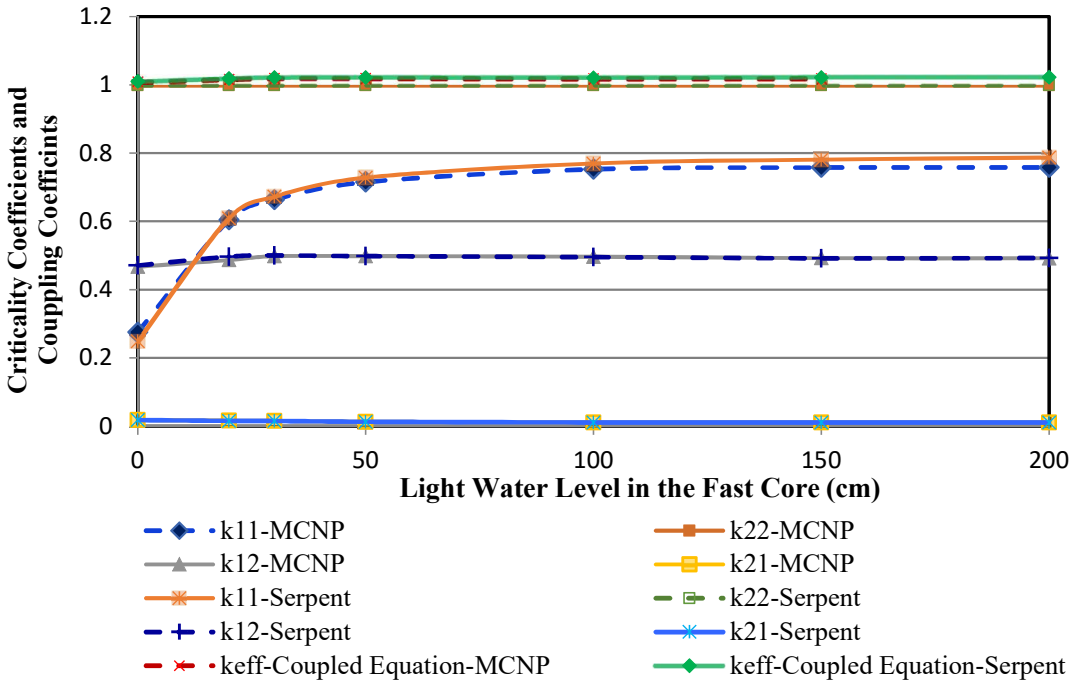

Figure (5-16): Criticality Factors and Coupling Coefficients for Different Light Water Levels in the Fast Core with the Heavy Water Level at 100 cm in the Thermal Core, Calculated by Serpent, MCNP5 Codes and with the Coupled Reactor Equation.

1) Figure (5-17) presents the comparison between the multiplication factors k_{eff} calculated directly by both MCNP5 and Serpent and that calculated by the coupled reactor equation. One observes good agreement as k_{eff} calculated by the two codes and from coupled reactor theory.

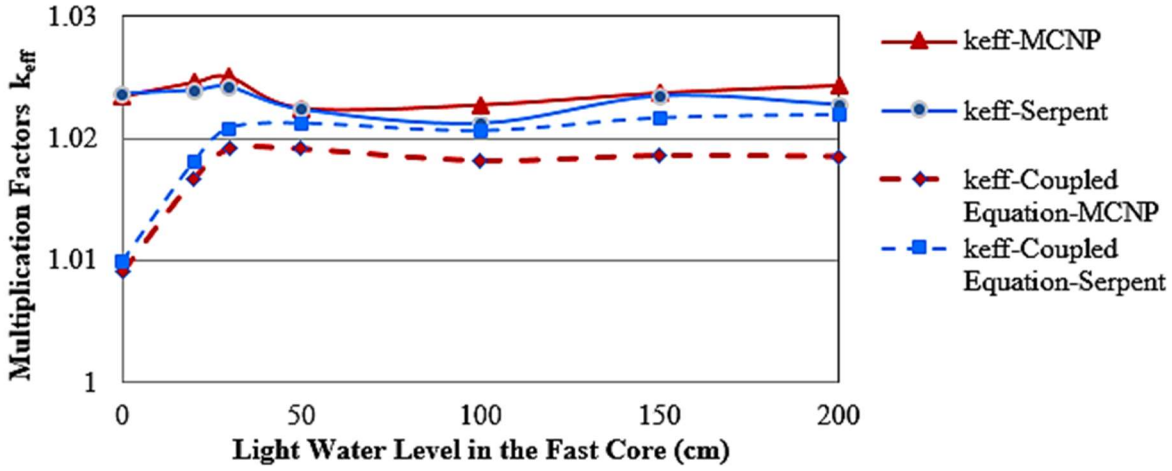

Figure (5-17): Multiplication Factors k_{eff} for Different Light Water Levels for a 100 cm Heavy Water Level as Calculated by Serpent and MCNP5 and with the Coupled Reactor Equation.

The average percentage differences were calculated according to Equation (5-7):

$$\Delta\%_{\substack{(MCNP5-Serpent)\ or;\\ Coupled\ Equation\ MCNP5\ or;\\ Coupled\ Equation\ Serpent}} = 100\times\left(\frac{(k_{eff})_{\substack{MCNP\ \ or;\\ MCNP5\ or;\\ Serpent}} - (k_{eff})_{\substack{Serpent\ or;\\ Coupled\ Equation\ MCNP5\ or;\\ Coupled\ Equation\ Serpent}}}{(k_{eff})_{\substack{MCNP\ \ or;\\ MCNP5\ or;\\ Serpent}}}\right) \quad (5\text{-}7)$$

Table (5-2) presents the average percentage differences for k_{eff} calculated by MCNP5 and Serpent and from the coupled reactor theory. The results demonstrate validated results between the codes and mathematical coupled reactor theory model.

Table (5-2): Average Percentage Difference between k_{eff} as Calculated by MCNP5, Serpent and the Coupled Reactor Theory when Setting the Levels of Heavy Water at 100 cm and Change the Level of the Light Water from 0 to 200 cm

	%Δkeff (MCNP5-Serpent)	%Δkeff (MCNP5-Coupling theory)	%Δkeff (Serpent-Coupling theory
Average percentage of difference of k_{eff}	0.07%	0.65%	0.38%

There is an excellent agreement with an average relative percentage ratio of 0.6%. The validation of the Serpent code for coupled reactor calculations provides the advantage that it can be used for designing of the multispectrum CANDU-based reactor. MCNP5 and Serpent codes therefore represent valid tools for the modelling of coupled reactors.

2) Figure (5-18) (A) and (B) represent close-ups of the criticality factors k_{11} and k_{22}. As the light water level increases in the fast core, the value of k_{22} is not affected because it was calculated when the thermal core was switched off. The criticality factors k_{22} from MCNP5 and Serpent are in good agreement within 0.13%. On the other hand, the criticality factor k_{11} strongly increases as the light water level increases because of neutron moderation. As the light water level increases to a 30-cm height, the rate of increase for k_{11} decreases gradually due to neutron absorption in light water.

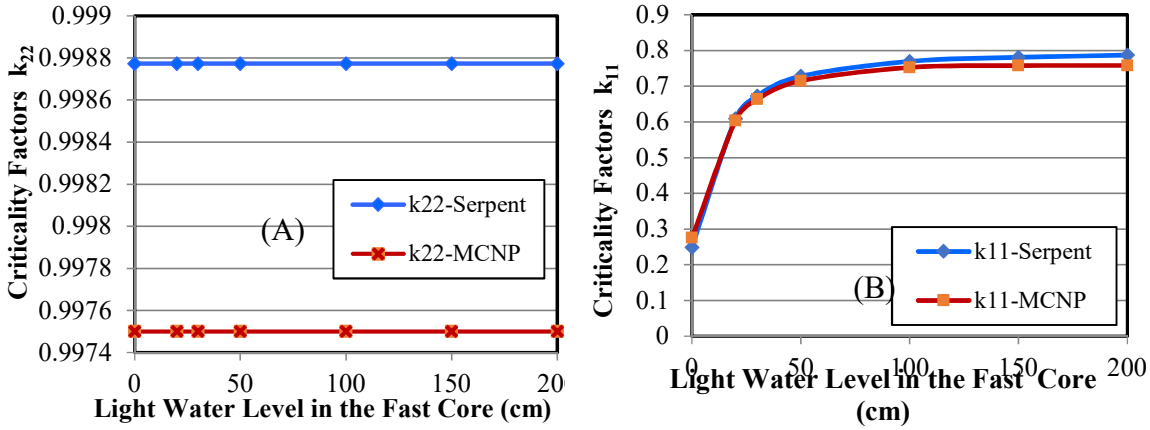

Figure (5-18): Criticality Factors k_{22} (A) and k_{11} (B) at Different Light Water Levels in the Fast Core with Heavy Water at 100 cm in the Thermal Core Calculated by Serpent and MCNP5.

The factor k_{11} becomes constant at a light water level of 100 cm and above, where the rates of fission are equal to that of absorption and leakage. The criticality factors k_{11} from MCNP5 and Serpent are in good agreement with a percent difference of 3.28%.

3) Figure (5-19)-(A) and (B) are close-ups of the coupling coefficients for k_{12} and k_{21} as the light water level increases in the fast core. The coupling coefficient k_{12} increases sharply due to neutron moderation in light water for those that are diffusing from the thermal to the fast core. As the light water level increases above 50 cm, the coupling coefficient the k_{12} starts to decrease gradually due to neutron absorption in light water.

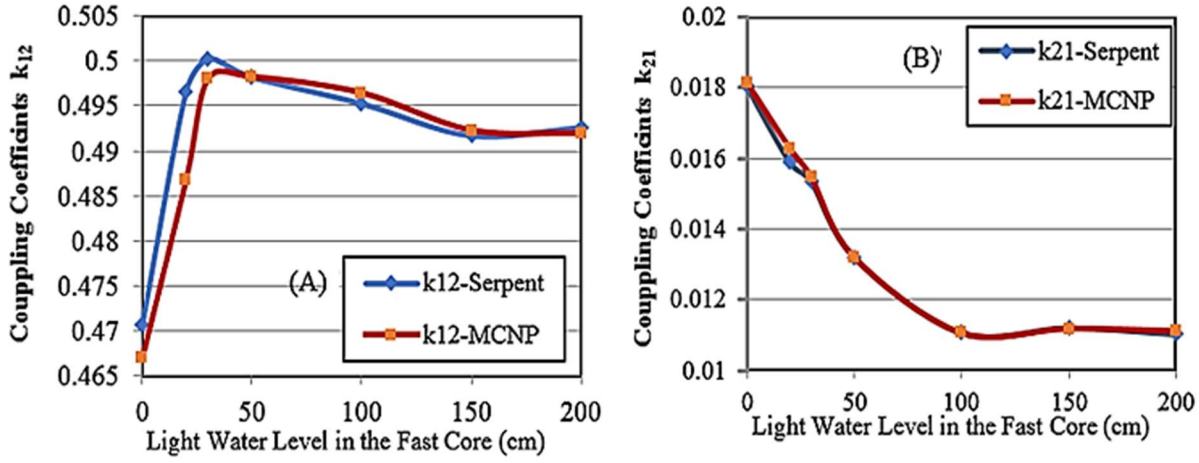

Figure (5-19): Coupling Coefficients k_{12} (A) and k_{21} (B) at Different Light Water Levels in the Fast Core with Heavy Water at 100 cm in the Thermal Core Calculated by Serpent and MCNP5.

- ***At Fixed Level of the Light Water in the Fast Core***

In this part of the simulation, the level of light water in the fast core is fixed at 100 cm while the level of the heavy water is changed from 0 to 200 cm as shown in Figure (5-20) to Figure (5-23)

1) From Figure (5-20) there is consistency of the criticality factors k_{11}, k_{22} and coupling coefficients k_{12} and k_{21} as calculated from the MCNP5 and Serpent codes. Consequently, the multiplication factor k_{eff} calculated by the coupled reactor equation match that as calculated with MCNP5 and Serpent independently.

2) Figure (5-21) also presents the multiplication factor k_{eff} calculated directly by both Serpent and MCNP5 codes in addtion to using the coupled reactor equation. the values .calculated by the two codes values calculated by the two codes correspond well and are in close agreement to that determined with coupled reactor theory

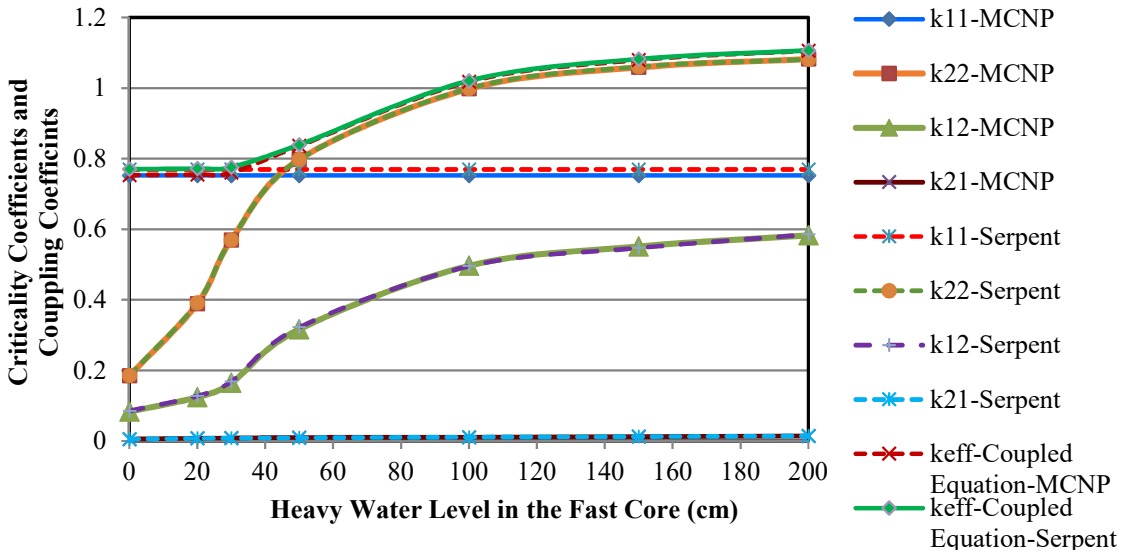

Figure (5-20): Criticality Factors and Coupling Coefficients for Different Heavy Water Levels in the Thermal Core with the Light Water Level at 100 cm in the Fast Core, as Calculated by Serpent, MCNP5 and using the Coupled Reactor Equation.

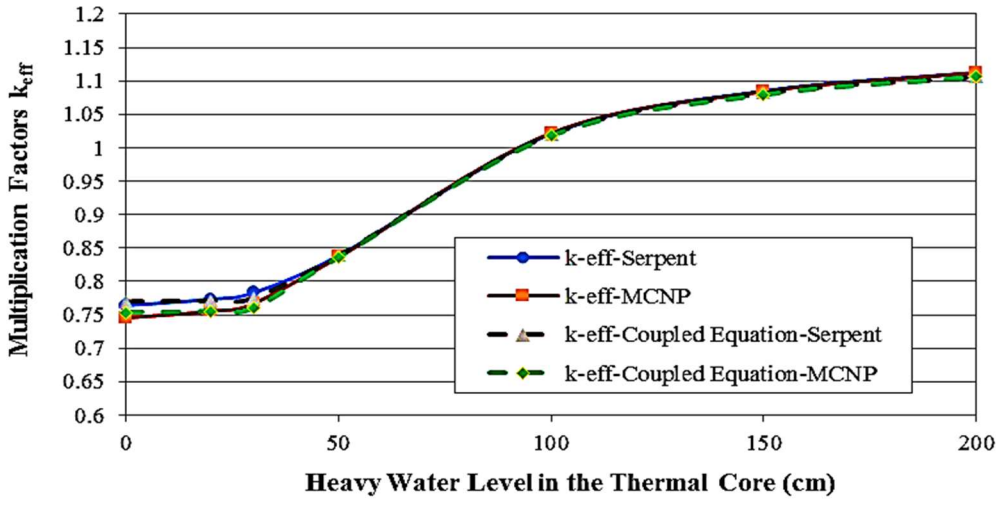

Figure (5-21): Multiplication Factors k_{eff}, for Different Heavy Water Levels in the Thermal Core with the Light Water Level at 100 cm in the Fast Core, as Calculated by Serpent and MCNP5 and Using the Coupled Reactor Equation.

Table (5-3) presents the average percentage difference between the k_{eff} calculated by MCNP5, Serpent and coupled reactor theory.

Table (5-3): Average Percentage Difference between k_{eff} as Calculated by MCNP5, Serpent and the Coupled Reactor Theory when Setting the Levels of Light Water at 100 cm and Changing the Level of the Heavy Water from 0 to 200 cm.

	%Δkeff (MCNP5-Serpent)	%Δkeff (MCNP5-Coupling theory)	%Δkeff (Serpent-Coupling theory
Average percentage of difference of k_{eff}	1.04%	0.54%	0.43%

3) Figure (5-22) (A) and (B) show the close-up of the results for the criticality factors k_{22} and k_{11}. In Figure (5-22) (A), the criticality factor k_{22} sharply increases as the heavy water level increases because of moderation. At 100 cm, the rate of increase of k_{22} decreases gradually to a constant value where the rate of fission equals that for absorption and leakage. The criticality factors k_{22} from MCNP5 and Serpent are in an excellent agreement with a difference 0.23%. In Figure (5-22) (B) as the water level increases in the thermal core, the value of k_{11} is not affected because it was calculated when the thermal core was switched off. The criticality factors k_{11} from MCNP5 and Serpent agree within 2.3%.

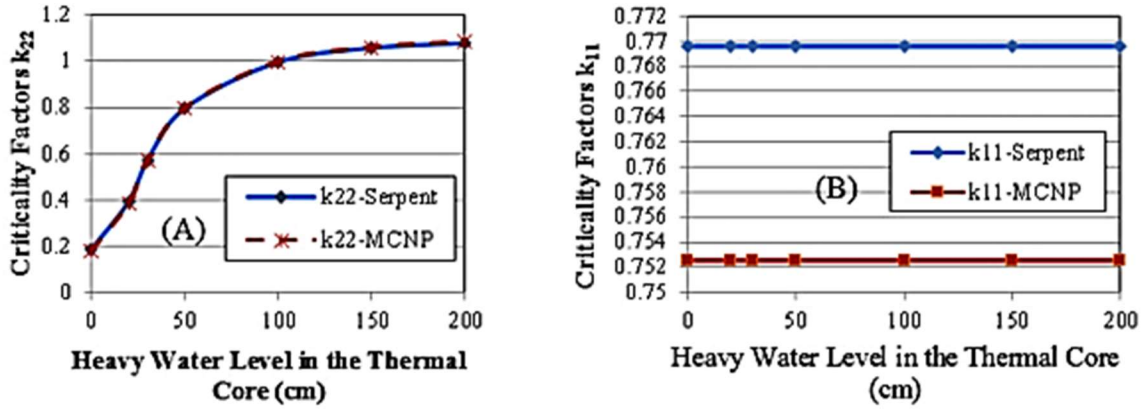

Figure (5-22): Criticality Factors k_{11} (A) and k_{22} (B), at Different Heavy Water Levels in the Thermal Core with the Light Water Level at 100 cm in the Fast Core, Calculated by Serpent and MCNP5.

Figure (5-23) (A) and (B) are close-up views of the change of the coupling coefficients k_{12} and k_{21} as the heavy water level increases in the thermal core when the light water level is set at 100 cm. The coupling coefficient k_{12} in Figure (5-23) (A) increases sharply because of moderation

in heavy water, i.e., there is more thermalization and more fissions are occurring as neutrons diffuse from the thermal to the fast core.

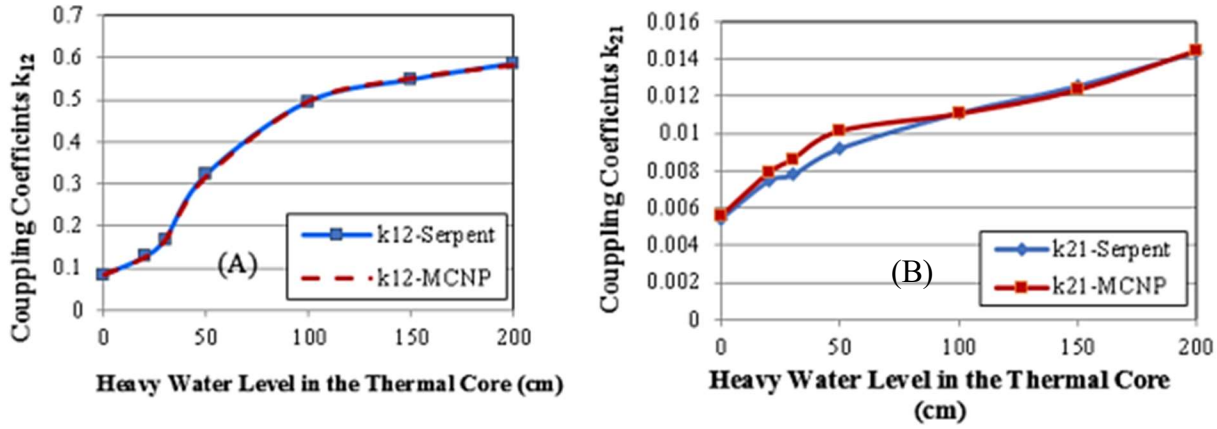

Figure (5-23): Coupling Coefficients k_{12} (A) and k_{21} (B), at Different Heavy Water Levels in the Thermal Core with the Light Water at 100 cm in the Fast Core, Calculated by Serpent and MCNP5.

4) As the heavy water level increases, the rate of change of the coupling coefficient k_{12} decreases gradually because of the heavy water internal reflector, which decreases the number of neutrons that have diffused from the thermal core to the fast core. In Figure (5-23) (B), as the heavy water increases in the thermal core, the k_{21} increases due to an increasing number of neutrons that have diffused from the thermal core to the fast core with more thermalization. Consequently, the rate of fission in the fast core increase then the rate of fission by neutrons of diffused from fast core to thermal one increases accordingly k_{21} increases.

5) The behaviour of the k_{21} curve in Figure (5-23) (B) is different from that of the corresponding curve in Figure (5-19)-(B) because of the difference in the volume and amount of fuel and volume and type of moderator at each core. The percentage difference between the MCNP5 and Serpent results for the coupling coefficients k_{12} and k_{21} were 1.52% and 4.28%, respectively.

5.6. Conclusion:

1) There is very good agreement between the results obtained numerically from the MCNP5 code and with the published results.

2) The multiplication factors calculated by the coupling coefficients k_{12} and k_{21}, and regional criticality factors k_{11} and k_{22} obtained directly from the MCNP5 and Serpent, agree well with those measured experimentally and with a reference code.

3) Coupled reactor theory has been verified with the use of both codes.

4) It is shown that the multiplication factor k_{eff} can be calculated with sufficient accuracy using these code predictions for the criticality factors k_{11} and k_{22} and the coupling coefficients k_{12} and k_{21}.

5) MCNP and Serpent can therefore be used with confidence for designing the multispectrum CANDU reactor.

6) By examining the changing effects of the flux at different energy groups, multiplication factor, criticality factors and coupling coefficients in the two cores provides a good understanding of the coupled behavior for a multispectrum reactor.

Chapter 6.

Validation of both MCNP6 and Serpent Codes for Power and Burnup Calculations for a CANDU6 Reactor Model

Evaluating the reliability of the reactor physics parameters calculations using Serpent code requires validation of the code. Results are subject to biases and uncertainties, which must be taken into account in the applications. Physical deficiencies and programming errors can be identified by comparing the results to reference data. Such data can be obtained from experimental measurements, or it can be produced by another code known to give reliable results such as MCNP6.1[49] and WIMS-AECL3.1.2.1[43]. It should be noted that all computer codes use methods that are more or less based on approximations so some uncertainty exists.

The Monte Carlo neutron transport code (e.g. MCNP6.1) [49] and the three-dimensional continuous-energy Monte Carlo reactor physics burnup calculation code Serpent (1.1.19) [45] have become common tools for calculations for other than criticality (KCODE). They can also be used for the calculation of core physical parameters, such as the power distribution, neutron flux, kinetic parameters, full-core burnup analysis, and fuel depletion capability.

Designing a multispectrum CANDU reactor as a possible actinide burner requires the validation of the Serpent code for full-core calculations and validation of both MCNP6 and Serpent1.1.19 codes for burnup calculations. Accordingly, these validations have been done using the design for a full-core CANDU6 reactor model. MCNP6.1 and Serpent were chosen owing to their capabilities for general modeling and continuous energy cross section. The continuous energy cross section is particularly important because it eliminates the need for collapsing multi-group cross sections.

The Serpent code requires a very good computational time compared to MCNP6.1 for the same tally calculation, burnup period, and KCODE calculation. These two codes are used to calculate the axial and radial flux and power distributions for a CANDU6 GENTILLY-2 nuclear reactor core with 37-element natural uranium fuelled bundles as shown in Figure (6-1). The reactor power is normalized at 2180 MWth[50]. Appendix (B) shows the optimum number of histories required for convergence of the track length estimator flux, the multiplication factor k_{eff}, actual

flux distribution, and power density distribution. A tallies combination of MCNP6 and detector analysis for Serpent are used to estimate the ratio of channel flux to fuel flux and calculate the radial power and axial power.

6.1. Design and Materials

The MCNP6 and Serpent codes are used to model the GENTILLY-2 nuclear reactor core with 37-element fuel bundles. These models are based on the geometrical and material parameters given in the design manual [50]. Figure (6-1) (A) and (B) show the models.

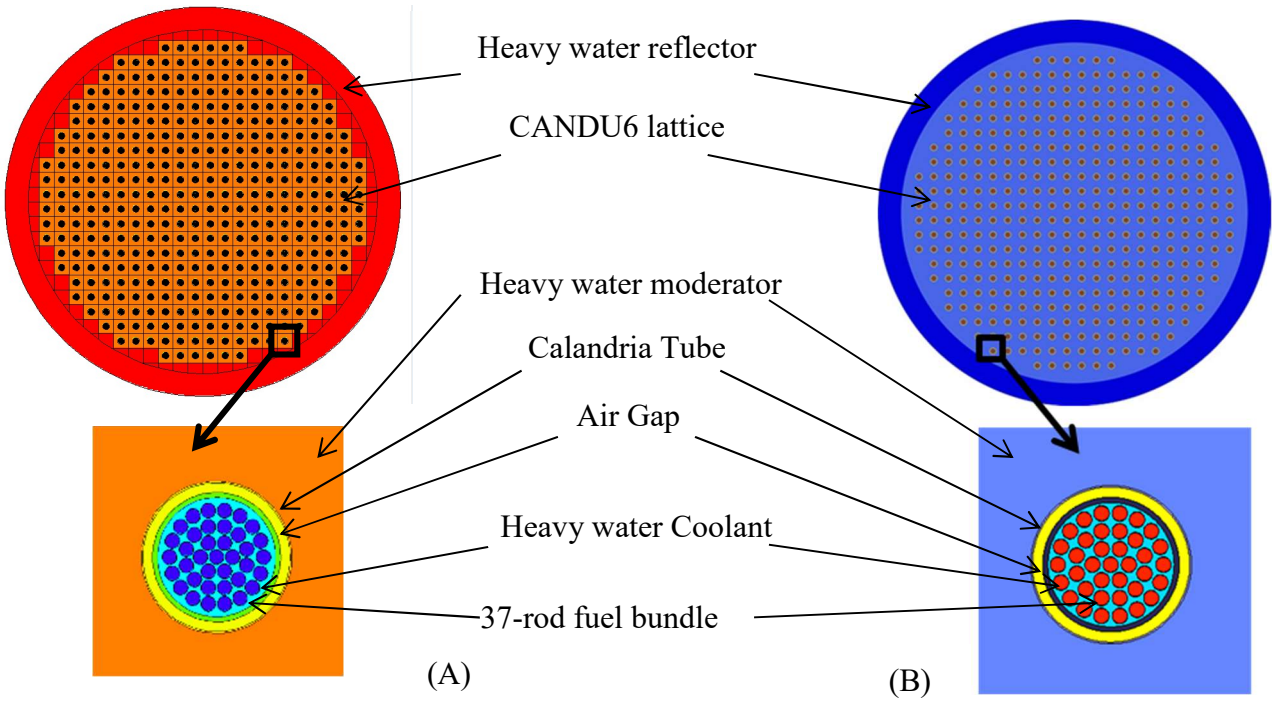

Figure (6-1): Full Core CANDU6 Design Model by (A) MCNP6-code and (B) Serpent code with the Corresponding Lattice Pitch, Fuel Channel, Fuel Bundle and Corresponding Lattice Pitch of Each.

For approximation, the end caps of the fuel element and the end-plates of the fuel bundles were not included because they have a negligible effect on the neutron economy. As such, the fuel bundle in a fuel channel is designed as one fuel bundle per channel with a length equal to the fuel channel length of 594 cm. All fuel bundles are fuelled with natural uranium. The heavy water coolant density is adjusted according to a heavy water density at 561 K and 11 MPa[51]. The material content percentage of the pressure tube and the calandria tube are taken from Ref. [52]

The material composition, mass or atomic ratio, temperature, density and properties of the cladding, coolant, pressure tube, calandria tube, moderator, and reflector used in both models appear in Appendix (C).

The cross-section data for the fresh core fuel, heavy water coolant, moderator, and reflector were taken from continuous-energy ENDF/B-VII library, while the material data for the cladding, pressure tube, and calandria tube are taken from endl92[49]. For the coolant, moderator, and reflector, the thermal scattering data are based on a free-gas treatment S (α, β), with hydrogen in light water and deuterium in heavy water, from ENDF/B-VII are added. The thermal scattering of the oxygen ($^{16}_{8}O$, $^{17}_{8}O$, $^{18}_{8}O$) in UO_2, and uranium-238 in UO_2, are considered at the corresponding fuel temperature from ENDF/B-VII in the MCNP6 code manual [49], but these libraries are not included in the Serpent code. The average values of reactivity and the total flux in the core as calculated using MCNP6 and Serpent code are shown in Table (6-1):

Table (6-1): Average converged value of the reactivity and average total flux in the core.

	Reactivity (mk)	Average total flux in the core (#n $cm^{-2}.sec^{-1}$)
MCNP6	83.838 ±0.755418	2.53666E+14 ±9.05539E-02%
Serpent	79.580±0.169435	2.48492E+14 ±3.10644E-02%

6.2. Method Used to Calculate the Radial and Axial Neutron Fluxes, and Radial and Axial Power Distributions

- ***Flux Calculation Using MCNP6 Code***

In MCNP, the easiest way to calculate the track length estimator of the neutron flux is by using a superimposed mesh tally card FMESHn. This allows the user to define a mesh tally that is superimposed over the problem geometry. By default, the mesh tally calculates the track length estimate of the particle flux averaged over the mesh cell located at the center of the mesh window. The size of the mesh is set to calculate the average flux per bundle length with the width and breadth of the fuel channel:

($x - mes$ 28.575, $y - mesh = 28.575, z - mes$ 49.5 all values in cm).

To calculate the average flux per fuel channel, the z-mesh width is integrated to the fuel channel length, i.e. z-mesh = 594 cm. The other method to calculate the track length estimator flux in the fuel channel is by using the lattice cell to universe reference as:[49].

$$\text{F4 } fuel\ cell\# < fuel\ universe[lattice\ address] \tag{6-1}$$

The limitation of this approach over the meshing method is that the user may need to write an F4 tally for 380 lines to cover the entire fuel channels. The latter is useful when a limited number of fuel channels are targeted as a reference.

- ***Flux Calculation Using Serpent Code***

The detectors method is equivalent to the tallies method used in MCNP to calculate the track length estimate of the particle flux lattice of the Serpent model.

- ***Power Calculation***

To calculate the radial power distribution the actual flux (φ) in the unit of n cm^{-2} s^{-1} is required. So, the track length estimator flux should be used to calculate the average actual flux in the fuel channel mesh dimension of $(28.757\ \text{cm} \times 28.757\ \text{cm} \times 594\ \text{cm})$. To calculate the power, the average actual flux at each energy bin in the fuel only should be calculated. The radial fuel flux could be calculated using MCNP6 code tallies and Serpent code detectors. The calculation of the axial power needs to introduce the Channel Flux to Fuel Flux Ratio (CFFFR) [53] at each energy bin. These ratios are used to calculate the actual fluxes at each energy bin and, consequently, the axial fuel channel power at each energy bin.

6.3. Radial and Axial Neutron Flux Distribution at the Center of the Core

The radial track length estimator flux was calculated at the central bundle position for the sixth bundle at the central fuel channel-11 in the row (M) as shown in the Figure (6-2) (A) and (B). The mesh size used is $(28.575\ \text{cm} \times 28.575\ \text{cm} \times 49.5\ \text{cm}$ (the bundle length)). The position of this mesh can be written as (6-M-11) (i.e., bundle number-horizontal row-vertical column).

(A)

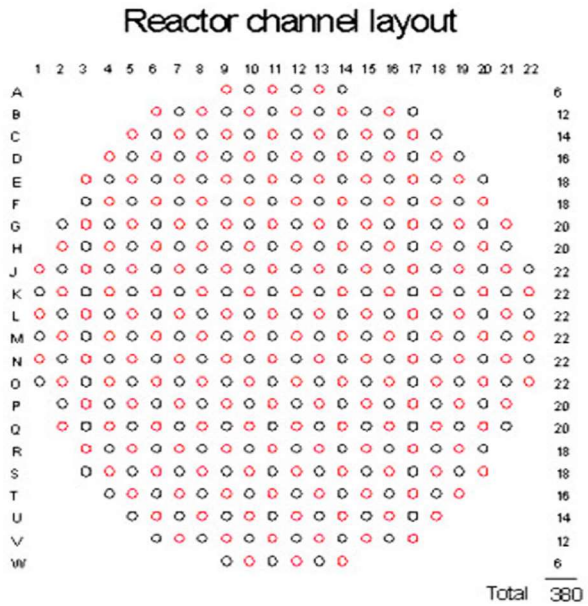

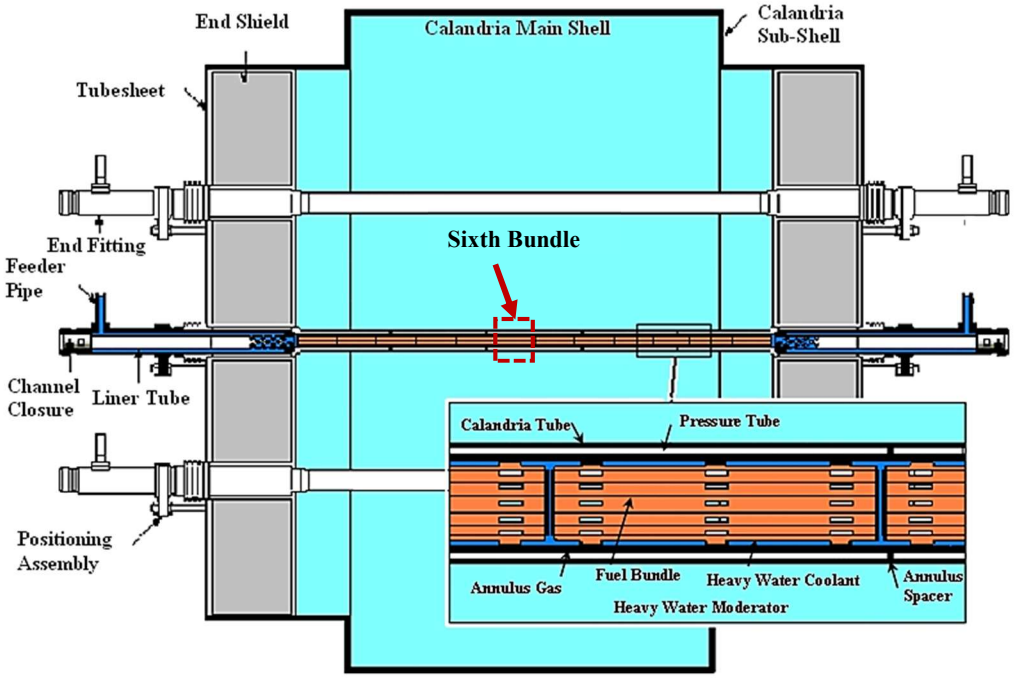

Figure (6-2): (A) Reactor Channel Layout (B) Fuel Channel Assemblies [54]**.**

The average track length estimator flux (TLE-flux) is calculated across this mesh dimension. F4 and Fmesh tallies from MCNP6 and lattice detectors and mesh detectors from Serpent1.1.19 codes were used to calculate the track length estimator flux Φ_E^{F4}in units of n cm^{-2}, which is normalized to one source neutron per volume. To calculate the actual flux per fuel channel

$\varphi_E^{actual(chann\ \ )}$in units of n cm^{-2} s^{-1} for the three energy groups, the track length estimator fluxes are scaled with a normalization to the reactor power as shown in Equation (6-2) [55] and [56].:

$$\varphi_E^{actual(Channel)}(n/cm^2.s) = \frac{\Phi_E^{F4(Channel)} \times (P_{total\ thermal} \times \upsilon)}{(q_{value/fission} \times k_{eff})} \qquad (6\text{-}2)$$

where,

$\Phi_E^{F4(Chann\ \ )}$ is the track length estimator flux calculated in unit of cm^{-2},

$P_{total\ thermal}$ is the total thermal power of the reactor in Watts,

υ is the average number of neutrons per fission,

$q_{value/fissio}$ is the average thermal energy dissipated in the core per fission in Joules, and

k_{eff} is the multiplication factor.

The actual flux is calculated at a mesh cell (6-M-11) dimension length of 49.5 cm with a width and breadth equal to the fuel channel's lattice pitch, i.e. 28.575 cm is shown in Figure (6-3).

MCNP6 and Serpent produced similar results for the thermal, epithermal, fast and total flux calculations at different neutron energy groups. These fluxes are expressed in the form of a Bessel function, and the percentage difference of the average flux values as calculated by MCNP6 and Serpent by Equation (6-3) is 3.21%:

$$Percentage\ Difference\ of\ the\ average = 100 \times \left(\frac{|\Delta\varphi|}{(\Sigma\varphi)/2}\right) \qquad (6\text{-}3)$$

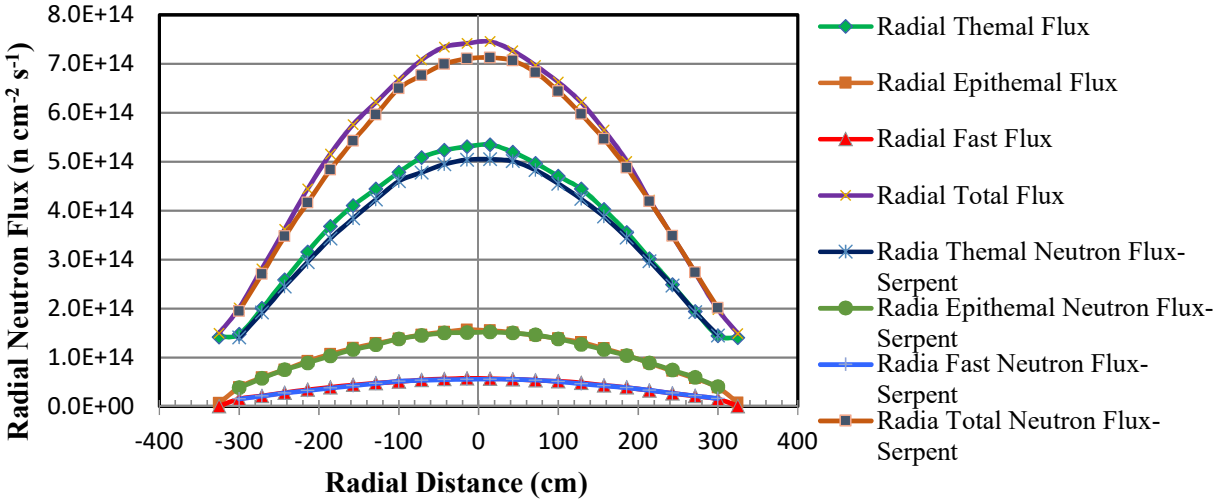

Figure (6-3): The Actual Radial Flux at the Central Bundle Number 6 and Radial Channel Plan Number M as Shown in Figure (6-2) (B) in the Core Layout.

Similarly, the average flux is calculated in the axial direction at each axial mesh of the same size in the central fuel (M-11). Figure (6-4) shows the axial flux for the central fuel channel M-11, which is calculated for each neutron energy bin for the thermal, epithermal, fast, and total flux. A cosine shape for the axial channel flux is seen for both codes. The percentage difference of the average flux values between the total axial flux calculated by MCNP6 and Serpent is 3.1%.

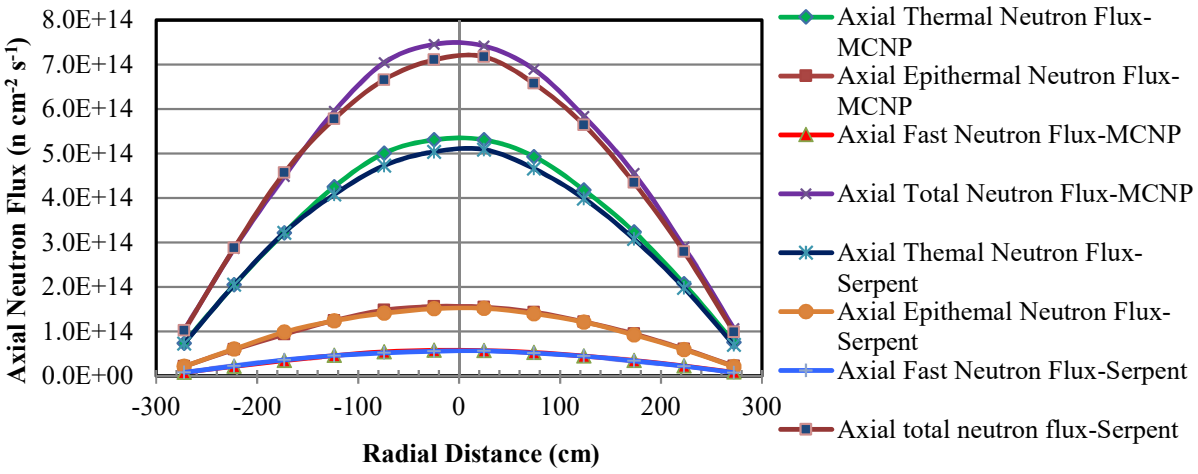

Figure (6-4): Total Axial Flux Distribution in the Central Channel #11

The total flux at the central point of the core calculated by MCNP6 is 7.4184E+14 n cm^{-2} s^{-1}, which represents the average flux at the central bundle 6-M-11 of the reactor with a radial tally. This

value is similar to the value at the center of the fuel channel M-11 in Figure (6-4) and was calculated with an axial arrangement tally. This scenario is valid for all energy groups.

In conclusion, the flux could be calculated with very good agreement by Serpent code in comparison with MCNP6 Code[53].

6.4. Calculation of Radial Neutron Flux Distributions in the Fuel and Fuel Channel.

Using the track length estimator flux calculated by both the MCNP6 and Serpent codes an Equation (6-2) the average radial flux of both the fuel channel and fuel only are calculated. The fuel flux at each energy bin is required to calculate the radial power distribution. The fuel flux can be calculated using the F4 tally syntax [49]with Equation (6-4):

$$Fn4: n(Fuel\ cell_1, Fuel\ cell_2, \dots Fuel\ cell_n < universe\ under\ which\ the\ fuel\ is\ defined)\ T \tag{6-4}$$

here $Fuel\ cell_n$ represents the fuel rod or a group of fuel rods. This tally should include the volume of each fuel cell for normalization. The "T" is added to sum up the flux in the cells that represent the fuel rods, at each energy bin. In other words, this provides the flux in the 37 fuel rods at each energy bin. Figure (6-5) and Figure (6-6) present the average radial flux distribution in the central fuel channels for the plane "M" position as calculated with MCNP6 and Serpent, respectively. The average thermal neutron flux in the channel is higher than the average thermal fluxes in the fuel because of moderation in both the coolant and moderator.

The epithermal neutron flux in the fuel channel and in the fuel, itself are almost the same, while the fast neutron flux in the fuel is higher than that in the channel due to the majority of fast neutrons produced from fission. The results are very similar for Serpent and MCNP6 for both types of fluxes calculated at each energy bin.

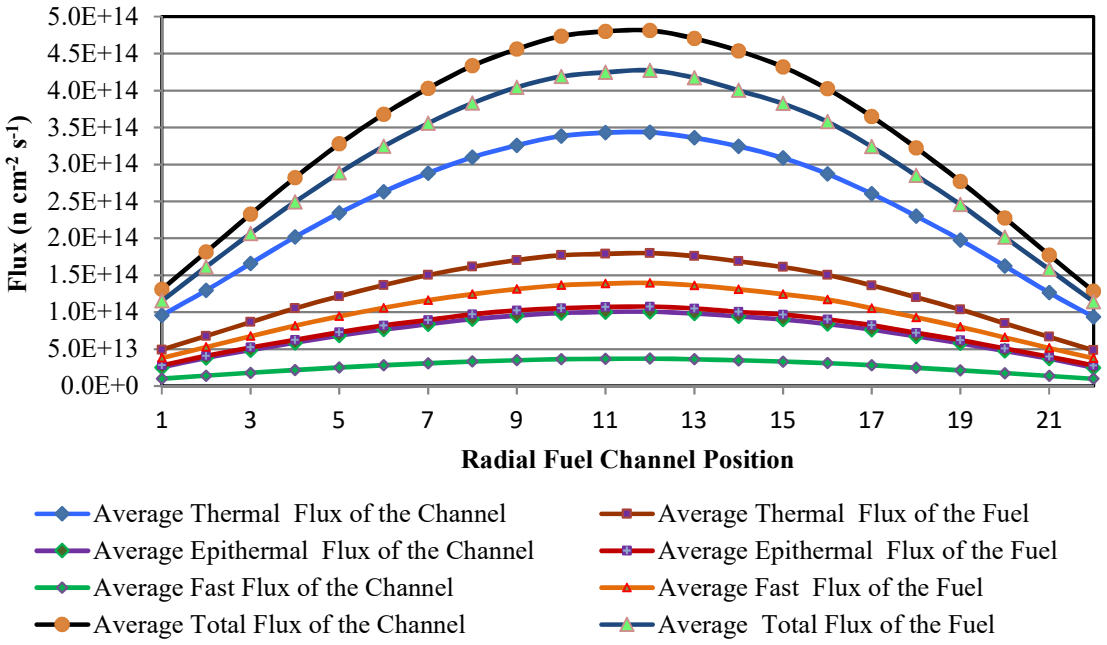

Figure (6-5): Average Fuel Channel Radial Flux and Average Fuel Radial Flux Channels –M as Calculated by MCNP6.

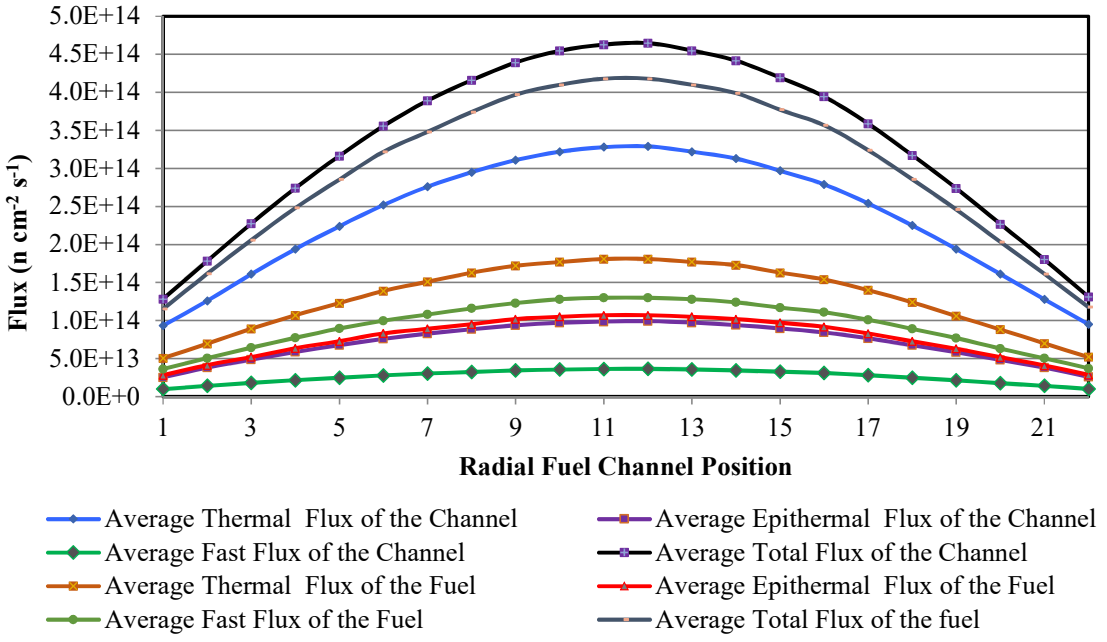

Figure (6-6): Average Fuel Channel Radial Flux and Average Fuel Radial Flux Channels –M as Calculated by Serpent.

6.4.1. Channel Flux to Fuel Flux Ratio (CFFFR)

To calculate the axial power per channel and per bundle, the actual flux in the fuel at each energy bin is required. Using the mesh tally FMESHn and the F4 tally, the average channel flux can be calculated, which includes the effect of the coolant and moderator on the neutron energy distribution. So, it is important to introduce the ratio between the average channel flux to the average fuel flux [53]:

$$Channel\ Flux\ to\ Fuel\ Flux\ Ratio\ (CFFFR)_E = \frac{(\ Average\ Channel\ Flux)_E}{(Average\ Fuel\ Flux)_E} \qquad (6\text{-}5)$$

Using the Channel Flux to Fuel Flux Ratio, CFFFR, the fuel flux per bundle can be calculated for each energy bin (Thermal, Epithermal, and Fast). The CFFFRs were calculated in the central fuel channel M-11. The ratio has almost the same value for each energy group except for the very small effect on the first and last channels because of the reflector and fuel-to-moderator ratio at these two channels. Figure (6-7) illustrates the Channel Flux to Fuel Flux Ratio, CFFFR, calculated using both the MCNP6 and Serpent codes. The results from the two codes were close for the CFFFR calculations for each neutron energy group. The average CFFFR values at each neutron energy group calculated by both codes and the percentage differences are summarized in Table (6-2).

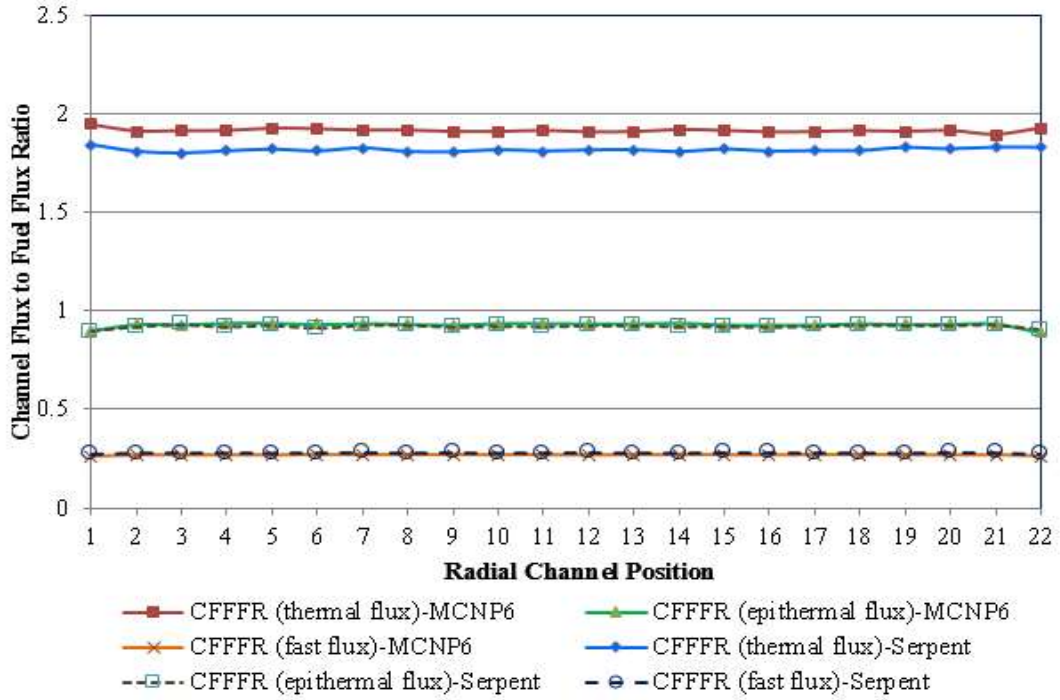

Figure (6-7): Channel Flux to Fuel Flux Ratio (CFFFR) as Calculated Using both MCNP6 and Serpent.

Table (6-2): Average Value of Channel Flux to Fuel Flux Ratio[53]

	MCNP	Serpent	Percentage Difference
Average value of thermal neutron CFFFR	1.92	1.82	5.4%
Average value of epithermal neutron group CFFFR	0.93	0.92	0.76%
Average value of fast neutron group neutron CFFFR	0.266	0.279	4.7%

The average value of the CFFFR for the thermal neutron fluxes in the fuel channel is higher than the average thermal flux in the fuel due to a thermalization by both the coolant and moderator. The average value of the CFFFR for the epithermal neutron flux in the channel is slightly less than one, which indicates that the epithermal neutron flux in the fuel is slightly larger than that in the fuel channel. For the fast neutron energy group, the average value of the CFFFR in the fuel is approximately four times higher than the average value in the fuel channel because of fast neutrons generated from fissions in the fuel region. Using these values of the CFFFR and the axial channel flux in Figure (6-4), the axial fuel flux at each neutron energy group can be calculated. Consequently, the axial power distribution is determined.

6.5. Power Distribution

Since the radial and axial fluxes in the fuel for each neutron energy group can be calculated, the radial and axial power density distributions can also be calculated for each energy bin of the fuel flux in the fuel channel [55] and [56].

$$Power(E) = \varphi_E^{actual\ (fuel)}\left(\frac{\#n}{cm^2.s}\right)\times\sigma_E(barn)\times N_D\left(\frac{\#n}{barn.cm}\right) \times q_{\frac{themal}{fission}}(MeV)\times S\left(\frac{Joule}{MeV}\right) \quad (6\text{-}6)$$

where *Power (E)* stands for the power produced from neutron at energy bin E, $\varphi_E^{actual}(n\ cm^{-2}s^{-1})$ is the actual neutron flux at energy E calculated from Equation (6-2) and, (6-6) where

$$\varphi_E^{actual\ (fuel)} = \varphi_E^{actual\ (Channel)_E}/(CFFFR)_E \quad (6\text{-}7)$$

$\sigma_E(barn)$ is the fission cross section corresponding to energy bin E

$N_D(n/barn.cm)$ is the number density of the fissile or fissionable materials?

$q_{thermal/fissi}$ (MeV) is the average total thermal energy per fission dissipated in the system from all neutron energies, and $S = 1.602\times10^{-13}$ is the conversion factor from MeV to Joules.

Figure (6-8) shows the average radial power per channel calculated by both codes using the radial flux Equation Figure (6-6). that determined directly by the Serpent code in the horizontal channel M-plane.

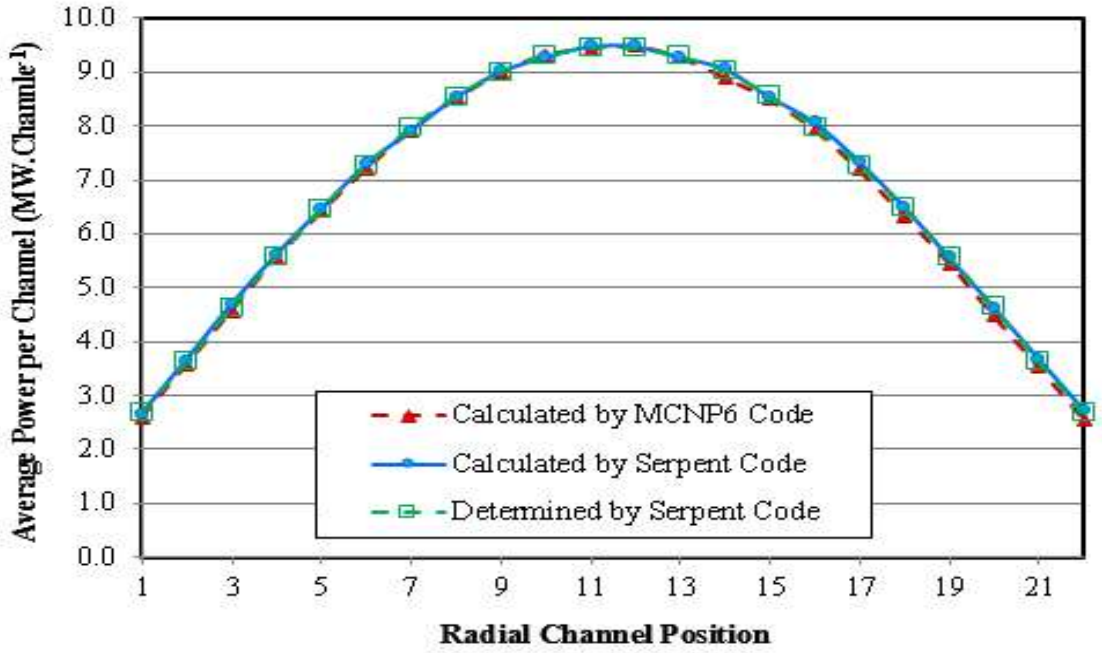

Figure (6-8): Radial Power Distribution Calculated with the MCNP6 and Serpent Codes.

Figure (6-2)(A) and Table (6-3) display the average channel power per channel. The calculated values are close to the average channel power of the reactor (6.7 MW per channel). The percentage difference between the average radial power calculated by Equation (6-3) by both codes is 1.26%. The percentage difference between the calculated average power per channel by MCNP6 code and Serpent code and that determined directly by Serpent code are 1.07% and 0.18%. This minor ratio of percentage difference in the average radial channel power provides confidence in the Serpent code for power calculations.

Table (6-3): Average Power per Channel of the Whole Reactor[53]**.**

Modelling Code	Average Power per Channel (MW channel^{-1})
Calculated by MCNP6	6.71
Calculated by Serpent	6.79
Determined by Serpent	6.78

Figure (6-9) shows the variation of the average axial power per bundle calculated in the central reactor channel (M-11).

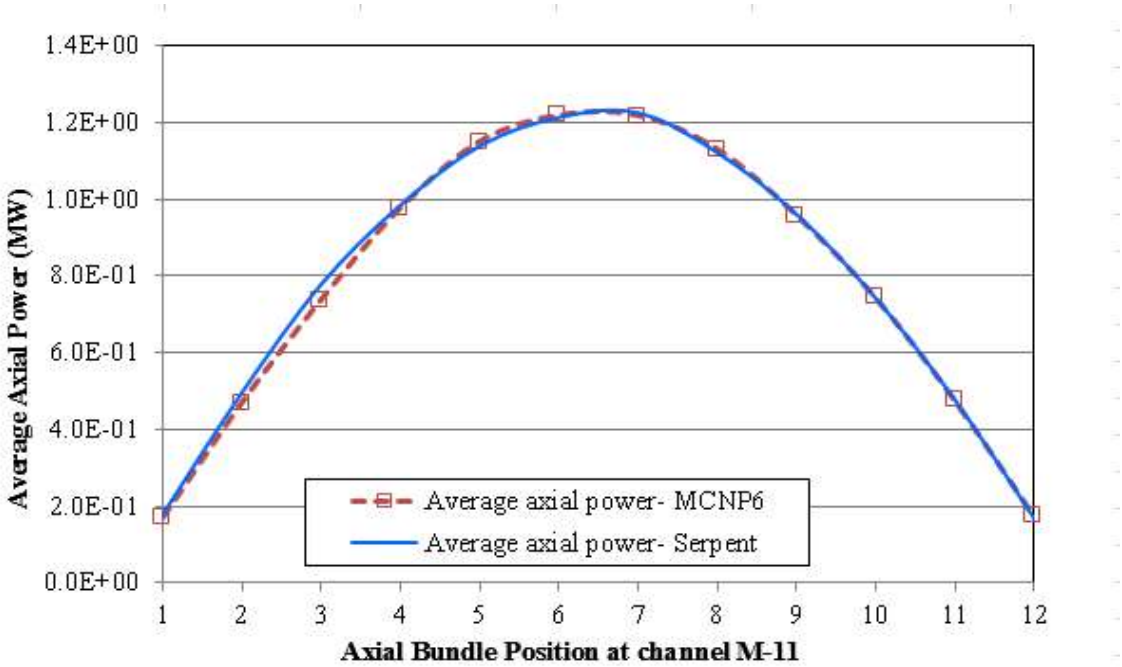

Figure (6-9) Axial Power Distribution as Calculated with MCNP6 and Serpent Codes

Each point in the graph Figure (6-9) represents the average power per bundle in this channel. Table (6-4) shows a comparison of the integrated axial power over this channel (M-11) in Figure (6-9) with the average power per channel from Figure (6-8). The integrated average power as calculated from the axial power distribution in the central channel as shown in Figure (6-9) is in excellent agreement with the average power calculated per channel. This agreement gives confidence in the predicted Channel Flux to Fuel Flux Ratio (CFFFR), which is then used to calculate the axial power.

Table (6-4): Comparison between Average Power in the Channel M-11 (Figure (6-8) and Integrated Flux over Channel M-11 (Figure (6-9)[53]

	Serpent	MCNP6
Average Channel M11 Power (Figure (6-8)	9.487 MW	9.427 MW
Integrated Channel M11 Power (Figure (6-9)	9.455 MW	9.41 MW

The radial and axial power distribution calculated using each code are in excellent agreement. It is also clear that the observed values are higher than the acceptable safety margin (7.3 MW/ channel). The reason for such high values is that the current model does not include borated

neutron poisons, adjuster rods, depleted uranium bundles, or any flux control devices such as control rods and liquid zone controllers, which are used to flatten the high flux and power in the central part of the reactor.

6.6. Calculation of the Burnup

The burnups and the effective multiplication factors were calculated for a burnup period of 180 days using MCNP6, Serpent 1.19 code and WIMS-AECL 3.1.2.1. The values of the effective multiplication factors, $k_{eff,}$ versus the burnup, as calculated using MCNP6.1, Serpent 1.19 , and WIMS-AECL 3.1.2.1, are shown in Figure (6-10)[57]. The variation of the multiplication factor k_{eff} is in excellent agreement between the three codes. The multiplication factors quickly decrease due to the consumption of ^{235}U and the build-up of xenon, samarium, as well as other neutron poisons and fission products in the core. The subsequent peak in the multiplication factor is caused by the production of ^{239}Pu known as the "plutonium peak". Then, there is a steady decrease of the multiplication factor due to the depletion of both ^{235}U and ^{239}Pu, and the accumulation of non-saturating fission products in the reactor fuel.

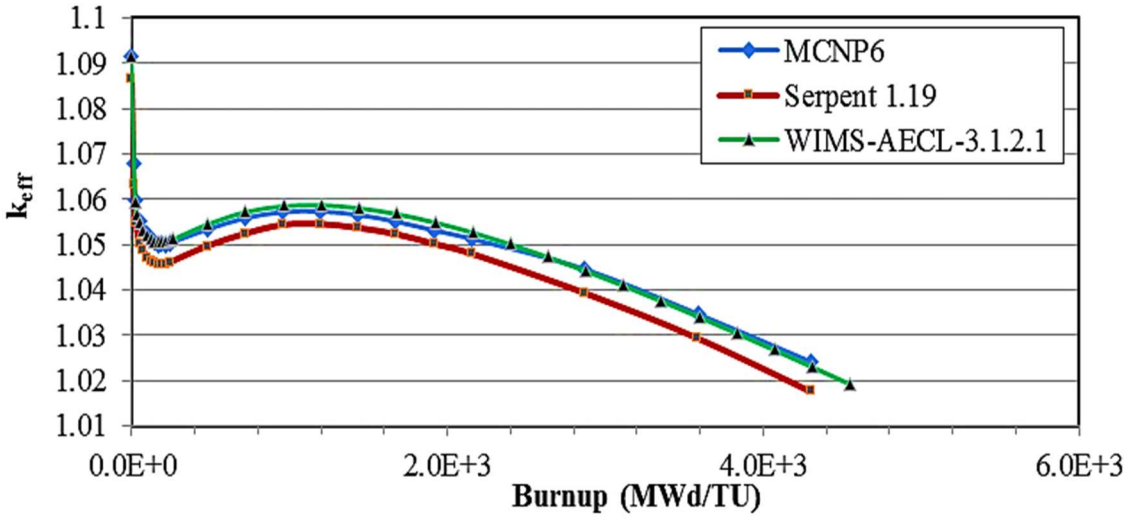

Figure (6-10): Effective Multiplication Factor versus Burnup as Calculated Using MCNP6, Serpent Code and WIMS-AECL for the CANDU-6 GENTILLY 2 Reactor.

The values of k_{eff} as calculated by WIMS-AECL are closer to the MCNP6 values because the buckling used in the WIMS-AECL calculation is related to the multiplication factor calculated

with MCNP6. The variation k_{eff} with burnup is like that of any CANDU 6 reactor with fresh fuel. In the first reactor operation period, the excess reactivity is in the range of 25 to 80 mk [7]. In the present case, it is 83.3 mk in the MCNP6 and WIMS-AECL analyses, and 79.8 k from Serpent. Under normal conditions, this large excess reactivity is compensated for by adding soluble boron to the moderator (which is not considered in the present work).

Figure (6-11) shows the variation of the burnup as calculated by Serpent, MCNP6 and WIMS-AECL as a function of the fluence in (n/kb). There is an excellent agreement between the three codes. As the fluence increases above the value of 1.5 n kb^{-1}, the burnup calculated by WIMS-AECL starts to deviate from that by MCNP6 and Serpent, both of which remain very close together. The deviation by the WIMS-AECL burnup line may be due to the difference in the data library, ENDF-VI.5 for WIMS-AECL, but ENDF-VII for both MCNP6 and Serpent. The calculation of the refuelling time when the excess reactivity becomes zero can be found by increasing the irradiation period to more than 180 days [57].

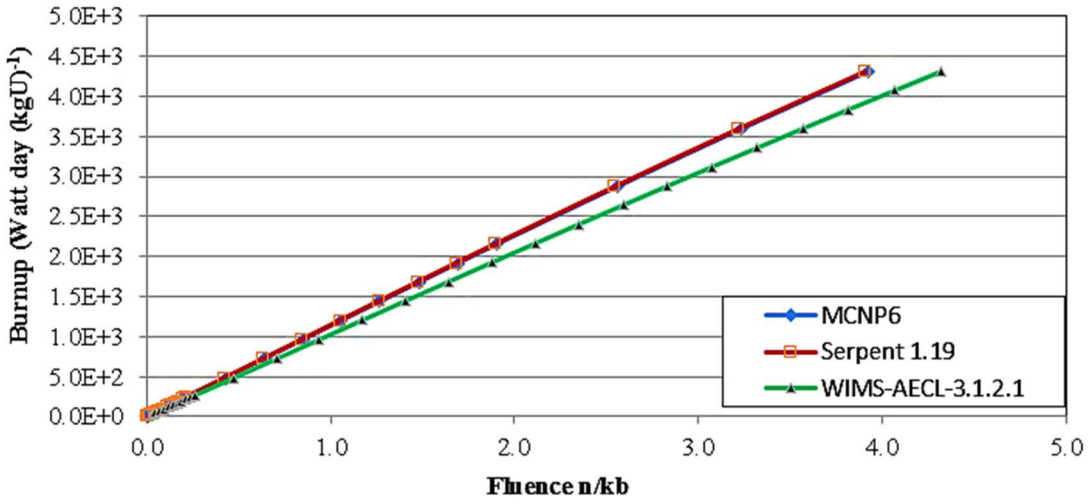

Figure (6-11): Burnup as Calculated Using the Codes MCNP6, Serpent, and WIMS-AECL for a CANDU-6 GENTILLY 2 Reactor versus the Fluence.

The computation time of Serpent1.1.19 code was 28 h on a Z800-intel processor with 16 parallel processing using an MPI shared a memory of 32 GB. The Serpent code calculation requires extensive memory. The calculation time is effectively improved as the memory size increases. The

computation time for MCNP6.1 using a Z820-Intel processor with 32 parallel processing threading and a 64 GB memory is one week or approximately 160 h. MCNP6 is processor dependent. It is recommended to use this code on a high-performance parallel computing system.

For WIMS-AECL3.1.2.1 code the computational time is extremely short in comparison. With other codes, it took about 10 minutes on the four-core Intel processor to achieve the 2D burnup calculations. The disadvantage of using WIMS-AECL code are: (1) It is only applicable for reactors with a similar size of fuel channels and similar fuel type with no zone controllers. (2) It is a 2D code so the axial flux profile of the multispectrum reactor cannot be explicitly calculated.

However, for a reactor with two different material zones such as multispectrum reactor, the code in its current version is not be applicable for such analysis. Consequently, the Serpent code is used for the design of the multispectrum CANDU based reactor.

6.7. Conclusion

1) The Monte Carlo-based probabilistic transport code, MCNP6, and the continuous energy reactor physics burnup calculation code, Serpent, were used to model a three dimension CANDU-6 nuclear reactor. Good agreement was obtained between the two codes for the criticality and total flux calculation.
2) The radial and axial fluxes are in very good agreement for the thermal, epithermal, and fast neutron energy bins.
3) The Channel Flux to Fuel Flux Ratio (CFFFR) is defined and calculated at each neutron energy bin with both codes. The CFFFR is used to calculate the radial and axial flux in the fuel.
4) The axial and radial power distributions calculated by the Serpent code are in excellent agreement with those calculated by MCNP6. The radial power distribution determined directly by Serpent is in an excellent argument with that calculated by MCNP6 and Serpent using a power formulation. Hence, Serpent offers an excellent method for the power calculation.

5) The Serpent has a much better computational time than MCNP6. The effective multiplication factors k_{eff} are calculated as a function of the burnup in order to validate the MCNP6 and Serpent 1.19 codes for use in burnup calculations for a full core CANDU 6 reactor. Excellent agreement for the burnup calculation is observed between MCNP6 and Serpent (as further benchmarked against WIMS-AECL).

6) The total actual flux in the CANDU 6 reactor core is calculated, and the value is in good agreement with that calculated by the WIMS-AECL model. The deterministic code WIMS-AECL 3.1.2.1 has exceptional computational time, but it could be used only for a unit cell calculation or for a full core with similar cells and fuel channel dimensions as a two-dimension calculation, so that it is not applicable for the multispectrum CANDU reactor analysis.

7) The MCNP6 and Serpent 1.19 codes have a very good tally flexibility for calculation of the flux and power distribution in three dimensions and can be used for the design of a multispectrum CANDU reactor. MCNP6 and Serpent are recommended for analysis of the multispectrum reactor for the burning of actinides where the bundle type, fuel enrichment, and lattice pitch may be different from one zone to another in the reactor. Overall, excellent agreement was found between the MCNP6 and Serpent codes in terms of the calculated flux and power distribution.

Chapter 7.

Design of a Multispectrum CANDU-Based Reactor, MSCR.

As mentioned in Chapter 1, more efficient transmutation of actinides occurs in fast neutron reactors. Thus, in the current chapter, the possibility of coupling a fast-thermal nuclear reactor system for the burning of actinides is presented for the design of a Multispectrum CANDU Reactor (MSCR) based on the CANDU 6 Gentilly-2 reactor[50]. This proposed reactor is designed with two concentric regions including an internal region with a predominant fast neutron energy spectrum and an external one with a predominant thermal neutron energy spectrum. The simulations for the design of the MSCR were carried out using the Serpent 1.19 code.

In the proposed designs, the inner core is fuelled with enriched uranium oxides with 19.9% of U-235/U or plutonium 13.89% (14.13% of fissile materials.). Helium is used as a coolant in the fast neutron core. The outer core is fuelled with natural uranium with heavy water as both moderator and coolant. Both of these cores use standard 37-element fuel bundles. A Stainless steel 316L(N) SS fuel bundle is used in the inner core while a Zircaloy-4 fuel bundle is used in the outer core. The size of the two cores and the level of enrichment of the fresh fuel in the fast core were optimized to ensure criticality, safety and to address non-proliferation concerns. The cores are independently subcritical (depending on the model), but the diffusion of neutrons from one core to another will drive the entire system to criticality. The details of both the fast and thermal cores are described in the following sections.

The Serpent three-dimensional continuous-energy code [58] has become a common tool for calculations of the criticality factor and the burnup. It can also be used to estimate core physical parameters such as the power distribution, neutron flux, and kinetic parameters in addition to fissile material depletion. The code has been verified for use in the design of the multispectrum reactor system for prediction of the reactor physics parameters as detailed in Chapters 5 and 6. This code was chosen for its ability to employ a continuous energy cross section, which eliminates the need for collapsing multigroup cross sections. An additional advantage of the Serpent code is that it provides an excellent computational time in comparison to MCNP6 for the same tally calculation and burnup analysis.

A design model of the MSCR is detailed as follows. The coolant and materials of the pressure tube, partition walls, and the filling of the fast neutron spectrum core were selected according to the function of the fast core. The thicknesses of the pressure tube and of the partition walls are optimized and calculated according to the pressure differential across them. The reactivity and the regeneration factors were calculated for different concentrations of the fissile isotope ^{235}U in the fuel of the fast core and with various lattice pitches to examine criticality, safety and the requirement for non-breeding. The behaviour of the radial flux distributions in the full-reactor is investigated for different enrichment concentrations of ^{235}U in the fast core (at different lattice pitches), and for each energy bin (e.g., thermal, epithermal and fast) in both the internal and external core.

7.1. Design Models of the Multispectrum CANDU Reactor

There are some design constraints or decision variables that affect the flux profile of the MSCR. The main design constraints considered in the current thesis are:

1) Radius of the fast core ($R_{n=1;2;or3}$),
2) Lattice pitch (Lp),
3) Concentration of the fissile materials for the fuel used in the fast core (En), and
4) Number of fuel channels in the fast core (Fc).

In the current work, three different radii for the fast core are chosen. Different models are designed and simulated using both types of fissile material in the fast core and at different fast core radii and lattice pitches. Six models of the MSCR are investigated in the current work. The main parameters of the different models are the radii of the fast core, the type of fissile material in the fast core, the lattice pitch, and the number of fuel channels in both the thermal and the fast core. This chapter concentrates on the use of uranium for the fast core while Chapter 8 covers the use of plutonium. The lattice pitch of the fast core is set at 28.575 cm or 14.585 cm for the uranium-fuelled reactor (Models (I) and Model (II)) presented in this chapter, and 28.575 cm or 14.287 cm for the plutonium-fuelled model (Models III, IV, V, and VI) in Chapter 8. The design parameters of the MSCR-Models are shown in the Appendix (D)

7.2. Optimizing the Number of Histories.

As is common in Monte Carlo calculations, the relative error in the computation is proportional to the inverse of the square root of the number of histories. Therefore, as the number of histories increase, the results obtained have greater confidence. For a converged solution for both flux and k_{eff}, the number of histories should be selected as high as possible with consideration given to the computational time.

For a converged solution for the uniform flux shape, the number of histories should be selected so that the flux and multiplication factor k_{eff} do not change within a certain error tolerance. Figure (7-1) and Figure (7-2) show the changing multiplication factor k_{eff} and the average total flux in the core of the MSCR model (I). The simulation was run at 15000 cycles with increasing neutron number per cycle from 40000 n per cycle to 55000 n per cycle. One notices that k_{eff} converges faster than the neutron flux. The multiplication factor converged to (1.0544±0.0009) with an average total flux of (3.6724 ±0.0001) x 10^{14} n cm^{-2} s^{-1}.

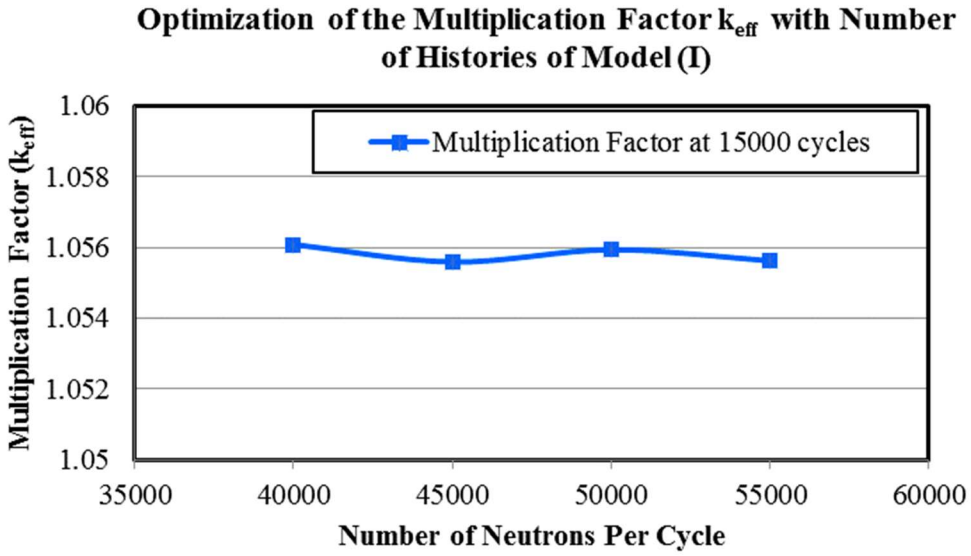

Figure (7-1): Optimization of the Multiplication Factor k_{eff} with Number of Histories Using the Serpent Code

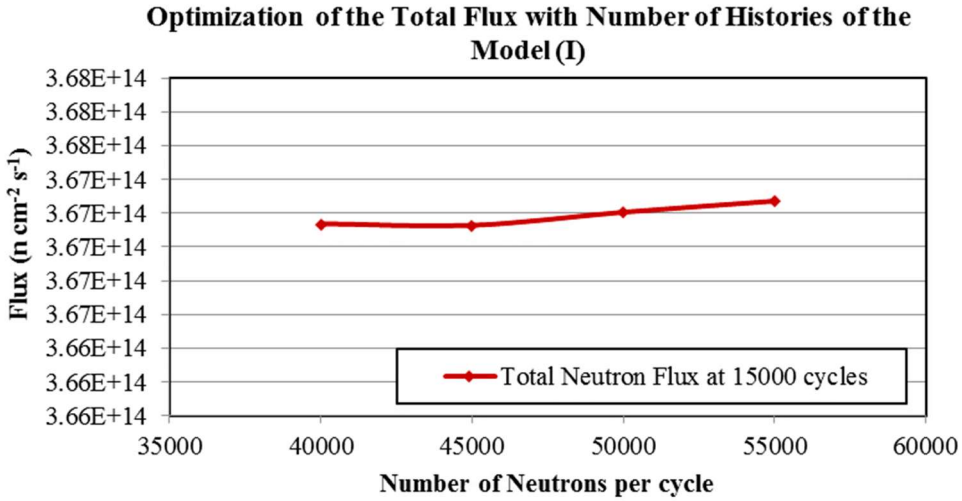

Figure (7-2): Optimization of the Total Flux with the Number of Histories Using the Serpent Code

To save computational time, there is no need to increase the number of histories; the corresponding values of the number of neutrons per cycle is chosen as 55000 n per cycle for 15000 cycles, and the number of the inactive cycles is optimized at 200 cycles.

Model (I) is used to investigate the effect of a changing lattice pitch size and fuel enrichment in the fast core for a constant radius and number of fuel channels for the fast core. So, there are four cases for Model (I) that will be used for this investigation as discussed in the next section.

7.3. Description of the Design of Multispectrum CANDU Reactor Model (I) and Model (II)

For the uranium-fuelled models, the radius is set at R_2 = 108.86 cm. The radii of the fast core are chosen as multiple lattice pitches to minimize the unfuelled spaces in the thermal core and fast core. The various geometric specifications of the MSCR-Models (I and II) and the mass of the fuel and fissile isotopes (U-235) are shown in Table (7-1) and Table (7-2). The common (constrained) parameters for the models are: (i) the full size of the reactor, which is the same as a CANDU 6 Gentilly-2 reactor (radius of 335 cm or 379.73 cm including the reflector with an axial dimension of 594 cm), and (ii) the standard 37-element fuel bundle. In the thermal core, the bundle is made of Zircaloy-4; however, in the fast core, the proposed bundle is of the same standard dimensions and sheath thickness as 37-fuel bundle but made of stainless steel 316L(N)SS.

Table (7-1): MSCR Models Designed and Simulated with Enriched Uranium

Model	Radius of the fast core measured from outer radius of partition wall. (cm)	Number of fuel channels in the thermal core	Number of fuel channels in the fast core	Lattice pitch of the fast core (cm)	Fuel type of the fast core and concentration of fissile materials (atomic ratio)
I	**R_2=108.86**	**320**	**32**	**28.575**	**^{235}U (19.9%)**
II	**R_2=108.86**	**320**	**148**	**14.575**	

Table (7-2): Mass of the Fuel and Fissile Materials in the MSCR Design with Enriched Uranium

Model	Total Mass of the UO_2 of the thermal core (g)	Mass of fissile materials in the thermal core (g)	Mass of the fuel in the fast core (g)	Mass of fissile materials in the fast core(g)	Total Mass of fissile material (g)	total mass of the fuel in the reactor Total mass of the fuel(g)
I	**8.70675E+07**	**5.45687E+05**	**8.70675E+06**	**1.51145E+06**	**2.05713E+06**	**9.577422E+07**
II	**8.70675E+07**	**5.45687E+05**	**4.0269E+07**	**6.99044E+06**	**7.53613E+06**	**1.27336E+08**

7.4. The Layout of the MSCR-Model (I) Design.

The multispectrum CANDU based reactor can be used for burning actinides and to produce electricity. As mentioned, it consists of two concentric cores as shown in Figure (7-3-A).

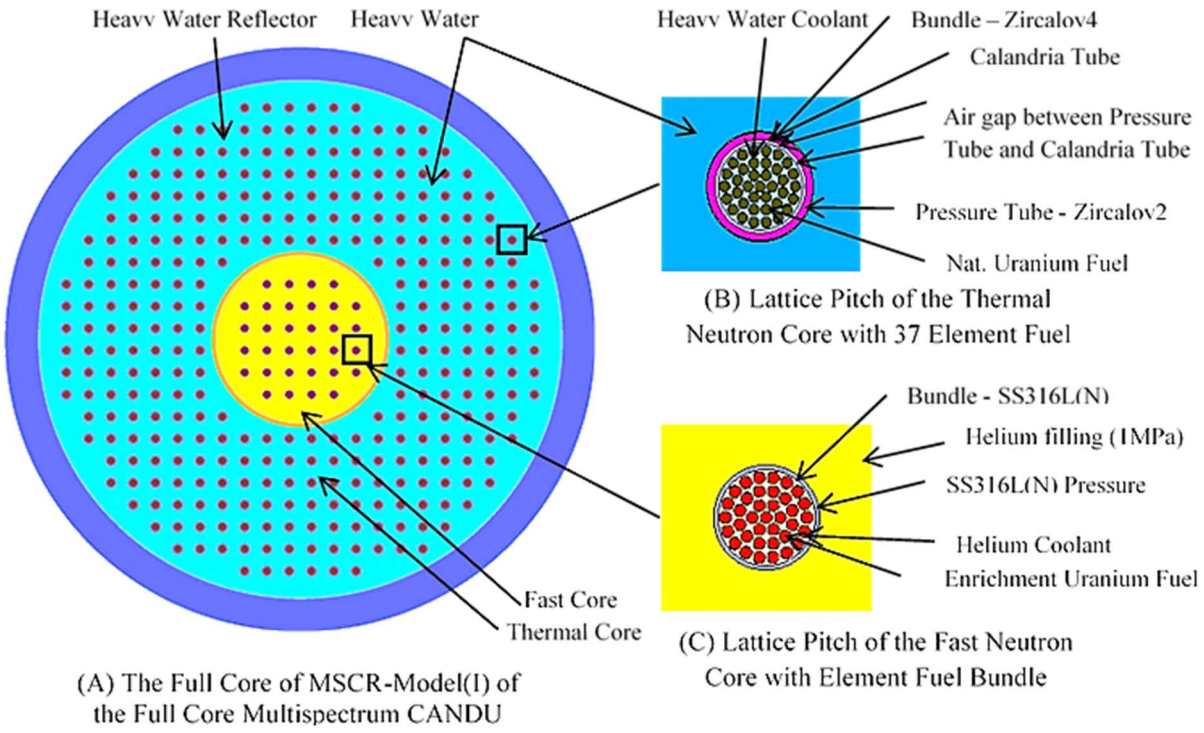

Figure (7-3): The Design Model of the Multispectrum CANDU Reactor Model (I)

The external fission region, or the outer core, has the same traditional CANDU structure, providing the external core with a predominant thermal neutron spectrum, with a lattice pitch shown in Figure (7-3-B). The internal fission region, or the inner core, is constructed to have a predominant fast neutron spectrum. For Model (I), the lattice pitch of the fast core is the same size as that of the thermal core equal to 28.575 cm. The structural materials and fuel for each core are presented in Figure (7-3-B,C) and Table (7-1)[59].

The fast and thermal cores, are separated by two stainless steel partition walls. The partition walls create a low-pressure helium gas-filled region to minimize the thermal diffusion from the fast core to the moderator of the thermal core that may affect the moderation quality.

7.4.1. The Fast Neutron Spectrum Core

The choice of coolant in the fast reactor is dictated by the desire to ensure a small or negligible amount of neutron absorption and moderation while still being able to remove reliably the heat from the fast core with a higher-powered density. In general, conventional coolants used in a fast nuclear reactor are: (1) liquid metals such as sodium and Pb-Bi lead (44.5%)-bismuth (55.5%) or eutectic alloys where sodium is the most common use as a coolant; and (2) a gas coolant. The most common choices for gas-cooled fast reactors are helium, supercritical CO_2, and steam [60][61] [62].

The use of Pb-Bi and sodium as coolants in the MSCR was avoided because both sodium and bismuth (at high-temperature 350^{o}C) have substantial chemical reactivity with water, which is used as both a coolant and moderator in the external thermal core. To avoid any inconvenient chemical reaction in case of an accident, and save on the requirement for a high pumping power, a liquid metal coolant is avoided.

Even though most of the gas coolants are composed of light isotopes, the amount of moderation is limited because of the low density of gas coolants, where most of the gas coolant isotopes have low neutron scattering and capture cross sections. At high temperatures, steam could be reactive with the stainless steel of the bundle sheath, pressure tube, and partition wall. The gas CO_2 degrades from radiolytic dissociation producing free oxygen and carbon monoxide. Oxygen at high temperature reacts with the stainless-steel structure. Consequently, steam and CO_2 are avoided as possible candidates in the fast neutron spectrum core. Therefore, helium represents the best choice as the coolant for the fast core of the MSCR.

The advantages of choosing helium as a gas coolant for the fast core are: (1) Chemical compatibility with heavy water in the case of accidents and leaks between the fast and thermal cores, eliminating the need of an intermediate coolant loop, and having generally a good chemical compatibility with structural materials, (2) Negligible activation of helium which has only two isotopes: $^{4}_{2}$He ($99.999863\ ^{a}/_{o}$) which has a negligible capture cross section) and $^{3}_{2}$He ($0.000137\ ^{a}/_{o}$) a reasonably high probable (n,p) reaction (due to the very small atomic percentage of this isotope, this reaction is negligible); (3) Optically transparent, simplifying fuel shuffling operations and inspection; (4) Impossibility of phase change of helium gas coolants in

the core, reducing the potential of reactivity swings under accidental conditions; (5) Generally harder neutron energy spectra allowed by helium gas coolants, which increase the burnup potential in the fast core reactor; and (6) Low density of helium gas coolants which can allow a larger coolant fraction in the core without an unacceptable increase in parasitic neutron capture. The latter property provides the opportunity to increase the helium coolant pressure, consequently increasing the efficiency for heat removal from the core[60].

1) Filling material of the fast core and the gap between the partition walls.

To obtain the highest burnup potential in a fast reactor, parasitic neutron absorption should be minimized. This translates into the choice of a very tightly packed core in which the volume fractions of structural materials and coolant are kept to a minimum. For reasons of economics for the fuel cycle and power production, it is desirable to have the highest possible burnup while respecting the safety margins. Thus, the reactor core is designed to have a very high fast neutron flux level. This high level translates into a high fast fission rate and high burnup of the actinides by fast neutrons, and, consequently, resulting in a high-power density. It should be noted that the power density in a fast reactor results from the design choices in addition to the features of reactor coolant type. The neutron spectrum will be affected if the coolant affects the fast neutron flux with absorption or moderation. Consequently, the rate of interaction at each energy bin and the power density distribution will be affected too. So, the choice of coolant is dictated by the desire to introduce the smallest amount of neutron absorption and moderation, while still being able to reliably remove the heat from this high-power density reactor configuration.

To ensure a predominant fast neutron spectrum, the filling materials must have a very small moderation power and be transparent to thermal, epithermal and fast neutrons. The perfect choice of coolant to meet these characteristics is helium gas. The filling gas outside of the pressure tube in the fast core is at pressure of 1 MPa. The use of helium as a filler material leads to a major fission reaction with fissile materials in the fast core taking place in the fast flux region where the fast core can be used to burn actinides. Helium is used in the fast core as a coolant at 6 MPa. In order to avoid heat transfer between the fast core and the thermal core, the space between the two stainless steel partition walls is filled with a low pressure (0.1 MPa) helium gas, benefitting from

the advantages of a low pressure gas as a thermal insulator[59]. Maintaining the pressure and high flow rate is provided by three separate pumps.

2) The material of fast core bundle, pressure tube and partition walls.

The recommended material for the bundle, pressure tube and partition walls of the fast core is Stainless Steel 316L(N)SS [52] rather than Zircaloy. Since the fuel used in the fast core has different enrichment levels, the temperature of the sheath may reach 900 K. Zircaloy is not suitable at such a high temperature for the fast reactor. Stainless Steel (316SS) grade is very applicable for high temperature operation. This alloy is more resistant to general corrosion and pitting/crevice corrosion than the conventional chromium-nickel austenitic stainless steels such as Type 304 SS. Type (316SS) also offer higher creep, stress rupture and tensile strength resistance at elevated temperatures[64] [65].

The choice of 316L(N)SS grade stainless steels is decided by several important factors such as high temperature (about 900 K), mechanical properties like creep, low cycle fatigue and creep-fatigue interaction, compatibility with the helium coolant, its ability to be welded and fabricated, and cost. Type 316L(N)SS austenitic stainless steel containing 0.02-0.03 wt.% carbon and 0.06–0.08 wt.% nitrogen is the current choice of material for high-temperature sodium-cooled fast reactors (SFRs)[66]. Increasing the nitrogen content from 0.06-0.08 wt % to levels of 0.12-0.14 wt% has been found to increase the creep rupture life of 316L(N)SS by order of magnitude[67]. Nitrogen in the 316L(N)SS alloy adds additional resistance to sensitization and provides some solid solution hardening, raising its minimum specified yield strength compared to 316L stainless steel[52][68]. The element contents of the Stainless Steel 316L(N)SS are shown in Table (7-3)

Table (7-3): Elemental composition of the Stainless Steel 316L(N)SS[52]

Reactor components	Material	Element	Mass ratio wt.%
Fuel bundle Pressure tube Internal partition wall External partition wall	Stainless steel 316L (N) Density= 8 g cm^{-3}	Fe	65.441
		N	0.14
		C	0.025
		Mn	1.74
		Cr	17.57
		Mo	2.53
		Ni	12.15
		Si	0.2
		S	0.004
		P	0.2

3) Bundle used in the fast core

The bundle used in the current fast core of the MSCR is a traditional 37-element bundle. The geometrical properties are the same as one used in the CANDU reactor but as explained above, the material used is stainless steel 316L(N)SS [63] instead of Zircaloy-4.

4) Pressure tube

One of the advantages of choosing the stainless steel 316L(N)SS is a high value of the maximum allowable stress of this type of alloy at high temperature. According to Equation (7-1), the thickness of the pressure tube or partition wall is inversely proportional to the maximum allowable design stress. A minimum thickness for the pressure tube and the partition walls is necessary to decrease their effect on the neutron flux. The thickness of the pressure tube is calculated according to the pressure difference across it. The pressure of the helium gas coolant inside most traditional gas-cooled fast reactors is around 5 to 7 MPa [60]. In the current MSCR reactor model, the helium coolant pressure is set to 6 MPa, which can affect the stainless-steel pressure tube. The tube thickness can be calculated according to: [65].

$$t = \frac{\Delta P \times R_{in}}{(S \times E) - (0.6 \times P)} \tag{7-1}$$

where,

t: is the thickness of the pressure tube or partition walls (inch)

ΔP: pressure difference between the inside and outside pressure tube or partition wall (psi)

R_{in}: inside radius of the tube (inch)

S: Maximum allowable design stress (psi),

E: Joint coefficient (which is supposed to be 1)

Equation (7-1) can be used to further calculate the thickness of the stainless-steel pressure tube used in the fast core. Given that the pressure on the inside the pressure tube is 6 MPa and at the outside it is 1 MPa, therefore the pressure differential is ΔP = 5MPa. The temperature of the pressure tube is around 650 K. The corresponding maximum allowable design stress is 17050 psi (117.556 MPa) found from tables in [69]. The required thickness of the pressure tube is calculated to be 0.467 cm.

5) Partition walls

The external thermal neutron spectrum core and the internal fast neutron spectrum core are separated by two stainless steel partition walls. These walls are separated with a 5-cm thick space filled with low-pressure helium gas (0.1 MPa). This low-pressure gap minimizes the heat transfer from the fast core to the moderator of the thermal core. As a result, moderation efficiency will not be affected. Subsequently, the thermalization rate of neutrons will not be affected in the thermal core. Therefore, this design provides insulation to keep the thermalization efficiency of the external core as desired in the traditional CANDU 6 thermal reactors and consequently the power density in the core. Criteria of designing the partition walls radii of the MSCR models are: i) keeping the lattice pitch size at the same value (28.575 cm) for the different radii designs (R_1, R_2 and R_3); ii) keeping the distance between the two partition walls at 5 cm, and, iii) the helium pressure inside the fast core equal to (1 MPa) [59]. Equation (7-1**)** can be used to calculate the thickness of the internal and external partition walls. The steps used to calculate the thickness of the partition walls are as follows:

1) Guessing the inner radius according to the internal pressure,
2) Find the thickness of the internal partition wall and the internal radius of the external partition wall,
3) Find the thickness of the external partition wall and add the thickness of the external partition wall to its internal radius to find the external radius,
4) The goal is to optimize the internal thickness of the internal partition wall.

The thicknesses at the three radii of the fast core used for the six models are presented in Table (7-4). The thermal and fast core specifications and materials are also shown in Table (7-4) and Table (7-5).

Table (7-4) Thickness of Partition Walls at the Three Radii Used to Design the Fast Core of the MSCR Models

Model	Thickness of Internal Partition Wall (cm)	Thickness of External Partition Wall (cm)
III and IV(R_1)	1.06	0.56
I, II and V (R_2)	0.84	0.44
VI (R_3)	0.62	0.34

6) The Fast Neutron Spectrum Core Fuel

In the current MSCR-model (I), the fuel used in the fast core is uranium dioxide, UO_2, of different (U-235) enrichments :0.7%, 5.0%, 10%, 15.0% and 19.9%. The model avoids a 20% enrichment because it represents the non-proliferation threshold. The fuel is in the form of cylindrical pellets stacked in 37 fuel rods or elements in a standard in a 37-element bundle, except that stainless steel 316L(N)SS replaces zirconium alloys. There is no need for the calandria tube because there is no moderator in the fast core. The number of fuel channels in the fast core depends on the radius and the lattice pitch chosen for the fast core. The common material characteristics of the fast core as used in this work are presented in Table (7-5).

Table (7-5): Materials for the Fast Core

Fast core components	Material	Density (g cm^{-3})	Temperature (K)	Pressure (MPa)
Fuel	Nat. UO_2	10.6	1400	n/a
Cladding	316L(N) SS	8	900	n/a
Coolant	He	6.618E-3	800	6
Pressure tube	316L(N) SS	8	650	n/a
Filling fast core material	He	1.99E-3		1
Internal partition wall	316L(N) SS	8	340	n/a
Gap between the partition walls	He	1.36E-4		0.1
External partition wall	316L(N) SS	8	330	n/a

7.4.2. The Thermal Neutron Spectrum Core

In the external thermal core, the major fission reaction taking place occurs with a predominant thermal neutron flux. This core is fuelled with natural uranium using 37-element Zr-4 bundle with

heavy water coolant and moderator. This configuration provides the main source of power generation in the MSCR. The external thermal core structure looks exactly like a traditional CANDU 6 reactor but with a lower number of fuel channels depending on the radius of the fast core. In all different models used, the lattice pitch of the thermal core is set at 28.575 cm. But the number of fuel channels in the thermal core may be different from one model to another depending on the relevant radius of the fast core as shown in Table (7-1). The actinide fuel burnup in the multispectrum reactor is affected primarily by the flux shape profiles of the three neutron energy groups (i.e., thermal, epithermal and fast) in both the thermal and fast cores.

7.5. Dependence of the Flux Profile on the Lattice Pitch and Fuel Enrichment of the Fast Core of U-235 Fuelled MSCR-Model (I)

In this section, the number of fuel channels is chosen to be a constant value of 32 fuel channels for all Model (I) simulations with a radius of the fast core of R_2=108.86 cm. Four cases are considered: Models (I-A), (I-B), (I-C), and (I-D), to investigate the radial flux profiles at different energy groups and find the dependence of the multiplication factor (k_{eff}) and the regeneration factor on the lattice pitch and enrichment concentrations. The design variables of these four cases of the model (I) are:

(a) Enrichment in the fast core fuel (En) are chosen as 0.7%, 5%, 10%, 15% and 19.9%.

(b) Lattice pitch of the fast core structure (Lp): chosen as 14.575 cm, 18.575 cm, 22.575 cm, and 28.575 cm. Table (7-6) provides a brief description of these four cases.

The characteristics of the thermal core for the four cases of Model (I) under consideration are similar to the traditional CANDU 6 lattice as shown in Figure (7-41) and Table (7-1) with a lattice pitch of 28.575cm and natural uranium fuel of 0.7% U-235. The four models differ only in the characteristics of the fast core as shown in Table (7-6) and Table (7-9).

Table (7-6): Description of the Four MSCR Cases of Model (I)

Thermal Core				Fast Core		
Case	Lattice Pitch (cm)	Number of fuel channel	Fuel enrichment concentration U-235	Lattice pitch (cm)	Number of fuel channels	Fuel enrichment concentration U-235
Model (I-A)	28.575	320	0.7%	14.575	32	0.7%, 5%, 10%, 15% and 19.9%.
Model (I-B)				18.575		
Model (I-C)				22.575		
Model (I-D)				28.575		

Figures (7-4), (7-5), (7-6), and (7-7) show the fast neutron cores for Models (I-A), (I-B), (I-C), and (I-D) as described in the Table (7 6). The differences between the four models are the lattice pitch values of 14.575 cm, 18.575 cm, 22.575 cm and 28.575 cm as fuelled with uranium at enrichments of 0.7%, 5%, 10%, 15%, 19.9% in U-235 for each lattice pitch.

In the following flux profiles of Figure (7-8) to Figure (7-9), the region (A) outside of the two-vertical blue dashed lines represent the external thermal core. The region (B) between the two-vertical red and blue dashed lines represents the region between the fast and thermal core, which is an unfuelled volume that contains the two partition walls, low pressure helium gas and a small volume of the thermal core moderator as shown in Figure (7-3) Finally, region (C) between the two-vertical dashed red lines represents the fuelled region of the fast core.

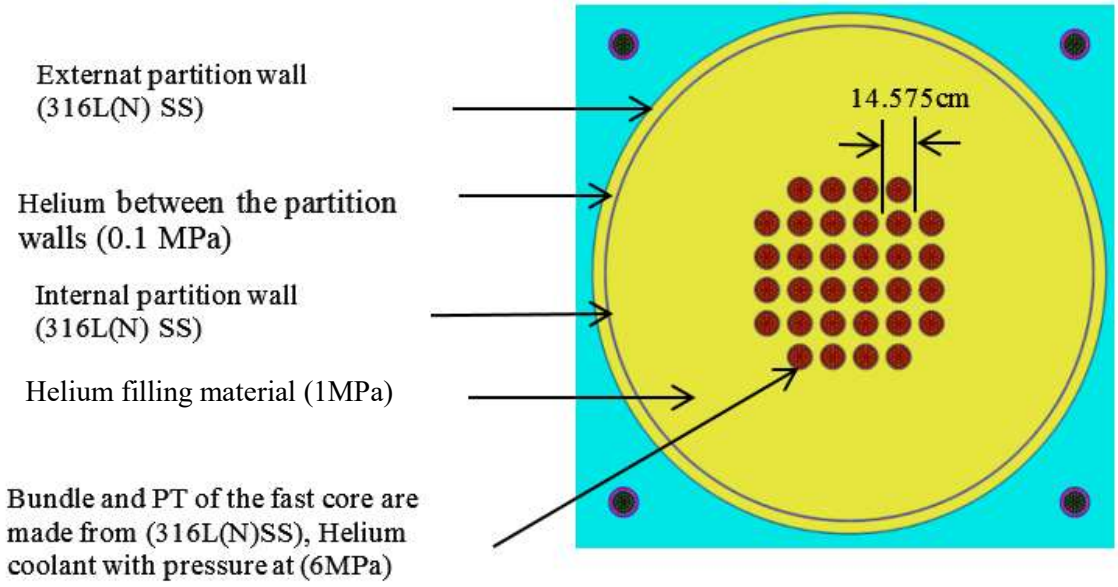

Figure (7-4): The fast core of the multispectrum CANDU reactor with 32 fuel channel and 14.575 cm lattice pitch of the fast core for Model (I-A).

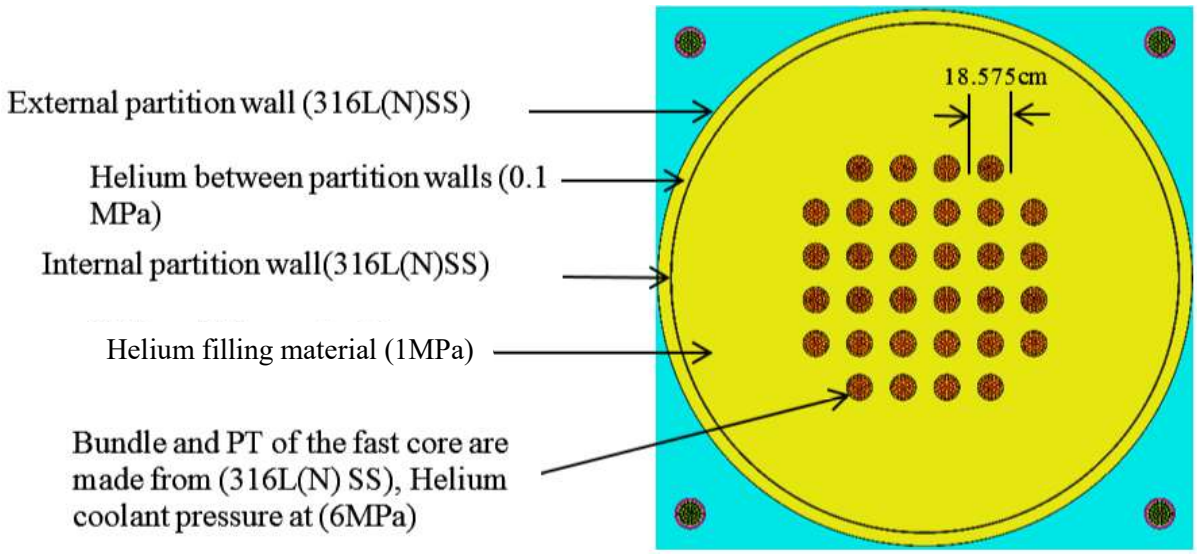

Figure (7-5): The fast core of the multispectrum CANDU reactor with 32 fuel channels and 18.575 cm lattice pitch of the fast core for Model (I-B).

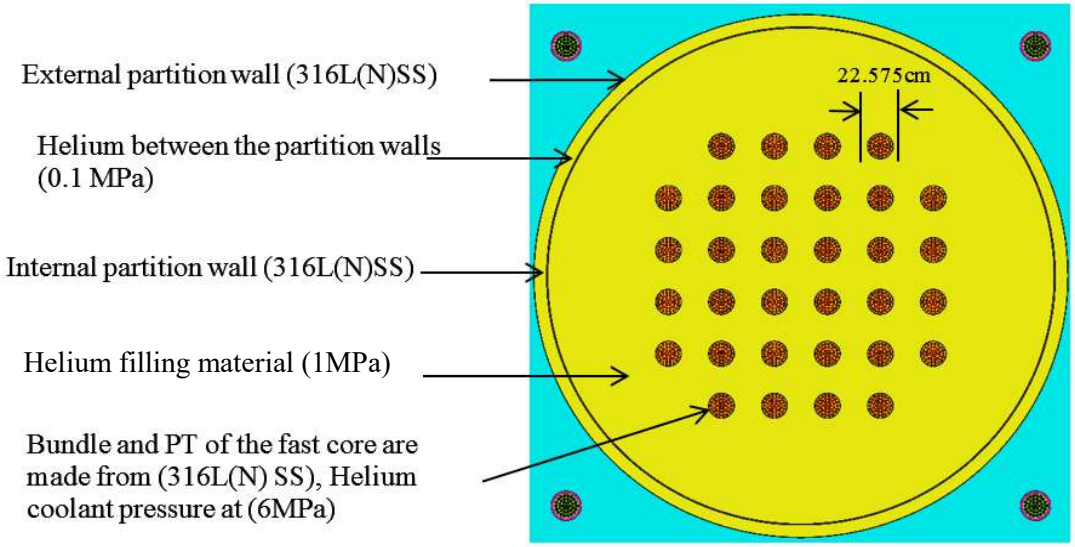

Figure (7-6): The fast core of the multispectrum CANDU reactor with 32 fuel channels and 22.575 cm lattice pitch of the fast core for Model (I-C).

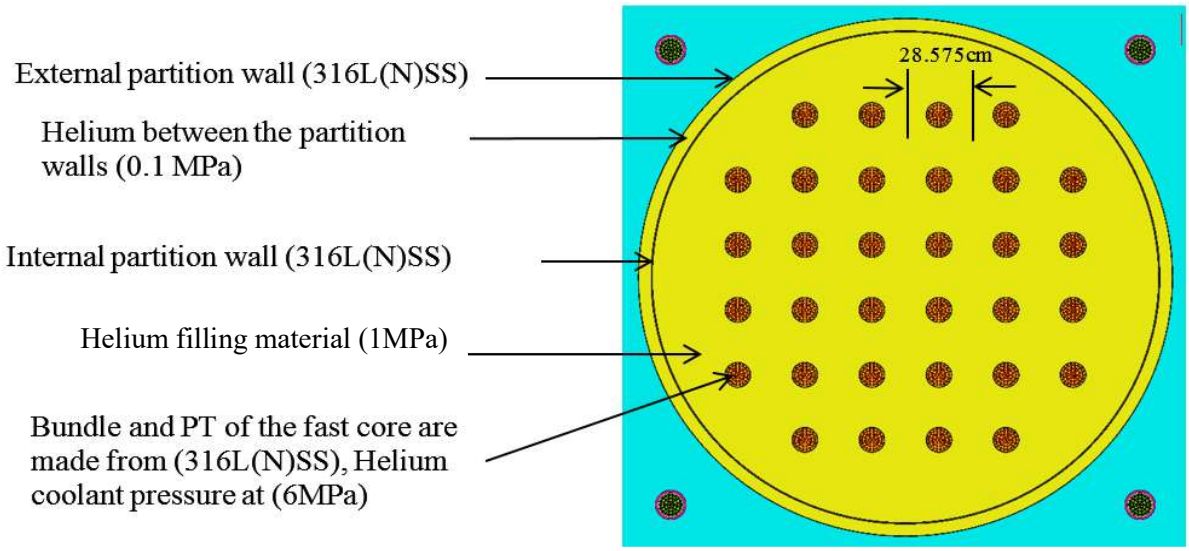

Figure (7-7): The fast core of the multispectrum CANDU reactor with 32 fuel channel and 28.575 cm lattice pitch of the fast core for Model (I-D).

7.5.1. Thermal Neutron Flux Distribution in the MSCR-Model (I) at Lattice Pitches for Different Enrichments.

Figure (7-8), Figure (7-11) show the radial thermal fluxes profiles in both the external thermal core and internal fast core of the four models (I-A, -B, -C, and-D) with lattice pitches 14.575, 18.575, 22.575 and 28.575 cm, respectively. For each case, the radial fluxes are calculated at different enrichments of ^{235}U at 0.7%, 5%,10%,15% and 19.9% for the fast core. One notices that:

1) The thermal flux in the thermal core, region (A), is slightly higher in the middle (~2.71E+14 n $cm^{-1}s^{-2}$) while at the edge of the thermal core, it is ~1.68E+14 n cm^{-1} s^{-2} and ~1.27E+14 n cm^{-1} s^{-2} because of the small fuel-to-moderator ratio. The thermal fluxes at a different fuel enrichment of the fast core have the same shape and value. Therefore, the thermal fluxes in the thermal core are not significantly affected by the enrichment concentration of the fuel in the fast-internal core.

2) In region (B), all the thermal fluxes at different enrichments are fast dropping down because there is no fuel or moderator in this region. The only materials in this region are stainless steel (partition walls) and the helium gas isolator. The thermal flux behaviour is almost the same for each enrichment concentration of the fast core for the four MSCR models under consideration.

3) In region (C), for Model (I-A) shown in) and Figure (7-8), the thermal flux remains steady in the unfuelled outer channels of the fast core because there is no moderator in the fast core. The only material in this region is helium. At the central fuel channels of the fast core, the thermal fluxes behave similarly at different enrichments where they drop down to their smallest values because most of the thermal neutrons were absorbed in the outer ring of fuel channels because of self-shielding. At the center of the fast core, the lowest value of the thermal flux of ~1.15E+12 n cm^{-2} s^{-1} for a 5% up to 19.9% enrichment concentrations of ^{235}U and ~2.55E+12 n cm^{-2} s^{-1} for the 0.7% enrichment occurs because of the high absorption cross section of ^{235}U. Therefore, Model (I-A) has the smallest value of the thermal neutron flux in the middle of the fast core.

4) For Model (I-B) in Figure (7-5) and Figure (7-9), where the lattice pitch is increased to 18.575 cm for all enrichments, the thermal fluxes in the fast core are steady at the outer unfuelled channels. The thermal flux at fuel enrichments of 5%, 10%, 15% and 19.9% all have the same behaviour and drop down to a value of ~ 1.95E+12 n cm^{-2} s^{-1}. For the 0.7% of ^{235}U natural uranium content, the flux drops down to 3.85E+12 n cm^{-2} s^{-1} because of the high absorption cross section of ^{235}U. These two values of the flux are greater than that in case of a lattice pitch equal to 14.575 cm for similar enrichments. This is due to the wide space between the fuel channels at higher lattice pitches that decrease the effect of self-shielding and allows for more thermal neutrons to reach the center of the fast core.

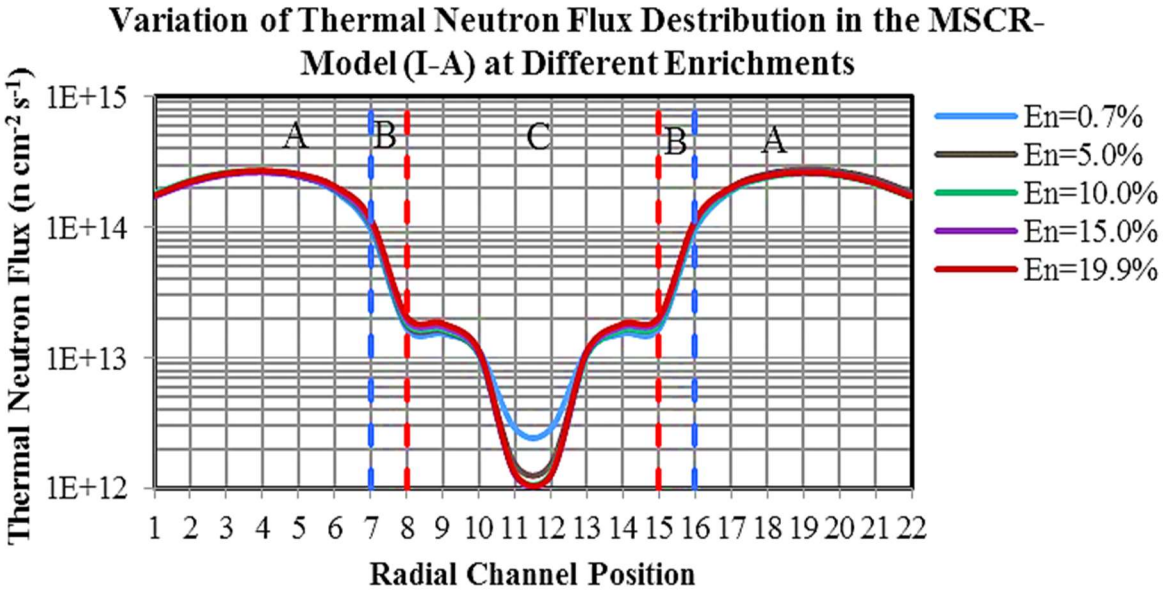

Figure (7-8): Variation of the Thermal Fluxes of MSCR with the Radial Positions at Different Enrichments of the Fuel in the Fast Core of Model (I-A).

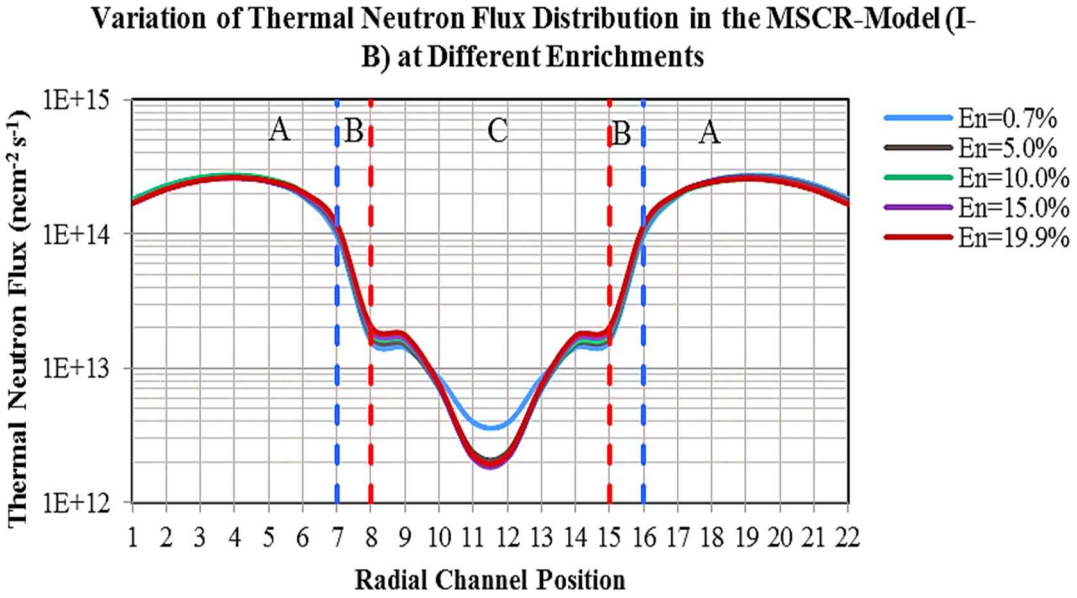

Figure (7-9): Variation of the Thermal Fluxes of MSCR with the Radial Positions at Different Enrichments of the Fuel in the Fast Core of Model (I-B)

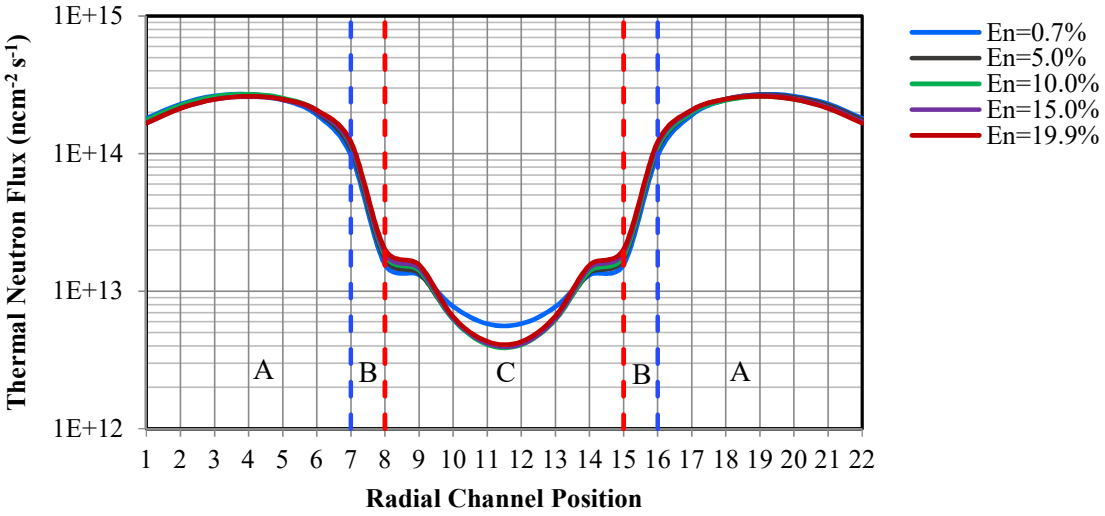

Figure (7-10): Variation of the Thermal Fluxes of MSCR with the Radial Positions at Different Enrichments of the Fuel in the Fast Core of Model (I-C)

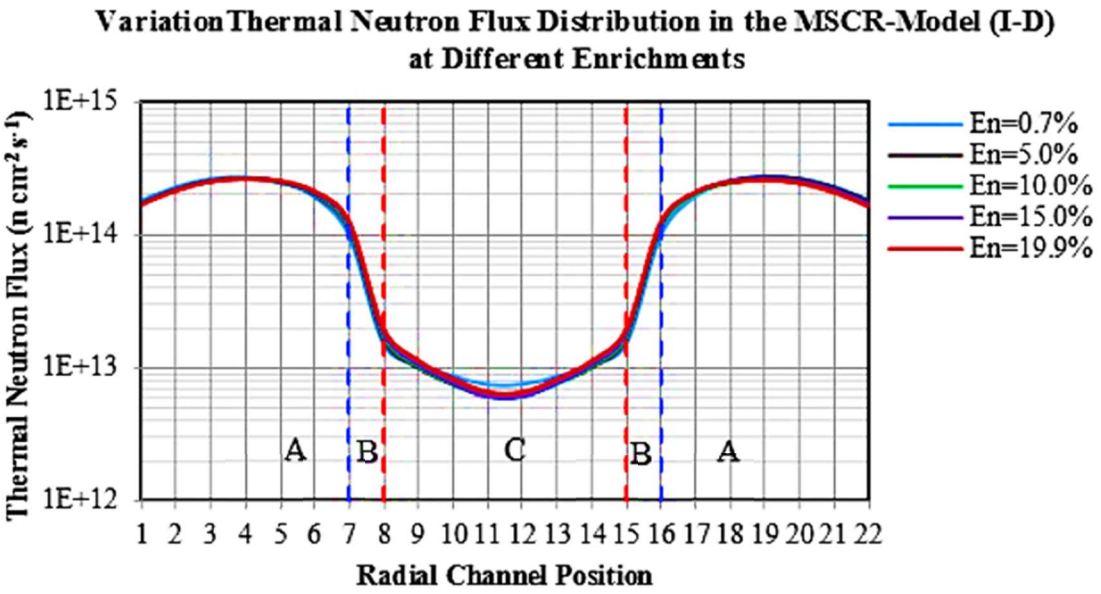

Figure (7-11): Variation of the Thermal Fluxes of MSCR with the Radial Positions at Different Enrichments of the Fuel in the Fast Core of Model (I-D)

5) For Model (I-C) in Figure (7-6) and Figure (7 10), where the lattice pitch increased to 22.575 cm for all enrichment concentrations, the thermal flux in the fast core is steady at the outer unfuelled channels. The thermal fluxes at fuel enrichments of 5%, 10%, 15% and 19.9% have the same behaviour and drop down to a value of ~ 4.1E+12 n cm^{-2} s^{-1}. For the ratio of ^{235}U 0.7%, the flux drops down to 5.5E+12 n cm^{-2} s^{-1} because of the high absorption cross section of ^{235}U. These two values of the flux are greater than that in the case of a lattice pitch equal to 14.575 cm and 18.575 cm for similar enrichment because there is more space between the fuel channels for the larger lattice pitches that decrease the effect of self-shielding and allow for more thermal neutrons to reach the center of the fast core.

6)

7) For Model (I-D) in Figure (7-7) and Figure (7-11), where the lattice pitch is increased to 28.575 cm for all enrichments, the thermal fluxes in the fast core decrease gradually toward the center of the core. The thermal fluxes at fuel enrichments of 5%, 10%, 15% and 19.9% have the same behaviour and decrease to ~ 7.5E+12 n cm^{-2} s^{-1}. For 0.7% of ^{235}U, the flux drops down to 7.85E+12 n cm^{-2} s^{-1} due to the absorption cross section of ^{235}U. These flux

values are higher than that in the case of lattice pitches equal to 14.575 cm, 18.575 cm and 22.575 cm for the similar enrichments with more space between the fuel channels.

8) One can conclude that as the lattice pitch of the fast core increases, the thermal fluxes increases slightly at the center of the fast core. At the lowest enrichment of the fuel at 0.7% U-235, the thermal fluxes are slightly higher at the center of the fast core. There are very small increases in the thermal flux at the internal edge of the thermal core as the lattice pitch of the fast core increases and as the enrichment also increases. At the same time, there is no significant increase in the thermal flux at the center of the thermal core due to changes in the lattice pitch or fuel enrichment of the fast core. This is because most of the diffused neutrons from the fast to thermal core are moderated at the internal edge of the thermal core in the fuel channels just outside the blue dashed lines and absorbed in these fuel channels.

7.5.2. Epithermal Neutron Flux Distribution in the MSCR at Lattice Pitches for Different Enrichment.

Figure (7-12) to Figure (7-15) show the variation of the radial epithermal fluxes profiles in both the external thermal core and the internal fast core for the four models (I-A, -B, -C, and -D). For each case, the radial epithermal flux is calculated at different enrichments of ^{235}U.

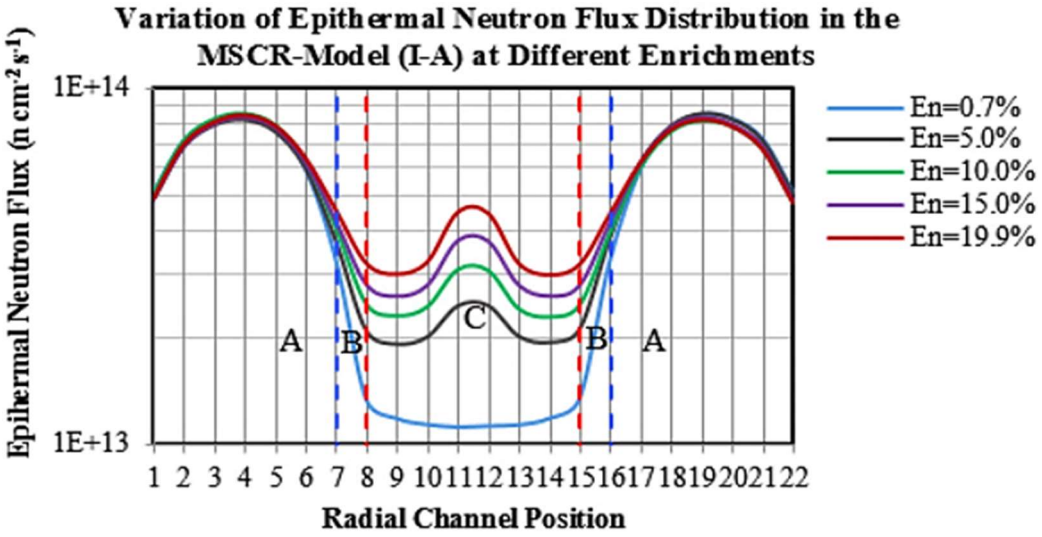

Figure (7-12): Variation of the Epithermal Fluxes of MSCR with the Radial Positions at Different Enrichments of The Fuel in the Fast Core for Model (I-A).

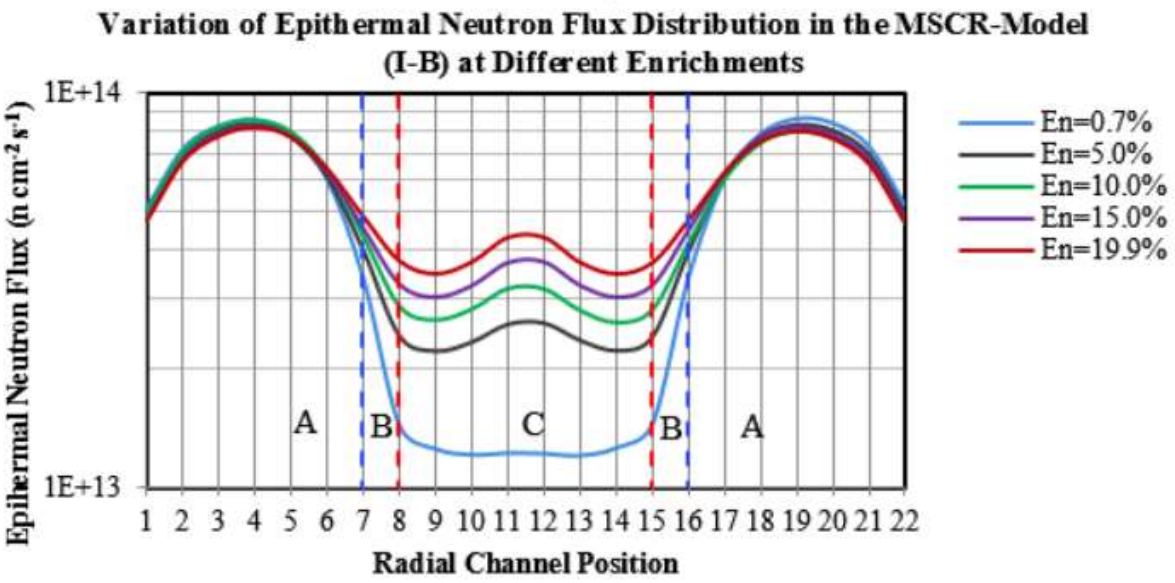

Figure (7-13): Variation of the Epithermal Fluxes of MSCR with the Radial Positions at Different Enrichments of the Fuel in the Fast Core for Model (I-B).

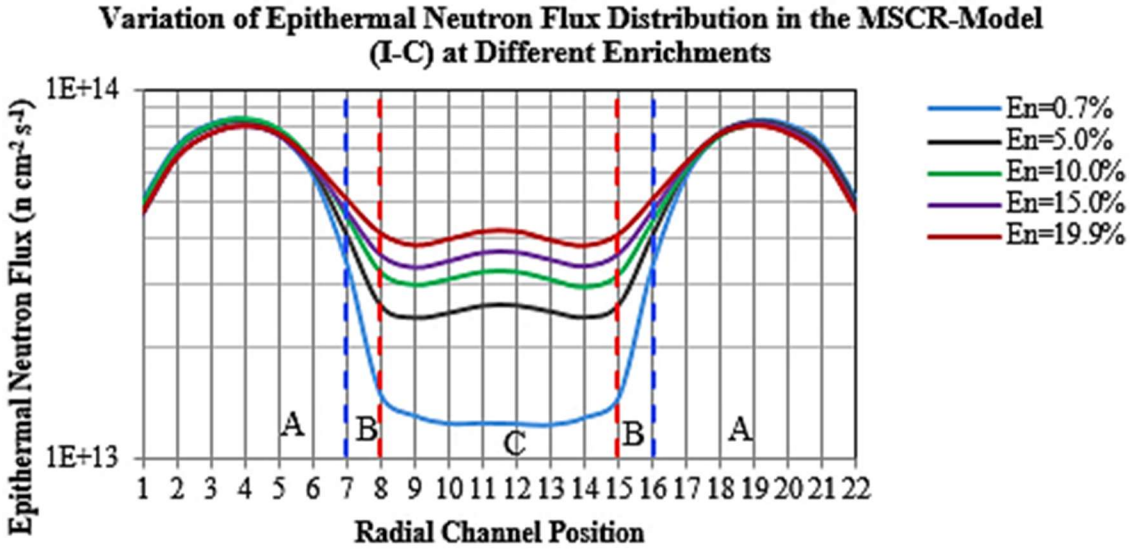

Figure (7-14): Variation of the Epithermal Fluxes of MSCR with the Radial Positions at Different Enrichments of the Fuel in the Fast Core for Model (I-C).

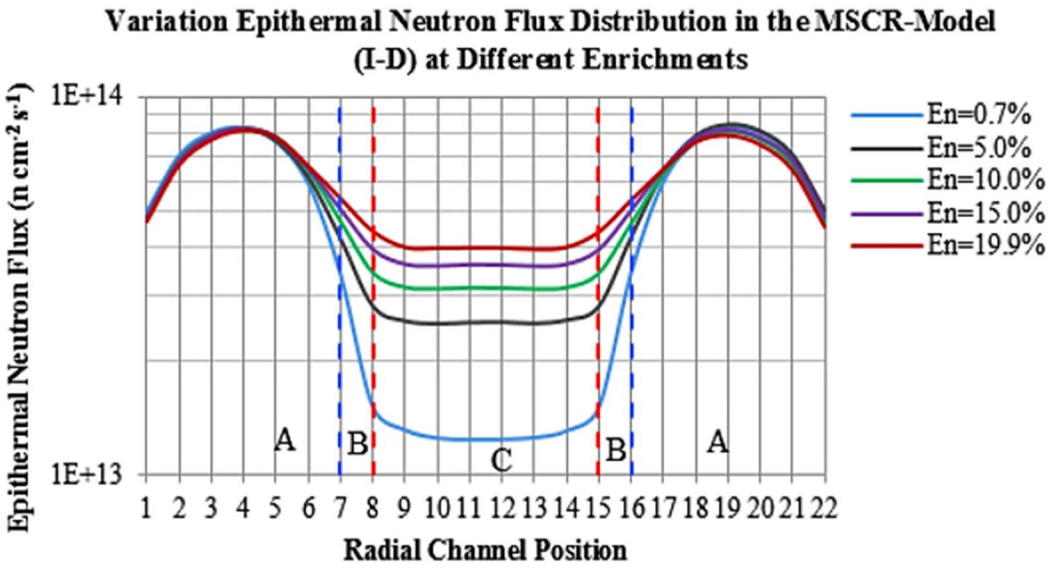

Figure (7-15): Variation of the Epithermal Fluxes of MSCR with the Radial Positions at Different Enrichments of the Fuel in the Fast Core for Model (I-D).

For the four models, one observes that:

1) The epithermal flux in the thermal core of region (A) is higher in the middle ~8.5E+13 n. cm^{-2} s^{-1}while that at the external edges (blue lines) of the thermal core it is ~5.0E+13 n cm^{-2} s^{-1}. At channels close to the external edges of the fast core, the epithermal fluxes decrease depending on the enrichment of the fuel because of diffusion of fast neutrons from the fast core to the thermal one in addition to lower values of the ratio of the fuel to the moderator.

2) In region (B), all the epithermal fluxes at different enrichments are dramatically decreasing with no fuel in this region (i.e., the only materials are stainless steel and helium). The epithermal flux behaviour is almost the same for each enrichment for the four models. The change in the gradient is different from one enrichment to another is explained by the production of epithermal neutrons in the fast core due to neutron collisions with stainless steel structural components and the partition walls and with some collisions in the moderator surrounding the fast core. As the enrichment in the fast core increases, the rate of production of fast neutrons increase and consequently, part of this fast spectrum is

affected from some collisions with stainless steel structure and falls into the epithermal energy region.

3) For region (C), the epithermal fluxes for all four models are different depending on the lattice pitch and enrichment. For natural uranium, the epithermal fluxes have the same behaviour. They are almost flat in the fast cores because the low U-235 content fails to produce many fast neutrons. There is a very small increase in epithermal neutrons as the lattice pitches increase from Model (I-A) to Model (I-D) at 0.7% U-235 concentration because, as the lattice pitch increases, there is a greater chance for neutrons to collide and to become epithermal before being absorbed or result in a new fast fission.

4) For Models (I-A) and (I-B), they have a peak in the middle of the fast core because of the higher epithermal flux at the loaded fuel channels than at the empty channels near the edge of the fast core. The heights of these peaks decrease as the lattice pitch increases from Model (I-C) and Model (I-D) from 14.575 cm to 22.575 cm. The flux shape at the center of the fast core becomes flat for a lattice pitch of 28.575 cm because, at higher values of the lattice pitch, the epithermal production becomes distributed at a similar rate in the radial direction of the fast core.

5) For all the models, the highest epithermal fluxes occur for the highest enrichment of 19.9% ^{235}U because of a high fission rate where the epithermal fluxes are proportional to the fast neutron fluxes.

7.5.3. Fast Neutron Flux Distribution in the MSCR at Different Lattice Pitches for Different Enrichments.

Figure (7-16) to Figure (7-19) show the variation of the fast radial fluxes in both the external and internal core for the four models (I-A,-B,-C, and -D), respectively. For each case, these fast radial fluxes are calculated for different enrichments of ^{235}U.

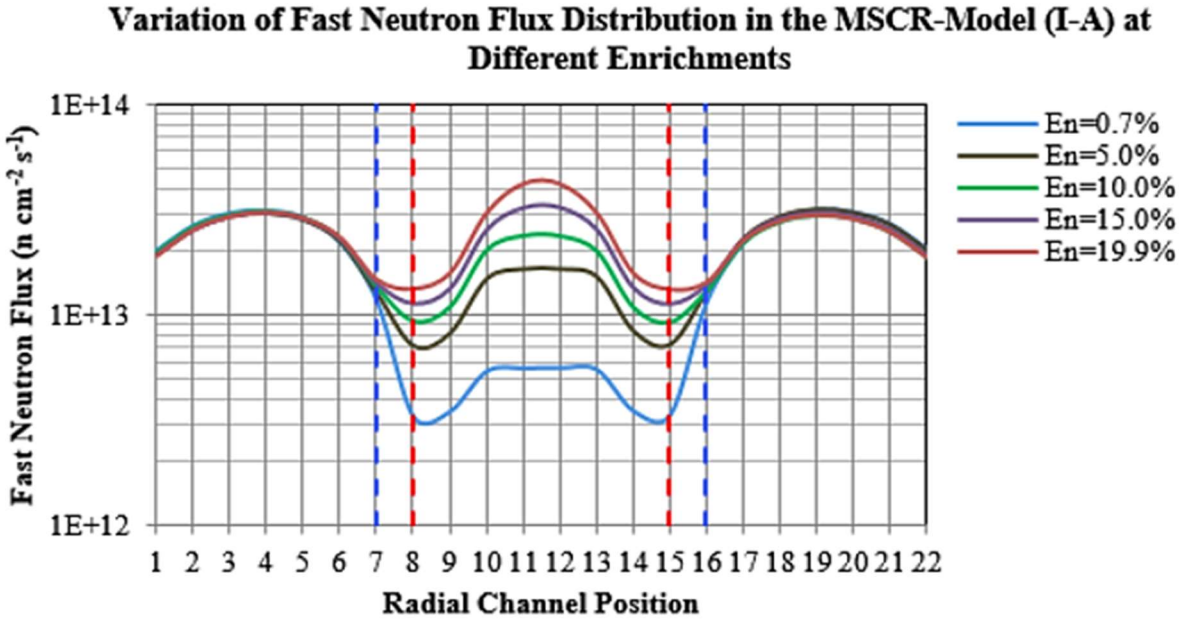

Figure (7-16): Variation of the Fast Fluxes of MSCR with The Radial Positions at Different Enrichments of the Fuel in the Fast Core for Model (I-A).

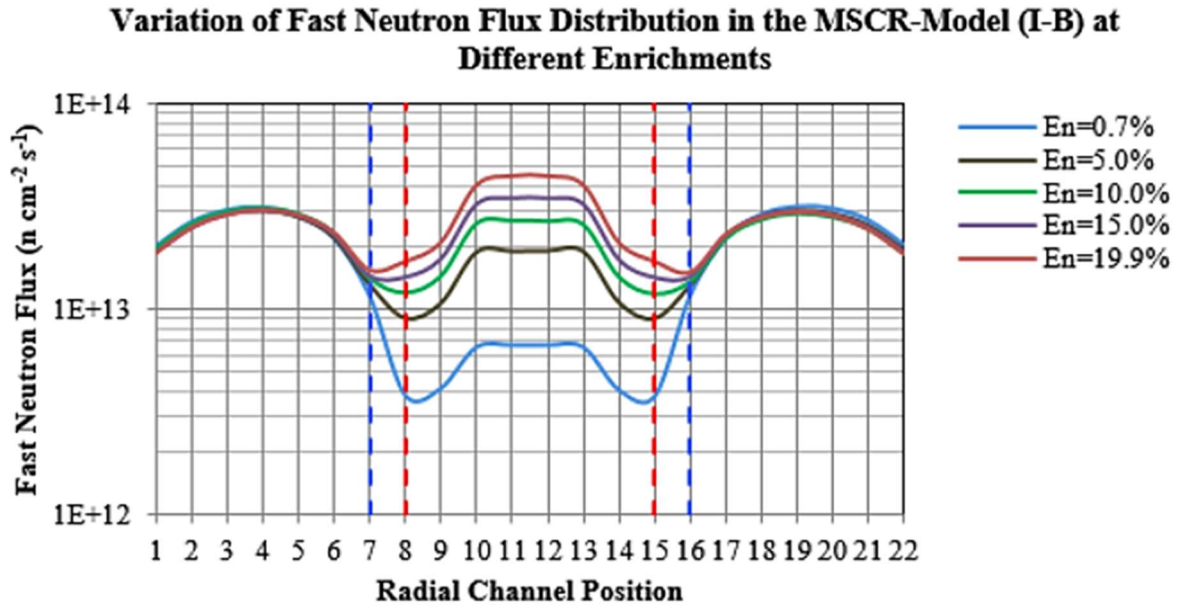

Figure (7-17): Variation of the Fast Fluxes of MSCR with The Radial Positions at Different Enrichments of the Fuel in the Fast Core for Model (I-B).

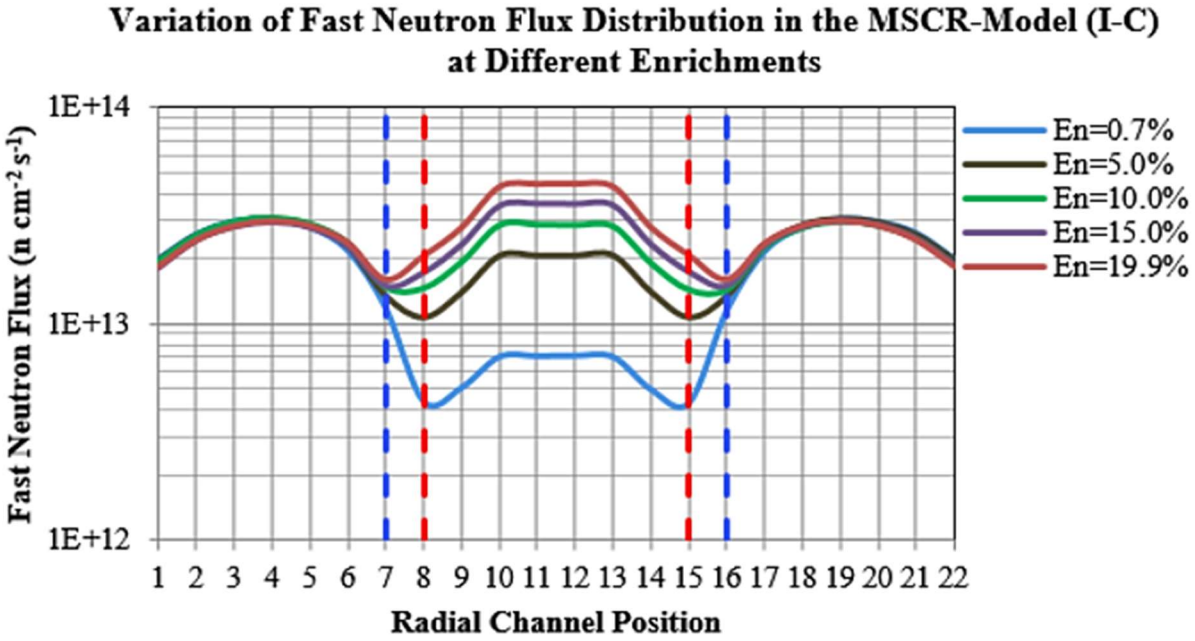

Figure (7-18): Variation of the Fast Fluxes of MSCR with The Radial Positions at Different Enrichments of the Fuel in the Fast Core for Model (I-C).

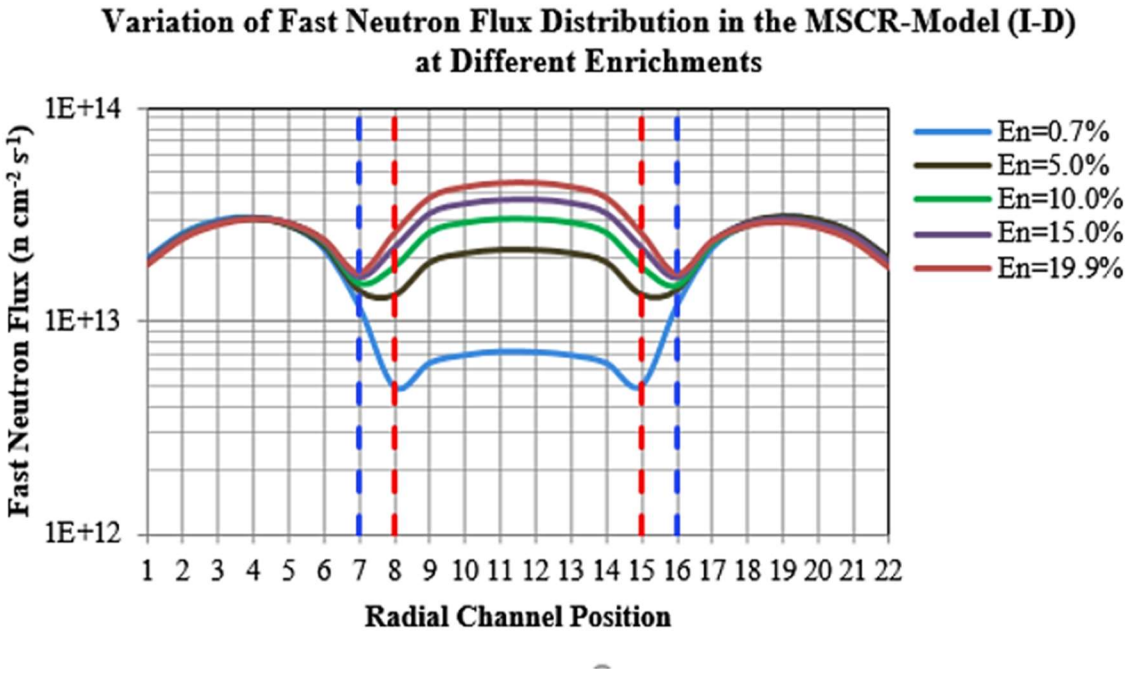

Figure (7-19): Variation of the Fast Fluxes of MSCR with the Radial Positions at Different Enrichments of the Fuel in the Fast Core for Model (I-D).

The inspection of Figure (7-16) to Figure (7-19) shows that:

1) In the thermal core region (A), at the middle of the thermal core, all the fast radial fluxes at different ^{235}U enrichments and at different lattice pitches do not change and are close to a constant value of ~3.0E+13 n cm^{-2} s^{-1}. For the different enrichments, the fast fluxes are almost identical at most positions in the thermal core. Close to the internal edge of the thermal core, there are very small changes of the flux value for different enrichments and different lattice pitches because most of the fast neutrons experience little moderation (e.g. at the right edge of the lattice pitch) that causes the fast neutrons to fall into the epithermal energy group. This explains the significant difference between the epithermal neutron fluxes at the region close to the fast core region of the of the epithermal flux in Figure (7-10) to Figure (7-13).

2) In region (B), the differences between the fast spectra of the four models are not significant because diffused neutrons from the fast core to the thermal core are thermalized and mostly contribute to the epithermal energy region. This explains the small difference in the fast flux right on the edge of the thermal core. This diffusion of fast neutrons increases with the enrichment. There is no fuel in this region made only of helium and stainless steel for which the cross section for the absorption of fast neutrons are low.

3) In the fast core region (C), as the enrichment increases, there is an increase in the fission rate. The fast neutron fluxes sources are mostly from fast fission in U-235.

4) For the enrichments of 0.7% and 5% of 235U, the fast flux in the fast core is less than that in the thermal core. However, for an enrichment of 10%, the fast neutron flux in the fast core is the same as that in the thermal core, while for enrichments of 15% and 19.9%, it is higher than that in the thermal core.

5) In the light of the analysis of this section, the objective of the current thesis work is to burn high-fissile concentrations of actinide. The fast neutron flux is more effective for actinide burning as previously demonstrated, while there is a minor effect of the thermal flux especially at the center of the fast core. Consequently, the design of the fast core should be driven in the direction which make the fast neutron flux in the fast core as high and as flat as possible to uniformly and efficiently burn actinides. Therefore, in conclusion, the

enrichment in the fuel channels should be at a highest possible level and the lattice pitch of the fast core should be reduced to include more enriched fuel and raise the fast neutron while respecting the safety constraints, breeding criteria, and non-proliferation requirements.

7.5.4. Dependence of the Multiplication Factor (k_{eff}) and the Regeneration Factor (η) on the Fuel Enrichment and on the Lattice Pitch in the Fast Core.

The multiplication factor (k_{eff}) is the main physical parameter that is needed to be calculated and considered in the reactor design because it impacts the reactor operation and safety. The regeneration factor as defined in Chapter 3 arises from the concept of the breeding ratio that represents the line between conversion and breeding. Here, the word "breeding" indicates a reactor condition in which the rate of production of fissile material is larger than the rate of consumption of fissile material. The criterion $\eta < 2$ represents the condition to avoid breeding of new fissile material. To study the effect of the variation of the lattice pitch and the enrichment on both the multiplication factor and regeneration factor of Models I-A, -B, -C, and -D, these two factors were additionally calculated at different lattice pitches and different enrichments.

1) Figure (7-20) shows the variation of multiplication factor (k_{eff}) with the enrichment concentration at various lattice pitches.

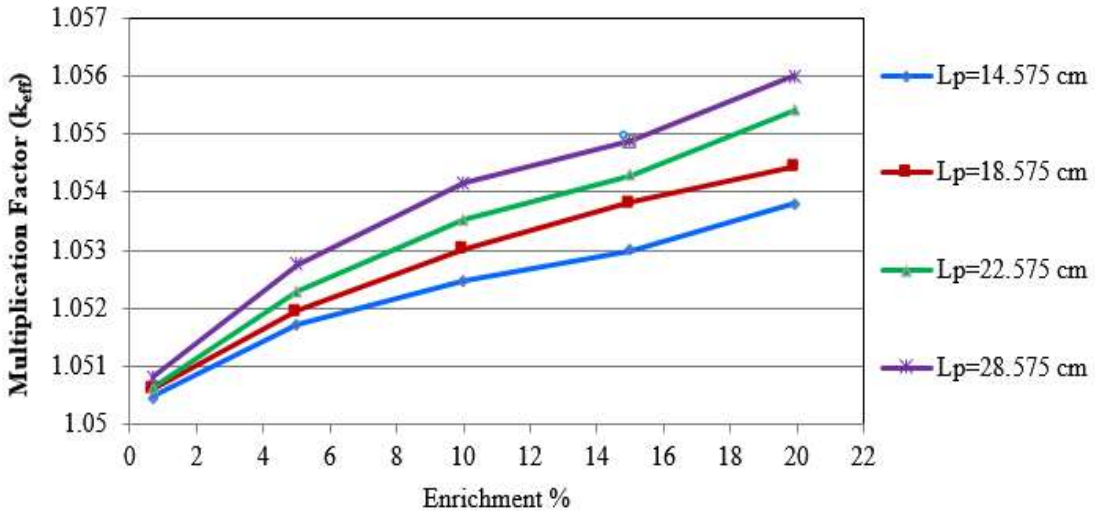

Figure (7-20): Variation of Multiplication Factor k_{eff} with Enrichment of U-235 at Different Lattice Pitch of the Fast Core of the MSCR.

2) From Figure (7-20), one notices that, as the enrichment increases in the fast core at certain lattice pitches, the multiplication factor increases gradually since the concentration of fissile material is increased. Since the number of fuel channels in the fast core is limited, there is no rapid increase.in the multiplication factor as the fast core fuel enrichment increases to 19.9%.

3) The multiplication factor k_{eff} increases with an increasing lattice pitch of the fast core because of the decrease in self-shielding in the outer fuel channels that reduces the diffused thermal neutrons from the thermal core. Hence, as the lattice pitch increases, the self-shielding decreases with a greater contribution for thermal neutrons to reach the central fuel channels. Also, the fission interaction takes place at different energy windows, where at a small lattice pitch, the probability of fast fission is higher particularly in the center of the fast core. As the lattice pitch increases, more fast neutrons fall in the epithermal energy region due to collisions with structures in the fast core. These neutrons also trigger fissions in the high enrichment concentrations of the fast core.

4) Figure (7-21) shows the variation of the regeneration factor (η) with enrichment at different lattice pitches. For the four models (I-A, -B, -C, and -D)

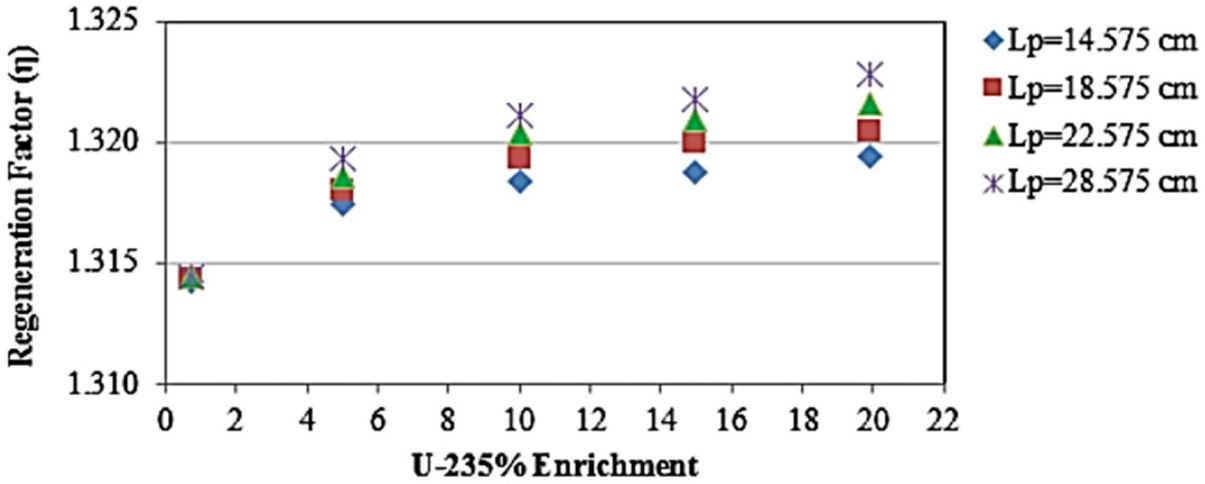

Figure (7-21): Variation of the Regeneration Factor η with Enrichment of U-235 at Different Lattice Pitch of the Fast Core of MSCR.

5) The regeneration factor slightly increases as the enrichment in the fast core fuel increases as the regeneration factor depends on the number of neutrons produced per absorption of

one neutron in the fuel. It also depends on the isotopic concentration of fissile material. At a certain enrichment, the regeneration factor increases slightly with an increased lattice pitch, whereas the regeneration factor is a material dependent quantity. The regeneration factor represents the entire core. As the lattice pitch increases, the neutron spectrum will have more chance for collision with structure materials of the fast core with a slight increase in the thermal neutrons that can reach to more fuel channels in that fast core and there is a change in the neutron energy distribution that diffused from one core to another

In the fast core, as the lattice pitch increases the fast neutrons incur more collisions with the structure, the number of epithermal neutrons increase with more inelastic collisions with U-238 and the stainless-steel structure. Also, the self-shielding with the outer ring of fuel channels of the fast core decreases so that more thermal neutron can reach the center of the fast core. However, this represents a small contribution in the neutron distribution such as shown in thermal flux distribution in figure Figure (7-8) to Figure (7-11)

7.6. MSCR-Model (I) Simulation

In this section, Model (I) is taken as a case study to calculate both radial and axial neutron flux distributions, the form factor, the multiplication factor and burnup. The geometrical specifications of the fast and thermal cores are presented in Table (7-9).

Table (7-7): The Geometry and Specifications of the Fast and Thermal Cores of the MSCR-Model (I)

	Thermal core	Fast core
Radius	335 cm (379.73 cm -including the reflector)	108.86 cm
Number of fuel channels	320	32
Type of fuel bundle	37 elements	37 elements
Type of fuel	UO_2 ,natural uranium	UO_2 19.9% enrichment

The change of the reactivity with burnup is presented in Figure (7-22). The reactor's reactivity starts at 51.6 mk and reaches a value below zero after 135 days. The behaviour of the reactivity curve is comparable to that of a traditional CANDU reactor with drop down in reactivity (with ~37 mk) in the first 10 days is due to the saturating fission products (xenon in particular) in the thermal core and a peak (~8 mk) at day 50 from the accumulation of plutonium in the both cores.

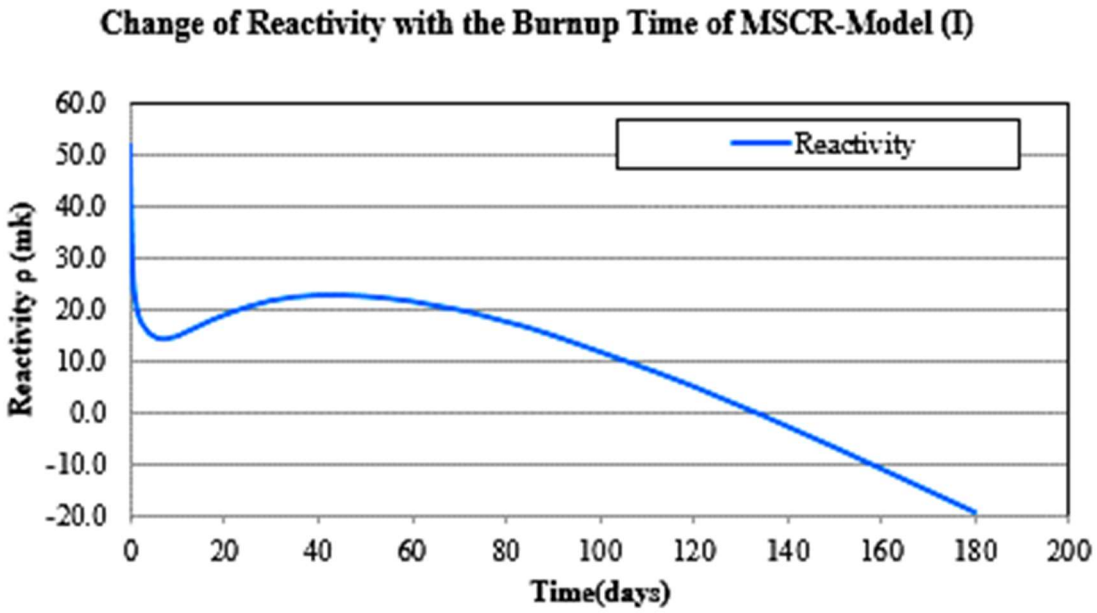

Figure (7-22): Variation of Reactivity with Time of the MSCR-Model (I)

Figure (7-23) shows the variation of the regeneration factor versus time. The behaviour of the regeneration factor (η) curve is similar to the reactivity curve. It is mainly correlated to the fuel composition with a decrease in the number of neutrons produced per neutron absorbed. The number of neutrons produced is decreased due to the production of xenon, but increases again after 20 days because of production of fissile plutonium. It then decreases again due to fuel burning in the thermal core and accumulation of the fission products.

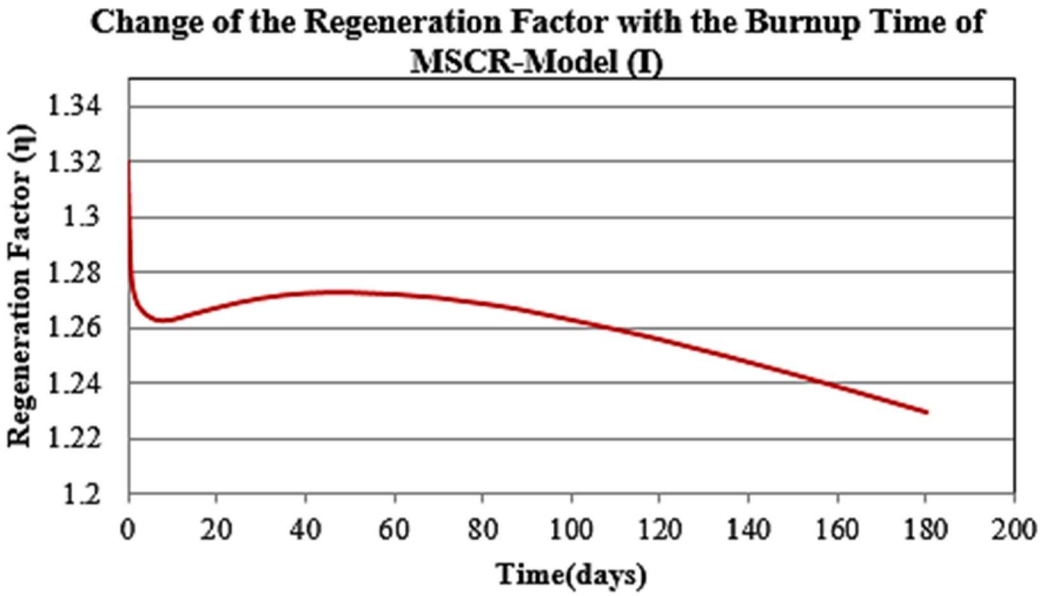

Figure (7-23) Variation of the Regeneration Factor with Time of the MSCR-Model (I)

7.6.1. Neutron Flux Distributions in the MSCR-Model (I)

The knowledge of the radial and axial neutron flux distributions $\varphi_r(r)$ and $\varphi_z(z)$ is of high importance in any reactor facility both in research reactors for the neutron source strength in irradiations and in power reactors as a source of heat. In the MSCR, the radial and axial neutron flux distributions are important to know the power distribution and the burnup in both cores. The flux shapes at each energy bin (thermal, epithermal and fast flux) have been calculated in both the radial and axial directions. These fluxes are normalized for a constant power of 2180 MWth which is the same power of the CANDU 6 Gentilly-2 reactor. The data library used for these calculations for both reactor materials and fuel is ENDF/B-VII. The three energy bins are defined as: thermal neutron energy bin (1E-5 eV to 0.625 eV), epithermal neutron energy bin (0.625 eV to 0.1 MeV) and fast neutron energy bin (0.1 MeV up to 14 MeV). The average radial and axial fluxes were calculated at 19.9% enrichment for the fast core. Since the neutron spectra distributions are different in the fuel and other materials in the fuel channel (coolant, bundle, moderator, pressure tube), the size of the mesh is taken as a size of the equivalent fuel channel. Therefore, the average flux is calculated as the average of the neutron spectra in the fuel channel. Figure (7-44) presents the average radial fluxes at each radial fuel channel of the thermal and fast cores. One notices that the thermal flux is highest in the thermal core while the fast flux is lowest there.

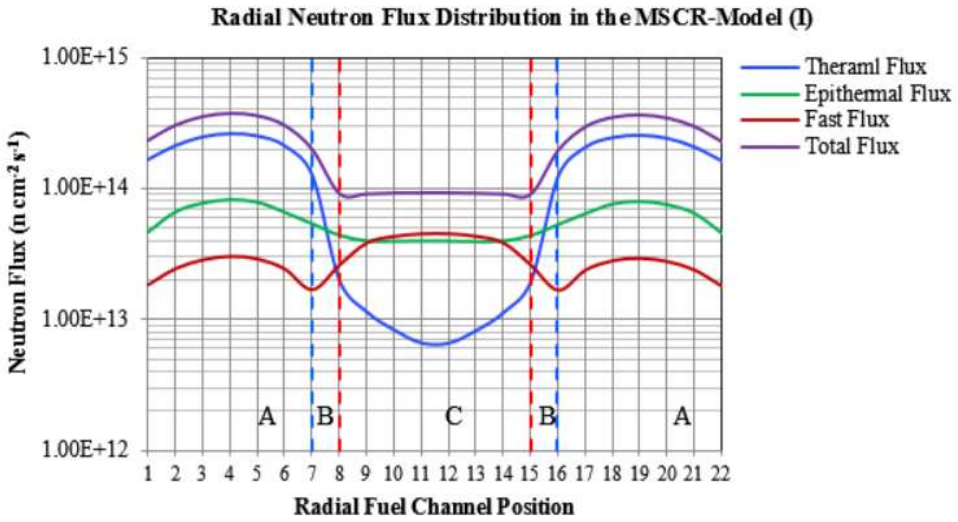

Figure (7-24) Radial Neutron Flux Distribution in the MSCR-Model (I)

Figure (7-25) presents the average axial fluxes at the central fuel channel as calculated at the center of the fuel bundle of the fast core. One can see that the sum of all points at a certain energy bin in the axial flux is equal to the central point at channel M-11 of the corresponding radial flux.

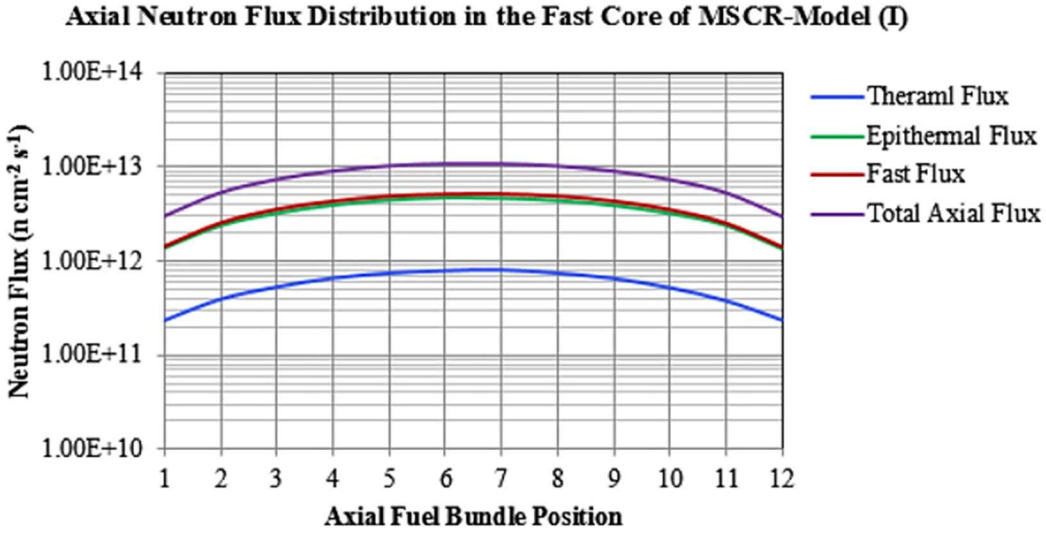

Figure (7-25): Axial Neutron Flux Distributions at the Central Channel of the Fast Core of the MSCR-Model (I)

7.6.2. Power Density Distribution

To show the depletion of the fuel as located in the fast and thermal cores, Figure (7-26) and Figure (7-27) present the power density distributions of the freshly-fuelled reactor at day zero, and after 150 days (at k_{eff}=0.995 just below criticality) of operation, respectively.

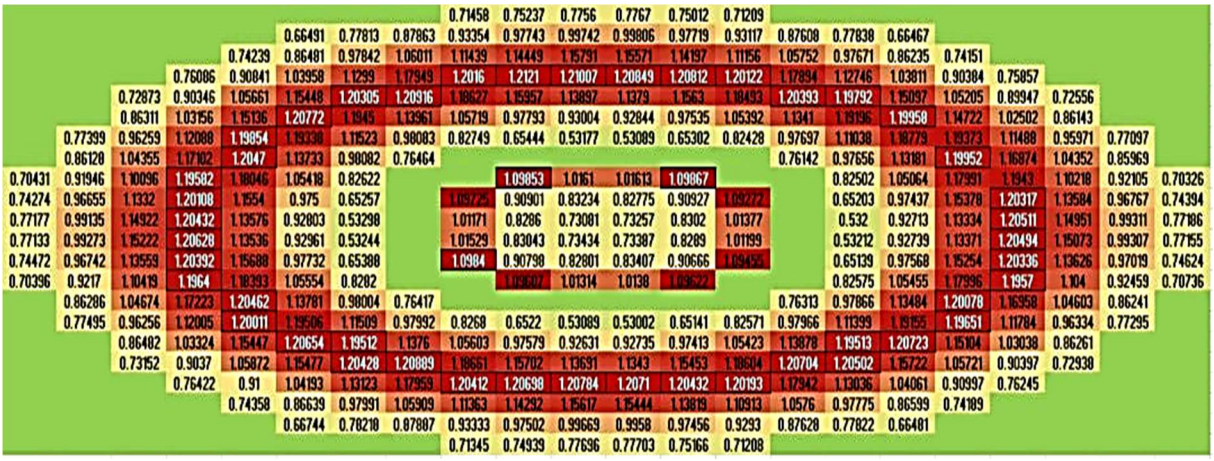

Figure (7-26): Power Density Distribution for the Freshly Fuelled Core of the MSCR-Model(I) (The power density units are in W cm^{-3})

Figure (7-27): Power Density Distribution in the MSCR Core after 150 Days of the MSCR-Model (I) (The power density units are in W cm^{-3})

The power density units in the two figures are in W cm^{-3}. From these two figures, it can be seen that:

1) In the thermal core, the higher and partial flattening of the thermal flux distribution at the center of the core produces a uniform high power density at its center. The channels closer to the fast core have a lower power density because of the lower thermal neutron flux at

these channel locations where the volume of a moderator is not enough to thermalize the fast neutrons that have diffused from the fast core.

2) The power density in the fast core is high for the fuel channels close to Region B due to the leakage of thermal neutrons from the thermal region that interacts with the high enrichment fuel in the fast region in addition to fast fission there.

3) The power density decreases towards the center of the fast core because of the self-shielding caused by the outer fuel channels that prevent thermal neutrons from reaching the center of the fast core and limits the fast fission rate due to the number of enriched fuel channels in the fast core

4) The highlighted numbers in Figure (7-26) and Figure (7-27) represent the highest 10% of the channels power density. The uniform distributions of these channels around the core in the first day and after 150 days of burnup indicate the consistency of burnup through this period in the whole reactor (no flux tilting).

5) Figure (7-28) and Figure (7-29) show that most of the power density is produced within the thermal core and the percentage of the power density produced from the thermal and fast core as normalized to the total power density generated in the whole reactor, respectively.

6) For the freshly fuelled reactor (day zero), the fast neutron core produces around 8.6% of the power density while the thermal core produces 91.4% of the total reactor power density.

7) After 150 days, when the reactor becomes subcritical, the fast core produces around 8.8% of the reactor power density, while the thermal core produces 91.2%. There is a slight increase in the percentage of power density produced in the fast core with a higher burnup of fuel in the thermal core after this period.

8) At the first 10 days of burnup, Figure (7-28) shows that the power density percentages produced for the thermal core decrease due to buildup of the neutron poisons in the thermal core; this decrease is correlated with the reactivity curve in Figure (7-29) After 20 days, it starts to increase to a peak value which is equivalent to the plutonium peak. In the same period for the first 10 days, the power density percentage produced from the fast core

increases to a higher value due to the burnup of the enrichment fuel where there is no xenon poisoning in the fast reactor.

9) After 80 days, the percentage power density of the thermal core decreases gradually due depletion of the fuel and accumulation of fission products. While the fast core is still rich with fissile material, fission products have a small effect on the fast neutron flux so the percentage of power density produced from the fast core increases.

10) With a high percentage of fissile material enrichment in the fast core, the depletion is very small as the fast flux is small.

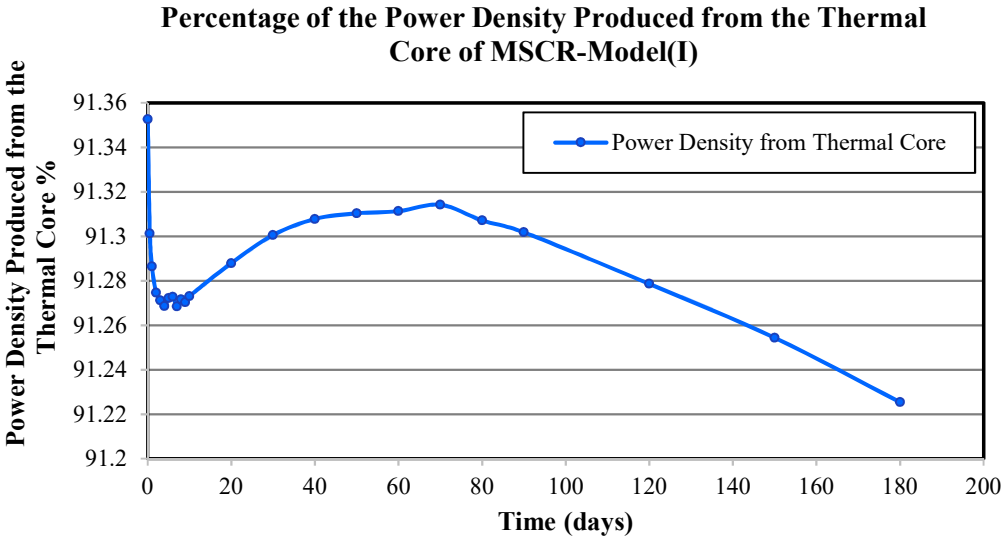

Figure (7-28): Percentage Ratio of the Power Density Produced from the Thermal Core for the MSCR-Model (I).

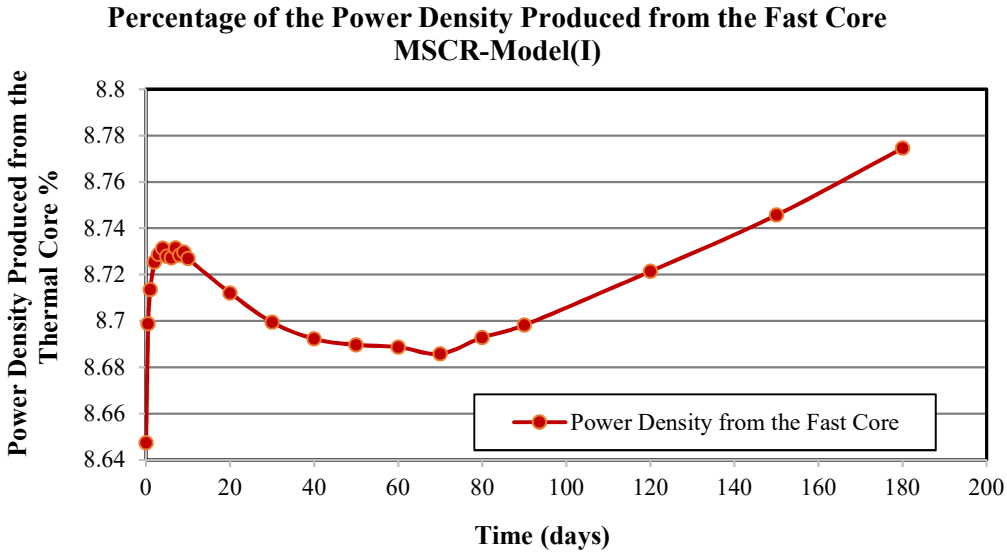

Figure (7-29): The Percentage Ratio of the Power Density Produced from the Fast Core for the MSCR-Model (I).

11) It is evident from the power density distributions shown in Figure (7-26) and Figure (7-27) that the outer fuel channel ring in the fast region provides self-shielding that absorbs thermal neutrons which diffuse from the thermal region to the fast region. However, the burning of actinides in the fast core depends mainly on the fast neutron spectrum. A larger lattice pitch decreases the self-shielding effect but does not affect the burning of actinides in the fast core very much. Packing more fuel in the fast core may improve the burning of U-235 as will be seen in the MSCR- Model (II) (see Section 7.7).

7.6.3. Form Factor.

The ratio between the maximum and average power is known as the form factor. The form factor represents one of the major safety factors. Figure (7-30) shows the form factors of the MSCR -Model (I) calculated independently for the fast core and thermal core for 23 burnup steps (or 180 days). The total form factor is normalized for the entire reactor.

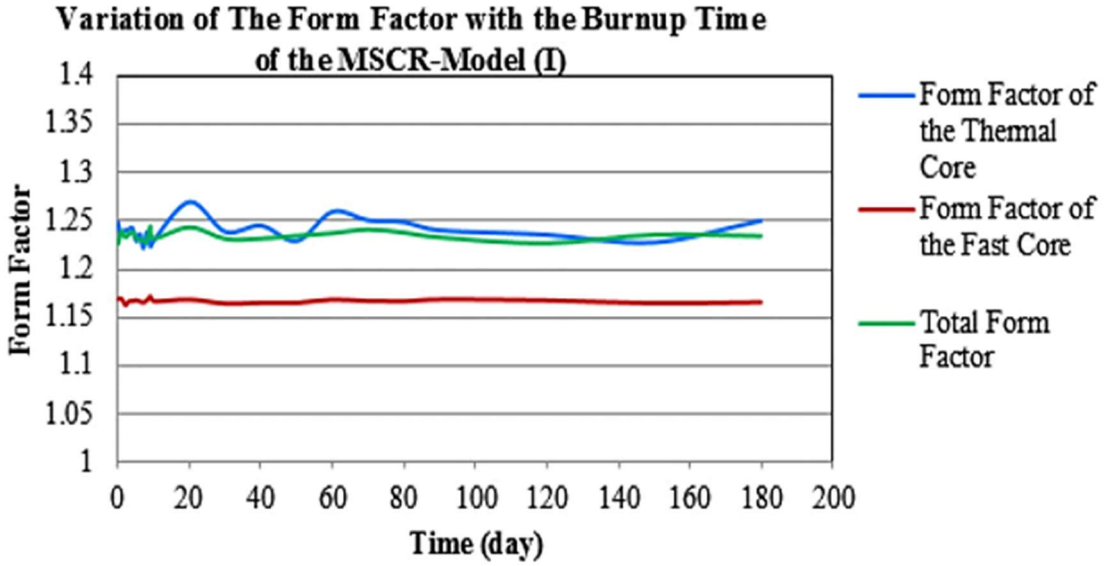

Figure (7-30): Total Channel Form Factors for both Fast and Thermal Cores and the entire of the MSCR-Model (I).

The form factor of the thermal core is between 1.23 and 1.24. The peak value at the around 20 days corresponds to the plutonium peak. There are no fluctuations in the form factor for the fast core. Both values are acceptable in comparison to the form factor of a traditional CANDU reactor. The total form factor for the whole reactor fluctuates between 1.23 and 1.26. The behaviour of the total form factor is similar to that of a thermal core because most of the power is produced in the thermal core. Both the thermal, fast and total form factor are almost constant values after 60 days.

7.6.4. Calculation of the Burnup.

The burnup and multiplication factor are calculated for a burnup period of 180 days using the Serpent 1.19 code. The results are shown in Figure (7-31).

The multiplication factor first decreases sharply because of the consumption of ^{235}U and the build-up of saturating fission products (Xe and Sm) in the thermal core. Since the volume of the fuel in the thermal core is ten times more than that in the fast core, and most of the power is produced in the thermal core, the behaviour of the multiplication factor of the thermal core is predominant. The peak in the multiplication factor is caused by ^{239}Pu production along with some other fissile nuclides. This plutonium peak is followed by a steady decrease of the multiplication factor due to the depletion of both ^{235}U and ^{239}Pu, and the accumulation of non-saturated fission

products along with the burnup of the fuel. The reactor becomes subcritical at a burnup of 2200 MW d (tonne H.E.)$^{-1}$.

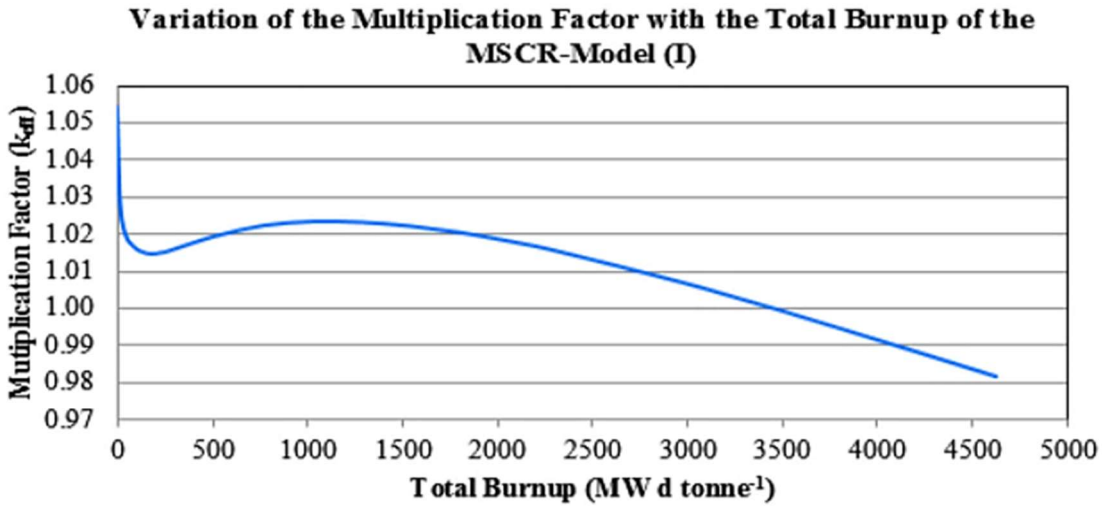

Figure (7-31): Variation of the Multiplication Factor with the Total Burnup of the MSCR-Model (I).

Figure (7-32) shows the variation of the burnup of the thermal (blue line) core, fast core (red line) and total MSCR-Model(I) (green line) with time. All burnups are normalized to the total mass of the fuel of the whole reactor. The regeneration factor of Model (I) was shown in Figure (7-23) and is equal to 1.332, which indicates that the MSCR-Model (I) is definitely not a breeder reactor.

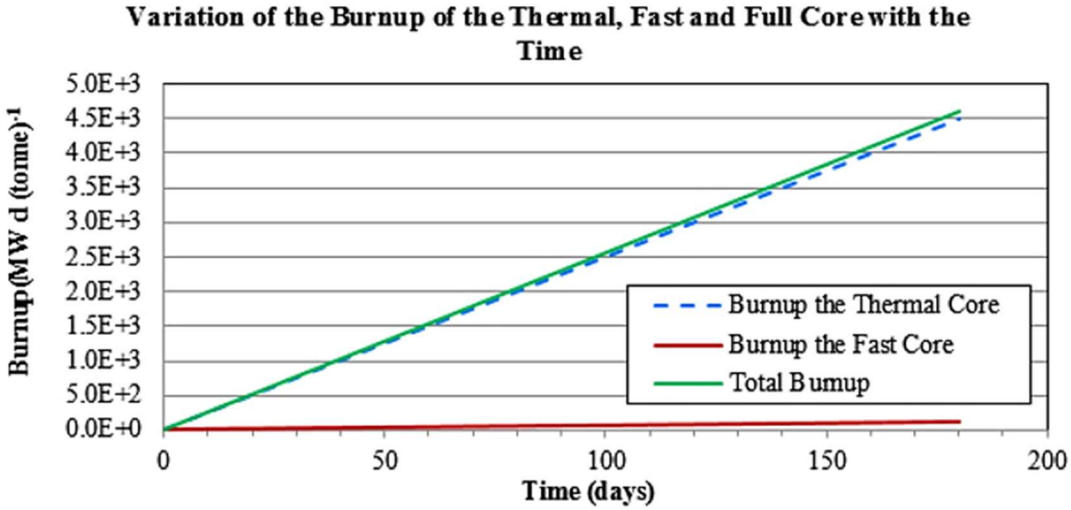

Figure (7-32): Variation of the Burnup with Time of Thermal Core, Fast Core and the Entire MSCR-Model (I).

The total burnup (green line) is normalized to the total mass of the fuel in the entire reactor core. The three burnups curves are linearly proportional to the time. It is evident that most of the fuel burnup is produced in the thermal core. The minor burnup arising from the fast core is due to the fresh fuel content in the fast core, self-shielding in the outer ring of the fuel channels and the low fast neutron flux in the fast core. Some of the fast neutron flux diffuses out to the thermal core without contributing to actinide burning. A leakage flux from the thermal core to the fast core is mostly in the epithermal region, which contributes slightly to the burnup of the fuel in the fast core or in the fuel conversions.

7.6.5. Change of Atomic Density of Actinides in the MSCR-Model (I).

1) Change of Atomic Density of Actinides in the Thermal Core of MSCR.

Figure (7-33) and Figure (7-34) show the variation of the atomic density concentrations in the thermal core of the MSCR-Model (I):

1) Figure (7-33) shows that the atomic density of the fissile isotope U-235 slightly decreases with burnup. The atomic densities of Pu-239 and Pu-241 sharply increase during the first 20 days due to the breeding of these fissile isotopes, and then their rate of accumulation decreases gradually.

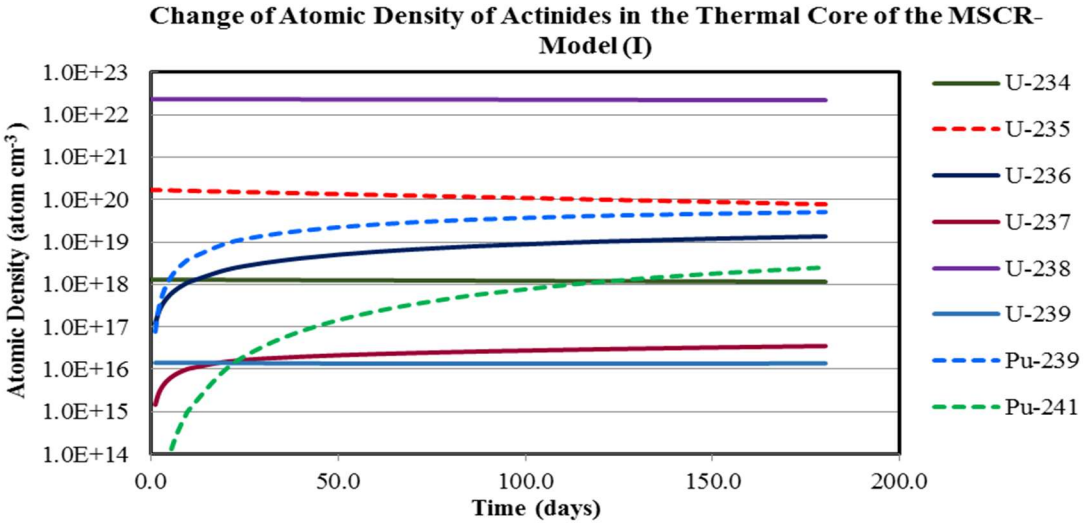

Figure (7-33): Atomic Densities of Uranium and Plutonium in the Thermal Core of the MSCR - Model (I) (1).

Later, the concentration of plutonium saturates when the rate of production is equal to the rate of consumption. It then eventually decreases with longer irradiation times.

2) Figure (7-34) presents the variations of the atomic density of some the transuranic isotopes. For the thermal core, the transuranic isotopes have initially zero concentration as expected for natural uranium fresh fuel. After a certain time, the transuranic isotopes reach different constant values for their concentrations. For the irradiation time longer than 180 days, these concentrations eventually decrease. The other transuranic isotopes are not included in the graph because they reach relatively small concentrations or are not considered important to the current discussion.

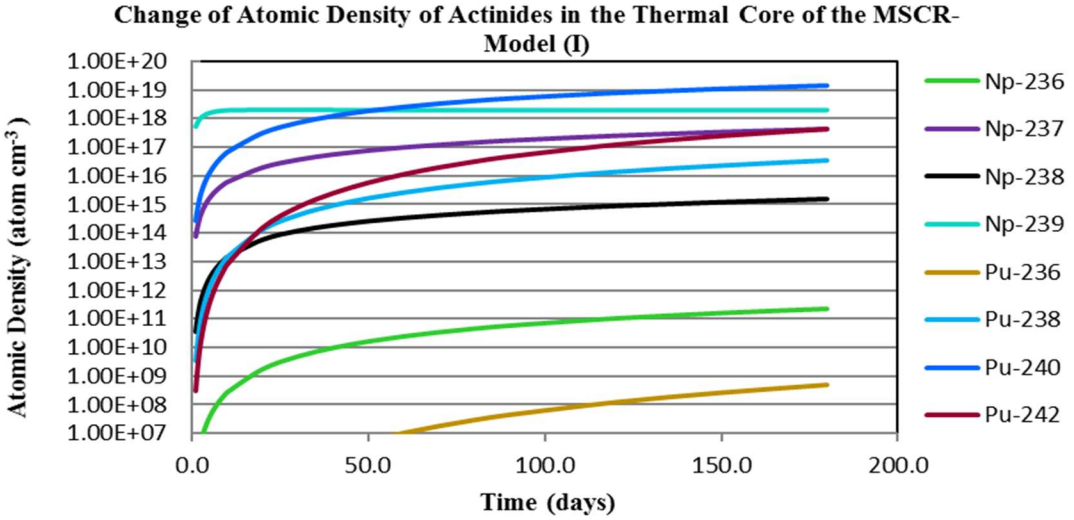

Figure (7-34): Atomic Density of Actinides in the Thermal Core of MSCR-Model (I) (2).

2) Change of Atomic Density of Actinides in the Fast Core of MSCR.

Figure (7-35) and Figure (7-36) show the variation of the atomic densities in the fast core for the MSCR-Model (I):

1) Figure (7-35) shows the atomic density of U-235, which is decreasing at a very small rate. As for the fissile Pu-239 and Pu-241, their densities increase quickly during the first 20 days due to breeding and then they increase at a very small rate.

2) Figure (7-36) presents the variations of the atomic densities of some of the transuranic isotopes. Some transuranic isotopes start at a zero concentration since the fuel is fresh. After

a certain time, they reach a constant value, and for irradiation times longer than 180 days, their concentrations start to decrease.

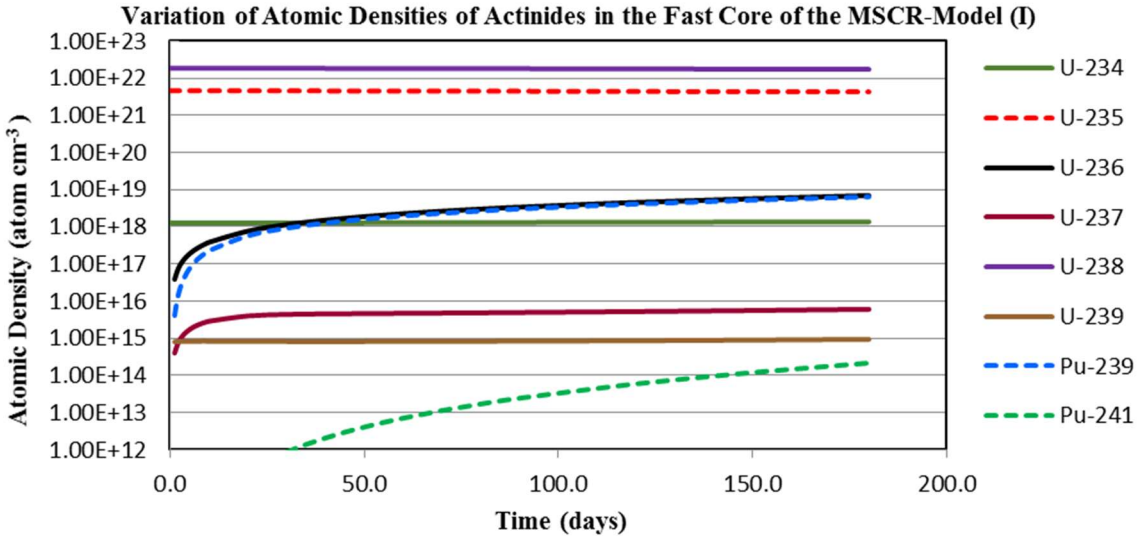

Figure (7-35): Atomic Density of Actinides Uranium and Plutonium in the Fast Core (1) of the MSCR-Model (I).

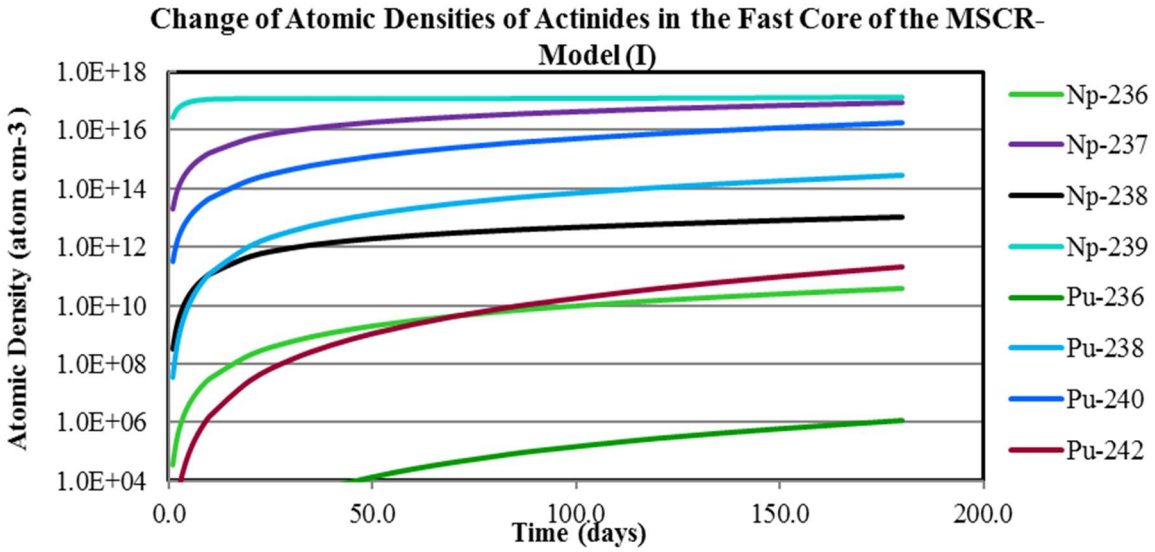

Figure (7-36): Atomic Density of Actinides in the Fast Core (2) of the MSCR-Model (I).

3) Change of Atomic Density of Fissile Actinides in the MSCR-Model (I)

Figure (7-37) and Figure (7-38) show the variation of U-235 in the entire reactor for both the fast and thermal cores.

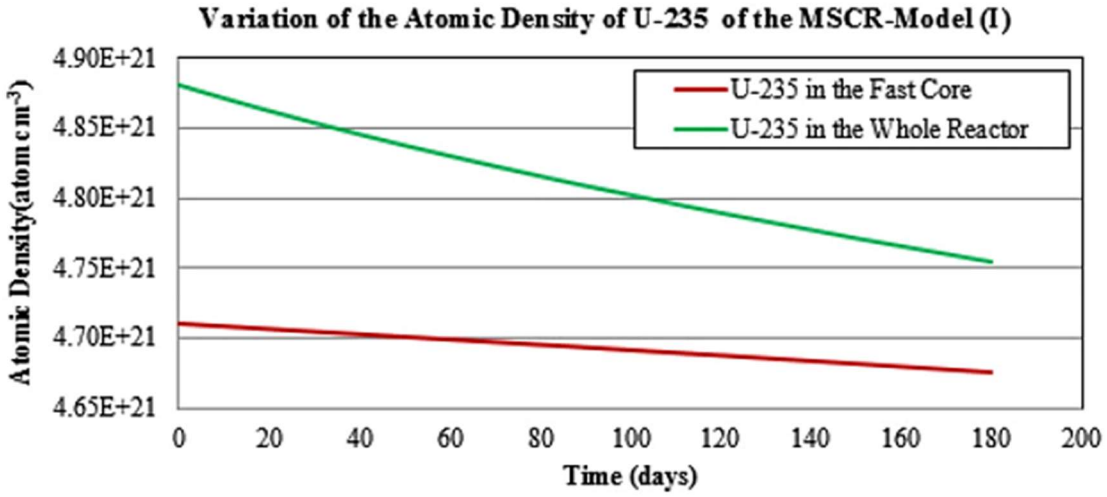

Figure (7-37): Atomic Density of the U-235 in the Fast Core and the Entire Reactor of the MSCR-Model (I) (1).

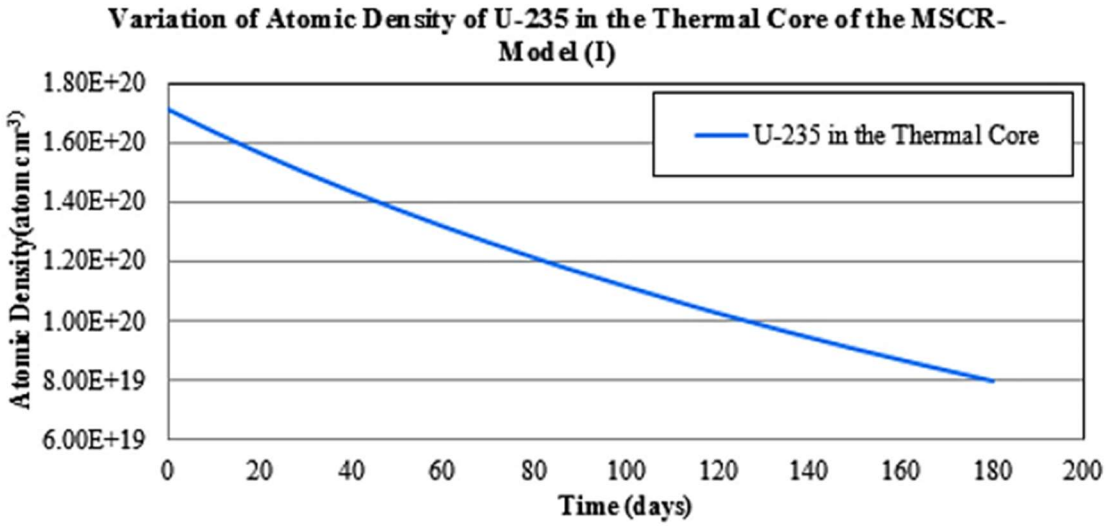

Figure (7-38): Atomic Density of U-235 in the Thermal Core the MSCR-Model (I) (2).

The rate of consumption per day (average gradient of the blue curve in Figure (7-39) in the thermal core is higher than that in the fast core because of the high thermal flux in the thermal core. Figure (7-39**)** shows the variation of the atomic density of Pu-239 with time in the thermal core (blue dashed curve), fast core (red curve) are and the entire reactor (green curve). The atomic density of Pu-239 sharply increases during the first 20 days; then shortly after a short duration steady state is reached that is then followed by a steady decrease for longer irradiation times.

The slope of the green curve shows the net rate of production of Pu-239 in both cores and in the entire reactor. Pu-239 is produced in both cores due to neutron capture in U-238 in the resonance energy region during moderation of the neutrons. The rate of production of Pu-239 in the fast core is around a tenth of that in the thermal core because of the mass of fuel in the fast core compared to that in the thermal core. The epithermal flux in the thermal core is higher than that in the fast core (the epithermal flux at the center of the thermal core is around double its value at the center of fast core). Also, the production of epithermal neutrons in the fast core is low because relatively little neutron moderation occurs as shown in Figure (7-24). This explains why the majority of Pu-239 is produced in the thermal core and why the rate of production of Pu-239 in the thermal core is very close to that of the total rate. However, some fast neutrons may also diffuse from the fast core to the thermal core, dependent on the enrichment of the fuel in the fast core and number of fuel channels in it.

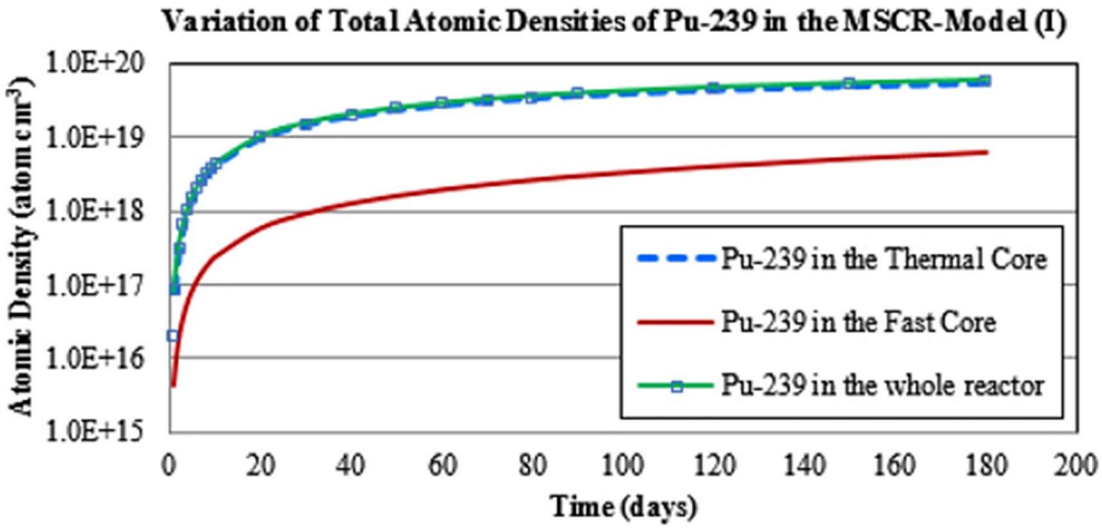

Figure (7-39) Variation of Atomic Density of Pu-239 in the Fast Neutron Core and the Entire MSCR-Model (I).

Figure (7-40) shows the variations of atomic density of the total fissile isotopes in the whole reactor. The slope of the line is less than that of Figure (7-37) and Figure (7-38) because of the added Plutonium isotopes Pu-239 and Pu241 due to breeding.

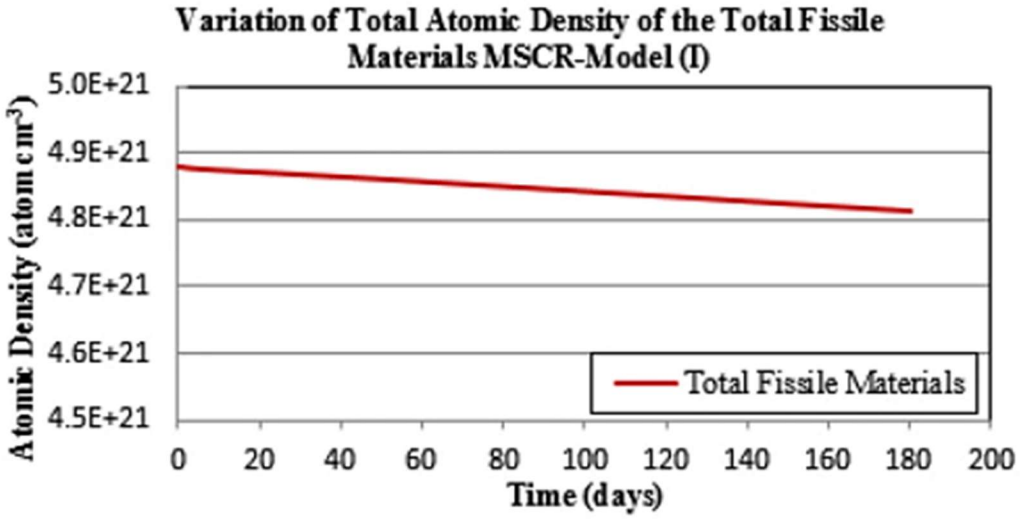

Figure (7-40): Atomic Density of the Total Fissile Materials in the Entire MSCR-Model (I) (1).

Table (7-10) shows the consumption rate of the U-235 in both cores and the entire reactor for the total fissile materials. The percentage of U-235 destructed in each core and the entire reactor is also presented in the table. The consumption rate of fissile material in the entire reactor is less than that of the U-235 due to the breeding of Pu-239 and Pu-241. However, the bred amounts of these fissile isotopes are very small as shown in Figure (7-35) and Figure (7-39). Most of the fuel is burnt (about 47.3% of the original U-235) in the thermal core. Only 0.62% of the original fuel concentration is burnt in the fast core. The percentage of U-235 burnt in the MSCR-Model (I) is 2.25% of the initial fissile isotope content of U-235.

Table (7-8) Mass Density Consumption Rate of the Fissile Material in the MSCR-Model(I) ($g\ cm^{-3}\ day^{-1}$)

	In the thermal core	In the fast core	In the entire reactor
Rate of consumption of U-235	2.11E-04 ($g\ cm^{-3}\ day^{-1}$)	7.555E-05 ($g\ cm^{-3}\ day^{-1}$)	2.86E-04 ($g\ cm^{-3}\ day^{-1}$)
Percentage destruction of the U-235 after 150 days	47.3%	0.62%	2.25%
Net rate of consumption of the total fissile actinides (U-235, P-239, Pu-241)	1.47E-04 ($g\ cm^{-3}\ day^{-1}$)		

7.7. MSCR-Model (II) Simulation

In this section, Model (II) is taken as a case study for the burning of high enrichment uranium in the fast core where the number of fuel channels is increased to 148, and the lattice pitch is set as 14.585 cm. The materials and geometrical core are the same MSCR-Model (I). The geometrical specifications of the fast and thermal cores of the MSCR-Model (II) are presented in Figure (7-41) and Table (7-9).

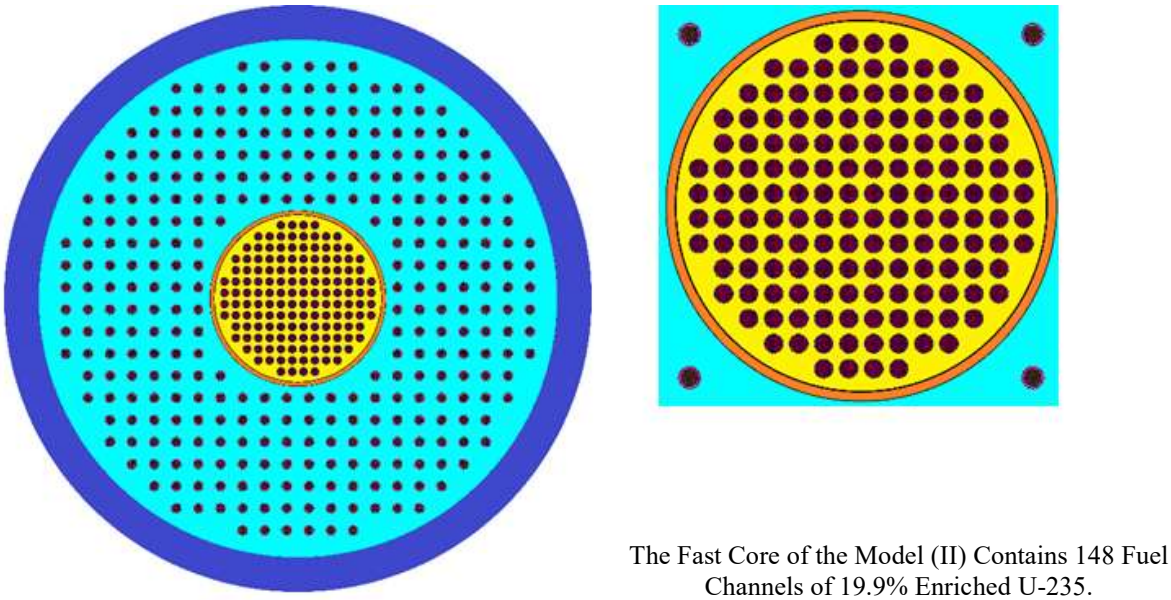

Figure (7-41): Design Model of the Multispectrum CANDU Reactor Model (II)

Table (7-9): Geometry and Specifications of the Fast and Thermal Cores of the MSCR-Model(II)

	Thermal core	Fast core
Radius	335 cm (379.73 cm -including the reflector)	108.86 cm
Number of fuel channels	320	148
Type of fuel bundle	37 elements	37 elements
Type of fuel	UO_2 ,natural uranium	$UO_2$19.9% enrichment
Lattice Pitch	28.575 cm	14.575 cm

The optimization of multiplication factor and total flux for number of cycles and number of neutrons per cycle are shown in the Appendix (E).

The analysis of the reactor physics parameters is focused on the calculations of the radial and axial neutron flux distributions, the form factor, the power distributions, the multiplication factor, the burnup, and the efficiency of the Model (II) to burn fissile actinides.

7.7.1. The Reactivity and the Regeneration Factor

The change of the reactivity with burnup time is presented in Figure (7-42). The reactivity starts at 80.16 mk (with an average error of 9.35E-5 mk) and becomes subcritical after 950 days. The average relative error of reactivity values is 9.66E-3%. The behaviour of the reactivity curve is comparable to that of a conventional CANDU reactor

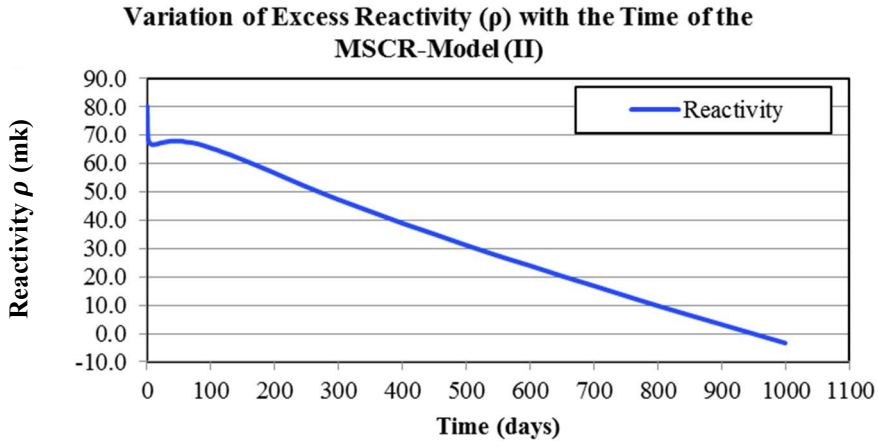

Figure (7-42): Variation of Reactivity with Time of the MSCR-Model(II)

The decrease in reactivity during the first ten days is 13.5 mk in comparison to that in Model (I) (37 mk). This difference is due to the saturating fission products (Xe-135 and Sm-149 in particular) with an accumulation in the entire reactor in Model (II). There is less effect in Model (I) because of the significant thermal neutron flux in the thermal and fast cores of the adjacent fuel channels. The external ring of fuel channels of the fast core produces some self-shielding, which decreases the thermal flux and consequently the thermal fission rate in the internal fuel channels of the fast core with a greater packing of fuel channels in the fast core of Model (II). In the case of Model (I), the larger value of the lattice pitch in the fast core allows for more leakage of the thermal neutrons from the thermal core to the center of the fast core. In Mode (II), the

smaller lattice pitch and channel packing increase the fast flux and consequently the fast fission rate. Since the saturating fission products are mainly affected by the thermal neutron flux, the effect of the neutron poisons in Model (II) is less than that of Model (I) because of the saturated fission products (mainly Xe-135 and Sm-149), which have a very low fast neutron absorption cross sections in comparison to the very high values for that of the thermal neutrons. This explains the significant fall in reactivity in Model (I).

The plutonium peak is due to an accumulation of plutonium in both cores. This peak in Model (II) is ~ 1 2 mk at day 50, which is smaller than that in Model (II) (~8 mk) because of the depth of the xenon dip, which is shorter in Model (II).

Figure (7-43) below shows the variation of the regeneration factor versus time. The behaviour of the regeneration factor (η) curve is like the reactivity curve. It is mainly correlated to the fuel concentration with a decrease in the number of neutrons produced per neutron absorbed. The number of generated neutrons is rapidly decreased due to xenon production, but increases again after 20 days because of the production of fissile plutonium. It then decreases again due to fuel burning in the reactor and the accumulation of non-saturating fission products. The regeneration factor is equal to 1.332 and decreases down to a value of 1.14 after 1000 days, which demonstrates that the MSCR-Model (II) is not a breeder reactor. The average relative error of regeneration factor is 5.16E-3%.

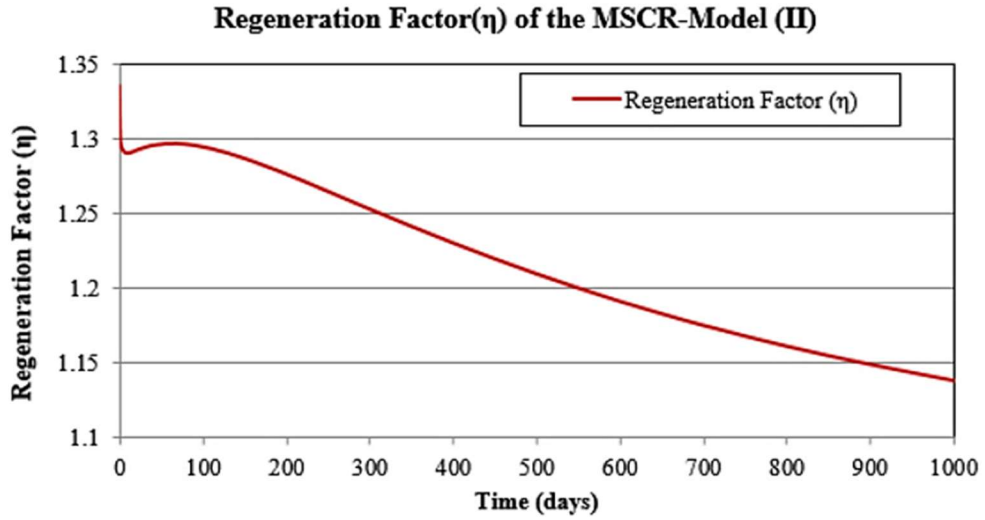

Figure (7-43): Variation of the Regeneration Factor with Time of the MSCR-Model(II)

7.7.2. Neutron Flux Distributions in the MSCR-Model (II)

In the MSCR-Model (II), the radial neutron flux $\varphi_r(r)$ and axial neutron flux $\varphi_z(z)$ distributions are necessary to determine the power distribution and burnup in both the thermal and fast cores. The flux shape at each energy bin (thermal, epithermal and fast flux) has been calculated in both the radial and axial directions. These fluxes are normalized for a constant power of 2180 MWth which is the same power of the CANDU 6 Gentilly-2 reactors. The data library used for these calculations for both reactor materials and fuel is ENDFB-VII. The three energy bins are defined as: thermal neutron energy bin (1E-5 eV to 0.625 eV), epithermal neutron energy bin (0.625 eV to 0.1 MeV) and fast neutron energy bin (0.1 MeV up to 14 MeV). The average radial and axial fluxes were calculated for a 19.9% uranium enrichment for the fast core. Figure (7-44) presents the average radial fluxes at each radial fuel channel of the thermal and fast cores.

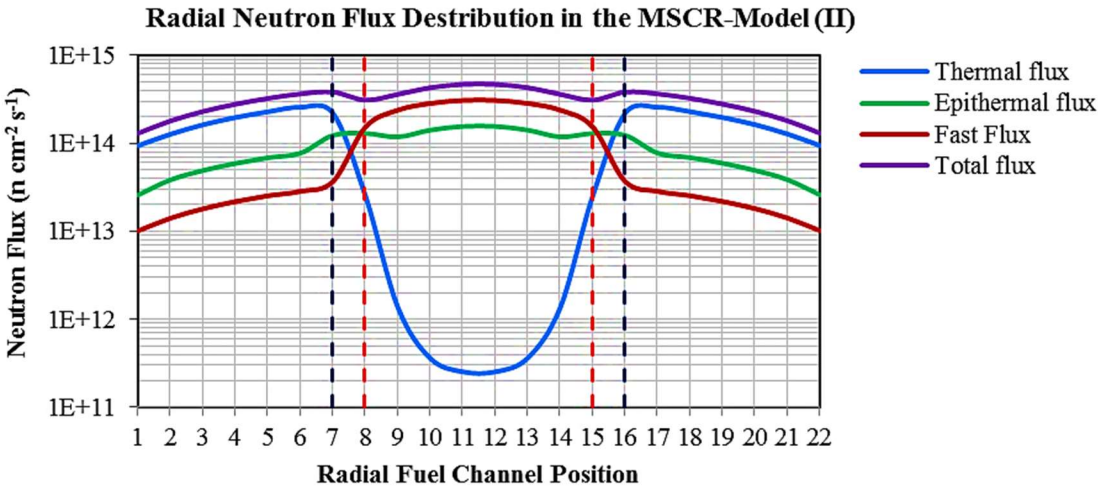

Figure (7-44): Radial Neutron Flux Distribution in the MSCR-Model(II)

In the fast core, one notices that:

1) The thermal flux is the smallest spectrum. The drop of the thermal flux at the center of the fast core, in comparison to that in the MSCR-Model (I), is due to the small value of the lattice pitch with highly packed fuel channels. This causes self-shielding which decreases the chance for thermal neutrons to reach to the center of the fast core in addition to the absence of a moderator in this core.

2) The maximum values of both the fast and epithermal spectra at the center of the core are increased in comparison with that in Model (I). An increased fast neutron spectrum causes an increase in the fast fission rate and consequently a better burning of the actinides.

3) However, increasing the epithermal neutron flux leads to an increased probability for the breeding of more fissile material.

4) The relative error in the thermal, epithermal and fast fluxes are 0.2214%, 0.0806% and 0.0924%. respectively.

For the thermal core, one notices that:

1) The maximum values of the three fluxes are shifted from the center of the core as shown in Model (I) in Figure (7-24) to near the edge of the fast core (beyond channels 7 and 16). These changes result because of an increasing number of fast and epithermal neutrons which have diffused from the fast core to the thermal one. Since the ratio of the moderator-to-fuel is higher at the inner edge of the thermal core, some of these neutrons are moderated to epithermal and thermal energies. The moderated thermal neutron flux is added to the thermal flux in the thermal core which makes it highest at these channels.

2) The increased fast and epithermal neutron spectra at the center of the fast core and the increased spectra for the three energy groups at the internal edges of the thermal core give rise to the given power density distribution as shown in Section 7.1.2.

Figure (7-45) presents the average axial fluxes at the central fuel channel (M-11) as calculated at the center of the fuel bundle of the fast core.

One can see that the sum of all points at a certain energy bin in the axial flux is equal to the central point at channel (M-11) of the corresponding radial flux of Figure (7-44). The three axial fluxes are flat at the middle which indicates a uniform axial burnup. The radial and axial total neutron fluxes have a predominant spectrum in each core.

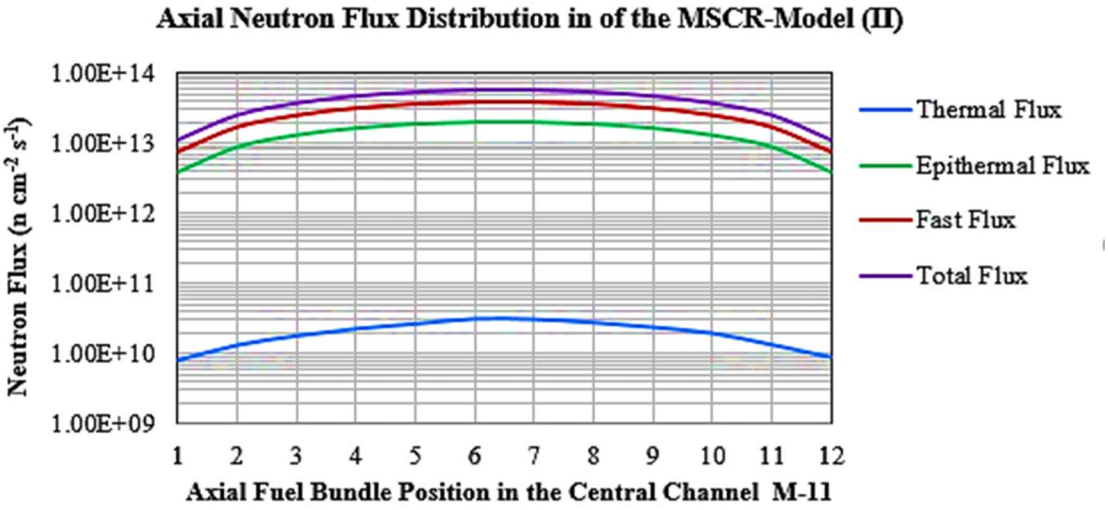

Figure (7-45) Axial Neutron Flux Distributions at the Central Channel of the Fast Core of the MSCR-Model (II)

7.7.3. Power Density Distribution

To show the depletion of the fuel, as located in the fast and thermal cores, Figure (7-46) and Figure (7-47) represent the power density distributions of the freshly-fuelled reactor at day zero. Figure (7-48) and Figure (7-49) present the power density distributions after 1000 days (at k_{eff} = 0.996) and just below criticality, respectively. The power density units in the two figures are in W cm^{-3}. From these two figures, it can be seen that:

1) In the thermal core of Figure (7-46), the higher thermal flux distribution near the inner edge of the thermal core (beyond channels 7 and 16) produces a high-power density at these channels. Towards the center of the thermal core, the power density decreases because of the decreasing thermal flux as shown in the radial flux distribution of Figure (7-44). The increasing fluxes in the fast and epithermal neutrons groups that diffuse from the fast core to the thermal core cause an increase for the three energy-group fluxes at the internal edge channels of the thermal core and consequently, result in an increase of power density.

2) Figure (7-47) shows the power density in the fast core is high for the fuel channels in the outer ring close to the edge of the fast core due to leakage of thermal neutrons from the thermal region that interacts with the high enriched fuel in the fast region in addition to any fast fission which occurs here.

Figure (7-46): Power Density Distribution for the Freshly Fueled Thermal Core of MSCR-Model(II) (The power density units are in W cm^{-3})

Figure (7-47): Power Density Distribution for the Freshly Fueled Fast Core of MSCR-Model(II) (The power density units are in W cm^{-3})

3) For the ring of two channels width, after the outer ring towards the center of the fast core, the power density decreases because of the self-shielding caused by the outer fuel channels that strongly decrease thermal neutrons from reaching the center of the fast core.

4) At the center of the fast core with an outward radius equal to the lattice pitch of three channels, the power density increases due to the high values of the fast flux that subsequently increases the fast fission rate and consequently the power density and burnup in these channels.

5) Figure (7-48) shows the power density distributions of the thermal and fast cores of the MSCR-Model (II) after 1000 days. In Figure (7-49) for the thermal core, the average power density distribution decreases due to a depletion of fuel in the thermal core, coincident with an increase in power density in the fast core due to the breeding of some fissile material because of neutron capture in U-238.

The highlighted numbers in the figures Figure (7-46), Figure (7-47), Figure (7-48), and Figure (7-49) represent the highest 10% of the channel power density. The uniform distributions of these channels power density around the reactor core in the first day and after 1000 days of burnup indicate the consistency of burnup throughout this period in the entire reactor.

Figure (7-48): Power Density Distribution in the Thermal Core of MSCR-Model (II) after 1000 Days (The power density units are in W cm^{-3})

Figure (7-49): Power Density Distribution in the Fast Core of MSCR-Model (II) after 1000 Days. (The power density units are in W cm^{-3})

Figure (7-50) and Figure (7-51) show the percentage of the power density produced from the thermal core and fast core respectively.

1) For the freshly fuelled reactor (day zero), the thermal core produces 67.7% of the total reactor power density while the fast core produces around 32.3%.

2) At the first 10 days of burnup, Figure (7-50) shows that the power density percentages produced for the thermal core decrease due to a build-up of neutron poisons in the thermal core; this decrease is correlated with the reactivity curve in Figure (7-42). After that, it starts to increase to a peak value due to a plutonium peak. In the same period for the first 10 days,

the power density percentage produced from the fast core increases to a higher value due to the burnup of the enriched fuel where there is no xenon poisoning in the fast reactor.

3) After 80 days, the percentage power density of the thermal core decreases gradually due to a depletion of fuel and accumulation of fission products. While the fast core is still rich with fissile material, the fission products have a small effect on the fast neutron flux so that the percentage of the power density produced from the fast core still increases.

4) After 1000 days, when the reactor becomes close to subcritical, the thermal core produces 61.7% of the power density. While the fast core produces around 38.3% of the reactor power density, there is an increase in the percentage of power density produced in the fast core with a higher burnup of fuel in the thermal core after this period. One can notice that the power density produced from the fast core of Model (II) is greater than that of the same core of the MSCR-Model (I). The high percentage of the fuel enrichment in the fast core, and the high fast and epithermal fluxes in this core of current MSCR-Model (II), cause high depletion in this core and consequently a higher power density.

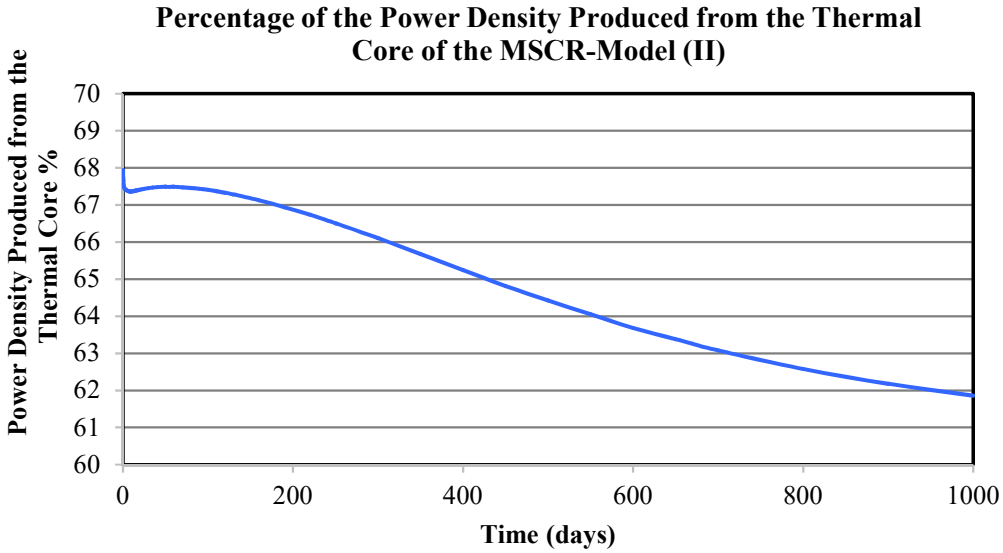

Figure (7-50): Percentage Ratio of the Power Density Produced from the Thermal Core for the MSCR-Model (II).

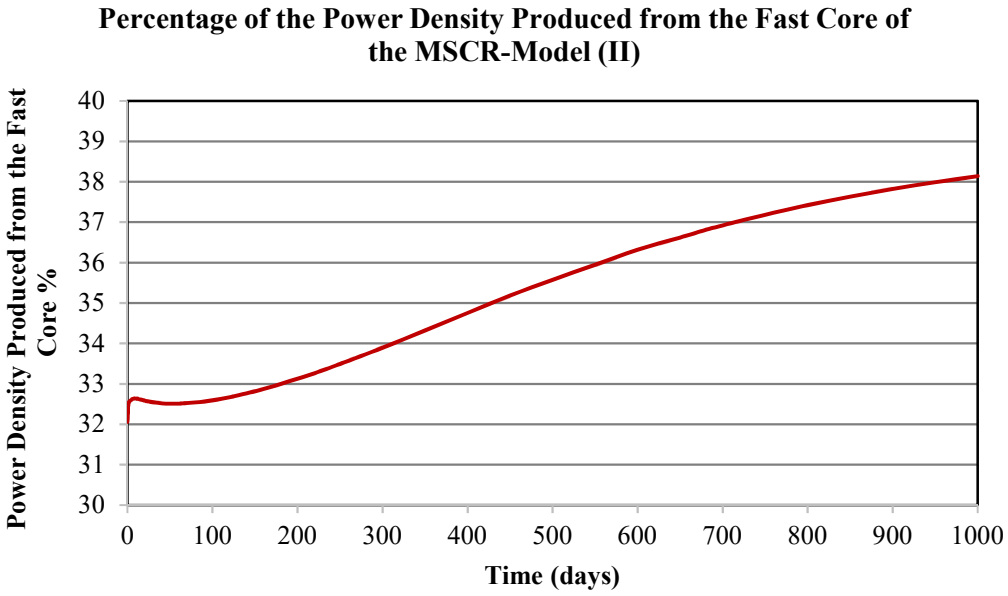

Figure (7-51): The Percentage Ratio of the Power Density Produced from the Fast Core for the MSCR-Model(II).

5) It is evident from the power density distributions shown in Figure (7-46) to Figure (7-49) that the outer fuel channel ring in the fast region provides self-shielding that absorbs thermal neutrons diffusing from the thermal region. These diffused thermal neutrons, in addition to the fast spectrum from the fast core, produce a maximum power density in the outer ring of the fast core. However, the burning of actinides in the rest of the fast core depends mainly on the fast neutron spectrum. A small lattice pitch and the packing of more fuel in the fast core improves the burning of U-235 and increases the power density percentage produced in the fast core. Self-shielding affects the burning of actinides in the fast core at the inner fuel channels (whereas the burnup in the outer fuel channel ring depends on both the fast and thermal neutron spectrum).

7.7.4. Form Factor

Figure (7-52) shows the form factors of the MSCR-Model (II) calculated independently for the fast core and thermal core for 54 burnup steps (or 1000 days). The total form factor is calculated by dividing the maximum channel power by the average power of the entire reactor.

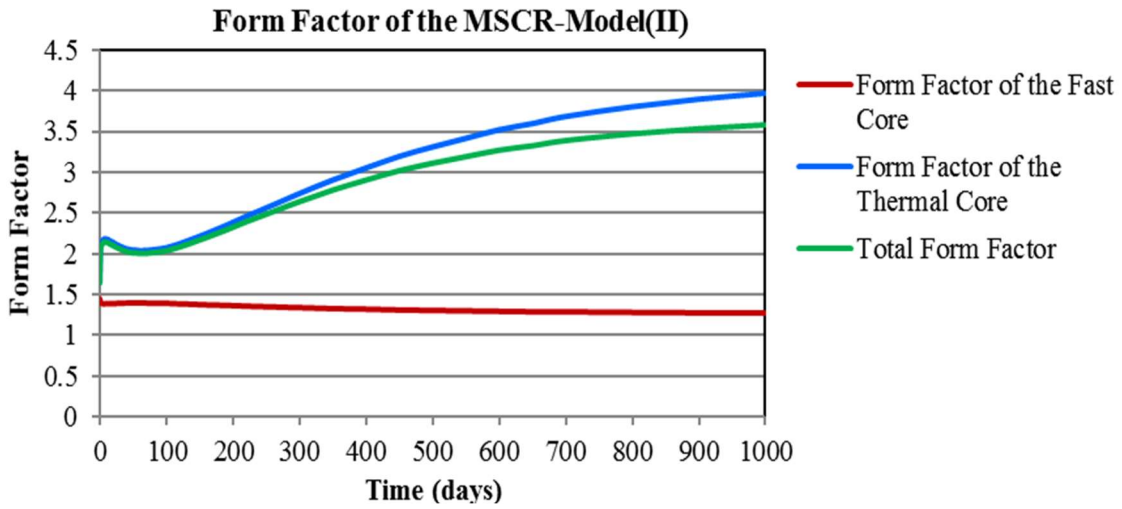

Figure (7-52): Total Channel Form Factors for both Fast and Thermal Cores and for the Entire of MSCR-Model(II)

In the thermal core, during the first 100 days, the form factor of the thermal core starts at 1.6 and then increases quickly up to 2.3. The form factor decreases again to ~ 2.0 at day 80. It increases gradually again up to the value of 3.9 after 1000 days. The increase in the form factor of the thermal core is due to an increase in the maximum channel power near the boundary between the two cores. At the same time, there is a decrease in the average total power produced in the thermal core because of the depletion of the fuel in the fuel channels. These values of the form factor are unacceptable from the perspective of the safety criteria. A decrease in the form factor could be controlled in the thermal core in future work. Control rods liquid zone controllers, or adjuster rods are not included in the current design.

The form factor for the fast core is almost flat; its value lies between 1.38 and 1.26, which are acceptable values in comparison to typical values for the form factor in a traditional CANDU 6 reactor. The behaviour of the total form factor is similar to that of the thermal core where it reaches a value of 3.6 after 1000 days because most of the power is produced in the thermal core.

7.7.5. Calculation of the Burnup.

The burnup and multiplication factor are calculated for a burnup period of 1000 days using the Serpent 1.19 code. The results are shown in Figure (7-53).

The multiplication factor first decreases sharply because of the consumption of ^{235}U and the build-up of saturating fission products (Xe and Sm). The saturating fission products quickly approach a constant value, which is higher in the thermal core. The drop in the multiplication factor is followed by a plutonium peak.

During the progressive burnup of the fuel in both cores, the non-saturating fission products that accumulate in the fuel limit the discharge burnup of the fuel. Because of these accumulated fission products, and the depletion of both fissile isotopes ^{235}U and ^{239}Pu, a steady decrease in the multiplication factor follows the plutonium peak. The reactor becomes subcritical at a burnup of 1.93E+4 MW d $(tonne)^{-1}$.

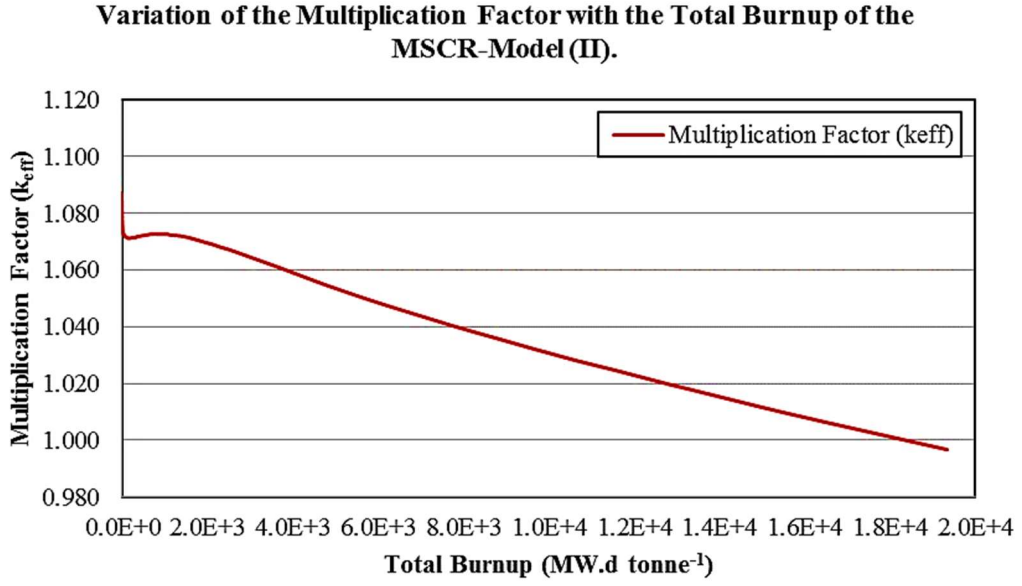

Figure (7-53): Variation of the Multiplication Factor with the Total Burnup of the MSCR-Model (II).

Figure (7-54) shows the variation of the burnup of the thermal (blue line) core, fast core (red line) and total MSCR-Model(II) (green line) with time. All burnups are normalized to the total mass of the fuel of the entire reactor.

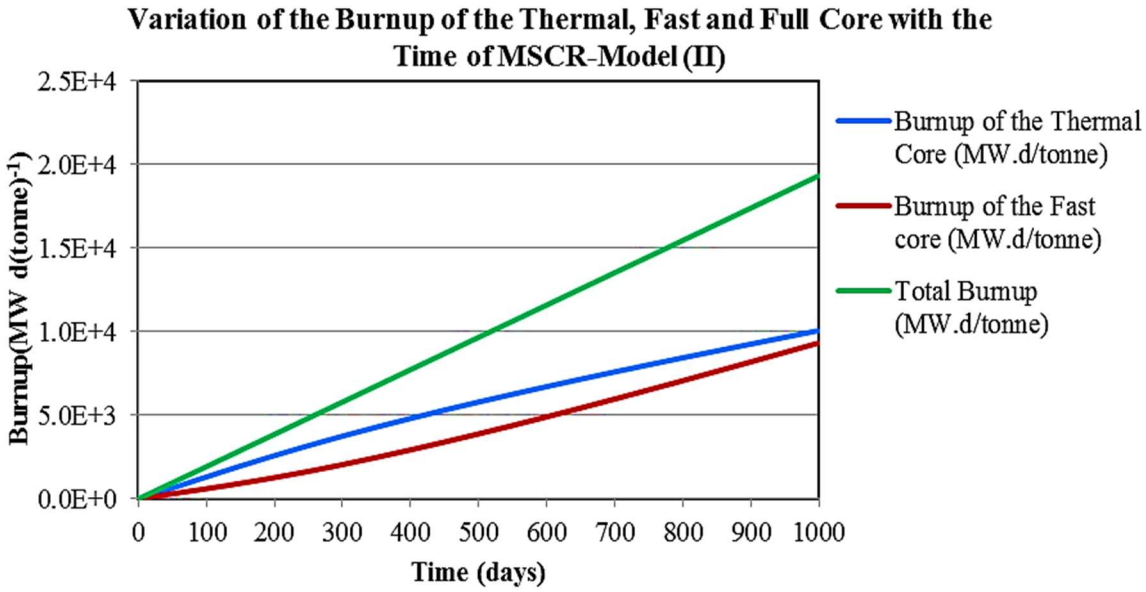

Figure (7-54): Variation of the Burnup with Time of Thermal Core, Fast Core and the Entire MSCR-Model(II).

The burnup of the thermal core slightly decreases after 300 days due to a reduced power production rate in that core. Correspondingly, the burnup of the fast core slightly increases with an increase in the power production rate. However, the total burnup is linearly proportional with time at a constant rate. The three burnup curves are proportional to time. It is evident that most of the fuel burnup is produced in the thermal core. The increased burnup in this model in comparison with Model (I) arises from the increased amount of fresh fuel in the fast core.

7.7.6. Change of Atomic Density of Actinides in the MSCR-Model(II).

1) Change of Atomic Density of Actinides in the Thermal Core of MSCR-Model (II)

Figure (7-55), and Figure (7-56) show the variation of the atomic density concentrations in the thermal core of the MSCR-Model (II):

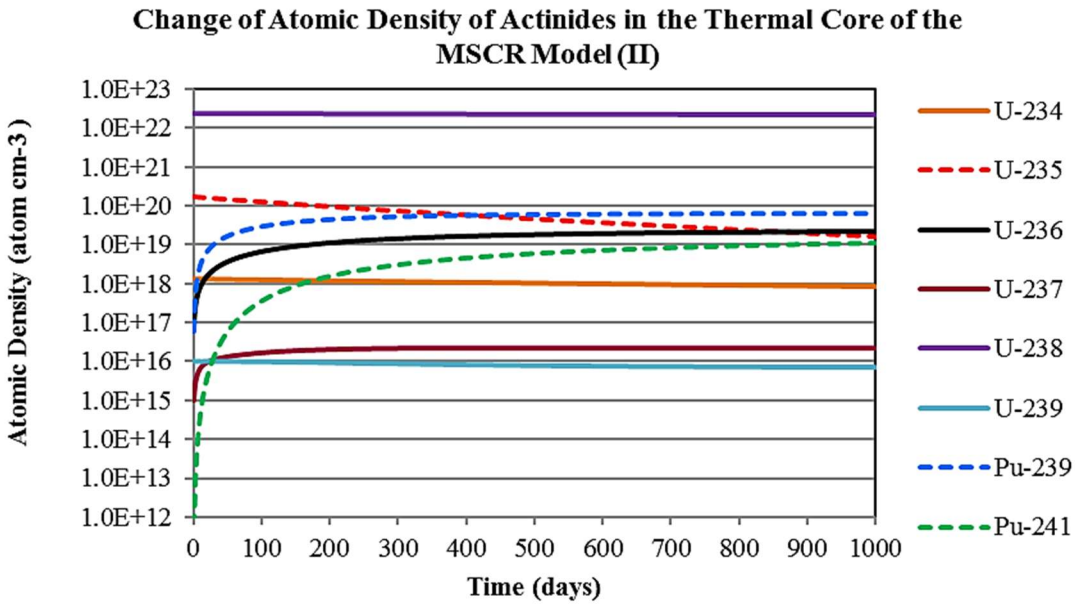

Figure (7-55): Variation of Atomic Density of Actinides in the Thermal Core of the MSCR-Model (II) (1).

Figure (7-55) shows that the atomic density of the fissile isotope U-235 slightly decreases with burnup. The atomic densities of Pu-239 and Pu-241 sharply increase during the first 20 days due to the breeding of these fissile isotopes, and then their rate of accumulation decreases gradually.

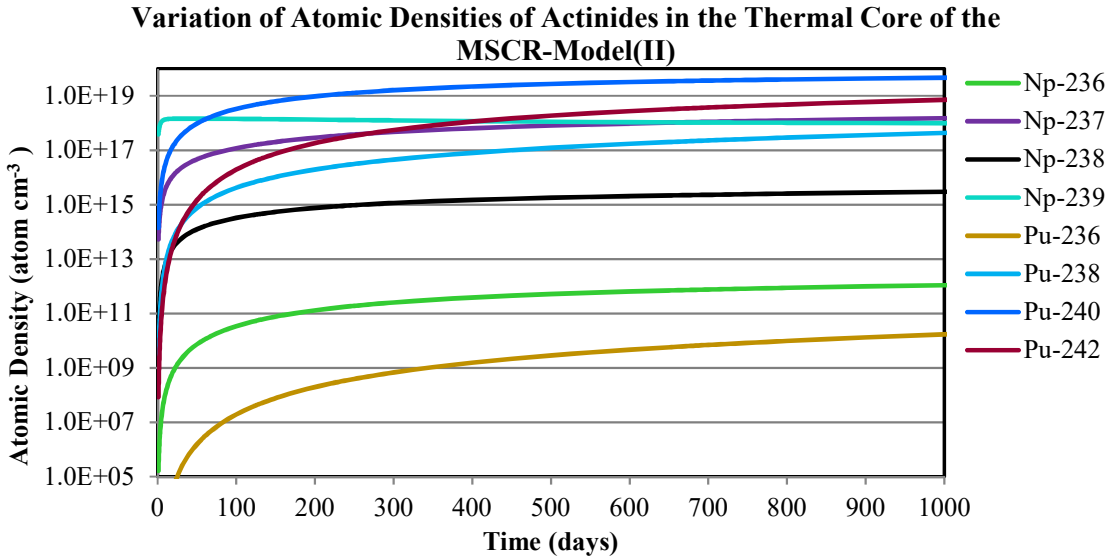

Figure (7-56): Variation of Atomic Density of Actinides in the Thermal Core of the MSCR-Model (II) (2).

Later, the concentration of plutonium saturates. It then eventually decreases with longer irradiation times with continued burnup.

Figure (7-56) presents the variations in atomic density of some transuranic isotopes. For the thermal core, the transuranic isotopes have initially zero concentration, as expected for fresh fuel with just natural uranium. After a certain time, the transuranic isotopes reach a constant value and then decrease for irradiation times longer than 1000 days. The other transuranic isotopes are not included in the graph because they have small concentrations.

2) Change of Atomic Density of Actinides in the Fast Core of MSCR Model(II).

Figure (7-57) and Figure (7-58) show the variation of the atomic densities in the fast core for the MSCR-Model (II):

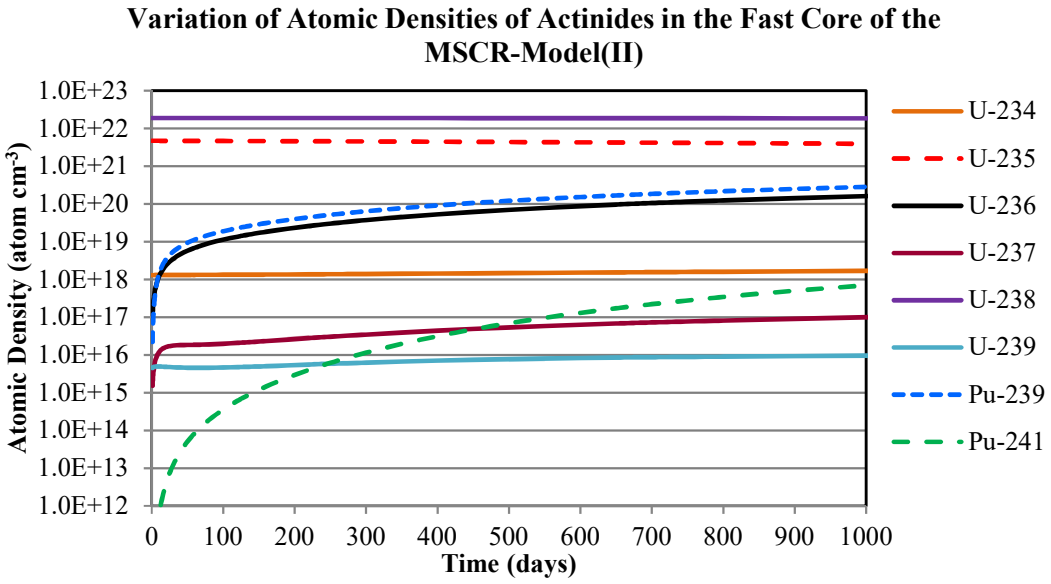

Figure (7-57): Variation of Atomic Density of Actinides in the Fast Core of the MSCR-Model (II) (1).

Figure (7-57) shows the atomic density of U-235, which is decreasing at a slight rate. The densities of the fissile Pu-239 and Pu-241 increase quickly during the first 20 days due to breeding and then increase at only a slight rate afterwards.

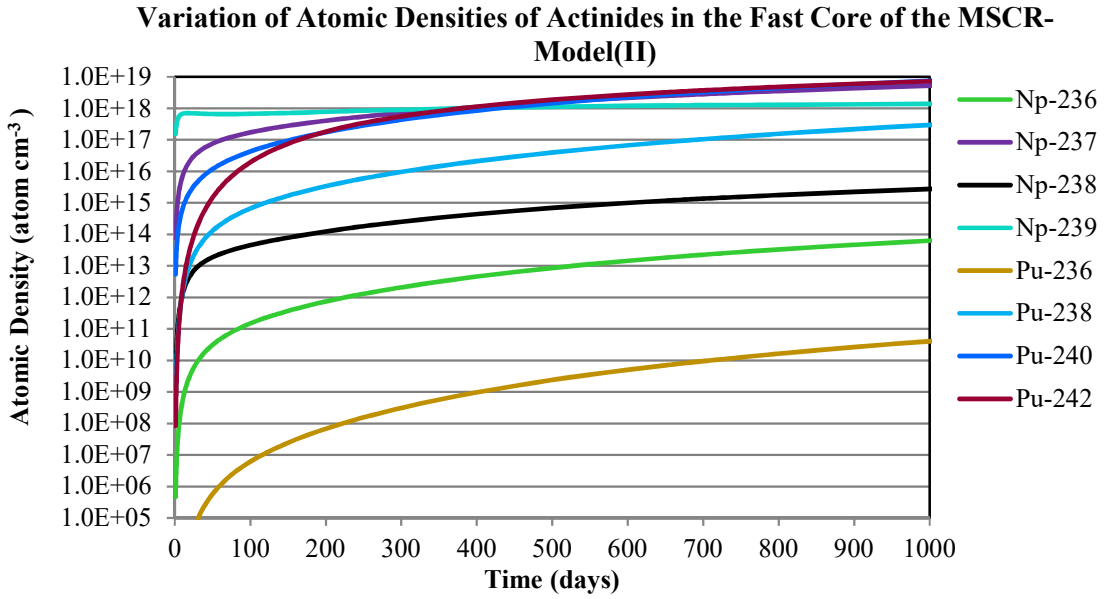

Figure (7-58): Variation of Atomic Density of Actinides in the Fast Core of the MSCR-Model (II) (2).

Figure (7-58) presents the variations of the atomic densities of some transuranic isotopes. Some isotopes start at a zero concentration since the fuel is fresh. After a certain time, they reach a constant value, and for irradiation times longer than 1000 days they decrease.

3) Change of Atomic Density of Fissile Actinides in the MSCR-Model(II)

Figure (7-59) and Figure (7-60) show the variation of U-235 for both the fast cores and the whole reactor. The rate of consumption per day in the fast core is higher than that in the thermal core because of the increased fast neutron flux in the fast core.

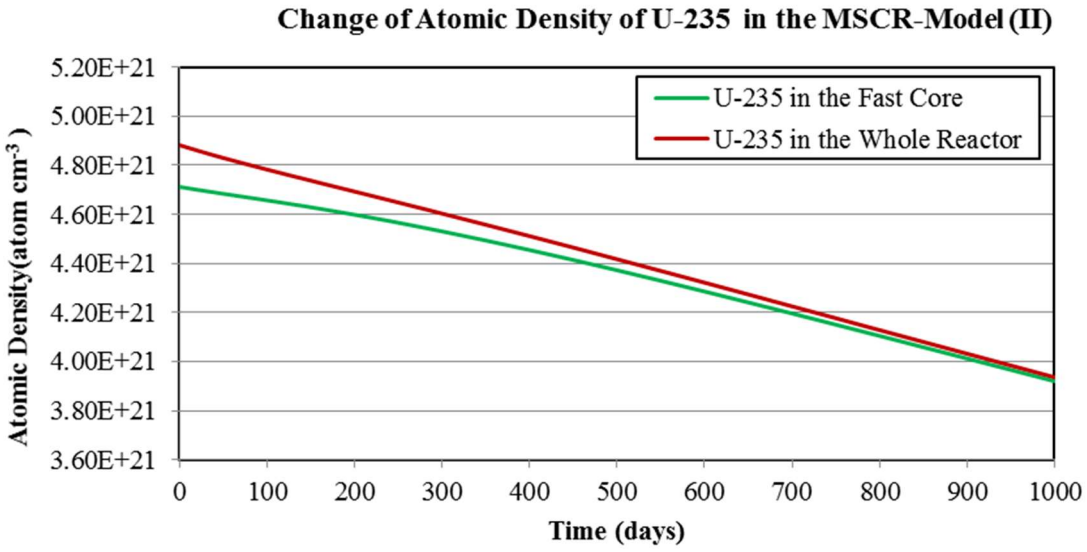

Figure (7-59): Atomic Density of the U-235 in the Fast Core and the Entire MSCR-Model (II)(1).

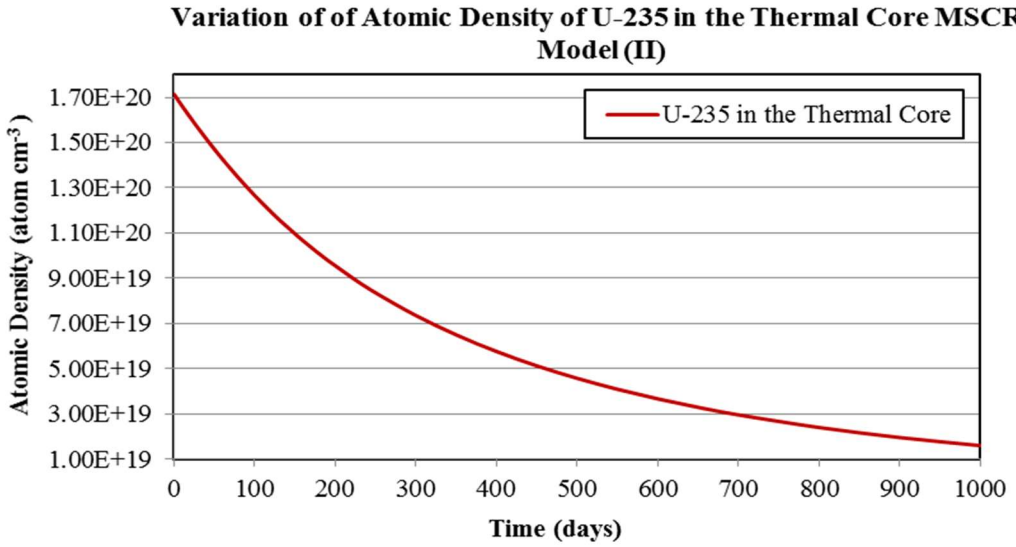

Figure (7-60): Atomic Density of the U-235 in the Fast Core and the Entire MSCR-Model (II) (2)

Figure (7-61) shows the variation of the atomic density of Pu-239 with time in the thermal core, fast core and the entire reactor (green curve). The atomic density of Pu-239 sharply increases during the first 20 days. After a short duration, steady state is reached, which is then followed by a steady decrease for longer irradiation times.

The slope at any point on the curve represents the instant rate of production of Pu-239 in g cm^{-3} day^{-1} in both cores and the entire reactor. Pu-239 is produced in both cores due to neutron capture in U-238 in the resonance energy region during moderation of the neutrons. The rate of production of Pu-239 in the fast core is higher than that in the thermal one because the average epithermal flux in the fast core is higher. Also, the production of epithermal neutrons in the fast core is higher because there is relatively little neutron moderation as fast neutrons scatter with the stainless-steel structure. This explains why most of the Pu-239 is produced in the fast core and why the rate of production of Pu-239 in the fast core is very close to that of the total rate. However, the fast neutrons that diffuse from the fast core to the thermal core are dependent on the fuel enrichment and its quantity in the fast core.

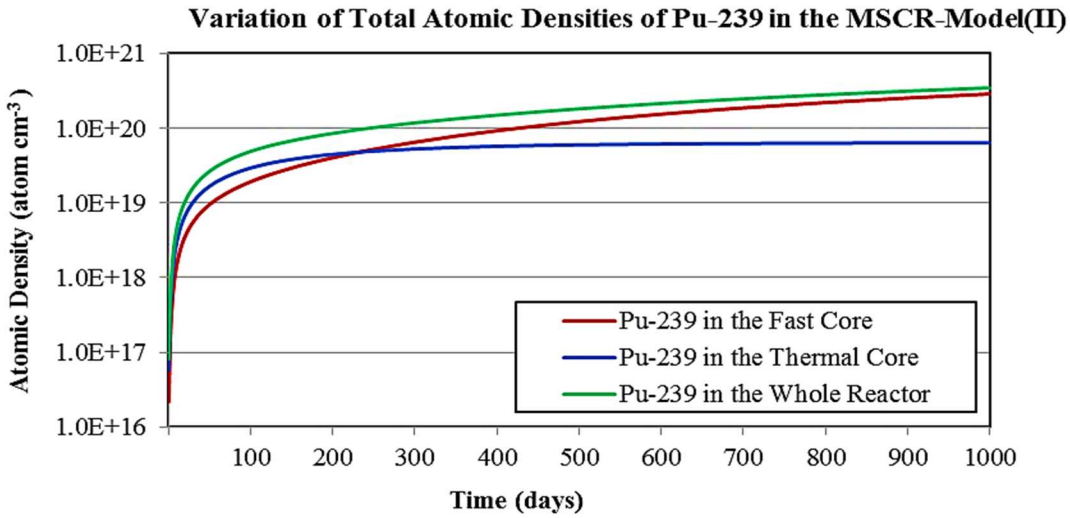

Figure (7-61): Variation of Atomic Density of Pu-239 in the Thermal Core, Fast Core and in the Entire MSCR-Model (II).

Figure (7-62) shows the variations of the atomic density of the total fissile isotopes in the entire reactor. The slope of the line is less than that of Figure (7-59) and Figure (7-60) because of the added isotopes of Pu-239 and Pu241 due to breeding.

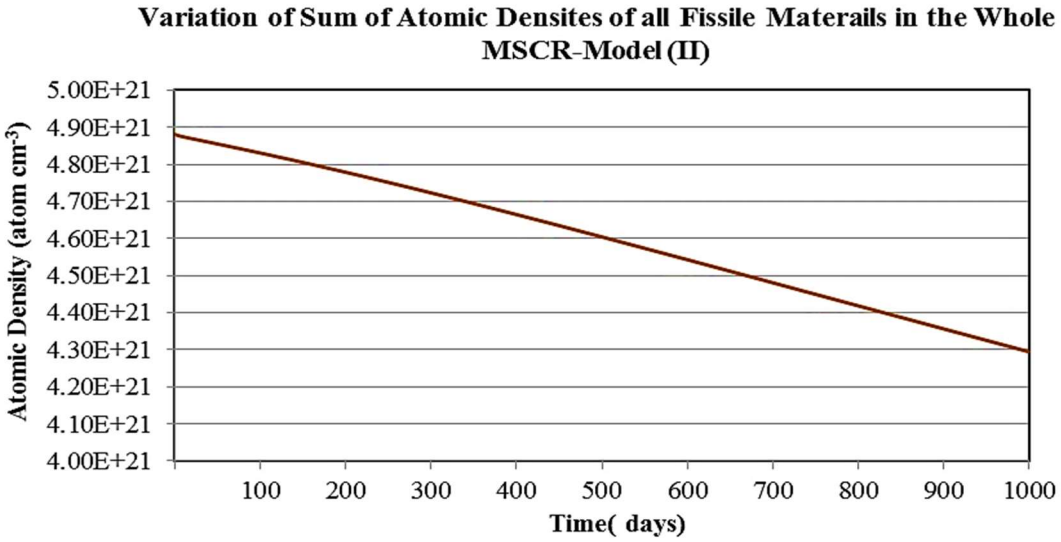

Figure (7-62): Atomic Densities of the Total Fissile Materials in the Entire Reactor Entire MSCR-Model (II) (1).

Table (7-10) shows the consumption rate and the percentage of the total fissile isotopes (U-235, Pu-239 and Pu-241) in both cores. The consumption rate in the fast core is around 5.9 times that in the thermal core. In comparison, in Model (I) the average rate of consumption in the thermal core was only slightly higher than that in the fast core.

Table (7-10): The Mass Density Consumption Rate and the Percentage of the Destructed of Fissile Material in the MSCR-Model(II)

	In the thermal core	In the fast core	In the entire reactor
Average Rate of Consumption of Fissile Isotopes ($g\ cm^{-3}\ day^{-1}$)	3.03E-05	1.96E-04	2.27E-04
Percentage of the Destructed Fissile Isotopes Weighted to the Original Fissile Material	46.15%	10.78%	12.02%

The percentage of destruction of fissile materials from the initial values in the thermal core is 46.15%, 10.78% in the fast core, and 12.02% for the entire reactor. This percentage is much better than that in the case of the MSCR-Model (I). Most of the fuel is burnt (about 46.15% of the initial U-235) in the thermal core, and 10.78% in the fast core. The percentage of U-235 burnt in the MSCR-Model (II) is 12.02% of the initial fissile isotope content of U-235.

7.8. Comparison between MSCR-Models (I) and (II)

The slopes of the lines in Figure (7-40) and Figure (7-62) represent the average rate of consumption of fissile materials. This average rate and the percentage of destruction of fissile material in each core and the entire reactor can be used to assess the capability of each model to burn fissile actinide during the periods of criticality. These values include destructed and produced concentrations of the fissile isotopes due to neutron capture. The rate of destruction as shown in Figure (7-63) is calculated in units of (g cm^{-3} day^{-1}). This chart shows that:

1) The rate of consumption of the fissile actinides in the thermal core of the model (I) is around seven times higher than that of the model (II). While the rate of consumption in the fast core of Model (II) is around ~2.6 times the consumption rate of the fast core in the model (I).

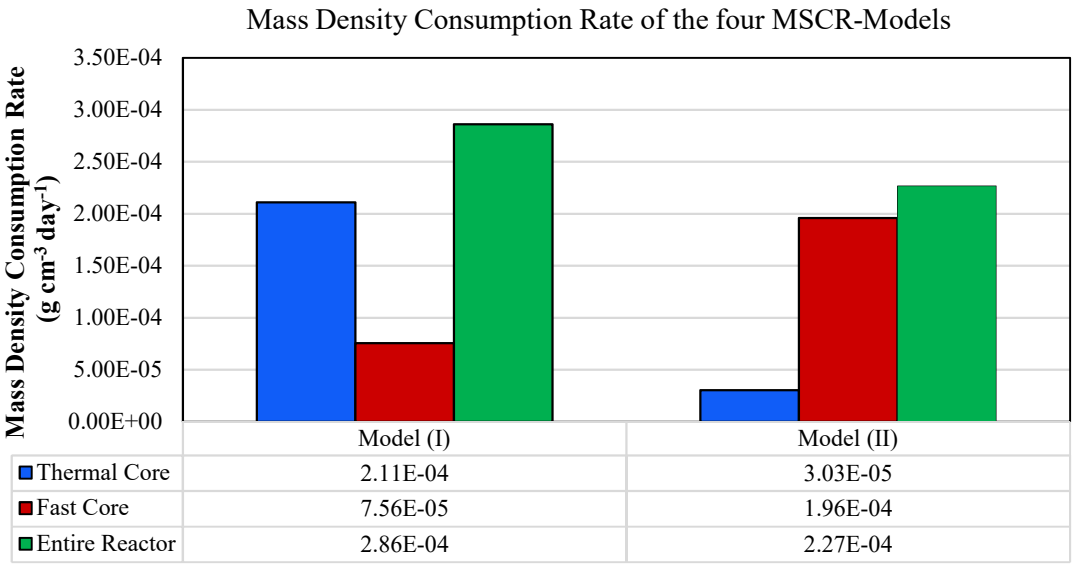

Figure (7-63): The Mass Density Consumption Rate of the Total Fissile Actinides in the four MSCR-Models

1) For the entire reactor model, the total consumption rate of model (I) is higher than that of model (II). But Model (I) is reach to subcriticality in shorter time in 135 days while model (II) needs 950 days to reach the subcriticality.

2) To evaluate the efficiency of burning actinides during the burnup time of each model, the percentage of districted actinides of each model is introduced as shown in Figure (7-64).

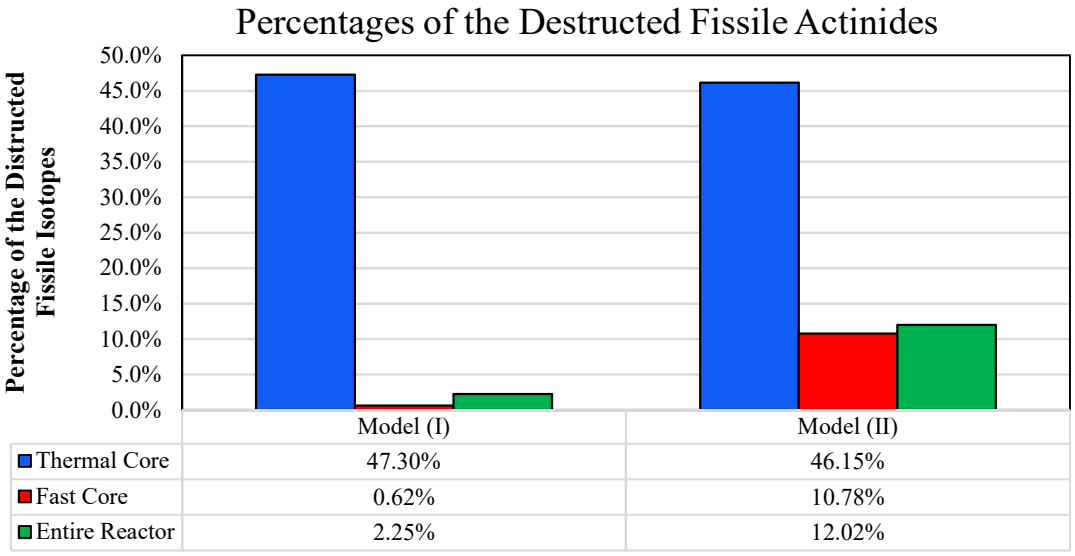

Figure (7-64): Percentages of Destruction of the Total Fissile Actinides in the four MSCR-Models

3) Form model (I), the percentage of destructed actinides is 0.62% while for the model(II) this percentage is 10.78% i.e. 17.4 times that of the model (II).

4) For the thermal core, the percentage of destructed materials of the model (I) is too close to that of the thermal core of the Model (II).

5) For the entire reactor, the percentage of destructed fissile actinides materials of model (II) is 12.02% with which is ~5.3 times of that for model (I) (2.25%)

6) As the fissile material in the fast core increase such as the case of model (II) the rate of burnup will be slow due to high percentage of the fissile actinides and higher average of the fast flux in the fast core. In addition to the buildup fission products that in the fast core that have a slightly similar moderate fast neutron cross section. Model (II) has higher efficiency for burning actinides in its fast core than Model (I) while the rate of destruction actinides in the thermal core of the Two models are similar.

7) Table (7-11) shows the mass of destructed fissile materials in the models (I) and (II) in each core as calculated at the end of the burnup period.

Table (7-11): The Actual Destructed mass of the Fissile materials in Models [(I) and (II)] at the end of the burnup period

Model	Burnup period (days)	Mass of fissile materials in the thermal core (g)	Mass of fissile materials in the fast core(g)	Percentage of fissile Mass Destructed in the thermal Core	Percentage of fissile Mass Destructed in the fast Core	Actual destructed mass the thermal core mass (g)	Actual destructed mass the fast core mass (g)	Actual destructed mass entire Model (g)
I	135	5.457E+5	1.511E+6	47.3%	0.62%	2.581E+05	9.371E+03	2.675E+05
II	950	5.457E+5	6.990E+6	46.15%	10.78%	2.518E+05	7.536E+05	1.005E+06

8) The destructed mass of the fissile material in the thermal core is slightly higher for Model (I) and but in the fast core and the entire reactor Model (II) is higher., it can burn 1.01 tonne of fissile material and ~ 0.75 tonne in the fast core only.

7.9. Conclusion

From results and discussion, one can conclude that:

1) The design model of the multispectrum CANDU reactor with U-235 as the fissile material has been implemented using the Serpent code. Helium gas is chosen as the coolant and filling material in the fast core. Stainless steel has been selected as the structural material of the fast core. The two cores are separated by a hollow cylinder filled with low-pressure helium between two partition walls.

2) Four cases based on MSCR-Model (I) are used to study the radial and axial flux distributions for different lattice pitches and enrichments of the fast uranium core, which demonstrate that:

   (a) There are no significant effects on the thermal neutron flux in both the thermal and fast cores with an increase in the fissile isotope concentration.

   (b) Increasing the fissile material concentration in the fast core causes an increase in the fast and epithermal fluxes in the fast core.

   (c) Increasing the lattice pitch width at the cost of decreasing the number of fuel channels in the fast core does not improve the burnup.

(d) Decreasing the lattice pitch of the fast core will increase the fast and epithermal fluxes at its center.

(e) Distribution of the fuel channels in the fast core makes the epithermal and fast fluxes are more uniform in that core.

(d) In the fast neutron core, both the epithermal and fast neutron fluxes are significantly increased with an increase in fissile isotope concentration. The epithermal fluxes in the thermal core are mostly independent of the enrichment except in channels near the fast region at certain lattice pitch values. Fast neutron fluxes in the thermal core are almost identical at different enrichments of the fuel of the fast core for certain lattice pitch values.

3) The calculated reactivity lies within the safety margin for criticality. To demonstrate the non-breeding characteristic of the current reactor, the regeneration factor is calculated and is shown to be smaller than the minimum value needed for breeding.

4) The MSCR-Model(I) is used as a first case study for burnup calculations. It shows that there are reasonable values for such safety parameters as the criticality and form factor. The model does not provide a significant level of burning of actinides in the fast core. This can be achieved by increasing the number of fuel channels in the fast core while respecting the criticality safety criteria.

5) MSCR-Model(II) is simulated with the same radius and enrichment ratio of the fuel in the fast core as Model (I). However, an increase in the number of fuel channels in the fast core to 148 and a decrease the lattice pitch to 14.575 cm are introduced.

6) The reactivity and regeneration factors were calculated proving that Model (II) is inside the criticality safety margin and that it can burn actinides more than breeding.

7) The form factor of the Model (II) is higher than acceptable safety margin.

8) For the thermal cores, the consumption rate of Model (I) is higher than that of Model (II). In contrast, for the fast core, the consumption rate of Model (II) is much better than in Model (I). However, for the entire reactor, Model (I) has a slightly higher consumption rate.

9) For the thermal core, both reactors have almost the same amount of destruction because both thermal cores are of the same size with the same amount of natural uranium. However, for the fast core in Model (II), there is a higher percentage of actinide burning, about 17.4 times more than that of Model (I). As such, overall, the entire reactor in Model (II) burns about 5.5 times more during it burnup time.

10) The relative error of the reactivity, regeneration factor, and the flux at each energy bin are very small. The error of Monti Carlo calculation algorithm that used in the Serpent or MCNP codes are very small and proportional inversely with the square root of number of histories.

11) Since the current MSCR models are represent as a preliminary design the relative error will not be considered in the other mode.

Hence, the MSCR-Model (II) is better than Model (I) in burning U-235. However, there are still safety concerns because of its high form factor.

Chapter 8.

Burning Plutonium from Dismantled Weapon Grade in the MSCR

8.1. Materials and Design

In this chapter, the Multispectrum CANDU reactor is used for burning plutonium from dismantled nuclear weapon grade material. The weapon-grade plutonium is added to the depleted uranium tail of U-238 with U-235 at 0.25%. The concentrations of isotopes of heavy elements in the fast neutron core are as shown in Table (8-1).

Table (8-1): Isotope Concentrations of the MOX Fuel Used in the Fast Core of Models (III to VI) [70][71]

Isotope	Pu-239	Pu-240	Pu-241	Am-241	U-234	U-235	U-238
Percentage ratio	13.88%,	1.05%	6.6E-5%	4.68E-2 %.	1.45E-3%	0.25%	84.8 %

The fast core is constructed to promote a fast neutron spectrum and fuelled by MOX fuel and depleted uranium. The ^{239}Pu, ^{235}U, and ^{241}Pu account for a total fissile isotope percentage of 14.13% of heavy elements. The temperature of the fuel in the fast core is set to 1400 K. The densities of UO_2 and PuO_2 are calculated at this temperature using Equation (8-1) [72].

$$\rho_T = \rho_{273}\times[0.99672 + (1.179\times10^{-5})\,T - (2.429\times10^{-9})T^2 + (1.219\times10^{-12})\,T^3]^{-3} \quad (8\text{-}1)$$

The density of the MOX fuel could be calculated using Equation (8-2) [73] by setting the ratio of UO_2 and PuO_2 respectively equal to 85.023% and 14.977%.

$$\rho_{(fuel\ in\ the\ fast\ core)} = \frac{(\rho_{UO_2}\times\rho_{PuO_2})}{(\rho_{PuO_2}\times R_{PuO_2}) + (\rho_{UO_2}\times R_{UO_2})} \quad (8\text{-}2)$$

The calculated density of the MOX fuel is 11.0634 g cm^{-3}, which is used as a fuel in the fast core of the MSCR-Models (III, IV, V and VI). The 14.13% percentage of the fissile materials is applied to all models. For the thermal core of the Pu-fuelled models, the fuel is supplied as natural uranium. The fuel bundle for the fast core is 37 fuel elements clad in stainless steel (316L(N) SS) with standard dimensions and sheath thickness. In the thermal core, the bundle cladding is made of Zircaloy-4.

The decision variables between these four models are the radius of the fast core and the number of fuel channels in each core. The lattice pitch of the fast core of Model (III) is 28.575 cm while for the other models (IV), (V) and (VI) it is chosen as 14.287 cm. The lattice pitch of the thermal core for the four models is 28.575 cm. The geometrical descriptions of the fast and thermal cores of the MSCR-Models (III, IV, V and VI) are presented in Figure (8-1) to (8-4), respectively. Table (8-2) presents the details of the specifications of the four models. Table (8-2) and Table (8-3) presents the mass of the fuel and fissile materials used in each model.

Figure (8-1) presents the design of the MSCR-Model (III)[74]. The Figure (8-1-A) show the layout of the full core design of this model. Figures (8-1-B) and (8-1-C) show the details of geometry and materials used in the fuel channels of the thermal and fast cores. The same materials and geometry of these fuel channels are used for Models (IV), (V) and (VI).

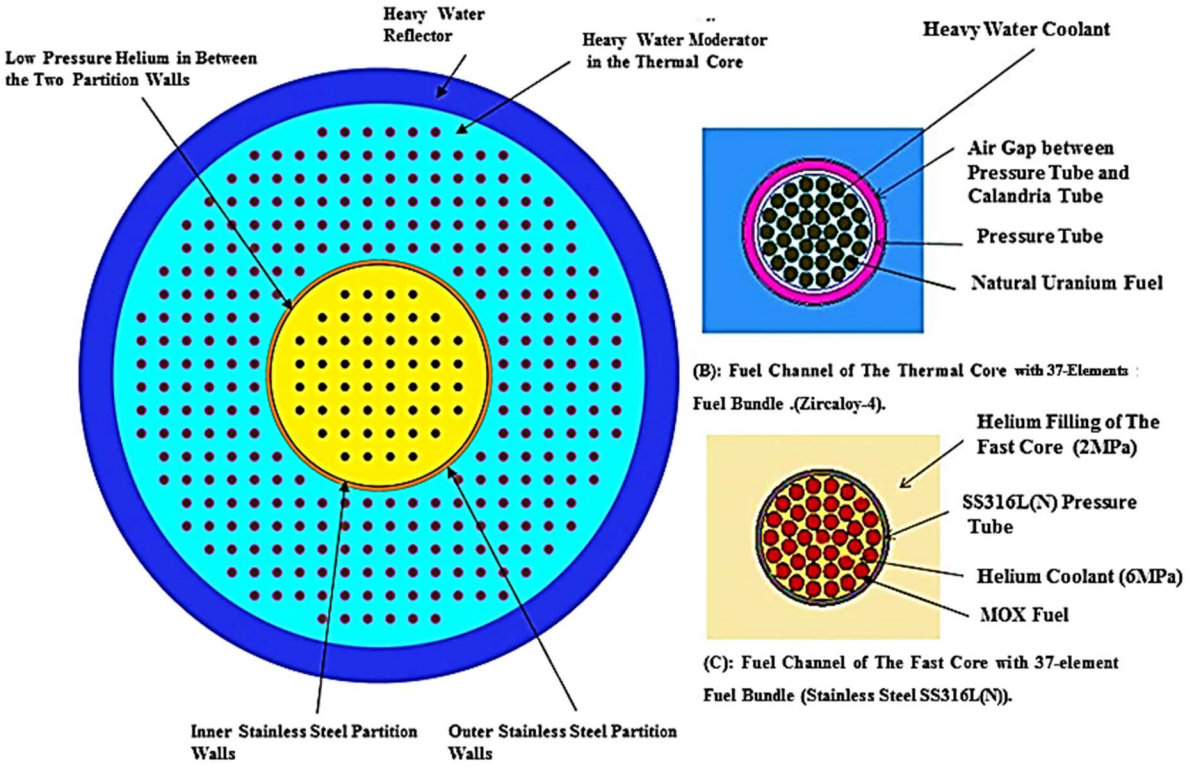

Figure (8-1): Design Model of the Multispectrum CANDU Reactor Model (III)

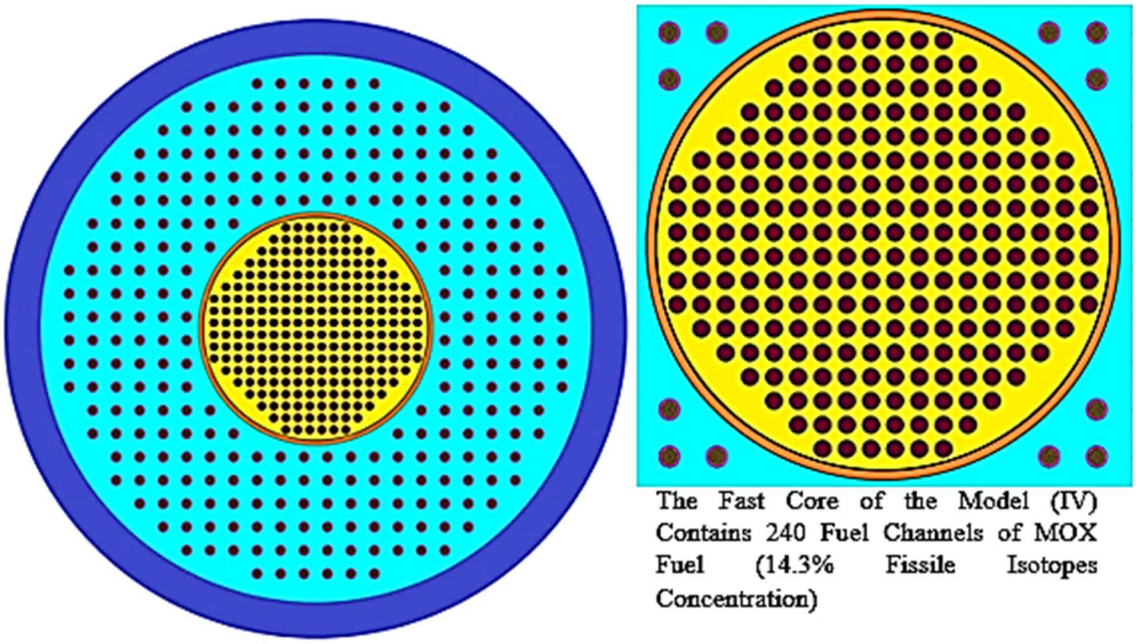

Figure (8-2): Design Model of the Multispectrum CANDU Reactor Model (IV)

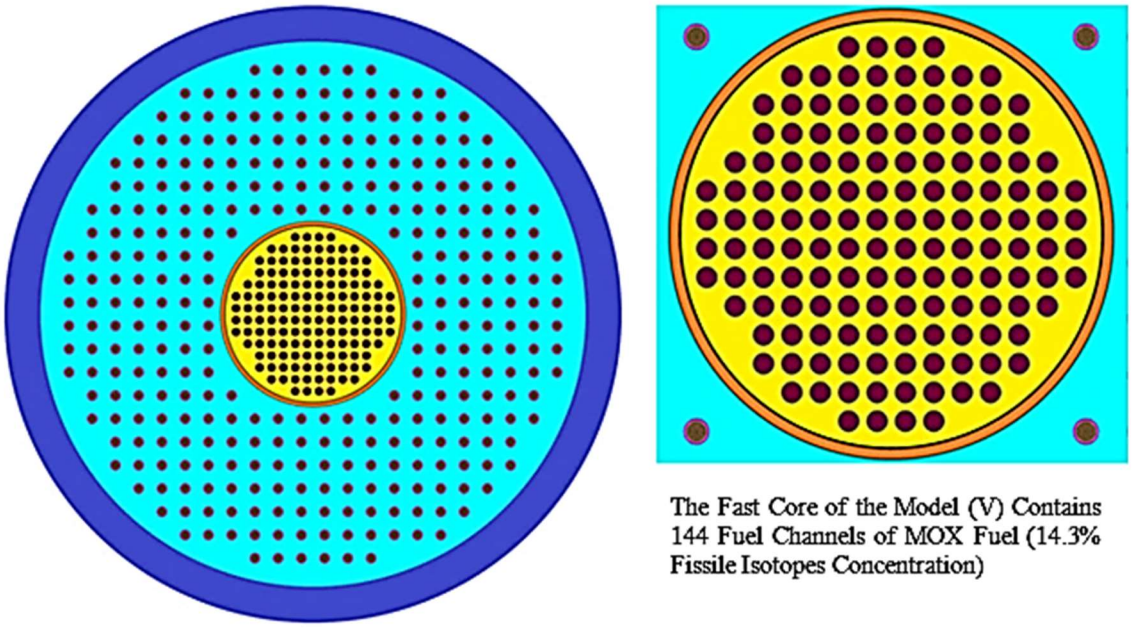

Figure (8-3): Design Model of the Multispectrum CANDU Reactor Model (V)

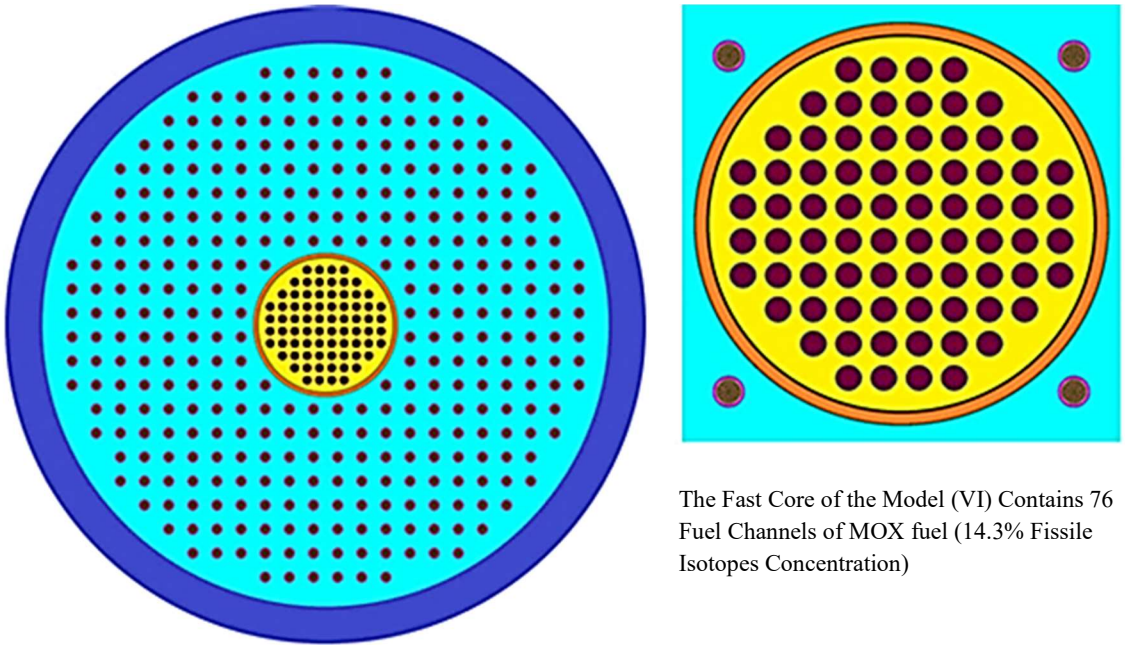

The Fast Core of the Model (VI) Contains 76 Fuel Channels of MOX fuel (14.3% Fissile Isotopes Concentration)

Figure (8-4): Design Model of the Multispectrum CANDU Reactor Model (VI)

Table (8-2): Geometry and Specifications of the Fast Core and Thermal Core of the Four of MSCR-Models Fuelled with Plutonium

Model	Radius of the fast core (cm) measured from the outer radius of the partition wall.	Number of fuel channels in the thermal core	Number of fuel channels in the fast core	Lattice pitch for the fast core (cm)	Fuel type of the fast core and concentration of fissile materials Enrichment) (atomic ratio)
III	R_1=137.32	292	52	28.575	Fissile material concentration 14.13% (^{239}Pu-13.89%) with depleted uranium base
IV	R_1=137.32	292	240	14.287	
V	R_2=108.86	320	144	14.287	
VI	R_3=80.39	348	76	14.287	

Table (8-3): Mass of the Fuel and Fissile Materials in the in the Design of the Four of MSCR-Models

Model	Total mass of the UO_2 of the thermal core (g)	Mass of fissile materials in the thermal core (g)	Total mass of the fuel in the fast core (g)	Mass of fissile materials in the fast core(g)	Total mass of fissile material (g)	Total mass of the fuel in the reactor (g)
III	7.9449E+07	4.9794E+05	1.4151E+07	1.7738E+06	2.2718E+06	9.3600E+07
IV	7.9449E+07	4.9794E+05	6.6400E+07	8.3233E+06	8.8212E+06	1.4585E+08
V	8.7067E+07	5.4569E+05	3.9187E+07	4.9121E+06	5.4578E+06	1.2625E+08
VI	9.4686E+07	5.9343E+05	2.0682E+07	2.5925E+06	3.1859E+06	1.1537E+08

In the four models, the analysis of the reactor physics parameters is focused on the calculations of the reactivity, the regeneration factors, the radial neutron flux $\varphi(r)$ and axial neutron flux $\varphi(z)$ distributions, power distributions, the percentage of the power produced from each core, the form factor, total burnup, the burning of fissile actinides in the different models, and finally, the percentage of destruction of fissile actinides and their consumption rate.

The radial neutron flux $\varphi(r)$ and axial neutron flux $\varphi(z)$ shape of the fresh fuel at each energy bin (thermal, epithermal and fast flux) have been calculated. These fluxes are normalized for a constant power of 2180 MWth which is the same power as for the CANDU 6 Gentilly-2 reactor.

The data library used for these calculations for the both reactor materials and fuel is ENDF/B-II. The three energy bins are defined similarly as for uranium-fuelled reactors.

The optimization of multiplication factor and total flux for number of cycles and number of neutrons per cycle are shown in the Appendix (E).

8.2. Excess Reactivity and the Regeneration Factor

8.2.1. Excess Reactivity

Figure (8-5) to (8-8) present the variation of the excess reactivity of the entire MSCR system with time. For the Models (III), (IV), (V), and (VI), the common behaviour of the reactivity is a decrease during the first few days, the magnitude of which depending on the model. This reduction is due to a build-up of saturated fission products (xenon in particular) mainly in the thermal core. This drop is followed by a plutonium peak due to the production of fissile plutonium isotopes in

both cores. The plutonium peak is followed by a steady decrease in the reactivity due to the burnup of the fuel and the accumulation of non-saturating fission products.

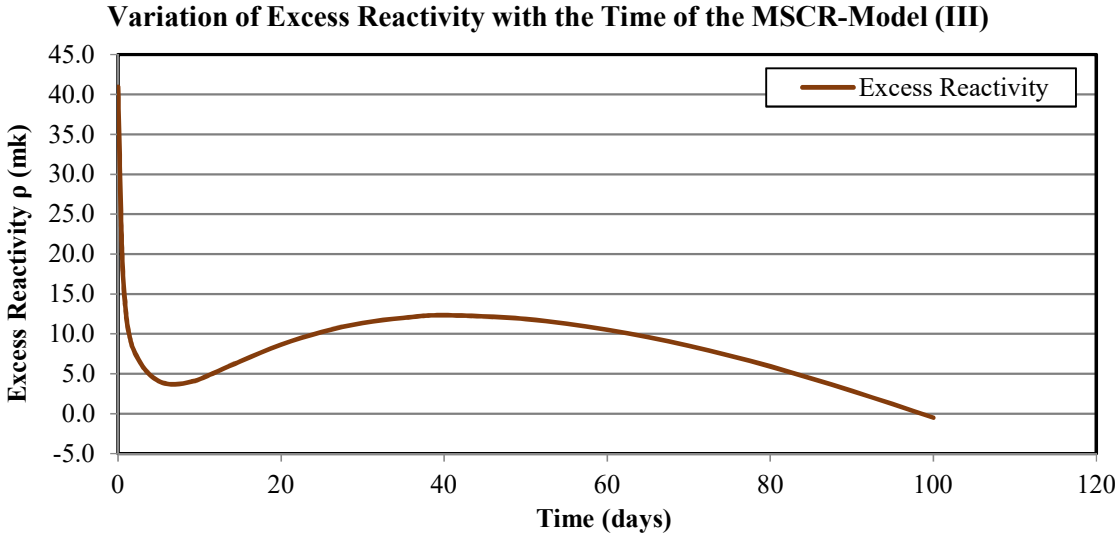

Figure (8-5): Variation of Reactivity with Time for the MSCR-Model (III)

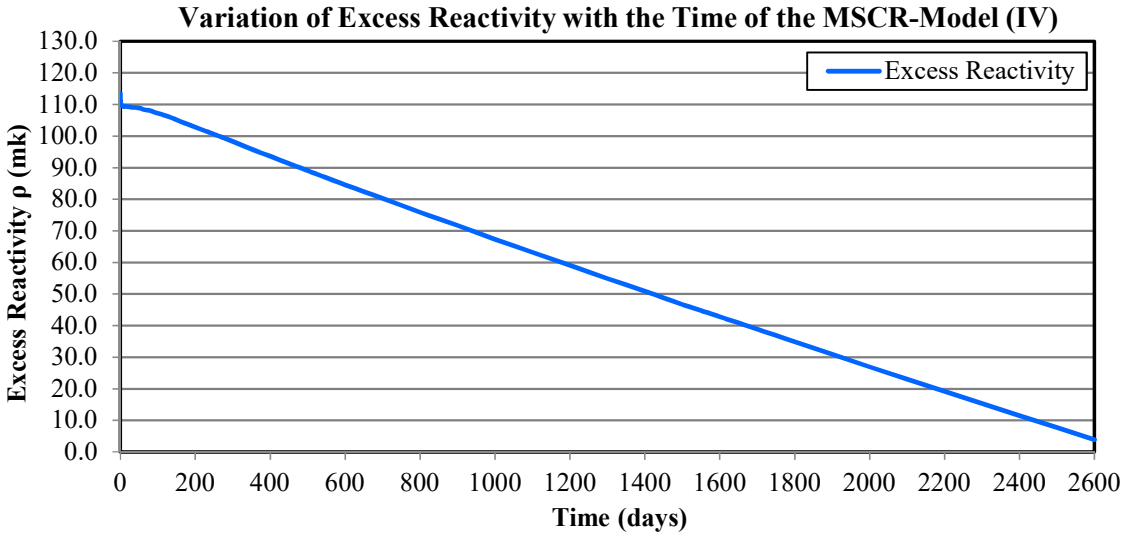

Figure (8-6): Variation of Reactivity with Time for the MSCR-Model (IV)

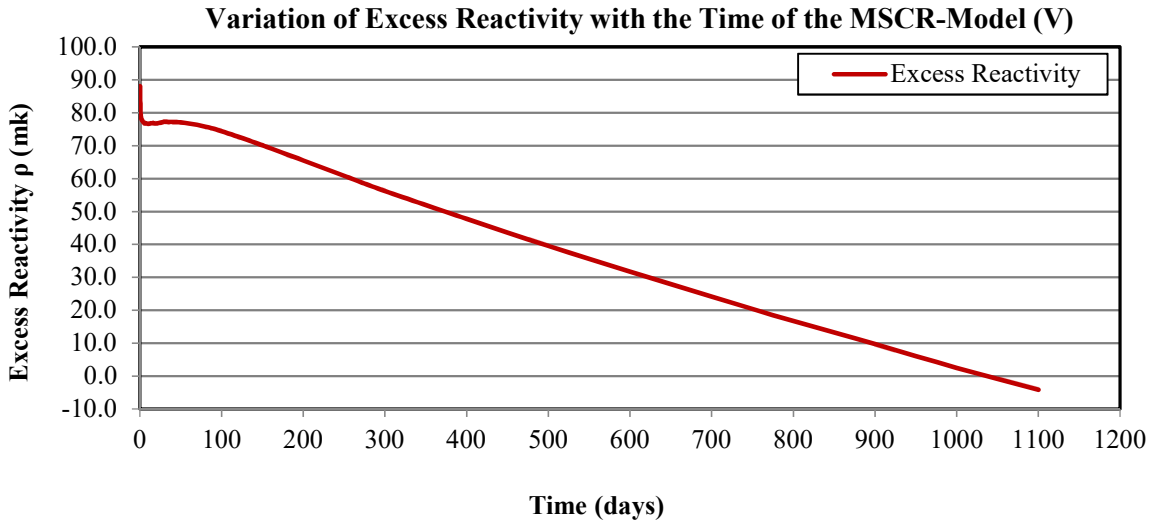

Figure (8-7): Variation of Reactivity with Time for the MSCR-Model (V)

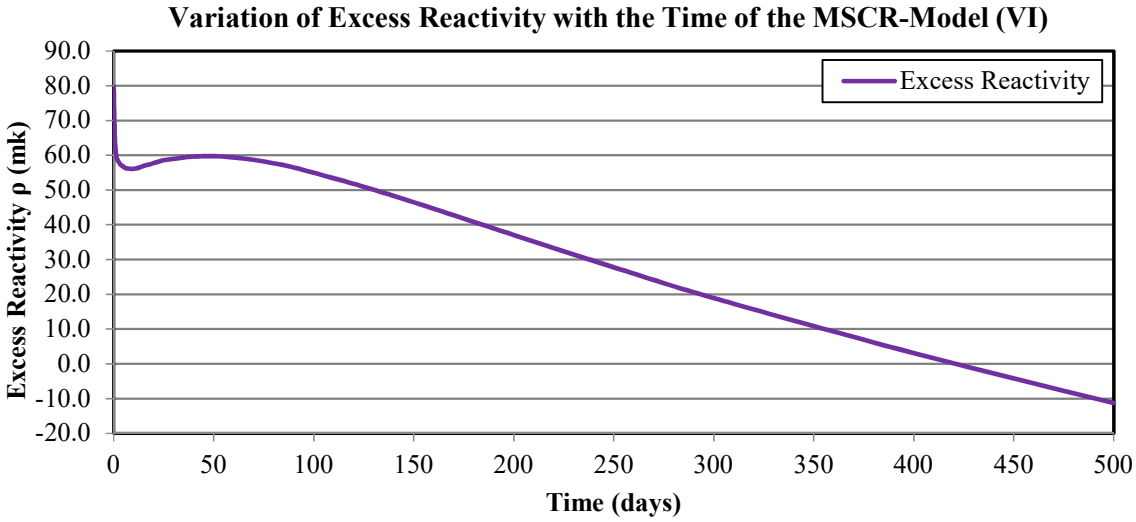

Figure (8-8): Variation of Reactivity with Time for the MSCR-Model (VI)

Table (8-4) shows the initial reactivity for all four models with a drop due to saturated fission products.

Table (8-4): Comparison between the Reactivity Curves Behaviour of the MSCR-Models (III, IV, V and VI)

	Initial reactivity (mk)	Drop in the reactivity $\Delta\rho$ due to saturated fission products (mk)	The Hight of plutonium peak (mk)	Time to reach subcritical (days)
Model (III)	41	-37.0	8.0	98
Model (IV)	113.5	-3.5	0	2700
Model (V)	88.1	-11.3	~0.7	1060
Model (VI)	79.5	-23.0	~4.0	420

The behaviour of the excess reactivity curves for Models (III), (V) and (VI) are similar to that of the traditional CANDU reactor except for Model (IV). The behaviour depends on the amount of fuel in the fast and thermal cores. From the excess reactivity curves of the four models and reactivity values in Table (8-4) one observes that:

1) The initial reactivity and the time to reach the sub-criticality is dependent on the amount of the fuel in both cores.

2) In comparison between reactivity curves of Model (III) and Model (IV) one can notice the large decrease in the reactivity of Model (III) (37 mk) while this decrease is only (3.5 mk) in case of the Model (IV) due to saturated fission products (mainly Xe-135 and Sm-147).

3) As the number of fuel channels increases and they are packed more closely in the fast core, the average fluxes at the three-energy bins in entire reactor of the two Models (III) and (IV) are shown in Table (8-5).

Table (8-5): Average Fluxes at the Three Energy Bins of the MSCR-Models (III)and (IV)

	Model (III)	Model (IV)	Relative change
Average Thermal Flux (n cm s^{-1})	1.27446E+14	8.12795E+13	-0.36
Average Epi Thermal Flux (n cm s^{-1})	4.95866E+13	1.42027E+14	1.86
Average Fast Flux (n cm s^{-1})	3.01565E+13	1.8098E+14	5.0

4) From Table (8-5) it can be seen that, the average thermal flux of Model (IV) decreases by 0.362 times the value in Model (III), while the average epithermal flux of Model (IV) increases by 1.86 times that of Model (III). The average fast flux of the entire reactor in Model (IV) increases by a factor of 5 times that of Model (III). Higher macroscopic fission cross section of fissile materials and an increase in the average fast flux in Model (IV), make the fast fission rate higher than in Model (III). Since the saturating fission products (xenon

and samarium) are mainly produced from thermal fission, as the fast fission rate increases and the thermal fission rate decreases in Model (IV), the effect of saturating fission products in Model (IV) decreases because it has low absorption cross section for the fast neutron spectrum as mentioned above in section (7.7.1) This explains the large differences in the reactivity drop between these two models.

5) For Models (V) and (VI), there is a decrease in the radius of the fast core by one fuel channel width (i.e. 28.575 cm) for model (V) and two fuel channels width (i.e. 57.150 cm) for model (VI). Therefore, the number of fuel channels in thermal core is increased to 320 in model (V) and to 348 for Model (VI) This results in an increase in the amount of moderator in the thermal core and consequently a greater thermal flux in the thermal core (as shown in later in the flux distribution section). The thermal fission rate increases in the thermal core for Model (VI). Consequently, the production of saturating fission products increases more in Model (VI) than that of Model (V) with a bigger drop in reactivity. A similar difference is observed for the reactivity drop between Models (IV) and (V) with more thermal fuel channels in Model (V) (320 fuel channels) compared to Model (IV) (292 fuel channels).

6) The peak in the reactivity curve of Model (III), (V) and (VI), and the corresponding constant value in Model (IV), are due to plutonium production in both cores for each model.

7) The fissile plutonium isotopes (Pu-239 and Pu-241) are mainly produced from the capture of epithermal neutrons by U-238 in the thermal core and in the fuel channels where the epithermal flux is high. In Model (III), the epithermal flux is higher at the center of the thermal core than in the fast core as shown in Section 8.3. In addition, there is a larger concentration of U-238 in the thermal core in comparison to the fast one. Also, the wide lattice pitch of the fast core increases the chance of neutron collision with structural materials before contributing to fast fission. Thus, the neutron falls into the epithermal energy region where it is captured by U-238 in the fast core. Consequently, the rate of production of plutonium is higher in Model (III)

8) For the other models [(IV), (V) and (VI)], with an increased number of fuel channels, and consequently a greater amount of U-238 and moderator in the thermal core, the rate of

plutonium production in the thermal core increases, thereby explaining the increase in the plutonium peak from Model (IV) through to Model (VI).

9) For Model (IV), the plutonium peak is flat indicating that the reactivity is practically constant from day 20 to day 60. The production of plutonium in the fast core has a small effect on the total fast core reactivity because of the higher percentage of Pu-239 in the fresh fuel. Hence, the amount of fuel burnup during this period is compensated for by the number of fissile isotopes produced during this period.

10) After the plutonium peak, the reactivity decreases in the four models at a steady rate. The time needed to reach subcriticality is dependent on the amount of fuel in the fast core. Model (IV) needs 2700 days or 7.4 y to become subcritical while Models (V), (VI) and (III) require 2.85 y, 1.15 y and 3.3 months, respectively.

11) For Models [(IV), (V) and (VI)] where the amount of fissile material in the fast core is large and the ratio of fast fission is increased from Model (VI) to (IV), the burnup of the fuel due to the accumulation of fission products is much slower. This occurs because most fission products have comparable cross-sections for fast neutrons. This demonstrates the proportionality of the burnup with the size of the fast core.

8.2.2. Regeneration Factor

Figure (8-9) to (8-12) show the change in the regeneration factor versus time. The behaviour of the regeneration factor (η) curve is similar to the reactivity curve, because it describes the number of the neutrons produced per neutron absorbed in the fuel, so it mainly depends on the fuel isotopic concentration.

During the first period, the regeneration factor decreases due to the production of saturated fission products in the fuel. Then the number of produced neutrons per neutron absorbed in the fuel is decreased with production of neutron poisons. The sharp decrease in the regeneration factor is followed by increases due to a change in the fuel concentration from the production of fissile plutonium. It then decreases again due to a change in the fuel content due to burnup and production of fission products.

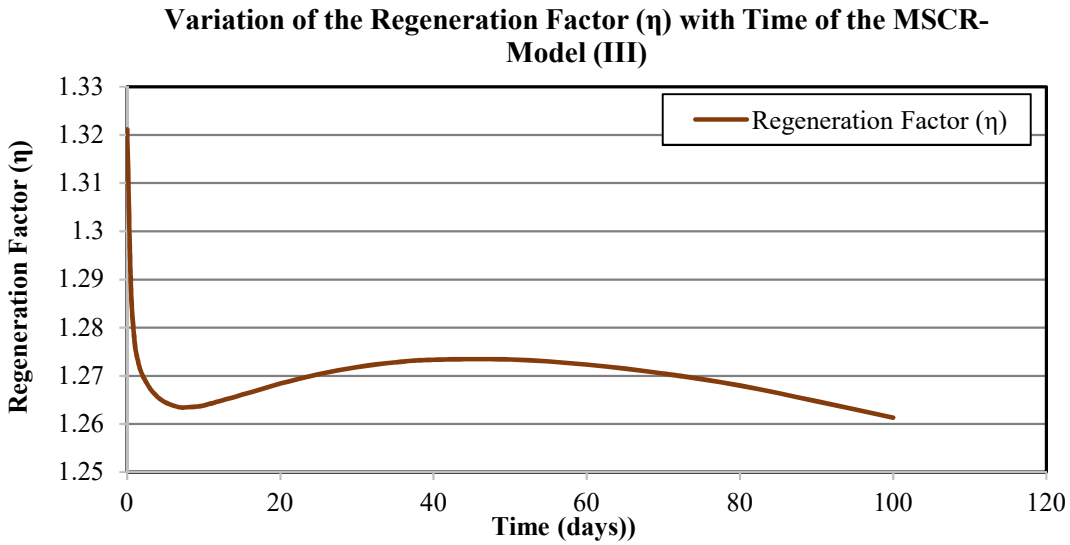

Figure (8-9): Variation of the Regeneration Factor with Time of the MSCR-Model (III)

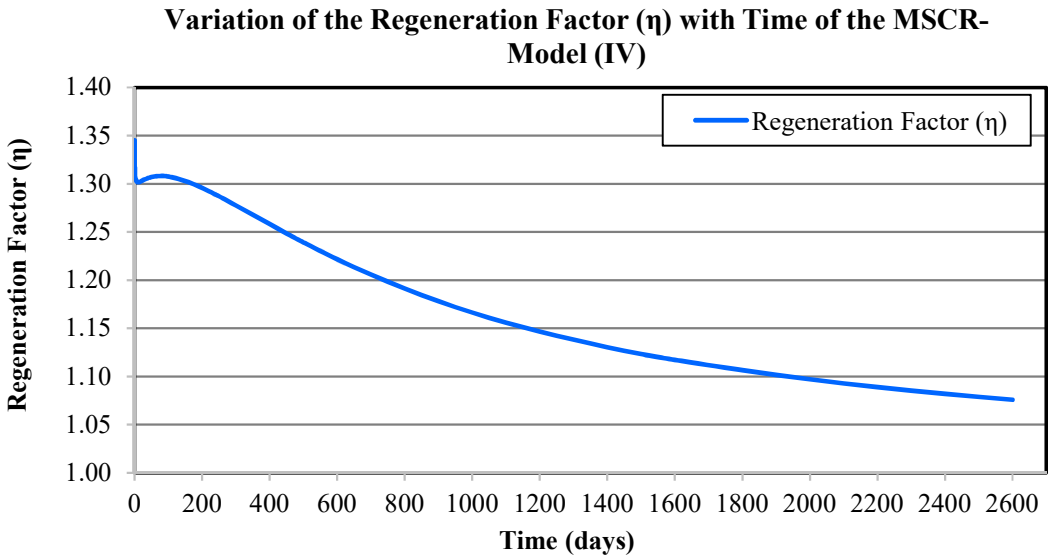

Figure (8-10): Variation of the Regeneration Factor with Time of the MSCR-Model (IV)

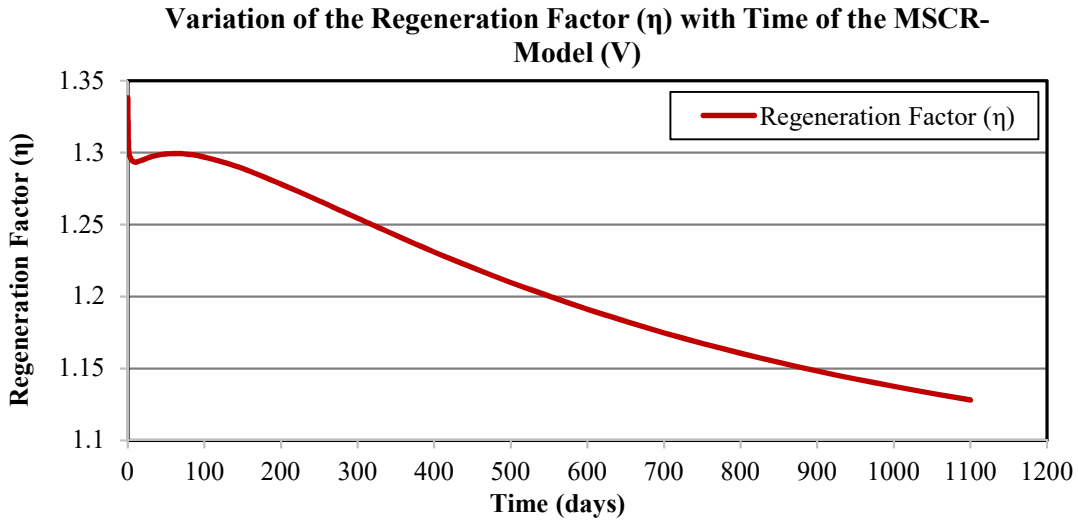

Figure (8-11): Variation of the Regeneration Factor with Time of the MSCR-Model (V)

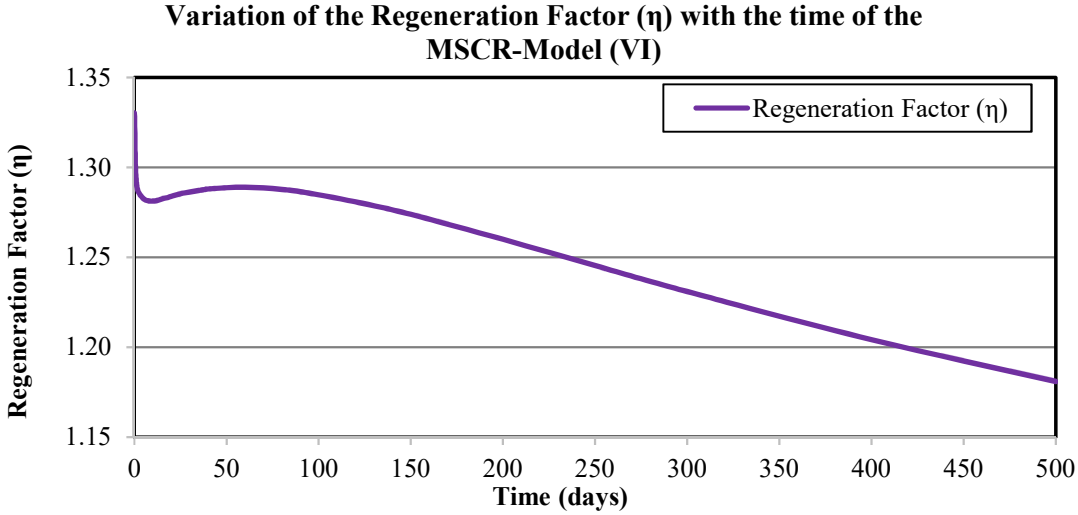

Figure (8-12): Variation of the Regeneration Factor with Time of the MSCR-Model (VI)

Table (8-6) shows the values of regeneration factors of the four models. The values of regeneration factors for the four models are less than 2 so that none of the models are breeder reactors.

Table (8-6): Values of the Regeneration Factors of the MSCR-Models (III, IV, V and VI)

	Starting	Final	Time of the final value (days)*
Model (III)	1.32	1.26	100
Model (IV)	1.35	1.08	2600
Model (V)	1.34	1.13	1060
Model (VI)	1.33	1.20	420

*At time of the reactivity is close to or equal zero

8.3. Neutron Flux Distributions in the MSCR

The average radial and axial fluxes were calculated at 14.13% of the fissile material percentage in MOX fuel for the fast core. Figure (8-13), (8-15), (8-17) and (819) present the average radial fluxes at each radial fuel channel of the thermal and fast cores of Models (III, IV, V and VI), respectively. While Figure (8-14), (8-16), (8-18) and (8-20) present the average axial flux at the central fuel channel of the fast core as calculated at the center of the fuel bundles.

One can see that from the radial flux profiles that:

1) For the four models, the thermal flux is highest in the thermal core while the fast flux is lowest there and conversely for the fast flux. The fast and epithermal fluxes are uniformly flat in the fast core.

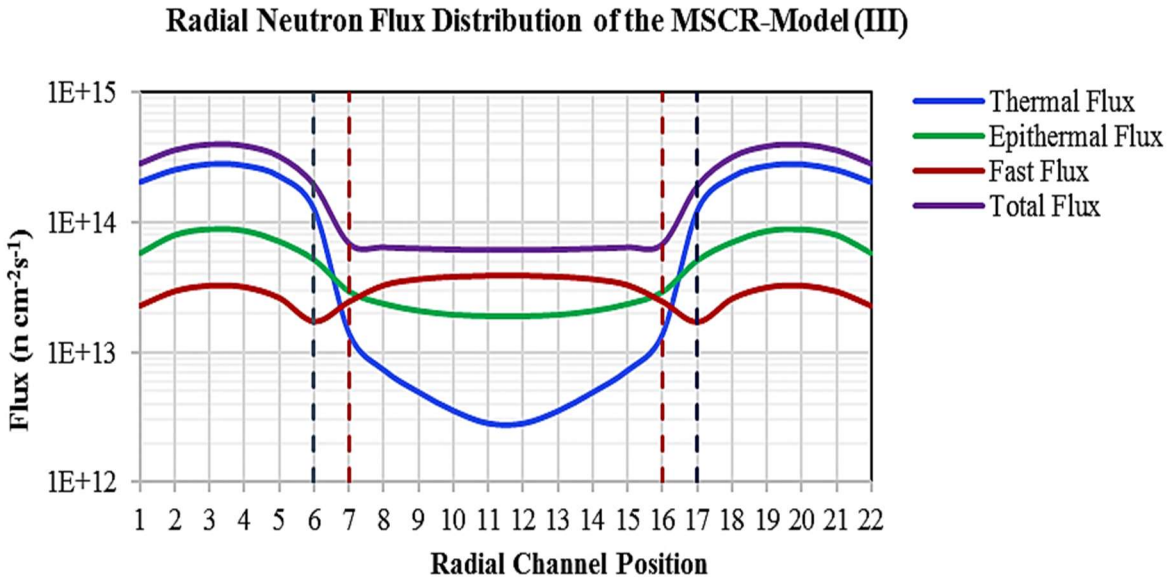

Figure (8-13) Radial Neutron Flux Distribution in the MSCR-Model (III)

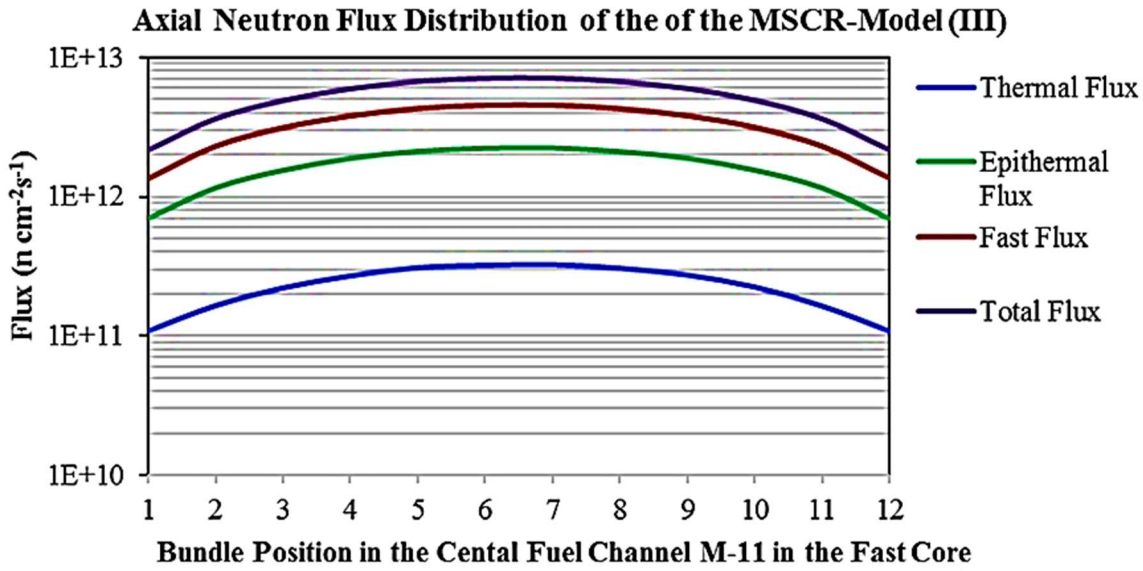

Figure (8-14): Axial Neutron Flux Distributions at the Central Channel of The Fast Core of the MSCR-Model (III)

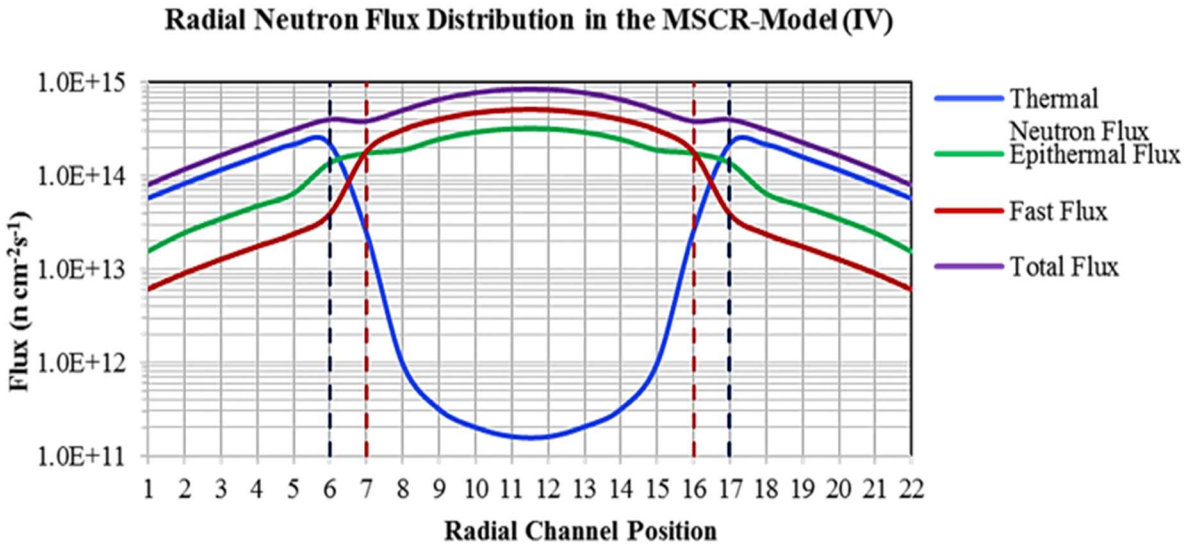

Figure (8-15): Radial Neutron Flux Distribution in the MSCR-Model (IV)

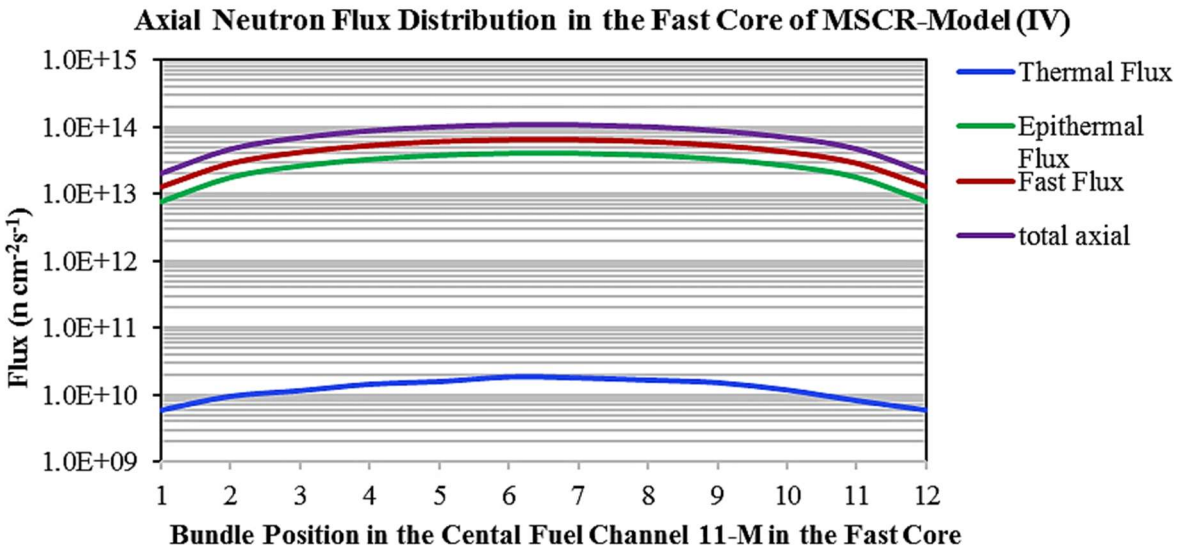

Figure (8-16): Axial Neutron Flux Distributions at the Central Channel of The Fast Core of the MSCR-Model (IV)

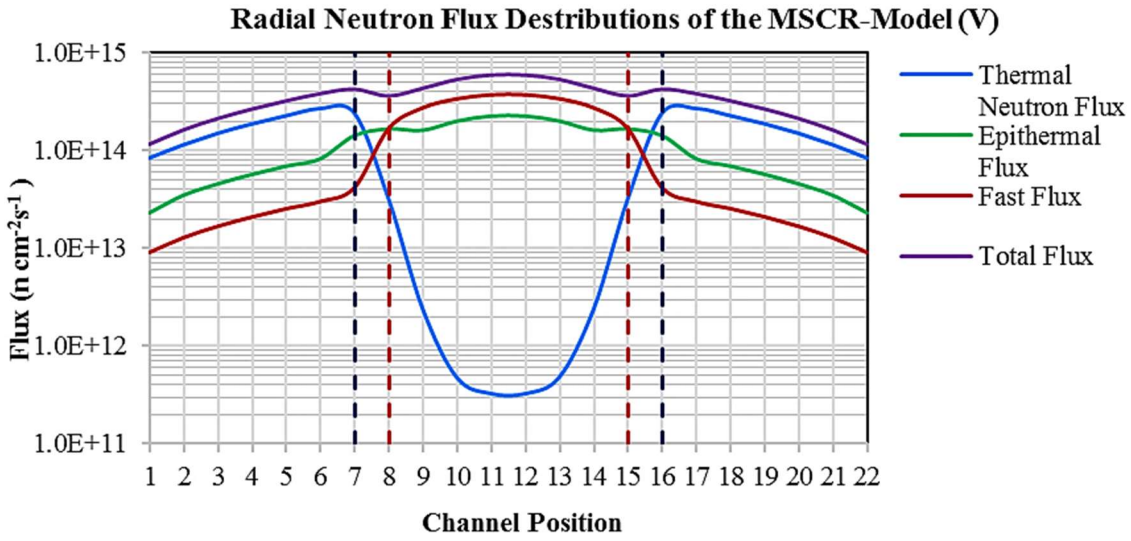

Figure (8-17): Radial Neutron Flux Distribution in the MSCR-Model (V)

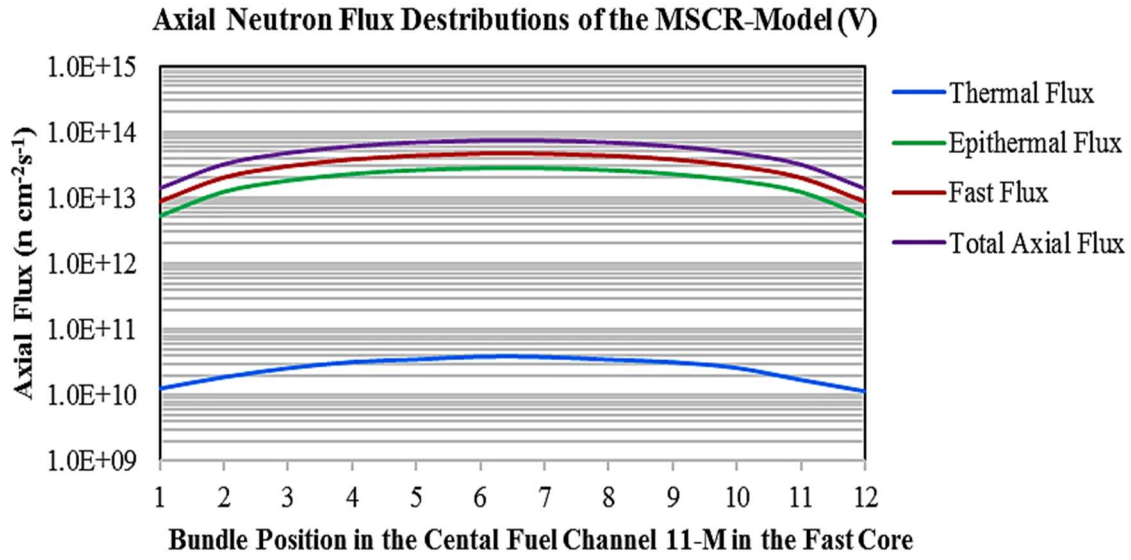

Figure (8-18): Axial Neutron Flux Distributions at the Central Channel of The Fast Core of the MSCR-Model (V)

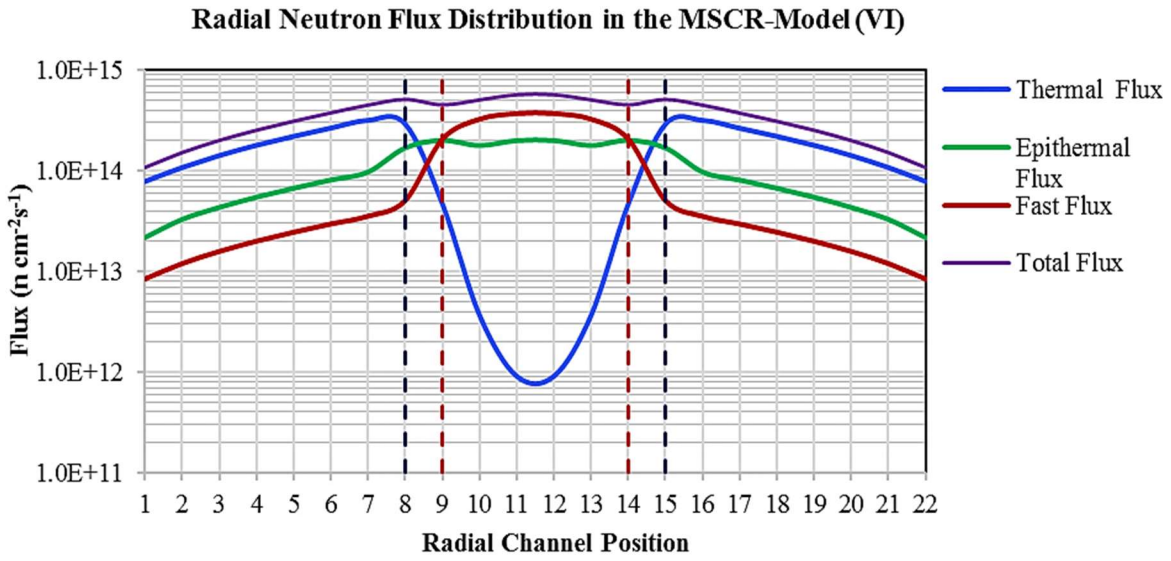

Figure (8-19): Radial Neutron Flux Distribution in the MSCR-Model (VI)

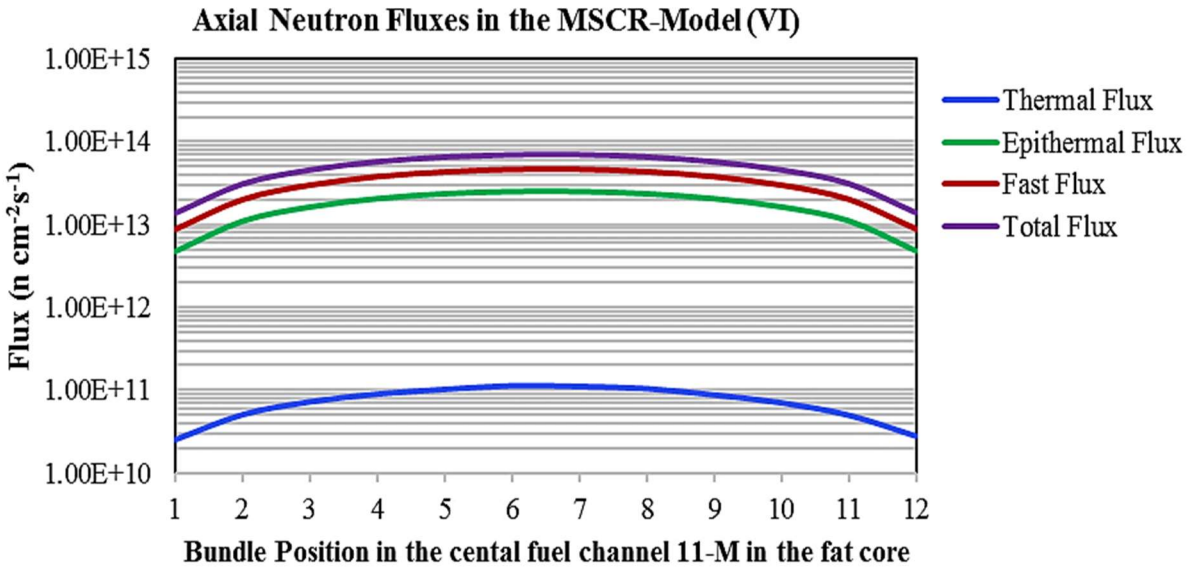

Figure (8-20): Axial Neutron Flux Distributions at the Central Channel of The Fast Core of the MSCR-Model (VI)

2) For Model (III), the epithermal flux in the thermal core is higher than that in the fast core. The behaviour of the three energy group fluxes is like that of Model (I) (section 7.6) where

both have the same lattice pitches for the fast core, whereas the fast core of Model (III) has a larger radius than for Model (I) and more fuel channels.

3) For Models (IV), (V) and (VI), as the number of fuel channels increases, the fast and epithermal fluxes are higher at the center of the fast core. The epithermal flux in the fast core is higher than that in the thermal core.

4) In Model (III), as shown in Figure (8-13), the three energy groups of radial flux profiles are uniformly distributed in each core. In the thermal core, these three fluxes are highest at the center of the core. Where the thermal flux is maximum, the epithermal and fast fluxes are respectively smaller. In the fast core, the fast flux is uniform, and where it is the highest, the epithermal and thermal fluxes are respectively smaller. The epithermal flux is also almost uniform but the thermal flux in the fast core decreases towards the center of the core due to self-shielding in the outer fuel channels.

5) For Models (IV), (V) and (VI) in the fast core, the fast and epithermal flux profiles are uniform and almost flat but, in the thermal core, the maximum value of each flux is shifted closer to the partition wall between the two cores. These fluxes decrease gradually towards the external edge of the thermal core due to the self-shielding by the internal fuel channels in the thermal core that are close to the partition walls.

6) For the axial flux in each model, the sum of all points at a certain energy bin is equal to the central point at channel M-11 for the corresponding radial flux.

8.4. Power Density Distribution

To show the depletion of the fuel as located in the fast and thermal cores, the power density distribution of the Models (III), (IV), (V), and (VI) are shown in Figures (8-21), (8-22), (8-25) to (8-28), (8-30) to (8-33) and (8-36) to (8-39).

1) Power Density Distribution and Percentage of the Power Density Produced from each Core of Model (III)

For Model (III), Figures (8-21) and (8-22) present the power density distributions of the freshly-fuelled reactor at day zero, and after 100 days (at k_{eff}=0.995, just below criticality) of

operation, respectively. The power density units in the two figures are in W cm^{-3}. From these two figures:

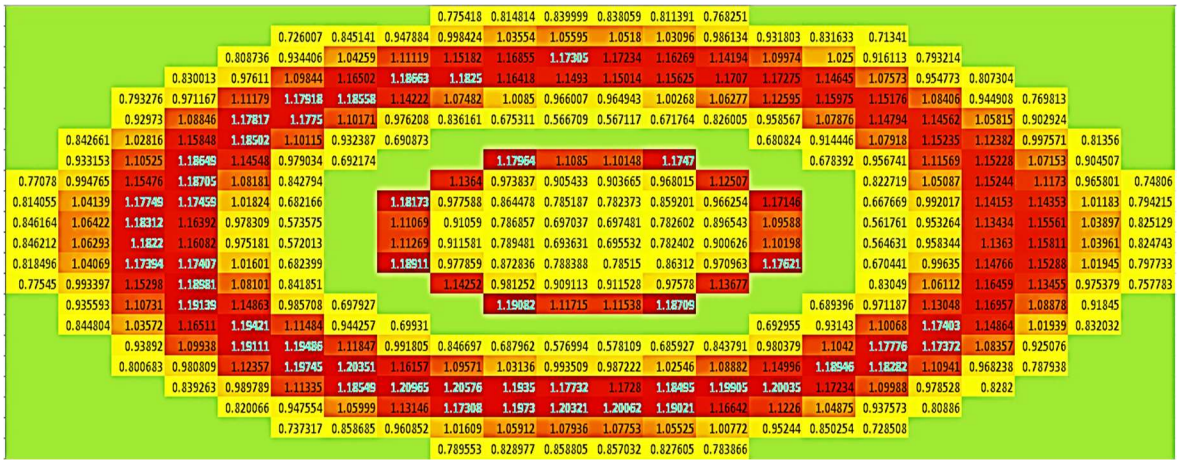

Figure (8-21): Power Density Distribution for the Freshly Fueled Core of the MSCR-Model (III) (The power density units are in W cm^{-3})

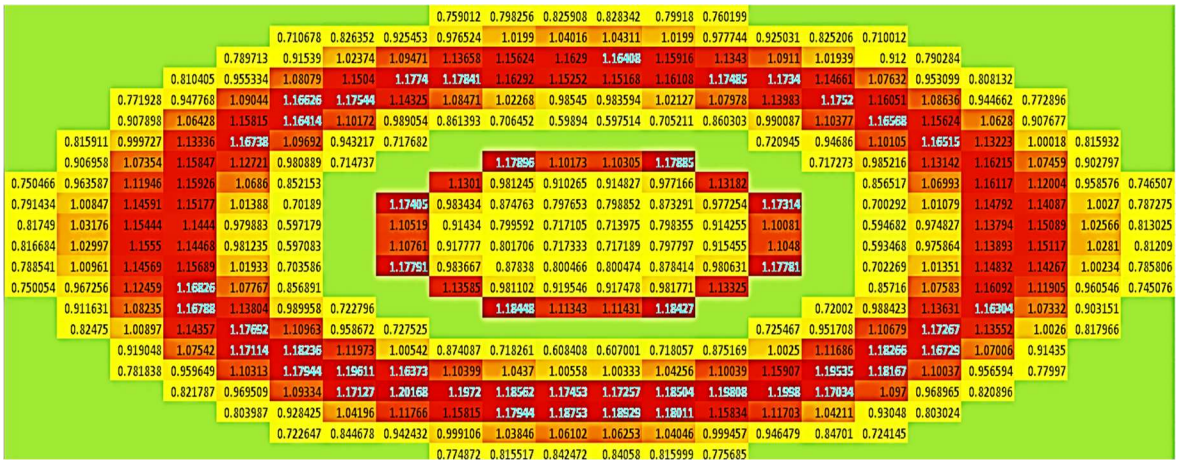

Figure (8-22): Power Density Distribution After 100 days of the MSCR Model (III) (The power density units are in W cm^{-3})

1) In the thermal core, the higher and partial flattening of the thermal flux distribution at the center of the thermal core produces a uniform high power density at its center. The channels closer to the fast core have a lower power density because of the low thermal neutron flux at these channel locations where the volume of a moderator is not enough to completely thermalize the limited number of fast neutrons that have diffused from the fast core.

2) The power density in the fast core is high for the outer ring fuel channels because of the leakage of thermal neutrons from the thermal region that interacts with the high enrichment

fuel in these fuel channels. The power density decreases towards the center of the fast core because of the self-shielding caused by the outer fuel channels that prevent most of the thermal neutrons from reaching the center of the fast core, which limits the fission rate in the fast core.

3) The highlighted numbers in Figure (8-21) and Figure (8-22) represent the highest 10% of the channel power density. The uniform distributions of these channels around the core after 100 days of burnup indicate the uniformity of the burnup profile through this period in the entire reactor. In other words, there is no flux tilting during this period. The power density distribution is of the Models (III) for the entire burnup steps are presented in the Appendix (G)

4) Figure (8-23) and (8-24) show that most of the power density is produced within the thermal core and the percentage of the power density produced from the thermal and fast core is normalized to the total power density produced in the entire reactor, respectively.

5) For the freshly fuelled reactor (day zero), the fast neutron core produces around 14.8% of the power density while the thermal core produces 85.2% of the total reactor power density.

6) After 100 days, when the reactor is just about to become subcritical, the fast core produces around 14.9% of the reactor power density, while the thermal core produces 85.1%. There is a slight increase in the percentage of power density produced in the fast core through 100 days with a higher burnup of fuel in the thermal core after this period.

7) During the first eight days of burnup, Figure (8-23) shows that the power density percentages produced by the thermal core decrease due to the accumulation of the neutron absorbing fission products in the thermal core; this decrease is correlated with the reactivity curve in Figure (8-5). After that, it starts to increase to a peak value which is equivalent to the plutonium peak. In the same period for the first eight days, the power density percentage produced by the fast core increases due to the burnup of the plutonium-rich MOX fuel where there is no or still little xenon poisoning in the fast reactor.

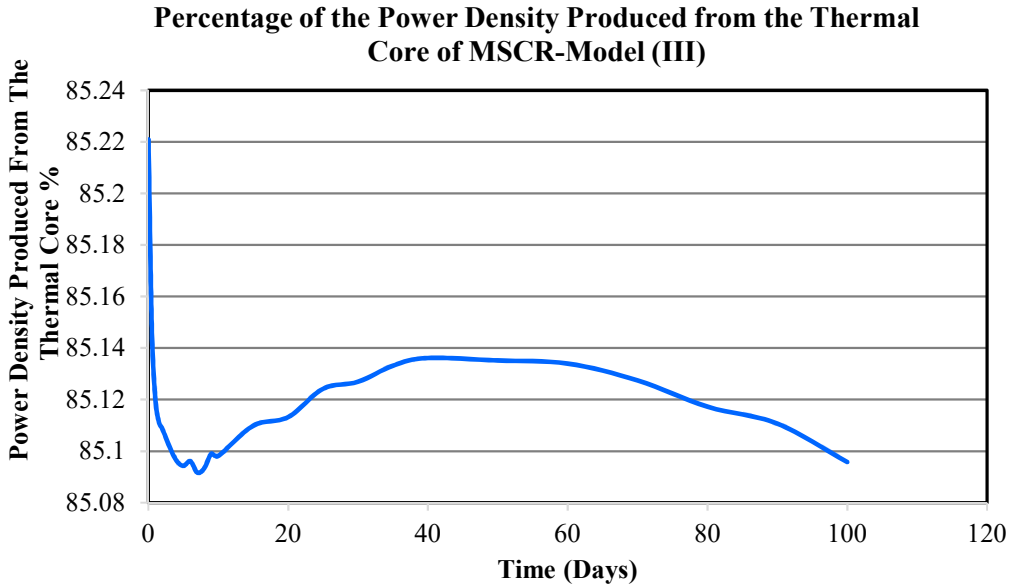

Figure (8-23): Relative Power Density Produced by the Thermal Core for the MSCR-Model (III).

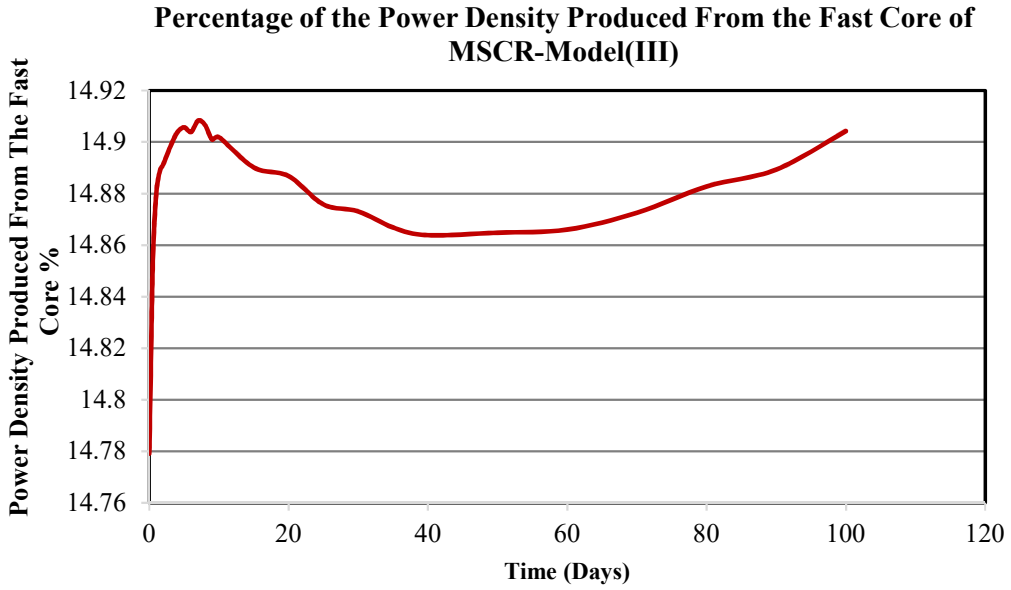

Figure (8-24): Relative Power Density Produced by the Fast Core for the MSCR-Model (III).

After 80 days, the percentage power density of the thermal core decreases gradually due to depletion of the fuel and the accumulation of fission products. While the fast core is still rich with fissile material, the percentage of power density produced from the fast core increases slightly as shown in Figure (8-24) due to a small fast flux.

2) *Power Density Distribution and Percentage of the Power Density Produced from each Core of Model (IV)*

The power density distributions of the Model (IV) for the freshly-fuelled reactor at day zero of the thermal and fast core are presented in Figure (8-25) and Figure (8-26), while the power density distributions of the thermal and fast cores after 2600 days (at k_{eff}=1.004 just before subcriticality are presented in Figure (8-27) and Figure (8-28) respectively. The power density units in the two figures are again in W cm^{-3}.

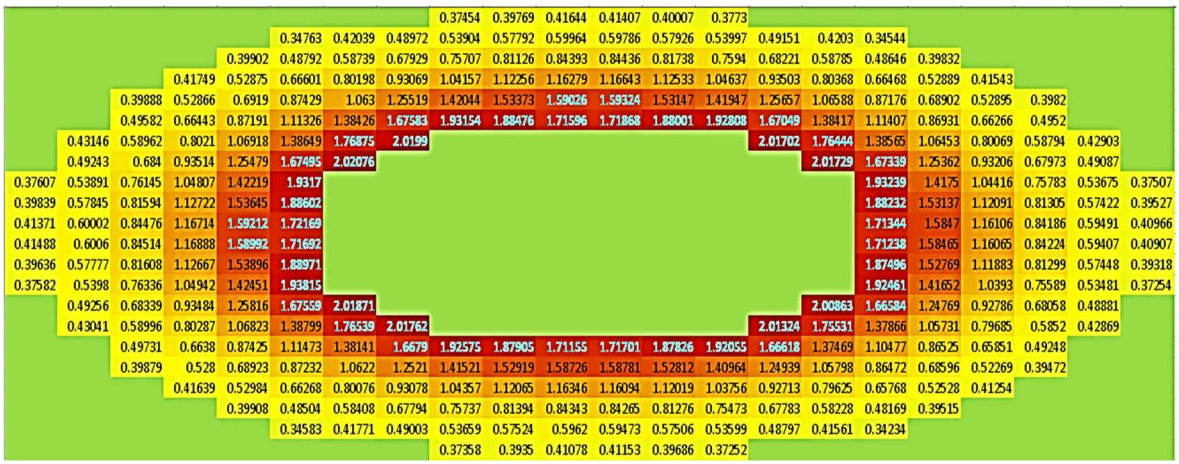

Figure (8-25): Power Density Distribution in the Thermal Core for the Freshly Fuelled Core of MSCR-Model (IV) (The power density units are in W cm^{-3})

Figure (8-26): Power Density Distribution in the Fast Core for the Freshly Fuelled Core of MSCR-Model (IV) (The power density units are in W cm^{-3})

Figure (8-27): Power Density Distribution in the Thermal Core after 2600 Days for the MSCR- Model (IV) (The power density units are in W cm^{-3})

Figure (8-28): Power Density Distribution in the Fast Core after 2600 Days for the MSCR- Model (IV) (The power density units are in W cm^{-3})

1) For the thermal core, Figure (8-25) shows a higher thermal flux distribution near the inner edge of the thermal core (beyond channels 6 and 17) that produces a higher power density at these channels. Towards the center of the thermal core, the power density decreases because of a decrease in the thermal flux as shown in the radial flux distribution of Figure (8-15). The fluxes increase in the fast and epithermal energy regions with diffusion from the fast to the thermal core. This diffusion causes an increase in the three energy-group fluxes at the internal edge of the thermal core and consequently the power density at these locations.

2) From Figure (8-26), the power density in the fast core is high for the fuel channels in the outer ring close to the edge of the fast core due to leakage of thermal neutrons from the thermal region that interact with the high enriched fuel in the fast region.

3) After the outer ring towards the center of the fast core, the power density decreases because of self-shielding in the outer fuel channels that prevents thermal neutrons from reaching the center of the fast core.

4) At the center of the fast core, with a radius equivalent to three lattice pitch widths, the power density increases due to a high value of the fast flux that causes an increase in the fast fission rate.

5) Figure (8-27) and Figure (8-28) show the power density distributions of the thermal and fast cores of Model (IV) after 2600 days. In Figure (8-27), for the thermal core, the average power density distribution decreases due to a depletion of fuel that is noticed in the color scheme. At the same time, the power density increases from the fast core.

6) The highlighted numbers in the Figure (8-25), Figure (8-26), Figure (8-27), and Figure (8-28), represent the highest 10% of the channel power density. The uniform distributions of these channels around the reactor core in the first day and after 2600 days of burnup indicate the consistency of burnup throughout this period for the entire reactor.

7) Figure (8-32) shows that most of the power density is produced within the thermal core. The percentages of the power density produced from the thermal and fast core are normalized to the total power density generated in the entire reactor.

8) For the freshly fuelled reactor (day zero), the thermal core produces 54% of the total reactor power density while the fast core produces around 46% of the power density.

9) At the first ten days of burnup, Figure (8-32) shows that the power density percentages produced for the thermal core decrease due to a build-up of neutron poisons in the thermal core. This decrease is correlated with the reactivity curve in Figure (8-6). It increases to a peak value for the plutonium peak. In the same period for the first ten days, the power density percentage produced from the fast core increases to a higher value due to burnup of the enriched fuel, where there is a little xenon poisoning effect in the fast reactor due to its

small cross section for the fast neutron spectrum. The only xenon effect in the fast core is due to thermal fission in the outer fuel channel ring by the thermal neutron that have diffused from the thermal core to the fast core.

10) After about 100 days, the percentage of power density in the thermal core decreases gradually due to depletion of the fuel and accumulation of fission products. Since the fast core is still rich with fissile material, the fission products have a relatively small effect on the fast neutron flux.

11) In 600 days, the powers density produced from both cores are comparable.

12) After 1800 days, the percentage of power density produced form each core is tend to be constant with the thermal core produces 46.5%, while the fast core produces around 53.5% of the reactor power density.

13) In comparison with Model (III), the relative power density produced from the fast core of Model (IV) is greater than that produced in the fast core of Model (III). The percentage of the fast core contribution to the total reactor power density becomes more than 50% when the burnup time increase due to the high amount in the fuel in the fast core.

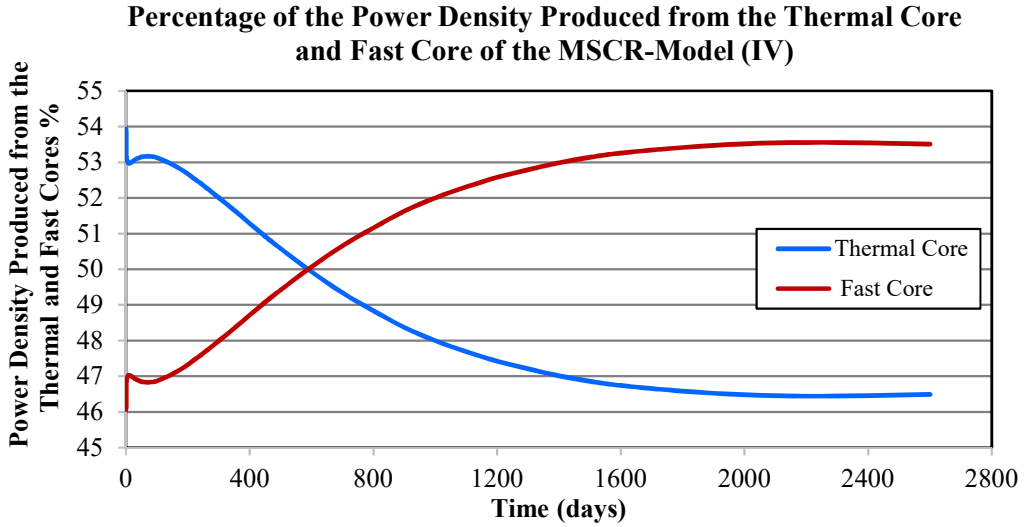

Figure (8-29): Relative Power Density Produced from the Thermal Core and Fast Core for the MSCR-Model (IV).

14) With a high percentage of fissile content in the fast core, the depletion of fissile nuclei is very small because the fast neutron flux is small.

3) Power Density Distribution and Percentage of the Power Density Produced from each Core of Model (V)

Figure (8-30) and Figure (8-31) show the power density distributions for the freshly-fuelled reactor at day zero of the thermal and fast cores of the Mode (V). While Figure (8-32) and Figure (8-33) present the power density distributions of the thermal and fast cores after 1060 days (at k_{eff}=1.003, just before the reactor becomes subcritical). The power density units in the two figures are in W cm^{-3}.

Figure (8-30): Power Density Distribution for the Freshly Fueled Thermal Core of the MSCR-Model (V) (The power density units are in W cm^{-3})

Figure (8-31): Power Density Distribution in the Fast Core for the Freshly Fueled of the MSCR-Model (V)(The power density units are in W cm^{-3})

Figure (8-32): Power Density Distribution in the Thermal Core after 1060 Days of the MSCR Model (V) (The power density units are in W cm^{-3})

Figure (8-33): Power Density Distribution in the Fast Core after 1060 days of the MSCR Model (V) (The power density units are in W cm-3)

Since the radial flux profiles of the three energy groups of the Model (IV) are similar to those of Model (IV) (in shape, but not in value), the power density distribution of Model (V) is similar to that of Model (IV). The number of fuel channels of the thermal core increases by 28 fuel channels, thus increasing the power density percentage produced from the thermal core of Model (V). The power density produced from the fast core increases with burnup. It is further shown that:

1) Figure (8-34) and Figure (8-35) show the percentage of the power density produced from both the thermal core and the fast core as normalized to the total power density generated in the entire reactor, respectively;

2) For the freshly fuelled reactor, the thermal core produces 68.5% of the total reactor power density while the fast core produces around 31.5% of the power density;

3) In the first 10 days of burnup, Figure (8-35) shows that the power density percentages generated for the thermal core decrease due to a build-up of neutron absorbing fission products in the thermal core. This decrease is correlated with the reactivity curve in Figure (8-7). After that, it starts to increase to a peak value which is equivalent to the plutonium peak. During the same period, the power density percentage produced from the fast core increases due to the fuel burnup while the fission products produced in the fast core are limited and less than that produced in the thermal core. Thermal fissions that takes place in the fast core are due to a leakage of thermal neutrons that takes place mainly in the outer ring of the fast core.

4) After about 100 days, the percentage power density of the thermal core decreases gradually due to the depletion of the fuel and the accumulation of fission products. While the fast core is still rich with fissile material, fission products have only a small effect on the fast neutron flux so the percentage of power density produced from the fast core increases.

5) After 1060 days, before the reactor becomes subcritical, the thermal core produces ~ 62.5% while the fast core produces around ~37.5% of the reactor power density. There is an increase in the percentage of power density generated in the fast core with a higher burnup of fuel in the thermal core after this period. The power density produced from the fast core of Model (V) is less than that for the fast core of the MSCR-Model (IV) reactor.

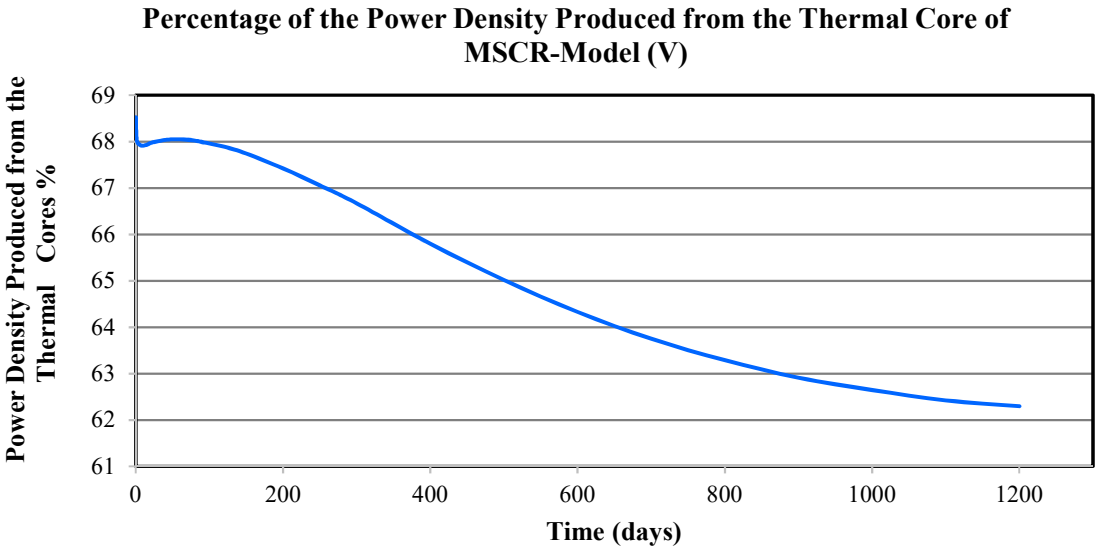

Figure (8-34): Relative Power Density Produced from the Thermal Core for the MSCR-Model (V).

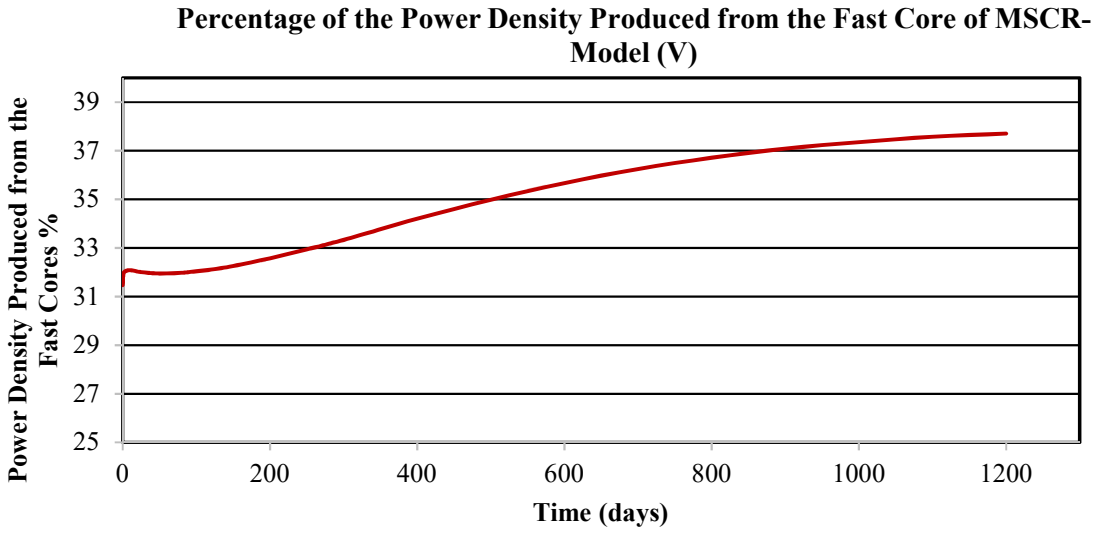

Figure (8-35): Relative Power Density Produced from the Fast Core for the MSCR-Model (V).

4) *Power Distribution and Percentage of the Power Density Produced from each Core of Model (VI)*

The power distributions of the Model (VI) reactor for the freshly-fuelled reactor at day zero of the thermal and fast core are presented in Figure (8-36) and Figure (8-37), while the power distributions of the thermal and fast cores after 2600 days (at k_{eff}=1.003, just before subcriticality) are presented in Figure (8-38) and Figure (8-39) respectively. The power density units in the two figures are in W cm^{-3}.

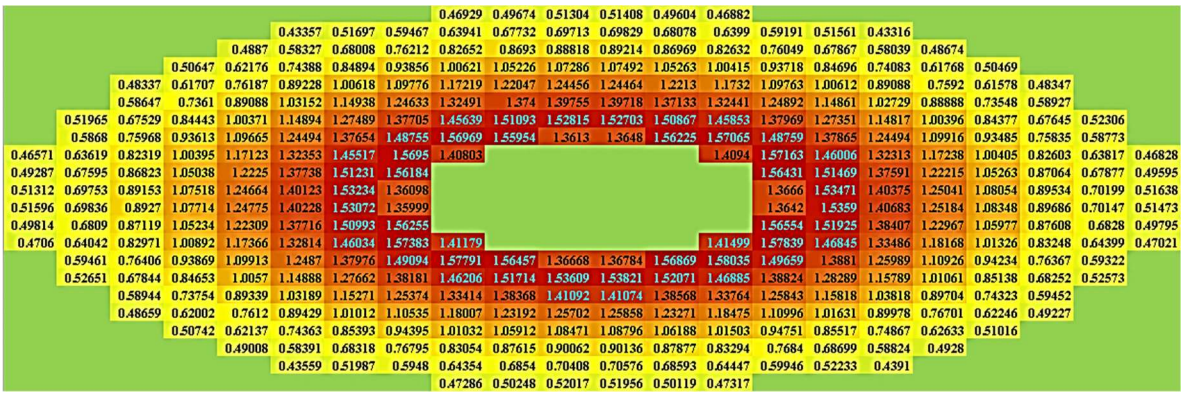

Figure (8-36): Power Density Distribution for the Freshly Fueled Thermal Core of the MSCR-Model (VI) (The power density units are in W cm^{-3})

Figure (8-37): Power Density Distribution for the Freshly Fueled Fast Core of the MSCR-Model (VI) (The power density units are in W cm^{-3})

Figure (8-38): Power Density Distribution for the Thermal core after 420 days of the MSCR Model (VI) (The power density units are in W cm^{-3})

Figure (8-39): Power Density Distribution for the Fast core after 420 days of the MSCR Model (VI) (The power density units are in W cm-3)

1) The radial flux profiles of the three energy groups of Models (VI) are like that of Models (IV) and (V). The number of fuel channels of the thermal core increases by 28 fuel channels from Model (V) and by 56 fuel channels from Model (IV), which increases the power density percentage produced by the thermal core of Model (VI). The power density percentage produced from the fast core of the Model (VI) is decreased because of a decrease in the number of fuel channels.

2) Figure (8-40) and Figure (8-41) show the percentage of the power density produced from the both thermal core and fast core as normalized to the total power density generated in the entire reactor.

3) For the freshly fuelled reactor (day zero), the thermal core produces 81.8% of the total reactor power density while the fast core produces around 18.2% of the power density.

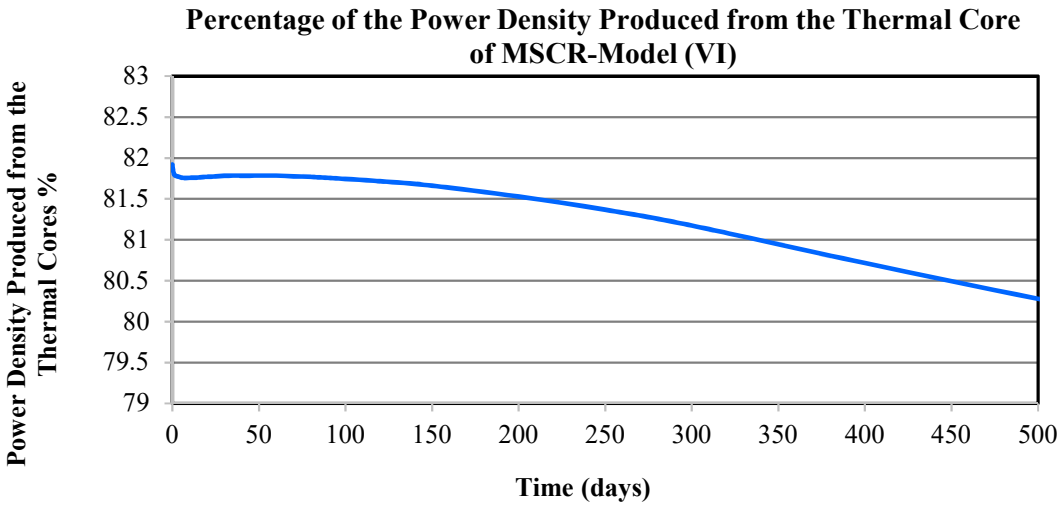

Figure (8-40): Relative Power Density Produced by the Thermal Core for the MSCR-Model (VI).

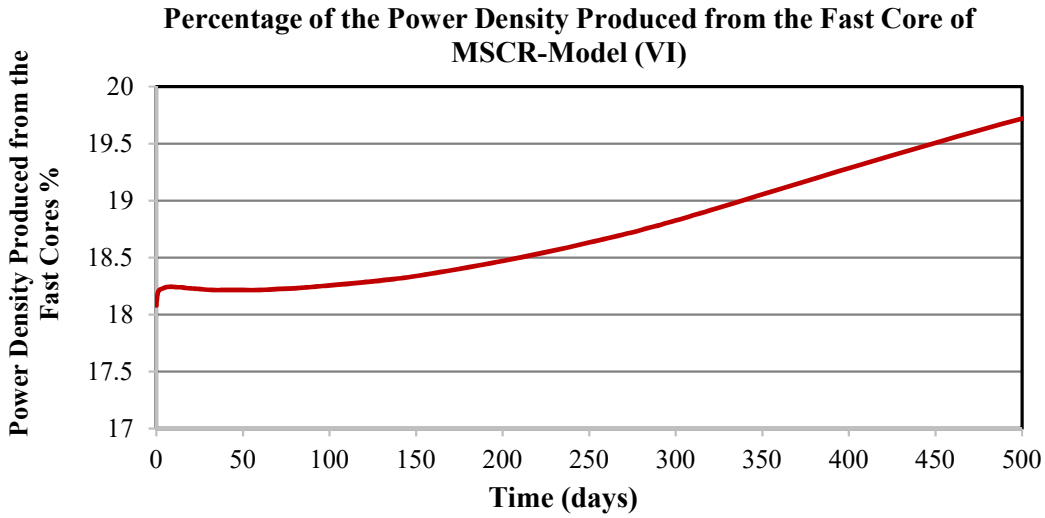

Figure (8-41): Relative Power Density Produced by the Fast Core for the MSCR-Model (VI).

4) For the first 10 days of burnup, Figure (8-40) shows a decrease of the power density percentages produced by the thermal core due to a neutron poison build-up as correlated with the reactivity curve in Figure (8-8). Similarly, a peak value is reached. During the same period, the power density percentage produced from in the fast core increases due to the burnup of enriched fuel where there is no or little xenon poisoning in the fast reactor.

Moreover, the percentage ratio from the fast core remains constant before it increases gradually again.

5) After about 50 days, the percentage of the power density of the thermal core decreases gradually due to the depletion of the fuel and accumulation of fission products. While the fast core is still rich with fissile material, the fission products have a small effect on the fast neutron flux resulting in an increase of the percentage of power density produced by the fast core.

6) After 420 days, just before subcriticality, the thermal core produces ~ 80.3%, while the fast core produces around ~19.7% of the reactor power density. There is a slight increase in the percentage of power density produced in the fast core at higher burnup of the fuel. The power density produced from the fast core of Model (VI) is less than that for MSCR-Models (IV) and (V).

8.5. Form Factor.

Figures (8-42), (8-43), (8-44) and (8-45) show the form factors of the MSCR -Models (III), (IV), (V) and (VI). The values of the form factors of the four models are simulated without any control devices such as adjuster, control and shutdown rods and liquid zone controllers.

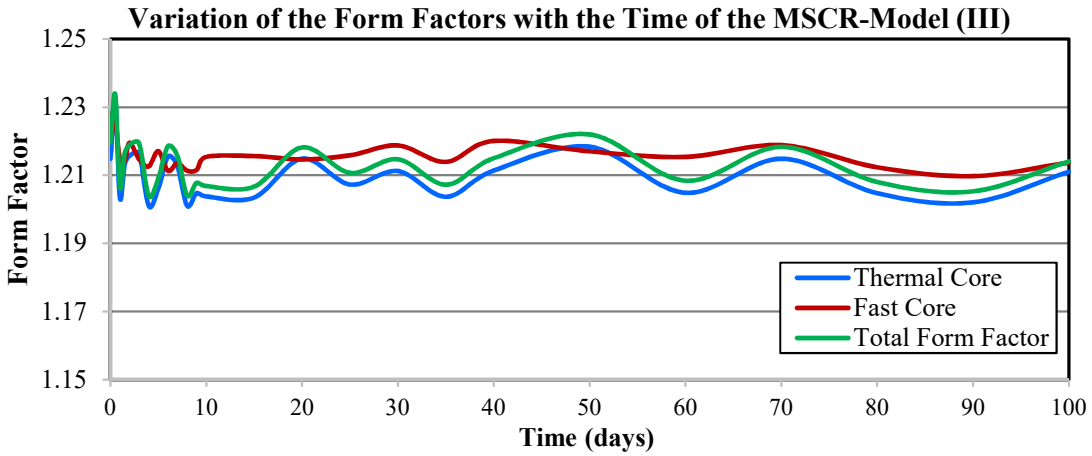

Figure (8-42): Total Channel Form Factors for both Fast and Thermal Cores, and the Entire MSCR-Model (III).

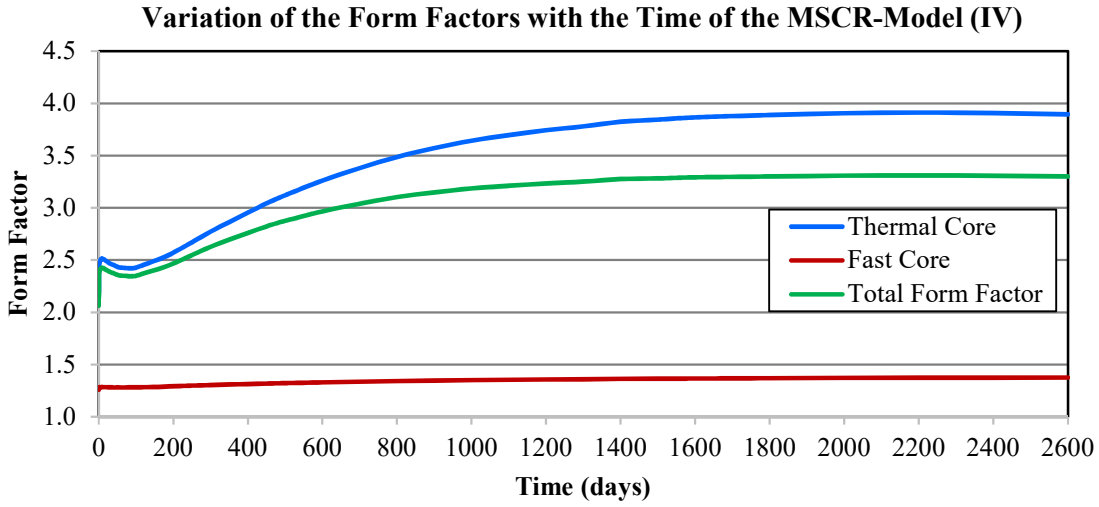

Figure (8-43): Total Channel Form Factors for both Fast and Thermal Cores and for the Entire MSCR-Model (IV).

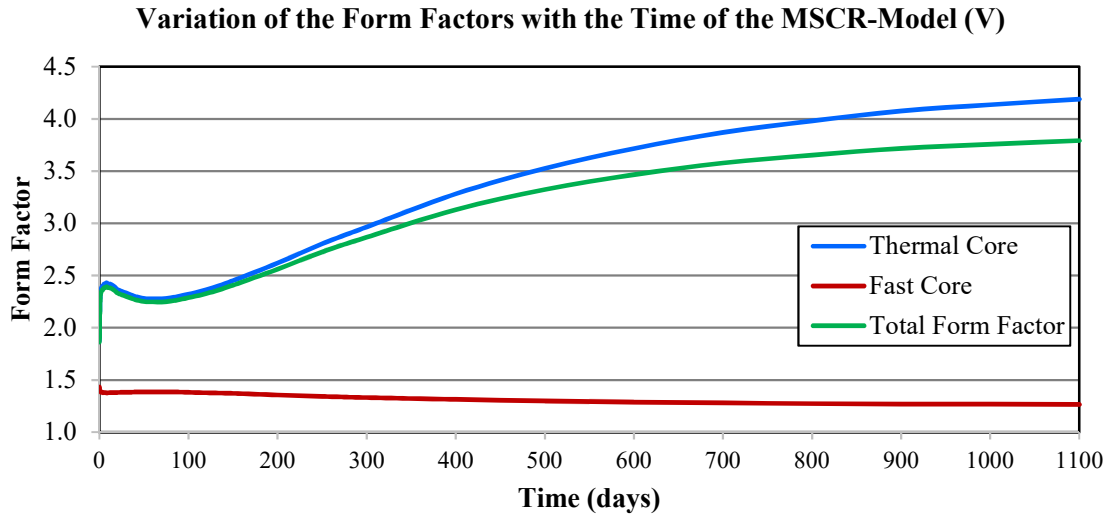

Figure (8-44): Total Channel Form Factors for both Fast and Thermal Cores and the Entire MSCR-Model (V).

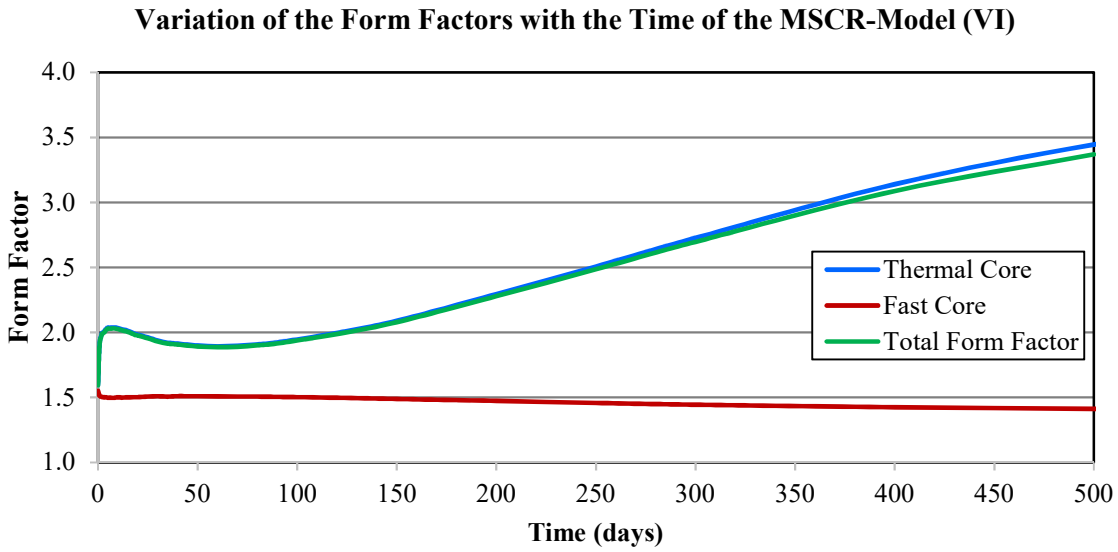

Figure (8-45): Total Channel Form Factors for both Fast and Thermal Cores and for the Entire MSCR-Model (VI).

Table (8-7) shows the form factor of the four Models (III), (IV), (V) and (VI) up to the final day just before subcriticality.

Table (8-7): Comparison Between the First and Final Form Factor of the Four MSCR-Models

	First Day			Last Day		
Model	Thermal Core	Fast Core	Total	Thermal Core	Fast Core	Total
III	1.23	1.22	1.23	1.21	1.21	1.21
IV	2.0	1.28	2.1	3.9	1.23	3.3
V	1.9	1.38	1.8	4.18	1.27	3.8
VI	1.6	1.5	1.55	3.45	1.45	3.4

One can see that:

1) In the Model (III), the form factor of the thermal core is between 1.23 and 1.20. There are fluctuations in the form factor for both cores. Both values are acceptable in comparison to the form factor of a traditional CANDU reactor. The total form factor for the entire reactor fluctuates between 1.23 and 1.20. The behaviour of the total form factor is like that of a thermal reactor core because most of the power is produced in the thermal core.

2) For the Models (IV), (V) and (VI), in the thermal core, the form factor starts at small values of 2.0, 1.9 and 1.6, respectively. Then it increases rapidly due to a decrease in the average power of the thermal core because of the production of saturating fission products

(particularly xenon and samarium). Later, with plutonium production in the thermal core, the average power increases resulting in a slight decrease in the form factor. The size and the time of the decrease in the form factor of each model depend on the size and position of the plutonium peak of that model. In the three models, the decreases are followed by a steady increase in the form factor. With increased irradiation, the form factor tends to a constant value as shown for Model (IV) in Figure (8-43) on the last day of burnup.

3) In the fast cores of Models (IV), (V) and (VI), the form factors start out at values of 1.28, 1.38 and 1.5, and reach values of 1.23, 1.27 and 1.45 on the last day, respectively. It is obvious that the form factor for the fast core is almost constant at a lower value than that for the thermal core.

4) The total form factor of each model is calculated by dividing the maximum channel power by the average power of the entire core. For Models (IV), (V) and (VI), the total form factor has the same behaviour because most of the power is produced from the thermal core. The maximum channel power in these three models is usually at the thermal core. Moreover, the average power of the entire reactor decreases that causes an increase in the total form factors of the three models. The total form factor is higher than the acceptable safety value for a traditional CANDU 6 reactor because there are no control rods in the models.

In conclusion, the distribution of the power density and the form factor depend mainly on the flux profiles at each energy bin for each model. As the number of fuel channels in the fast core increases with decreasing lattice pitch, there is an increase of the number of fast and epithermal neutrons that diffuse from the fast core to the channels beside to the partition walls in the thermal core (e.g., channels 6 and 15 of Model (IV)). The high moderator-to-fuel ratio in these channels in the thermal core cause:1) An increase in the thermal flux beside the partition walls with an increase in the thermal fission rate there and power density 2) An increase in the epithermal fluxes at these channels which increases the rate of plutonium production and consequently the power density. 3) An increase in the fast fission rate due to an increase of diffused fast neutrons. For these three reasons, the maximum fuel channel power is located close to partition wall in the thermal core for the three MSCR-Models (IV), (V) and (VI). With longer irradiation times, the average power of the entire reactor is decreasing at the same time the maximum power in channels is increasing,

resulting in an increase in the total form factor. The power density distribution is of the Models (IV) for the entire burnup steps are presented in the Appendix (G).

Future work is needed to: 1) Assign the best position of the control rods and other control devices; 2) modify the lattice pitch of the fast core and the reflector materials in the fast core to decrease the diffusion of fast neutrons from the fast core to the thermal core (i.e., to move the maximum values of the three energy group fluxes from the internal edge of the thermal core to the center similar to that seen in Model (III)).

8.6. Calculation of the Burnup.

1) Variation of the Multiplication Factor versus the Burnup

The burnup and the multiplication factor are calculated for a burnup period for Models (III), (IV), (V) and (VI). The multiplication factors of each model versus the burnup are presented in Figure (8-46), Figure (8-47), Figure (8-48), and, Figure (8-49) respectively. The behaviour of the curves for the multiplication factor and the burnup are like those for the reactivity curves shown in Section 8.2.

The multiplication factor first decreases sharply because of a build-up of saturating fission products (Xe and Sm). With increasing burnup, the multiplication factor increases due to the plutonium peak followed by a steady decrease with burnup.

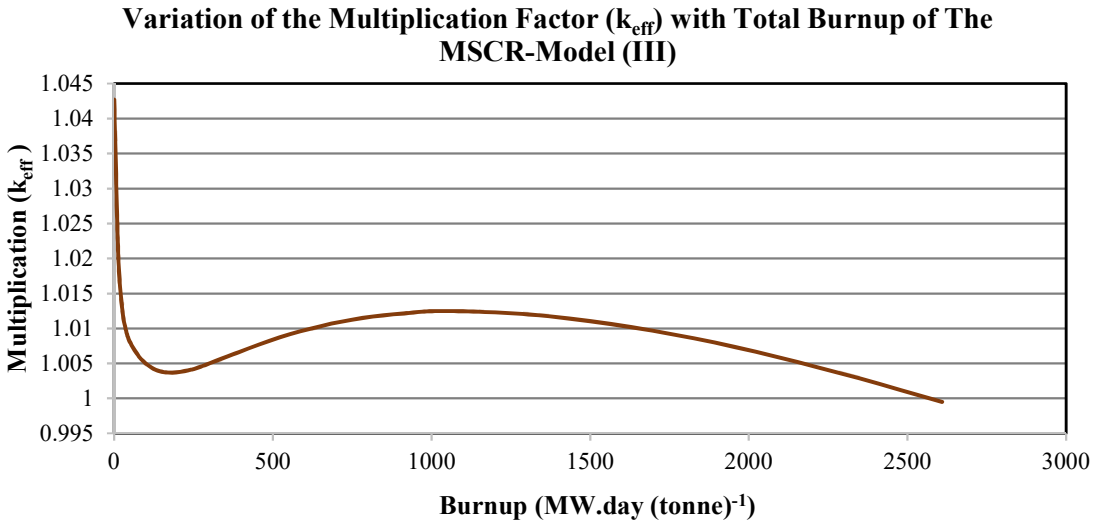

Figure (8-46): Variation of the Multiplication Factor with the Total Burnup for the MSCR-Model (III)

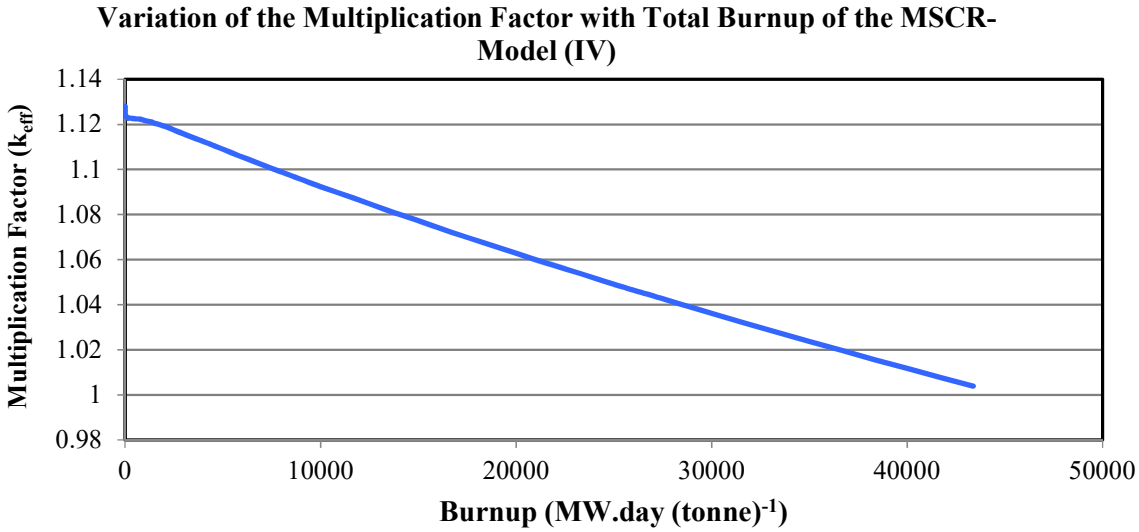

Figure (8-47): Variation of the Multiplication Factor with the Total Burnup for the MSCR-Model (IV).

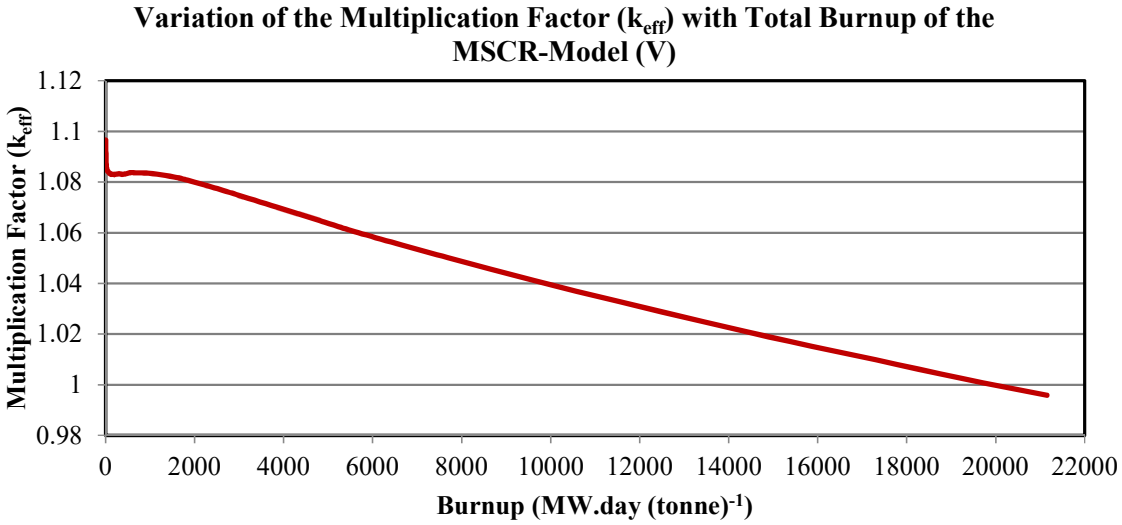

Figure (8-48): Variation of the Multiplication Factor with the Total Burnup for the MSCR-Model (V).

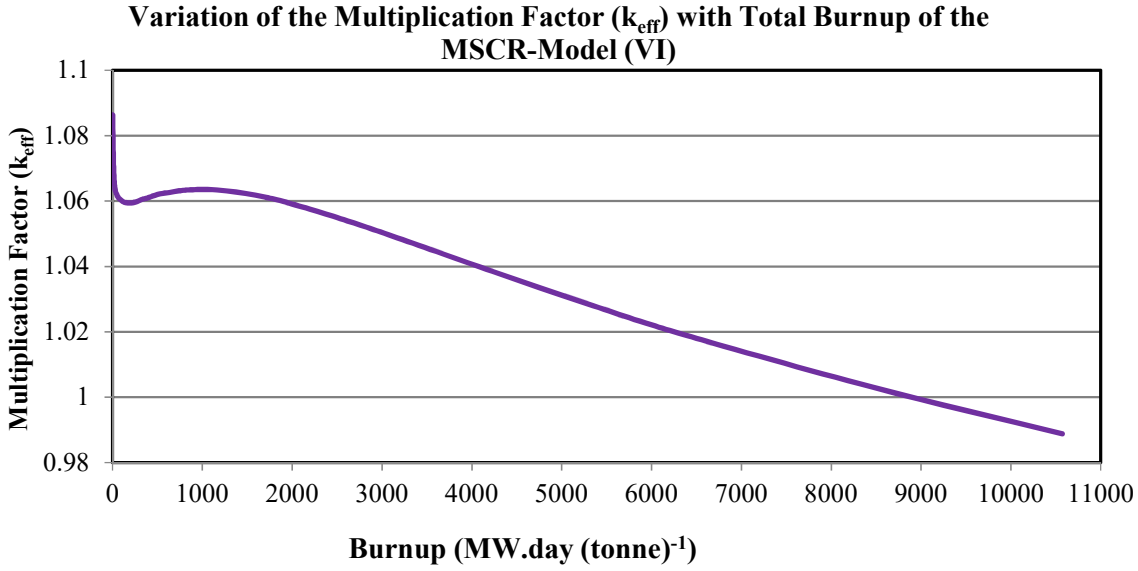

Figure (8-49): Variation of the Multiplication Factor with the Total Burnup for the MSCR-Model (VI).

2) *Variation of the Burnup versus Time*

Figure (8-50), (8-51), (8-52) and (8-53), show the variation of burnup of the thermal core (blue line), fast core (red line) and total MSCR-Models (III, IV, V, VI) (green line) with time. All the burnups are normalized to the total fuel mass for each reactor model. For all these, the time dependence of the burnup is essentially linear.

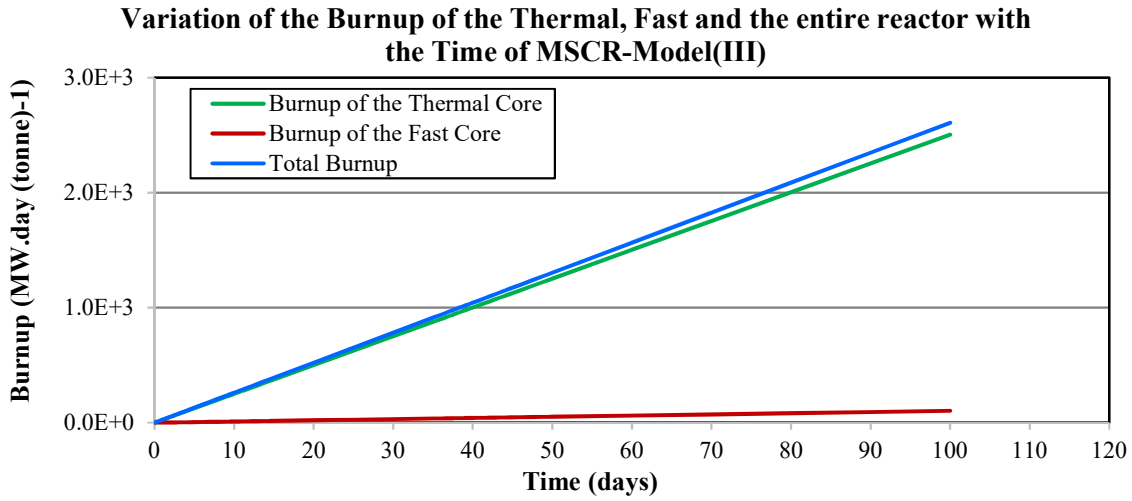

Figure (8-50): Variation of the Burnup of Thermal Core, Fast Core and Entire MSCR-Model (III) with Time.

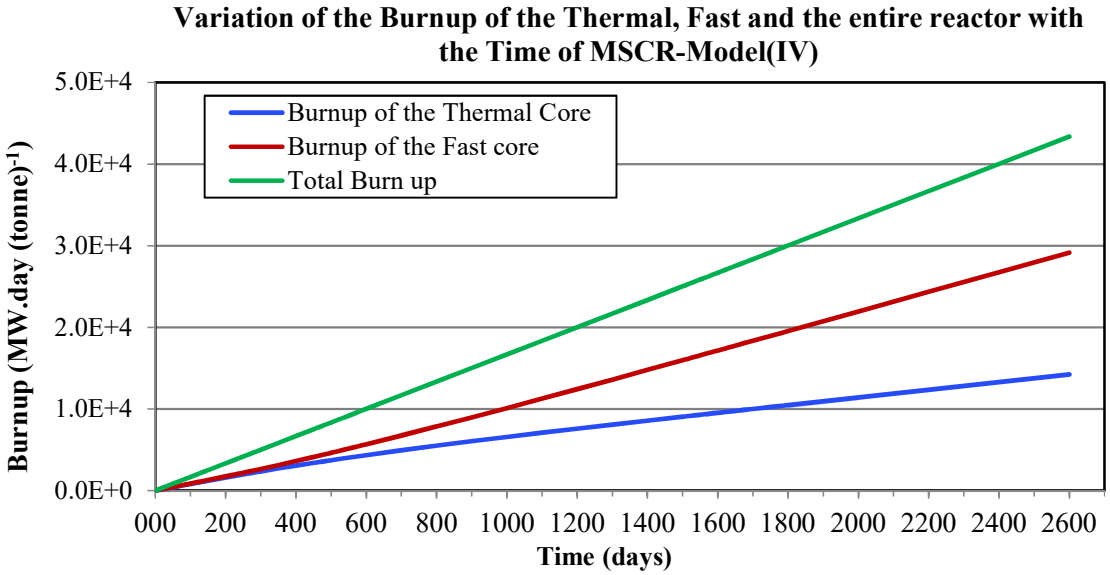

Figure (8-51): Variation of the Burnup of Thermal Core, Fast Core and Entire MSCR-Model (IV) with Time.

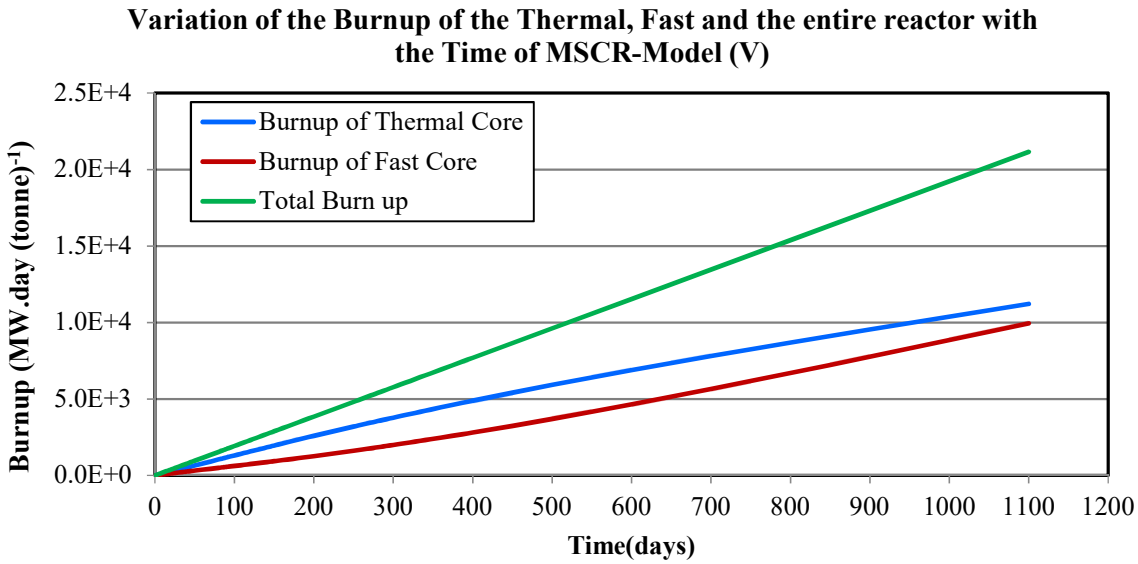

Figure (8-52): Variation of the Burnup of Thermal Core, Fast Core and the Entire MSCR-Model (V) with Time.

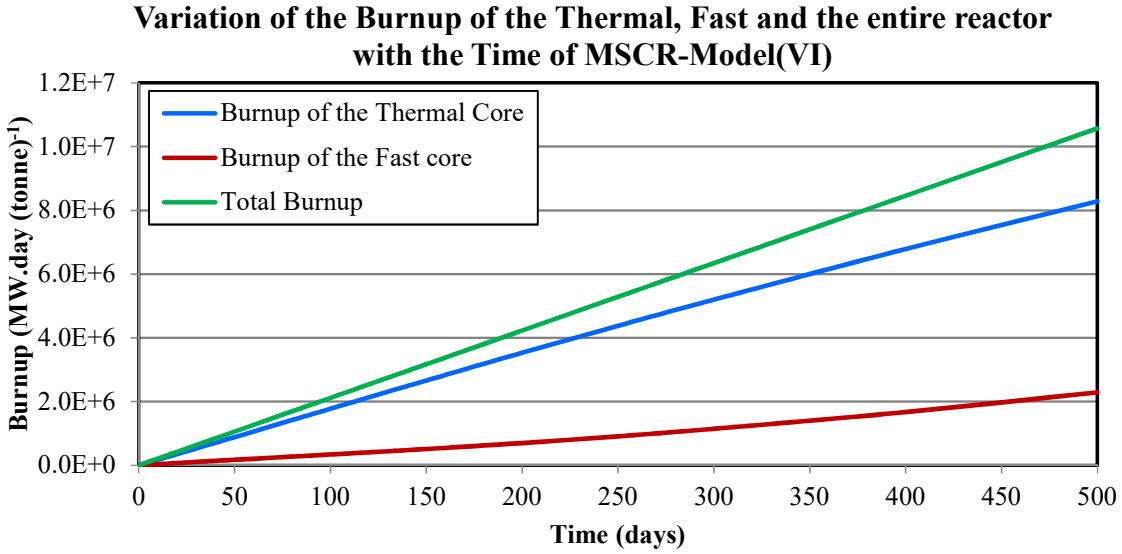

Figure (8-53): Variation of the Burnup of Thermal Core, Fast Core and Entire MSCR-Model (VI) with Time.

1) For Model (III), it is evident that most of the fuel burnup is produced in the thermal core. The minor burnup arising from the fast core is due to the fresh fuel content in the fast core with self-shielding by the external ring of fuel channels in the fast core. The lattice pitch of the fast core produces leakage of fast neutrons from the fast core to the thermal one. There

is some thermal leakage of neutrons from the thermal core to the fast core. These can escape from the fast core back into the thermal core without interaction.

2) For Model (IV), as the amount of fuel is increased in the fast core with a smaller lattice pitch, in the first 400 days the burnup from both cores is the same. However, after 400 days, the burnup curve for the thermal core falls slightly downwards due to a decrease in burnup. Similarly, the burnup line of the fast core is rising with an increase in time. These compensating effects maintain a linear burnup with time in the entire reactor. The majority of the fuel burnup occurs in the fast core. The high burnup arising from the fast core is due to a higher concentration of fissile materials for the fresh fuel core and a higher fast neutron flux.

3) For Model (V), between 300 and 400 days, the burnup curve of the thermal core is slightly decreased, indicating a slight decrease of burnup in the thermal core with time and a slight increase in burnup of the fast core, so that the burnup for the entire reactor is linear. These slight changes with burnup arise from the difference in composition of the fresh fuel and variations in the isotopic concentrations with time. Most the fuel burnup is produced in the thermal core.

4) For Model (VI) between the 150 and 200 days, the burnup curve of the thermal core slightly decreases with time, with a slight increase in burnup of the fast core.

8.7. Change of Atomic Density of Actinides in the MSCR-Models

8.7.1. Change of Atomic Density of Actinides in the Thermal Core of MSCR.

Figures (8-54), (8-56), (8-58) and (8-60) show that the variation of atomic densities of actinides concentrations in the thermal core for Models (III), (IV), (V) and VI). The fissile isotopes are represented with dashed lines. The U-235 is slightly decreased with time due to the burnup in the thermal core, while the atomic densities of Pu-239 and Pu-241 sharply increase during the first 20 days due to breeding after which their accumulation rates decreases gradually. Later, the concentration of plutonium saturates when the rate of production is equal to the rate of consumption. It then eventually decreases with longer irradiation times.

Figures (8-55), (8-57), (8-59) and (8-61) present the variations of the atomic density of some the transuranic isotopes of for Models (III, IV, V and VI). For the thermal core, the transuranic isotopes have initially zero concentration as expected for natural uranium fresh fuel. After a certain time, the transuranic isotopes reach a constant value. For longer irradiation times, they eventually decrease.

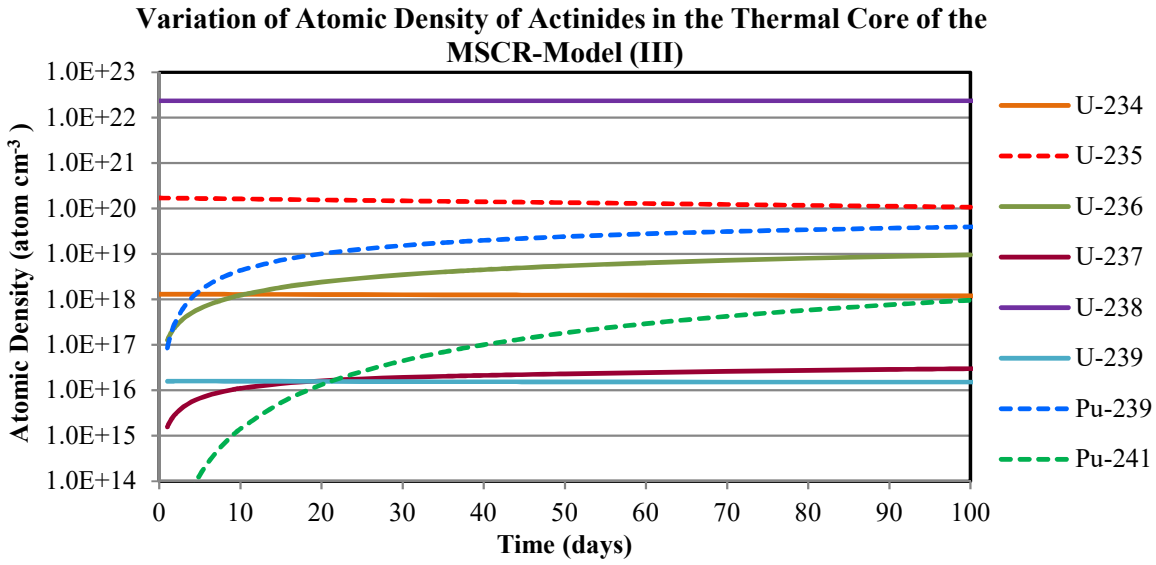

Figure (8-54): Variation of Atomic Density of Actinides in the Thermal Core of the MSCR-Model (III) (1).

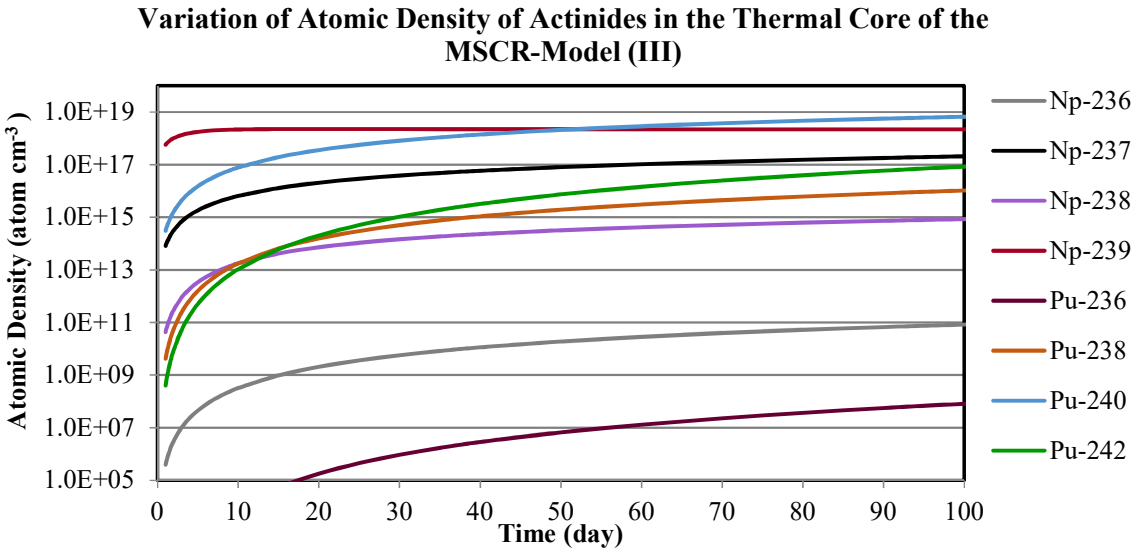

Figure (8-55): Variation of Atomic Density of Actinides in the Thermal Core of the MSCR-Model (III) (2).

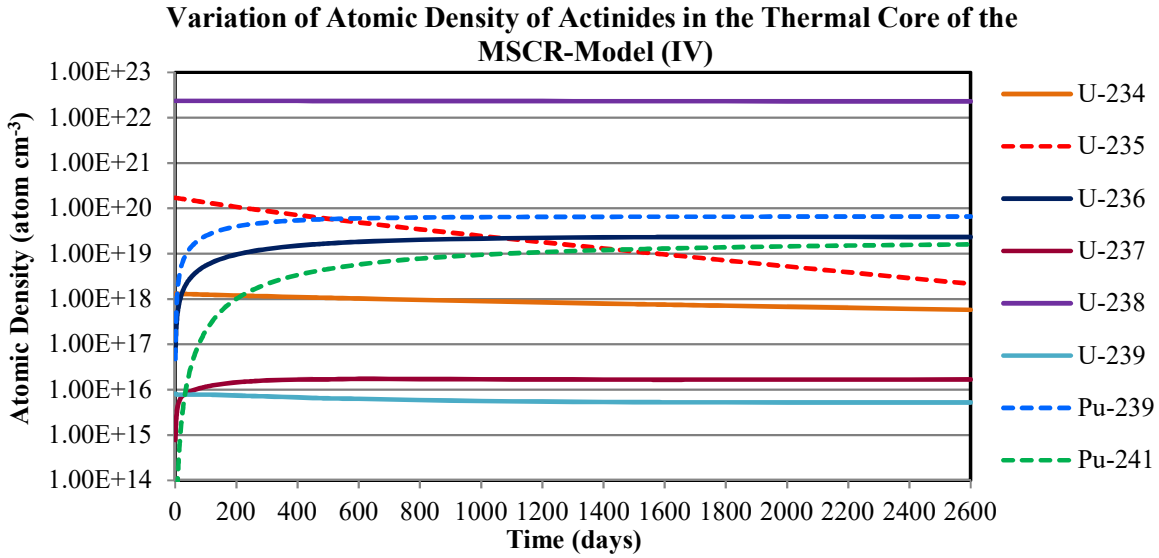

Figure (8-56): Variation of Atomic Density of Actinides in the Thermal Core of the MSCR-Model (IV) (1).

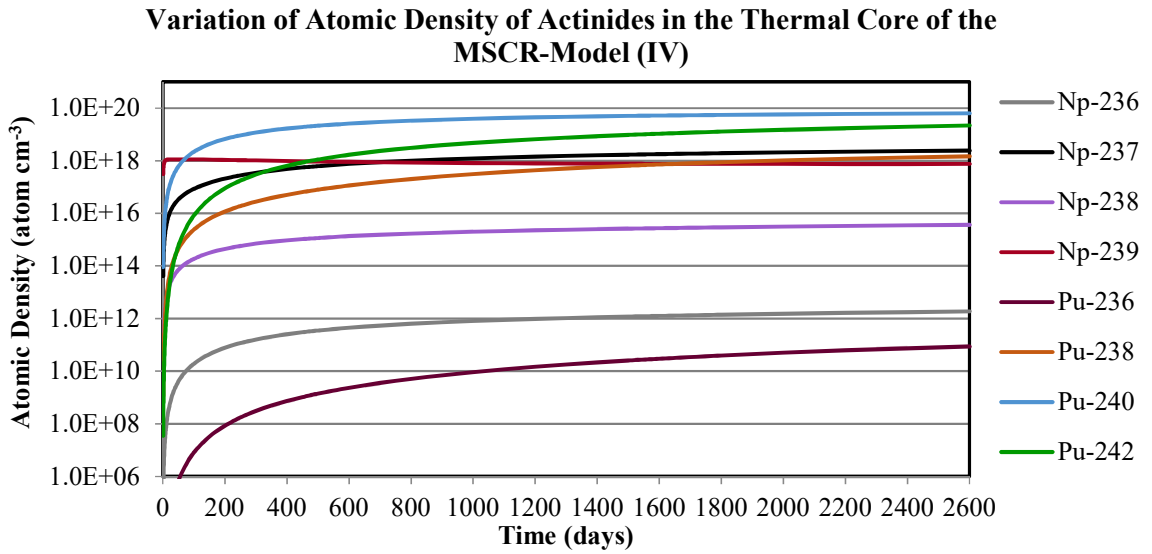

Figure (8-57): Variation of Atomic Density of Actinides in the Thermal Core of the MSCR-Model (IV) (2).

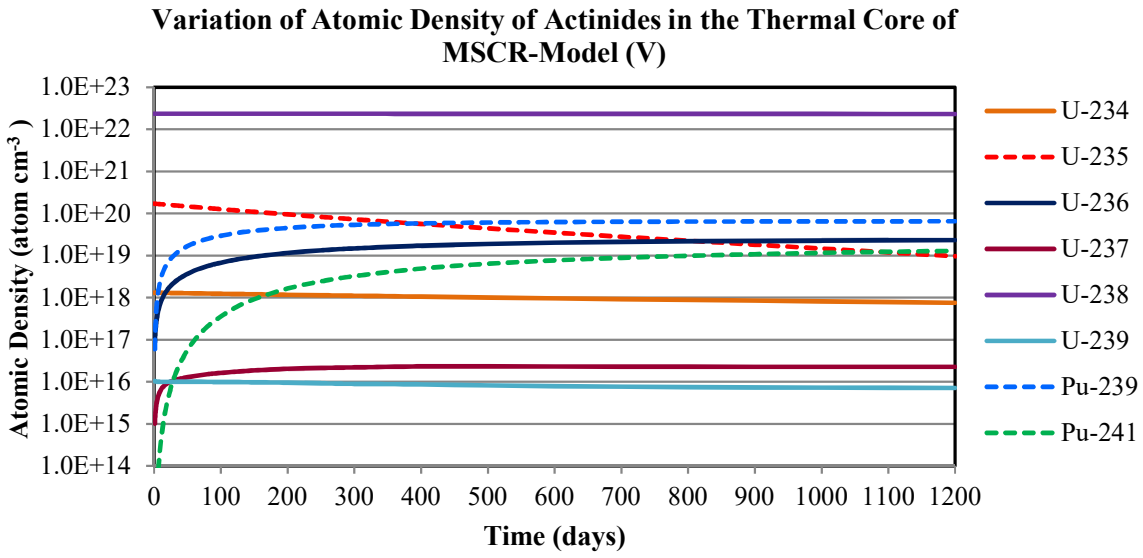

Figure (8-58): Variation of Atomic Density of Actinides in the Thermal Core of the MSCR-Model (V) (1).

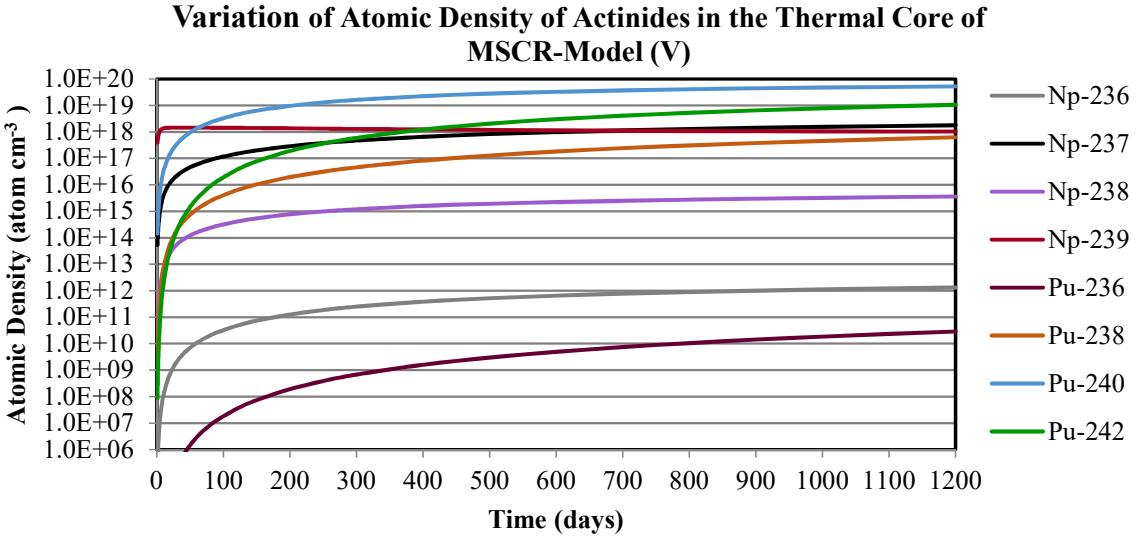

Figure (8-59): Variation of Atomic Density of Actinides in the Thermal Core of the MSCR-Model (V) (2).

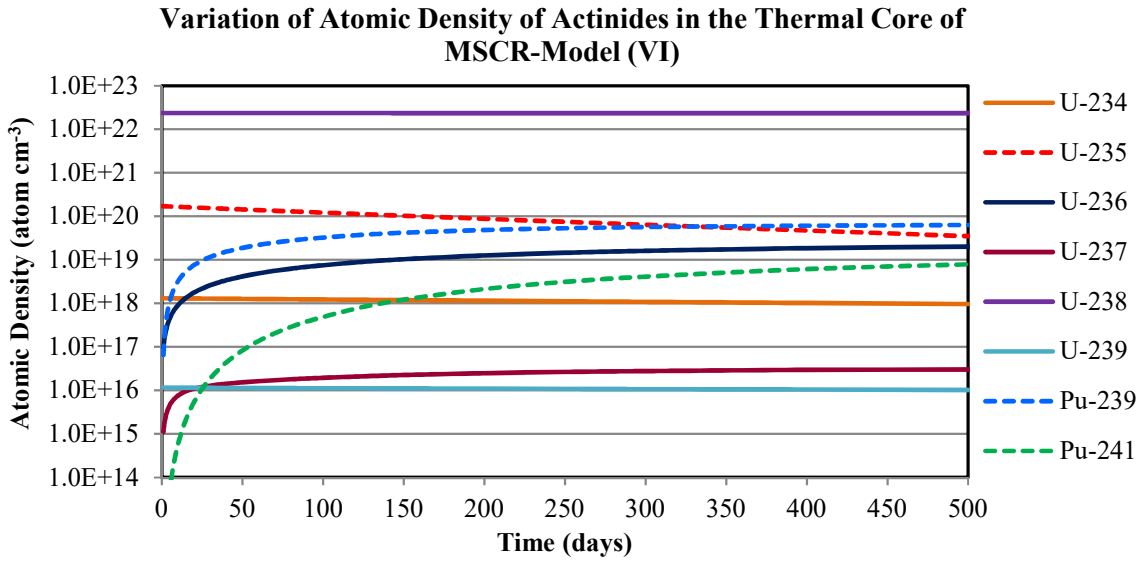

Figure (8-60): Variation of Atomic Density of Actinides in the Thermal Core of the MSCR-Model (VI) (1).

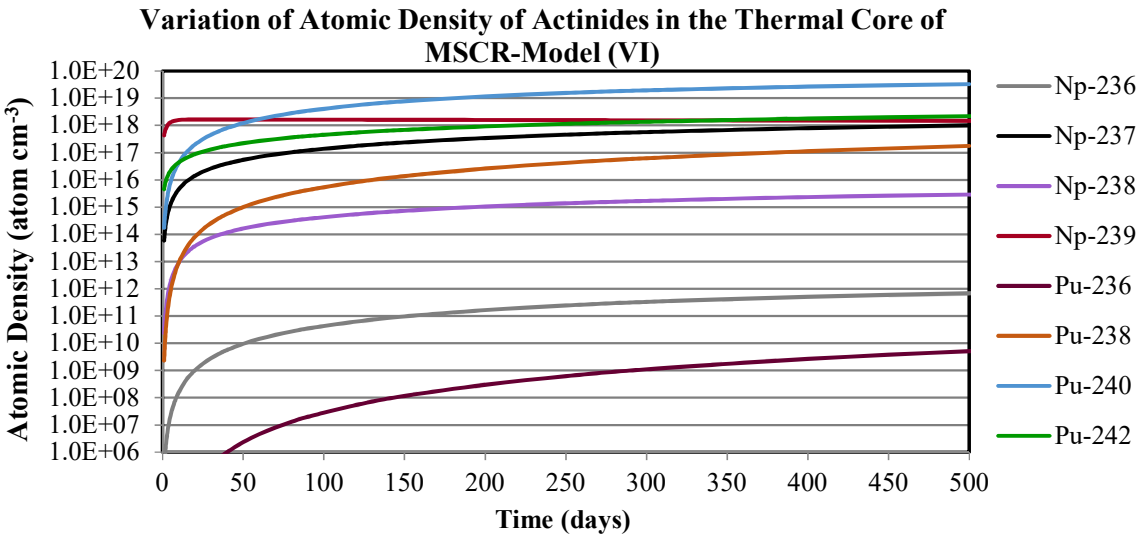

Figure (8-61): Variation of Atomic Density of Actinides in the Thermal Core of the MSCR-Model (VI) (2).

8.7.2. Change of Atomic Density of Actinides in the Fast Core of MSCR for Models (III) to (VI)

Figure (8-62) to Figure (8-69) show the variation of the atomic densities in the fast core for Model III to Model VI of the MSCR:

1) Figures (8-62), (8-64), (8-66) and (8-68) show that the concentration of Pu-239 is decreased with burnup. The traces of U-235 arise from the initial depleted uranium base of the fresh MOX fuel (0.25%). Pu-241 is one of the initial contents of the MOX fuel from the weapon great source. The atomic density of Pu-241 increases during the first period of irradiation and then it increases very slightly. The density of Pu-240 starts from a certain value as shown in Table (8-1).
2) Figures (8-63), (8-65), (8-67) and (8-69) presents the variations of the atomic densities of some of the transuranic isotopes. Some of the transuranic isotopes start at a zero concentration since the fuel is fresh. After a certain time, they reach a constant value that is burnt by the fast flux.

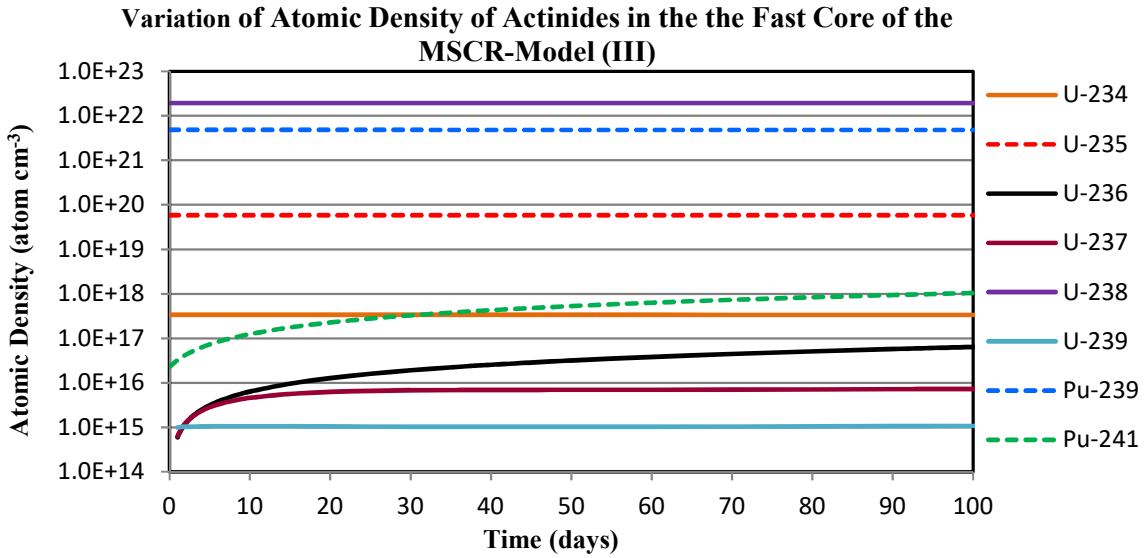

Figure (8-62): Variation of Atomic Density of Actinides in the Fast Core of the MSCR-Model (III) (1).

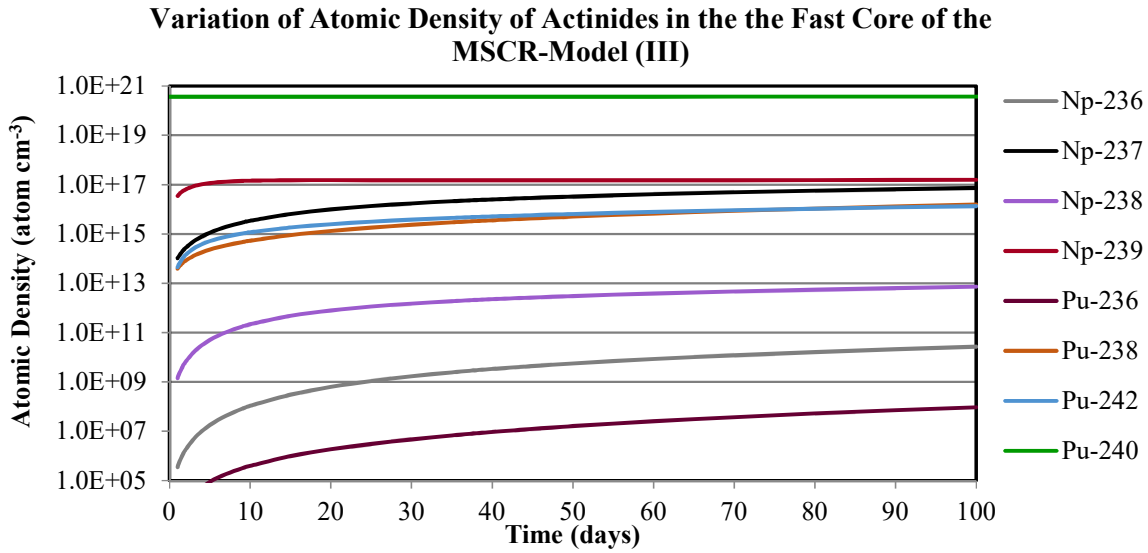

Figure (8-63): Variation of Atomic Density of Actinides in the Fast Core of the MSCR-Model (III) (2).

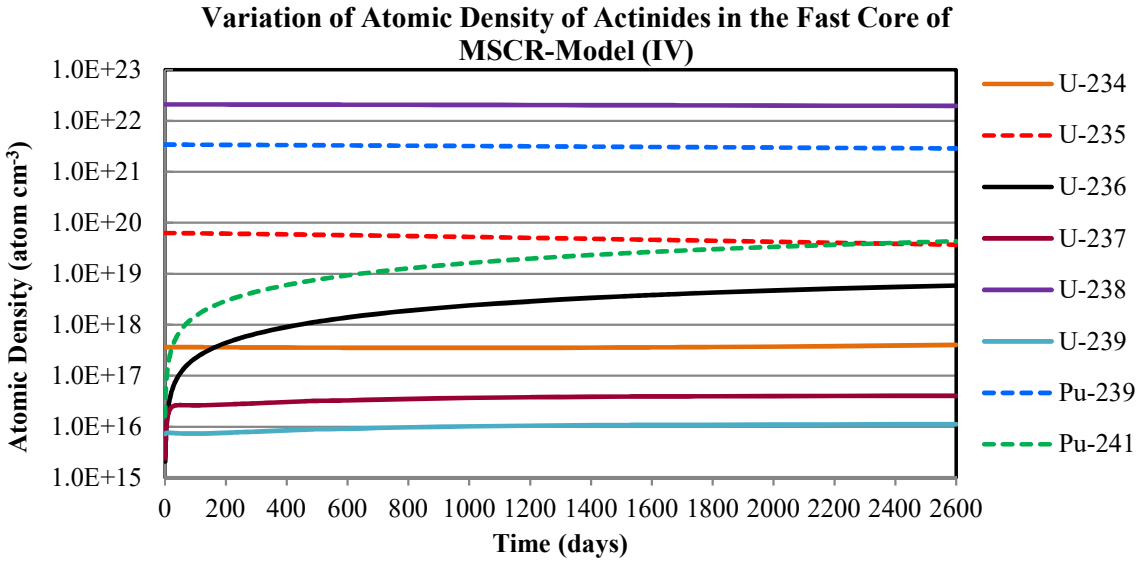

Figure (8-64): Variation of Atomic Density of Actinides in the Fast Core of the MSCR-Model (IV) (1).

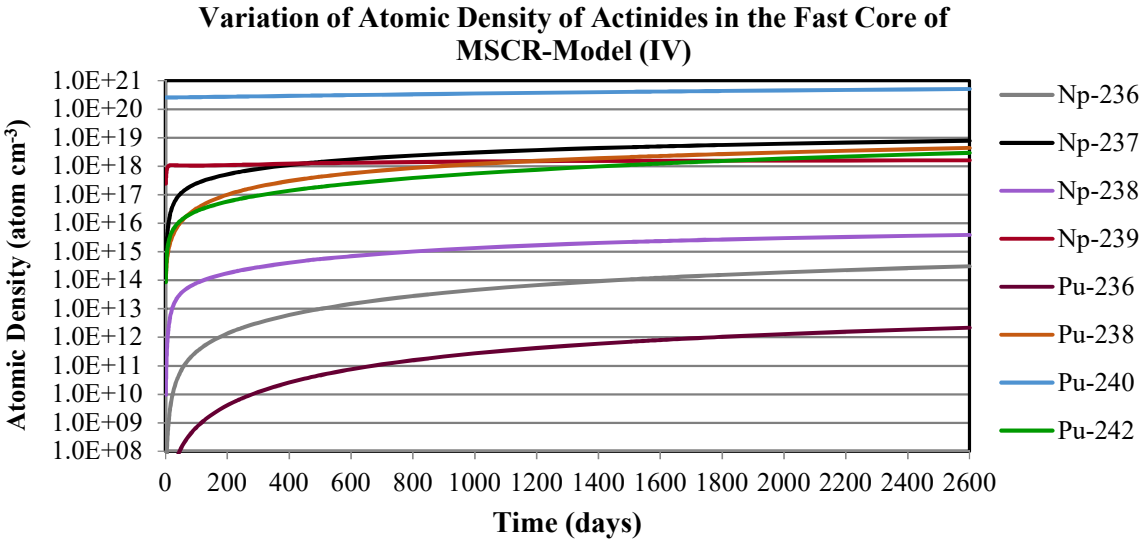

Figure (8-65): Variation of Atomic Density of Actinides in the Fast Core of the MSCR-Model (IV) (2).

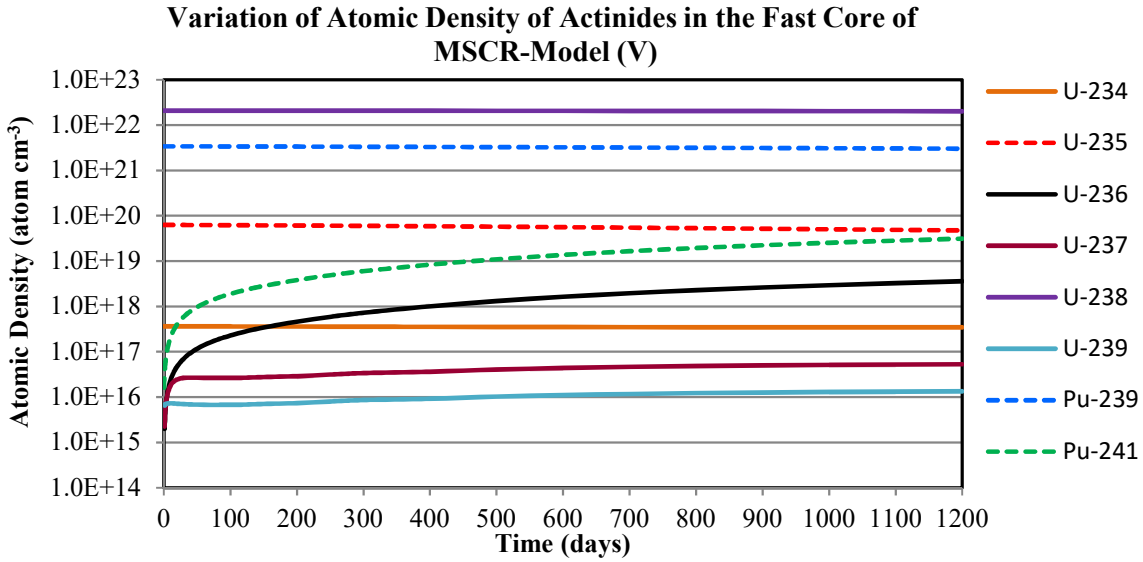

Figure (8-66): Variation of Atomic Density of Actinides in the Fast Core of the MSCR-Model (V) (1).

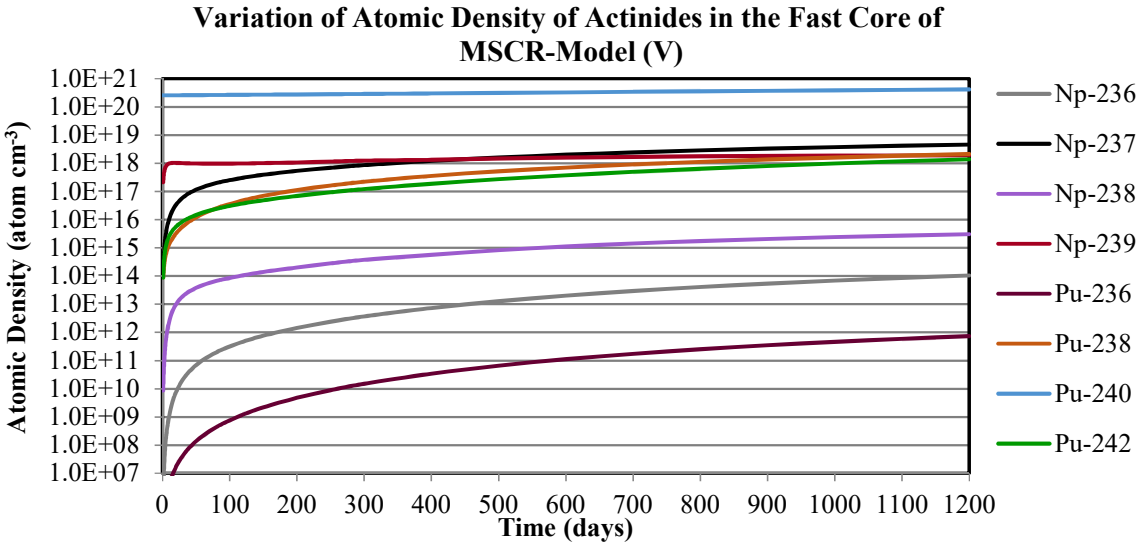

Figure (8-67): Variation of Atomic Density of Actinides in the Fast Core of the MSCR-Model (V) (2).

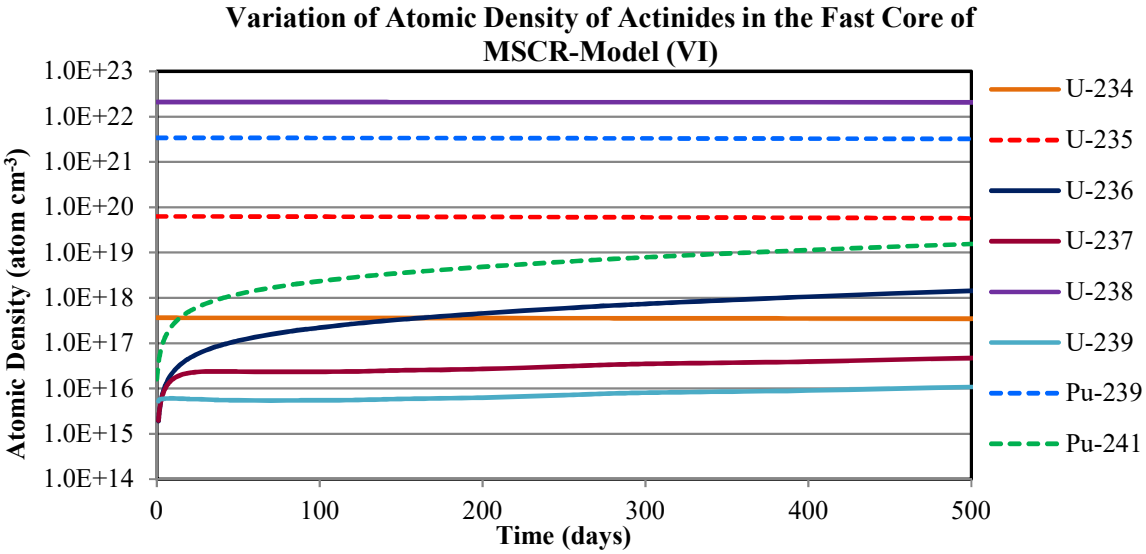

Figure (8-68): Variation Atomic Density of Actinides in the Fast Core of the MSCR-Model (VI) (1).

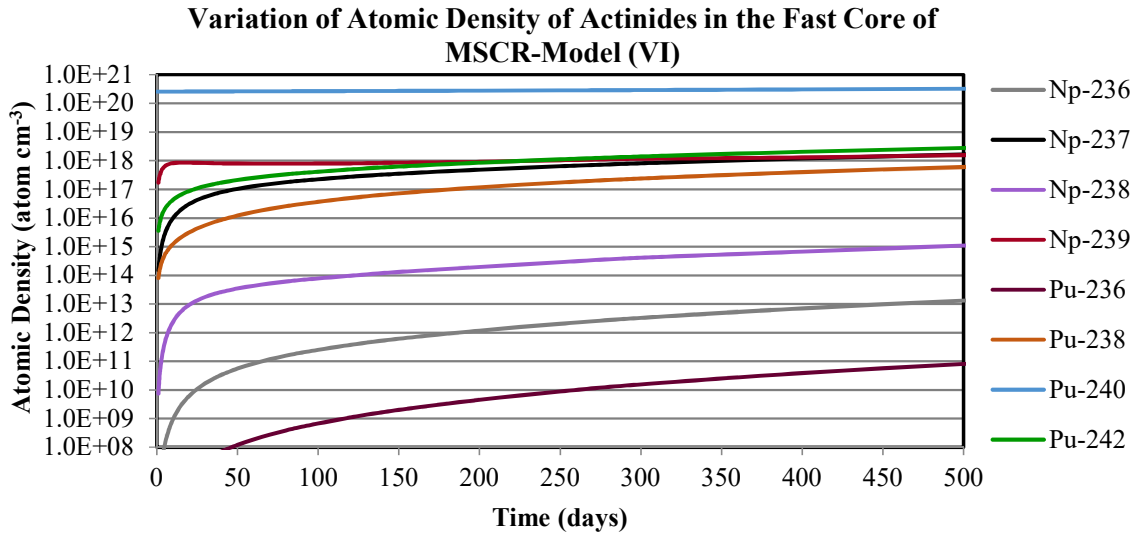

Figure (8-69): Variation Atomic Density of Actinides in the Fast Core of the MSCR-Model (VI) (2).

8.7.3. Variations of Atomic Density of Fissile Actinides in the MSCR-Models

1) Variations of Pu-239 Concentration in the Fast Core and Entire MSCR-Models

The variation of atomic density of Pu-239 isotope in the entire reactor and the fast core of the four reactor Models (III, IV, V, and VI) are shown in Figure (8-70) to Figure (8-73). The red lines represent the Pu-239 concentration in the fast core and the green line represent the concentration in the entire reactor. In the fast core, the concentration of plutonium is decreasing with time while the concentration in the entire reactor increases first after very short time of criticality and then increases due to production of plutonium in the thermal core. one can see that:

1) For Model (III), since the initial reactivity was 41 mk, the criticality period is the shortest in comparison to the other models (subcriticality is reached within 98 days). The model will be subcritical within the plutonium peak. However, for longer irradiation times, the green curve of the entire reactor for the Pu-239 concentration will decrease.

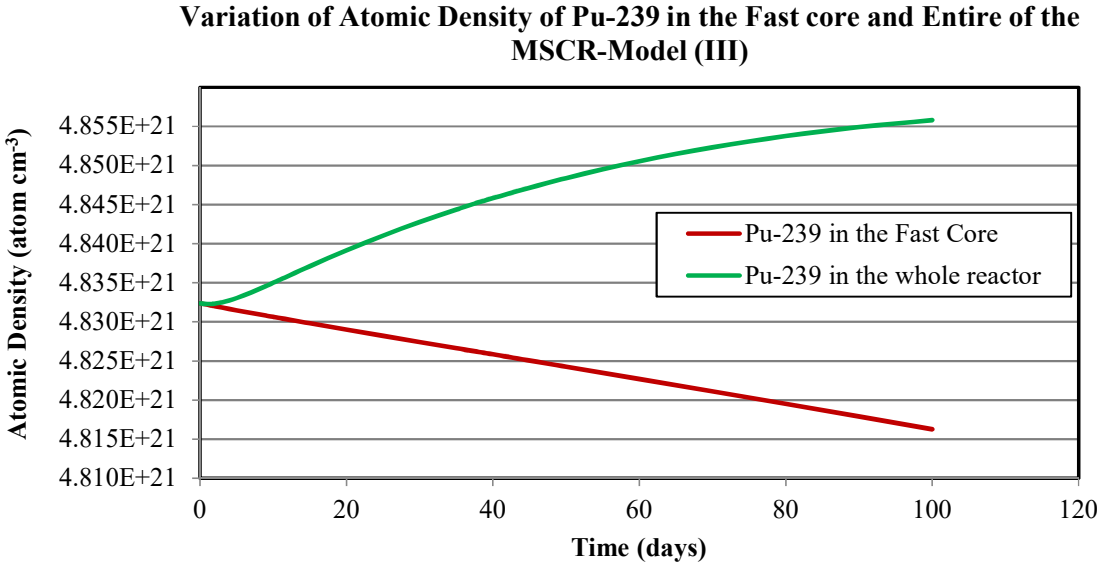

Figure (8-70): Variation of the Atomic Densities of Pu-239 in MSCR-Model (III).

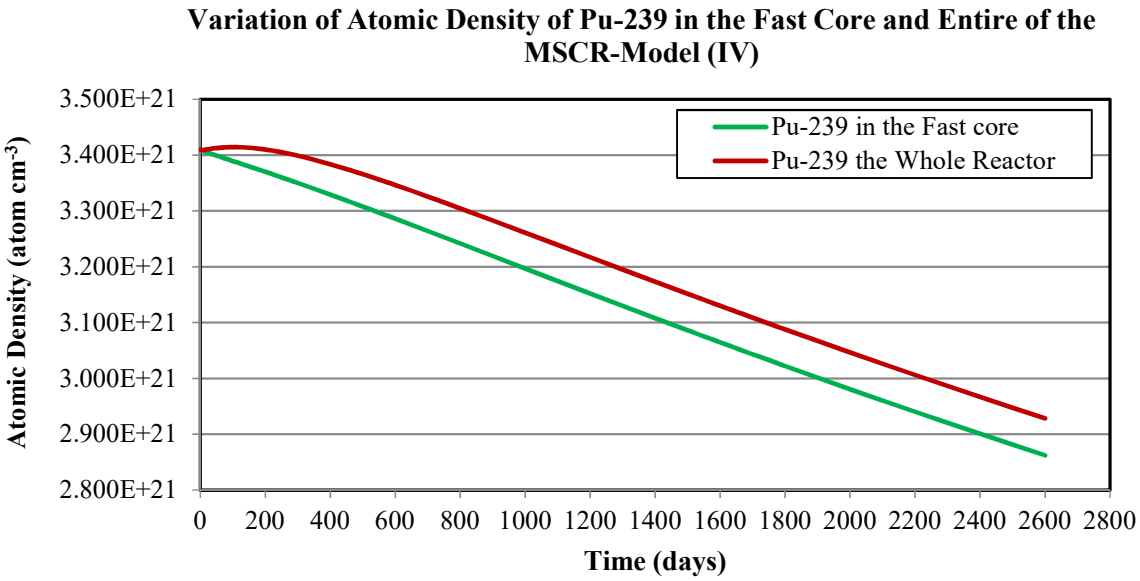

Figure (8-71): Variation of the Atomic Densities of Pu-239 in MSCR-Model (IV)

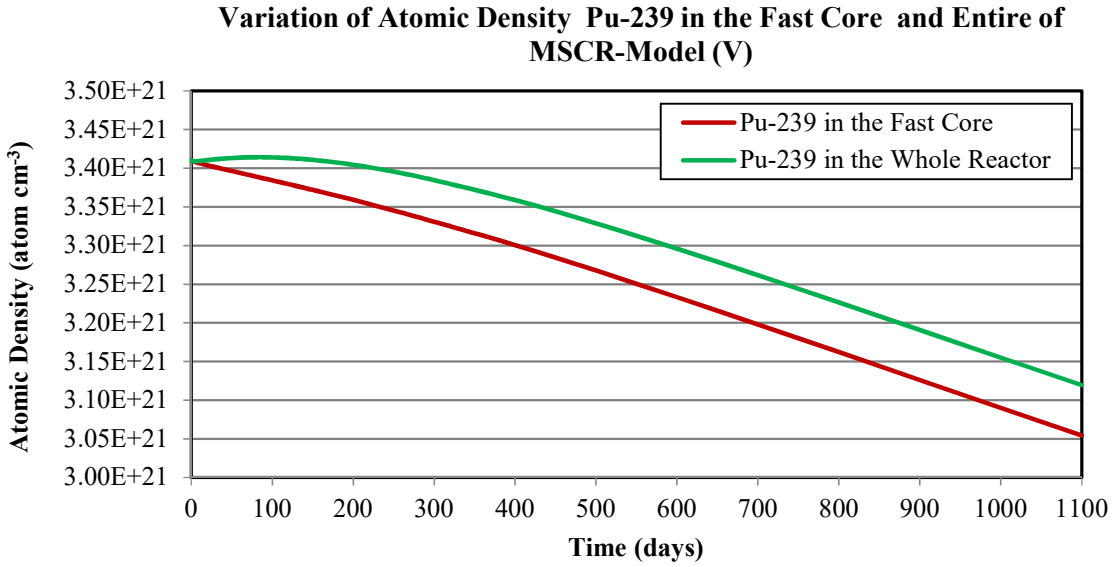

Figure (8-72): Variation of the Atomic Densities of Pu-239 in MSCR-Model (V).

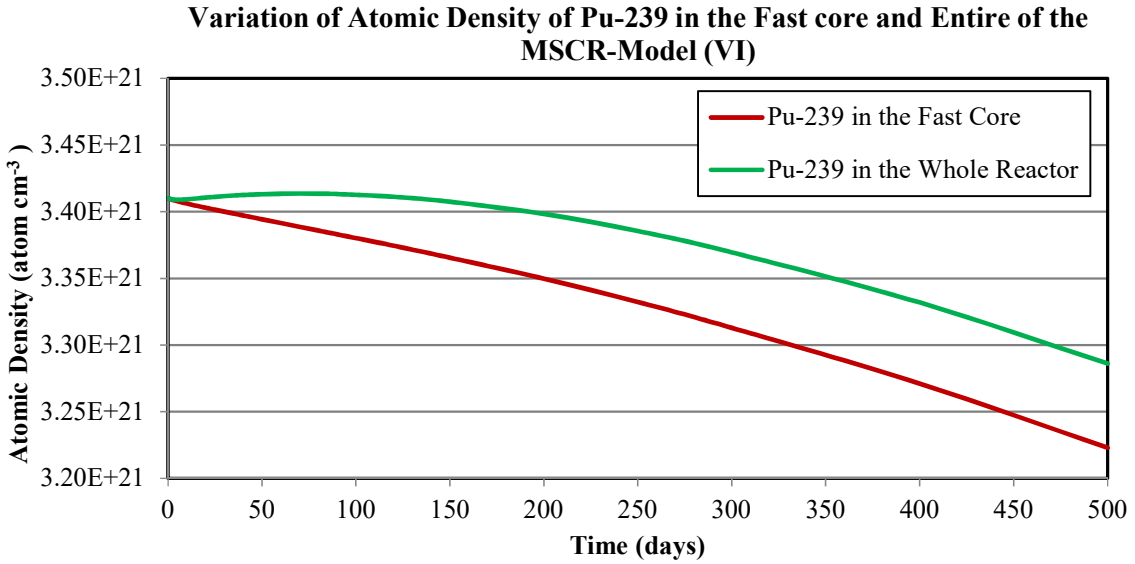

Figure (8-73): Variation of the Atomic Densities of Pu-239 in MSCR-Model (VI)

2) In the fast core, the concentration of Pu-239 is represented by the red lines which decrease with burnup time. The rate of these decreasing is different from one model to another. No initial increase in the red lines indicates that the destruction of plutonium in the fast core is much more than its production. This can also explain the absence of a plutonium peak in the reactivity curves in Section 8.2.1 in the fast core.

3) The green curves show the variation of the concentrations of Pu-239 with time in the entire core. The atomic density of Pu-239 increases during the first period of irradiation due to the high rate of Pu-239 production in the thermal core with the presence of U-238; then after a short duration, steady state is reached after which there is a steady decrease for longer irradiation times with the burning of Pu-239.

4) Pu-239 is produced in both cores due to neutron capture in U-238 mainly in the resonance energy region during neutron moderation. The rate of production of Pu-239 is dependent on the epithermal flux and the ratio of U-238 in the core. In the thermal core, the ratio of U-238 is much higher than that in the fast core, which causes an increase in the concentration of plutonium during the first period in the entire reactor. The rate can be represented by the slope of the green curve.

Figure (8-74) shows the destruction percentage of the Pu-239 in the fast core from the initial atomic density of this isotope in the fresh fuel. Model (IV) has the highest percentage of destruction of Pu-239 in the fast core while Model (III) has the lowest. For the models with the same lattice pitch but of with different sizes for the fast and thermal cores (Models (IV), (V) and (VI)), the destruction percentage for Model (IV) is about three times that of Mode (VI) and 1.5 times that for Model (V).

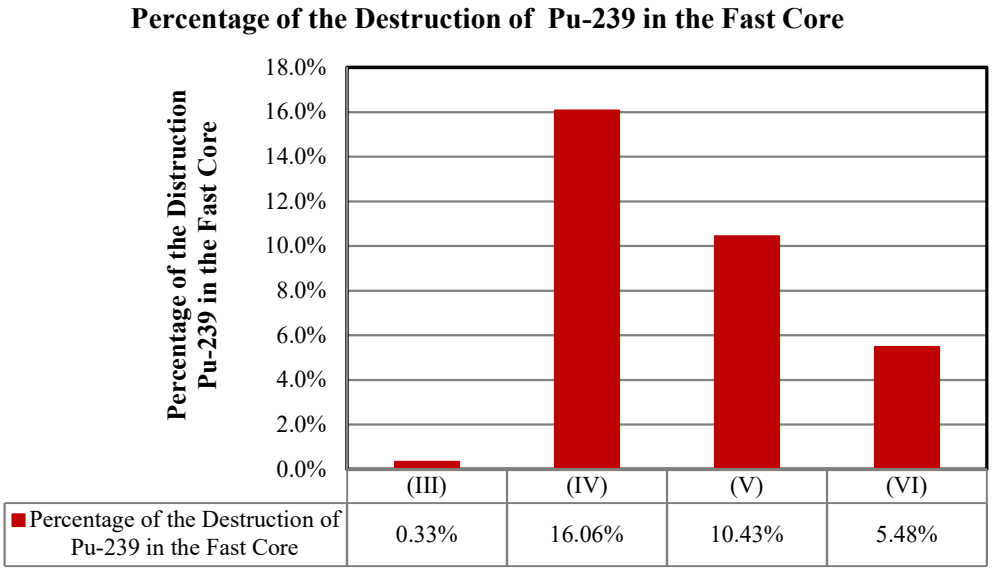

Figure (8-74): Percentage of Destruction of P-239 in the Fast Core of the MSCR-Models (III, IV, V, and VI)

These reactors can be run at continuous power before subcriticality for 2600, 1060 and 420 days for Models (IV, V, VI), respectively. The average consumption rate of plutonium needs to be counted for these periods. Figure (8-75) shows the average consumption rate of Pu-239 in the fast core in a unit of (g cm^{-3} day^{-1}). It is obvious that the Model (VI) has the highest rate per day. Correlating these results with the flux distribution and the power distribution one concludes that as the radius of the fast core decreases and the number of fuel channels in the thermal core increases, there are increasing in the number of thermal neutrons which can diffuse from the thermal to the fast core. This results in an increase in the thermal fission rate with an increase in the rate of consumption of plutonium by thermal fission in addition to fast fission in the fast core.

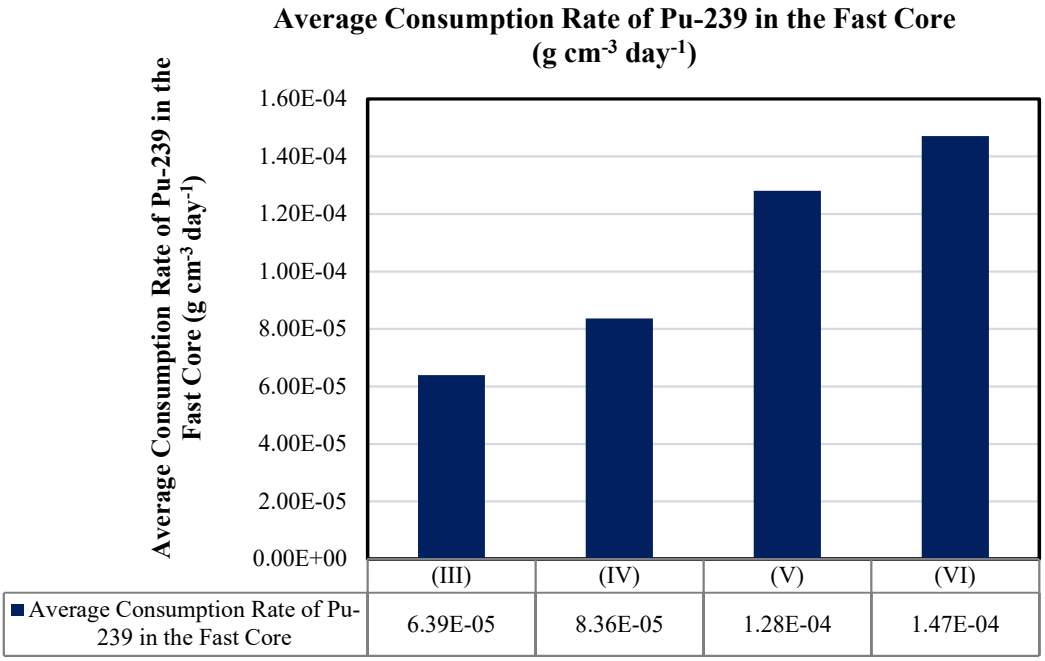

Figure (8-75) Average Consumption Rate of Pu-239 in the Fast Core

2) Variations of the Total Fissile Actinides Concentration in the Entire MSCR-Models

Considering the other fissile isotopes in the thermal and fast cores of each model in the fresh fuel, or those that are produced by neutron captures in both cores, the total destruction of the fissile isotopes is shown in Figures (8-76), (8-77), (8-78) and (8-79). These figures show the variations the total atomic density of the fissile actinides isotopes in the entire reactor for Models (III IV, V, and VI), respectively. Four reactors are burners, where a number of the fissile materials destructed are more than that produced.

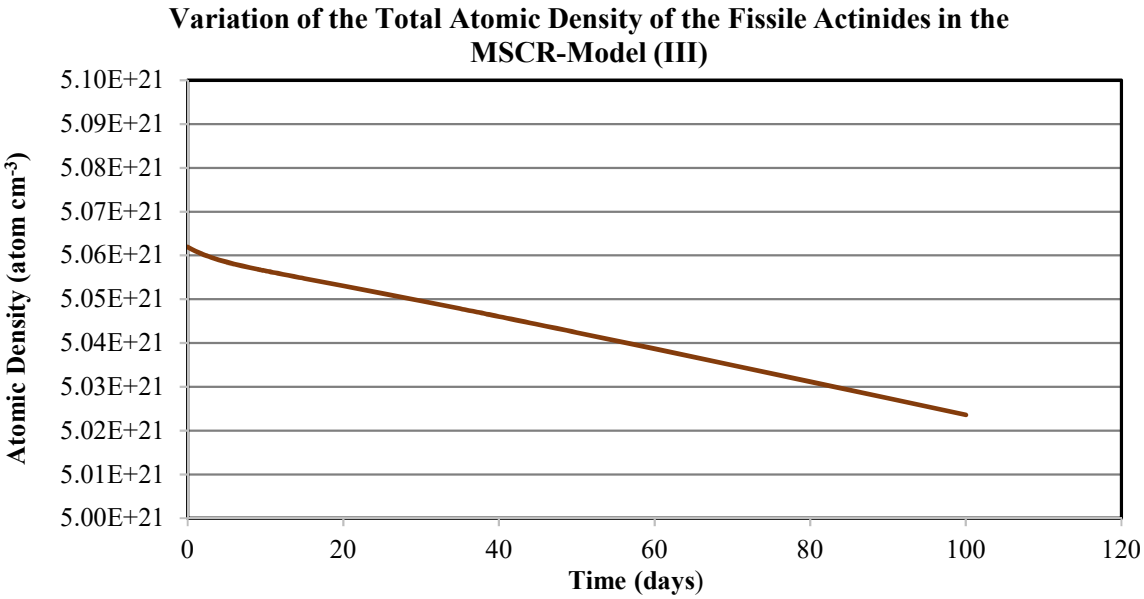

Figure (8-76): Variation of the Total Atomic Density of Fissile Actinides in the Entire MSCR-Model (III).

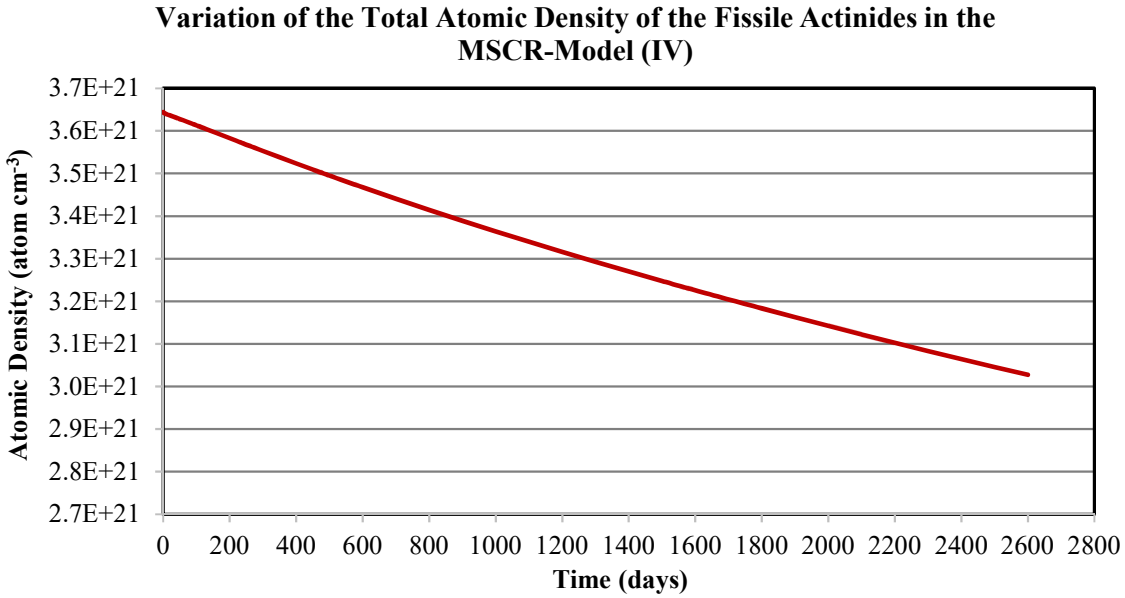

Figure (8-77): Variation of the Total Atomic Density of Fissile Actinides in the Entire MSCR-Model (IV).

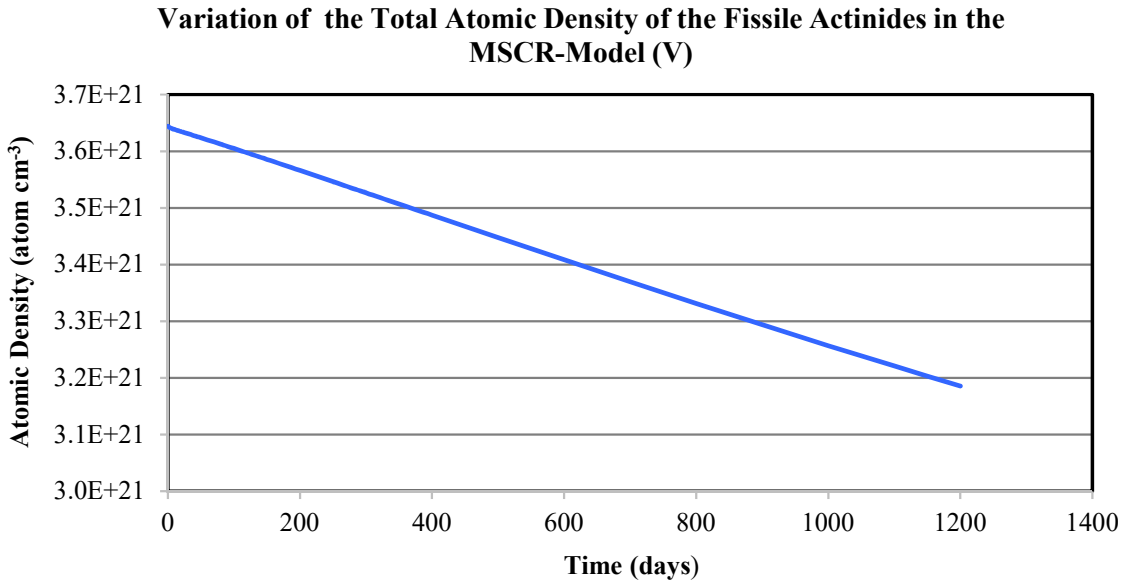

Figure (8-78): Variation of the Total Atomic Density of Fissile Actinides in the Entire MSCR-Model (V).

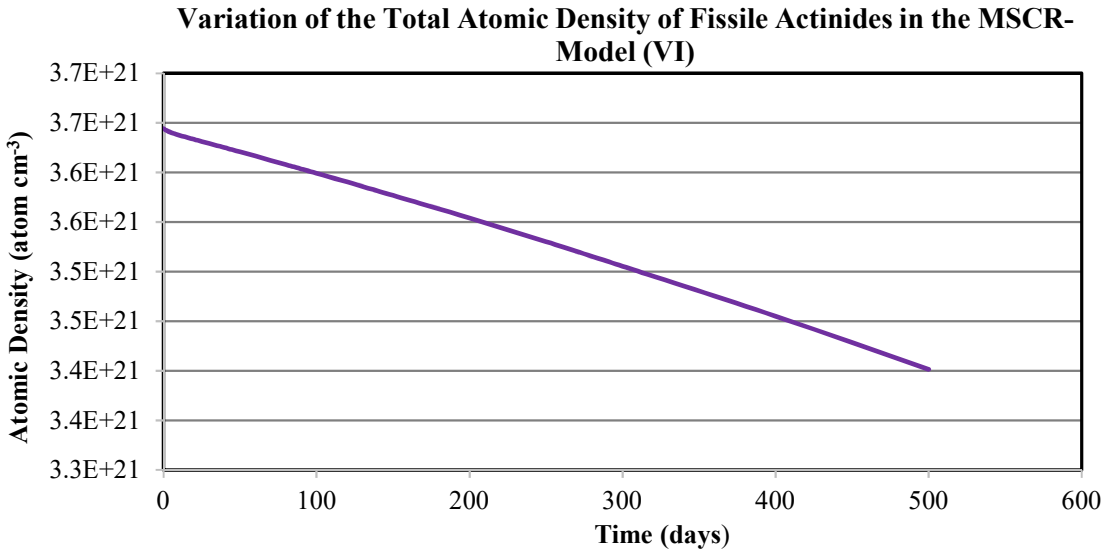

Figure (8-79): Variation of the Total Atomic Density of Fissile Actinides in the Entire MSCR-Model (VI).

The rate of destruction of the fissile materials are different from one model to another. To assess the average of this rate in both thermal and fast cores, and in the entire reactor during the periods of criticality, the slopes of these lines in Figure (8-76) to Figure (8-79) must be evaluated. These values include the destructed and produced concentrations of fissile isotopes due to neutron

capture. The rates of destruction are shown in Figure (8-80), calculated in units of (g cm^{-3} day^{-1}). From the bar chart, it can be concluded that:

1) For the thermal cores, the highest consumption rate of the total fissile materials in the thermal core is seen for Model (III).
2) For the fast cores, the highest consumption rate of the total fissile materials is introduced by Model (VI) while the smallest in the fast core of Model (III).
3) For the entire reactor models, Model (VI) produces the highest consumption rate followed by Model (V), (III) and then (IV).

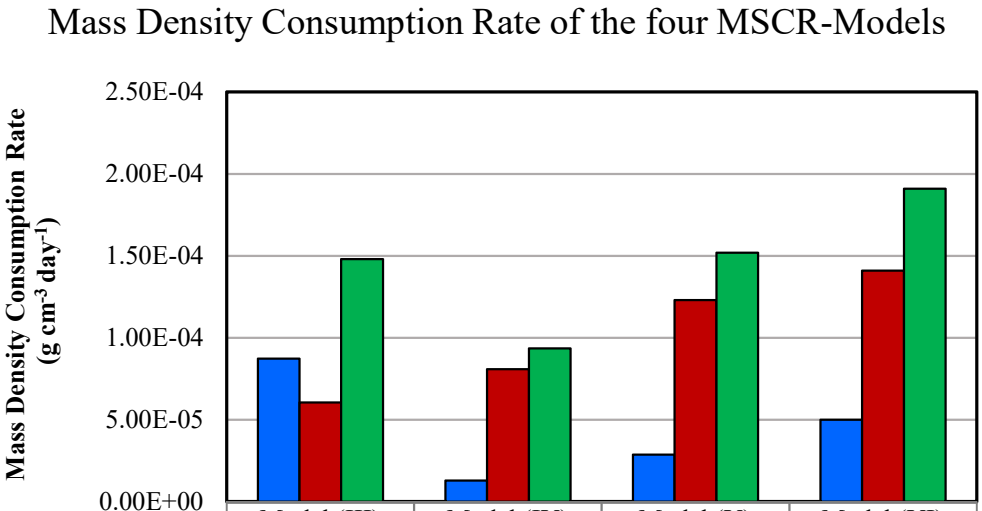

	Model (III)	Model (IV)	Model (V)	Model (VI)
Thermal Core	8.73E-05	1.28E-05	2.86E-05	4.99E-05
Fast Core	6.05E-05	8.08E-05	1.23E-04	1.41E-04
In the EntireMSCR-Model	1.48E-04	9.36E-05	1.52E-04	1.91E-04

:

Figure (8-80): Mass Density Consumption Rate of the Total Fissile Actinide in the four MSCR-Models

Equation (8-3) can be used to determine the amount of actinides burned in each model for the thermal and fast core, and the entire reactor:

$$Percentages\ of\ the\ Destructed\ Fissile\ Actinides = 100\times\frac{\left(\begin{matrix}(sum\ of\ the\ initial\ \ atomic\\densites\ of\ \ fissile\ actinides\end{matrix}\right)-\left(\begin{matrix}sum\ of\ the\ final\ atomic\\densities\ of\ fissile\ \ actinides)\end{matrix}\right)}{\left(\begin{matrix}sum\ of\ the\ initial\ atomic\\densities\ of\ actinides\end{matrix}\right)} \quad (8\text{-}3)$$

Table (8-8) shows the initial and final sum of fissile actinides mass densities for Model (III). that is used by Equation (8-3) to calculate of the percentages of the destructed fissile actinides in the thermal core, fast core and the entire reactor of the MSCR-Model (III).

Table (8-8): Calculation of the percentages of the destructed fissile actinides in Model (III)

	Thermal core (atom cm^{-3})	Fast Core (atom cm^{-3})	Entire reactor (atom cm^{-3})
Sum of the mass densities of fissile actinides at (0) day	1.7129E+20	4.8907E+21	5.0619E+21
Sum of the mass densities of fissile actinides after (100) days	1.4817E+20	4.8754E+21	5.0236E+21
The percentages of the destructed fissile actinides in Model (III)	13.50%	0.31%	0.76%

Figure (8-81) shows the percentages of the destruction of the total fissile actinides in each reactor model. The highest percentage in the thermal, fast and entire reactor was seen in Model (IV) with the smallest percentage in Model (III). Model (IV) shows the most destruction of fissile isotopes in the thermal core, fast core and entire reactor with ratios of 50.76%, 15.26% and 16.93 respectively when running for 2600 days without refueling. These percentages can be increased by utilizing the features of online refueling by shifting bundles from one fuel channel to another in each core. This refuelling would need a special fuel management that is different from that of traditional CANDU reactors. However, safety criteria must be considered for Model (IV) because of its higher form factor.

Model (VI) provides the highest rate of consumption of actinides with percentages of actinides destruction of 6.66 % of fissile actinides in the entire reactor, and 38.1% and 5.11% for the thermal and fast core. For this reactor model, although it has a short criticality period of only 420 days, in comparison to Model (IV), but with continuous refuelling in the fast core of Model (VI), it will burn more actinides than Model (IV) operating for the same period of time.

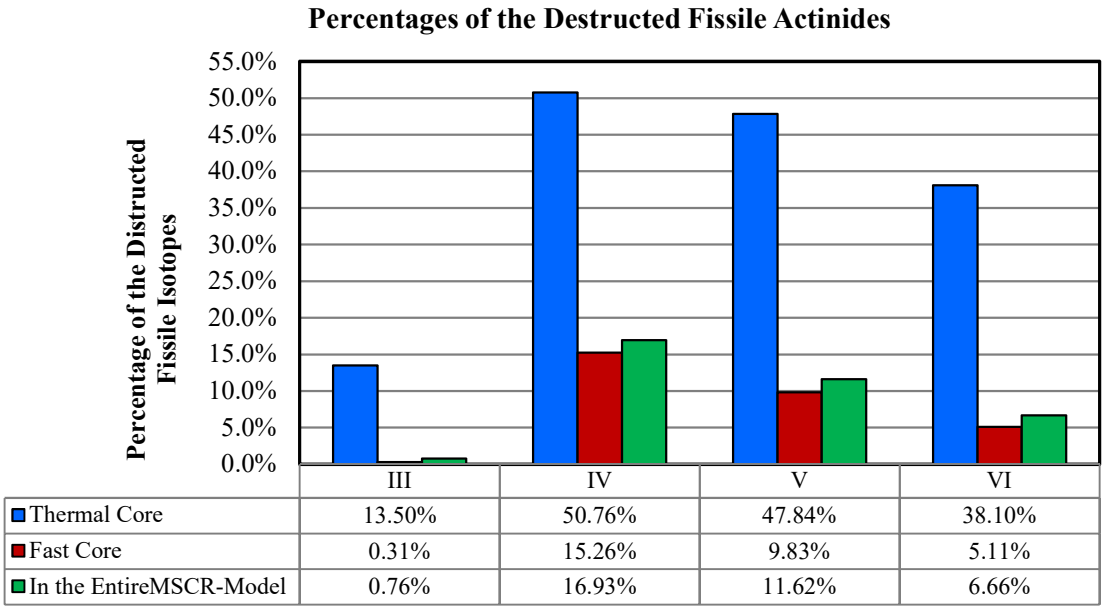

Figure (8-81): Percentages of Destruction of the Total Fissile Actinides in the four MSCR-Models

Table (8-9) shows the mass of destructed fissile materials in the four models in each core as calculated at the end of the burnup period.

Table (8-9): The Actual Destructed mass of the Fissile materials in in Models [(III) to (VI)] at the end of the burnup period

Model	Burnup period (days)	Mass of fissile materials in the thermal core (g)	Mass of fissile materials in the fast core(g)	Percentage of fissile Mass Destructed in the thermal Core	Percentage of fissile Mass Destructed in the fast Core	Actual destructed mass the thermal core mass (g)	Actual destructed mass the fast core mass (g)	Actual destructed mass entire (g)
III	98	4.98E+05	1.77E+06	13.50%	0.31%	6.72E+04	5.53E+03	7.28E+04
IV	2600	4.98E+05	8.32E+06	50.76%	15.26%	2.53E+05	1.27E+06	1.52E+06
V	1100	5.46E+05	4.91E+06	47.84%	9.83%	2.61E+05	4.83E+05	7.44E+05
VI	420	5.93E+05	2.59E+06	38.10%	5.11%	2.26E+05	1.32E+05	3.59E+05

The highest mass of fissile material destructed in the thermal core is for Model (V). The reactor of entire Model (IV) can burn 1.52 tonne of fissile material and 1.27 tonne in the fast core only.

8.8. Conclusion

1) Four models of the MSCR are simulated by Serpent code for the burning of plutonium in the fast core. The concentration of the fissile actinides in the fast core is 14.13%.
2) For the four models, the calculated reactivity lies within the safety margin of criticality. To demonstrate the non-breeding characteristic of the current reactor, the regeneration factor is calculated and is shown to be smaller than the minimum criteria needed for breeding.
3) The flux distributions at the three energy bins are calculated for the four models. As the amount of fuel increases in the fast core the fast and epithermal fluxes also increase.
4) Model(III) shows a reasonable value for such safety parameters as the criticality and form factor. The model does not provide a significant level of burning of actinides in the fast core. For future work, this can be achieved by increasing the concentration of the fissile materials up to 19.9% while respecting criticality safety criteria.
5) Models (IV) to (VI) show a reasonable value for the criticality parameter but their form factors are higher than the acceptable safety criteria. These models provide a significant level of burning of actinides in the fast core.
6) For the thermal cores, the consumption rate of fissile actinides by Model (III) is the highest in comparison to the other three models. On the other hand, Model (VI) introduces the highest consumption rate in the fast core and entire reactor.
7) The highest percentage of destruction of fissile materials in the thermal core, fast and entire reactor is provided in Model (IV).

Chapter 9.

Achievement of Goals

The current work addresses the preliminary design of multispectrum reactor based on the unique features of a CANDU reactor to burn fissile actinides obtained from dismantled nuclear-grade weapons material. For this study, one has the following conclusions:

1) The theory of coupled reactors was successfully verified against experimental and numerical results in the literature for the design of a Deuterium Critical Assembly using the probabilistic computer code (MCNP5) and the continuous-energy Monte Carlo reactor physics burnup code (Serpent 1.1.19). This benchmark provides confidence in the use of the Serpent code for the design of a multispectrum reactor.

2) The Serpent and MCNP6 codes were further benchmarked for burnup calculations with natural uranium fuel for a CANDU 6 Gentilly-2 reactor as well as against burnup calculations with the WIMS-AECL code. Agreement was obtained for three energy bins for the Channel Flux to Fuel Flux Ratio (CFFFR) and radial and axial power in the reactor.

3) The Serpent code has been successfully used to design a multispectrum reactor (MSCR). It has a significantly reduced computation time as compared to MCNP6 for burnup calculate.

4) The MSCR design is at the same thermal power (2180 MWth) and size of a CANDU 6 - Gentilly-2 reactor with common design features of: a natural uranium thermal core and lattice pitch of 28.575 cm for the fast core using a standard 37-element bundle design (Zircaloy-4 for the thermal core and Stainless Steel (SS316L(N) for the fast core); and heavy water for the coolant and moderator in the thermal core and helium gas as coolant for the fast core.

5) The characteristics of the six models investigated for the MSCR design are given in Table (4-1). Two models (Models I and II) use enriched uranium (19.9%) for the fast core with a fast core radius of 108.38 cm. The other four models use enriched plutonium (as MOX fuel with depleted uranium and 13.9% of Pu-239). Models (III and IV) have a fast core radius

of 137.00 cm, while Models (IV, V and VI) have the same lattice pitch in the fast core but different core sizes and number of fuel channels for both cores.

6) The work investigated the influence of: (i) the radius, lattice pitch, type of fissile material (uranium and plutonium) and fissile enrichment of the fast core; (ii) number of fuel channels in the thermal and fast core, on the multiplication and regeneration factors for the reactor design, and (iii) the flux profile at different energy bins in the fast and thermal cores.

7) Several reactor physics parameters/metrics have been calculated in this study for the MSCR including: (i) reactivity, (ii) regeneration factor, (iii) flux distribution, (iv) power density distribution, (v) percentage of power produced from each core, (vi) form factor, (vii) total burnup and (viii) rate of destruction of actinides. The major findings for these parameters are:

   i. Reactivity: The initial reactivity for all models met the safety margin of a traditional CANDU 6 reactor (~41 to ~113 mk). This study demonstrated an initial drop in reactivity due to production of saturating fission products, a plutonium peak, and the required amount of time for refuelling.

   ii. Regeneration factor: This criterium demonstrated that all reactor designs were in fact burners of actinides (and not breeders). This factor is principally influenced by the size of the lattice pitch, number of fuel channels and fuel enrichment of the fast core.

   iii. Flux distribution: The radial and axial flux distributions are calculated for the thermal, epithermal and fast energy groups. The flux shape depends on the lattice pitch and number of fuel channels in the fast core. For the thermal core, it is affected by the fissile material concentration, number of fuel channels and the lattice pitch of the fast core.

   iv. Power density distribution: The distribution depends mainly on the flux profile, where the highest 10% of the power density does not change over the operating period. This result indicates that flux tilting does not occur. In Models (I and III), a decreased power density at the center of the fast core is due to self-shielding in the outer channels of the fast core, while for Models (II), (IV), (V) and (VI) self-shielding also occurs within

the inner ring of channels in the thermal core. With time, the average power density increases in the fast core, depending on the radius and number of fuel channels in the fast core in contrast to the thermal core.

v. Percentage of power produced from each core: The percentage of power produced from the fast core is directly proportional to the number of channels and inversely proportional to the lattice pitch with an increase in the average value of the fast flux. For Models (I) and (III), most of the power is produced from the thermal core with a ratio of 91.4% and 85.2%, respectively, with a small change in these percentages over the irradiation period. For Models (II), (IV), (V) and (VI), the power percentage generated from the fast core is greater and increases with continuous irradiation depending on the amount of fuel in the fast core. Only in Model (IV) is the relative power produced in the fast core greater than that in the thermal core.

vi. Form factor: For Models (I) and (III), the form factors change slightly with a value between 1.15 to 1.23 (which is acceptable from a safety perspective). However, for Models (II), (IV), (V) and (VI), the form factor of the fast core is less than 1.5, with a starting value higher in the thermal core that eventually reaches an unacceptable value of 3.4 and 4.2.

vii. Total burnup: The fuel burnup of Models (I) and (III) is small in the entire reactor due to the small number of fuel channels and fast flux in the fast core. Burnup mainly occurs in the thermal core. Models (II), (IV), (V) and (VI) have a higher burnup before subcriticality is reached with the highest burnup occurring in Model (IV) up to 2700 days before refuelling is needed. For the fast core, as the number of fuel channels increase, the burnup becomes predominate in the reactor.

viii. Percentage and rate of destruction of actinides: These parameters principally depend on the size and amount of fuel in the fast core. For the uranium-fuelled reactors, Model (II) has the higher consumption rate (10.78%) with the reactor running for 950 days before refueling. For the MOX-fuelled reactors, Model (IV) shows the greatest destruction of fissile isotopes in the thermal core, fast core and entire reactor with ratios of 50.76%, 15.26% and 16.93, respectively while running for 2600 days. Model

(VI) has the highest consumption rate in the fast core and entire reactor operating for 420 days. The percentages for Models (II) and (IV) can be increased with on-line refuelling with bundle shifting from one channel to another. However, safety criteria are an important consideration for Model (IV) because of the resulting form factor. The most effective design for burning actinides in a fast core with high burnup is Model (II) for an uranium-fuelled reactor and Model (VI) for a MOX-fuelled reactor, although once again safety criteria need to be met.

Chapter 10.

Recommendations

The following recommendations are made as a carry on of the research work, which is outside the scope of the current thesis:

1) Improvement in the reactor design could be made. For instance, one could investigate the use of thorium fuel as a base material for the MOX fuel component rather than the use of depleted uranium. Th-232 is the major abundant isotope that can produce the fissile U-233 isotope with the capture of one neutron followed by two successive beta decays. Also, the delayed neutron fraction for U-233 (0.0027) is slight greater than that of Pu-239 (0.0023)[75]. With two further neutrons captures in U-233, U-235 is produced that has a greater delayed neutron fraction (0.0068) than for the similar process that produces Pu-241. The delayed neutron fraction is an important factor for reactor control. On the other hand, the thorium fuel cycle has some concerns in regards to its chemistry because of the production of U-232, which is a by-product of the thorium fuel cycle due to the (n,2n) interactions between fast neutrons and U-233, Th-232 and Pa-233. The U-232 particularly have hard gamma rays that represent a challenge for thorium fuel reprocessing.

2) An expanded study could be considered for Model (III) by considering higher enrichments in the MOX fuel, while respecting non-proliferation and safety concerns. In addition, a multidimensional optimization could be performed to optimize the lattice pitch, number of fuel channels, enrichment and radius of the fast core. A CANFLEX (43-element) bundle design could also be considered which has been developed by Atomic Energy of Canada Limited (this might also include the use of slightly-enriched uranium in the thermal core). The design could consider a 480-channel CANDU reactor, which would allow a greater size for the fast core and consequently a greater destruction of fissile material.

3) One could also develop improved designs to address safety criteria and provide better safety margins. A model can be used to normalize the flux to find the maximum power

produced to meet required safety criteria. Also, the design of Models (II, IV, V, VI) could be expanded to obtain a uniform flux profile in the thermal core and relocate the maximum value of the fluxes for the three energy groups to the center of the thermal core. The current analysis also does not include the use of control rods and liquid zone controllers. The addition of control devices may help to address and improve safety margins including an improvement in the form factor in each core of the entire reactor. Additional work is also needed to study the xenon transient effect in the thermal and fast core.

4) Investigate other applications of the MSCR; for example, in the burning of minor actinides and to produce medical isotopes.

5) In addition to considering the use of the CANFLEX fuel bundle design, other new bundle designs based on higher numbers of fuel rods (such as 62) could be investigated if thorium is a component of the fresh fuel mixture.

References

[1] K. Davenport, “Nuclear Weapons: Who Has What at a Glance,” 2016. [Online]. Available: https://www.armscontrol.org/factsheets/Nuclearweaponswhohaswhat. [Accessed: 12-Dec-2016].

[2] M. V Ramana, “Nuclear power: Economic, safety, health, and environmental issues of near-term technologies,” *Annu. Rev. Environ. Resour.*, vol. 34, 2009.

[3] Dwight D. Eisenhower, “Atoms for Peace Speech,” *International Atomic Energy Agency*, 1953. [Online]. Available: https://www.iaea.org/about/history/atoms-for-peace-speech. [Accessed: 01-Dec-2016].

[4] C. A. Ford, “Debating Disarmament:,” *Nonproliferation Rev.*, vol. 14, no. 3, pp. 401–428, 2007.

[5] Department of Energy, “Report to Congress on Advanced Fuel Cycle Initiative: The Future Path for Advanced Spent Fuel Treatment and Transmutation Research,” *Rep. to Congr.*, no. January, 2003.

[6] A. C. Morreale, M. R. Ball, D. R. Novog, and J. C. Luxat, “the Behaviour of Transuranic Mixed Oxide Fuel in a Candu - 900 Reactor,” in *PHYSOR 2012 – Advances in Reactor Physics*, 2012, no. January 2012.

[7] H. W. Bonin, *Management,Course notes for Course CC56*. Kingston: Royal Military College of Canada, 2012.

[8] B. Bergeslon and A. S. G. and G. V. Tikhomiro, “Application of Power Reactors for Transmutation of Actinides,” in *12th International Conference on Nuclear Engineering*, 2004.

[9] J. Brown, F. McLachlan, M. Sarsfield, R. Taylor, G. Modolo, and A. Wilden, “Plutonium Loading of Prospective Grouped Actinide Extraction (GANEX) Solvent Systems based on Diglycolamide Extractants,” *Solvent Extr. Ion Exch.*, vol. 30, no. 2, pp. 127–141, Mar. 2012.

[10] C. W. Forsberg, E. D. Collins, J. P. Renier, and C. W. Alexander, “Can thermal reactor recycle eliminate the need for multiple repositories?,” 2005.

[11] Koria Atomic Energy Research Institute, “Nuclear Data Center at KAERI,” 2011. [Online]. Available: http://atom.kaeri.re.kr/nuchart/. [Accessed: 01-Jan-2011].

[12] NUCLEAR ENERGY AGENCY, “Minor Actinide Burning in Thermal Reactors A Reby the Working Party on,” 2013.

[13] Encyclopaedia Britannica, “Encyclopaedia Britannica, ‘Strategic Arms Reduction Talks,’” 2011. [Online]. Available: http://www.britannica.com/EBchecked/topic/568184/Strategic-Arms-Limitation-Talks-SALT.

[14] “Environmentalists Against War.” [Online]. Available:

http://www.envirosagainstwar.org/know/read.php?itemid=17838. [Accessed: 24-Jan-2017].

[15] “USEC marks final uranium shipment in ‘megatons to megawatts’ program.,” 2013. [Online]. Available: http://generationhub.com/2013/12/10/usec-marks-final-uranium-shipment-in-megatons-to-m.

[16] “Uranium and Depleted Uranium - World Nuclear Association.” [Online]. Available: http://www.world-nuclear.org/information-library/nuclear-fuel-cycle/uranium-resources/uranium-and-depleted-uranium.aspx. [Accessed: 26-Jan-2017].

[17] IAEA, “Status and Advances in MOX Fuel Technology,” 2003.

[18] NNSA, “Under U.S.-Russia Partnership, Final Shipment of Fuel Converted From 20,000 Russian Nuclear Warheads Arrives in United States and Will Be Used for U.S. Electricity,” 2013. [Online]. Available:

https://nnsa.energy.gov/mediaroom/pressreleases/megatonstomegawatts. [Accessed: 20-Apr-2012].

[19] A. C. Morreale, “Analysis of Transuranic Mixed Oxide Fuel in a CANDU Nuclear Reactor,” McMaster University, 2013.

[20] J. Whitlock, “The Canadian Nuclear FAQ - Section F: Security and Non-Proliferation,” 2011. [Online]. Available: http://www.nuclearfaq.ca/cnf_sectionF.htm. [Accessed: 05-Nov-2016].

[21] F. C. Dimayuga, Y. N. Zhou, M. A. Ryz, and R. M. Hoyd, “Status of Irradiation Testing

and PIE of MOX (Pu-Containing Fuel)," in *the Fourth International Conference on CANDU Fuel*, 1995.

[22] F. C. Dimayuga, "Fabrication of Simulated Mid-Burnup CANDU Fuel in the RFFL," in *5th Intl. Conf. on CANDU Fuel*, 1997.

[23] P. G. Boczar and et. al., "Advanced CANDU Systems for Plutonium Destruction," *NATO Advanced Research Workshop on Advanced*. Moscow, Russia, Oct-1996.

[24] B. Hyland, "Transmutation of Actinides Using Heavy Water Reactors and Sodium Cooled Fast Reactors," Ph.D. thesis, Royal Military College of Canada, 2017.

[25] R. Avery, "Theory of Coupled Reactor," in *2nd International Conference on the Peaceful Uses Atomic Energy*, 1958, pp. 182–188.

[26] R. Avery, "Coupled Fast-Thermal Power Breeder," *Nucl. Sci. Eng.*, vol. 3, pp. 129–144, 1957.

[27] K. Nishihara, "Numerical Validation of the Theory of Coupled Reactors for the Heavy Water Critical Assembly DCA," *J. Nucl. Sci. Technol.*, vol. 36, pp. 265–272, 1999.

[28] M. Pesic and et. al., "Study on Criticality Of Coupled Fast-Thermal Core ,HERBE, At (RB) Reactor," *Ann. Nucl. Energy*, vol. 18, no. 7, pp. 413–420, 1991.

[29] M. Komata, "On the Derivation of Avery's Coupled Reactor Kinetic Equations," *J. Nucl. Sci. Eng.*, vol. 38, pp. 193–204, 1969.

[30] K. Kobayashi, "Rigorous derivation of nodal equations for coupled reactors," *Ann. Nucl. Energy*, vol. 18, no. 1, pp. 13–18, 1991.

[31] K. Kobayashi, "Rigorous derivation of Static and Kinetic Nodal Equations for Coupled Reactors Using Transport Equations," *J. Nucl. Sci. Technol.*, vol. 28, pp. 389–398, 1991.

[32] F. Allen, "Extending the CANDU Nuclear Reactor Concept: The Multi- Spectrum Nuclear Reactor. Feasibility Study of Designing the Multi-Spectrum Nuclear Reactor Using the CANDU's Unique Features," Royal Military College of Canada, 2009.

[33] S. Glasstone and A. Sesonsky, *Nuclear Reactor Engineering*, 4th editio. Springer, 1994.

[34] T. Kiguchi, *Nuclear Reactor Design*. 2014.

[35] K. D. Kok, *Nuclear engineering handbook*. CRC Press, 2009.

[36] J. Duderstadt and L. Hamilton, *Nuclear Reactor Analysis*. John Wiley and Sons, Inc. New York, NY, USA, 1976.

[37] Yoshiaki Oka, *Nuclear Reactor Design*, vol. 2. 2014.

[38] D. G. Cacuci, *Handbook of Nuclear Engineering*, vol. 2 and 3. Springer Science & Business Media, 2010.

[39] A. E. Waltar, D. R. Todd, and P. V. Tsvetkov, Eds., *Fast Spectrum Reactors*. Boston, MA: Springer US, 2012.

[40] M. J. Anthiny, *An Introduction to the Engineering of Fast Nuclear Reactors*, First publ. Cambridge University Press, 2014.

[41] W. S. Yang, "Fast reactor physics and computational methods," *Nucl. Eng. Technol.*, vol. 44, no. 2, pp. 177–198, 2012.

[42] J. R. Lamarsh, *Introduction to Nuclear Reactor Theory*, Second. New York: ddison-Wesley Publishing Copmany, 1972.

[43] Atomic Energy of Canada Limited, "WIMS-AECL 3.1.2.1." Chalk River Laboratories Chalk River, Ontario, Canada, 2004.

[44] Los Alamos National Laboratory of university of, "Theory and use of the general geometry TWOTRAN program." California, New Mixico, 1970.

[45] J. Leppänen, *Development of a New Monte Carlo reactor physics code*, no. 640. 2007.

[46] L. A. N. Lab, "'Monte Carlo N–Particle Transport Code System, MCNP5 1.51.' Radiation Safety Information" Computational Center." 2008.

[47] M. S. Hussein, H. W. Bonin, and B. J. Lewis, "Numerical Verification of the Theory of Coupled Reactors for Deuterium Critical Assembly Using MCNP5 code," in *Canadian Nuclear Society*, 2013.

[48] R. Schwarz, "The Visual Editor for MCNP." Visual Editor Consultants, 2014.

[49] J. T. Goorley *et al.*, “MCNP6 User’s Manual, Version 1.0, LA-CP-13-00634,” p. 765, 2013.

[50] Atomic Energy of Canada Limited, “GENTILLY-2 Nuclear Power Station DATA-AECL,” 1974.

[51] Atomic Energy of Canada Limited, “Table of thermodynamic properties of heavy water in S.I. Units," Document AECL 7531,” Chalk River.

[52] “A. Technologies, ‘ATI wah Chang,’ Allegheny Technologies.” [Online]. Available: http://www.atimetals.com/businesses/atispecialtyalloysandcomponents/products/Documents/Zr nuke waste disposal.pdf. [Accessed: 20-Feb-2014].

[53] M. S. Hussein, H. W. Bonin, and B. J. Lewis, “Calculation of the Radial and Axial Flux and Power Distribution for a CANDU 6 Reactor with both the MCNP6 and Serpent Codes,” *Pbnc 2014*, no. Pbnc, pp. 1–13, 2014.

[54] G. T. Bereznai and G. Harvel, “Workshop on Nuclear Power Planet Simulators: Introduction to CANDU Systems and Applications,” pp. 1–258, 2011.

[55] M. H. Rabir, J. Abdul Karim, and M. . Salleh, “Power and Neutron Flux Calculation for the Puspati Triga Reactor Using MCNP,” *J. Sains Nukl. Malaysia*, vol. 24, no. 1, pp. 22–32, 2012.

[56] L. Snoj and M. Ravnik, “Calculation of Power Density with MCNP in TRIGA Reactor,” 2006.

[57] M. S. Hussein, H. W. Bonin, and B. J. Lewis, “Burnup Calculation of a CANDU6 Reactor Using the Serpent and MCNP6 Codes,” *Pbnc 2014*, no. Pbnc, pp. 1–7, 2014.

[58] J. Leppänen, “Development of a new Monte Carlo reactor physics code,” Helsinki University of Technology, VTT Publications, 2007.

[59] M. S. Hussein, H. W. Bonin, B. J. Lewis, and P. K. Chan, “Design of a Multispectrum CANDU-Based Reactor, MSCR, with 37-Element Fuel Bundles Using Sserprnt Code,” in *The 7th International Conference on Modelling and Simulation in Nuclear Science and Engineering (CMSNSE 2015),* 2015.

[60] W. F. G. van Rooijen, “Gas-Cooled Fast Reactor: A Historical Overview and Future

Outlook," *Sci. Technol. Nucl. Install.*, vol. 2009, pp. 1–11, 2009.

[61] W. Rooijen, "Improving Fuel Cycle Design and Safety Characteristics of a Gas Cooled Fast Reactor," Delft University, 2006.

[62] J. C. Lefèvre, C. H. Mitchell, and G. Hubert, "European fast reactor design," *Nucl. Eng. Des.*, vol. 162, no. 2–3, pp. 133–143, Apr. 1996.

[63] A. T. Incorporated, "Technical Data Sheet ,ATI 316 Stainless Steel: Austenitic (UNS S31600)."

[64] ATI, "Technical Data Sheet ,ATI 316 Stainless Steel: Austenitic (UNS S31600)," Pittsburgh, PA 15222-5479 U.S.A., 2014.

[65] A. S. of M. Engineers., *ASME boiler and pressure vessel code: an international code. Section I, Section I,*. New York: American Society of Mechanical Engineers, 2010.

[66] S. L. Mannan, S. C. Chetal, B. Raj, and S. B. Bhoje, "Selection of materials for prototype fast breeder reactor," *Trans. Indian Inst. Met.*, vol. 56, no. 2, pp. 155–178, 2003.

[67] M. D. Mathew, "Evolution of creep resistant 316 stainless steel for sodium cooled fast reactor applications," *Trans. Indian Inst. Met.*, vol. 63, no. 2–3, pp. 151–158, Apr. 2010.

[68] ATI Allegheny Ludlu, "TECHNICAL DATA BLUE SHEET," USA, Technical Data Sheet, Oct. 2014.

[69] P. A. Schweitzer, *Metallic materials: physical, mechanical, and corrosion properties*, no. 19. New York: M. Dekker, 2003.

[70] World Nuclear Association, "Military Warheads as a Source of Nuclear Fuel Title," 2012. [Online]. Available: http://www.world-nuclear.org/information-library/nuclear-fuel-cycle/uranium-resources/military-warheads-as-a-source-of-nuclear-fuel.aspx. [Accessed: 20-Mar-2012].

[71] U. Gat, J. R. Engel, and H. L. Dodds, "Molten Salt Reactors for Burning Dismanteld Weapons Fuel," *Nucl. Technol.*, vol. Journal Vo, no. 3, p. 100, 1992.

[72] D. G. Martin, "The thermal expansion of solid UO2 and (U, Pu) mixed oxides — a review and recommendationse," *J. Nucl. Mater.*, vol. 152, no. 2, pp. 94–101, 1988.

[73] W. World Information Service on Energy, “MOX Fuel Calculator,” 2012. [Online]. Available: http://www.wise-uranium.org/nfcmx.html. [Accessed: 15-Jun-2014].

[74] M. S. Hussein, H. W. Bonin, and B. J. Lewis, “Burning Plutonium in the Multi-Spectrum CANDU-Based Reactor (MSCR) Using the Serpent Code,” in *13th International Conference on CANDU Fuel*, 2016.

[75] D. Rozon, *Introduction to Nuclear Reactor Kinetics*. Polytechnic International Press, 1998.

[76] European Commission Research Center, “Introduction to the Monte Carlo method,” *Engineering*, 2008. [Online]. Available:

https://www.nucleonica.com/wiki/images/d/df/EMC_2008_short.pdf.

Appendices

Appendix (A)

Monti Carlo Calculations Scoring or Tallying

- **There are two Fundamental Tallies in the neutron transport in the media Particle**

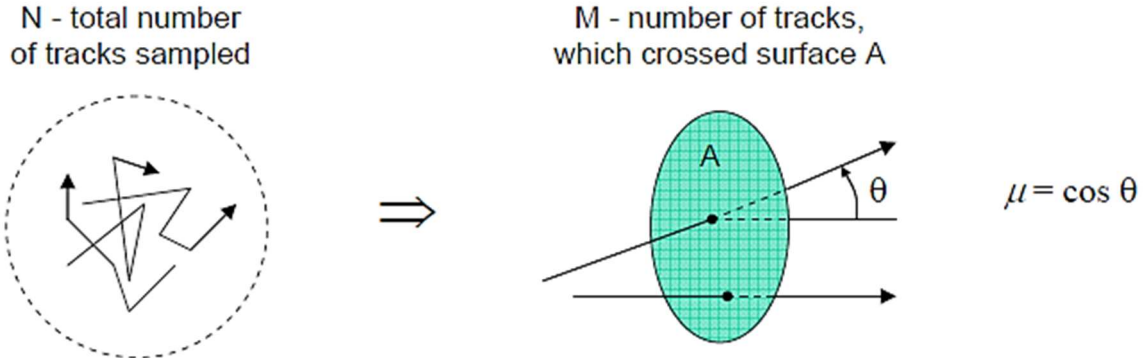

1) **Particle Current:** The number of particles crossing surface A normalized per one source particle

$$J = \frac{\sum_{i=1}^{M} 1}{N} = \frac{M}{N} \qquad [J] = 1$$

2) **Particle Flux:** The number of particles crossing surface A normalized per one source particle and per square centimeter of the surface area seen from the direction of the particle. This area is calculated as $A_\mu = A \cdot |\mu|$, where $|\mu|$ is the absolute value of cosine of angle between surface normal and particle trajectory.

$$\Phi = \frac{\sum_{i=1}^{M} 1/|\mu_i|}{NA} \qquad [\Phi] = cm^{-2}$$

- **Cell Particle Flux or Track-Length Estimator**

The particle flux definition above gives the value of the flux averaged over a surface, so called the Surface Flux Tally. If we are interested in the particle flux averaged over a cell such as the fuel channel; fuel pin or part of the fuel channel of the bundle length as applied in Chapters 6 then the track-length estimator tally will be more suitable.

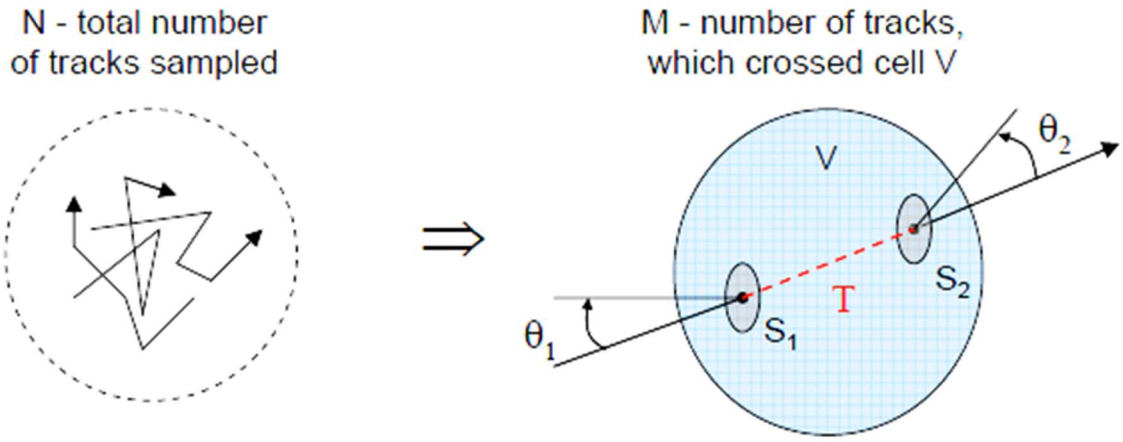

The estimate of the particle flux averaged over cell is given by the following formula [76]:

$$\Phi = \frac{\sum_{i=1}^{M} T_i}{N\,V}$$

Where, T is the track length of particles inside the cell, and V is the cell volume.

This track length estimator flux is measured in unit n.cm^{-2} and this represent the output flux in the MCNP to convert this into the average flux per cell the relation

- **Calculation of Actual Flux**

$$\Phi_E^{actual(Channel)}(n/cm^2.s) = \frac{\varphi_E^{F4(Channel)} \times (P_{total\ thermal} \times \upsilon)}{(q_{value/fission} \times k_{eff})}$$

where,

$\varphi_E^{F4(Channel)}$ is the F4 tally results of the track length estimator flux calculated in unit of cm^{-2} (using the codes),

$P_{total\ therm}$ is the total thermal power of the reactor in Watts,

υ is the average number of neutrons per fission,

$q_{value/fission}$ is the average thermal energy dissipated in the core per fission in Joules, and

k_{eff} is the multiplication factor.

This equation is suitable to calculate the actual flux in the unit of (n cm^{-2} s^{-1}) from the results of the MCNP code but for the Serpent code one sets the normalized power at fixed value in the core. The Serpent code can calculate the average cell flux at each energy bin.

- **Neutron Transport in Monte Carlo calculation**

Figure (A-1)) shows the generating the "history" of neutrons in a Monte Carlo calculation.

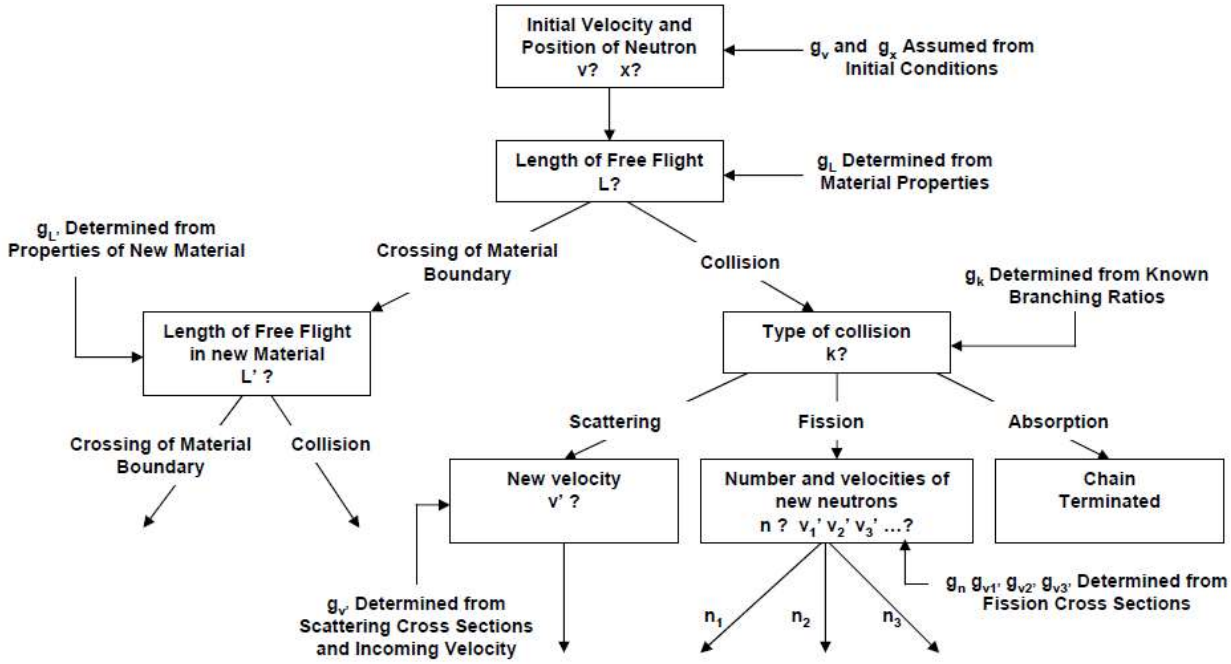

Figure (A-1): schematic of some of the decisions that are made to generate the "history" of a neutron in a Monte Carlo calculation[76]**.**

Appendix (B)

Optimizing the Number of Histories of the CANDU 6 GENTILLY-2 Reactor Model

As common in Monte Carlo calculations, the relative error of the calculation is proportional to the inverse of the root of the number of histories. Therefore, as the number of histories increases, the results become more accurate. The number of histories is chosen so that the flux and the multiplication factor k_{eff} converge. In addition, the flux results of each tally pass the error checker in the calculation of the code and the figure of merit of each tally remains the same. All calculated tallies in this work passed the various confidence tests.

- MCNP6

Figure (B-1) to Figure (B-4) show the changing multiplication factors k_{eff} and the average total flux for a fresh CANDU-6 core using the MCNP6 code. The simulation was run from 500 cycles to 18000 cycles with an increasing neutron number per cycles from 500 to15000 n cycle^{-1}.

One notices that the k_{eff} converges before the flux. The convergence number of histories has been chosen according to the flux convergence value. The convergence value of the k_{eff} and the average total flux in the core are (1.09157 ±0.00003) and (1.6667E-6 ±0.00001 n cm^{-2}) at 15000 n cycle^{-1}/18000 cycles, respectively.

The k_{eff} and the average total flux start to converge to a constant value at 5000 n/cycle for 5000 cycles with k_{eff} =1.09151±0.0009 and a total average fluence of 1.6666E-6 ±0.0001 n cm^{-2}. To save computational time, the chosen number of histories for the MCNP6 simulation was 5000 n/cycle for 5000 cycles, and the number of inactive cycles is optimized at 100 cycles.

- Serpent

Similarly, one can show the variation of the k_{eff} and average total flux of the CANDU-6-simulation model of the fresh core using the Serpent code. The simulation was run with an increasing number of neutron per cycle from 500 to 15000 n cycle^{-1}.

One notices that the k_{eff} is converging before the total flux converges. The convergence number of histories has been chosen according to the total flux convergence value. The convergence value of k_{eff} and the total average fluence in the core are 1.08676 ±0.00008 and

1.62557E-6 ±0.00002 n cm^{-2} at 15000 n $cycle^{-1}$ /15000 cycle respectively. The multiplication factor k_{eff}, and the flux converge at smaller histories of 8000 n $cycle^{-1}$ for 5000 cycles at k_{eff} =1.08646 ±0.0002 and the total average track length estimator flux is at 1.62505E-6 ±0.00014 n cm^{-2}. To save computational time, the chosen number of histories is 8000 n $cycle^{-1}$ for 5000 cycles.

In both simulations, the change in the final average values of k_{eff} and the total average flux was not significant as the number of inactive cycle increases above 100 so the number of inactive cycles is optimized at 100 cycles. The reactivity and the average total flux are comparable in the MCNP and Serpent simulations with that reported in Reference[53].

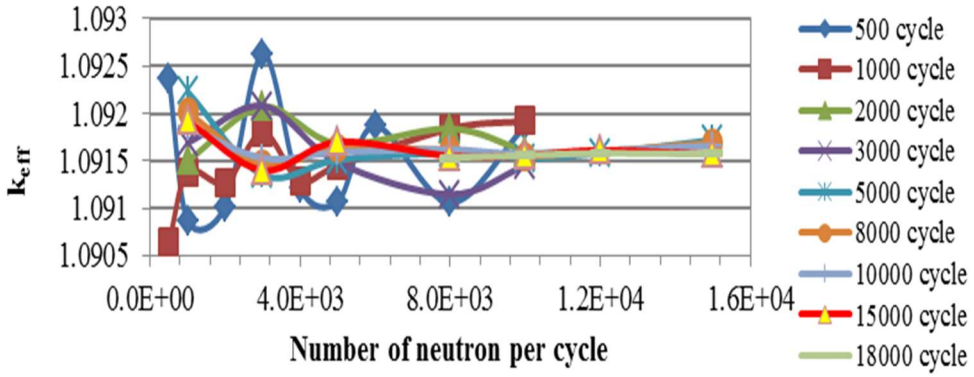

Figure (B-1): Optimization of the Multiplication Factor k_{eff} with the Number of Histories Using MCNP6.

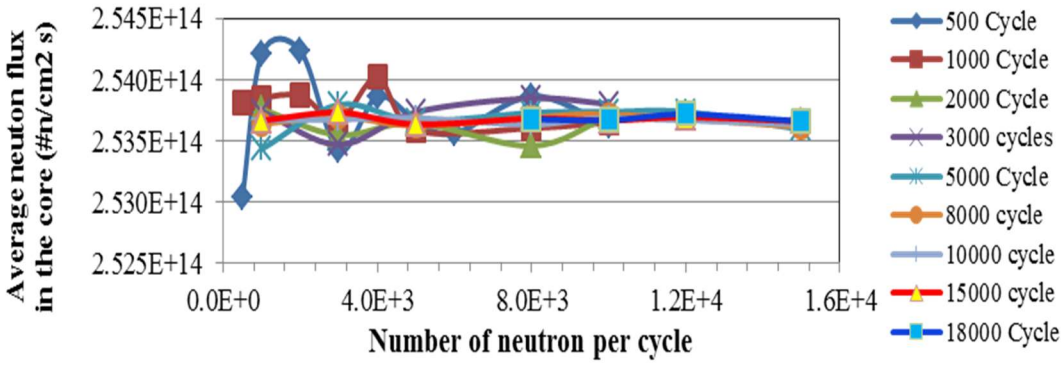

Figure (B-2): Optimization of the Average Total Flux in the Core

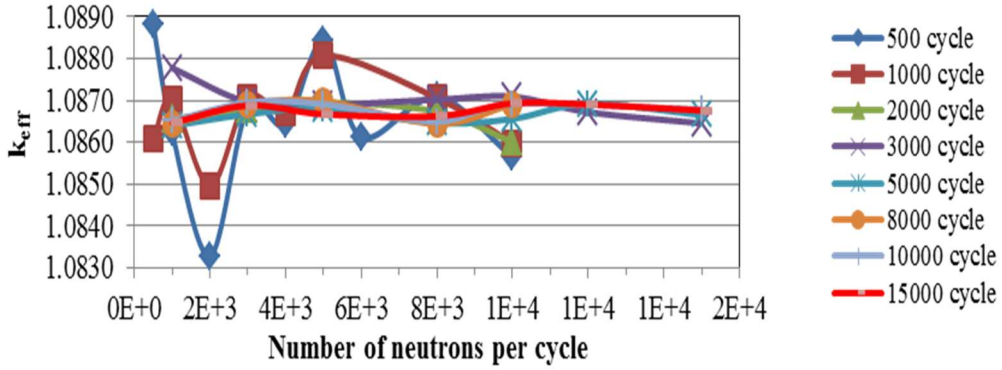

Figure (B-3)10: Optimization of the Multiplication Factor k_{eff} Histories Using the Serpent Code.

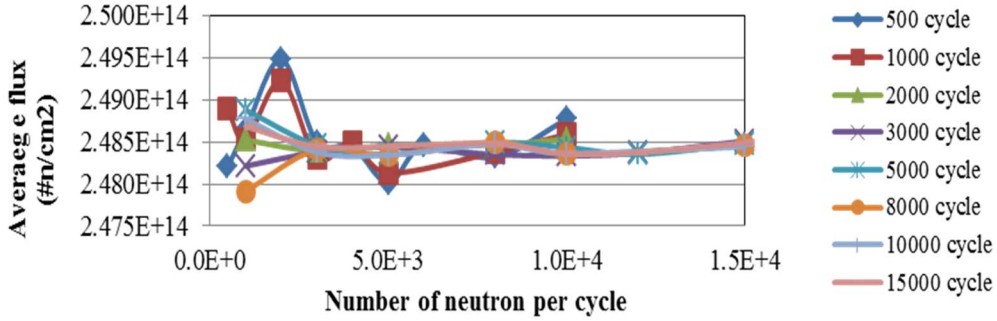

Figure (B-4): Optimization of the Average Total Flux with Number of Histories Using the Serpent Code

Appendix (C)

Design Parameters of the CANDU6 GENTILLY-2 Reactor

The material composition, mass or atomic ratio, temperature, density and properties of the cladding, coolant, pressure tube, calandria tube, moderator and reflector used in both models are summarized in Table (A-1)

Table (C-1): Mass Ratio, Temperature and Density of Material in the CANDU-6 Reactor.

Component	Material	Mass Ratio or Atomic Ratio			Density g cm^{-3}	Temperature K
Fuel	Nat.U (UO_2)	U-234	4.767E-5	w/0	10.6	1200
		U-235	6.2670E-3			
		U-238	8.7516533E-1			
		O_2	1.1852E-1			
Cladding	Zircaloy-4 Grade-R60804	Zr	0.982	w/0	6.55	600
		Sn	0.015			
		Fe	0.002			
		Cr	0.001			

Coolant (Purity %99.3)	D_2O	H_2	7.051965E-04	a/0	0.818985	561
		D_2	1.999064E-01			
		^{16}O	7.990650E-01			
		^{17}O	3.234771E-04			
Pressure tube	Zircaloy-2.5% Nb	Zr	0.975	w/0	6.55	530
		Nb	0.025			
Air Gap		N_2	0.767	w/0	0.001293	350
		O_2	0.233			
Calandria Tube	Zircaloy-2 Grade-R60802	Zr	0.982	w/0	6.55	350
		Sn	0.015			
		Fe	0.0015			
		Cr	0.001			
		Ni	0.0005			
Moderator (Purity %99.75)	D_2O	H_2	2.517743E-04	a/0	1.1037265	330
		D_2	2.007214E-01			
		^{16}O	7.987034E-01			
		^{17}O	3.233307E-04			
Reflector	D_2O	H_2	2.517743E-04	a/0		330

(Purity %99.75)		D_2	2.007214E-01		1.1037265	
		^{16}O	7.987034E-01			
		^{17}O	3.233307E-04			

Appendix (D)

Design Parameters of the MSCR Reactor

Table (D-1): Design parameters of the Thermal Core of the MSCR Models

Component	Material	Mass Ratio or Atomic Ratio			Density g cm^{-3}	Temperature K
Fuel	Nat.U UO_2	U-234	4.76717E-5	w/0	10.664	1200
		U-235	6.267403E-3			
		U-238	8.752123E-1			
		O_2	1.1847263E-1			
Cladding	Zircaloy-4 Grade-R60804	Zr	0.982	w/0	6.55	600
		Sn	0.015			
		Fe	0.002			
		Cr	0.001			
Coolant (Purity %99.3)	D_2O	H_2	7.051965E-04	a/0	0.818985	561
		D_2	1.999064E-01			
		^{16}O	7.990650E-01			
		^{17}O	3.234771E-04			
Pressure tube	Zircaloy-2.5% Nb	Zr	0.975	w/0	6.55	530
		Nb	0.025			
Air Gap	Nitrogen and Oxygen	N_2	0.767	w/0	0.001293	350
		O_2	0.233			
Calandria Tube	Zircaloy-2 Grade-R60802	Zr	0.982	w/0	6.55	350
		Sn	0.015			
		Fe	0.0015			
		Cr	0.001			
		Ni	0.0005			
Moderator and Reflector (Purity %99.75)	D_2O	H_2	2.517743E-04	a/0	1.1037265	330
		D_2	2.007214E-01			
		^{16}O	7.987034E-01			
		^{17}O	3.233307E-04			

Table (D-2): Design parameters of the Fast Core of MSCR-Model (I) and (II) fuelled by U-19.9

Component	Material	Mass Ratio or Atomic Ratio			Density g cm^{-3}	Temperature K
		O_2	0.118726205			
Fuel	Enrichment UO_2.(19.19U-235/U)	U-234	4.77737E-5	w/0	10.6	1200
		U-235	0.173594822			
		U-238	0.707631199			
		O_2	1.1852E-1			
Cladding	Stainless Steel (316L(N))	Zr	0.982	w/0	6.55	600
		Sn	0.015			
		Fe	0.002			
		Cr	0.001			
Coolant (Purity %99.3)	He	H_2	7.051965E-04	a/0	0.818985	561
		D_2	1.999064E-01			
		^{16}O	7.990650E-01			
		^{17}O	3.234771E-04			
Pressure tube	Stainless Steel (316L(N))	Zr	0.975	w/0	6.55	530
		Nb	0.025			
Filling material	He	N_2	0.767	w/0	0.001293	350
		O_2	0.233			
Partition walls	Zircaloy-2 Grade-R60802	Zr	0.982	w/0	6.55	350
		Sn	0.015			
		Fe	0.0015			
		Cr	0.001			
		Ni	0.0005			

Table (D-3): Plutonium Fuel mass ratio

Component	Material	Mass Ratio or Atomic Ratio			Density g cm^{-3}	Temperature K
Fuel	Depleted uranium and Plutonium weapon grade	O_2	0.118354881		11.0634	1200
		U-234	1.27958E-05			
		U-235	2.219456E-3			
		U-238	0.747368487			
		Pu-239	0.122352287			
		Pu-240	9.278873E-3			
		Pu-241	5.82353E-07			
		Am-241	4.12638E-4			

Appendix (E)

Optimization of the Multiplication Factor (k_{eff}) and Total Flux of the MSCR Models with the Number of Histories Using the Serpent Code

MSCR-Model (II):

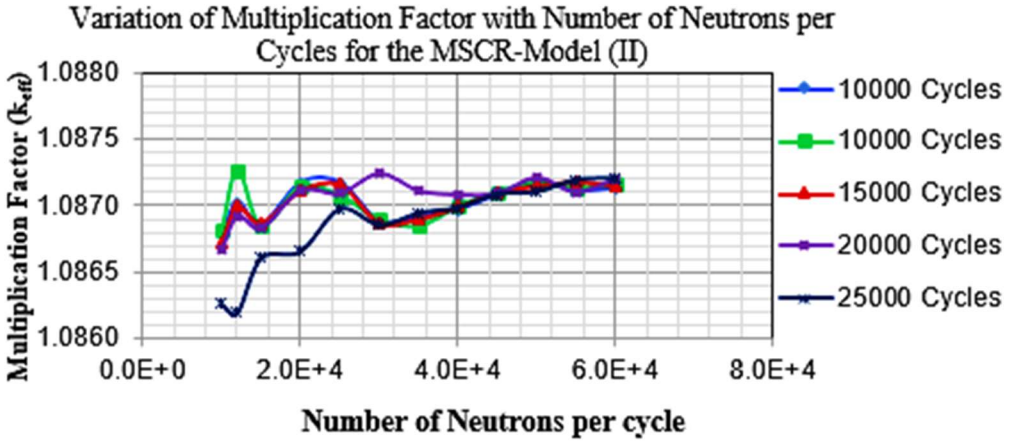

Figure (E-1): Optimization of the Multiplication Factor k_{eff} with the Number of Histories Using the Serpent Code for MSCR-Model (II)

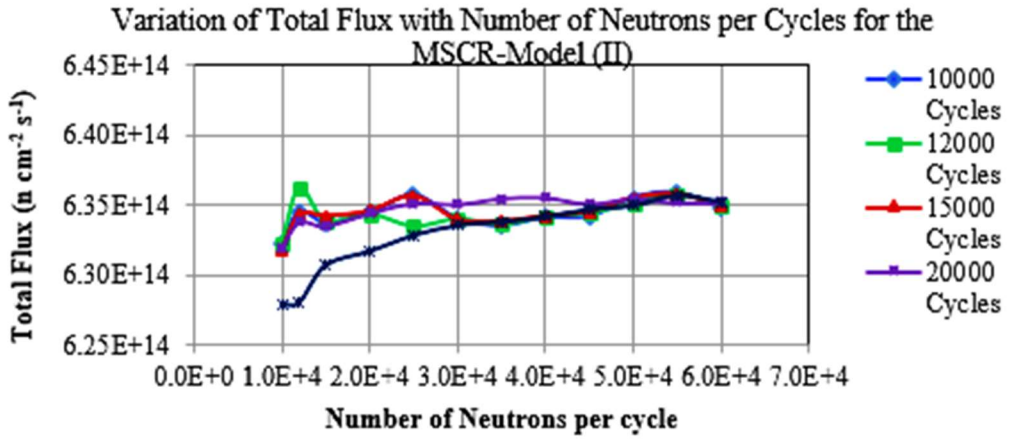

Figure (E-2): Optimization of the Total Flux with the Number of Histories Using the Serpent Code for MSCR-Model (II)

MSCR-Model (IV):

In the Model (IV), (V) and (VI), to save the computational time, the number of cycles are set at 15000 with the changing number of neutrons per cycles between 35,000n's /cycle to 60,000 n's/cycles. The multiplication factor and total flux are converging between these two values

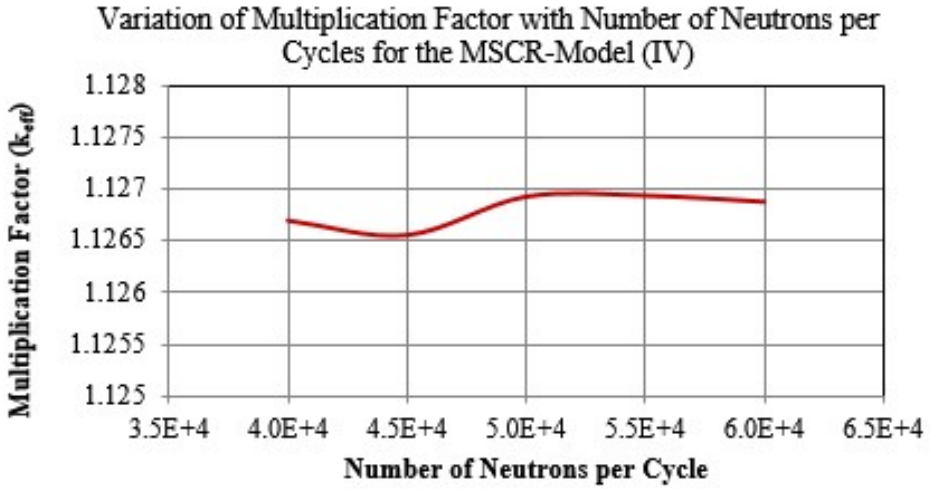

Figure (E-3): Optimization of the Multiplication Factor k_{eff} with the Number of Histories Using the Serpent Code for MSCR-Model (IV)

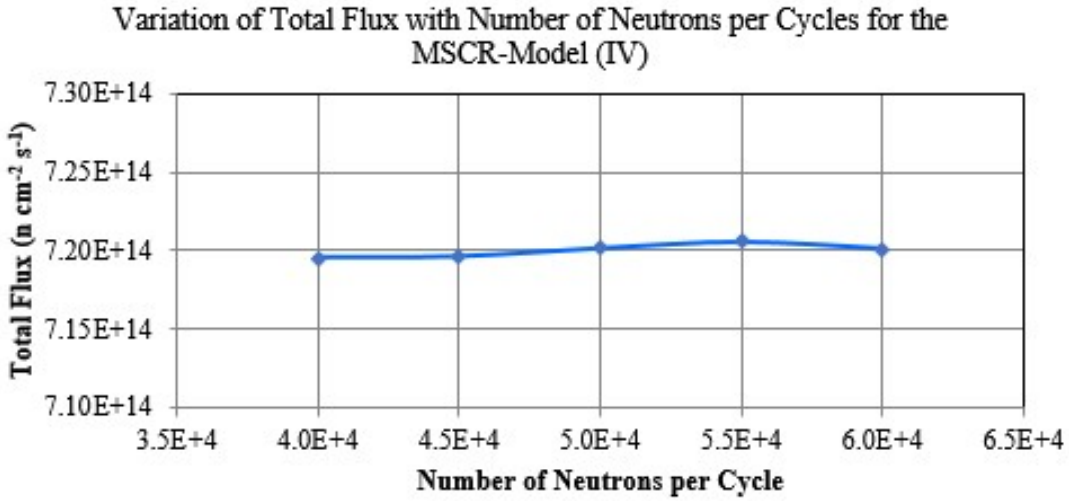

Figure (E-4): Optimization of the Total Flux with the Number of Histories Using the Serpent Code for MSCR-Model (IV)

MSCR-Model (V):

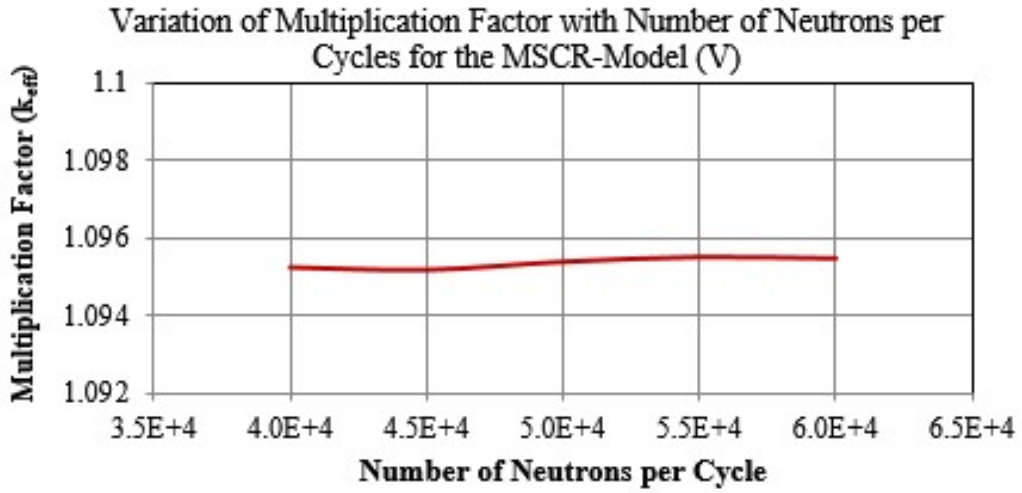

Figure (E-5): Optimization of the Multiplication Factor k_{eff} with the Number of Histories Using the Serpent Code for MSCR-Model (V)

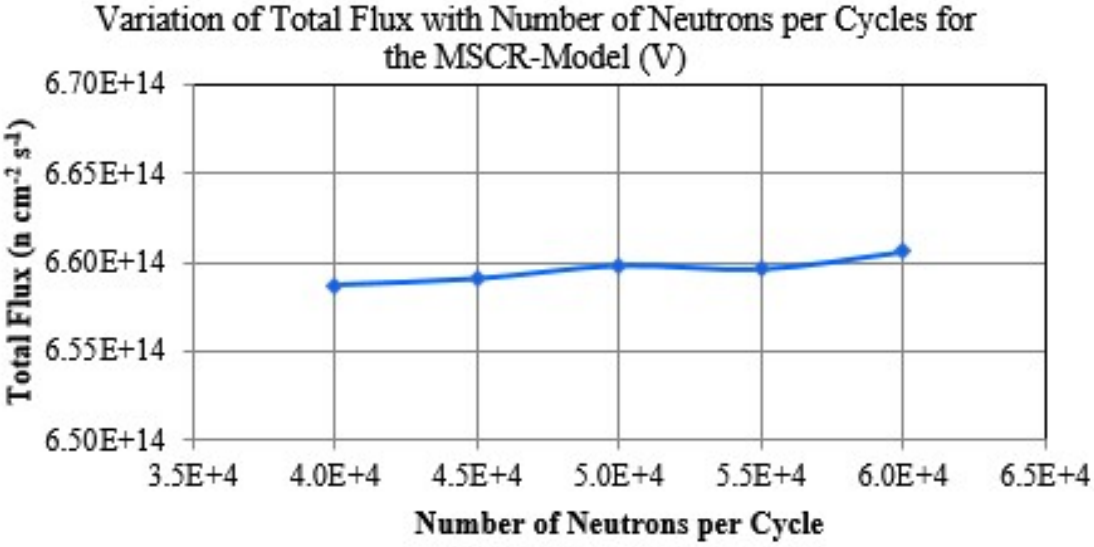

Figure (E-6): Optimization of the Total Flux with the Number of Histories Using the Serpent Code for MSCR-Model (V)

MSCR-Model (VI)

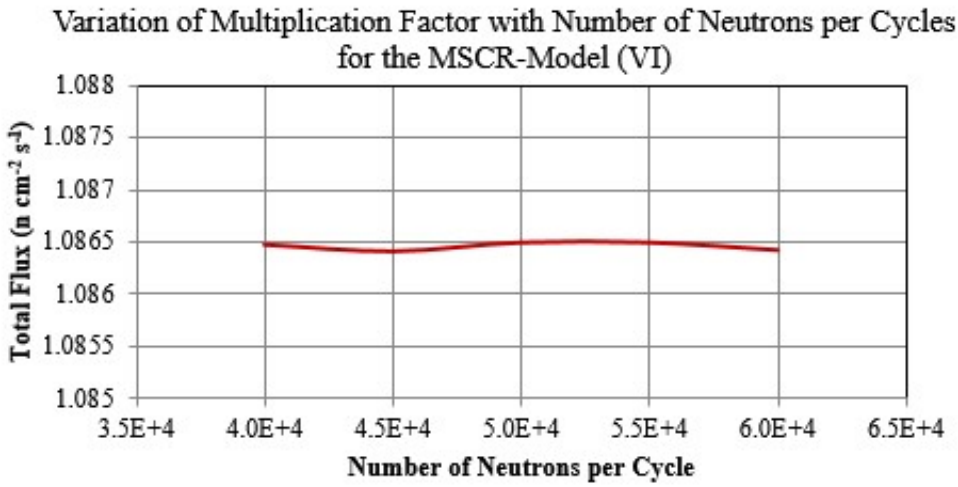

Figure (E-7): Optimization of the Multiplication Factor k_{eff} with the Number of Histories Using the Serpent Code for MSCR-Model (VI)

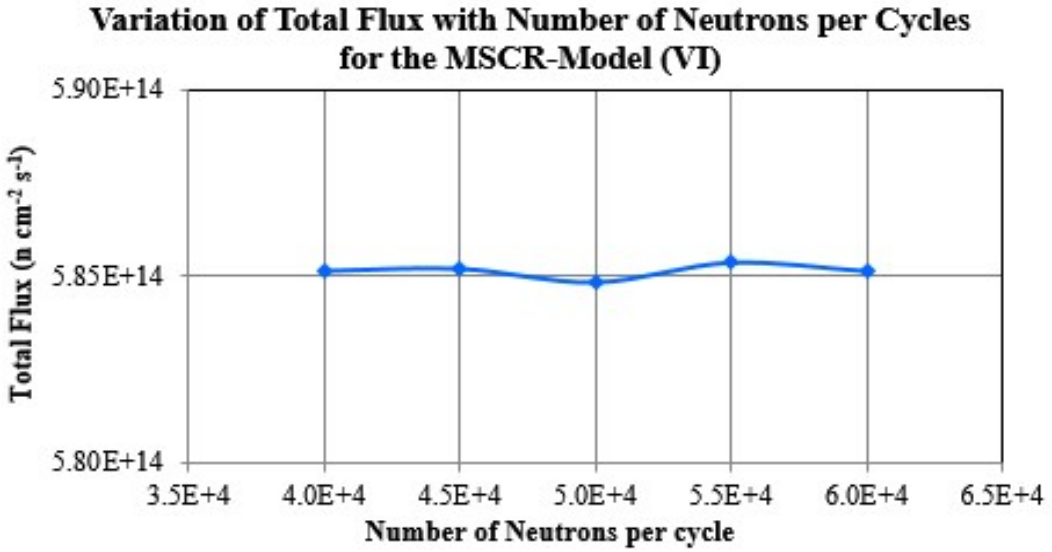

Figure (E-8): Optimization of the Total Flux with the Number of Histories Using the Serpent Code for MSCR-Model (VI)

Appendix (F)

Power Distribution of the MSCR-Model (III)

The following schematic diagrams represent the power density distributions of MSCR-Model (III) for the burnup time of 160 days in the unit of (Wcm^{-3})

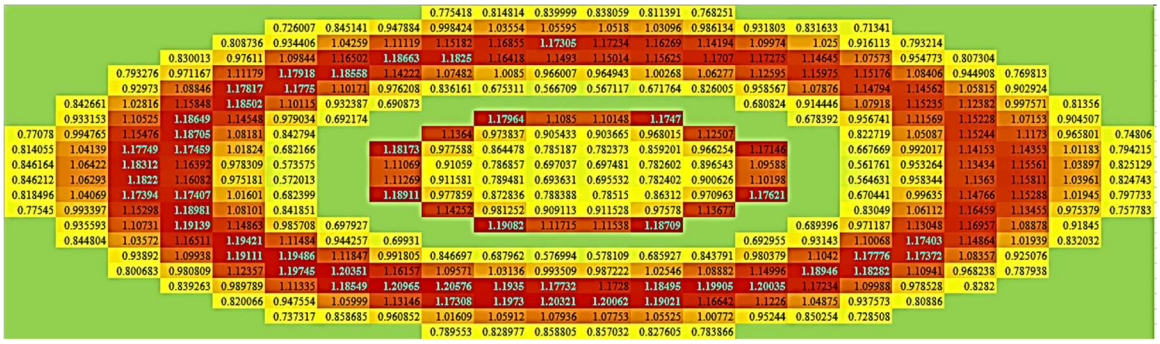

Power Distribution of the MSCR-Model (III) at Day (0)

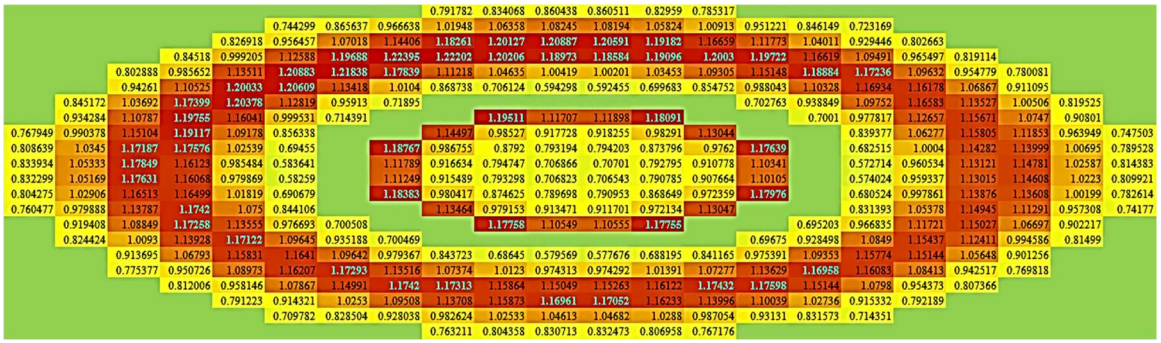

Power distribution of the MCNP-Model (III) after (0.5 day)

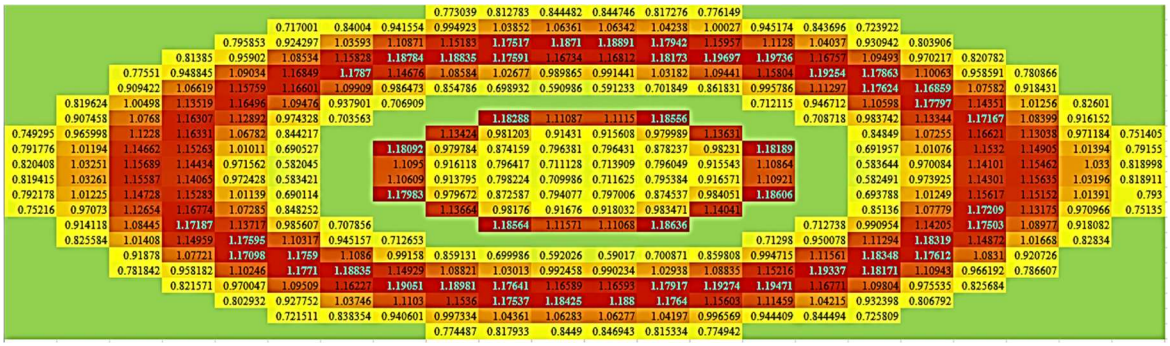

Power Distribution of the MSCR-Model (III) after (1 day)

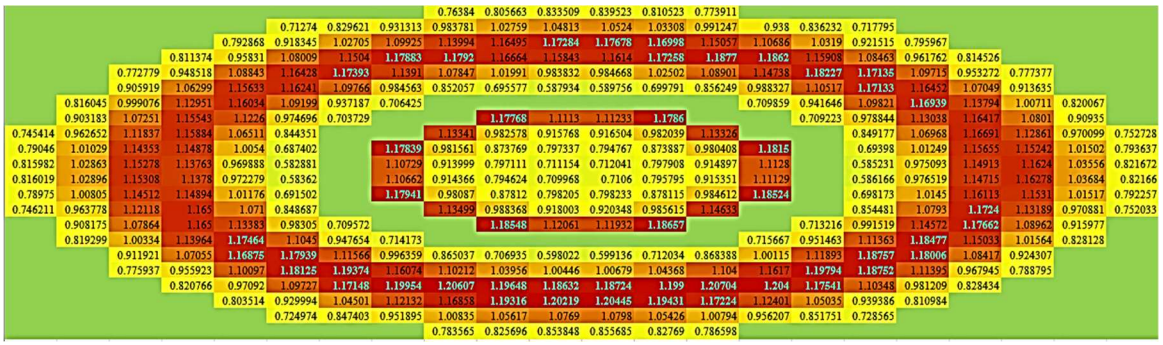

Power Distribution of the MSCR-Model (III) after (1.5 days)

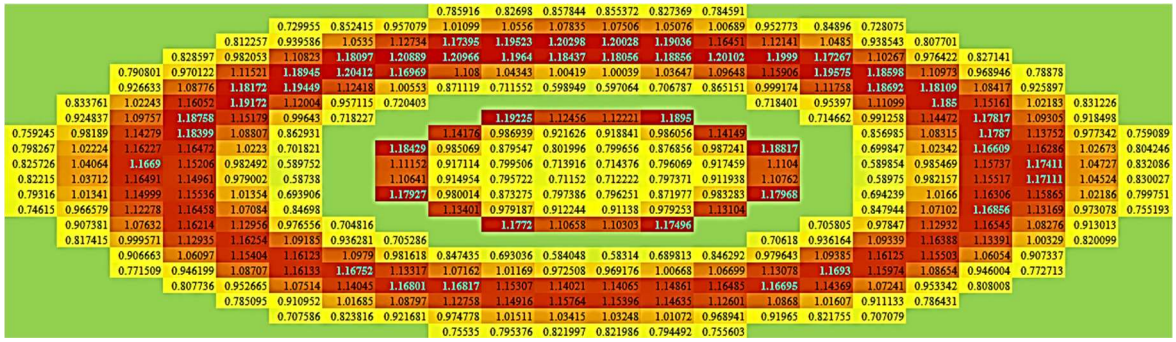

Power Distribution of the MSCR-Model (III) after (2 days)

Power Distribution of the MSCR-Model (III) after (3 days)

Power Distribution of the MSCR-Model (III) after (4 days)

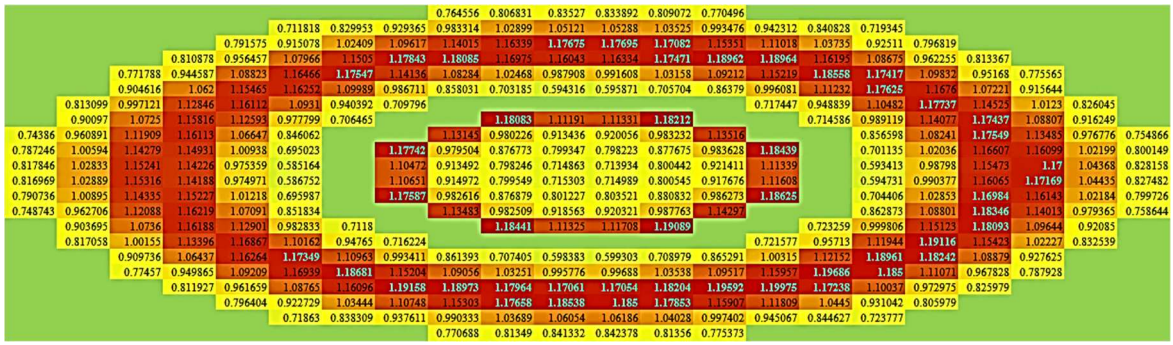

Power Distribution of the MSCR-Model (III) after (5 days)

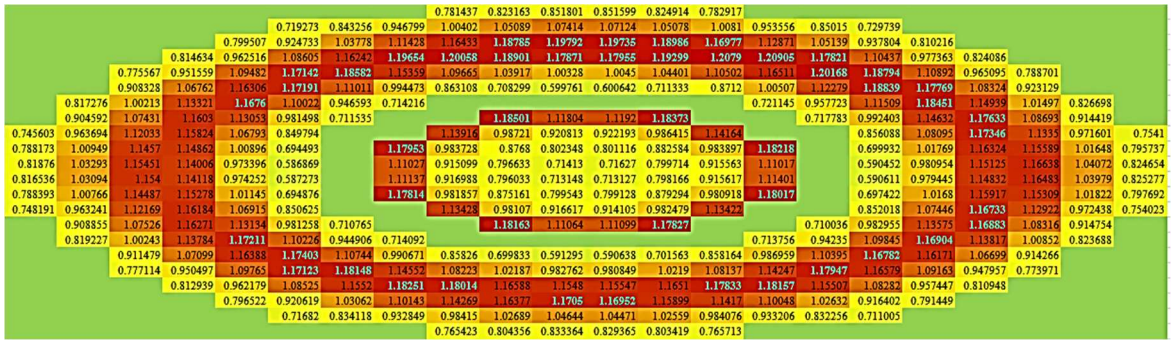

Power Distribution of the MSCR-Model (III) after (6 days)

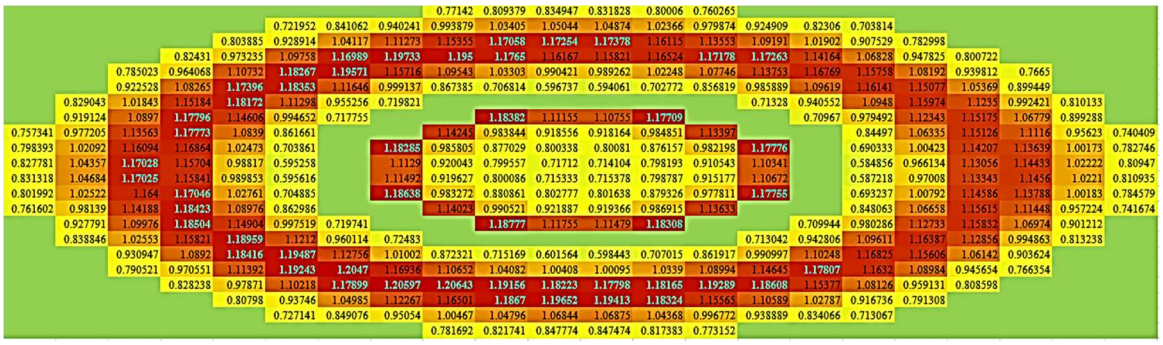

Power Distribution of the MSCR-Model (III) after (7 days)

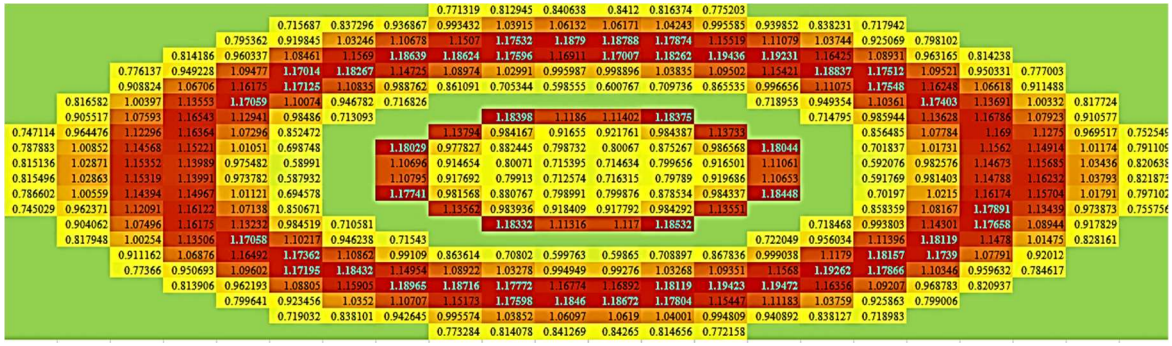

Power Distribution of the MSCR-Model (III) after (8 days)

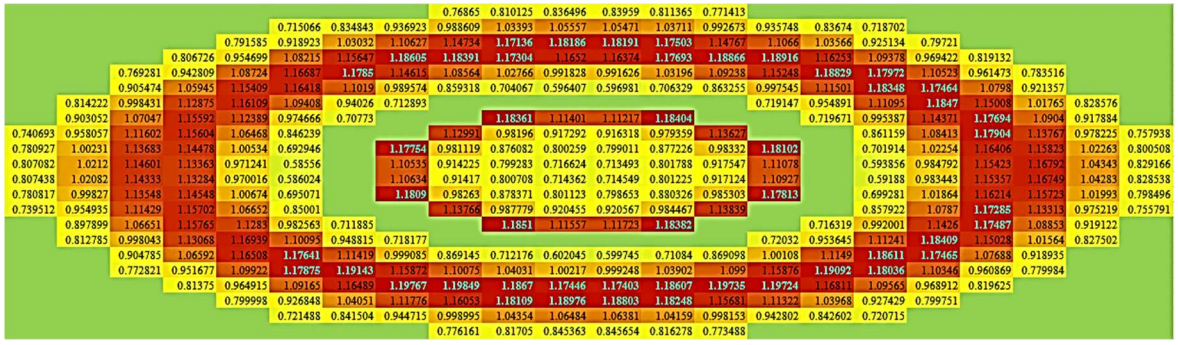

Power Distribution of the MSCR-Model (III) after (9 days)

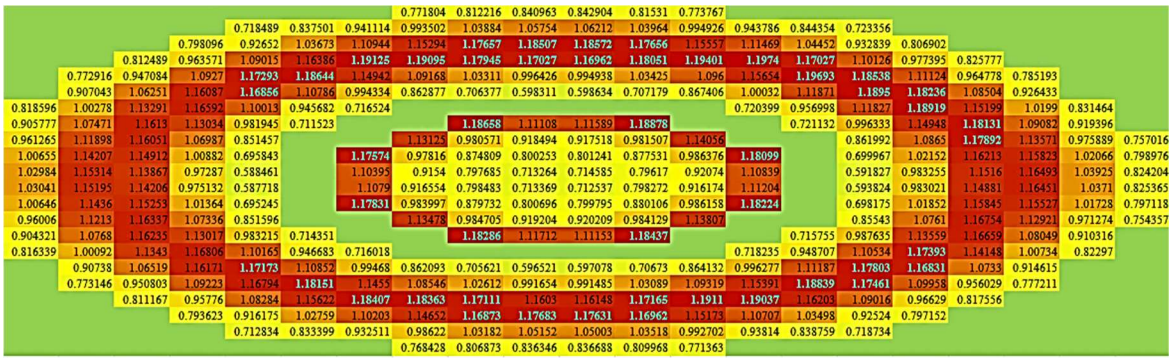

Power Distribution of the MSCR-Model (III) after (10 days)

Power Distribution of the MSCR-Model (III) after (15 days)

Power Distribution of the MSCR-Model (III) after (20 days)

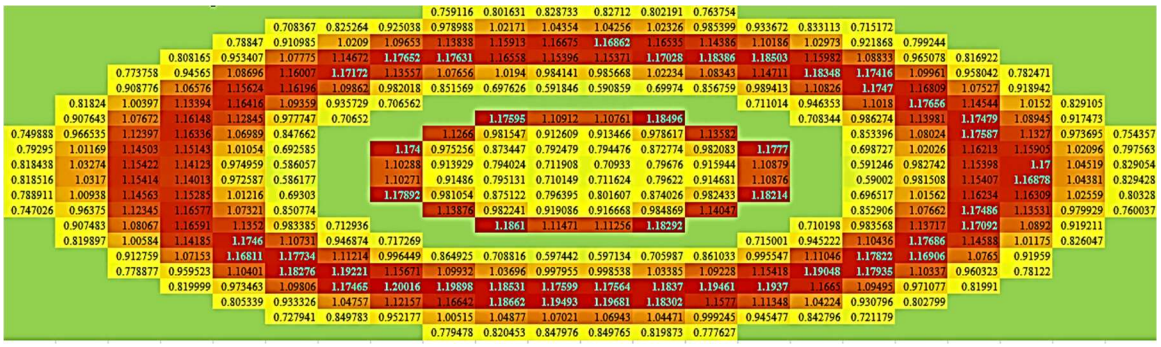

Power Distribution of the MSCR-Model (III) after (25 days)

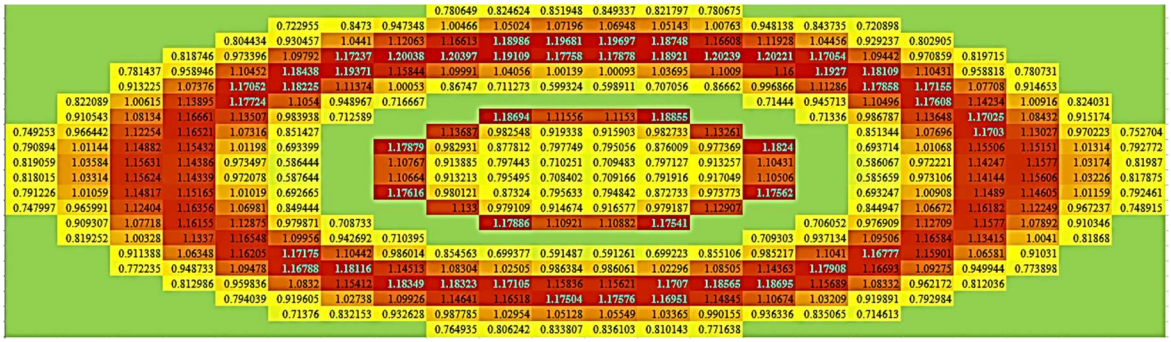

Power Distribution of the MSCR-Model (III) after (30 days)

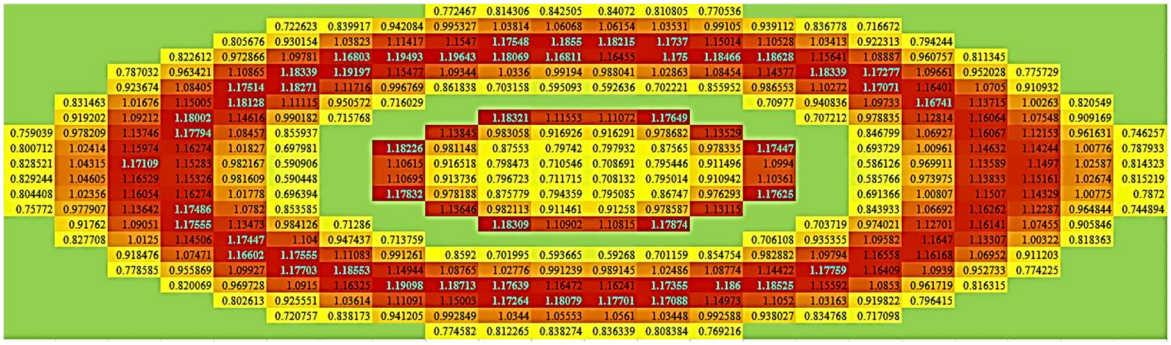

Power Distribution of the MSCR-Model (III) after (35 days)

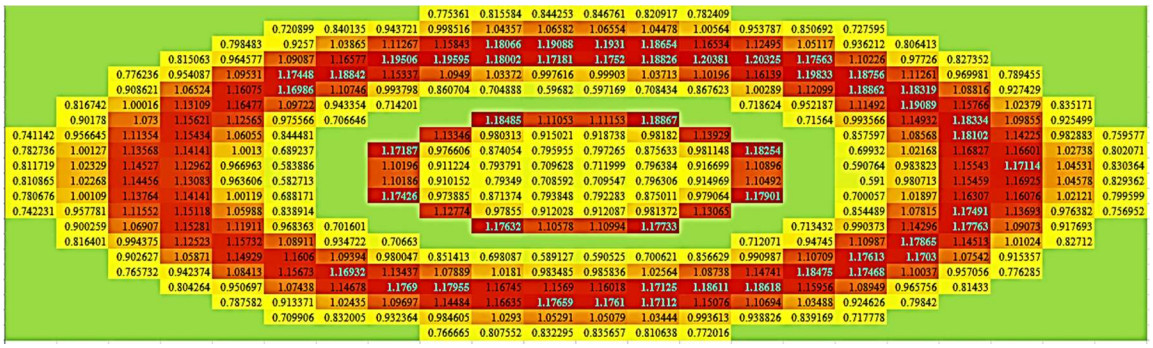

Power Distribution of the MSCR-Model (III) after (40 days)

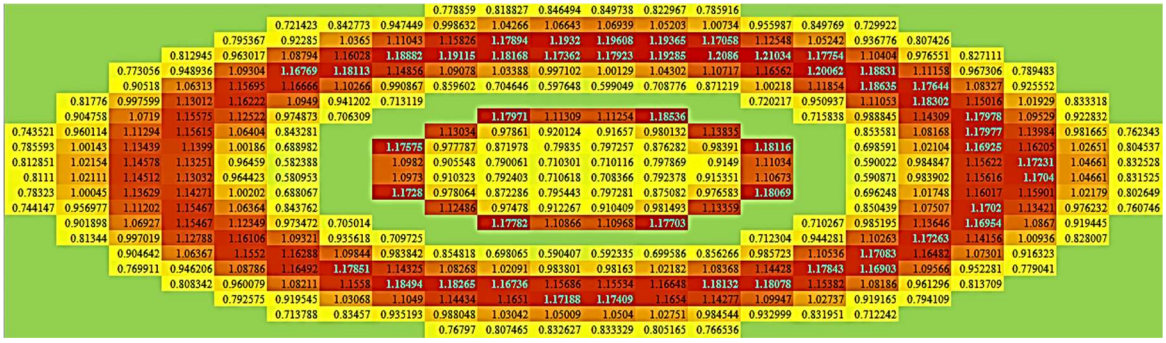

Power Distribution of the MSCR-Model (III) after (50 days)

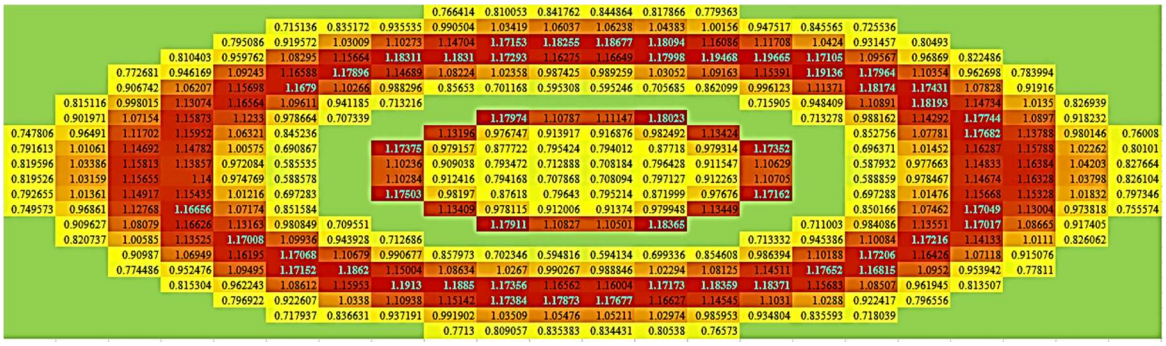

Power Distribution of the MSCR-Model (III) after (60 days)

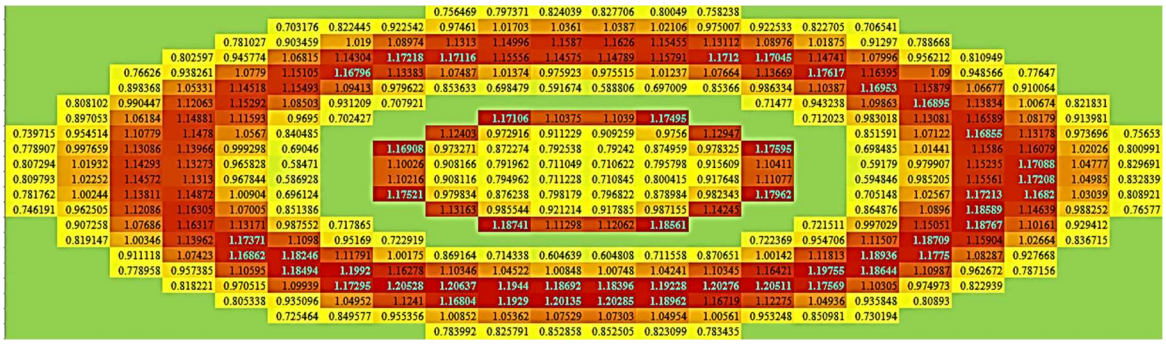

Power Distribution of the MSCR-Model (III) after (70 days)

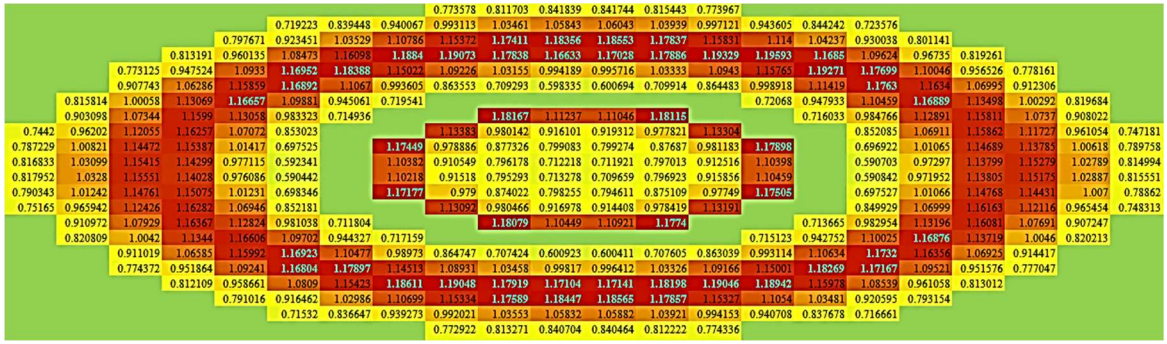

Power Distribution of the MSCR-Model (III) after (80 days)

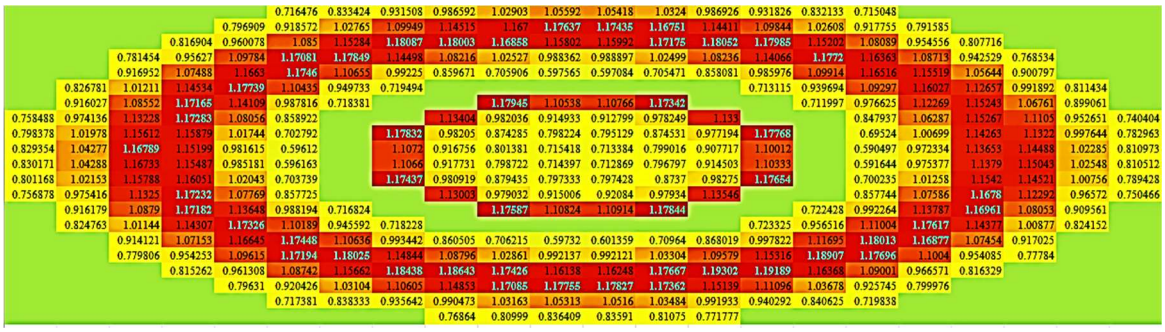

Power Distribution of the MSCR-Model (III) after (90 days)

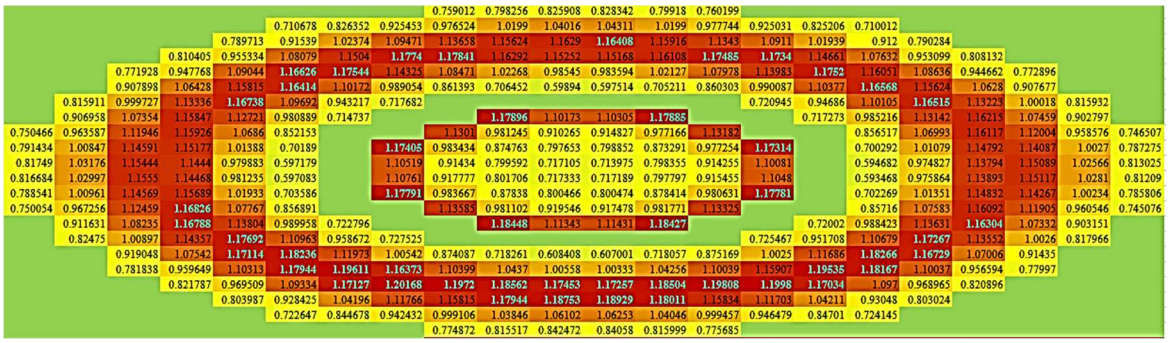

Power Distribution of the MSCR-Model (III) after (100 days)

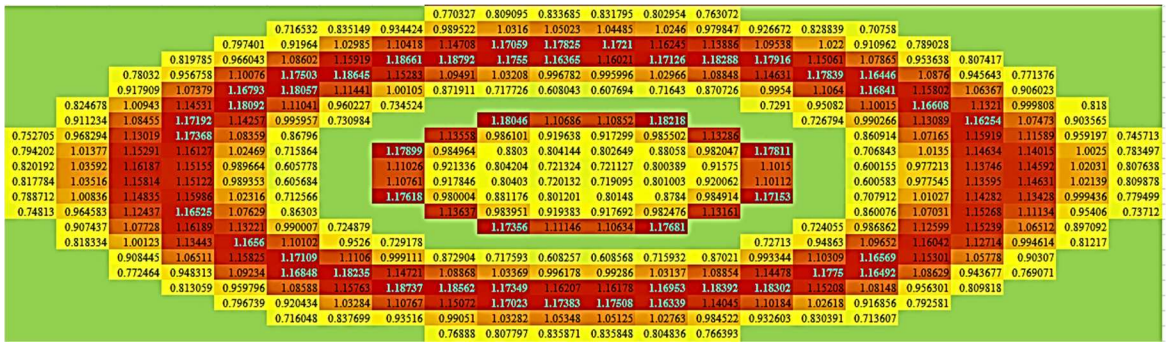

Power Distribution of the MSCR-Model (III) after (130 days)

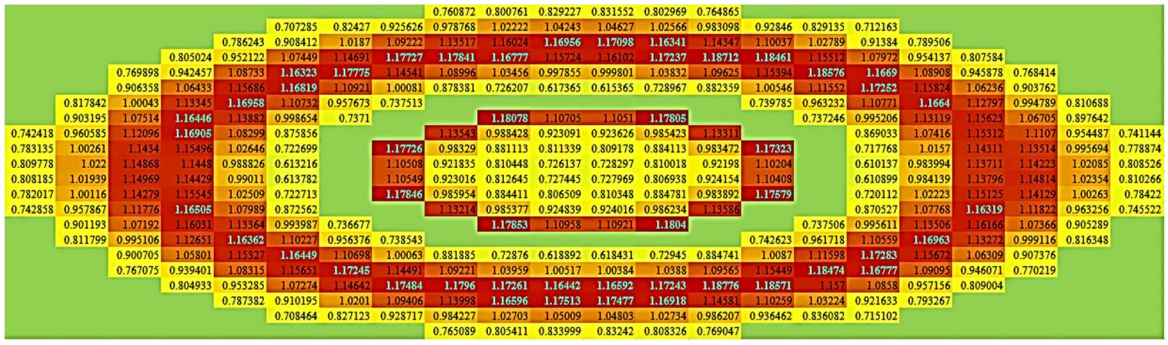

Power Distribution of the MSCR-Model (III) after (160 days)

Appendix (G)

Power Distribution of the MSCR-Model (IV)

The following schematic diagrams represent the power density distributions of MSCR-Model (IV) for the burnup time of 2600 days in the unit of (Wcm^{-3})

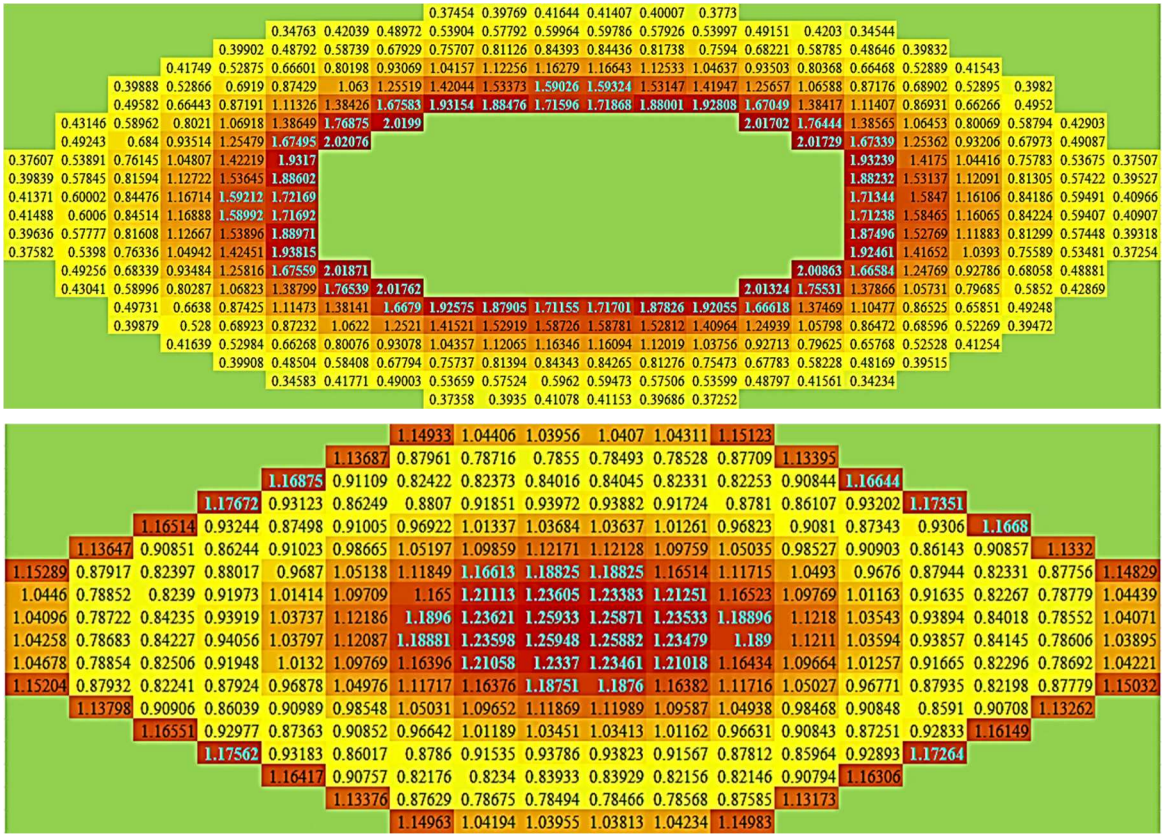

Power Distribution in the Thermal Core and Fast Core of MSCR-Model (IV) at Day (0)

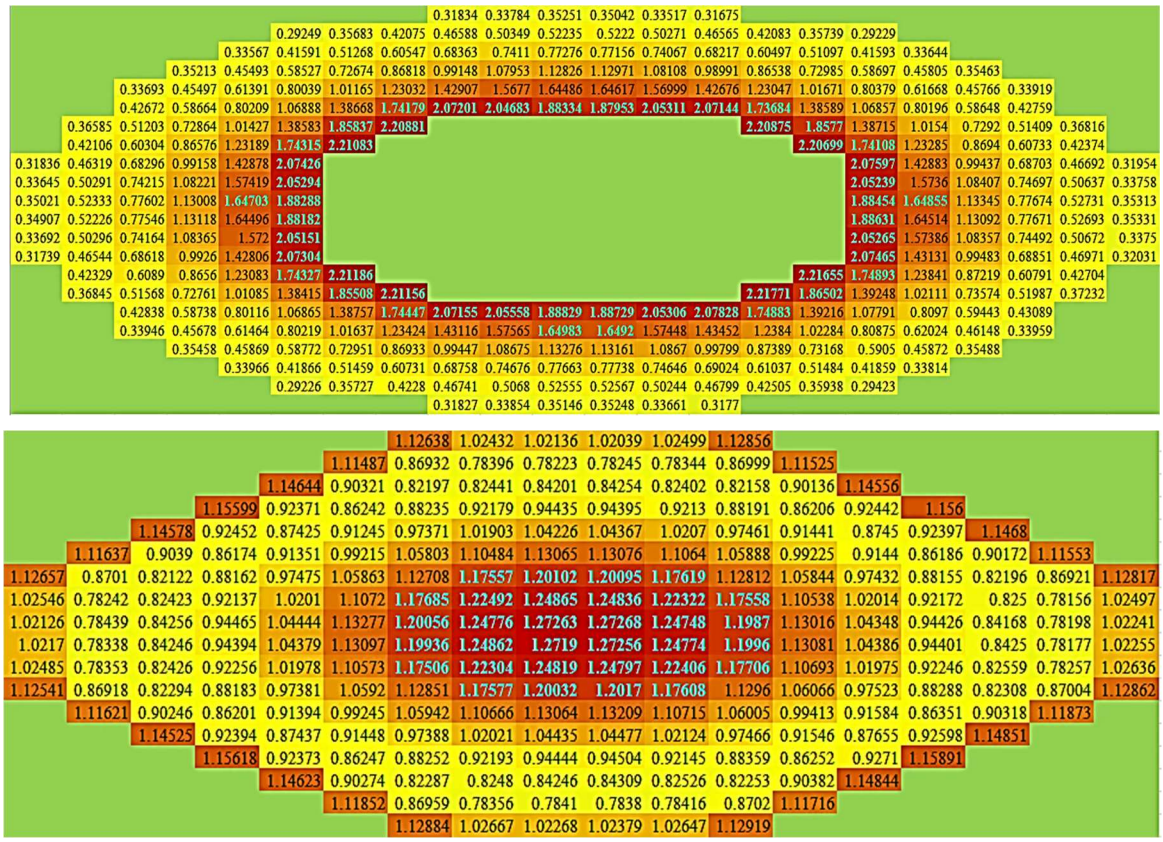

Power Distribution in the Thermal Core and Fast Core of MSCR-Model (IV) after (0.5 day)

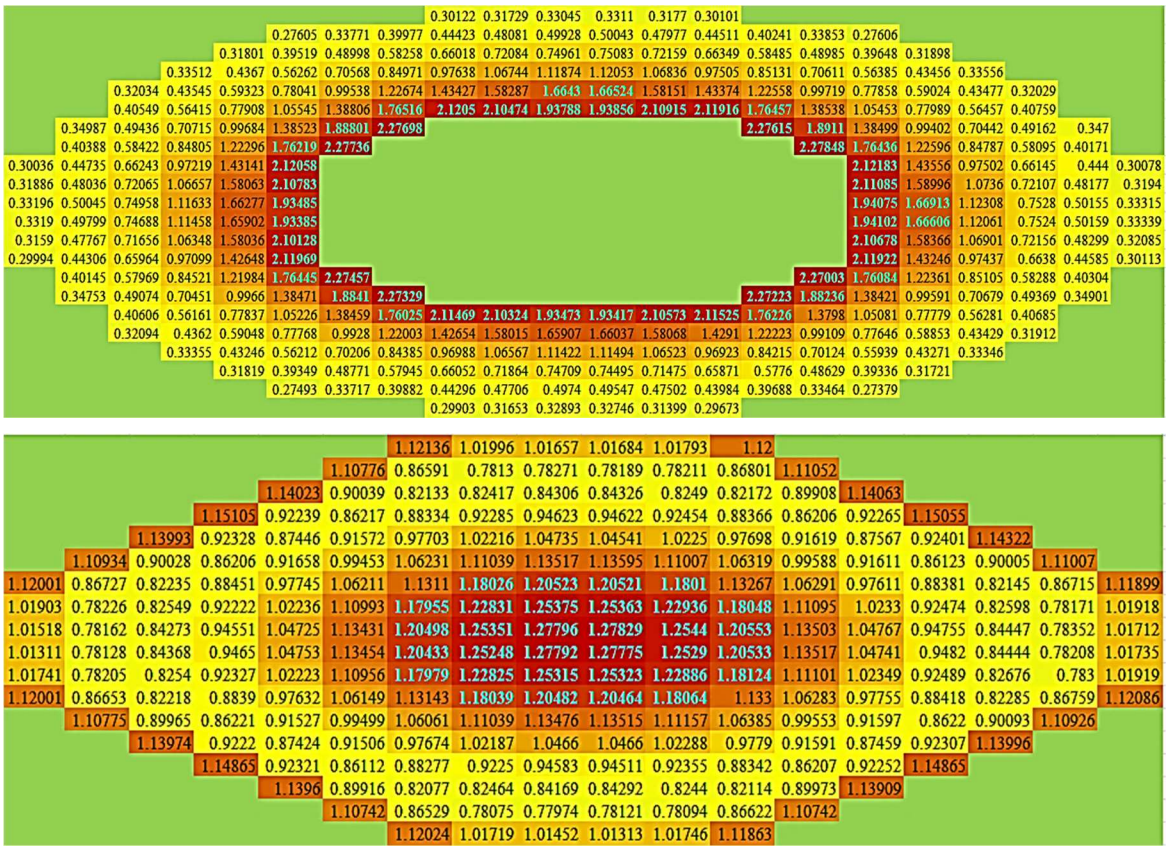

Power Distribution in the Thermal Core and Fast Core of MSCR-Model (IV) after (1 day)

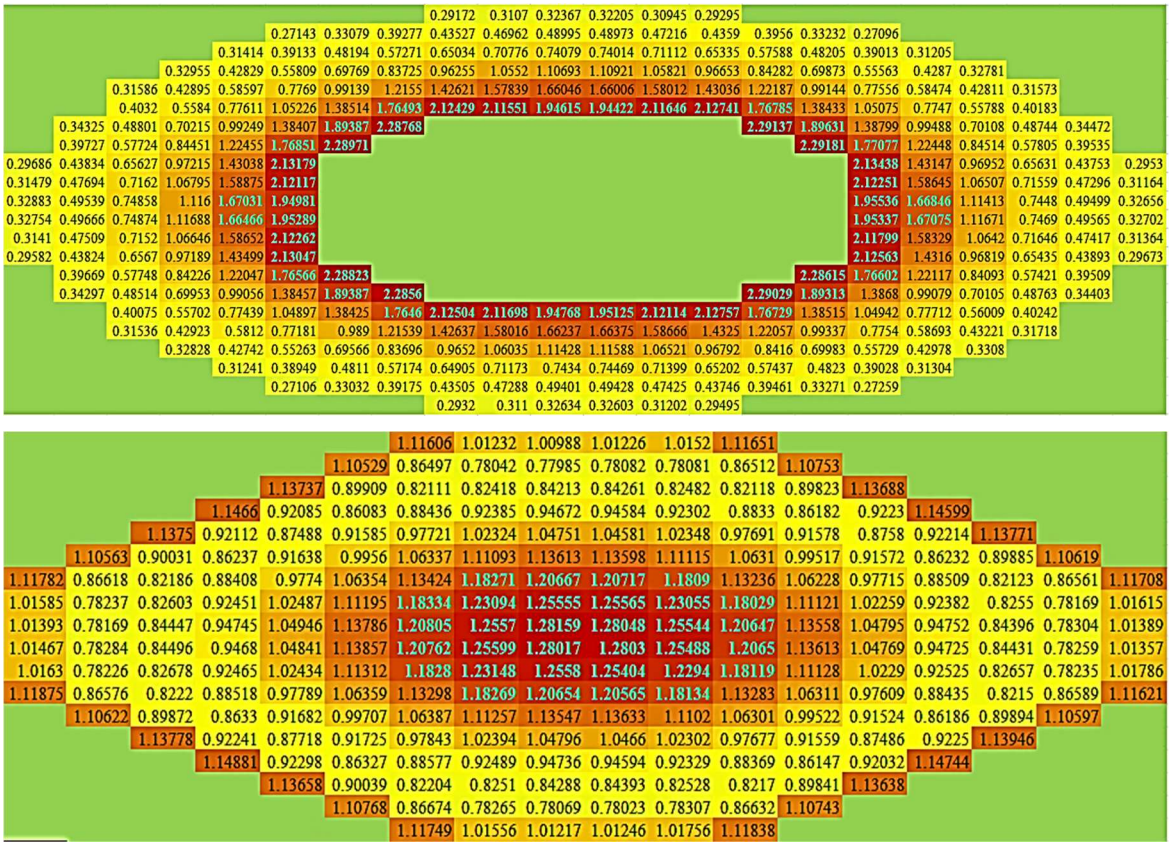

Power Distribution in the Thermal Core and Fast Core of MSCR-Model (IV) after (1.5 days)

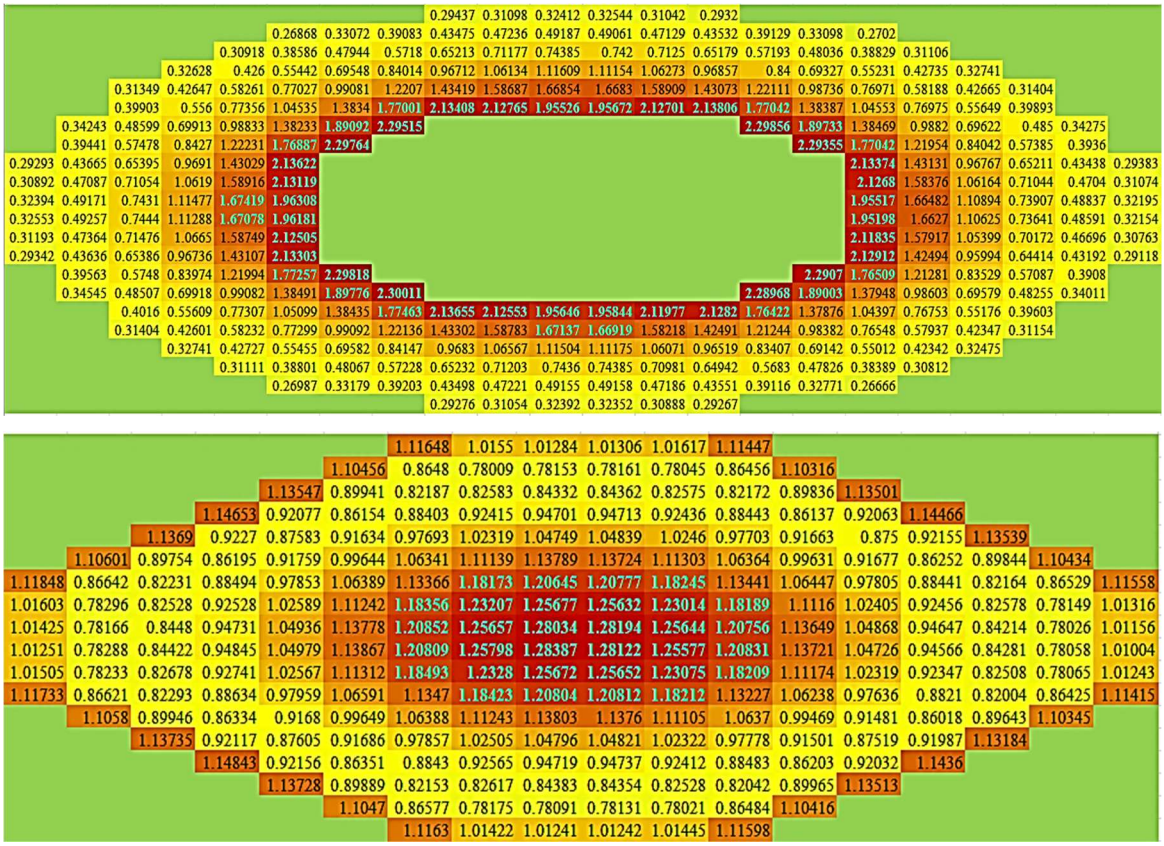

Power Distribution in the Thermal Core and Fast Core of MSCR-Model (IV) after (2 days)

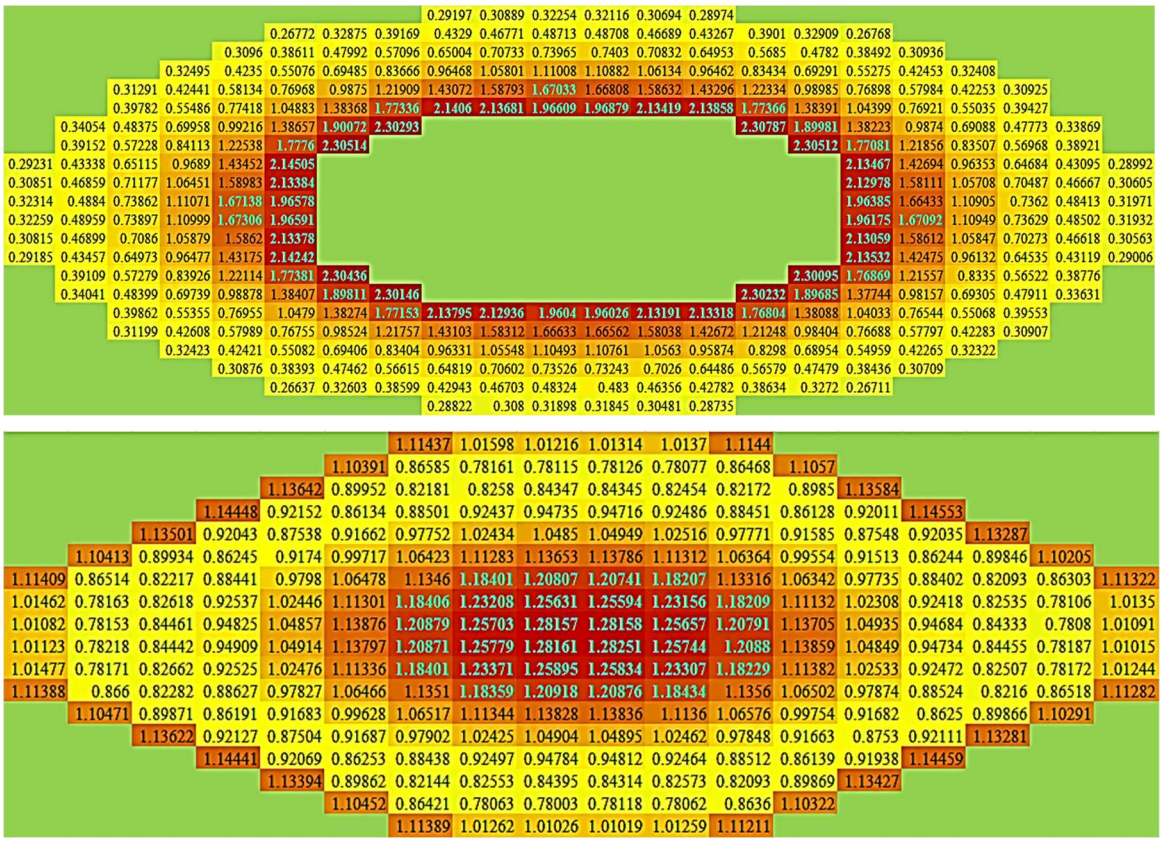

Power Distribution in the Thermal Core and Fast Core of MSCR-Model (IV) after (3 days)

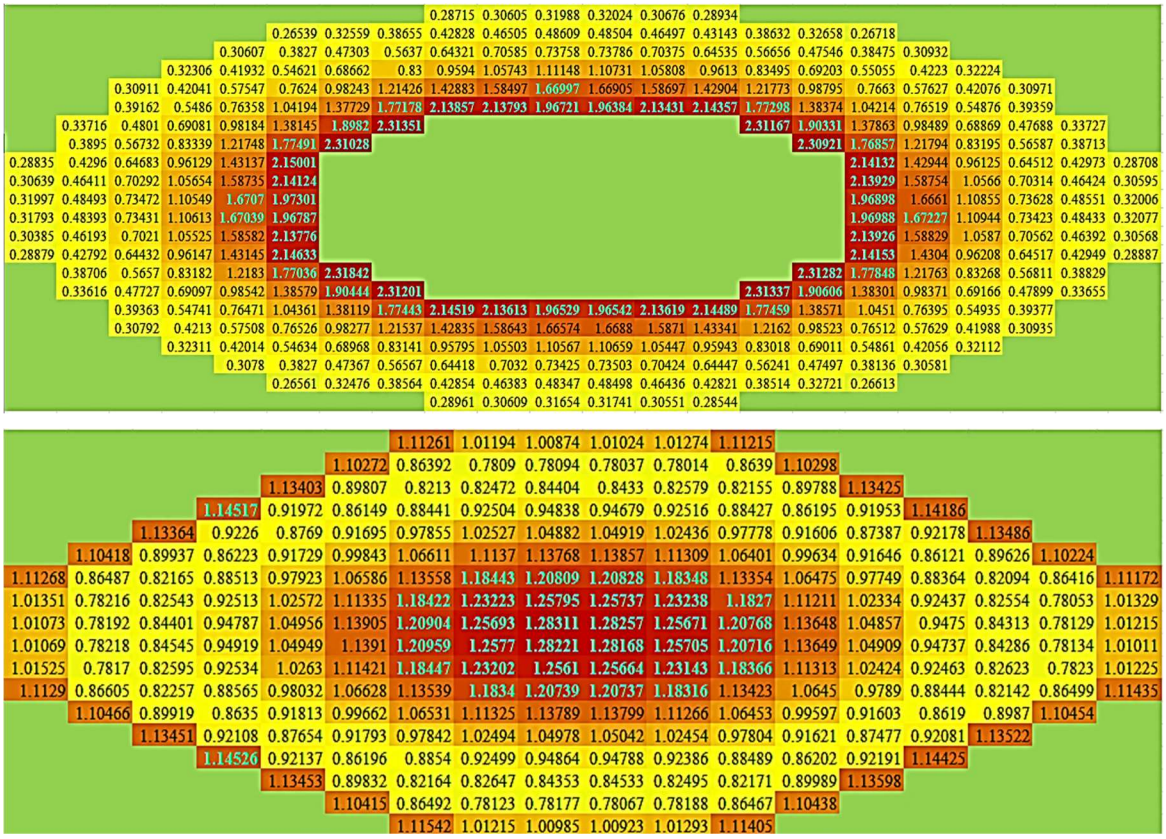

Power Distribution in the Thermal Core and Fast Core of MSCR-Model (IV) after (4 days)

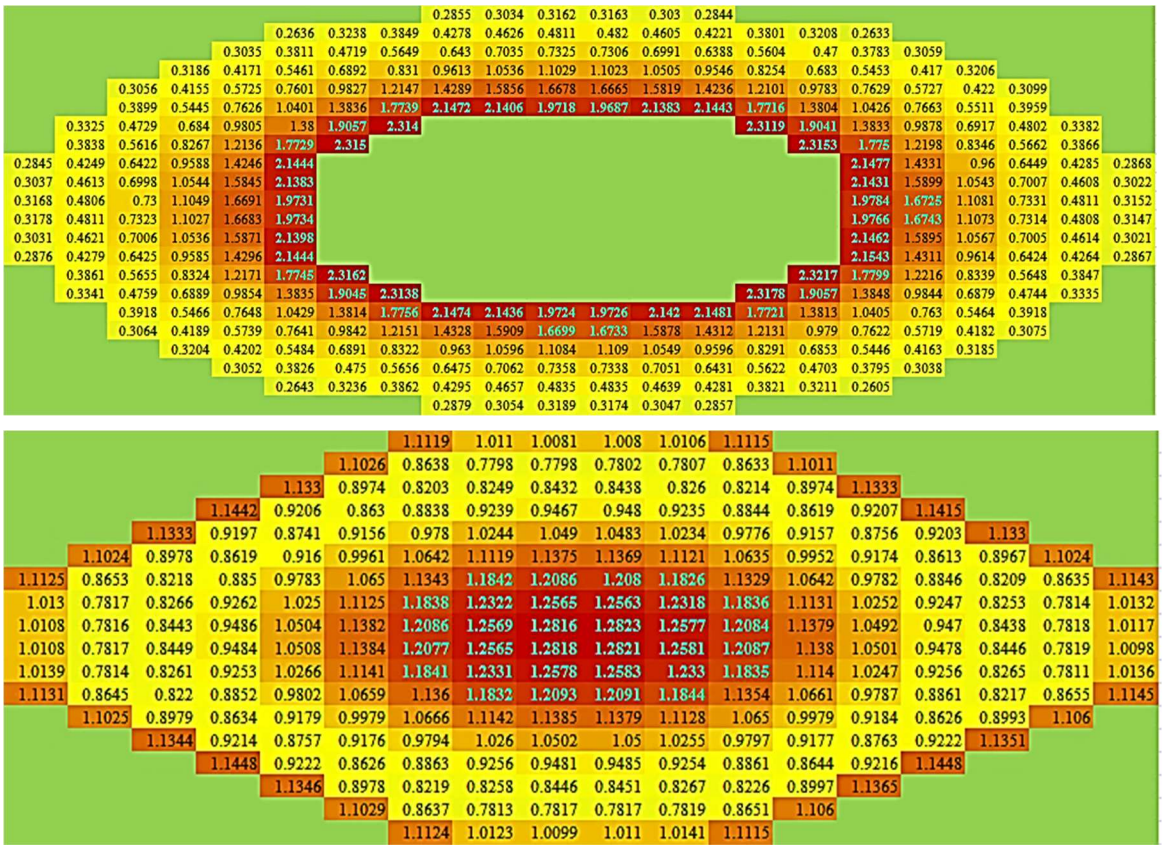

Power Distribution in the Thermal Core and Fast Core of MSCR-Model (IV) after (5 days)

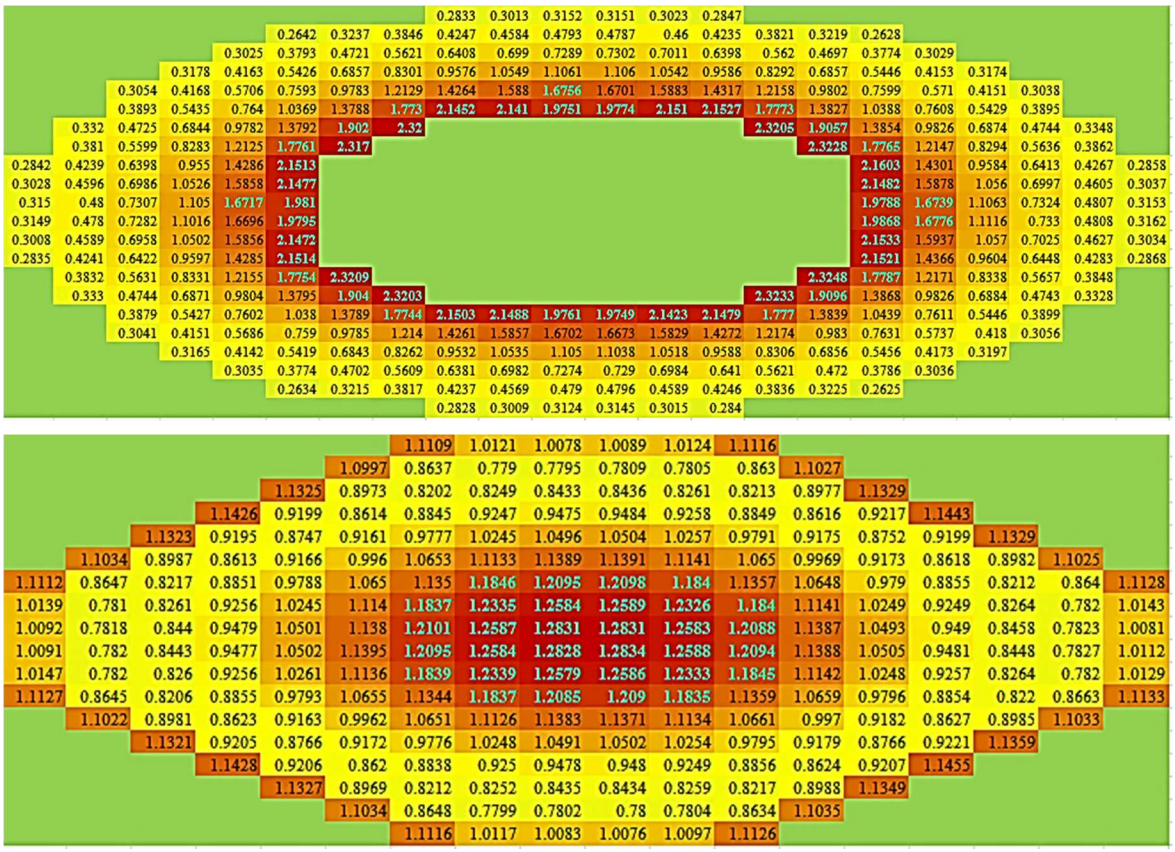

Power Distribution in the Thermal Core and Fast Core of MSCR-Model (IV) after (6 days)

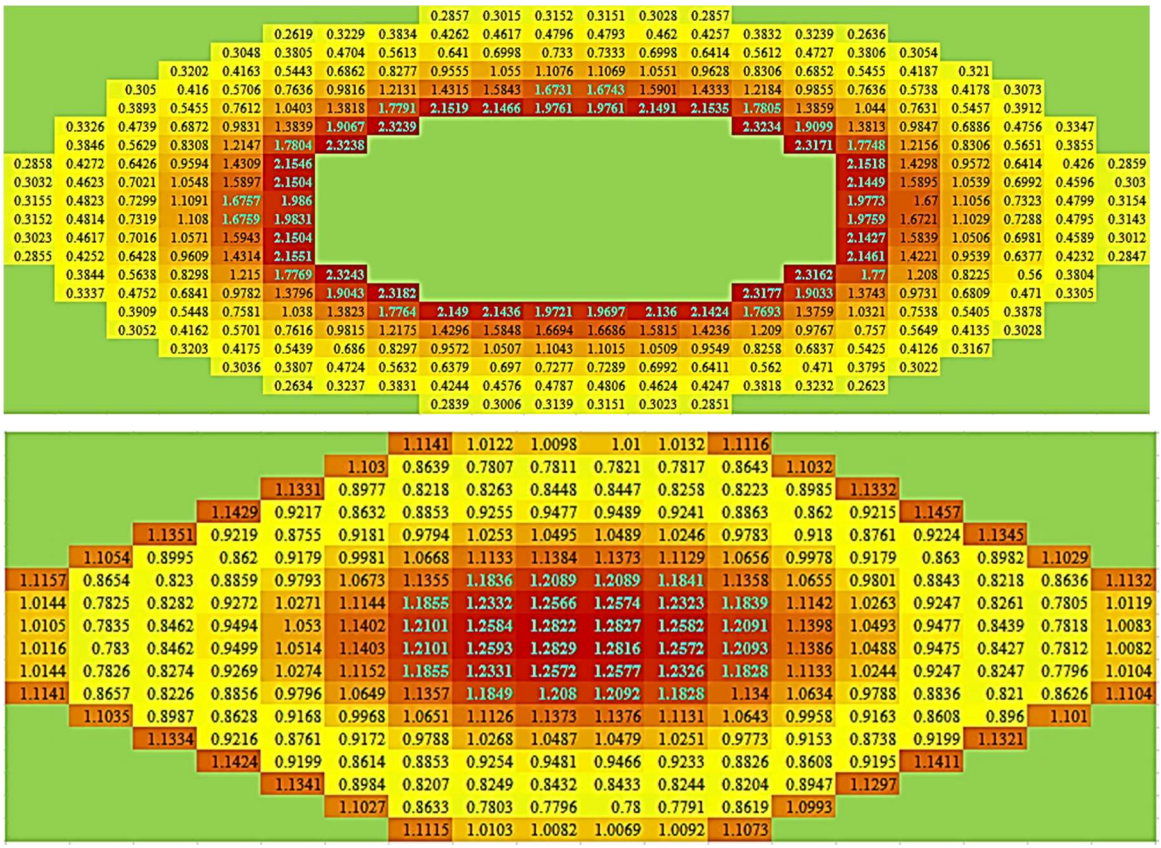

Power Distribution in the Thermal Core and Fast Core of MSCR-Model (IV) after (7 days)

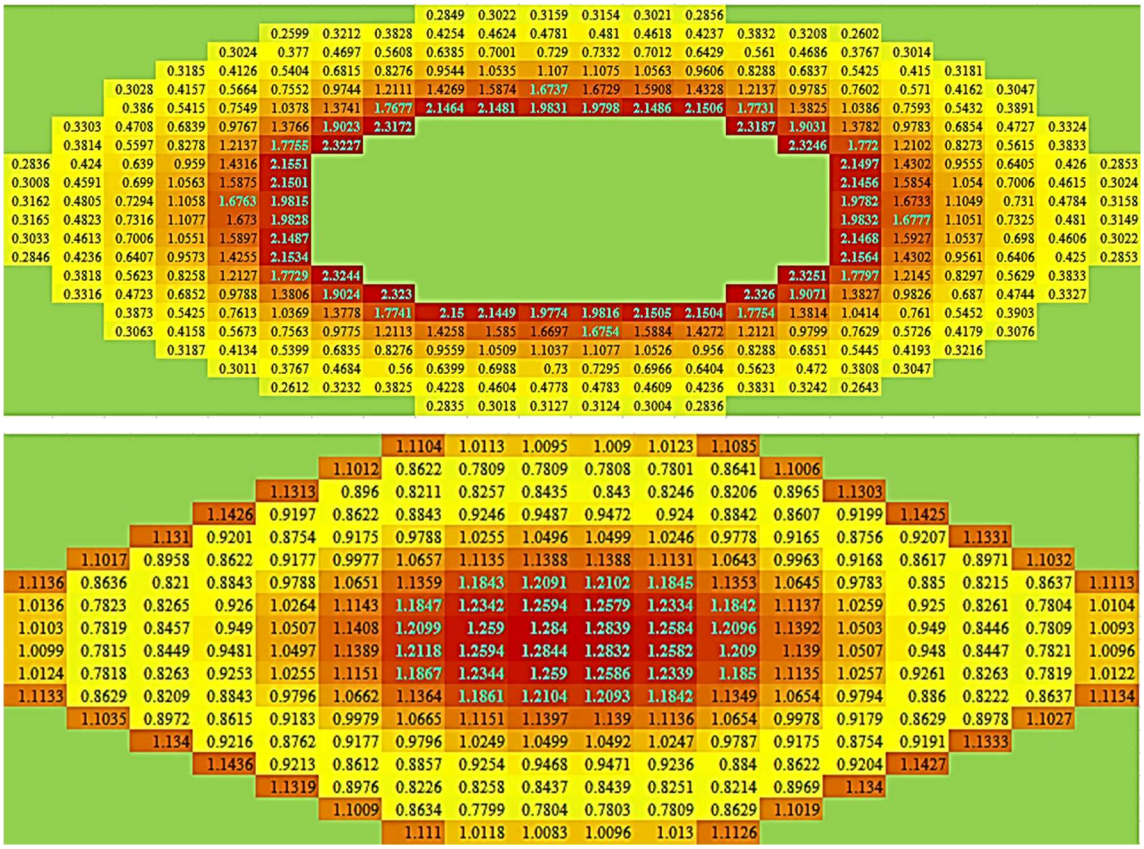

Power Distribution in the Thermal Core and Fast Core of MSCR-Model (IV) after (8 days)

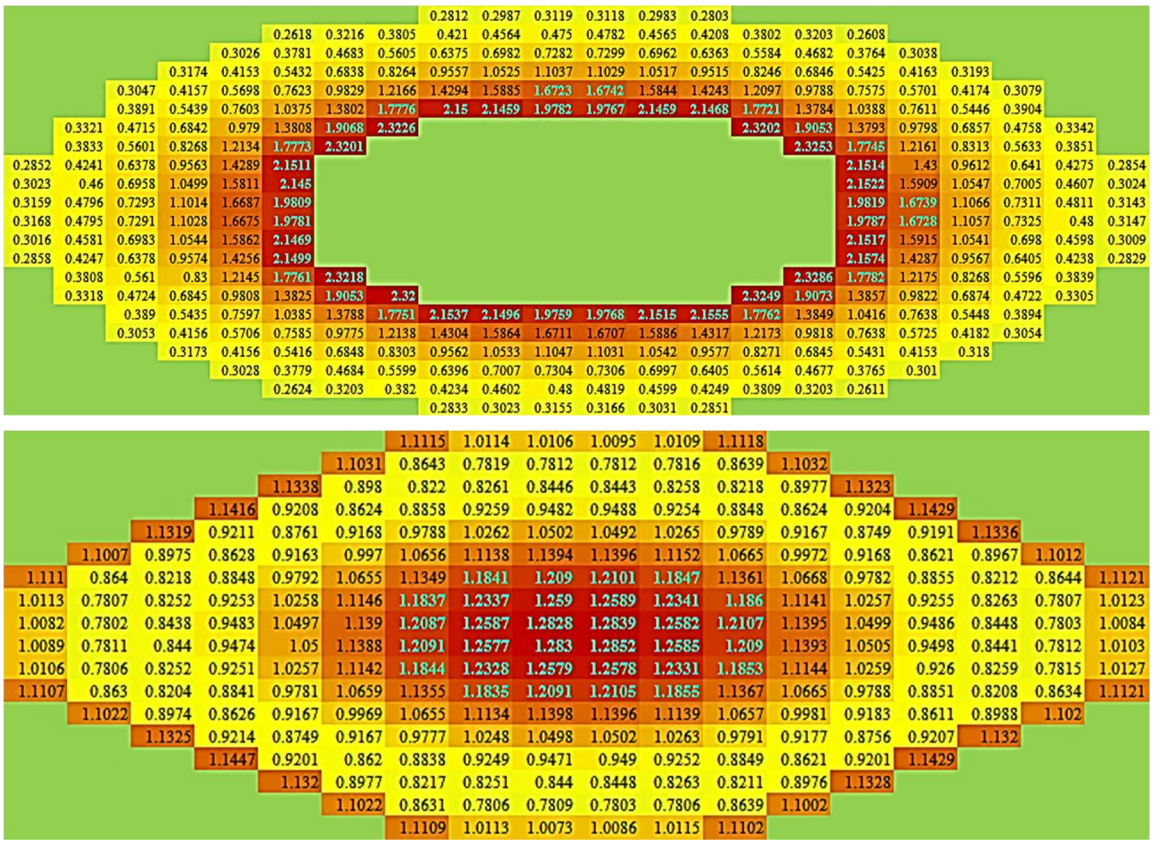

Power Distribution in the Thermal Core and Fast Core of MSCR-Model (IV) after (9 days)

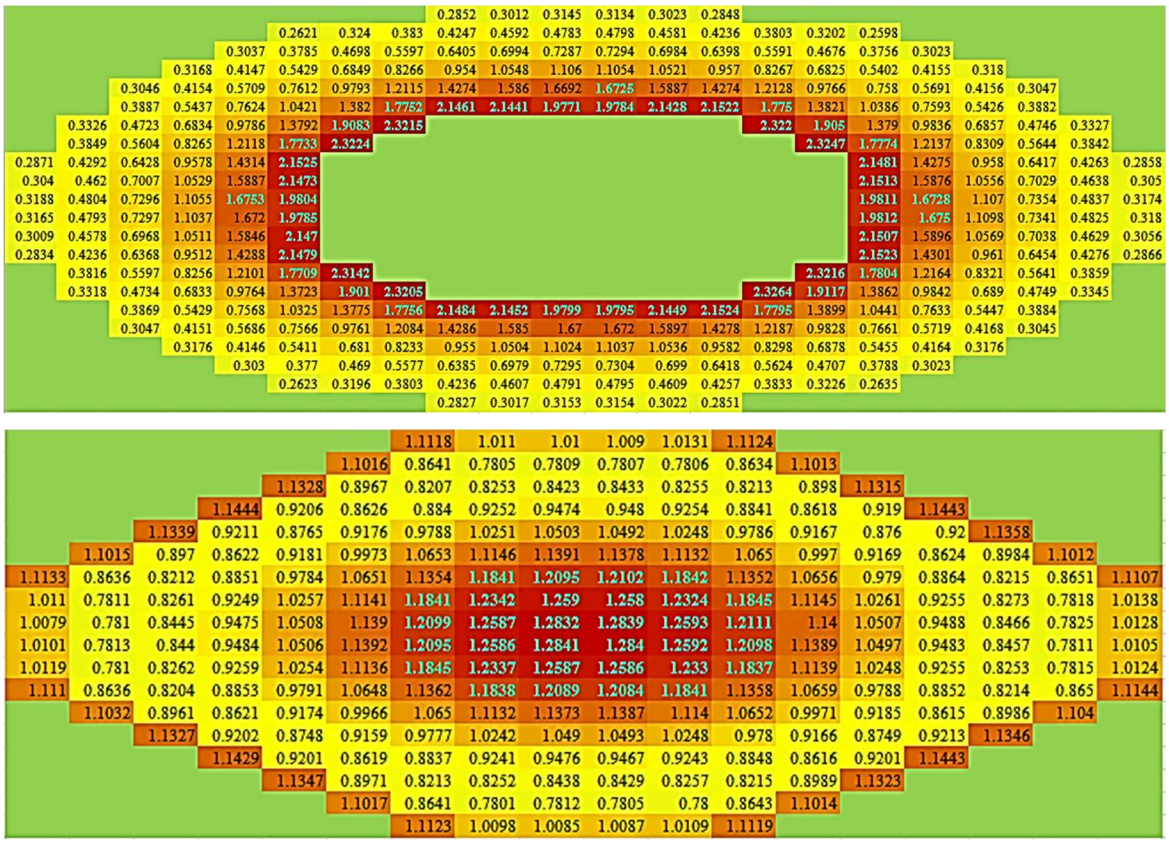

Power Distribution in the Thermal Core and Fast Core of MSCR-Model (IV) after (10 days)

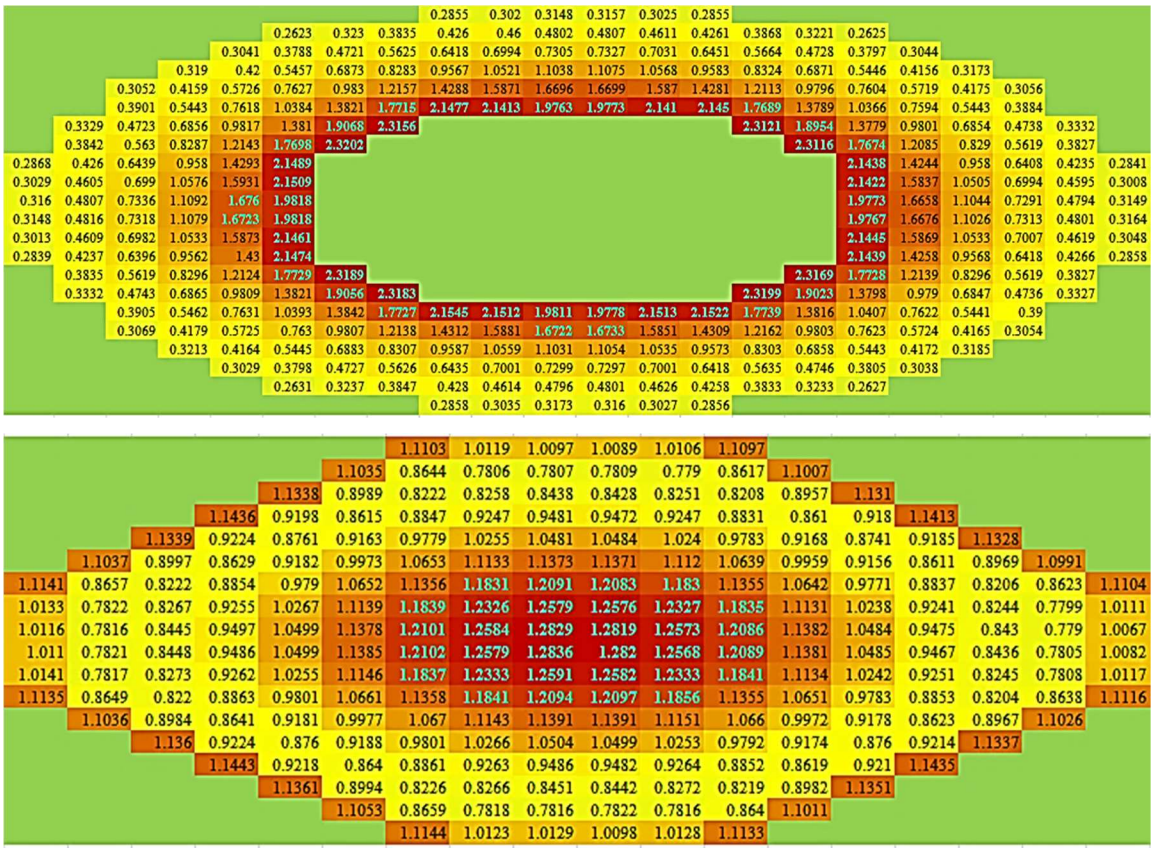

Power Distribution in the Thermal Core and Fast Core of MSCR-Model (IV) after (15 days)

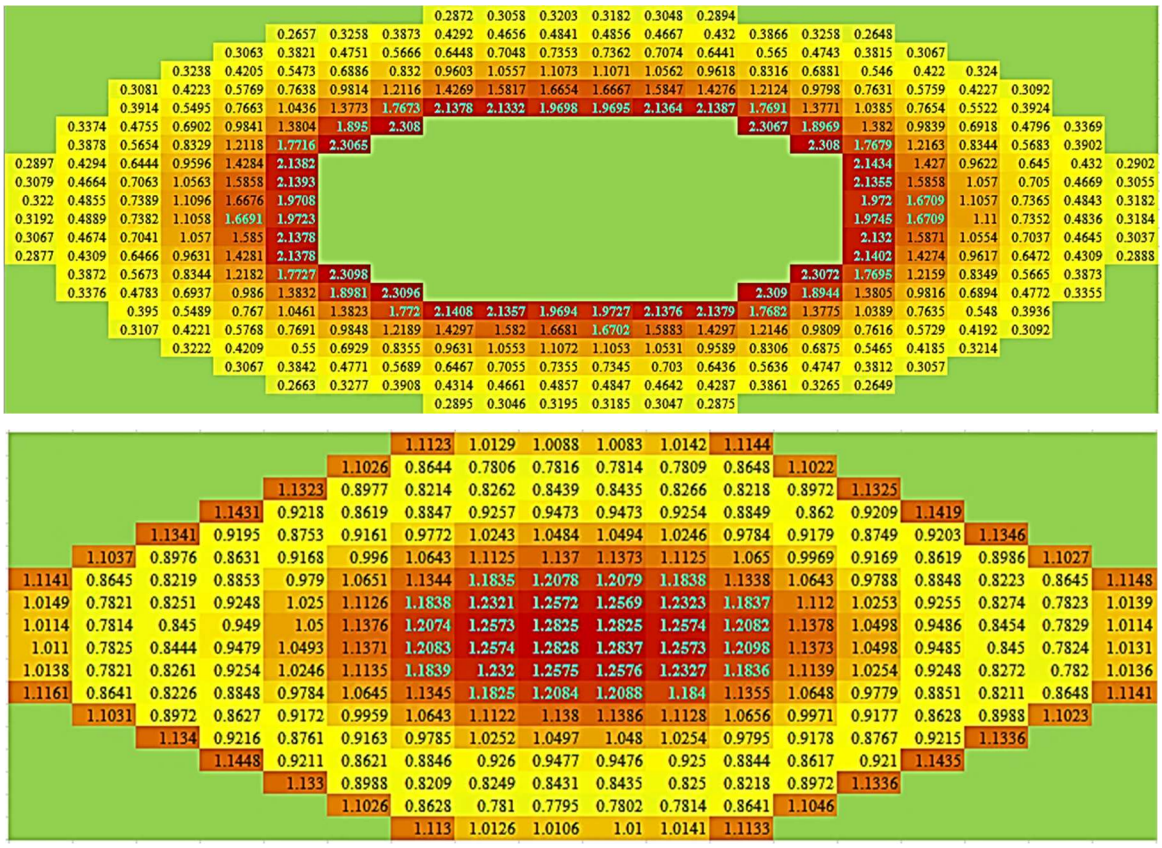

Power Distribution in the Thermal Core and Fast Core of MSCR-Model (IV) after (20 days)

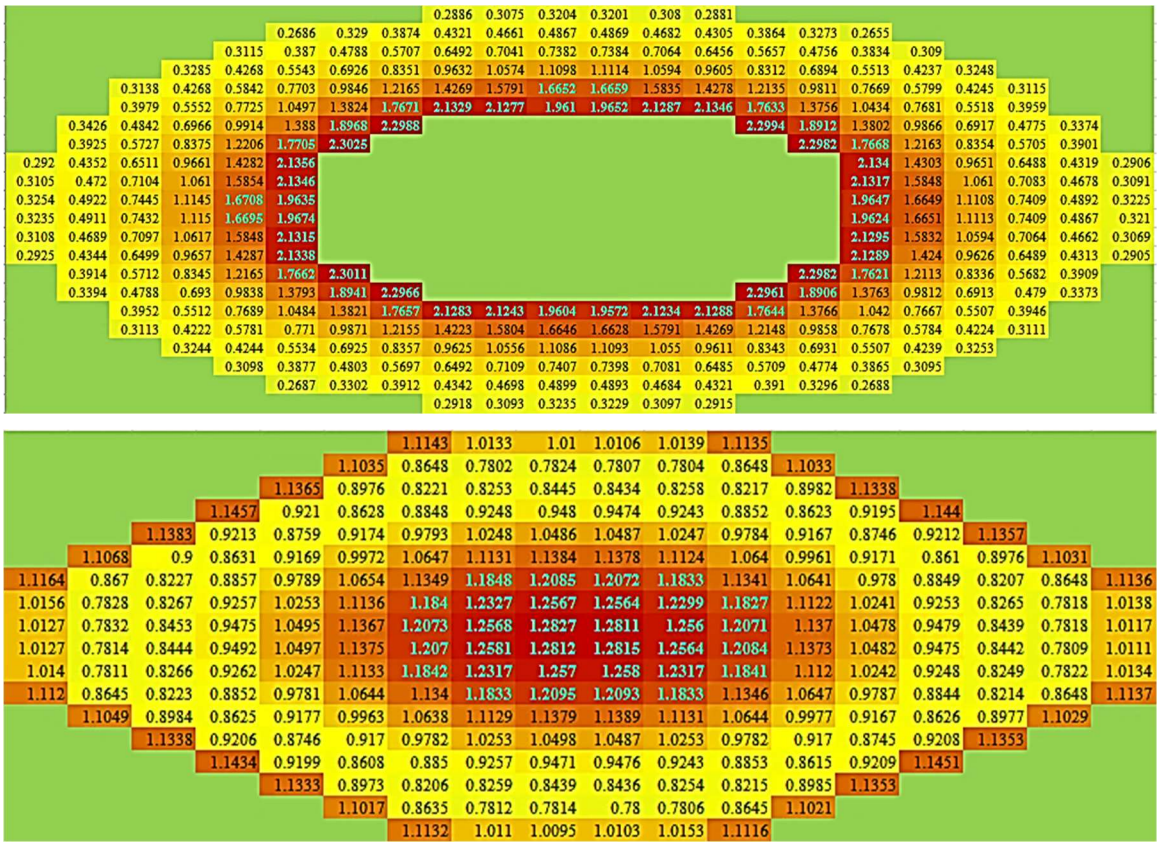

Power Distribution in the Thermal Core and Fast Core of MSCR-Model (IV) after (25 days)

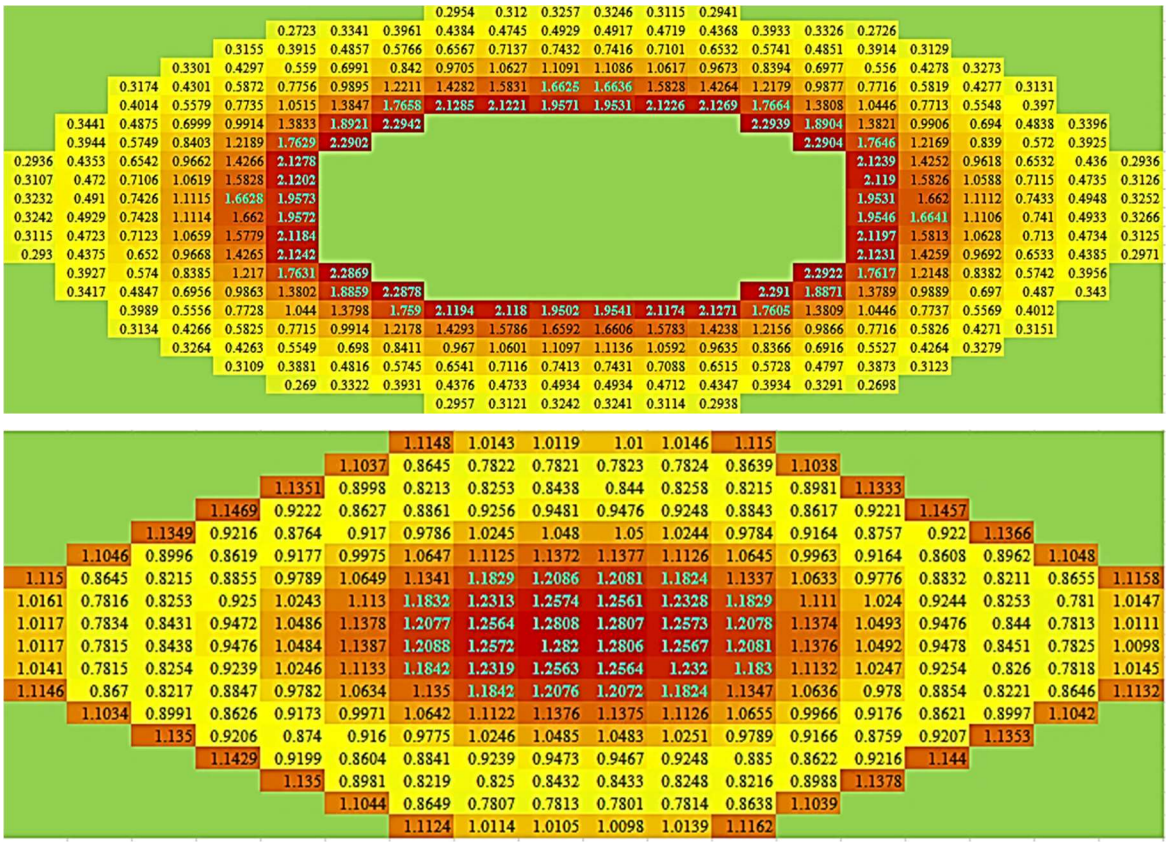

Power Distribution in the Thermal Core and Fast Core of MSCR-Model (IV) after (30 days)

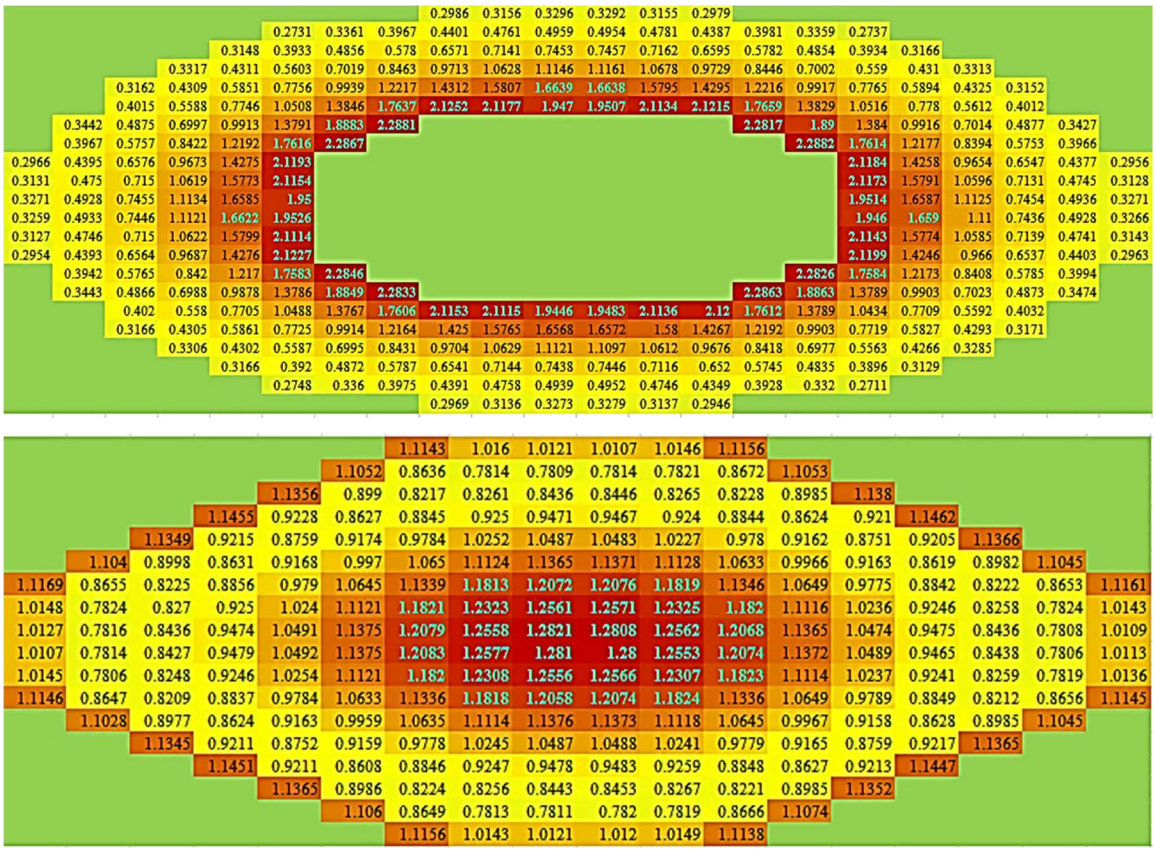

Power Distribution in the Thermal Core and Fast Core of MSCR-Model (IV) after (35 days)

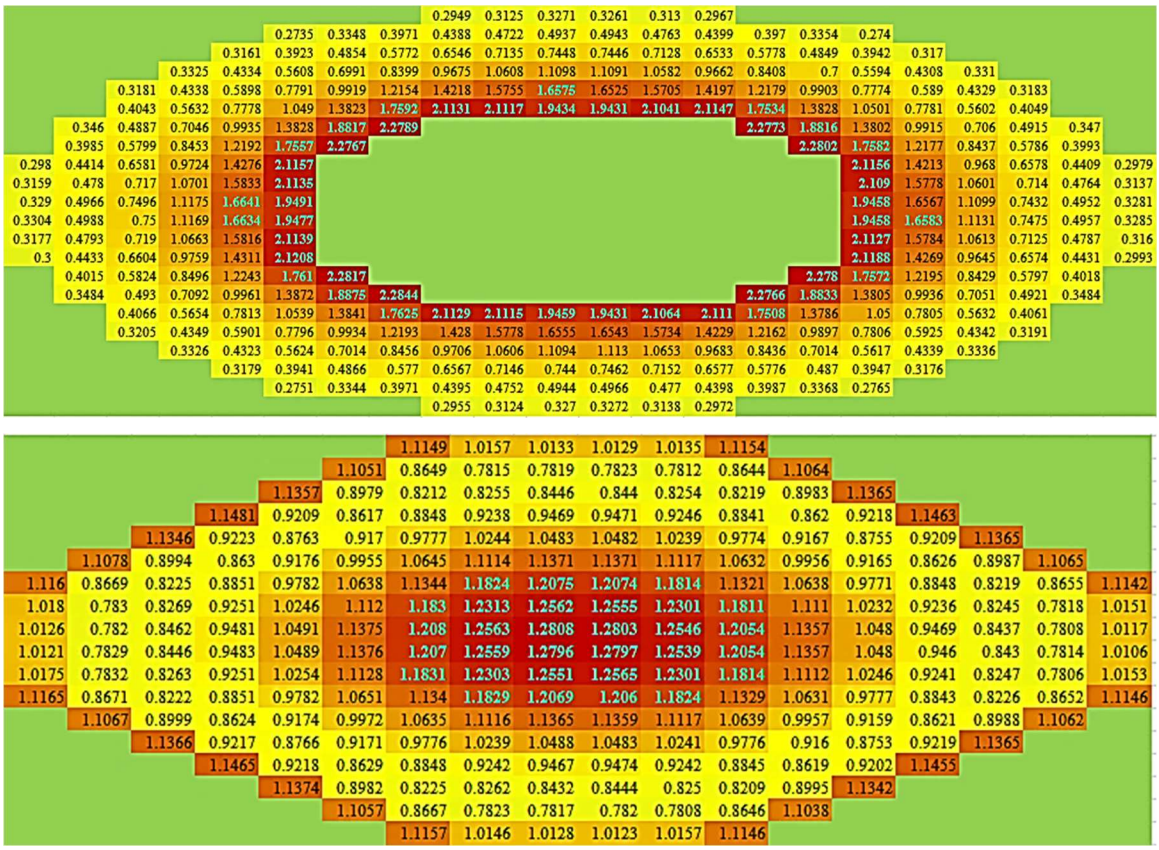

Power Distribution in the Thermal Core and Fast Core of MSCR-Model (IV) after (40 days)

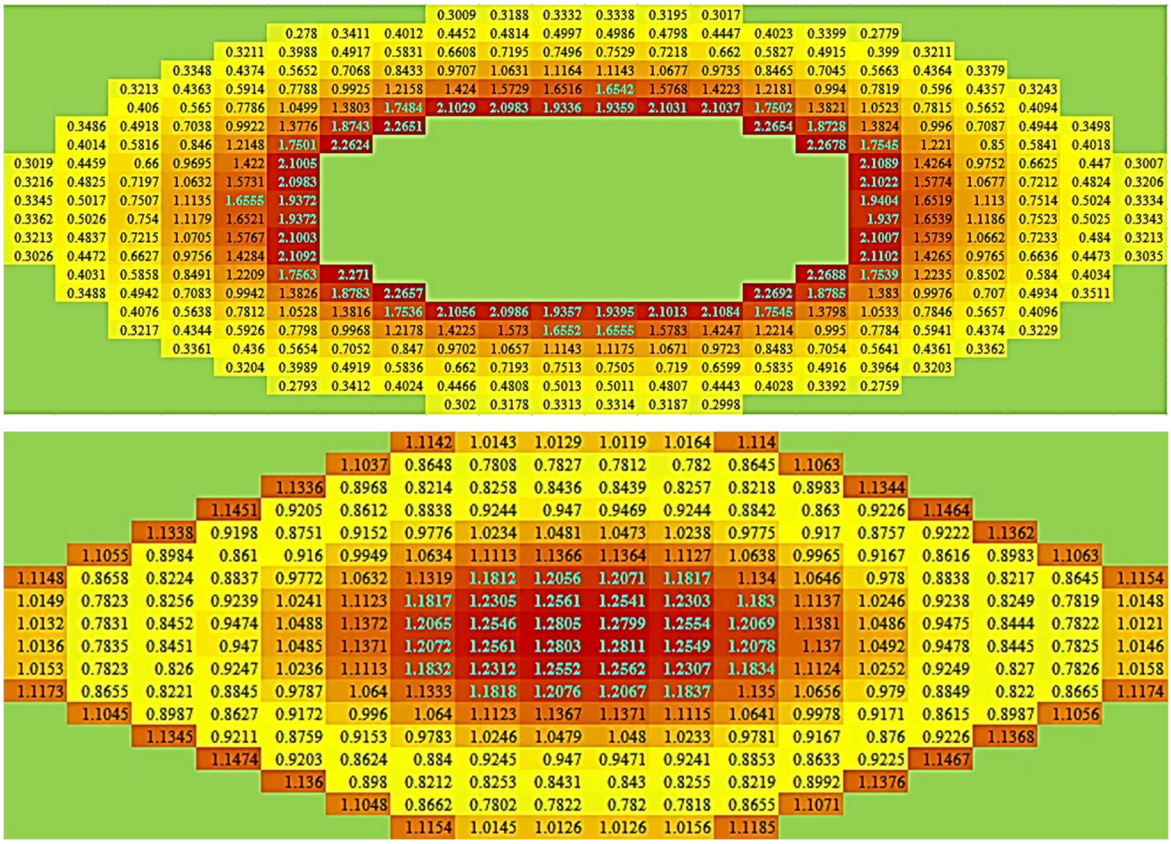

Power Distribution in the Thermal Core and Fast Core of MSCR-Model (IV) after (50 days)

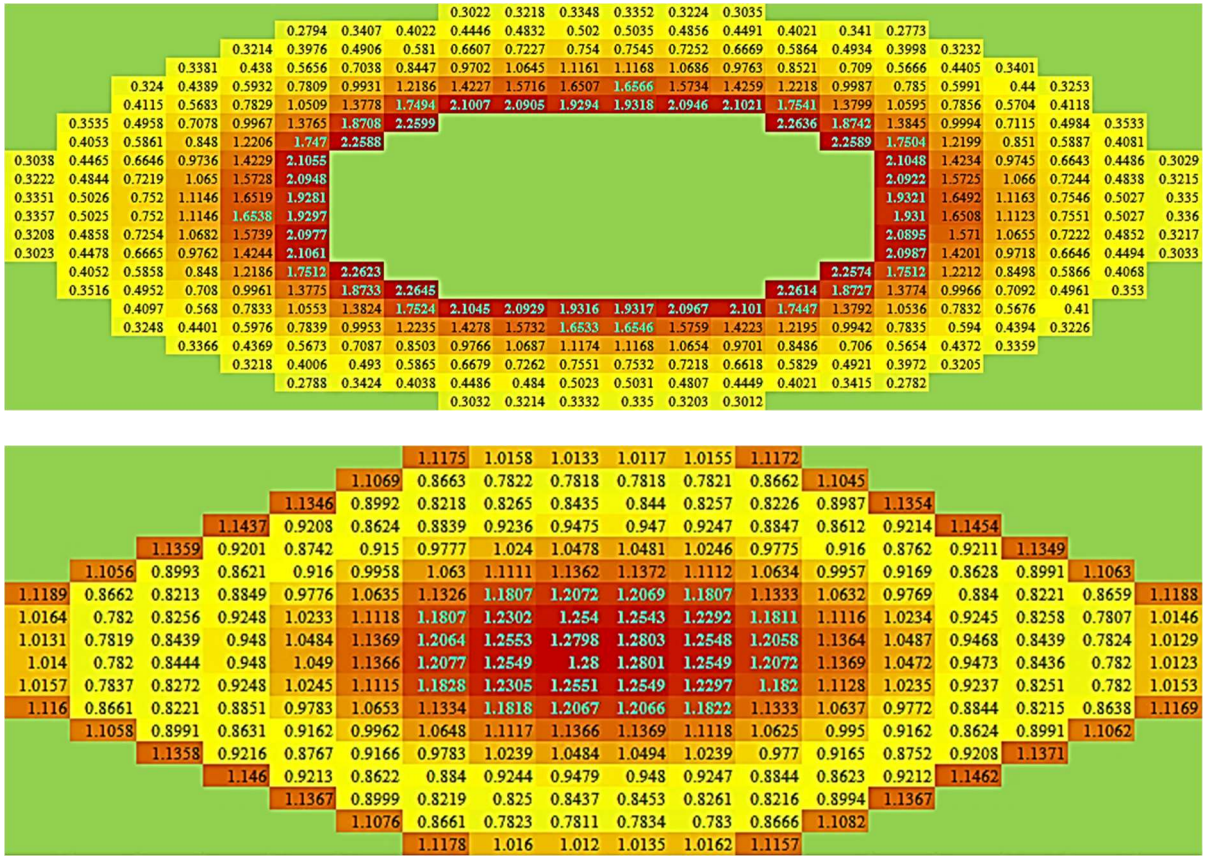

Power Distribution in the Thermal Core and Fast Core of MSCR-Model (IV) after (60 days)

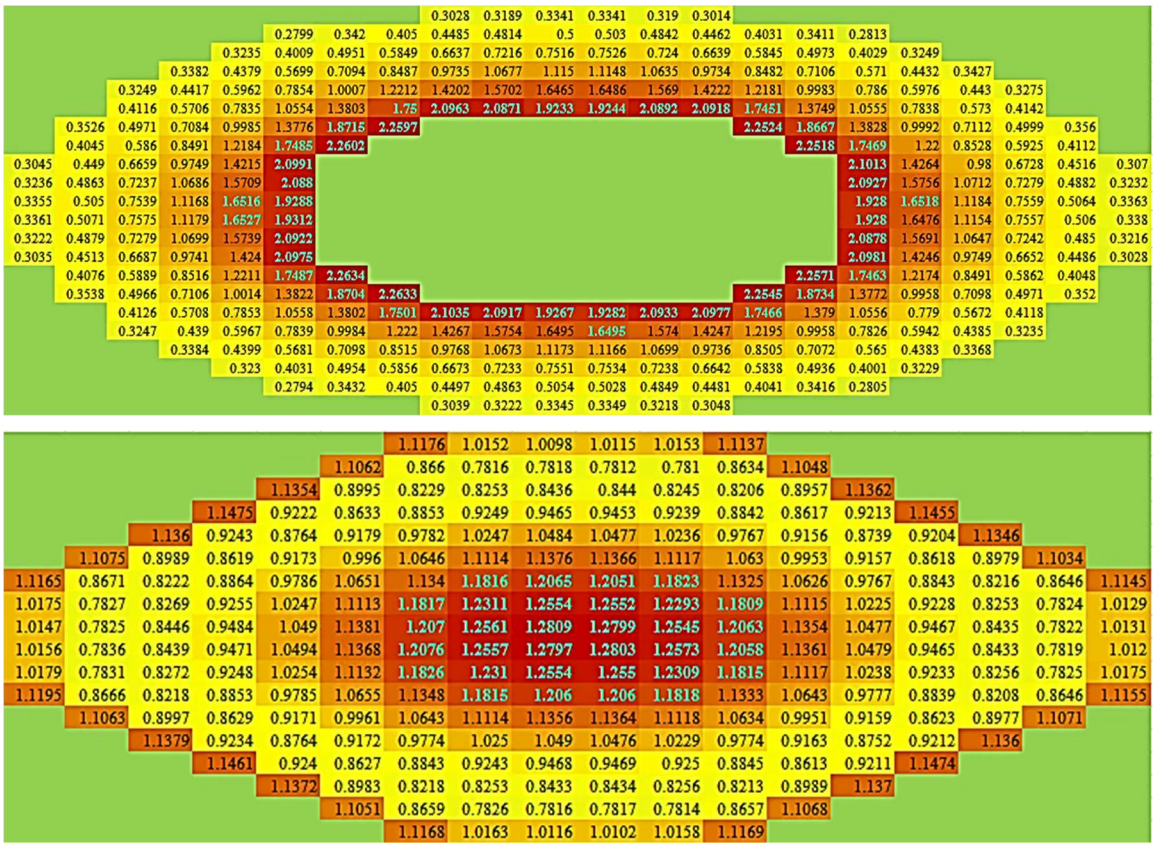

Power Distribution in the Thermal Core and Fast Core of MSCR-Model (IV) after (70 days)

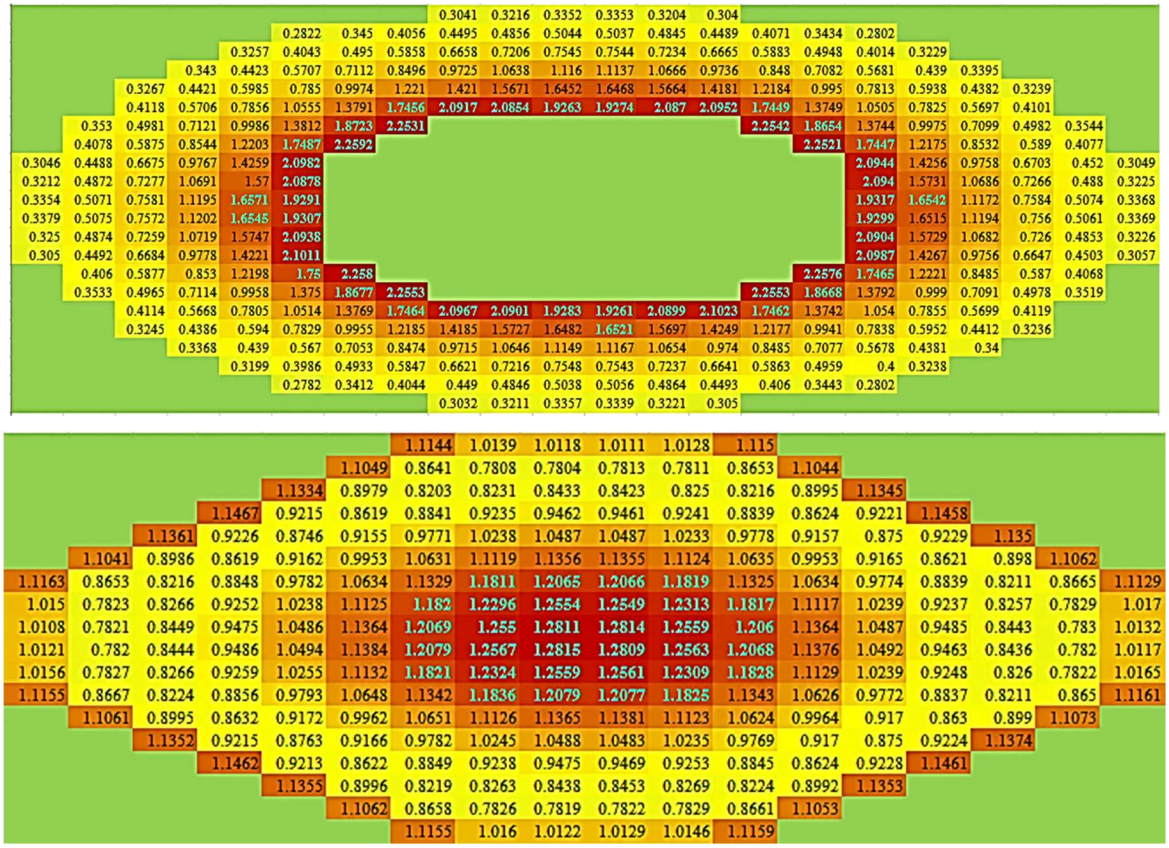

Power Distribution in the Thermal Core and Fast Core of MSCR-Model (IV) after (80 days)

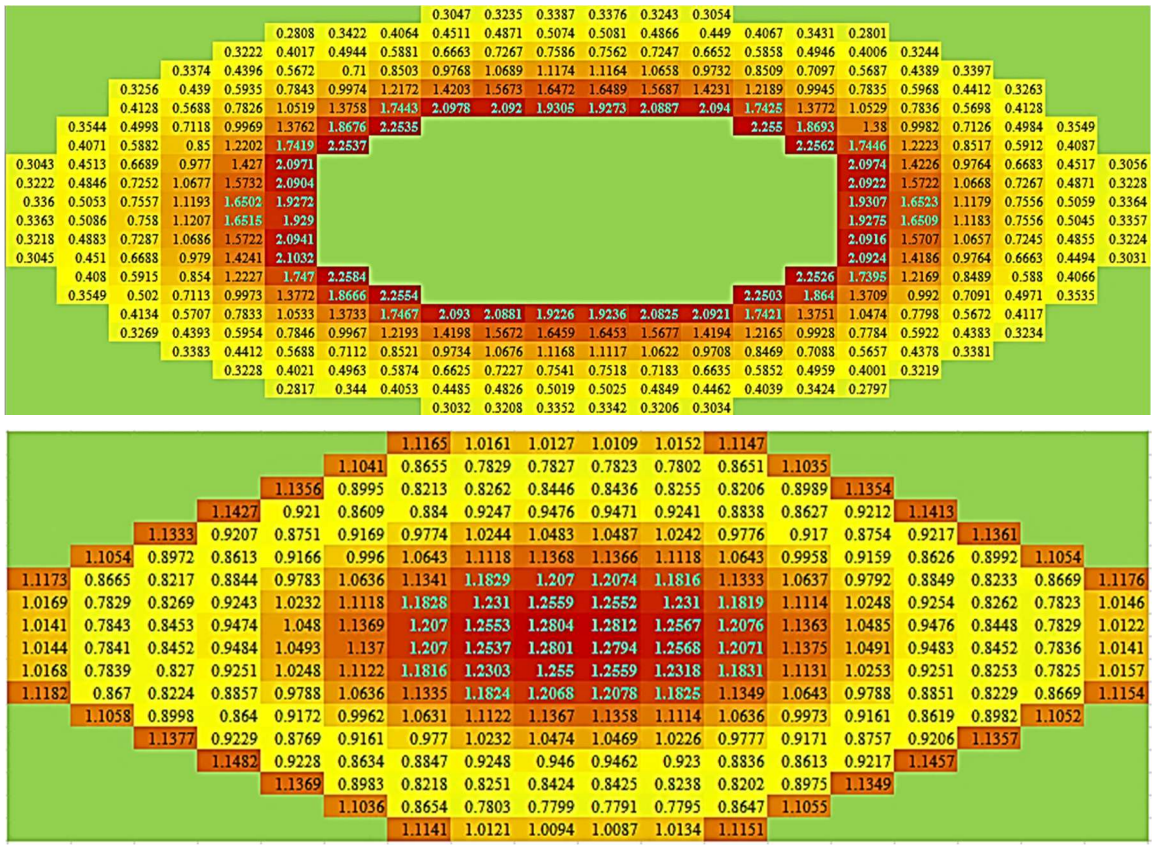

Power Distribution in the Thermal Core and Fast Core of MSCR-Model (IV) after (90 days)

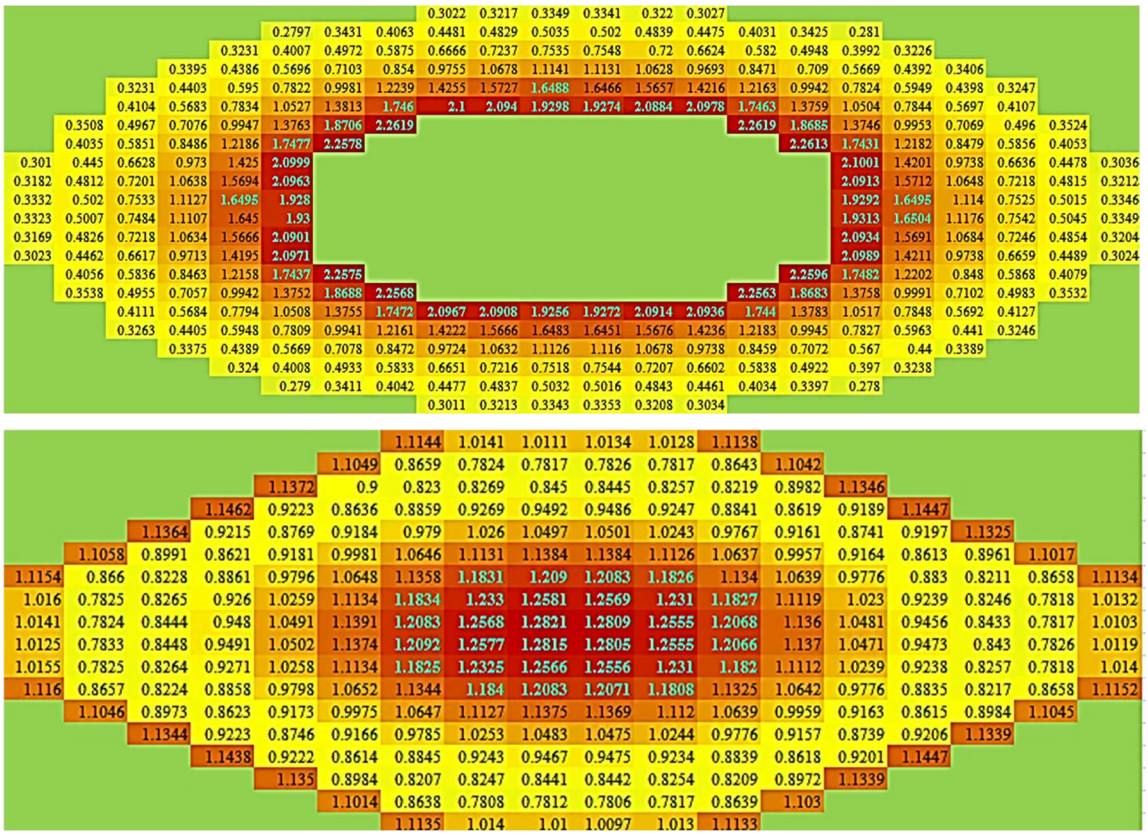

Power Distribution in the Thermal Core and Fast Core of MSCR-Model (IV) after (100 days)

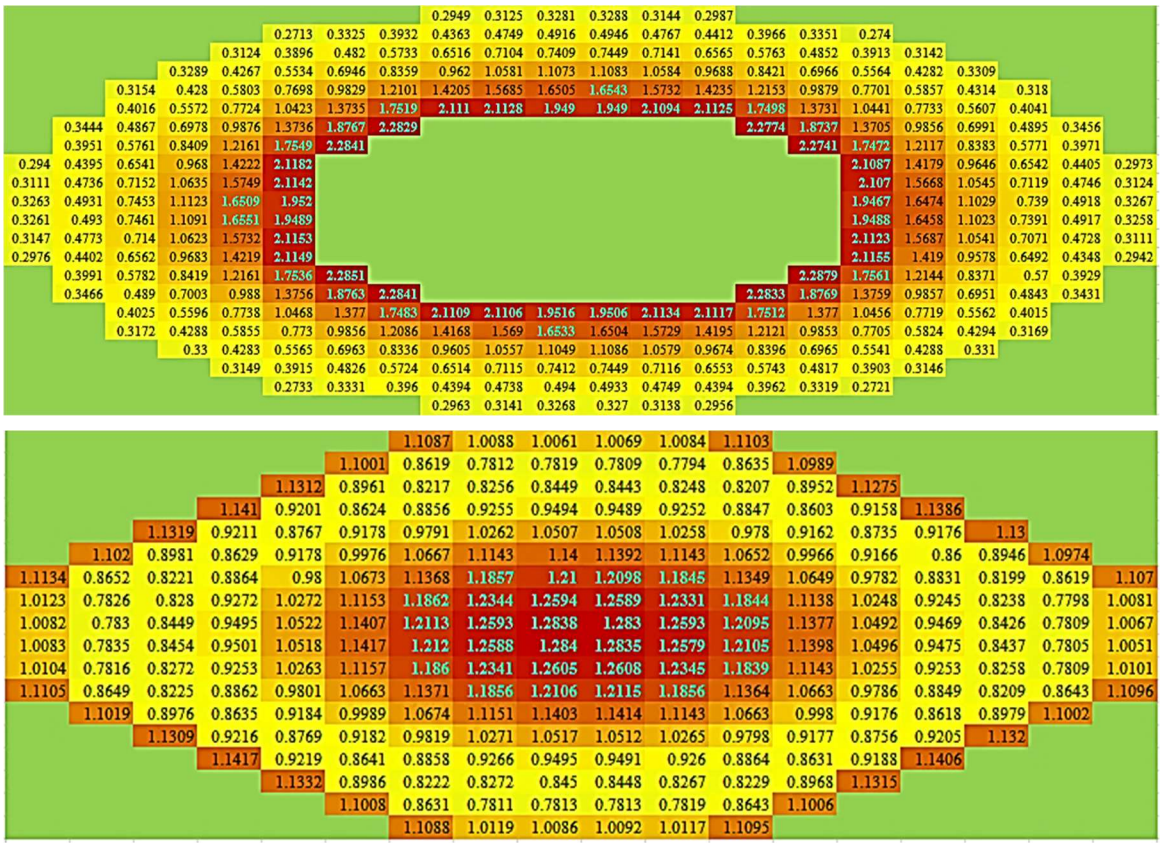

Power Distribution in the Thermal Core and Fast Core of MSCR-Model (IV) after (130 days)

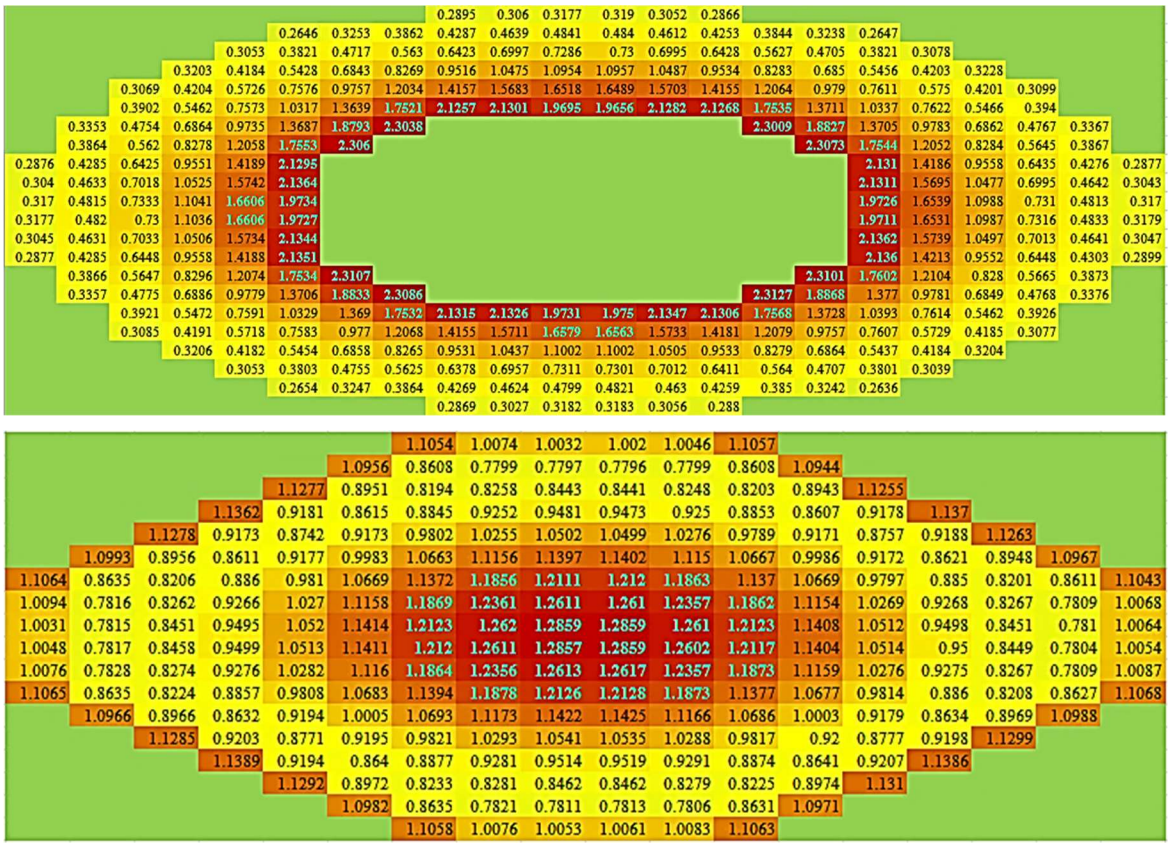

Power Distribution in the Thermal Core and Fast Core of MSCR-Model (IV) after (160 days)

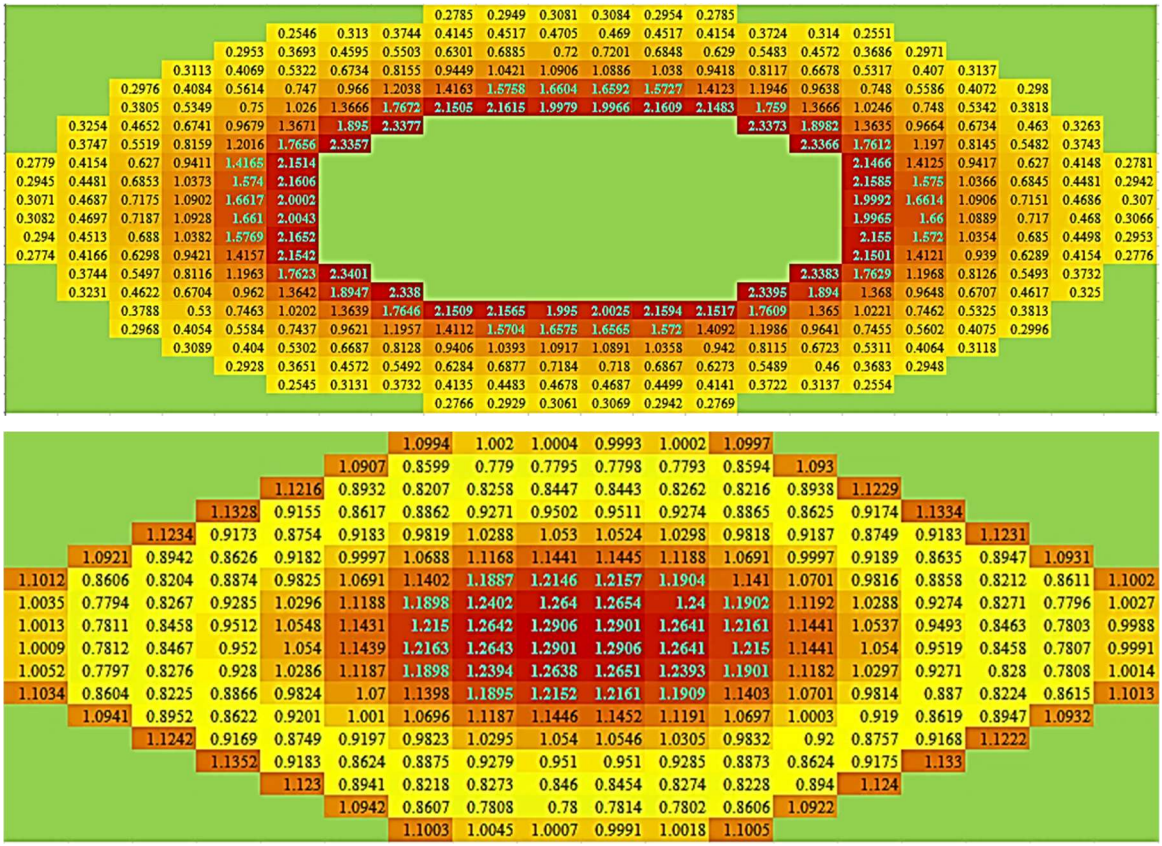

Power Distribution in the Thermal Core and Fast Core of MSCR-Model (IV) after (190 days)

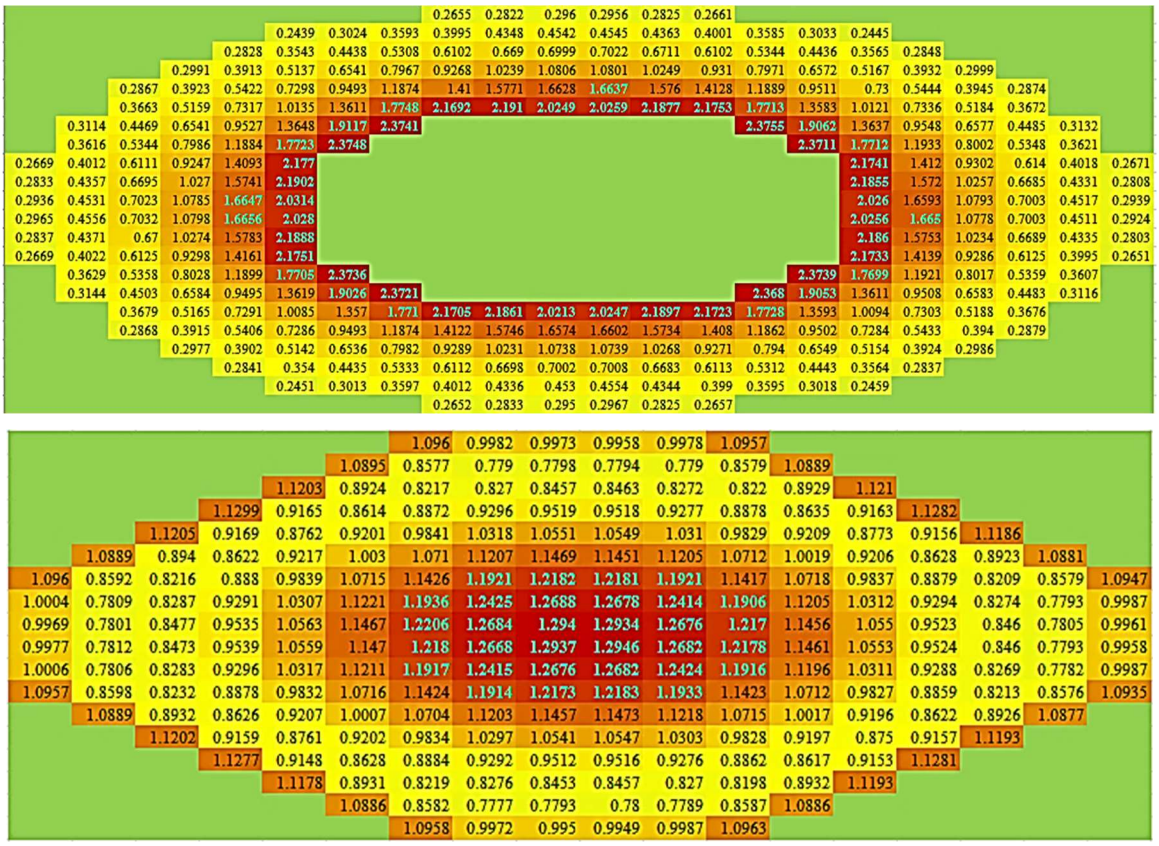

Power Distribution in the Thermal Core and Fast Core of MSCR-Model (IV) after (220 days)

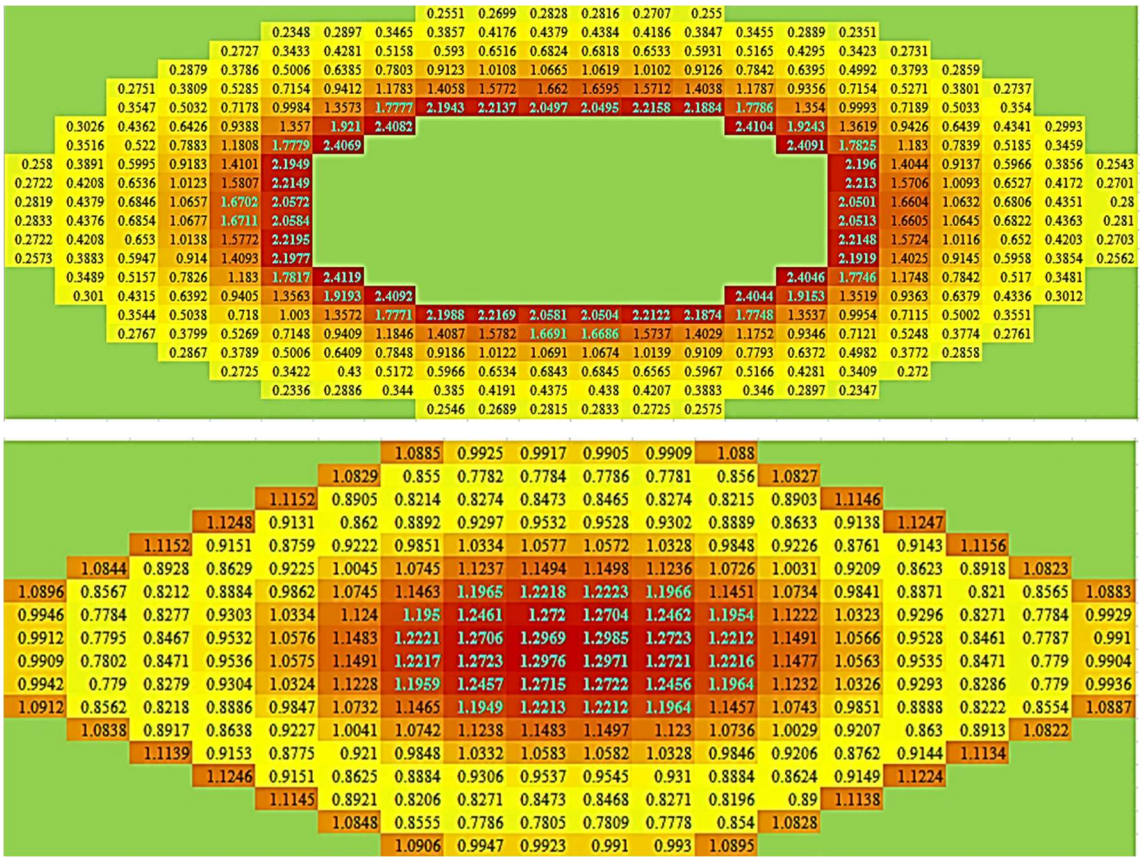

Power Distribution in the Thermal Core and Fast Core of MSCR-Model (IV) after (250 days)

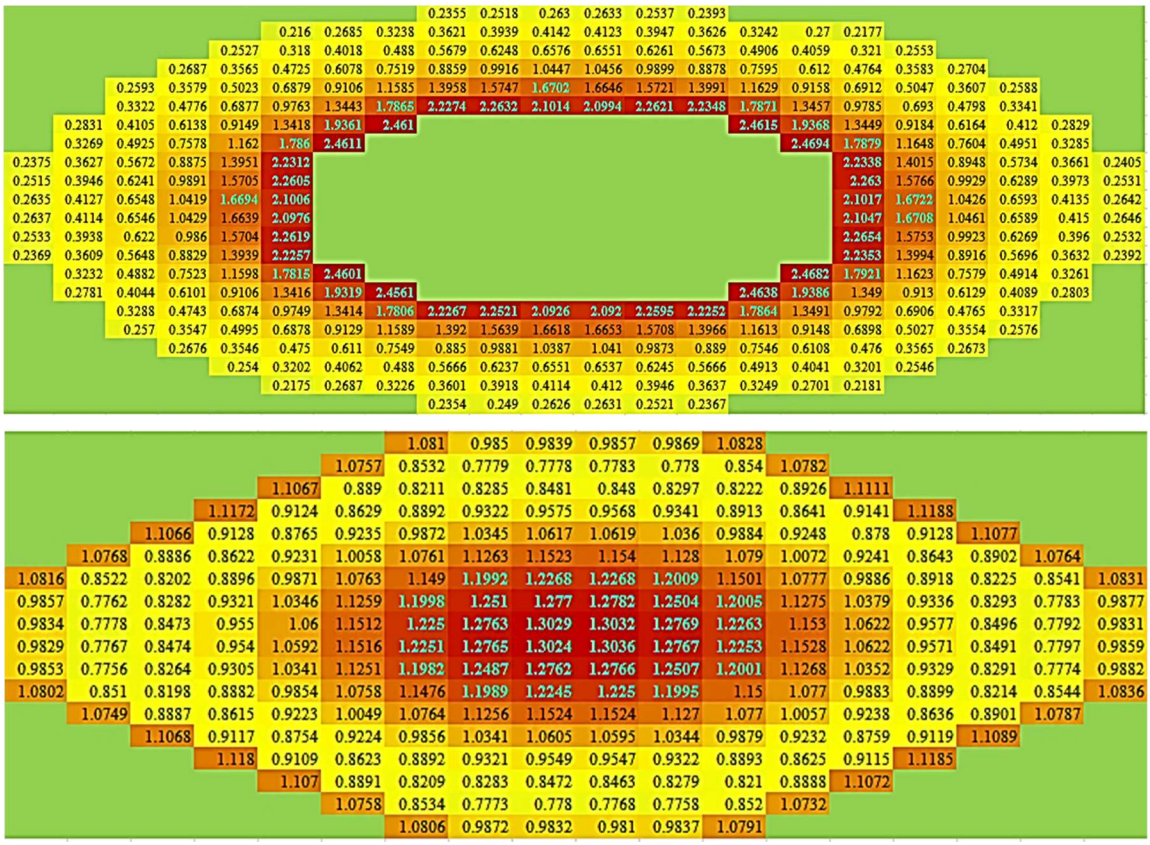

Power Distribution in the Thermal Core and Fast Core of MSCR-Model (IV) after (300 days)

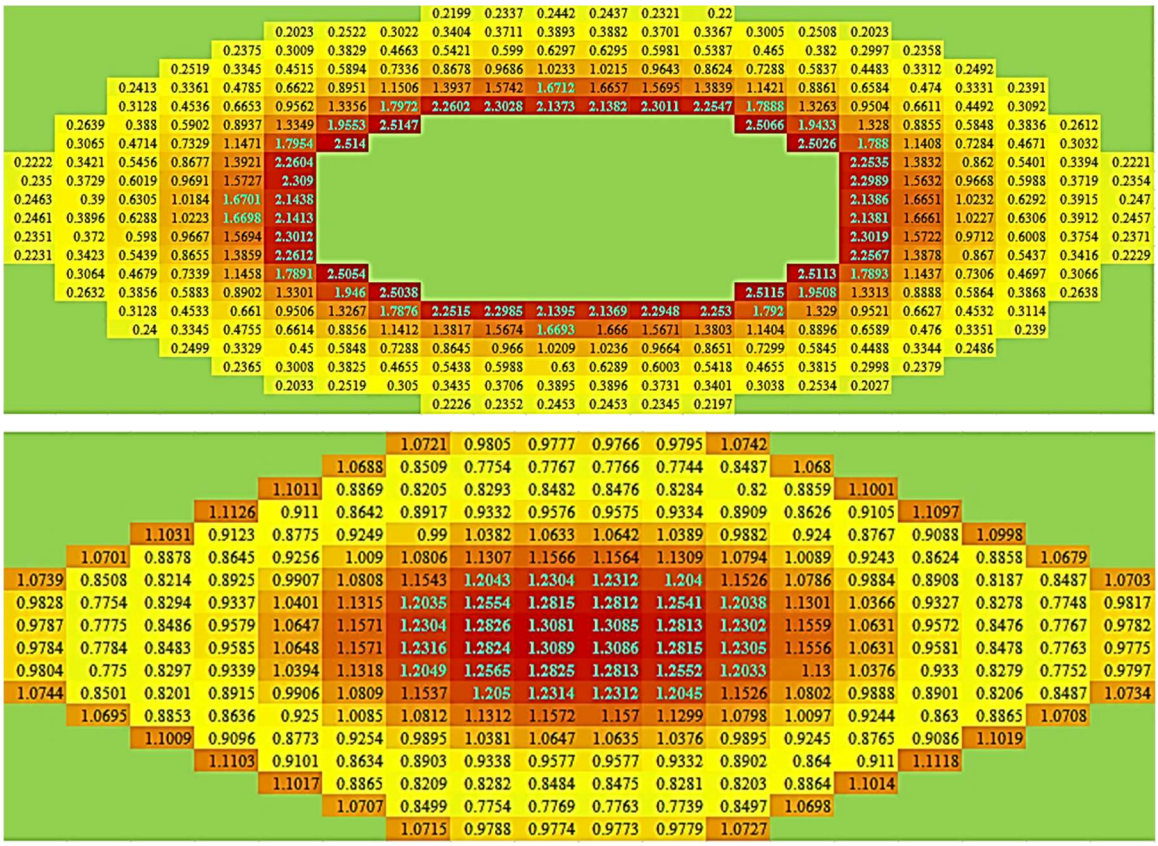

Power Distribution in the Thermal Core and Fast Core of MSCR-Model (IV) after (350 days)

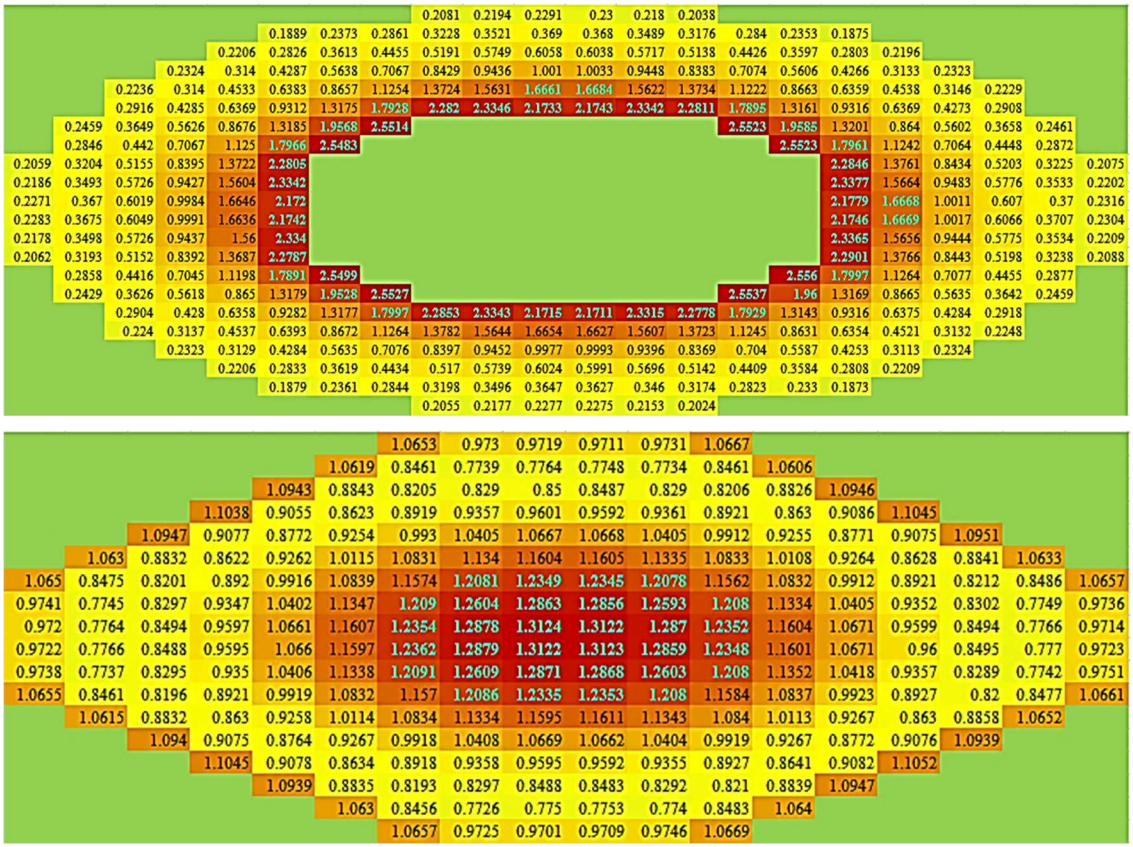

Power Distribution in the Thermal Core and Fast Core of MSCR-Model (IV) after (400 days)

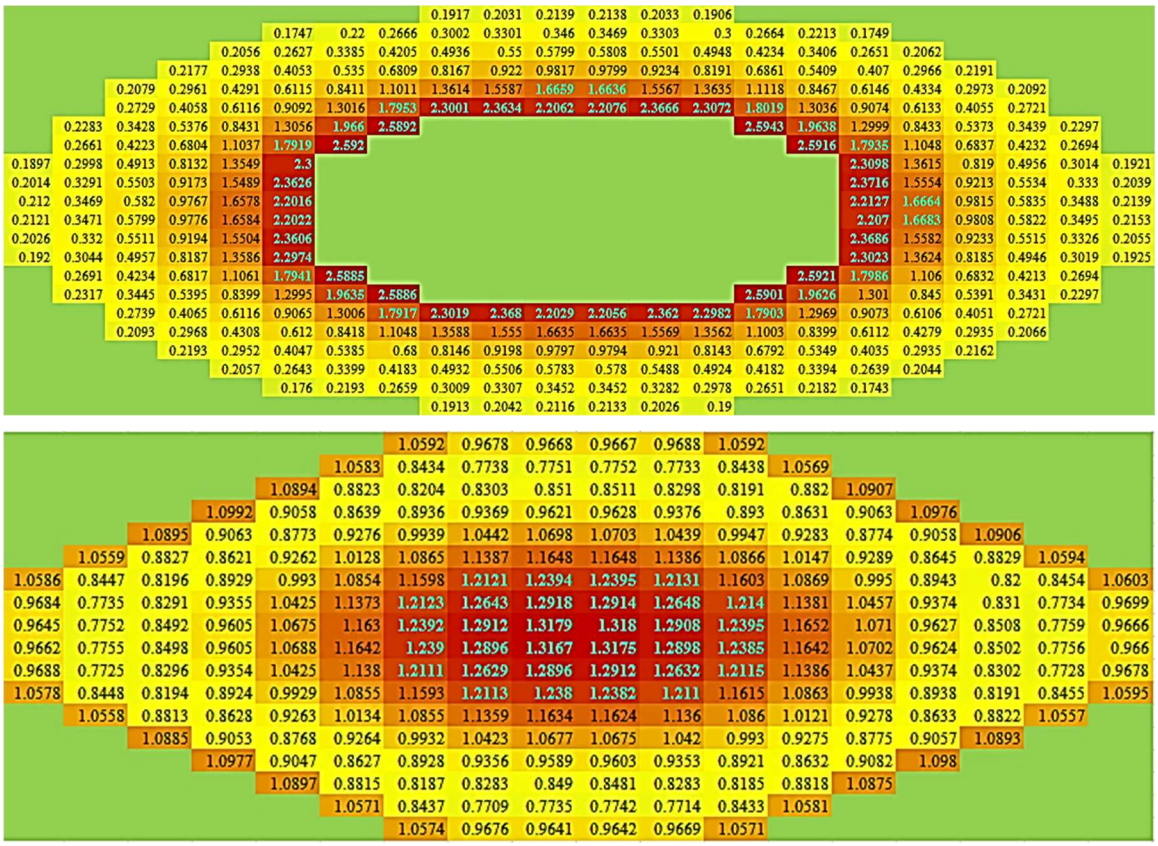

Power Distribution in the Thermal Core and Fast Core of MSCR-Model (IV) after (450 days)

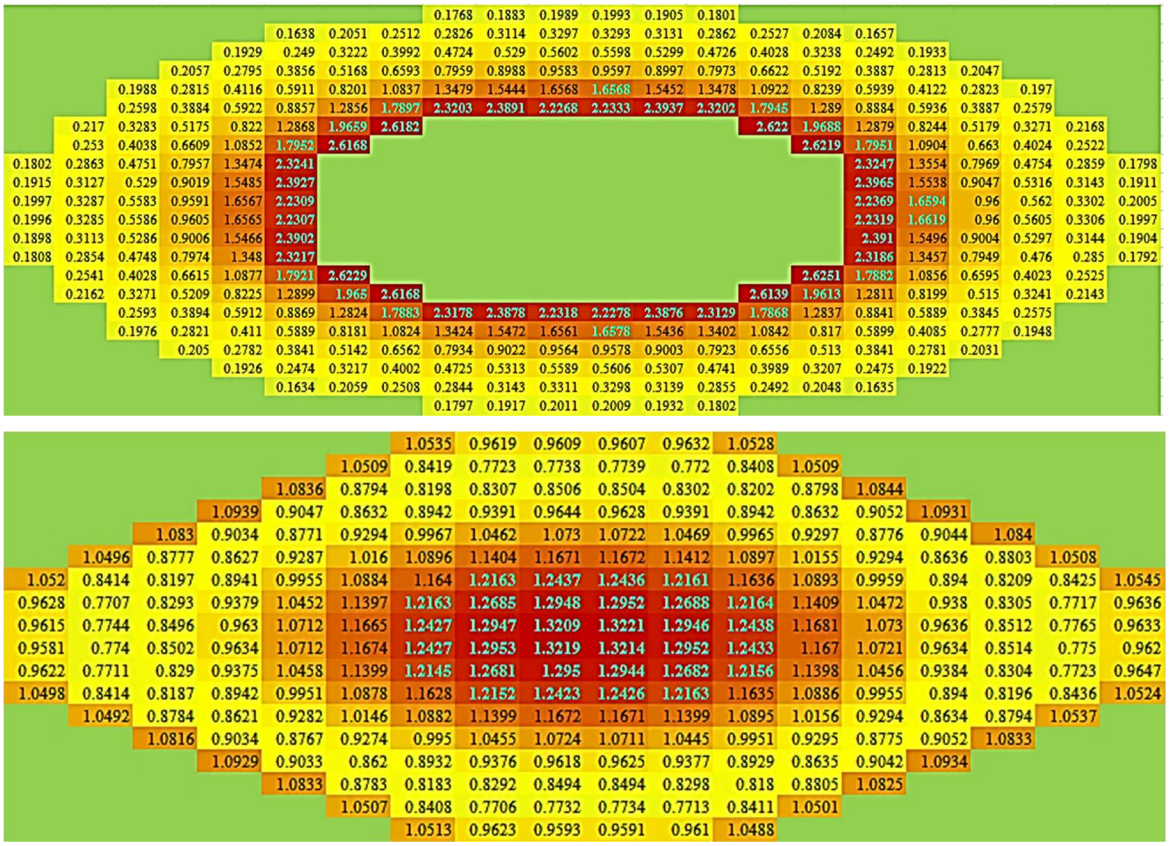

Power Distribution in the Thermal Core and Fast Core of MSCR-Model (IV) after (500 days)

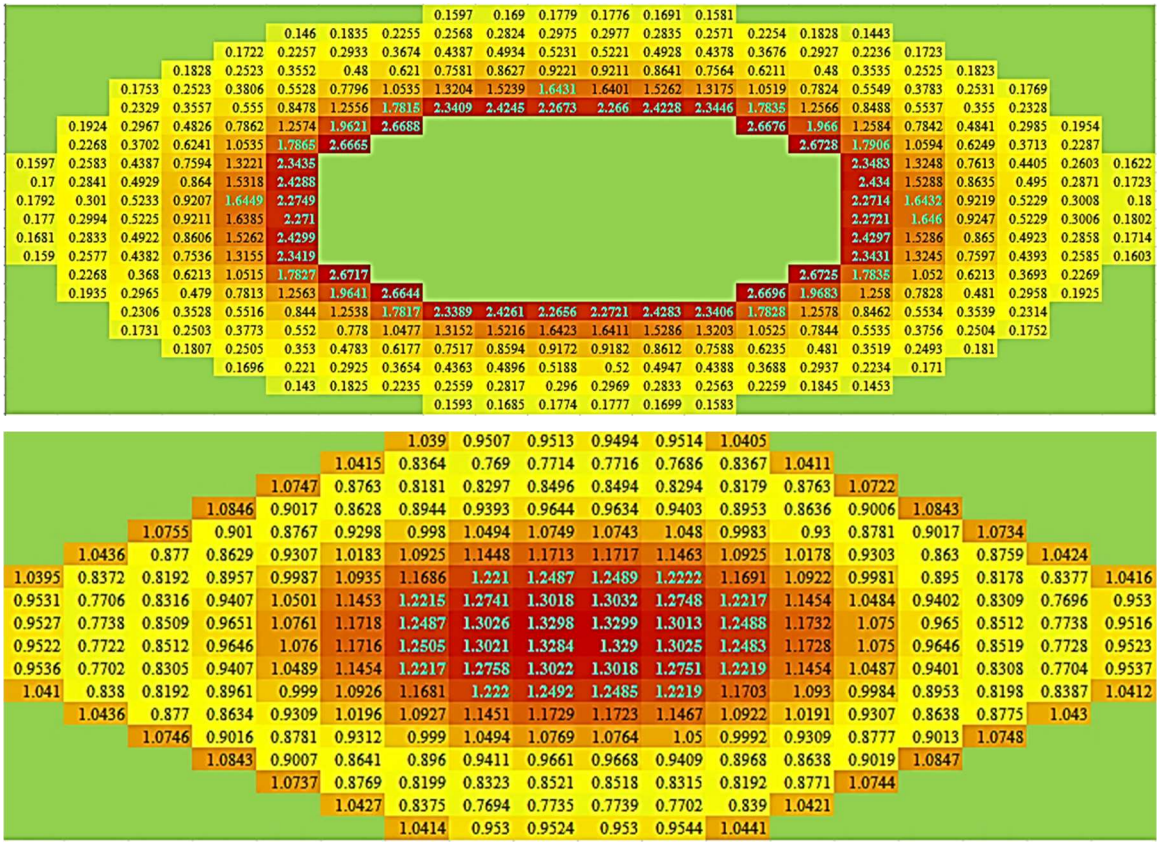

Power Distribution in the Thermal Core and Fast Core of MSCR-Model (IV) after (600 days)

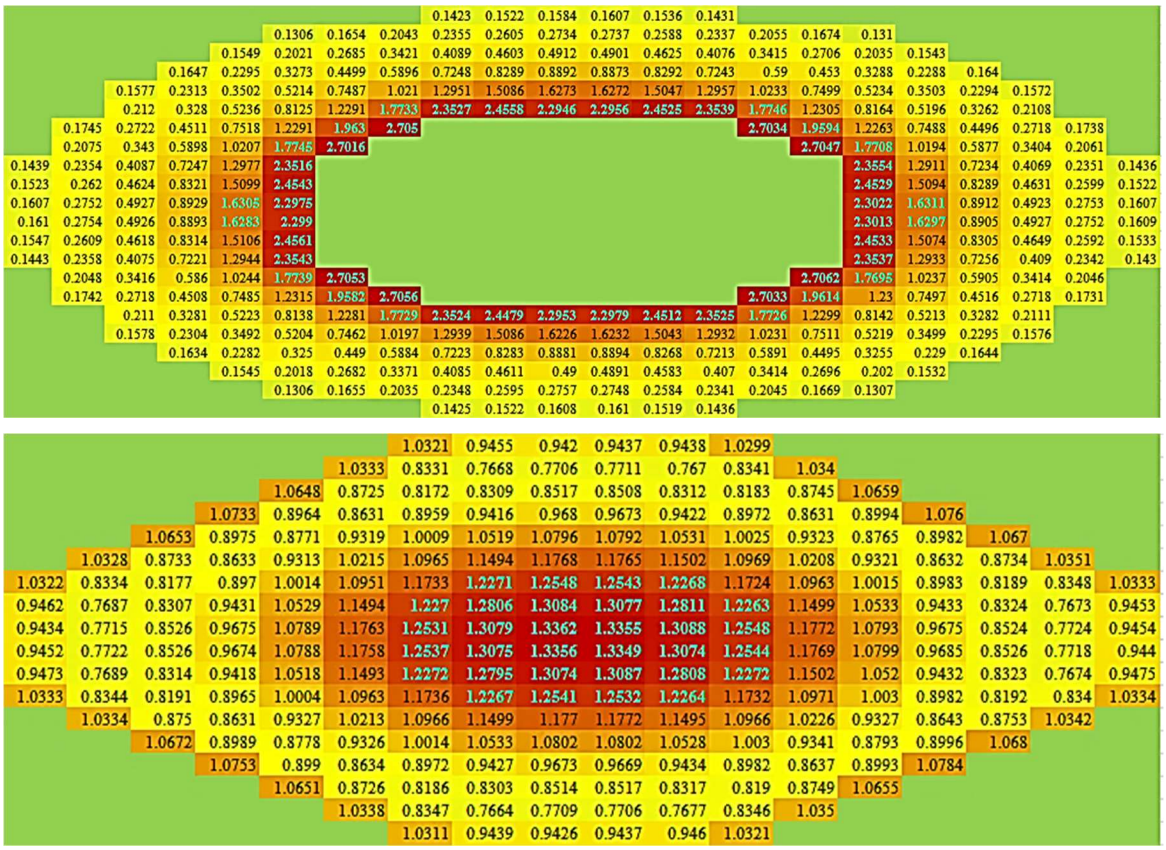

Power Distribution in the Thermal Core and Fast Core of MSCR-Model (IV) after (700 days)

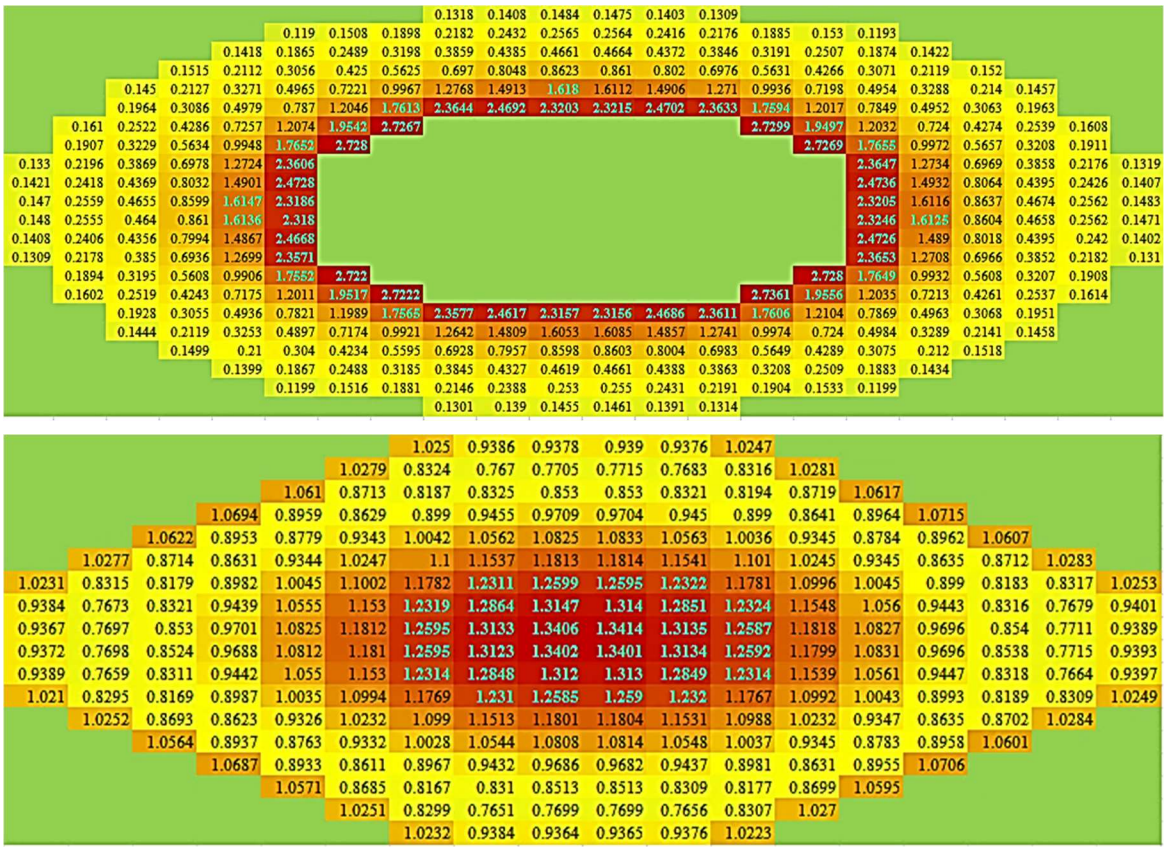

Power Distribution in the Thermal Core and Fast Core of MSCR-Model (IV) after (800 days)

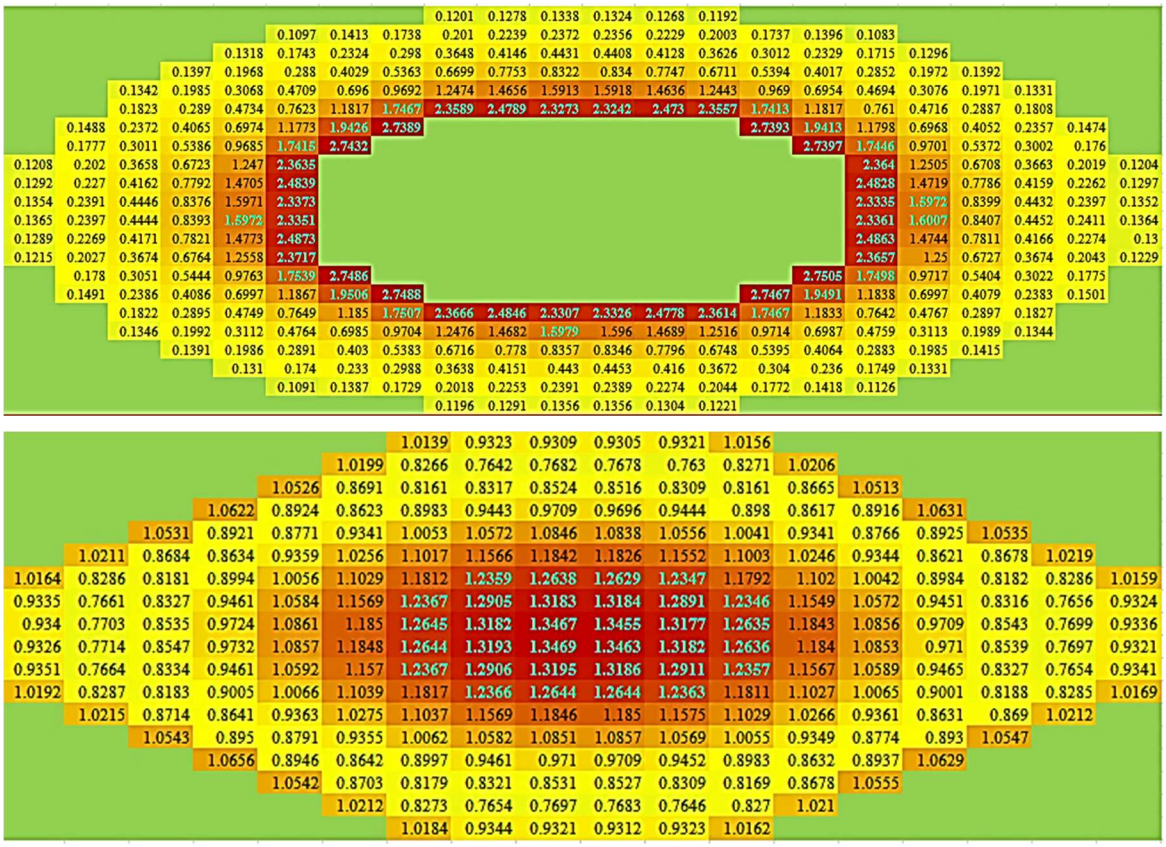

Power Distribution in the Thermal Core and Fast Core of MSCR-Model (IV) after (900 days)

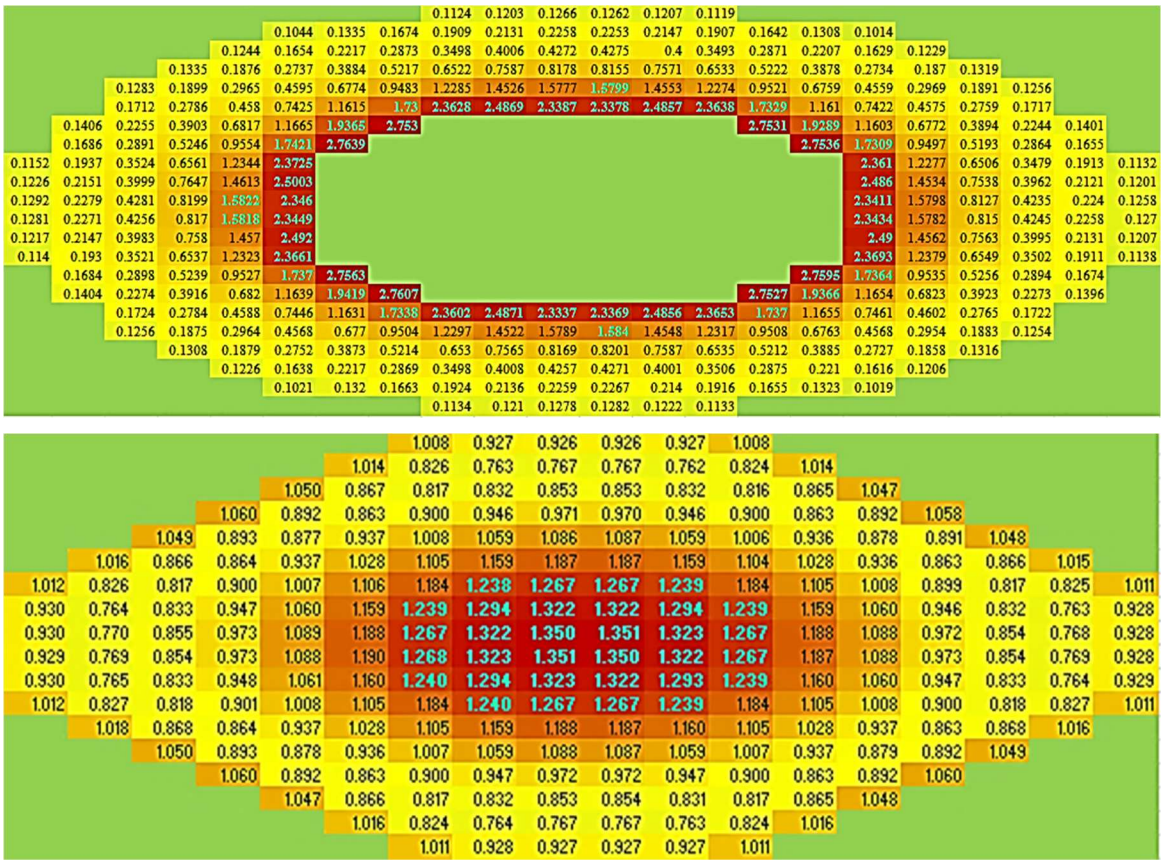

Power Distribution in the Thermal Core and Fast Core of MSCR-Model (IV) after (1000 days)

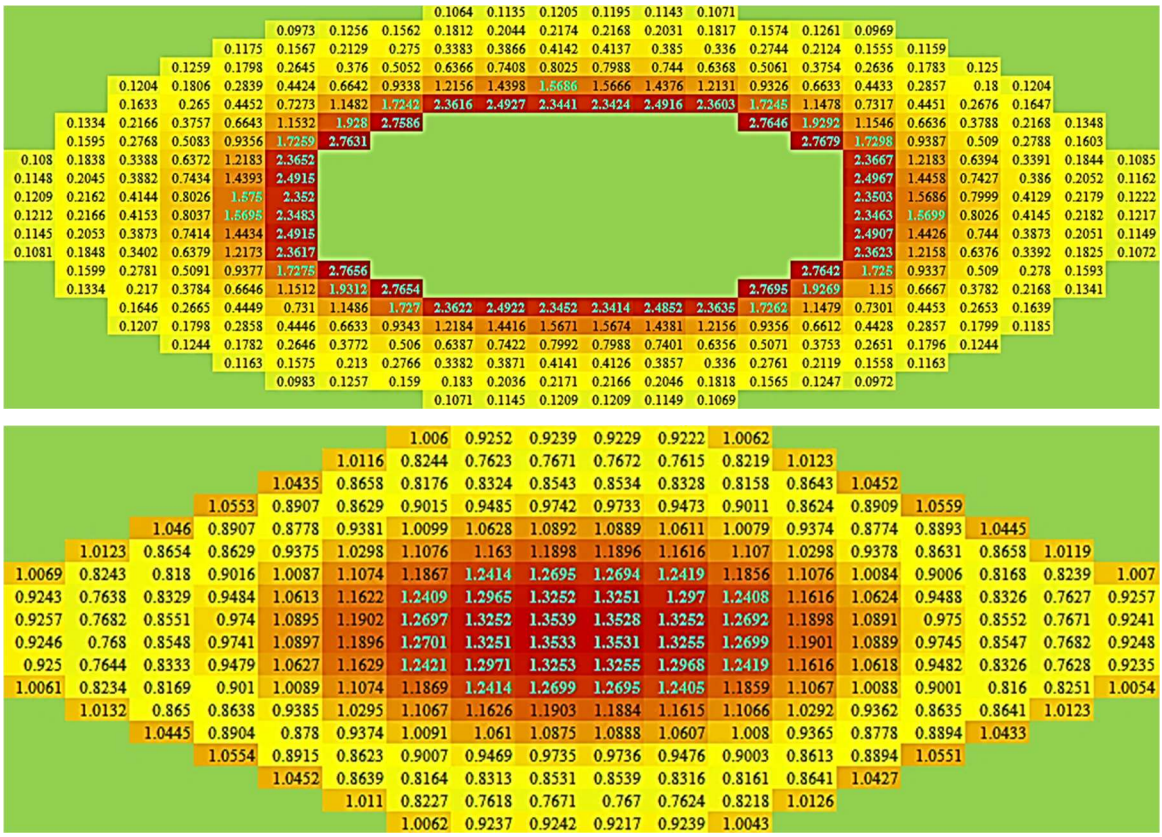

Power Distribution in the Thermal Core and Fast Core of MSCR-Model (IV) after (1100 days)

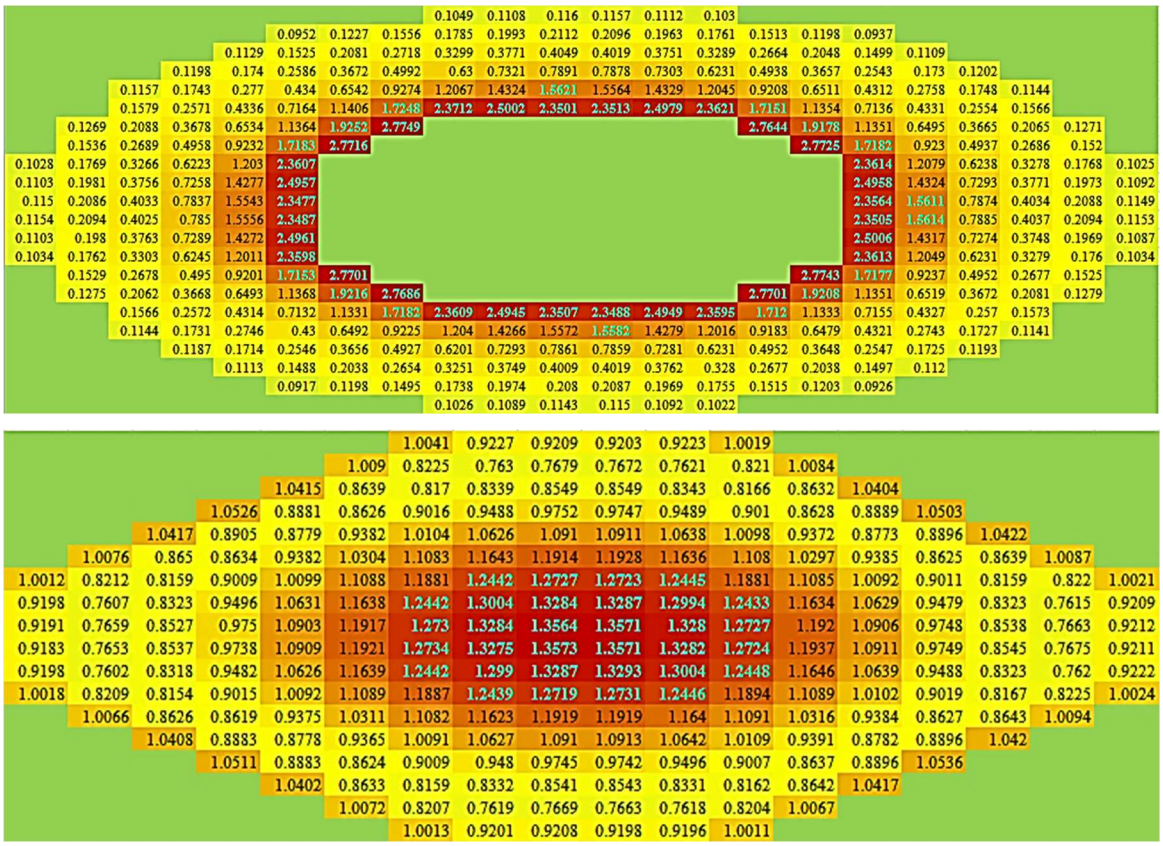

Power Distribution in the Thermal Core and Fast Core of MSCR-Model (IV) after (1200 days)

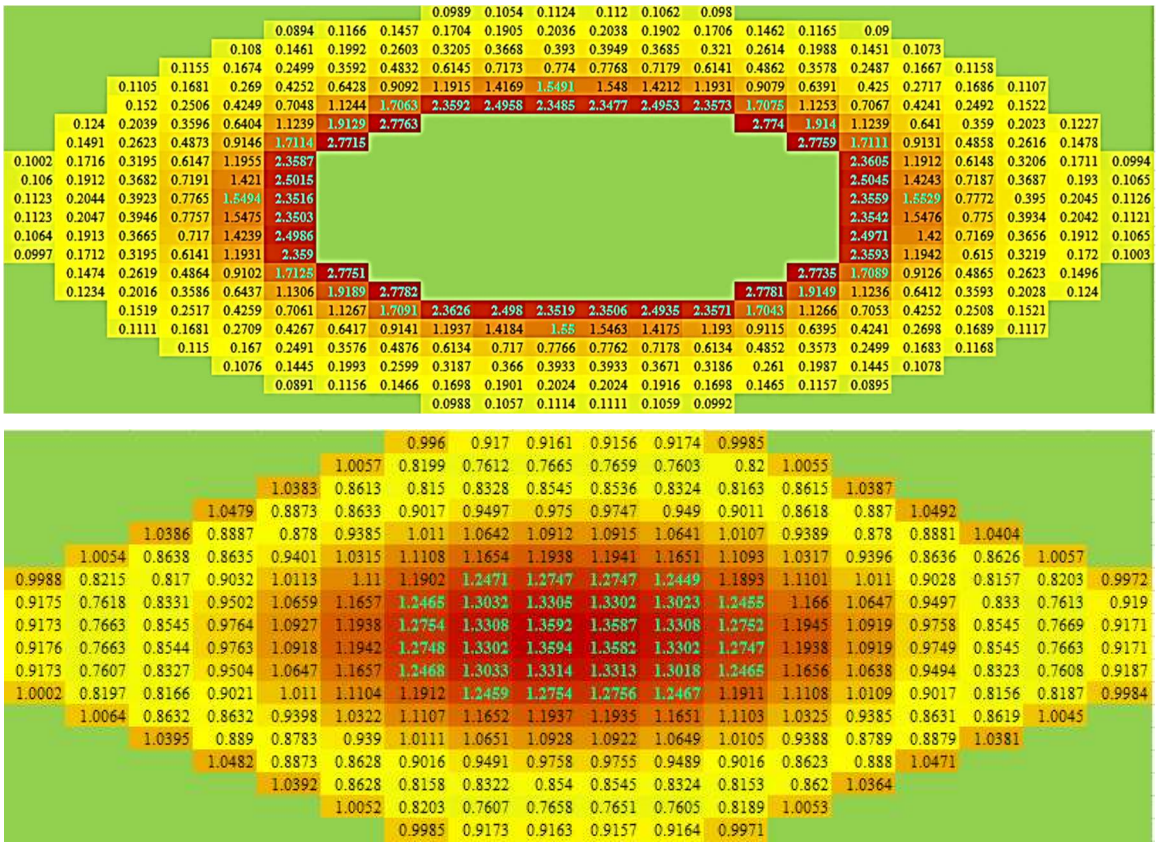

Power Distribution in the Thermal Core and Fast Core of MSCR-Model (IV) after (1300 days)

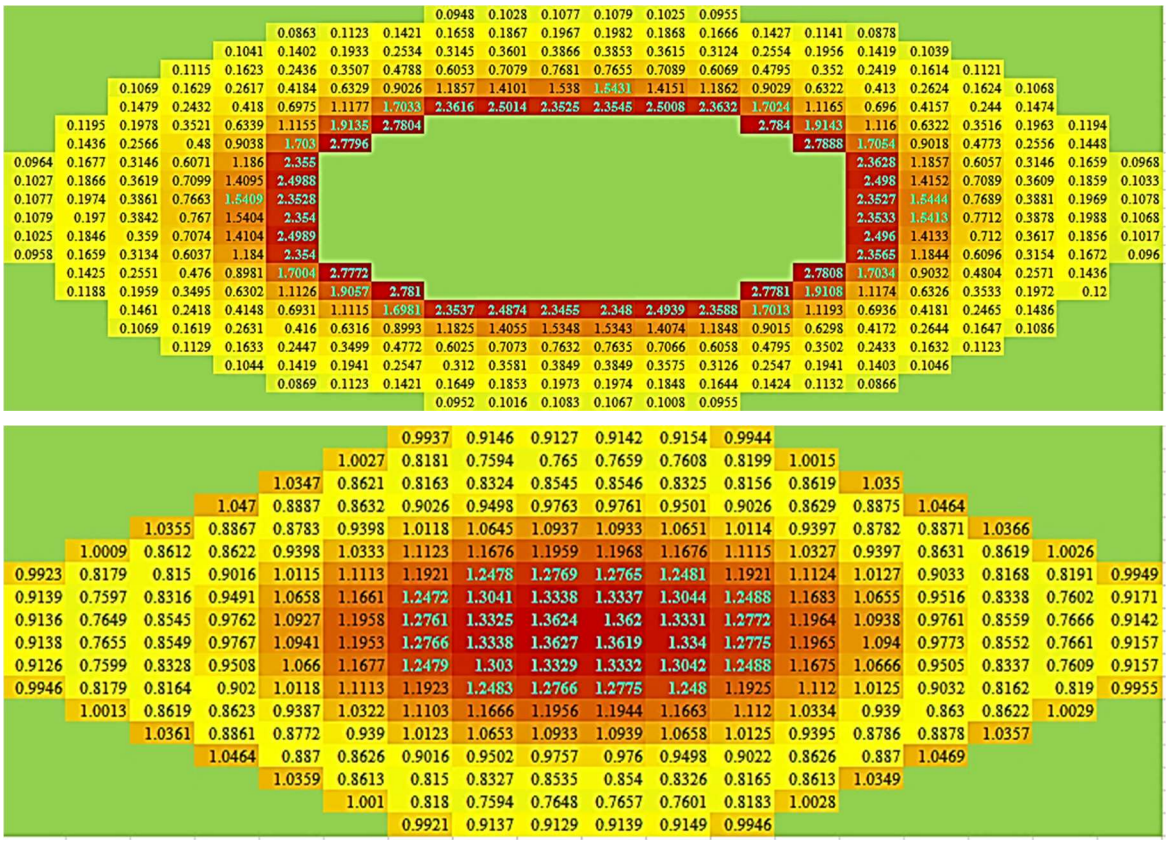

Power Distribution in the Thermal Core and Fast Core of MSCR-Model (IV) after (1400 days)

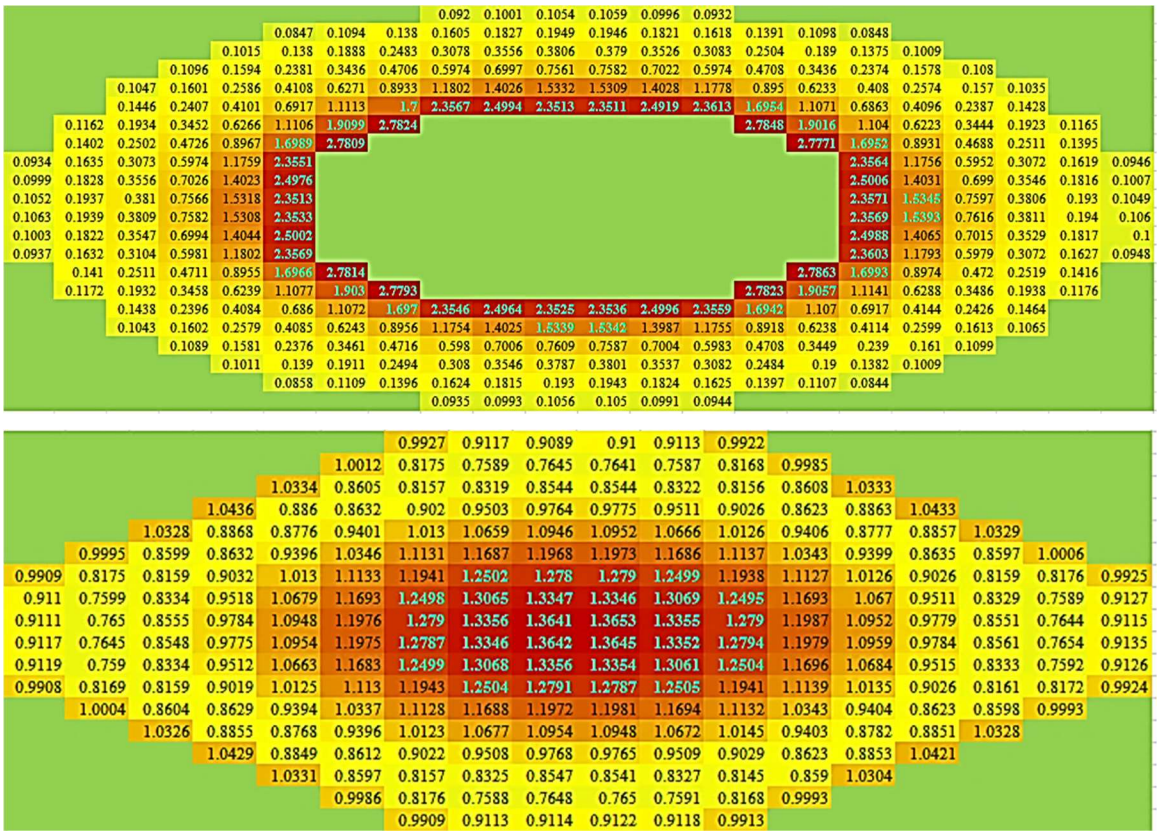

Power Distribution in the Thermal Core and Fast Core of MSCR-Model (IV) after (1500 days)

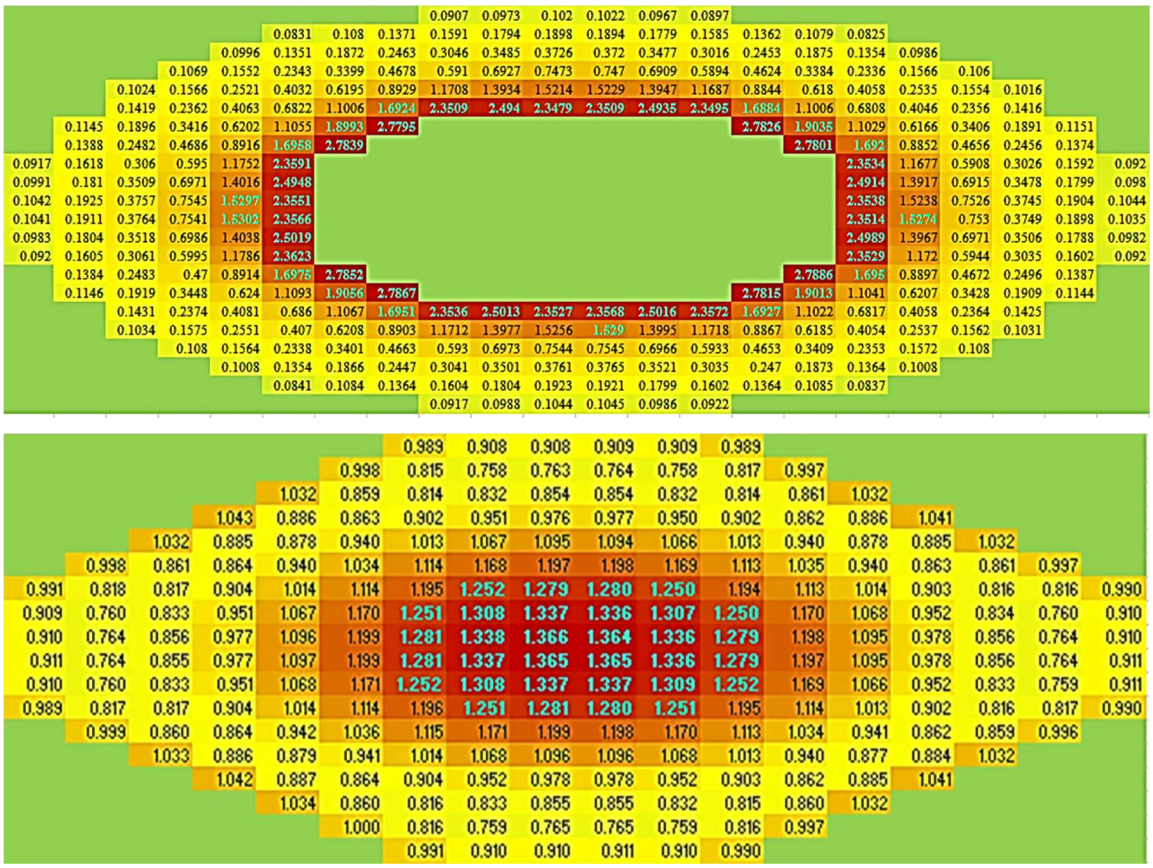

Power Distribution in the Thermal Core and Fast Core of MSCR-Model (IV) after (1600 days)

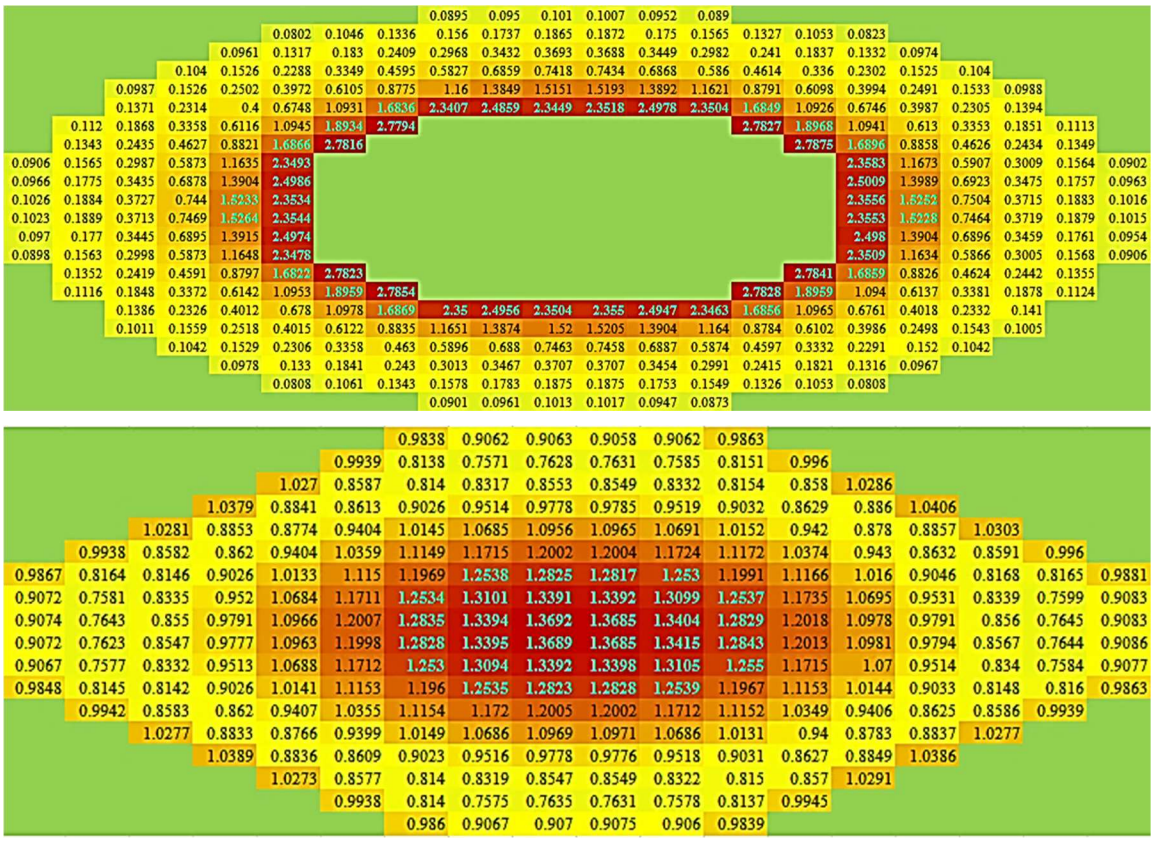

Power Distribution in the Thermal Core and Fast Core of MSCR-Model (IV) after (1800 days)

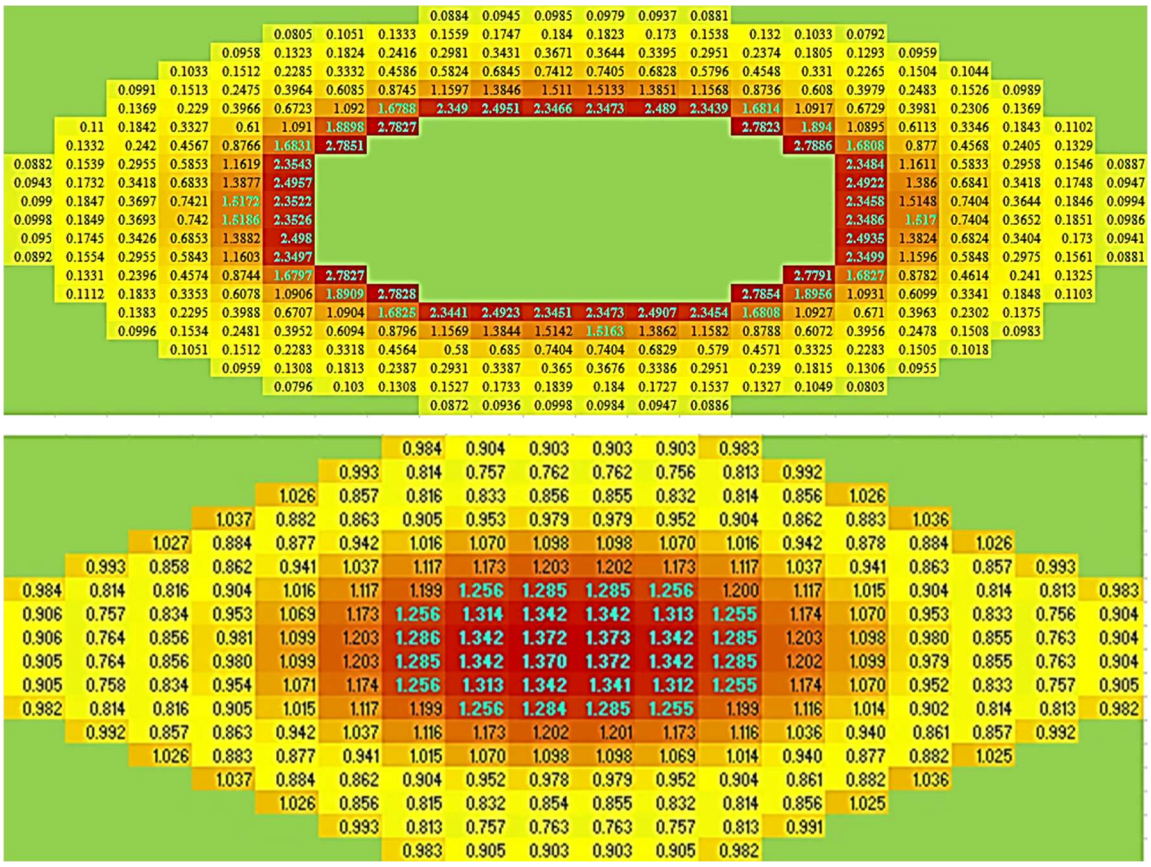

Power Distribution in the Thermal Core and Fast Core of MSCR-Model (IV) after (2000 days)

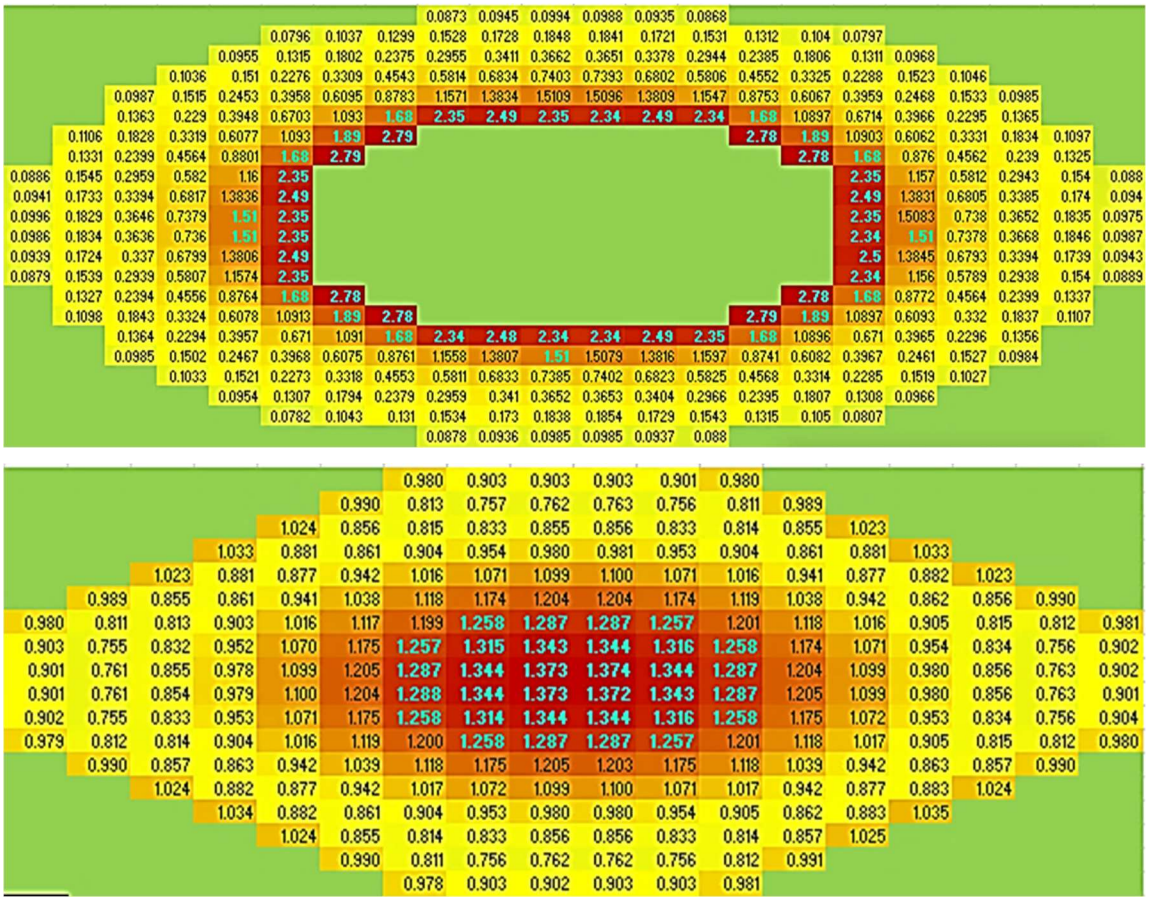

Power Distribution in the Thermal Core and Fast Core of MSCR-Model (IV) after (2200 days)

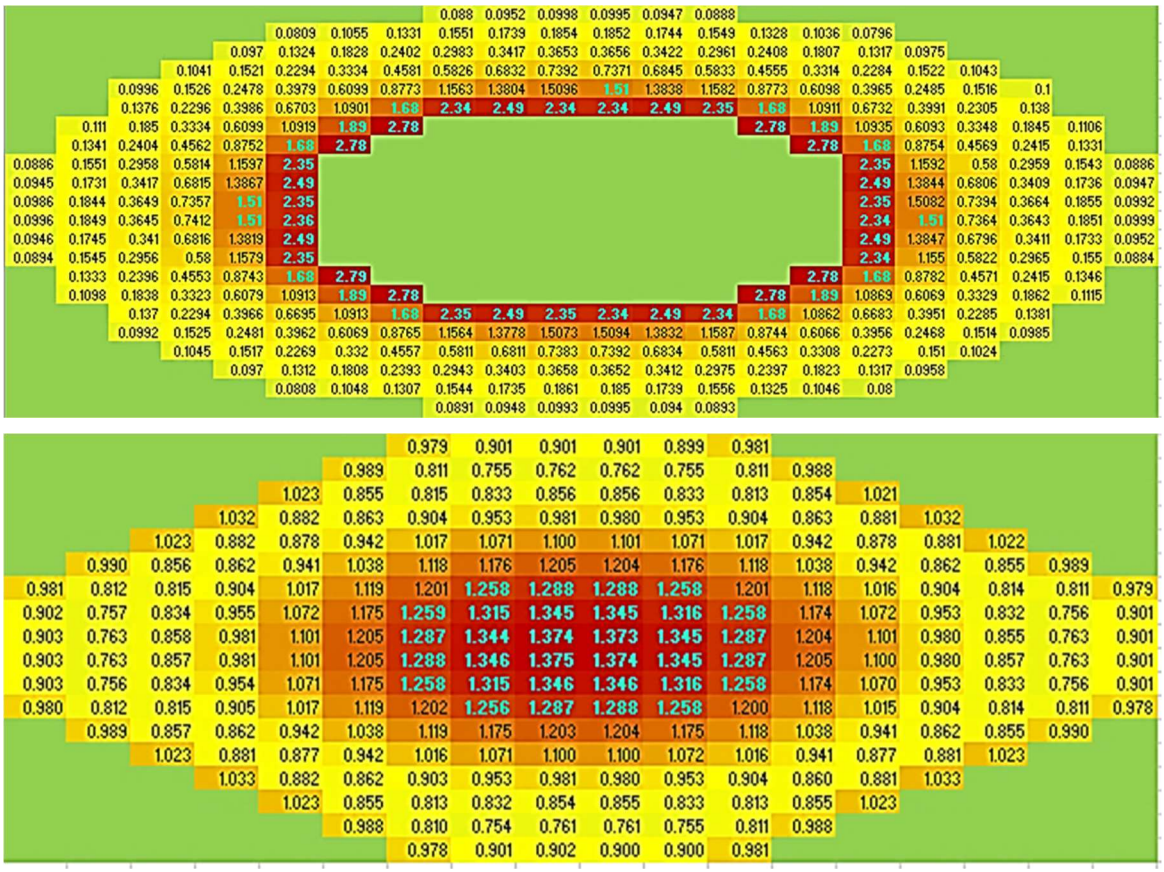

Power Distribution in the Thermal Core and Fast Core of MSCR-Model (IV) after (2400 days)

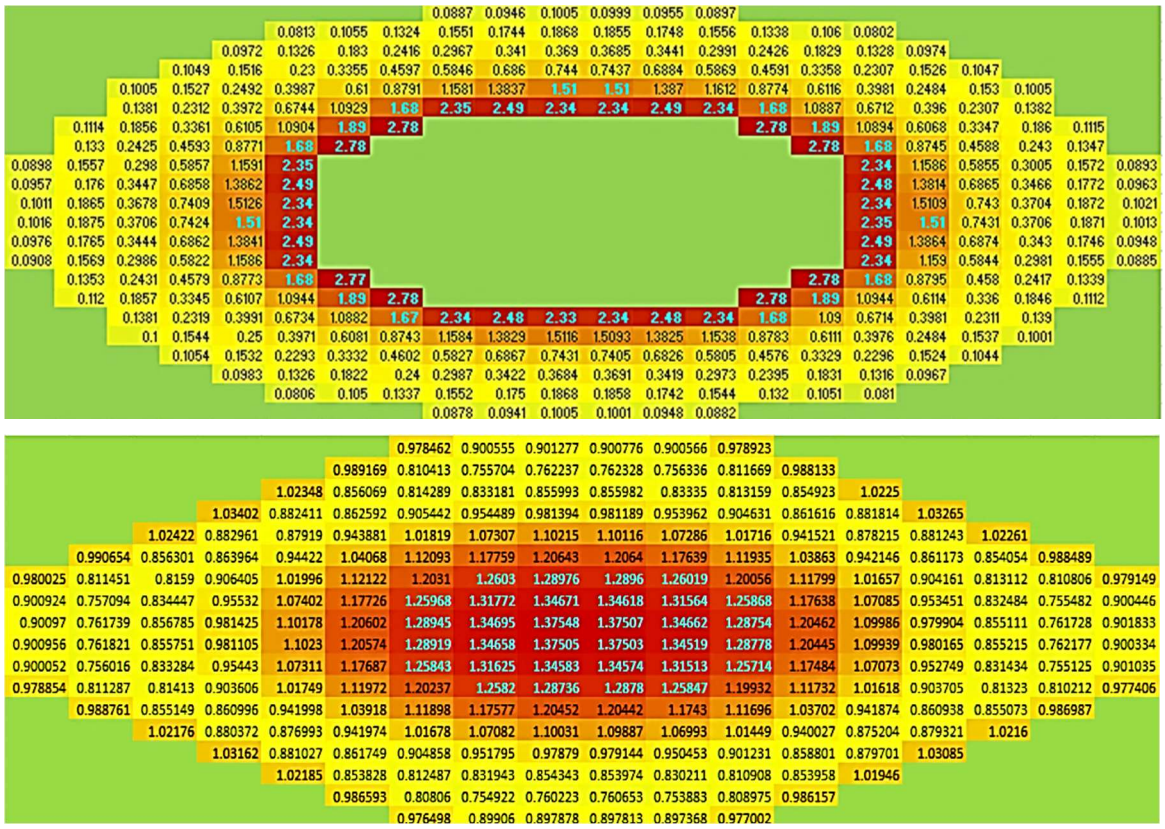

Power Distribution in the Thermal Core and Fast Core of MSCR-Model (IV) after (2600 days)